Cp*M-Mediated P-H Activation Reactions: Activity and Mechanisms

by

Jin Yang
B.Sc. (Honors), St. Francis Xavier University, 2014
M.Sc., University of Victoria, 2016

A Dissertation Submitted in Partial Fulfillment
of the Requirements for the Degree of

DOCTOR OF PHILOSOPHY

in the Department of Chemistry

Supervisory Committee

Cp*M-Mediated P-H Activation Reactions: Activity and Mechanisms

by

Jin Yang
B.Sc. (Honors), St. Francis Xavier University, 2014
M.Sc., University of Victoria, 2016

Supervisory Committee

Dr. Lisa Rosenberg, Department of Chemistry
Supervisor

Dr. David Berg, Department of Chemistry
Departmental Member

Dr. Robin Hicks, Department of Chemistry
Departmental Member

Dr. Kim Venn, Department of Physics & Astronomy
Outside Member

Dr. David Glueck, Department of Chemistry
Additional Member

Abstract

This thesis presented the synthesis and reactivity of metal complexes for the hydrophosphination of alkenes and dehydrocoupling of phosphines. The mechanism of these metal-catalyzed P-H activation reactions was explored.

Half-sandwich Cp*Ru complexes (Cp*= 1,2,3,4,5-pentamethylcyclopentadienyl) were developed as catalysts for hydrophosphination, based on the previous work in the Rosenberg group. Cp*Ru phosphido complexes, Ru(η^5-Cp*)(PR_2)(PR_2H)$_2$ (**Ru-1**) were found to be the vital intermediates for the hydrophosphination. Preliminary mechanistic studies also indicate that the catalyst resting state is Ru(η^5-Cp*)(PR_2)(PR_2H)(**P**) (**P** = hydrophosphination product) and intramolecular P-H bond cleavage is turnover-limiting. These investigations provide sufficient parallels to our established chemistry of the indenyl analogues to imply that conjugate addition of metal phosphido at alkene plays a significant role in these half-sandwich catalytic systems. The increased steric crowding at the Cp*Ru fragment and P-basicity/nucleophilicity of its phosphido complexes lead to a 30-fold increase in the hydrophosphination activity in the Cp* system compared to the indenyl catalysts.

A half-sandwich Co catalyst, Co(η^5-Cp*)I_2(CO) (**Co-1**), was also developed for hydrophosphination along the lines of the conjugate addition mechanism. Similar to the Cp*Ru system, the substrate scope for alkene is limited to electron-deficient alkene. However, the Cp*Co catalyst significantly expands the substrate scope for phosphines (PR_2H and PRH_2, R = alkyl and aryl). A detailed mechanistic study on the Cp*Co system was performed. The results show that the Co-catalyzed hydrophosphination occurs through

an outer-sphere mechanism and the stoichiometric formation of diphosphine is a critical catalyst activation step.

Since the side product diphosphine was formed during the Co-catalyzed hydrophosphination, using complex **Co-1** as a catalyst for dehydrocoupling phosphines was investigated. The preliminary studies reveal the role of base and Cp* ligand in the catalysis. Additionally, the study highlights the importance of removing dihydrogen throughout the process. Thus, hydrogen acceptors (HA) were used to facilitate the dehydrocoupling reactions. Last, the novel P-H activation process between Cp*Co complexes $[Co(\eta^5\text{-}Cp^*)(NCCH_3)_3][SbF_6]_2$ (**Co-5**) and excess PPh_2H was investigated through various analytical techniques.

Table of Contents

Supervisory Committee ..... **ii**
Abstract ..... **iii**
Table of Contents ..... **v**
List of Tables ..... **x**
List of Figures ..... **xii**
List of Schemes ..... **xix**
List of Abbreviations ..... **xxiv**
List of Numbered Compounds ..... **xxvii**
Acknowledgments ..... **xxviii**
Dedication ..... **xxix**
1. Introduction **1**
1.1 Overview 1
1.2 Background: why we care about phosphines 1
1.2.1 Tertiary phosphines PR_3 2
1.2.2 Diphosphines $R_2P\text{-}PR_2$ 3
1.3 Synthesis of phosphines 4
1.3.1 Traditional stoichiometric P-C bond and P-P bond formation 4
1.3.2 P-C bond formation *via* hydrophosphination 5
1.3.3 P-P bond formation *via* dehydrocoupling 9
1.4 Metal-catalyzed hydrophosphination 10
1.4.1 Challenges in metal-catalyzed hydrophosphination 11
1.4.2 Mechanisms of metal-catalyzed hydrophosphination 11
1.5 Metal-catalyzed dehydrocoupling of phosphines 16
1.5.1 Activity of metal-catalyzed dehydrocoupling 17
1.5.2 Mechanisms of metal-catalyzed dehydrocoupling 17
1.6 Scope of the thesis 20
1.7 References 23
2. Investigation of Cp* Ru-catalyzed hydrophosphination **32**
2.1 Introduction 32
2.2 Designing Cp*Ru phosphido catalysts for hydrophosphination 35
2.2.1 Ligand substitution reactions of $Ru(\eta^5\text{-}Cp^*)Cl(PPh_3)_2$ (**Ru-3**) to generate $Ru(\eta^5\text{-}Cp^*)Cl(PR_2H)_2$ (**Ru-4**) 36
2.2.2 Attempted isolation of $Ru(\eta^5\text{-}Cp^*)(PPh_2)(PPh_2H)_2$ (**Ru-1a**) 37
2.2.3 Dehydrohalogenation of $Ru(\eta^5\text{-}Cp^*)Cl(PR_2H)_2$ (**Ru-4**) generated *in situ* 39
2.2.4 Effect of the "free" base in catalytic hydrophosphination 40
2.3 Investigation of $Ru(\eta^5\text{-}Cp^*)(PR_2)(PR_2H)_2$ (**Ru-1(a-c)**) and $Ru(\eta^5\text{-}Cp^*)(PCy_2)(PCy_2H)$ (**Ru-2d**) in catalytic hydrophosphination 43
2.3.1 Comparison of $Ru(\eta^5\text{-}Cp^*)(PPh_2)(PPh_2H)_2$ (**Ru-1a**) with the indenyl analogue in hydrophosphination catalysis 43
2.3.2 Substrate scope in Cp*Ru-catalyzed hydrophosphination 48
2.3.3 Proposed mechanism for Cp*Ru-catalyzed hydrophosphination 51
2.4 Conclusion 52
2.5 Experimental 52
2.5.1 General comments 52

2.5.2 In-situ generation of **Ru-1** and **Ru-2** for spectroscopic identification 53
2.5.3 Monitoring catalytic reactions using **Ru-1** or **Ru-2** 55
2.6 References 59
3. Synthesis and characterization of Cp*Co complexes 61
3.1 Introduction 61
3.2 Synthesis of Cp*Co(III) phosphine complexes 63
3.2.1 Iodide complexes Co(η^5-Cp*)I_2(PR_2H) (**Co-2**), Co(η^5-Cp*)I_2(PRH_2) (**Co-3**) and [Co(η^5-Cp*)I(PR_2H)$_2$]I (**Co-4**) 63
3.2.2 Dicationic phosphine complexes [Co(η^5-Cp*)($NCCH_3$)$_2$(PR_2H)][SbF_6]$_2$ (**Co-6**) and [Co(η^5-Cp*)($NCCH_3$)(PR_2H)$_2$][SbF_6]$_2$ (**Co-7**) 66
3.3 Characterization of Cp*Co(III) phosphine complexes 67
3.3.1 NMR characterization of **Co-2**, **Co-3**, **Co-4**, **Co-6** and **Co-7** 68
3.3.2 X-ray analysis of **Co-1**, **Co-2c**, **Co-3c**, **Co-4e** and **Co-6a,c** 70
3.3.3 UV-vis spectra of **Co-1**, **Co-2(a-d)**, **Co-3(a,c)**, **Co-4(a,e)**, **Co-5** and **Co-6(a-d)** 73
3.3.4 Electrochemical behaviour of **Co-1**, **Co-2a**, **Co-4e**, **Co-5** and **Co-6a** 77
3.4 Preliminary investigation of the participation of Cp*Co complexes in reactions involving P-H activation. 82
3.4.1 Preliminary investigation of Cp*Co complexes in catalytic hydrophosphination of *tert*-butyl acrylate with PPh_2H 83
3.4.2 Preliminary investigation of Cp*Co complexes in catalytic dehydrocoupling of PPh_2H 85
3.4.3 Reactions of **Co-1** and **Co-5** with excess PPh_2H involving an interesting dynamic process 87
3.5 Conclusion 89
3.6 Experimental 90
3.6.1 Modified synthesis of Co(η^5-Cp*)I_2(CO) (**Co-1**) 90
3.6.2 General procedure for the synthesis of Co(η^5-Cp*)I_2(PR_2H) (**Co-2**) 91
3.6.3 General procedure for the synthesis of Co(η^5-Cp*)I_2(PRH_2) (**Co-3**) 93
3.6.4 General procedure for the synthesis of [Co(η^5-Cp*)I(PR_2H)$_2$]I (**Co-4**) 94
3.6.5 Modified synthesis of [Co(η^5-Cp*)($NCCH_3$)$_3$][SbF_6]$_2$ (**Co-5**) 97
3.6.6 General procedure for the synthesis of [Co(η^5-Cp*)($NCCH_3$)$_2$(PR_2H)][SbF_6]$_2$ (**Co-6**) 99
3.6.7 ^{1}H and ^{13}C{^{1}H} NMR data for Cp*Co phosphine complexes 100
3.6.8 UV-vis spectroscopy of Cp*Co complexes 104
3.6.9 General procedure for preliminary catalytic hydrophosphination reactions using Cp*Co complexes 107
3.6.10 General procedure for preliminary dehydrocoupling reactions using **Co-1** or **Co-5** 107
3.6.11 Reaction of **Co-1** or **Co-5** with excess phosphine. 108
3.6.12 Reaction of **Co-1** or **Co-5** with excess *tert*-butyl acrylate 108
3.7 References 109
4. Investigation of Cp*Co-catalyzed hydrophosphination 113
4.1 Introduction 113
4.2 Optimizing conditions for Co-catalyzed hydrophosphination 117
4.2.1 Optimizing the Co:base ratio for catalytic hydrophosphination 118

4.2.2 Screening different bases for the catalytic hydrophosphination 121
4.2.3 Optimizing the solvent for catalytic hydrophosphination 124
4.3 Investigating substrate scope for Co-catalyzed hydrophosphination 126
4.3.1 Alkene scope 126
4.3.2 Phosphine scope 128
4.4 Investigating the mechanism of Co-catalyzed hydrophosphination 130
4.4.1 Substitution chemistry of complex **Co-1** with substrate phosphines and *tert*-butyl acrylate 130
4.4.2 Identifying Co intermediates in the catalytic mixture by NMR 132
4.4.3 Investigating the reduction of Co(III) phosphido to Co(II) and diphosphine 135
4.4.4 Investigating the participation of Co(II) species in catalytic hydrophosphination 143
4.4.5 Proposed steps for the reduction of Co(III) to a catalytically active Co(II) phosphido complex 147
4.4.6 Preliminary kinetic studies of Co-catalyzed hydrophosphination 149
4.4.7 Proposed mechanism for Co-catalyzed hydrophosphination 153
4.5 Conclusion 155
4.6 Experimental 156
4.6.1 General procedure for Co-catalyzed hydrophosphination 157
4.6.2 Reactions of complex **Co-2a** with different bases 158
4.6.3 Reactions of PPh_2H with different bases 159
4.6.4 Optimization of Co:base ratio 159
4.6.5 NMR characterization of hydrophosphination products 160
4.6.6 Reaction of **Co-1** with excess phosphine or *tert*-butyl acrylate 165
4.6.7 Reaction of **Co-2a** with DBU in the presence of TEMPO. 165
4.6.8 Attempted isolation of Co(II) complex $[Co(\eta^5\text{-}Cp^*)(\mu\text{-}I)]_2$ 166
4.6.9 Reaction of in-situ-generated Co(II) species with *tert*-butyl acrylate and PPh_2H. 168
4.6.10 Reactions of complex **Co-2a** with hydrogen atom abstraction agents 168
4.6.11 The "same excess" experiment 169
4.6.12 The initial rates method 170
4.7 References 171
5. Investigation of Cp*Co-catalyzed dehydrocoupling 177
5.1 Introduction 177
5.2 Investigating catalytic dehydrocoupling of PPh_2H using **Co-1** 178
5.2.1 Screening catalytic conditions for dehydrocoupling of PPh_2H using **Co-1** ... 178
5.2.2 Identifying Co intermediates in catalytic dehydrocoupling 180
5.3 Using hydrogen acceptors (HAs) in catalytic dehydrocoupling using **Co-1** 193
5.3.1 Screening for the optimal HA for Co-catalyzed dehydrocoupling of PPh_2H 193
5.3.2 Phosphine substrate scope in catalyzed dehydrocoupling using 10 mol% **Co-1** in the presence of **HA-1** 195
5.4 Conclusion 197
5.5 Experimental 197
5.5.1 General procedure for Co-catalyzed dehydrocoupling of PPh_2H. 198
5.5.2 General procedure for Co-catalyzed dehydrocoupling of phosphines in the presence of hydrogen acceptors (HAs) 199

5.5.3 NMR data for Co complexes **Co-10**, **Co-11** and **[Co-12]I** 199
5.5.4 $^{31}P\{^{1}H\}$ NMR data for diphosphines and other P-containing products. 200
5.7 References 204
6. Investigation of Cp*Co(III) complexes in non-base-mediated P-H activation 208
6.1 Introduction 208
6.2 Spectroscopic evidence for reversible P-H activation of PPh_2H by Cp*Co(III) complexes 212
6.2.1 Investigating the dynamic process using VT-NMR 213
6.2.2 Evidence for paramagnetic species by the Evans method 214
6.2.3 Identifying paramagnetic species using EPR spectroscopy 216
6.2.4 Identifying charged species using ESI-MS 217
6.2.5 Investigating the dynamic process using UV-vis spectroscopy 219
6.2.6 Investigating the reversible P-H activation using deuterium labelling experiments 223
6.3 Two proposed mechanisms for P-H activation at Cp*Co(III) 226
6.4 Conclusion 230
6.5 Experimental 230
6.5.1 VT-NMR 230
6.5.2 The Evans method 231
6.5.3 EPR 231
6.5.4 ESI-MS 231
6.5.5 UV-vis spectroscopy 232
6.5.6 Deuterium labelling experiments 232
6.6 References 234
7. Future work 237
7.1 Short-term work 237
7.1.1 Investigation of highly active Cp*Ru catalysts for hydrophosphination of activated alkenes 237
7.1.2 Publication on synthesis and physical properties of Cp*Co(III) complexes . 239
7.1.3 Publication on Cp*Co-catalyzed hydrophosphination 240
7.1.4 Publication based on Chapters 5 and 6 241
7.2 Long-term work: developing chiral metal catalysts for asymmetric hydrophosphination 242
7.3 References 244
Appendix A – Survey of first-row transition metal-catalyzed hydrophosphination and metal-catalyzed dehydrocoupling of phosphines 246
Appendix B – NMR spectra of Cp*Ru phosphido complexes generated *in situ* 257
Appendix C – NMR spectra of isolated Cp*Co compounds 263
Appendix D – NMR spectra of hydrophosphination products 284
Appendix E – Survey of Co phosphido complexes 299
Appendix F – ^{1}H and $^{31}P\{^{1}H\}$ NMR spectra from Chapter 5 305
Appendix G – X-ray crystallographic structure report for complex Co-1 314
Appendix H – X-ray crystallographic structure report for complex Co-2c 324
Appendix I – X-ray crystallographic structure report for complex Co-3c 335
Appendix J – X-ray crystallographic structure report for complex Co-4e 346
Appendix K – X-ray crystallographic structure report for complex Co-6a 358

Appendix L – X-ray crystallographic structure report for complex Co-6c 372

List of Tables

Table 2.1 $^{31}P\{^{1}H\}$ NMR (121.55 MHz, C_6D_6) data for complexes **Ru-4(a-d)**: δ (ppm) (multiplicity). 36

Table 2.2 $^{31}P\{^{1}H\}$ NMR (121.55 MHz, C_6D_6) data for complexes **Ru-1(a-c)** and **Ru-2d** generated *in situ* in the presence of excess PR_2H: δ (ppm) (multiplicity, J or $\omega_{1/2}$ in Hz)..... 39

Table 2.3 ^{1}H NMR (500.27 MHz, C_6D_6) data for complexes **Ru-1(a-c)** and **Ru-2d**: δ in ppm (multiplicity, J in Hz, RI). 54

Table 2.4 $^{13}C\{^{1}H\}$ NMR (125.77 MHz, C_6D_6) data for complexes **Ru-1(a-c)** and **Ru-2d**: δ in ppm (multiplicity, J in Hz)..... 55

Table 3.1 $^{31}P\{^{1}H\}$ NMR (202.51 MHz, solvent[a]) data for complexes **Co-2**, **Co-3**, **Co-4**, **Co-6** and **Co-7**. 69

Table 3.2 Selected interatomic distances (Å) and bond angles (°) in the structure of **Co-1**, **Co-2c**, **Co-3c**, **Co-4e** and **Co-6a,c**.[a] 72

Table 3.3 Selected peak potentials E_{pc}(red) and E_{pa}(ox) of complex **Co-1**, **Co-2a**, **Co-4e**, **Co-5** and **Co-6a** from cyclic voltammetry (CV) data.[a] 77

Table 3.4 ^{1}H NMR (500.27 MHz, solvent) data for complexes **Co-2**, **Co-3** and **Co-4**: δ in ppm (multiplicity, J or $\omega_{1/2}$ in Hz, RI,) 100

Table 3.5 $^{13}C\{^{1}H\}$ NMR (125.77 MHz, solvent) data for complexes **Co-2**, **Co-3** and **Co-4**: δ in ppm (multiplicity, J or $\omega_{1/2}$ in Hz). 102

Table 3.6 ^{1}H NMR (500.27 MHz, CD_3CN) data for complexes **Co-6**: δ in ppm (multiplicity, J or $\omega_{1/2}$ in Hz, RI)[a] 103

Table 3.7 $^{13}C\{^{1}H\}$ NMR (125.77 MHz, CD_3CN) data for complexes **Co-6**: δ in ppm (multiplicity, J or $\omega_{1/2}$ in Hz).[a] 104

Table 3.8 UV-vis data for complexes **Co-1**, **Co-2(a-d)** and **Co-4(a,e)** in CH_2Cl_2 and **Co-5** and **Co-6(a-d)** in CH_3CN..... 106

Table 4.1 Screening the catalytic activity of complex **Co-1** and DBU for the hydrophosphination of *tert*-butyl acrylate with PPh_2H.[a] 119

Table 5.1 Assessing catalytic activity of **Co-1** for catalytic dehydrocoupling of PPh_2H.[a] 179

Table 5.2 ^{1}H NMR (500.27 MHz, C_6D_6 or CD_3CN) data of complexes **Co-10**, **Co-11** and **[Co-12]I**: δ in ppm (multiplicity, J or $\omega_{1/2}$ in Hz, RI)..... 199

Table 5.3 $^{31}P\{^{1}H\}$ NMR (202.51 MHz, C_6D_6 or CD_3CN) data of complexes **Co-10**, **Co-11** and **[Co-12]I**: δ in ppm (multiplicity)..... 200

Table 5.4 $^{13}C\{^{1}H\}$ NMR (125.77 MHz, C_6D_6 or CD_3CN) data of complexes **Co-10**, **Co-11** and **[Co-12]I**: δ in ppm (multiplicity, J or $\omega_{1/2}$ in Hz)..... 200

Table 5.5 $^{31}P\{^{1}H\}$ NMR (121.55 MHz, C_6D_6) data for P-P coupling products (diphosphines and polyphosphines): δ (ppm) (multiplicity, J in Hz)..... 201

Table 5.6 $^{31}P\{^{1}H\}$ NMR (121.55 MHz, C_6D_6) data for tentatively assigned products containing P-N and P-C bonds observed in the catalytic dehydrocoupling reactions in the presence of HAs: δ (ppm) (multiplicity)..... 202

List of Figures

Figure 2.1 $^{31}P\{^{1}H\}$ NMR (121.55 MHz, C_6D_6) spectrum of the isolated mixture, including **Ru-1a**, the orthometallation product (•) and other impurities (•). 38

Figure 2.2 ^{1}H NMR spectra (300.13 MHz, C_6D_6) of: **a)** $NaN(SiMe_3)_2$; **b)** reaction of 1 equiv $NaN(SiMe_3)_2$ with 10 equiv PPh_2H (PPh_2^- generated *in situ*); **c)** reaction of 10 equiv *tert*-butyl acrylate with a previously prepared mixture of 1 equiv $NaN(SiMe_3)_2$ and 10 equiv PPh_2H (PPh_2^- generated *in situ*); **d)** the reaction of 1 equiv $NaN(SiMe_3)_2$ with 10 equiv *tert*-butyl acrylate. 41

Figure 2.3 $^{31}P\{^{1}H\}$ NMR spectrum (121.55 MHz, C_6D_6) of a reaction where 10 equiv of *tert*-butyl acrylate was added to a premixed solution of 1 equiv $NaN(SiMe_3)_2$ and 10 equiv PPh_2H (10 mol% PPh_2^- generated *in situ*). P = $Ph_2P(CH_2CHCO_2Bu^t)$. 42

Figure 2.4 Rate profiles for the reaction of PPh_2H with *tert*-butyl acrylate catalyzed by **Ru-1a** (□) and Ru(η^5-indenyl)(PPh_2)(PPh_2H)(PPh_3) (Δ), as monitored by ^{1}H NMR (500.27 MHz, C_6D_6, RT). Conditions: 1 mol% Cp*Ru and 10 mol% indenyl Ru. Error bars show uncertainty over triplicate runs. The turnover frequencies (TOFs) shown were calculated for the 90% conversion. 44

Figure 2.5 $^{31}P\{^{1}H\}$ NMR spectra (121.55 MHz, C_6D_6) of catalysis using 1 mol % **Ru-1a** showing the catalyst resting state **Ru-6a**. Note: unreacted **Ru-4a** in the catalytic mixture arises from the uncomplete dehydrohalogenation using less base (0.8 mol%) with respect to Ru (1 mol%). 45

Figure 3.1 $^{31}P\{^{1}H\}$ NMR spectra (121.55 MHz, C_6D_6) of the mixture of **Co-1** and 10 equiv of PR_2H. R = (**a**) Ph, (**b**) Tol^p, (**c**) Cy, (**d**) Pr^i, (**e**) Et. 65

Figure 3.2 $^{31}P\{^{1}H\}$ NMR spectra (121.55 MHz, C_6D_6) of the mixture of **Co-1** and 10 equiv of PRH_2. R = Ph (**a**), Cy (**c**). 66

Figure 3.3 X-ray structures of: **a)** Co(η^5-Cp*)I_2(CO) **Co-1**; **b)** Co(η^5-Cp*)I_2(PCy_2H) **Co-2c**;[a] **c)** Co(η^5-Cp*)I_2($PCyH_2$) **Co-3c**; **d)** ion $[Co(\eta^5\text{-Cp*})I(PEt_2H)_2]^+$ of **Co-4e**;[b] **e)** ion $[Co(\eta^5\text{-Cp*})(NCCH_3)_2PPh_2H]^{2+}$ of **Co-6a**;[c] **f)** ion $[Co(\eta^5\text{-Cp*})(NCCH_3)_2PCy_2H]^{2+}$ of **Co-6c**;[c] showing the atom labeling. Non-hydrogen atoms are represented by Gaussian ellipsoids at the 30% probability level. Hydrogen atoms are shown with arbitrarily small thermal parameters. 71

Figure 3.4 UV-vis absorption spectra of iodide complexes **Co-1** and **Co-2(a-d)** in CH_2Cl_2 at RT. 73

Figure 3.5 UV-vis absorption spectra of iodide complexes **Co-3(a,c)** in CH_2Cl_2 at RT. 74

Figure 3.6 UV-vis absorption spectra of iodide complexes **Co-1** and **Co-4(a,e)** in CH_2Cl_2 at RT. 75

Figure 3.7 UV-vis absorption spectra of dicationic complexes **Co-5** and **Co-6(a-d)** in CH_3CN at RT. 76

Figure 3.8 Cyclic voltammograms of complexes (**a**) **Co-1** and (**b**) **Co-2a**. 1 mM [Co] in CH_3CN, scan rate ν = 0.1 V s^{-1}, 0.1 M supporting electrolyte Bu_4NPF_6. The voltammogram is referenced to the Fc/Fc^+ redox couple. 79

Figure 3.9 Effect of the scan rate (ν) on the CV of complex **Co-2a**. 1 mM [Co] in CH_3CN, 0.1 M supporting electrolyte Bu_4NPF_6. The voltammogram is referenced to the Fc/Fc^+ redox couple. 80

Figure 3.10 Cyclic voltammogram of complex **Co-4e**. 1 mM [Co] in CH_3CN, scan rate ν = 0.1 V s^{-1}, 0.1 M supporting electrolyte Bu_4NPF_6. The voltammogram is referenced to the Fc/Fc^+ redox couple. 81

Figure 3.11 Cyclic voltammograms of **a) Co-5** and **b) Co-6a**. 1 mM [Co] in CH_3CN, scan rate ν = 0.1 V s^{-1}, 0.1 M supporting electrolyte Bu_4NPF_6. The voltammogram is referenced to the Fc/Fc^+ redox couple. 82

Figure 3.12 $^{31}P\{^1H\}$ NMR spectra (121.55 MHz, C_6D_6) of the hydrophosphination of *tert*-butyl acrylate with PPh_2H using 10 mol% **a) Co-1**, **b) Co-2a** or **c) Co-4a**. 84

Figure 3.13 ^{31}P NMR (121.55 MHz, C_6D_6) spectrum of the reaction of **Co-1** with 10 equiv of PPh_2H, showing the absence of $^1J_{PH}$ coupling in free PPh_2H. Inset: P-H region of the ^1H NMR (300.27 MHz, C_6D_6) spectrum of the mixture. 88

Figure 3.14 $^{31}P\{^1H\}$ NMR (202.51 MHz, CD_3CN) spectrum of the mixture of **Co-5** with 3 equiv of PPh_2H, showing the broadening of signal due to free PPh_2H. Note: the internal standard PPh_3 is in a sealed capillary. Inset: partial ^{31}P NMR of the mixture. 88

Figure 3.15 ^1H NMR (300.27 MHz, C_6D_6) spectrum of complex **Co-2d** dried under vacuum for 1 h, showing its decomposition to several Co-containing species. Residual proteo-solvent is marked with •. 93

Figure 3.16 VT $^{31}P\{^{1}H\}$ NMR (145.78 MHz, $CDCl_3$) spectra of the isolated **Co-4a**, showing a ligand redistribution in the solution. 95

Figure 3.17 ESI-MS spectrum of **Co-4e** in CH_2Cl_2 and MS/MS of the peak at *m/z* = 501.30 (inset). Other unidentified peaks could be due to the decomposition of this reactive Co complex. Conditions: a solution of **Co-4e** (0.02 mmol) in CH_2Cl_2 (0.6 mL) was further diluted 20 times for the ESI-MS experiments. 96

Figure 3.18 ^{1}H NMR (300.27 MHz, C_6D_6) spectrum of complex **Co-4e** dried under vacuum for 1 h, showing its decomposition to **Co-2e**. Residual proteo-solvent (•). 97

Figure 3.19 ^{1}H NMR (300.27 MHz, CD_3CN) spectrum of isolated complex **Co-5** in CD_3CN and scheme illustrating substitution of CH_3CN ligand by CD_3CN. Residual proteo-solvent (•). 98

Figure 3.20 Photograph of UV-vis samples (from left to right): blank, **Co-2**, **Co-4**, **Co-5**, **Co-1** and **Co-6**. 105

Figure 4.1 Conversion to hydrophosphination product after 2 h, as a function of DBU loading. (a) Reactions using 2 mol% **Co-1** and the DBU loading shown on the top axis, Δ; (b) reactions using the DBU loading shown on the bottom axis (corresponds to DBU in excess of 2 mol% used in (**a**)), □. Error bars represent standard deviation over triplicate runs. 121

Figure 4.2 $^{31}P\{^{1}H\}$ NMR (202.51 MHz, C_6D_6) spectra of the hydrophosphination of *tert*-butyl acrylate with PPh_2H using 2 mol% **Co-1** and 4 mol% base after 2 h. 122

Figure 4.3 ^{1}H NMR (500.27 MHz, C_6D_6) spectra of the reaction of PPh_2H with 4 mol% of base ((**a**) NEt_3 or (**b**) DBU), showing that no deprotonation occurs. 124

Figure 4.4 $^{31}P\{^{1}H\}$ NMR (121.55 MHz, CD_2Cl_2) spectrum of the hydrophosphination of *tert*-butyl acrylate with PPh_2H catalyzed by 2 mol% of **Co-1** and 4 mol% of DBU, after 24 h. Note: the oxidized product arises from using insufficiently dried CD_2Cl_2 or slowly oxidized substrate PPh_2H. 125

Figure 4.5 $^{31}P\{^{1}H\}$ NMR (202.51 MHz, C_6D_6) spectrum of the reaction of *tert*-butyl acrylate with PPh_2H catalyzed by 10 mol% **Co-1** and 20 mol% DBU. Inset shows trace amounts of complexes **Co-8** and **Co-9** in the catalytic mixture. 134

Figure 4.6 $^{1}H/^{31}P\{^{1}H\}$ HMBC (500.27 MHz, C_6D_6) spectrum of the reaction of 10 equiv of *tert*-butyl acrylate and PPh_2H catalyzed by **Co-1**, showing correlations of the ^{31}P signals in Co-P species with their Cp* signals and phenyl *ortho*-H signals..... 134

Figure 4.7 Wide $^{31}P\{^{1}H\}$ NMR (121.55 MHz, C_6D_6, up to 2000 ppm) spectrum of the reaction of complex **Co-2a** with DBU, showing no Co-PPh_2 observed in the mixture. 136

Figure 4.8 ^{1}H NMR (300.27 MHz, C_6D_6) spectrum of the reaction of **Co-2a** with DBU, showing the broad paramagnetic ^{1}H signals. Note: deuterated solvent (•). 137

Figure 4.9 X-band EPR spectrum of the reaction of **Co-2a** with DBU measured in d_8-toluene at ~20 mM concentration at 100 K with a microwave frequency of 9.39 GHz. Parameters used in preliminary simulation in EasySpin: $g_1 = 2.348$, $g_2 = 2.039$, $g_3 = 2.001$, $A_1(^{59}Co) = 74$ G, $A_3(^{59}Co) = 16$ G, $A_1(^{31}P) = 39$ G, 1G. 138

Figure 4.10 ^{1}H NMR (300.27 MHz, C_6D_6, 1 scan) spectrum of the reaction of [**Co-2a** +DBU] with 1 equiv of *tert*-butyl acrylate and internal standard $O(SiMe_3)_2$, showing the possible coordination of *tert*-butyl acrylate to the resulting paramagnetic Co species. 144

Figure 4.11 $^{31}P\{^{1}H\}$ NMR (121.55 MHz, C_6D_6) spectra of **a)** the reaction of complex **Co-2a** with 1 equiv of DBU; **b)** the reaction of the mixture generated in (**a**) with 10 equiv each of *tert*-butyl acrylate and PPh_2H; **c)** the reaction of the mixture generated from (**b**) with 1 equiv of DBU, showing catalytic activity. 146

Figure 4.12 Monitoring the hydrophosphination of *tert*-butyl acrylate by PPh_2H catalyzed by 2 mol% **Co-1** and 4 mol% DBU by ^{1}H NMR (500.27 MHz, C_6D_6) spectra. 150

Figure 4.13 Reaction profiles for the hydrophosphination of *tert*-butyl acrylate by PPh_2H following the "same excess" protocol. Profile **R-a** (green) and **R-b** (red) have different initial concentrations of *tert*-butyl acrylate and PPh_2H. Profile **R-c** (blue) has the same initial concentrations as **R-b** and added the product phosphines to match the initial concentration of PPh_2H in **R-b**. Error bars represent standard deviation over triplicate runs. 151

Figure 4.14 Reaction rate dependence on [cat] (cat = **Co-1**) determined by the initial rate method. Conditions: [**Co-1**] 0.003 M (1 mol%), 0.006 M (2 mol%), 0.012 M (4

mol%). Error bars represent standard deviation over triplicate runs. Initial rates = % conversion/15 min. 152

Figure 4.15 Representative ^{1}H NMR (500.27 MHz, C_6D_6) spectra of the reaction of *tert*-butyl acrylate with PPh_2H catalyzed by **Co-1** (2 mol%) and DBU (4 mol%). The first spectrum (first data point) was collected within 15 minutes of mixing the catalytic solution (bottom). The remaining spectra were with a delay of 5 minutes between each (from bottom to up). 158

Figure 4.16 $^{31}P\{^{1}H\}$ NMR (121.55 MHz, C_6D_6) spectra of the reaction of complex **Co-2a** with 1 equiv of **a)** $NaN(SiMe_3)_2$, **b)** $KOBu^t$, **c)** DBU or **d)** NEt_3. 159

Figure 4.17 $^{31}P\{^{1}H\}$ NMR (121.55 MHz, C_6D_6) spectra of the reaction of complex **Co-2a** with DBU in the presence of TEMPO, showing the different species. Note: some small signals are not identified. 166

Figure 4.18 ^{1}H NMR (300.27 MHz, $CDCl_3$) spectrum of isolated [HDBU]I. Residual proteo-solvent (•). 167

Figure 4.19 ESI-MS spectrum of isolated [HDBU]I, showing *m/z* 153.24 (M^+, 153.14 calcd, 100%) and *m/z* 433.30 ($2M^+ + I^-$, 433.18 calcd, 50%). Conditions: a solution of [HDBU]I (0.02 mmol) in (CH_3CN) (0.6 mL) was further diluted 20 times for the ESI-MS experiments. 167

Figure 4.20 $^{31}P\{^{1}H\}$ NMR (121.55 MHz, C_6D_6) spectra of experiments using complex **Co-2a** and (**a**) Mes*O or (**b**) TEMPO. 168

Figure 5.1 $^{31}P\{^{1}H\}$ NMR (121.55 MHz, C_6D_6) spectrum of the dehydrocoupling reaction of PPh_2H using 10 mol% **Co-1** and 20 mol% DBU at RT after 15 min (before heating). 182

Figure 5.2 X-band EPR spectrum of the reaction of complex **Co-1** with 2 equiv of DBU in the presence of 10 equiv of PPh_2H. Measured in CD_3CN at ~20 mM concentration at 100 K with a microwave frequency of 9.39 GHz. Parameters used in preliminary simulation in EasySpin: $g_1 = 2.351$, $g_2 = 2.065$, $g_3 = 1.979$, $A_1(^{59}Co) = 80$ G, $A_3(^{59}Co) = 72$ G, $A_1(^{31}P) = 6$ G. 184

Figure 5.3 ^{1}H NMR (300.27 MHz, C_6D_6) spectrum of the dehydrocoupling reaction of PPh_2H using 10 mol% **Co-1** and 20 mol% DBU after heating 3 h, showing the formation of cationic **Co-10** fragment. 185

Figure 5.4 $^{31}P\{^{1}H\}$ NMR (121.55 MHz, CD_3CN) spectrum and partial ^{1}H NMR (300.27 MHz, CD_3CN, inset) spectrum of the dehydrocoupling reaction of PPh_2H using 10 mol% **Co-1** and 20 mol% DBU, after heating 3 h. 186

Figure 5.5 ^{1}H NMR (300.27 MHz, CD_3CN) spectrum of the dehydrocoupling reaction of PPh_2H using 10 mol% **Co-1** and 20 mol% DBU, after heating 3 h. Note: ⋆ signals due to [HDBU]I. 186

Figure 5.6 $^{31}P\{^{1}H\}$ NMR (121.55 MHz, CD_3CN) spectrum of the dehydrocoupling of PPh_2H using 10 mol% **Co-5** and 20 mol% DBU, after heating at 80 °C for 2 h. Residual proteo-solvent (●). 187

Figure 6.1 $^{31}P\{^{1}H\}$ NMR (202.51 MHz, CD_3CN) and partial ^{31}P NMR (inset) spectra of a mixture of **Co-5** with 3 equiv of PPh_2H, showing the broadening of signal due to free PPh_2H. Internal standard PPh_3 is in a sealed capillary..... 212

Figure 6.2 VT ^{31}P NMR (202.51 MHz, CD_3CN) spectra of the reaction of **Co-5** with 3 equiv of PPh_2H, showing variable broadening of the free PPh_2H signal at different temperatures. Internal standard PPh_3 (⋆) is in a sealed capillary; a tiny peak at ~ –14 ppm is due to $Ph_2P\text{-}PPh_2$. 213

Figure 6.3 Partial $^{13}C\{^{1}H\}$ NMR (121.55 MHz, CD_2Cl_2/CD_3CN = 4:1, ⋆) spectra of samples in CD_2Cl_2/CD_3CN (4:1) containing inserted coaxial tubes containing just the identical solvent (CD_2Cl_2 : CD_3CN = 4:1, ◆). Samples: **a) Co-5** and 3 equiv of PPh_2H, **b) Co-5** and 2 equiv of PPh_2H, **c) Co-6a**, **d) Co-5**. 215

Figure 6.4 X-band EPR spectrum of the reaction of complex **Co-5** in the presence of 3 equiv of PPh_2H. Measured in CD_3CN at ~20 mM concentration, at 100 K, with a microwave frequency of 9.39 GHz. Inset shows an extra tiny signal due to an organic radical. Parameters used for preliminary simulation in EasySpin: g_1 = 2.271, g_2 = 2.090, g_3 = 1.970, $A_1(^{59}Co)$ = 30 G, $A_2(^{59}Co)$ = 20 G, $A_3(^{59}Co)$ = 50 G. 216

Figure 6.5 ESI-MS spectrum of the reaction mixture of complex **Co-5** in the presence of 3 equiv of PPh_2H. Inset: MS/MS spectrum of the peak at *m/z* = 566.17. Other unidentified peaks could be due to the decomposition of highly reactive Co species. Peaks at higher *m/z* could be due to unidentified dimeric Co species after the decomposition. 218

Figure 6.6 UV-vis absorption spectra of **Co-5**, **Co-6a** and the mixtures of **Co-5** with 2, 3, 25, 500, and 1500 equiv of PPh_2H in CH_3CN at RT. 221

Figure 6.7 a) VT-UV-vis absorption spectra of the mixture of **Co-5** in the presence of 25 equiv of PPh_2H in CH_3CN; **b)** original and post-VT spectra recorded at 20 °C. ... 222

Figure 6.8 a) $^{31}P\{^1H\}$ NMR (121.55 MHz, CD_3CN) spectrum of the mixture of **Co-5** and PPh_2D (10 equiv), showing the multiple unidentified species in the reaction. **b)** $^{31}P\{^1H\}$ NMR (121.55 MHz, C_6D_6) spectrum of the mixture of **Co-1** and PPh_2D (10 equiv). 224

Figure 6.9 $^{31}P\{^1H\}$ NMR (121.55 MHz, C_6D_6) spectrum of the reaction of complex **Co-1** with 5 equiv of PPh_2D and 5 equiv of $PTol^p{}_2H$ after 15 min. Inset: Co phosphine complex region of the $^{31}P\{^1H\}$ NMR spectrum..... 226

List of Schemes

Scheme 1.1 Examples of chiral phosphine ligands used for asymmetric catalysis. 2

Scheme 1.2 Phosphine-mediated Michael addition.[4] 3

Scheme 1.3 Examples of compounds containing P-P bonds in coordination chemistry.... 4

Scheme 1.4 Selected traditional stoichiometric methods for forming P-C and P-P bonds. 5

Scheme 1.5 a) Hydrophosphination of an alkene with PR_2H under different conditions. **b)** Homolytic or heterolytic cleavage of the P-H bond of PR_2H. 6

Scheme 1.6 Free radical addition of PH_3 to an alkene (IN• is a radical initiator). 7

Scheme 1.7 Base-catalyzed hydrophosphination of alkynes with PPh_2H.[22] 8

Scheme 1.8 Stereochemistry and regiochemistry of hydrophosphination of alkenes with PR_2H. 9

Scheme 1.9 Homo- or hetero-dehydrocoupling (E, E' = B, N, P, Si). 9

Scheme 1.10 Examples of catalysts (transition metals[52,56] and main group molecules[61,64,69]) and reagents[65,68] for P-P bond formation *via* dehydrocoupling of phosphines. 10

Scheme 1.11 P-H activation mechanisms (left) and selected examples (right). The phosphido lone pair is shown to highlight the nucleophilicity of the M-PR_2 fragment. 12

Scheme 1.12 Possible outcomes following the deprotonation with a base. 13

Scheme 1.13 P-C bond formation mechanisms and selected examples.[78–80,87] 14

Scheme 1.14 C-H bond formation mechanisms and selected examples.[78,79] 16

Scheme 1.15 P-H activation mechanisms and selected examples.[52,55] 18

Scheme 1.16 P-P bond formation mechanisms and selected examples. [56,58,89] 19

Scheme 1.17 H-H bond formation mechanisms. 20

Scheme 2.1 Proposed catalytic cycles for outer-sphere hydrophosphination using Ru(η^5-indenyl)(PPh_2)(PPh_2H)(PPh_3) involving intramolecular and intermolecular proton transfers. [Ru] = indenylRu, L = PPh_3 or $Ph_2P(CH_2CH_2CO_2Bu^t)$, R = CO_2Bu^t. 33

Scheme 2.2 Proposed catalytic cycle for outer-sphere hydrophosphination using Ru(η^5-indenyl)(PPh_2)(CO)(PPh_3). [Ru] = indenyl Ru, R = CO_2Bu^t. P-capped oligomers are probably terminated by abstracting a proton from PPh_2H. 34

Scheme 2.3 Undesired orthometallation of Ru(η^5-Cp*)(PR_2)(PPh_3) and the Cp* catalysts described in this chapter..... 35

Scheme 2.4 Reactions of **Ru-3** with 10 equiv of PR_2H. The equilibrium is only spectroscopically observed for bulky PR_2H (R = Cy (d)); ^{31}P δ for **Ru-5d**: 49.6 (d, $^2J_{PP}$ = 40 Hz, PPh_3), 48.2 (d, PCy_2H). 36

Scheme 2.5 Strategy of generating the Cp* complex **Ru-1**. Base = $NaN(SiMe_3)_2$ or $KOBu^t$. 37

Scheme 2.6 Attempted synthesis of complex **Ru-1a**, showing possible mechanisms for the undesired orthometallation..... 38

Scheme 2.7 Impacts of the size of PR_2H on **Ru-1** and **Ru-2**. 40

Scheme 2.8 Proposed relative rates of each step in the catalytic hydrophosphination of *tert*-butyl acrylate with PPh_2H using **Ru-1a**. **P** = $Ph_2P(CH_2CH_2CO_2Bu^t)$, R = CO_2Bu^t. 46

Scheme 2.9 Deactivation process of **Ru-7a** at the end of catalysis in the absence of PPh_2H. **P** = $Ph_2P(CH_2CH_2CO_2Bu^t)$, R = CO_2Bu^t. 47

Scheme 2.10 Regeneration of **Ru-1a** at the end of catalysis with a slight excess of PPh_2H with respect to the alkene. P = $Ph_2P(CH_2CH_2CO_2Bu^t)$, R = CO_2Bu^t. 48

Scheme 2.11 Hydrophosphination of *tert*-butyl and methyl acrylate with various phosphines using Cp*Ru phosphido catalysts (generated *in situ*).[a]..... 49

Scheme 2.12 Two competitive processes depend on the P-H bond acidity of the coordinated PR_2H. R = Ph (**a**), Tol^p (**b**), Et (**c**); R' = CO_2Bu^t, CO_2Me. P = hydrophosphination product. 50

Scheme 2.13 Proposed cycle for outer-sphere hydrophosphination catalyzed by **Ru-1** (R = Ph, Tol^p, Et), relying on conjugate addition. R' = electron withdrawing group (EWG). 51

Scheme 3.1 Synthesis of complexes Co(η^5-Cp*)I_2(PR_2H) (**Co-2**) and Co(η^5-Cp*)I_2(PRH_2) (**Co-3**) from Co(η^5-Cp*)I_2(CO) (**Co-1**). 63

Scheme 3.2 Substitution chemistry of complex **Co-1** in the presence of excess PR_2H or PRH_2. 64

Scheme 3.3 Synthesis of complex **Co-6** through the reaction of **Co-5** with 1 equiv PR_2H, highlighting an equilibrium involving **Co-6** and **Co-7** in CH_3CN solution (bottom box). 67

Scheme 3.4 Catalytic hydrophosphination using complex **Co-5** and DBU. 85

Scheme 3.5 Preliminary assessments of dehydrocoupling of PPh_2H using **Co-1** and **Co-5**. 86

Scheme 3.6 Reactions of complex **Co-1** (top) and **Co-5** (bottom) with excess PPh_2H, showing the formation of corresponding bis(phosphine) complexes as major products. 87

Scheme 4.1 Literature examples of Co-catalyzed hydrophosphination. 114

Scheme 4.2 Proposed cycle for the Co-catalyzed hydrophosphination involving Co(0)/Co(II). 115

Scheme 4.3 Proposed cycle for the Co-catalyzed hydrophosphination involving conjugate addition of substrate PPh_2H at metal-alkene complexes. 116

Scheme 4.4 Alkene scope for Co-catalyzed hydrophosphination with PPh_2H.[a] 127

Scheme 4.5 Phosphine scope for Co-catalyzed hydrophosphination of *tert*-butyl acrylate.[a] 128

Scheme 4.6 Reactions of complex **Co-1** with excess **a)** secondary phosphine or **b)** primary phosphine. R = Ph (**a**), Tol^p (**b**), Cy (**c**), Pr^i (**d**) and Et (**e**). 132

Scheme 4.7 Dehydrohalogenation of **Co-2a** by DBU, showing the formation of Ph_2P-PPh_2 and a paramagnetic Co(II) complex. 135

Scheme 4.8 Proposed equilibria of Co(II) complexes in the reaction mixture of **Co-2a** and DBU. 139

Scheme 4.9 a) Representation of valence tautomerism/electromerism (M = transition metal, L = ligand). **b)** An example of valence tautomerism in a cobalt bis(dioxolene) complex. 140

Scheme 4.10 Dehydrohalogenation of **Co-2a** by DBU in the presence of TEMPO (top), showing phosphinyl trapping products. Box inset shows possible valence tautomerism of Co(III)-PPh_2. Plausible mechanisms of the phosphinyl trapping (bottom). 141

Scheme 4.11 Thermochemical cycle used for measuring $E_{1/2}(PPh_2^-/PPh_2\bullet)$ of the Co(III)-PPh_2. C_G is the constant used to convert reduction potentials and pK_a values into bond dissociation free energies (BDFEs), which varies in different solvents. 142

Scheme 4.12 Estimations of pK_a and bond dissociation free energies (BDFE) for complex **Co-2a**. 143

Scheme 4.13 Addition of *tert*-butyl acrylate and PPh_2H to the mixture containing Co(II) complexes. 145

Scheme 4.14 Proposed formation of Co(II)-PR_2 intermediates for catalysis. 147

Scheme 4.15 Possible pathways for the formation of Co(II)-PPh_2 from the literature about Co-catalyzed hydrophosphination. 149

Scheme 4.16 Proposed catalyst activation and mechanism for the hydrophosphination of an electron-deficient alkene with PR_2H using **Co-1** and DBU. R = alkyl and aryl, R' = CO_2Bu^t. 154

Scheme 5.1 Equilibrium of dehydrocoupling of PPh_2H, showing the reaction heavily lies on the left side. 178

Scheme 5.2 Equilibrium of dehydrocoupling of PPh_2H using **Co-1**. 180

Scheme 5.3 Catalytic dehydrocoupling of PPh_2H using **Co-1** in the presence of (**a**) base or (**b**) not. 181

Scheme 5.4 Proposed process for the formation of **Co-8** and **Co-9** in the base-mediated dehydrocoupling reaction of PPh_2H using **Co-1** in C_6D_6, before heating. R = Ph. 182

Scheme 5.5 Proposed process for the formation of the Co species observed by NMR (red) and EPR (blue) in the catalytic mixture in CD_3CN, before heating. R = Ph. 183

Scheme 5.6 Stepwise mechanism for the formation of **Co-8** and **Co-9** in the base-mediated dehydrocoupling reaction of PPh_2H using **Co-1**. R = Ph. 188

Scheme 5.7 Proposed process for the formation of Co species involving protonation of the Co(I) fragment and subsequent proton transfer. 189

Scheme 5.8 Proposed catalytic cycle for dehydrocoupling PPh_2H using Cp*Co(III) and DBU. 191

Scheme 5.9 Screening of different hydrogen acceptors (HAs) in the dehydrocoupling reactions of PPh_2H using 10 mol % **Co-1**.[a] 194

Scheme 5.10 Substrate phosphine scope for the dehydrocoupling reactions using 10 mol % **Co-1** in the presence of **HA-1**.[a] 196

Scheme 6.1 Transition metal-mediated P-H activation giving a metal phosphido intermediate. 209

Scheme 6.2 Transition metal-mediated P-H activation *via* hydride (H^-) abstraction. ... 210

Scheme 6.3 Examples of transition metal-mediated homolytic P-H cleavage. 211

Scheme 6.4 Possible equilibria in the mixture of complex **Co-5** and excess PPh_2H. 220

Scheme 6.5 Deuterium labelling experiments using **Co-1**: **a)** reaction of **Co-1** with 10 equiv of PPh_2D; **b)** reaction of **Co-1** with 10 equiv of PPh_2H; **c)** reaction of **Co-1** with 5 equiv of PPh_2D and 5 equiv of $PTol^p{}_2H$; **d)** the mixture of PPh_2D and $PTol^p{}_2H$ (1:1). 225

Scheme 6.6 Proposed mechanism (#1) for reversible homolytic P-H bond cleavage by complex **Co-7a**..... 227

Scheme 6.7 Proposed mechanism (#2) for reversible P-H activation by a Cp*Co(III) complex with an FLP adduct. 229

Scheme 7.1 Proposed mechanism for outer-sphere hydrophosphination catalyzed by **Ru-1**. (R = Ph; R' = CO_2Bu^t) 238

Scheme 7.2 Proposed Cp*Ru-catalyzed hydrophosphination reactions using primary phosphine or methyl methacrylate (prochiral alkene) giving chiral phosphine products. R = Ph and Cy, R' = Me, Bu^t. 239

Scheme 7.3 Paramagnetic species resulting from the reaction of **Co-2a** with DBU. 241

Scheme 7.4 Synthesis of binuclear Co(II) complex $[Co(\eta^5\text{-}Cp^*)(\mu\text{-}Cl)]_2$. 241

Scheme 7.5 Synthesis of chiral $Cp^xCo(III)$ complexes. 243

List of Abbreviations

Å	Angstrom (1 x 10^{-10} m)
Anal.	analysis
atm	atmosphere
Ar	aryl
br	broad
Bu or *n*-Bu	butyl
Bu^t	*tert*-butyl, -C(CH_3)$_3$
°C	degrees Celsius
C_{ipso}	*ipso*-carbon
C_{meta}	*meta*-carbon
C_{ortho}	*ortho*-carbon
C_{para}	*para*-carbon
Calcd	calculated
$^{13}C\{^1H\}$	Observed carbon while decoupling proton
cm^{-1}	wavenumber
COSY	correlation spectroscopy
Cp	cyclopentadienyl group, $C_5H_5^-$
Cp*	1,2,3,4,5-Pentamethylcyclopentadienyl, $C_5(CH_3)_5^-$
Cy	cyclohexyl group, -C_6H_{11}
D	dimension
d	doublet *or* days
DBU	1,8-diazabicyclo[5.4.0]undec-7-ene
dd	doublet of doublets
ddd	doublet of doublet of doublets
dec	decomposes
deg (or °)	degrees
DEPT	distortionless enhanced polarization transfer
DFT	density functional theory
dm	doublet of multiplets
dt	doublet of triplets
δ	NMR chemical shift in parts per million
E	element (usually main group)
EPR (or ESR)	electron paramagnetic (spin) resonance
equiv	equivalent(s)
eq	equation
ESI	electrospray ionization
Et	ethyl group, -C_2H_5
η^n	hapticity
g	gram
h	hour(s)
^1H	observed proton
H_m	*meta*-proton
H_o	*ortho*-proton
H_p	*para*-proton

HMBC	heteronuclear multiple-bond connectivity
HSQC	heteronuclear single quantum coherence
Hz	hertz
i	iso
IR	infrared
J	scalar nuclear spin-spin coupling constant (NMR)
κ^n	denticity
K	Kelvin
L	liter or neutral donor ligand
LR	low-resolution
M	molarity *or* metal
M^+	parent ion
m	mutiplet (NMR)
Me	methyl, $-CH_3$
mg	milligram(s)
MHz	megahertz
min	minutes(s)
mL	milliliter
mm	millimeter
mmol	millimole(s)
mol	mole(s)
mp	melting point (°C)
MS	mass spectrometry
m/z	mass to charge ratio
µL	microliter
n	normal
NMR	nuclear magnetic resonance
nOe	nuclear Overhauser effect
NOESY	nuclear Overhauser effect spectroscopy
o	ortho
^{31}P	observed phosphorus
$^{31}P\{^1H\}$	observed phosphorus wihle decoupling proton
p	para
Ph	phenyl group, $-C_6H_5$
Pr	Propyl group, $-C_3H_7$
R	alkyl or aryl group
RI	relative integration
RT	room temperature
s	singlet (NMR)
T	temperature
t	triplet (NMR)
t	tertiary
td	triplet of doublets
θ	Tolman cone angle
THF	tetrahydrofuran
TOCSY	Total correlation spectroscopy

Tol	tolyl group, $-C_6H_4CH_3$
Tol^p	*para*-tolyl group
VT	variable temperature
VTNA	Variable Time Normalization Analysis
$\omega_{1/2}$	line width at half height
X	anionic donor ligand
X_i	Tolman electronic factor

List of Numbered Compounds

Ru(II) complexes:

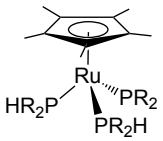

Ru-1

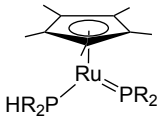

Ru-2

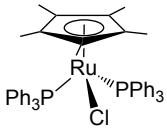

Ru-3

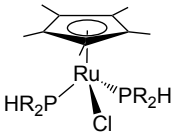

Ru-4

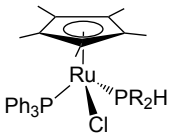

Ru-5

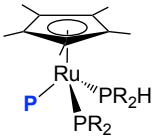

Ru-6

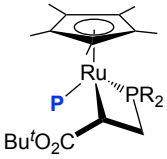

Ru-7

R= Ph (**a**), Tol^{p} (**b**), Et (**c**), Cy (**d**)

P = $PR_2(CH_2CH_2CO_2Bu^t)$

Co complexes:

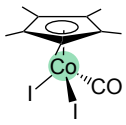

Co-1

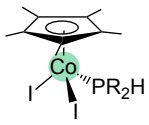

Co-2

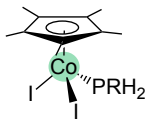

Co-3

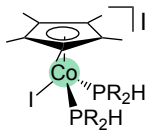

Co-4

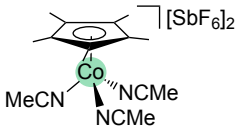

Co-5

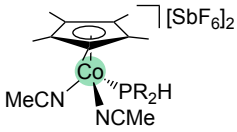

Co-6

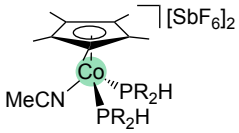

Co-7

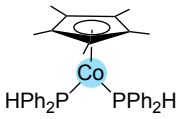

Co-8

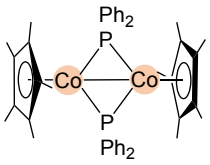

Co-9

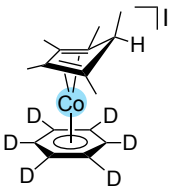

[Co-10]I

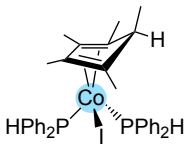

Co-11

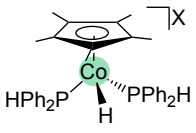

[Co-12]X

X = I^- or SbF_6^-

R = Ph (**a**), Tol^{p} (**b**), Cy (**c**), Pr^{i} (**d**), Et (**e**) Co = Co^{III} Co = Co^{II} Co = Co^{I}

Acknowledgments

I would like to express my heartfelt appreciation to everyone who has contributed to my Ph.D. experience. First and foremost, I want to thank my supervisor (academic mother), Dr. Lisa Rosenberg, who provided me with precious opportunities and constant support during my Ph.D. (and M.Sc.). I am grateful to her for the profound influence she has had on my growth as a scientific researcher. During these eight years at the University of Victoria, I am fortunate to work with the outstanding Rosenberg group members, both past and present. I am quite appreciative of their assistance and advice. Roman Belli, who has been at my side from the very beginning, deserves special thanks for his constant support and encouragement.

My gratitude also goes to my committee members. I am especially grateful to Dr. David Berg for his insightful conversations about my projects. In addition, I want to thank Dr. Scott McIndoe for his assistance and use of the ESI-MS in his lab. I am thankful to Dr. Chris Barr for his support in NMR spectroscopy and the knowledge he has shared with me. I would like to thank Dr. Charles Walsby (at Simon Fraser University) for his help in EPR spectroscopy. I appreciate Dr. Robert McDonald and Dr. Michael Ferguson (at the University of Alberta) for solving the crystal structures presented in this thesis.

Finally, I want to thank my family and friends for their inspiration, love, and support.

Dedication

For my family

1. Introduction

1.1 Overview

Organophosphorus chemistry has a substantial impact on contemporary synthetic chemistry.[1] In contrast to well-established stoichiometric methods, which continue to dominate in this area, catalytic routes of synthesizing phosphorus(P)-containing molecules provide a very intriguing alternative synthetic strategy.

Our group has been developing catalytic methodologies for P-H activation reactions to synthesize organophosphorus compounds containing P-P or P-C bonds. Hydrophosphination (P-C bond formation) provides an atom-economic route to various organophosphines. Dehydrocoupling (P-P bond formation) enables the formation of diphosphines and novel polyphosphines with attractive features.

My Ph.D. studies focused on exploring, investigating, and developing transition metal catalysts for hydrophosphination and dehydrocoupling. The knowledge gathered will assist in developing and improving future catalysts for P-H activation reactions. In the long term, this work will contribute to the synthesis of chiral phosphines and additional compounds containing P-E bonds (E = main group element).

1.2 Background: why we care about phosphines

Molecular compounds containing P-C and P-P bonds (phosphines and diphosphines) offer a wide range of applications in coordination and synthetic chemistry, which are summarized in this section.

1.2.1 Tertiary phosphines PR_3

Phosphines (PR_3) are effective Lewis bases for transition metals (ligands) because they enable facile manipulation of their steric and electronic characteristics by substituent (R) alteration.[2] For example, chiral phosphines can be "privileged" ligands widely used in metal-mediated asymmetric catalysis.[3] As shown in Scheme 1.1, a phosphine (e.g. PR_3) can have chirality on the carbon atom, phosphorus atom, or both. The ring conformations of chelating phosphine ligands can provide further control over the stereochemical environment of the metal center.

Scheme 1.1 Examples of chiral phosphine ligands used for asymmetric catalysis.

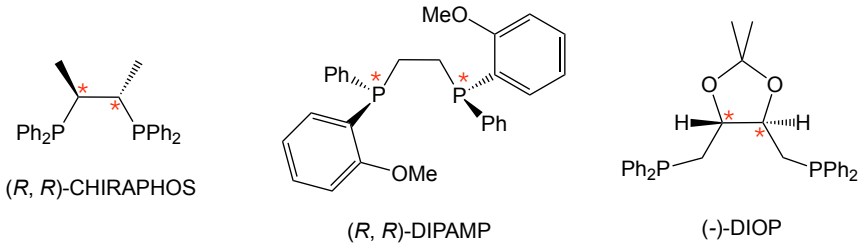

In addition to being ligands for metal complexes, organophosphines have seen increasing use as organocatalysts/initiators in organic synthesis over the last several decades.[4] One of the distinguishing features of nucleophilic phosphine catalysis (Scheme 1.2) is that reactions are often initiated by conjugate addition of tertiary phosphines to activated unsaturated C-C bonds to generate β-phosphonium α-carbanion intermediates.

Scheme 1.2 Phosphine-mediated Michael addition.[4]

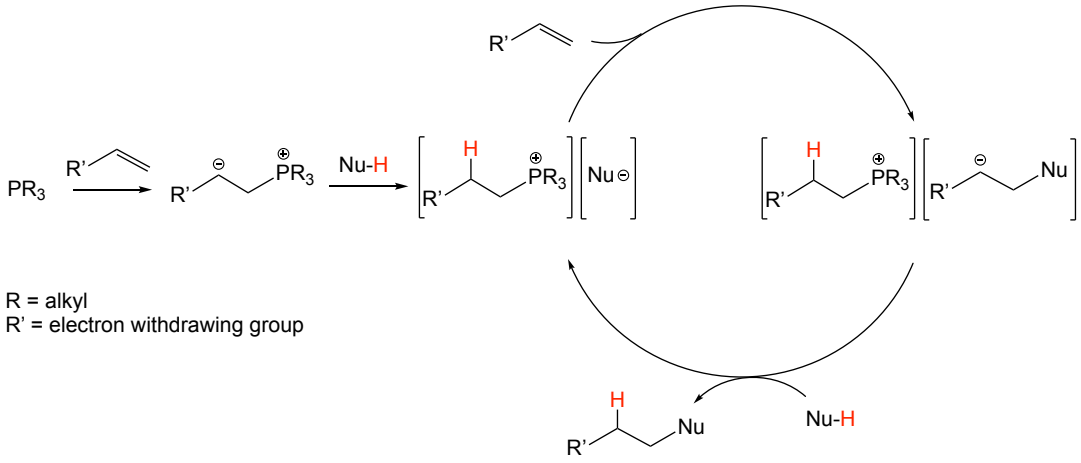

1.2.2 Diphosphines R_2P-PR_2

Diphosphines (R_2P-PR_2) are the simplest molecules containing P-P bonds, in which R can be hydrogen, halogen, silyl, amine, alkyl, aryl, boryl or borazinyl groups, resulting in a variety of structures. The type of substituents at P-atoms has a significant impact on diphosphine properties. For example, the addition of sterically demanding and electron-withdrawing substituents to the P-atoms enhances the propensity of homolytic P-P bond cleavage in the diphosphine, resulting in an equilibrium between the radical monomer and the dimer forms.[5]

Molecules containing P-P bonds (e.g. diphosphines) have various applications in coordination (Scheme 1.3)[6,7] and synthetic chemistry.[8–11] Indeed, P-P bonds in diphosphines are considered active (i.e. easy to be broken).[6] Studies on the P-P bond activation of diphosphines have emerged during the previous two decades.[8–11] In these studies, diphosphines can be used to prepare a variety of compounds (also materials and polymers) containing phosphorus-carbon (P-C) and phosphorus-element (P-E) bonds (e.g. E = Si and N).

Scheme 1.3 Examples of compounds containing P-P bonds in coordination chemistry.

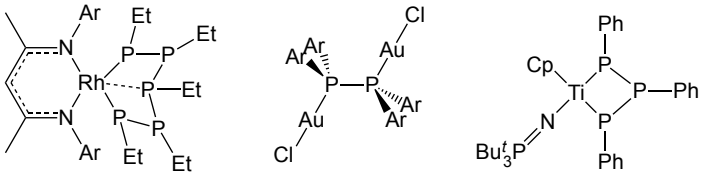

Stephan Gessner Stephan

1.3 Synthesis of phosphines

Some phosphines (especially secondary phosphines PR_2H and primary phosphines PRH_2) are air-sensitive, have a foul odour, and are pyrophoric, neurotoxic chemicals that are often challenging to synthesize and purify.[12] Thus, many phosphines are isolated in "protected" forms: phosphine borane $H_3B{\bullet}PR_3$, phosphine oxide $O{=}PR_3$, or phosphine sulfide $S{=}PR_3$. These protected phosphines are more accessible (easier to isolate and purify) and exhibit good configurational stability.[12]

The literature on compounds containing P-C or P-P bonds includes many synthetic methods. This section summarizes the most common synthetic approaches for generating P-C and P-P bonds from P(III) starting materials.

1.3.1 Traditional stoichiometric P-C bond and P-P bond formation

A classic approach for making P-containing molecules with P-C or P-P bonds (Scheme 1.4) is through salt metathesis reactions using halophosphines (PR_2X) or metal (group I or II) phosphido reagents (e.g. MPR_2).[12] However, these methods are constrained by a lack of selectivity and the formation of byproducts, which requires additional separation steps to isolate the desired phosphine product.

Scheme 1.4 Selected traditional stoichiometric methods for forming P-C and P-P bonds.

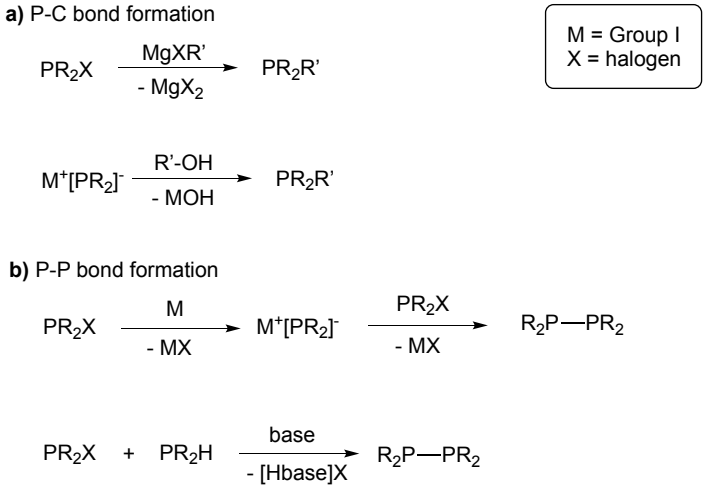

1.3.2 P-C bond formation *via* hydrophosphination

Hydrophosphination, the addition of P-H bonds of PRH_2 or PR_2H to unsaturated organic molecules, is an attractive alternative to the traditional methods discussed above because it is an atom-economical process with no byproducts (Scheme 1.5a).[13] Hydrophosphination is a spontaneous reaction that can be initiated or promoted by light/ radical initiators,[14–20] acids,[21] bases,[22–24] main group metals,[25–28] transition metals[29–38] or even heat[39–42] (Scheme 1.5a). Most hydrophosphination reactions use alkenes and alkynes because P-C bond formation is desirable (making alkyl phosphines), which also takes advantage of the high proportion of unsaturated hydrocarbons in the traditional petroleum-derived chemical feedstock.

Scheme 1.5 a) Hydrophosphination of an alkene with PR_2H under different conditions. **b)** Homolytic or heterolytic cleavage of the P-H bond of PR_2H.

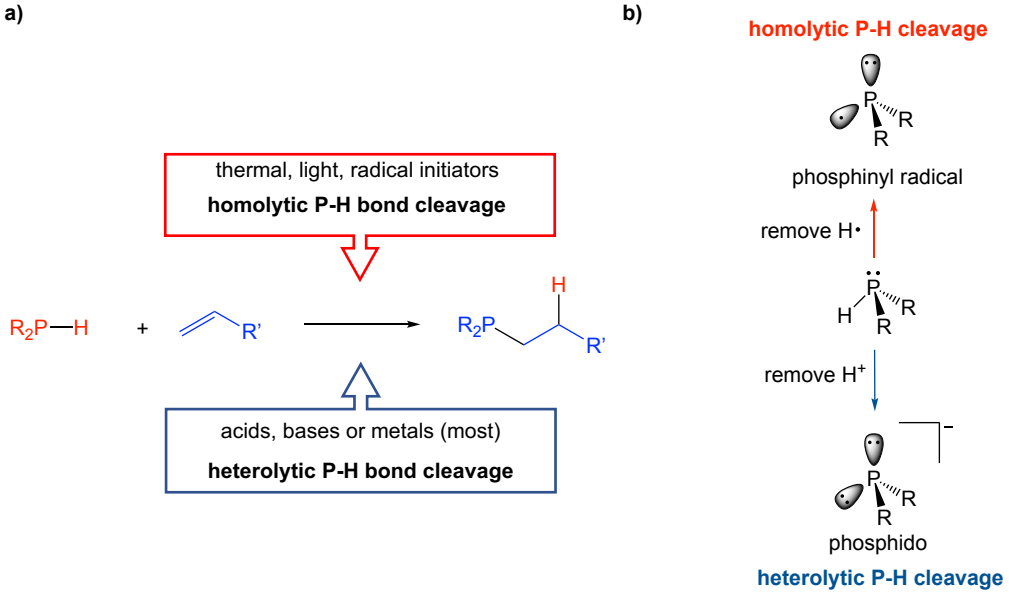

Since the Pauling electronegativities of hydrogen and phosphorus are close (2.20 and 2.19, respectively),[43] a P-H bond at a substrate phosphine (Scheme 1.5b) can be cleaved homolytically (removing a hydrogen atom H•) or heterolytically (e.g. removing a proton H^+). Thus, hydrophosphination could be classified into two categories based on different mechanisms for activating the P-H bonds (Scheme 1.5).

A widely used method for making P-C bonds in industry is homolytic cleavage of P-H bonds in a simple phosphine PH_3 (Scheme 1.6). Since the 1950s,[19] radical initiators (e.g. azobis(isobutyronitrile), AIBN) have been commonly used for this reaction with a wide variety of phosphine and alkene substrates.[44] The reaction (Scheme 1.6[14,45]) is typically initiated by homolytic cleavage of a P-H bond at the PH_3 (step A). Subsequently, the resulting phosphinyl radical ($\bullet PH_2$) is added to an alkene, forming a C-centered radical (step B). The C-centered radical propagates the reaction, finally terminated by abstracting H• from a P-H bond at the PH_3 (step C). In addition, well-established catalyst-free (thermal) hydrophosphination seems to have seen a recent revival.[41,42]

Scheme 1.6 Free radical addition of PH_3 to an alkene (IN• is a radical initiator).

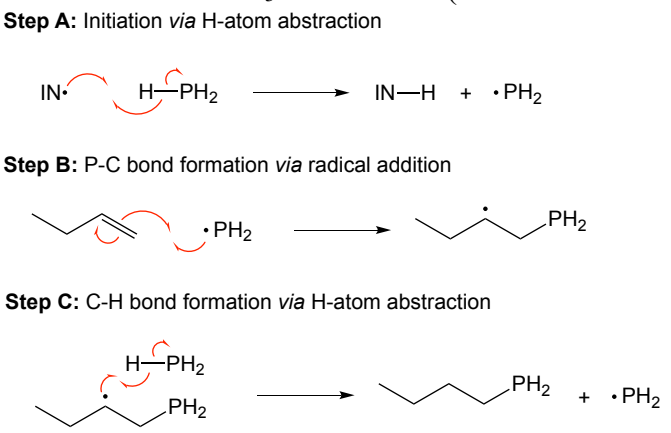

Unlike radical-mediated hydrophosphination, base- or acid-mediated hydrophosphination proceeds *via* heterolytic P-H bond cleavage of substrate phosphines. Stoichiometric base-mediated hydrophosphination (i.e. a traditional method to give metal phosphido reagents) is more common than base-catalyzed hydrophosphination. A catalytic example (Scheme 1.7) [22] involves a phosphido anion generated from deprotonation (step A), which undergoes conjugate addition at a unsaturated substrate to form a P-C bond (step B). The most significant difference between this process and the conventional technique using metal phosphido reagents (Scheme 1.4) is that the resulting conjugate acid acts as a proton shuttle (Scheme 1.7, step C), quenching the carbanion and therefore regenerating the base catalyst.

Scheme 1.7 Base-catalyzed hydrophosphination of alkynes with PPh_2H.[22]

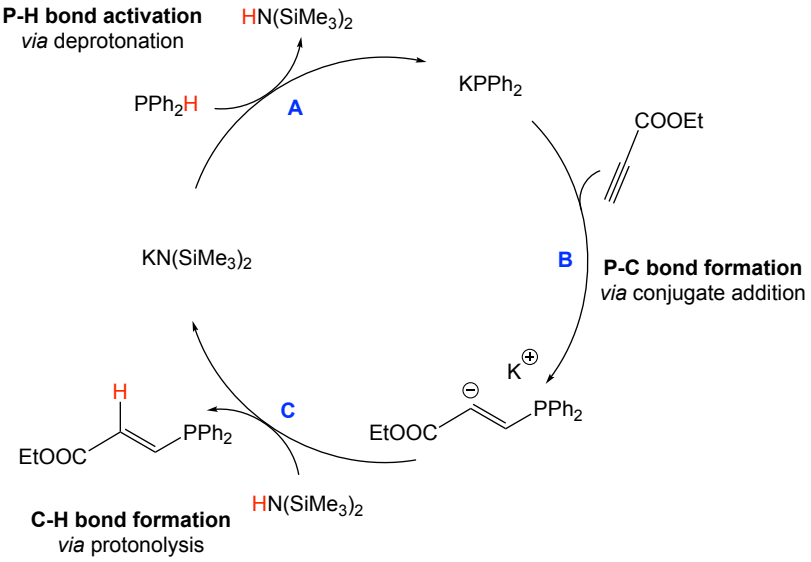

As previously stated, hydrophosphination is a thermodynamically and kinetically spontaneous favoured reaction that various approaches may accomplish. Hence, why should metal catalysts be used for hydrophosphination? The answer is to introduce the desired selectivity in these reactions, avoiding the time- and reagent-consuming separation procedures that generally precede the isolation of high-value phosphines. Scheme 1.8 illustrates the stereo- and regioselectivity possible for transition metal-catalyzed hydrophosphination of alkenes. These targets, chiral phosphines, are more sophisticated and advanced than the phosphine ligands employed in current fine chemical synthesis.

Scheme 1.8 Stereochemistry and regiochemistry of hydrophosphination of alkenes with PR_2H.

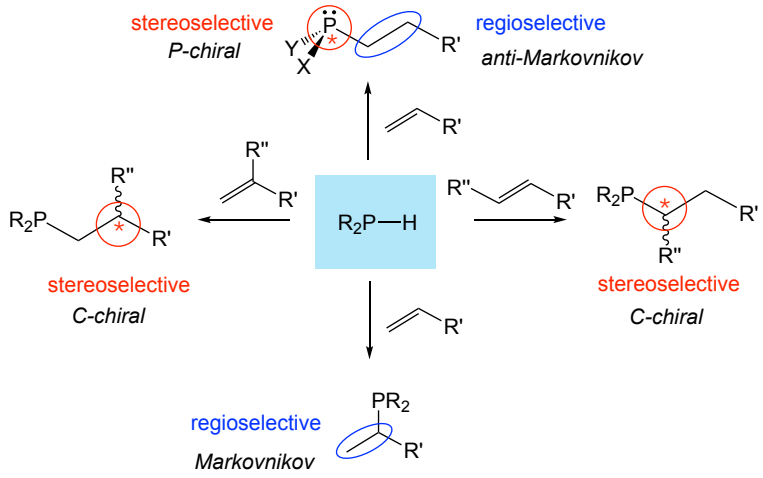

Metal-catalyzed phosphination (cross-coupling) is an alternative P-C bond-forming technique for preparing phosphines (also chiral phosphines).[46–48] While it is an efficient and effective technique, it does result in salt byproducts, like traditional methods (see Section 1.3.1). Thus, metal-catalyzed phosphination is not included.

1.3.3 P-P bond formation *via* dehydrocoupling

Catalytic dehydrocoupling could provide an alternative and "green" route in forming homonuclear element-element (E–E) or heteronuclear element-element (E–E') bonds (E, E' = B, N, P, Si).[49,50] Dehydrocoupling (Scheme 1.9) occurs when two molecules that have element-hydrogen (E-H or E'-H) bonds undergo a "condensation" reaction, resulting in the formation of the E-E (or E-E') bond and dihydrogen (H_2) as the only byproduct.

Scheme 1.9 Homo- or hetero-dehydrocoupling (E, E' = B, N, P, Si).

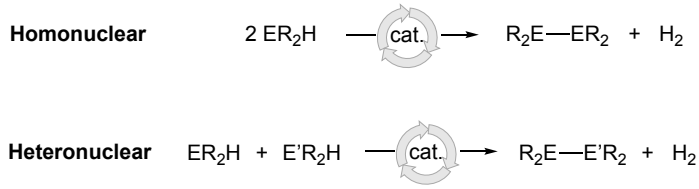

Catalytic dehydrocoupling of P-H precursors has received less attention than dehydrocoupling of other E-H compounds, probably due to difficulty activating the P-H bond at the catalyst.[51] Transition metal catalysts (Zr,[52–54] Rh,[55–57] Fe[58,59] and Co[60]) have been used to make P-P bonds through catalytic dehydrocoupling of phosphines (Scheme 1.10 blue). In addition, transition metal-free catalysts (e.g. $(Cp^*)_2SnCl_2$,[61,62] $B(p\text{-}C_6F_4H)_3$[63] and $KOBu^t$[64]) and stoichiometric reagents (e.g. lithium chloride carbenoids,[65] bismuth amides,[66] radical initiators[67] and *N*-heterocyclic carbenes[68]) are known for facilitating phosphine dehydrocoupling (Scheme 1.10 purple and green).

Scheme 1.10 Examples of catalysts (transition metals[52,56] and main group molecules[61,64,69]) and reagents[65,68] for P-P bond formation *via* dehydrocoupling of phosphines.

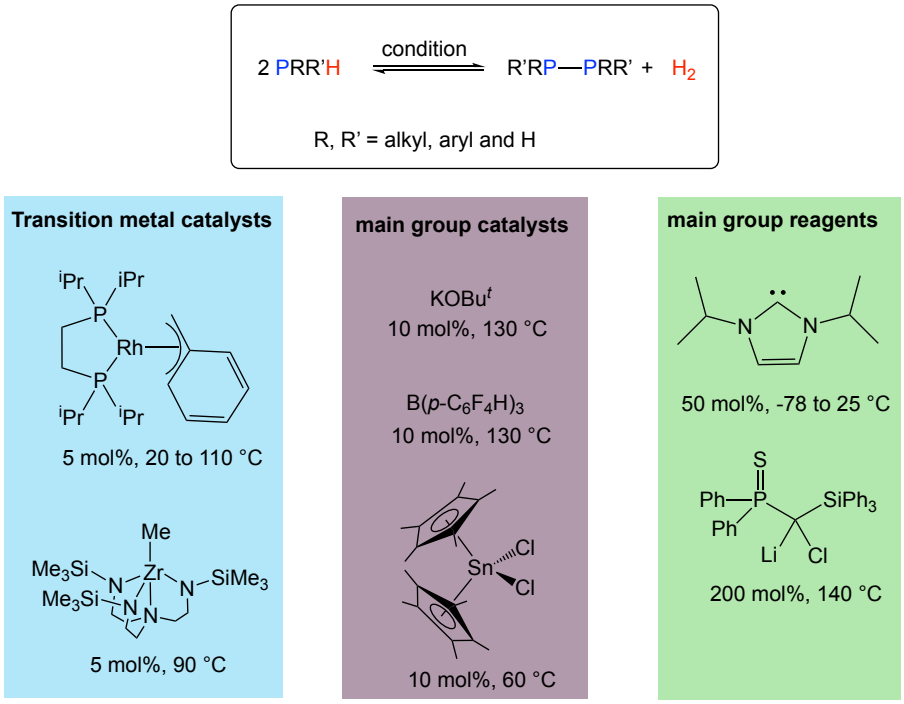

1.4 Metal-catalyzed hydrophosphination

It is worth mentioning that transition metal-catalyzed hydrophosphination has been thoroughly reviewed, emphasizing specific aspects such as stereoselectivity,[29,32,36] mechanisms[38] and challenges.[35] Selective catalysts and a broader substrate scope are

required for metal-catalyzed hydrophosphination to enter the mainstream of synthetic chemistry and become a common synthetic technique. Thus, further development in this field requires novel methodologies (e.g. new catalyst designs) with in-depth mechanistic understanding.

1.4.1 Challenges in metal-catalyzed hydrophosphination

Despite advancements, challenges persist for metal-catalyzed hydrophosphination: selectivity, substrate scope[35] and activity.[70] The issue of selectivity is often divided into three categories: stereoselectivity, regioselectivity and chemoselectivity. Stereoselectivity, the primary driving force for developing metal-catalyzed hydrophosphination, has been achieved using a few catalysts with specific substrates.[29,30,32,36]

Metal-catalyzed hydrophosphination also has a very limited substrate scope. Most reactions include only PPh_2H, which contains a reasonably acidic P-H bond. Using secondary alkylphosphines or primary phosphines as substrates is less common. Many catalysts only work with electron-deficient alkenes or alkynes. Metal-catalyzed hydrophosphination of simple and unactivated alkenes/alkynes remains rare.

In general, metal-catalyzed hydrophosphination suffers from insufficient catalytic activity. The turnover frequencies (TOFs) reported for most cases are often in the tens of h^{-1}.[70] A few examples show the TOFs (h^{-1}) in the hundreds or higher. [70]

1.4.2 Mechanisms of metal-catalyzed hydrophosphination

As described above, an in-depth understanding of fundamental mechanisms is necessary and will guide us to design better metal catalysts for hydrophosphination. The catalytic mechanisms are generally dissected into three steps: P-H activation, P-C bond

formation and C-H bond formation.[38] It is worth noting that some of these steps might be concerted in the catalytic process. In this section, the fundamental steps are illustrated with first-row metal examples because of the extensive use of cobalt (Co) in this thesis. In addition, the use of 3d metals in catalytic hydrophosphination has shown an increasing trend over years (details in Appendix A), so their mechanisms are worth to be highlighted.

P-H bond activation

Metal phosphido (M-PR_2) intermediates are proposed in most metal-catalyzed hydrophosphination reactions.[38] As a result, practically all P-H activation pathways are directed toward forming M-PR_2 species. The formation of M-PR_2 can rely on protonolysis reactions between a phosphine and a high valent metal alkyl or amido complex (Scheme 1.11a),[59,71] deprotonation of metal-coordinated PH_2R or PR_2H by an external base (Scheme 1.11b)[72–74] or oxidative addition of a P-H bond at a low valent metal (Scheme 1.11c)[75,76]

Scheme 1.11 P-H activation mechanisms (left) and selected examples (right). The phosphido lone pair is shown to highlight the nucleophilicity of the M-PR_2 fragment.

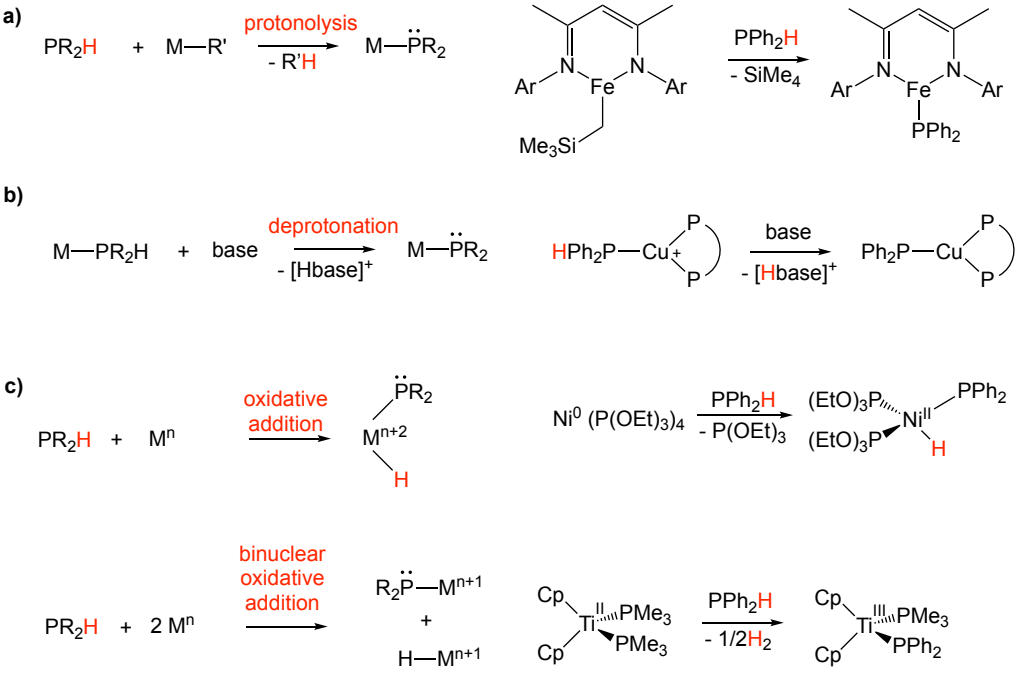

Using an external base is common in metal-catalyzed hydrophosphination. The role of the base varies. In most cases, the external base deprotonates a metal phosphine complex M-PR_2H to generate an active M-PR_2 intermediate (Scheme 1.11c), which is proposed as a catalyst activation step (Scheme 1.12, Role 1). In some specific examples, a base also acts as a "proton shuttle" (Scheme 1.12, Role 2).[73] The base deprotonates a M-PR_2H to give a M-PR_2 initially. The resulting conjugate acid later protonates a M-C bond to regenerate the base and liberate the hydrophosphination product. Additionally, one example exhibits that the deprotonation of a M-PR_2H by a base can form diphosphine and change the oxidation state of the metal (Scheme 1.12, Role 3).[77]

Scheme 1.12 Possible outcomes following the deprotonation with a base.

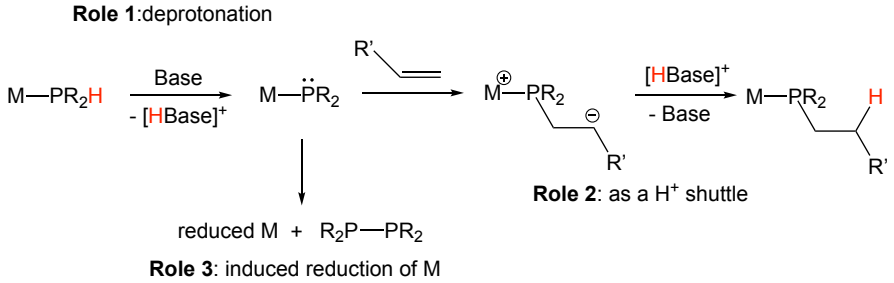

P-C bond formation

A nucleophilic M-PR_2 intermediate can participate in inner-sphere insertion of an alkene/alkyne (Scheme 1.13a)[78,79] or outer-sphere conjugate addition at an activated alkene (Scheme 1.13b top) [80]. The M-PR_2 species can also undergo reductive elimination with an alkyl ligand at the metal to form a P-C bond (Scheme 1.13c).[75]

Some metal catalysts (e.g. Ti[81] and Ni[75,82–84]) were presumed to participate in insertion chemistry, probably because they work for both unactivated and activated alkenes. Conjugate addition of M-PR_2 or PR_2H is unlikely to occur at unactivated alkenes. Thus, a conjugate addition mechanism is proposed for some late metal systems because catalysis only works for activated alkenes.[74,85]

Scheme 1.13 P-C bond formation mechanisms and selected examples.[78–80,87]

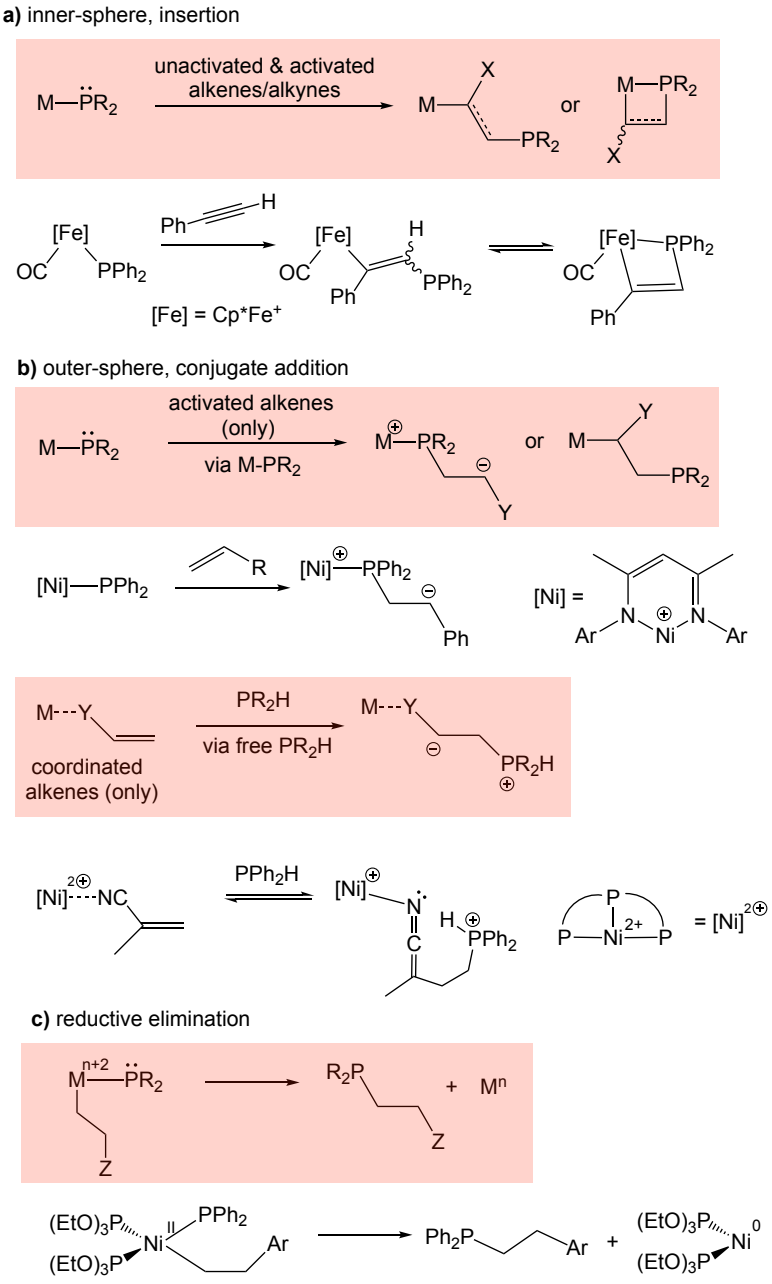

Two types of P-C bond formation by conjugate addition have been proposed (Scheme 1.13b). The first, most common mechanism (Scheme 1.13b top) involves conjugate addition of a metal phosphido ligand at an activated alkene.[73,74,86] An alternative process (Scheme 1.13b bottom), involving the initial formation of a metal-alkene complex initially, has been reported mainly for late transition metals (e.g. Ni,[87] Co[85], Ru[88]). In these cases, a

substrate phosphine undergoes conjugate addition at the coordinated, activated alkene, followed by a proton shift to give a hydrophosphination product bound to the metal complex.

C-H bond formation

Common C-H bond formation mechanisms (again using first-row metal examples) are listed in Scheme 1.14. For most redox-neutral catalytic cycles (i.e. no oxidation state change for the active metal catalyst), a C-H bond can be formed through protonolysis of a metal-alkyl bond with a free[71] or coordinated substrate phosphines[79] (Scheme 1.14a). In some redox-active catalytic cycles involving a metal alkyl hydride intermediate, reductive elimination could occur at the H-M-R'PR_2 complex, resulting in C-H bond formation (Scheme 1.14b).[78] Alternatively, an alkene could insert into a M-H bond in the H-M-PR_2 complex to form a C-H bond (Scheme 1.14c).[78]

Scheme 1.14 C-H bond formation mechanisms and selected examples.[78,79]

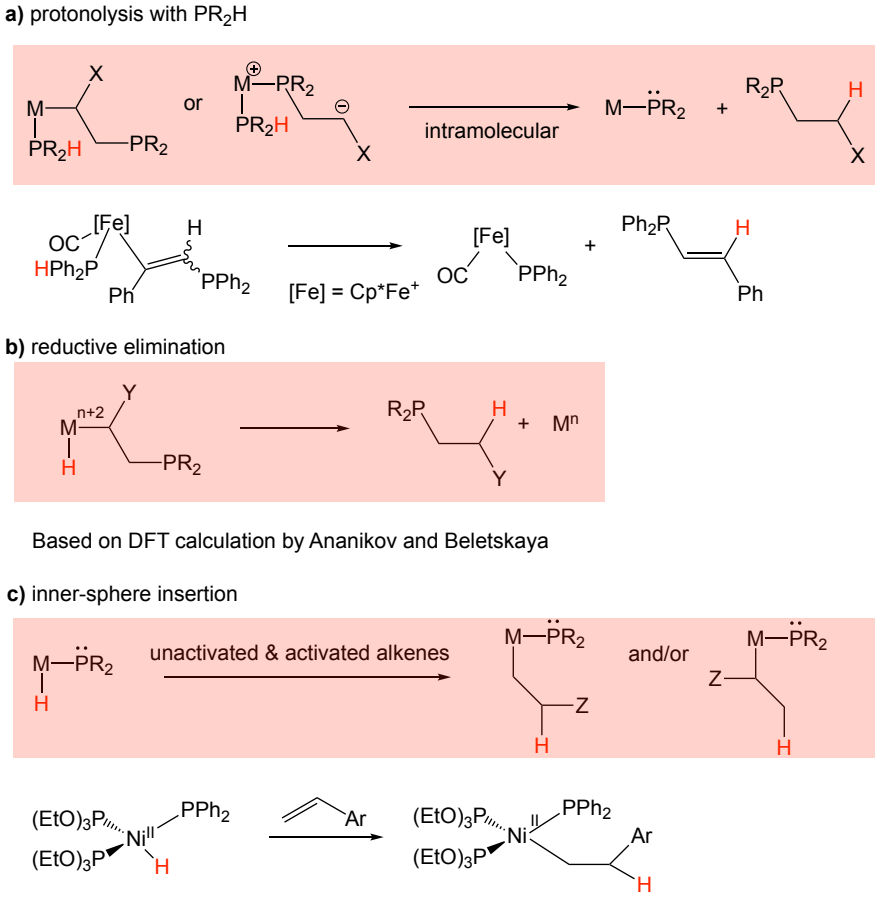

1.5 Metal-catalyzed dehydrocoupling of phosphines

Metal-catalyzed dehydrocoupling of phosphines is generally more efficient and selective than dehydrocoupling using main group catalysts.[49] Also, dehydrocoupling of substrate phosphines could be a side reaction in first-row metal-catalyzed hydrophosphination. Thus, a better understanding of the catalytic dehydrocoupling is required, opening avenues for developing new catalysts for both dehydrocoupling and hydrophosphination.

Dehydrocoupling of phosphines has been reviewed by Harrod,[50] Stephan,[6] Waterman[51,89] and Manners[49]. This section briefly overviews known transition metal

catalysts for dehydrocoupling phosphines, focusing on the activities and proposed mechanisms for these catalysts.

1.5.1 Activity of metal-catalyzed dehydrocoupling

The activity for catalytic dehydrocoupling of phosphines is generally low, even with a transition metal catalyst and at high temperatures (Appendix A). The range of activity for the reported dehydrocoupling reactions of PPh_2H and $PPhH_2$ involving transition metals is TOF = 0.06–2.3 h^{-1} (Appendix A). As shown in Appendix A, most catalytic reactions do not give full conversion. Recently, Manners and coworkers demonstrated the thermodynamic limitation of this condensation reaction, which could be the main reason for the low activity.[64] According to their recently reported computational study, the direct dehydrocoupling of PPh_2H to Ph_2P-PPh_2 and H_2 is endergonic by 2.64 kcal/mol; the thermodynamic equilibrium lies heavily toward the side of PPh_2H. See Appendix A for more details.

1.5.2 Mechanisms of metal-catalyzed dehydrocoupling

This section focuses on the mechanisms of metal-catalyzed dehydrocoupling of phosphines to form diphosphine products. Notably, dehydrocoupling of phosphines can also yield polyphosphines (e.g. $(PR)_n$). While the dehydrocoupling reactions generating diphosphines and polyphosphines may have the same intermediates, mechanisms of extending P-P bonded chains are more complicated than those for diphosphines. Thus, the mechanisms of forming polyphosphines are not included here.

The proposed mechanisms of metal-catalyzed dehydrocoupling typically include metal phosphido (M-PR_2) intermediates, which are also intermediates in catalytic

hydrophosphination as described above. This explains why hydrophosphination and dehydrocoupling can be competing reactions. For catalytic dehydrocoupling, M-PR_2 complexes are often formed by similar P-H activation mechanisms to those described above for catalytic hydrophosphination. The resulting M-PR_2 forms a P-P bond with an additional phosphido ligand at the metal or a substrate phosphine.

P-H bond activation

P-H activation mechanisms of metal-catalyzed dehydrocoupling are similar to those of hydrophosphination (Scheme 1.11). Protonolysis reactions (Scheme 1.15a) have been proposed for Zr and Ti.[52,90] Oxidative addition mechanisms (Scheme 1.15b) have been mainly proposed for dehydrocoupling reactions catalyzed by Rh.[55]

Scheme 1.15 P-H activation mechanisms and selected examples.[52,55]

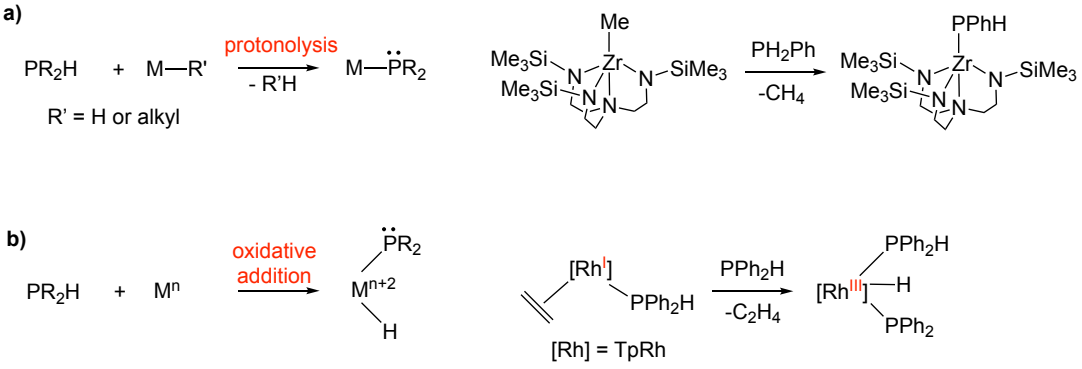

P-P bond formation

σ-Bond metathesis has been implicated in forming P-P bonds (Scheme 1.16a),[89] which appears to be favourable for early transition metal catalysts. Late transition metal phosphido complexes, formed through the oxidative addition (Scheme 1.15b), undergo reductive elimination, resulting in P-P bonds (Scheme 1.16b). Indeed, the reductive elimination pathway is proposed for only a few Rh-catalyzed reactions.[55–57] Preliminary investigations on Fe catalysts established that dehydrocoupling of phosphines could occur

through a radical-mediated process.[58] Terminal phosphido Fe(II) complexes may serve as generators of unidentified phosphinyl radicals in this scenario (Scheme 1.16c). The P-P bond might be generated *via* metal-mediated coupling of phosphinyl radicals.

Scheme 1.16 P-P bond formation mechanisms and selected examples. [56,58,89]

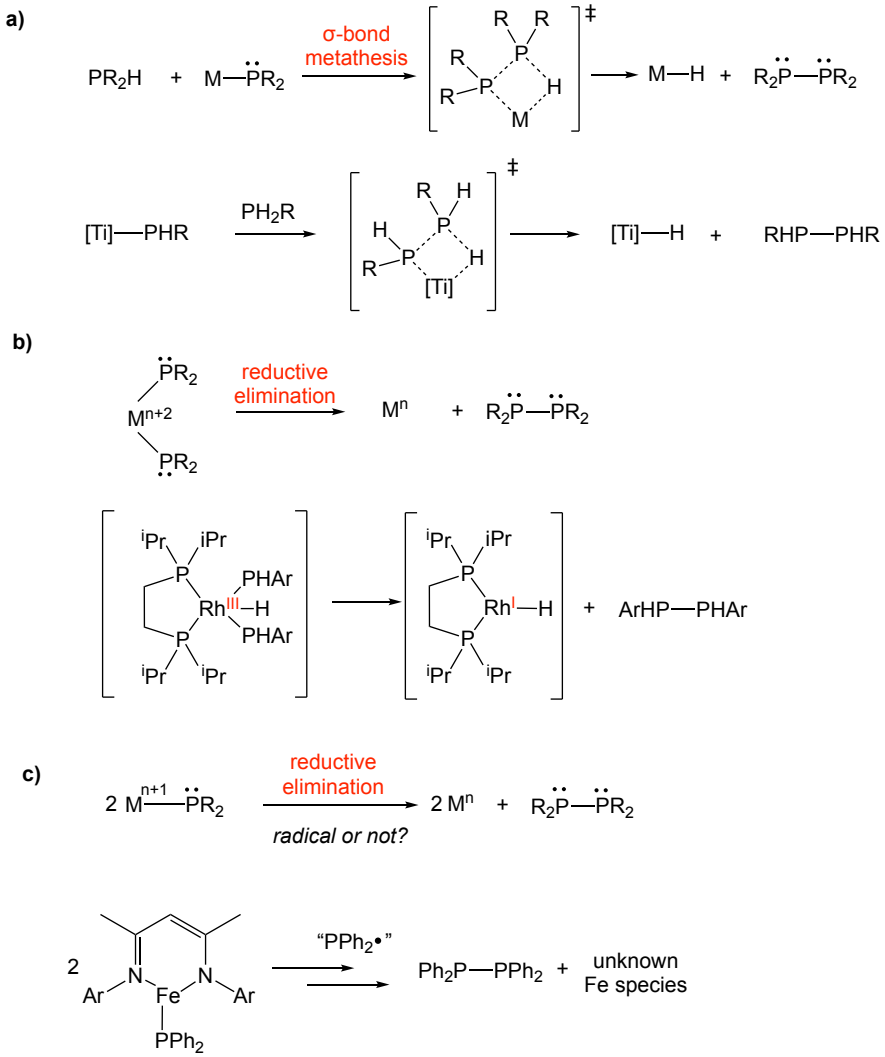

H-H bond formation

Metal-mediated dehydrogenative coupling of E-H bonds to form H_2 is a much more well-established field than dehydrocoupling of just phosphines. Thus, the details are not discussed here. Generally, H-H bond formation can simply be reductive elimination of a metal hydride (M-H) complex (Scheme 1.17a).[55,56] Indeed, protonolysis reactions of a M-

H bond, primarily *via* σ-bond metathesis, are mainly proposed to form H_2 in metal-catalyzed dehydrocoupling (Scheme 1.17b).[52,90]

Scheme 1.17 H-H bond formation mechanisms.

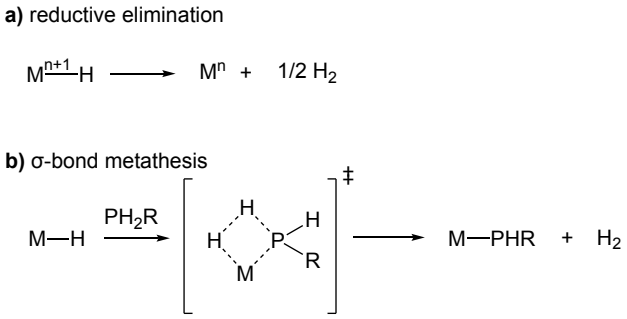

1.6 Scope of the thesis

The original goal of my studies was to overcome difficulties in metal-catalyzed hydrophosphination by developing new transition metal catalysts. I aimed to solve problems associated with low activities and a limited substrate scope in metal-catalyzed hydrophosphination, by using Cp*Ru and Cp*Co complexes. Additionally, I developed a metal-catalyzed dehydrocoupling system using the Cp*Co catalysts, intrigued by the observation that Co-catalyzed hydrophosphination produced a diphosphine byproduct. Furthermore, I demonstrated a unique interaction and activation of P-H bonds in this Co system, which might aid in designing more catalysts for dehydrocoupling and hydrophosphination through a different mechanism.

Chapter 2 describes the discovery and development of Cp*Ru complexes for catalytic hydrophosphination of activated alkenes with different phosphines. In this study, I designed Cp*Ru phosphido complexes, similar to our previous indenyl Ru complexes, for catalytic hydrophosphination. While the reaction mechanism of the Cp*Ru catalyst is identical to that of the indenyl Ru catalysts,[70] a simple ligand change from indenyl to Cp* leads to a 30-fold increase in hydrophosphination activity, by addressing a slow

substitution step in the indenyl system. Despite its high activity, the Cp*Ru catalyst has a limited specific substrate scope (activated alkenes and diaryl phosphines). This led me to develop a new Cp*M catalyst (Chapters 3 and 4).

Chapter 3 describes the synthesis and characterization of various Cp*Co(III) complexes. According to preliminary investigations, these Co(III) complexes can participate in catalytic hydrophosphination and dehydrocoupling. Besides that, they show interesting interactions with phosphines. Assessing the physical properties and solution behaviour of these Co complexes (especially Co phosphine complexes) helped us lay the groundwork for exploring mechanisms.

In Chapter 4, I present the hydrophosphination using Cp*Co complexes as catalysts. Even though the scope of alkenes remains constrained, the Cp*Cp catalyst substantially broadens the substrate scope for phosphines. Based on preliminary mechanistic investigations of this catalytic system, I established that Co-catalyzed hydrophosphination occurs through an outer-sphere mechanism similar to that proposed for our Ru half-sandwich complexes. In addition, I discovered how observed diphosphine formation is related to catalyst activation.

Chapter 5 presents investigations of the Cp*Co complex in catalytic dehydrocoupling of phosphines. This work highlights the critical importance of removing product dihydrogen from the entire process (i.e. shifting a thermodynamic equilibrium toward diphosphine). Additionally, preliminary mechanistic investigations suggest that non-innocent involvements of the Cp* ligand and/or the base as proton shuttles play roles in the formation of H_2. Knowledge of the cooperative participation of Cp* and/or base in this

catalysis may provide new prospects for building catalysts for dehydrocoupling of other E-H molecules.

Chapter 6 demonstrates a novel P-H activation process between the Cp*Co complexes and PPh_2H, which is based on the interesting solution behaviour described in Chapter 3. This new type of P-H activation is distinct from the deprotonation relied on in the hydrophosphination (Chapters 2 and 4) and base-mediated dehydrocoupling reactions (Chapter 5) I have studied. This P-H activation mechanism is also relevant to the "base-free" dehydrocoupling reaction described in Chapter 5.

1.7 References

(1) Corbridge, D. E. C. *Phosphorus 2000: Chemistry, Biochemistry & Technology*; Studies in Inorganic Chemistry; Elsevier, 2000.

(2) Temkin, O. N. *Homogeneous Catalysis with Metal Complexes: Kinetic Aspects and Mechanisms*; Plenum Publishing Corporation: New York, 2012.

(3) Grabulosa, A. P-Stereogenic Ligands in Enantioselective Catalysis. *RSC Catal. Ser.* **2010**, 1–521.

(4) Guo, H.; Fan, Y. C.; Sun, Z.; Wu, Y.; Kwon, O. Phosphine Organocatalysis. *Chem. Rev.* **2018**, *118*, 10049–10293.

(5) Szynkiewicz, N.; Ponikiewski, Ł.; Grubba, R. Symmetrical and Unsymmetrical Diphosphanes with Diversified Alkyl, Aryl, and Amino Substituents. *Dalton Trans.* **2018**, *47*, 16885–16894.

(6) Greenberg, S.; Stephan, D. W. Stoichiometric and Catalytic Activation of P–H and P–P Bonds. *Chem. Soc. Rev.* **2008**, *37*, 1482–1489.

(7) Molitor, S.; Mahler, C.; Gessner, V. H. Synthesis and Solid-State Structures of Gold(i) Complexes of Diphosphines. *New J. Chem.* **2016**, *40*, 6467–6474.

(8) Hirano, K.; Miura, M. Recent Advances in Diphosphination of Alkynes and Alkenes. *Tetrahedron Lett.* **2017**, *58*, 4317–4322.

(9) Wu, L.; Chitnis, S. S.; Jiao, H.; Annibale, V. T.; Manners, I. Non-Metal-Catalyzed Heterodehydrocoupling of Phosphines and Hydrosilanes: Mechanistic Studies of $B(C_6F_5)_3$-Mediated Formation of P-Si Bonds. *J. Am. Chem. Soc.* **2017**, *139*, 16780–16790.

(10) Chitnis, S. S.; Sparkes, H. A.; Annibale, V. T.; Pridmore, N. E.; Oliver, A. M.; Manners, I. Addition of a Cyclophosphine to Nitriles: An Inorganic Click Reaction Featuring Protio, Organo, and Main-Group Catalysis. *Angew. Chem. Int. Ed.* **2017**, *56*, 9536–9540.

(11) Feldmann, K. O.; Weigand, J. J. P-N/P-P Bond Metathesis for the Synthesis of Complex Polyphosphanes. *J. Am. Chem. Soc.* **2012**, *134*, 15443–15456.

(12) Murphy, P. *Organophosphorus Reagents*; Oxford University Press: New York, 2004.

(13) Delacroix, O.; Gaumont, A. Hydrophosphination of Unactivated Alkenes, Dienes and Alkynes: A Versatile and Valuable Approach for the Synthesis of Phosphines. *Curr. Org. Chem.* **2005**, *9*, 1851–1882.

(14) Pellon, J. Reversibility in the Reaction of Phosphinyl Radicals with Olefins. *J. Am. Chem. Soc.* **1961**, *83*, 1915–1916.

(15) Leca, D.; Fensterbank, L.; Lacôte, E.; Malacria, M. Recent Advances in the Use of Phosphorus-Centered Radicals in Organic Chemistry. *Chem. Soc. Rev.* **2005**, *34*, 858–865.

(16) Daeffler, C. S.; Grubbs, R. H. Radical-Mediated Anti-Markovnikov Hydrophosphonation of Olefins. *Org. Lett.* **2011**, *13*, 6429–6431.

(17) Trofimov, B. A.; Malysheva, S. F.; Parshina, L. N.; Gusarova, N. K.; Belogorlova, N. A. Metal-Free Hydrophosphanation of 1-Vinylimidazoles with Secondary Phosphanes: A Straightforward Atom-Economic Route to Tertiary Phosphanes with Imidazolyl Substituents. *Synlett* **2011**, *2011*, 94–98.

(18) Arbuzova, S. N.; Gusarova, N. K.; Trofimov, B. A. Nucleophilic and Free-Radical Additions of Phosphines and Phosphine Chalcogenides to Alkenes and Alkynes. *Arkivoc* **2006**, *2006*, 12–36.

(19) Stiles, A. R.; Rust, F. F.; Vaughan, W. E. The Preparation of Organo-Phosphines by the Addition of Phosphine to Unsaturated Compounds. *J. Am. Chem. Soc.* **1952**, *74*, 3282–3284.

(20) Jiménez, M. V.; Pérez-Torrente, J. J.; Bartolomé, M. I.; Oro, L. A. Convenient Methods for the Synthesis of a Library of Hemilabile Phosphines. *Synthesis.* **2009**, *2009*, 1916–1922.

(21) Dombek, B. D. Acid-Catalyzed Addition of Secondary Phosphines to Vinyl Ethers. *J. Org. Chem.* **1978**, *43*, 3408–3409.

(22) Coles, N. T.; Mahon, M. F.; Webster, R. L. 1,1-Diphosphines and Divinylphosphines via Base Catalyzed Hydrophosphination. *Chem. Commun.* **2018**, *54*, 10443–10446.

(23) Perrier, A.; Comte, V.; Moïse, C.; Richard, P.; Le Gendre, P. NBuLi-Mediated Hydrophosphination: A Simple Route to Valuable Organophosphorus Compounds. *Eur. J. Org. Chem.* **2010**, *2010*, 1562–1568.

(24) Bunlaksananusorn, T.; Knochel, P. T-BuOK-Mediated Hydrophosphination of Functionalized Alkenes: A Novel Synthesis of Chiral P,N- and P,P-Ligands. *J. Org. Chem.* **2004**, *69*, 4595–4601.

(25) Sarazin, Y.; Carpentier, J. F. Molecular S-Block Catalysts for Alkene Hydrophosphination and Related Reactions. In *Early Main Group Metal Catalysis: Concepts and Reactions*; Wiley, 2019; pp 93–121.

(26) Krieck, S.; Westerhausen, M. H-N and H-P Bond Addition to Alkynes and Heterocumulenes. In *Early Main Group Metal Catalysis: Concepts and Reactions*; Wiley, 2019; pp 123–149.

(27) Sarazin, Y.; Carpentier, J. F. Calcium, Strontium and Barium Homogeneous Catalysts for Fine Chemicals Synthesis. *Chem. Rec.* **2016**, *16*, 2482–2505.

(28) Hill, M. S.; Liptrot, D. J.; Weetman, C. Alkaline Earths as Main Group Reagents in Molecular Catalysis. *Chem. Soc. Rev.* **2016**, *45*, 972–988.

(29) Seah, J. W. K.; Teo, R. H. X.; Leung, P. H. Organometallic Chemistry and Application of Palladacycles in Asymmetric Hydrophosphination Reactions. *Dalton Trans.* **2021**, *50*, 16909–16915.

(30) Glueck, D. S. Metal-Catalyzed P-C Bond Formation via P-H Oxidative Addition: Fundamentals and Recent Advances. *J. Org. Chem.* **2020**, *85*, 14276–14285.

(31) Wei, D.; Darcel, C. Organophosphorus and Iron Catalysis: Good Partners for Hydrometalation of Olefins and Alkynes. *J. Org. Chem.* **2020**, *85*, 14298–14306.

(32) Liu, J. K.; Gong, J. F.; Song, M. P. Chiral Palladium Pincer Complexes for Asymmetric Catalytic Reactions. *Org. Biomol. Chem.* **2019**, *17*, 6069–6098.

(33) Webster, R. L. β-Diketiminate Complexes of the First Row Transition Metals: Applications in Catalysis. *Dalton Trans.* **2017**, *46*, 4483–4498.

(34) Trifonov, A. A.; Basalov, I. V.; Kissel, A. A. Use of Organolanthanides in the Catalytic Intermolecular Hydrophosphination and Hydroamination of Multiple C-C Bonds. *Dalton Trans.* **2016**, *45*, 19172–19193.

(35) Bange, C. A.; Waterman, R. Challenges in Catalytic Hydrophosphination. *Chem. – Eur. J.* **2016**, *22*, 12598–12605.

(36) Pullarkat, S. A. Recent Progress in Palladium-Catalyzed Asymmetric Hydrophos-Phination. *Synthesis* **2016**, *48*, 493–503.

(37) Koshti, V.; Gaikwad, S.; Chikkali, S. H. Contemporary Avenues in Catalytic PH Bond Addition Reaction: A Case Study of Hydrophosphination. *Coord. Chem. Rev.* **2014**, *265*, 52–73.

(38) Rosenberg, L. Mechanisms of Metal-Catalyzed Hydrophosphination of Alkenes and Alkynes. *ACS Catal.* **2013**, *3*, 2845–2855.

(39) Bissessar, D.; Egly, J.; Achard, T.; Steffanut, P.; Bellemin-Laponnaz, S. Catalyst-Free Hydrophosphination of Alkenes in Presence of 2-Methyltetrahydrofuran: A Green and Easy Access to a Wide Range of Tertiary Phosphines. *RSC Adv.* **2019**, *9*, 27250–27256.

(40) Gusarova, N. K.; Chernysheva, N. A.; Trofimov, B. A. Catalyst- and Solvent-Free Addition of the P-H Species to Alkenes and Alkynes: A Green Methodology for C-P Bond Formation. *Synthesis* **2017**, *49*, 4783–4807.

(41) Moglie, Y.; González-Soria, M. J.; Martín-García, I.; Radivoy, G.; Alonso, F. Catalyst- and Solvent-Free Hydrophosphination and Multicomponent Hydrothiophosphination of Alkenes and Alkynes. *Green Chem.* **2016**, *18*, 4896–4907.

(42) Alonso, F.; Moglie, Y.; Radivoy, G.; Yus, M. Solvent- and Catalyst-Free Regioselective Hydrophosphanation of Alkenes. *Green Chem.* **2012**, *14*, 2699–2702.

(43) Haynes, W. M. *CRC Handbook of Chemistry and Physics, 94th Edition*; 100 Key Points; CRC Press, 2016.

(44) Trofimov, B. A.; Gusarova, N. K.; Sukhov, B. G.; Malysheva, S. F.; Tarasova, O. A.; Belogorlova, N. A.; Maximova, M. A.; Tunik, S. P. Atom-Economic, Solvent-Free, High Yield Synthesis of 2-(Pyrrol-1-Yl) Propyldiorganylphosphines. *Synthesis* **2005**, *2005*, 965–970.

(45) Rauhut, M. M.; Currier, H. A.; Semsel, A. M.; Wystrach, V. P. The Free Radical Addition of Phosphines to Unsaturated Compounds. *J. Org. Chem.* **1961**, *26*, 5138–5145.

(46) Glueck, D. S. Catalytic Asymmetric Synthesis of P-Stereogenic Phosphines: Beyond Precious Metals. *Synlett* **2020**, *32*, 875–884.

(47) Tappe, F. M. J.; Trepohl, V. T.; Oestreich, M. Transition-Metal-Catalyzed C-P Cross-Coupling Reactions. *Synthesis* **2010**, *2010*, 3037–3062.

(48) Glueck, D. S. Recent Advances in Metal-Catalyzed C-P Bond Formation. *Top. Organomet. Chem.* **2010**, *31*, 65–100.

(49) Leitao, E. M.; Jurca, T.; Manners, I. Catalysis in Service of Main Group Chemistry Offers a Versatile Approach to P-Block Molecules and Materials. *Nat. Chem.* **2013**, *5*, 817–829.

(50) Gauvin, F.; Harrod, J. F.; Woo, H. G. Catalytic Dehydrocoupling: A General Strategy for the Formation of Element-Element Bonds. *Adv. Organomet. Chem.* **1998**, *42*, 363–405.

(51) Waterman, R. Dehydrogenative Bond-Forming Catalysis Involving Phosphines: Updated Through 2010. *Curr. Org. Chem.* **2012**, *16*, 1313–1331.

(52) Waterman, R. Selective Dehydrocoupling of Phosphines by Triamidoamine Zirconium Catalysts. *Organometallics* **2007**, *26*, 2492–2494.

(53) Masuda, J. D.; Hoskin, A. J.; Graham, T. W.; Beddie, C.; Fermin, M. C.; Etkin, N.; Stephan, D. W. Catalytic P-H Activation by Ti and Zr Catalysts. *Chem. – Eur. J.* **2006**, *12*, 8696–8707.

(54) Fermin, M. C.; Stephan, D. W. Catalytic Oligomerization of Primary Phosphines by the Anionic Zirconocene Trihydride: $[Cp^*_2ZrH_3]^-$. *J. Am. Chem. Soc.* **1995**, *117*, 12645–12646.

(55) Geer, A. M.; Serrano, Á. L.; De Bruin, B.; Ciriano, M. A.; Tejel, C. Terminal Phosphanido Rhodium Complexes Mediating Catalytic P-P and P-C Bond Formation. *Angew. Chem. Int. Ed.* **2015**, *54*, 472–475.

(56) Han, L. B.; Tilley, T. D. Selective Homo- and Heterodehydrocouplings of Phosphines Catalyzed by Rhodium Phosphido Complexes. *J. Am. Chem. Soc.* **2006**, *128*, 13698–13699.

(57) Böhm, V. P. W.; Brookhart, M. Dehydrocoupling of Phosphanes Catalyzed by a Rhodium(I) Complex. *Angew. Chem. Int. Ed.* **2001**, *40*, 4694–4696.

(58) Kaniewska, K.; Dragulescu-Andrasi, A.; Ponikiewski, Ł.; Pikies, J.; Stoian, S. A.; Grubba, R. Syntheses, Structures and Reactivity of Terminal Phosphido Complexes

of Iron(II) Supported by a β-Diketiminato Ligand. *Eur. J. Inorg. Chem.* **2018**, *2018*, 4298–4308.

(59) King, A. K.; Buchard, A.; Mahon, M. F.; Webster, R. L. Facile, Catalytic Dehydrocoupling of Phosphines Using β-Diketiminate Iron(II) Complexes. *Chem. – Eur. J.* **2015**, *21*, 15960–15963.

(60) Wang, D.; Chen, Q.; Leng, X.; Deng, L. Reactions of Low-Coordinate Cobalt(0)-N-Heterocyclic Carbene Complexes with Primary Aryl Phosphines. *Inorg. Chem.* **2018**, *57*, 15600–15609.

(61) Erickson, K. A.; Dixon, L. S. H.; Wright, D. S.; Waterman, R. Exploration of Tin-Catalyzed Phosphine Dehydrocoupling: Catalyst Effects and Observation of Tin-Catalyzed Hydrophosphination. *Inorg. Chim. Acta* **2014**, *422*, 141–145.

(62) Naseri, V.; Less, R. J.; Mulvey, R. E.; McPartlin, M.; Wright, D. S. Stoichiometric and Catalytic Sn-Mediated Dehydrocoupling of Primary Phosphines. *Chem. Commun.* **2010**, *46*, 5000–5002.

(63) Dobrovetsky, R.; Takeuchi, K.; Stephan, D. W. Metal-Free Lewis Acid Mediated Dehydrocoupling of Phosphines and Concurrent Hydrogenation. *Chem. Commun.* **2015**, *51*, 2396–2398.

(64) Wu, L.; Annibale, V. T.; Jiao, H.; Brookfield, A.; Collison, D.; Manners, I. Homo- and Heterodehydrocoupling of Phosphines Mediated by Alkali Metal Catalysts. *Nat. Commun.* **2019**, *10*, 2786.

(65) Molitor, S.; Becker, J.; Gessner, V. H. Selective Dehydrocoupling of Phosphines by Lithium Chloride Carbenoids. *J. Am. Chem. Soc.* **2014**, *136*, 15517–15520.

(66) Oberdorf, K.; Hanft, A.; Ramler, J.; Krummenacher, I.; Bickelhaupt, F. M.; Poater, J.; Lichtenberg, C. Bismuth Amides Mediate Facile and Highly Selective Pn–Pn Radical-Coupling Reactions (Pn=N, P, As). *Angew. Chem. Int. Ed.* **2021**, *60*, 6441–6445.

(67) Baker, R. J.; Hashem, E. A Study of the Reactivity of Secondary Phosphanes with Radical Sources: A New Dehydrocoupling Reaction. *Helv. Chim. Acta* **2010**, *93*, 1081–1085.

(68) Schneider, H.; Schmidt, D.; Radius, U. The Reductive P-P Coupling of Primary and Secondary Phosphines Mediated by N-Heterocyclic Carbenes. *Chem. Commun.* **2015**, *51*, 10138–10141.

(69) Dobrovetsky, R.; Takeuchi, K.; Stephan, D. W. Metal-Free Lewis Acid Mediated Dehydrocoupling of Phosphines and Concurrent Hydrogenation. *Chem. Commun.* **2015**, *51*, 2396–2398.

(70) Belli, R. G.; Yang, J.; Bahena, E. N.; McDonald, R.; Rosenberg, L. Mechanism and Catalyst Design in Ru-Catalyzed Alkene Hydrophosphination. *ACS Catal.* **2022**, *12*, 5247–5262.

(71) King, A. K.; Gallagher, K. J.; Mahon, M. F.; Webster, R. L. Markovnikov versus Anti-Markovnikov Hydrophosphination: Divergent Reactivity Using an Iron(II) β-Diketiminate Pre-Catalyst. *Chem. – Eur. J.* **2017**, *23*, 9039–9043.

(72) Pérez, J. M.; Postolache, R.; Castiñeira Reis, M.; Sinnema, E. G.; Vargová, D.; De Vries, F.; Otten, E.; Ge, L.; Harutyunyan, S. R. Manganese(I)-Catalyzed H-P Bond Activation via Metal-Ligand Cooperation. *J. Am. Chem. Soc.* **2021**, *143*, 20071–20076.

(73) Yue, W.; Xiao, J.; Zhang, S.; Yin, L. Rapid Synthesis of Chiral 1,2-Bisphosphine Derivatives through Copper(I)-Catalyzed Asymmetric Conjugate Hydrophosphination. *Angew. Chem. Int. Ed.* **2020**, *59*, 7057–7062.

(74) Li, Y. B.; Tian, H.; Yin, L. Copper(I)-Catalyzed Asymmetric 1,4-Conjugate Hydrophosphination of α,β-Unsaturated Amides. *J. Am. Chem. Soc.* **2020**, *142*, 20098–20106.

(75) Kazankova, M. A.; Shulyupin, M. O.; Borisenko, A. A.; Beletskaya, I. P. Synthesis of Alkyl(Diphenyl)Phosphines by Hydrophosphination of Vinylarenes Catalyzed by Transition Metal Complexes. *Russ. J. Org. Chem.* **2002**, *38*, 1479–1484.

(76) Perrier, A.; Comte, V.; Moïse, C.; Le Gendre, P. First Titanium-Catalyzed 1,4-Hydrophosphination of 1,3-Dienes. *Chem. – Eur. J.* **2010**, *16*, 64–67.

(77) Yuan, J.; Zhu, L.; Zhang, J.; Li, J.; Cui, C. Sequential Addition of Phosphine to Alkynes for the Selective Synthesis of 1,2-Diphosphinoethanes under Catalysis. Well-Defined NHC-Copper Phosphides vs in Situ $CuCl_2$/NHC Catalyst. *Organometallics* **2017**, *36*, 455–459.

(78) Ananikov, V. P.; Beletskaya, I. P. Alkyne Insertion into the M-P and M-H Bonds (M=Pd, Ni, Pt, and Rh): A Theoretical Mechanistic Study of the C-P and C-H Bond-Formation Steps. *Chem. Asian J.* **2011**, *6*, 1423–1430.

(79) Itazaki, M.; Katsube, S.; Kamitani, M.; Nakazawa, H. Synthesis of Vinylphosphines and Unsymmetric Diphosphines: Iron-Catalyzed Selective Hydrophosphination Reaction of Alkynes and Vinylphosphines with Secondary Phosphines. *Chem. Commun.* **2016**, *52*, 3163–3166.

(80) Webster, R. L. Room Temperature Ni(II) Catalyzed Hydrophosphination and Cyclotrimerization of Alkynes. *Inorganics* **2018**, *6*, 120.

(81) Zhao, G.; Basuli, F.; Kilgore, U. J.; Fan, H.; Aneetha, H.; Huffman, J. C.; Wu, G.; Mindiola, D. J. Neutral and Zwitterionic Low-Coordinate Titanium Complexes Bearing the Terminal Phosphinidene Functionality. Structural, Spectroscopic, Theoretical, and Catalytic Studies Addressing the Ti-P Multiple Bond. *J. Am. Chem. Soc.* **2006**, *128*, 13575–13585.

(82) Shulyupin, M. O.; Kazankova, M. A.; Beletskaya, I. P. Catalytic Hydrophosphination of Styrenes. *Org. Lett.* **2002**, *4*, 761–763.

(83) Kazankova, M. A.; Shulyupin, M. O.; Beletskaya, I. P. Catalytic Hydrophosphination of Alkenylalkyl Ethers. *Synlett* **2003**, No. 14, 2155–2158.

(84) Kazankova, M. A.; Efimova, I. V.; Kochetkov, A. N.; Afanas'ev, V. V.; Beletskaya, I. P.; Dixneuf, P. H. New Approach to Vinylphosphines Based on Pd- and Ni-Catalyzed Diphenylphosphine Addition to Alkynes. *Synlett* **2001**, *2001*, 497–500.

(85) Nolla-Saltiel, R.; Geer, A. M.; Taylor, L. J.; Churchill, O.; Davies, E. S.; Lewis, W.; Blake, A. J.; Kays, D. L. Hydrophosphination of Activated Alkenes by a Cobalt(I) Pincer Complex. *Adv. Synth. Catal.* **2020**, *362*, 3148–3157.

(86) Yan, J.; Wang, Y. B.; Hou, S.; Shi, L.; Zhu, X.; Hao, X. Q.; Song, M. P. NCC Pincer Ni (II) Complexes Catalyzed Hydrophosphination of Nitroalkenes with Diphenylphosphine. *Appl. Organomet. Chem.* **2020**, *34*, e5954.

(87) Sadow, A. D.; Togni, A. Enantioselective Addition of Secondary Phosphines to Methacrylonitrile: Catalysis and Mechanism. *J. Am. Chem. Soc.* **2005**, *127*, 17012–17024.

(88) Jérôme, F.; Monnier, F.; Lawicka, H.; Dérien, S.; Dixneuf, P. H. Ruthenium Catalyzed Regioselective Hydrophosphination of Propargyl Alcohols. *Chem. Commun.* **2003**, No. 6, 696–697.

(89) Waterman, R. Mechanisms of Metal-Catalyzed Dehydrocoupling Reactions. *Chem. Soc. Rev.* **2013**, *42*, 5629–5641.

(90) Xin, S.; Woo, H. G.; Harrod, J. F.; Samuel, E.; Lebuis, A. M. Synthesis and Crystal Structure of Some Novel Titanocene Phosphido Compounds by P-H Activation in the Presence of Hydrosilanes. *J. Am. Chem. Soc.* **1997**, *119*, 5307–5313.

2. Investigation of Cp* Ru-catalyzed hydrophosphination

In this chapter, I present the development and characterization of Cp*Ru complexes Ru(η^5-Cp*)(PR_2)(PR_2H)$_2$ (**Ru-1**, R = aryl, alkyl) as catalysts for the hydrophosphination of electron-deficient alkenes with secondary phosphines. These Cp*Ru catalysts are compared with our previous indenyl Ru catalysts described in this chapter. The results for **Ru-1a** (R = Ph) presented in this chapter are reproduced with permission from Belli, R. G.; Yang, J.; Bahena, E. N.; McDonald, R.; Rosenberg, L. Mechanism and Catalyst Design in Ru-Catalyzed Alkene Hydrophosphination. *ACS Catal.* **2022**, 12(*9*), 5247–5262.[1] This chapter includes contributions from Roman Belli (a former Ph.D. student), Alexis Kellinghusen and Hayley Parkin (undergraduate honours students).

2.1 Introduction

Roman Belli explored a series of complexes, Ru(η^5-indenyl)(PPh_2)(L)(PPh_3) (L = PPh_2H, CO, PhCN), as catalysts for hydrophosphination.[1] The study elucidates critical aspects of the design of metal catalysts for outer-sphere hydrophosphination relying on conjugate addition (Scheme 2.1). For Ru(η^5-indenyl)(PPh_2)(PPh_2H)(PPh_3), the study demonstrates that a half-sandwich metal system with easily accessible *cis*-coordination sites enables fast, intramolecular carbanion quenching from coordinated substrate phosphines (Scheme 2.1, step B) while concurrently regenerating the essential metal phosphido species (M-PR_2). As described in Chapter 1, this intramolecular C-H bond formation is scarcely reported for metal catalyst systems *via* conjugate addition. However, the relatively slow ligand substitution (step C – turnover-limiting step) limits the catalytic activity, which allows a competing cycle (Scheme 2.1, left) where intermolecular

carbanion quenching is the turnover-limiting step (step E). Additionally, steps E and F could be a concerted proton transfer/ligand substitution. These two competing processes will inevitably have a detrimental effect on the desired stereoselectivity in further studies if we want to use this indenyl Ru system for asymmetric hydrophosphination.

Scheme 2.1 Proposed catalytic cycles for outer-sphere hydrophosphination using Ru(η^5-indenyl)(PPh_2)(PPh_2H)(PPh_3) involving intramolecular and intermolecular proton transfers. [Ru] = indenylRu, L = PPh_3 or $Ph_2P(CH_2CH_2CO_2Bu^t)$, R = CO_2Bu^t.

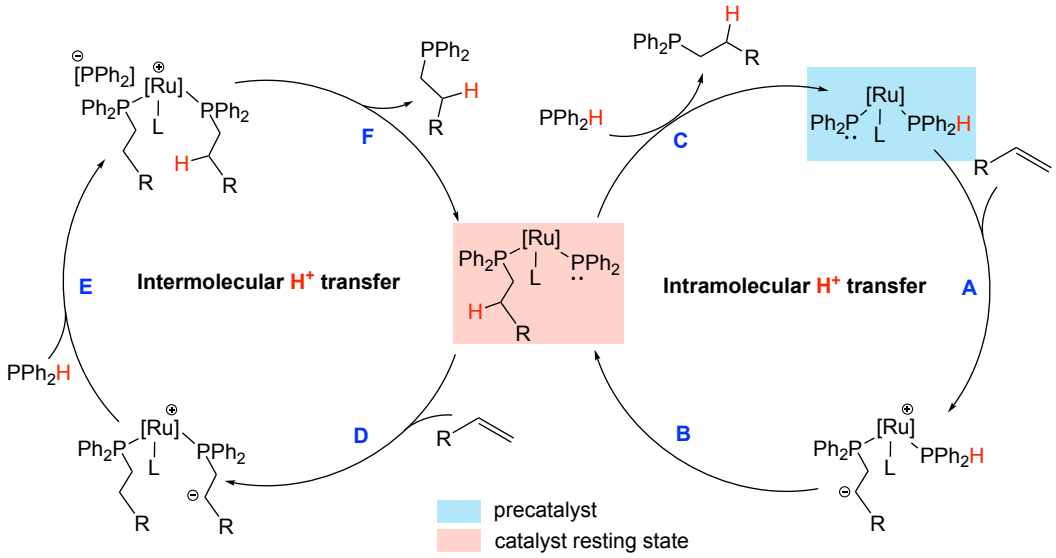

Another takeaway from the previous study is that the nucleophilicity of carbanion-containing intermediates can lead to potential off-cycle reactivities that compete with productive catalysis (i.e. poor chemoselectivity) in a hydrophosphination system relying on conjugate addition. For example, an outer-sphere cycle proposed for the catalyst Ru(η^5-indenyl)(PPh_2)(CO)(PPh_3) relies on intermolecular proton transfer from free PPh_2H (Scheme 2.2, step B – turnover-limiting step). The catalyst resting state is a long-lived zwitterionic intermediate (i.e. carbanion) that can participate in oligomerization to produce P-capped and alkene-terminated oligomers.[3-6]

Scheme 2.2 Proposed catalytic cycle for outer-sphere hydrophosphination using Ru(η^5-indenyl)(PPh_2)(CO)(PPh_3). [Ru] = indenyl Ru, R = CO_2Bu^t. P-capped oligomers are probably terminated by abstracting a proton from PPh_2H.

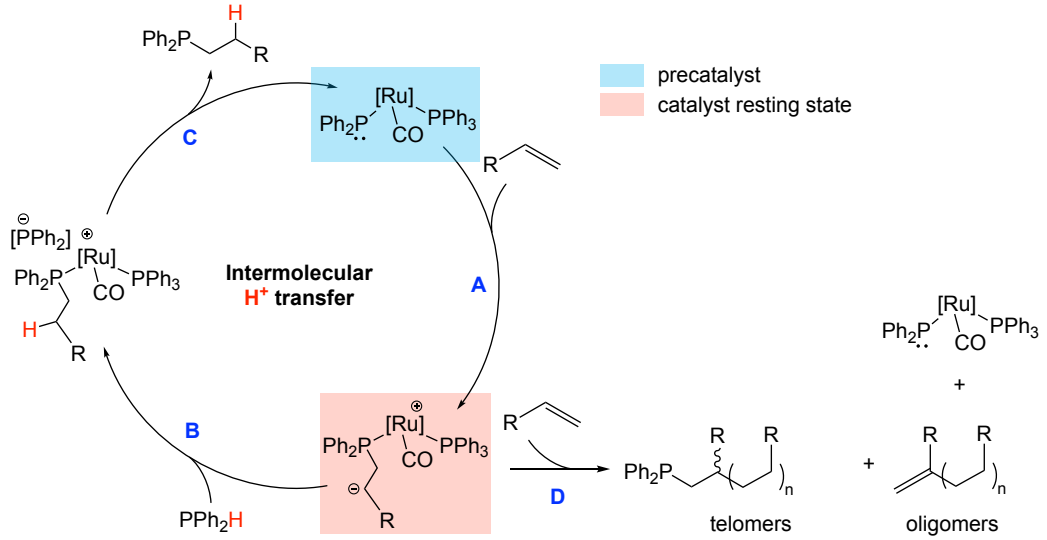

I studied the stoichiometric reactivities of Cp*Ru complexes in my M.Sc. project and wondered what impact of Cp* ligand (compared to indenyl) would have on the hydrophosphination catalysis. According to my previous work,[7] Cp*Ru phosphido complexes Ru(η^5-Cp*)(PR_2)(PPh_3) (R = aryl, alkyl) show increased basicity/nucleophilicity and substitutional lability in comparison to our well-studied analogues Ru(η^5-indenyl)(PR_2)(PPh_3), owing to the higher electron density at the Ru and increased steric crowding caused by the Cp* ligand. The more basic/nucleophilic phosphido ligands at the Cp*Ru complexes should increase the rate of conjugate addition in catalysis. Additionally, the more sterically congested Cp*Ru center should address the issues of slow product substitution associated with Ru(η^5-indenyl)(PPh_2)(PPh_2H)(PPh_3) in catalysis (i.e. two competing processes in Scheme 2.1). However, these coordinatively unsaturated complexes Ru(η^5-Cp*)(PR_2)(PPh_3) may pose an issue for catalytic hydrophosphination due to their rapid PPh_3 orthometallation (Scheme 2.3, left). The orthometallation hinders their isolation and subsequent reactivity. Such orthometallation

also occurs for the Ru(η^5-indenyl)(PR_2)(PPh_3), but it is much faster for the Cp* complexes.[7] This indicates the need for a new Cp*Ru catalyst in which the PPh_3 ligand is removed. Also, the indenyl system highlights the importance of the coordinated PPh_2H, which allows the intramolecular P-H cleavage (Scheme 2.1, step B). My strategy is to make a Cp*Ru complex containing just phosphido and substrate phosphine ligands (i.e. Ru(η^5-Cp*)(PR_2)(PR_2H)$_2$) as a potential catalyst for hydrophosphination.

Scheme 2.3 Undesired orthometallation of Ru(η^5-Cp*)(PR_2)(PPh_3) and the Cp* catalysts described in this chapter.

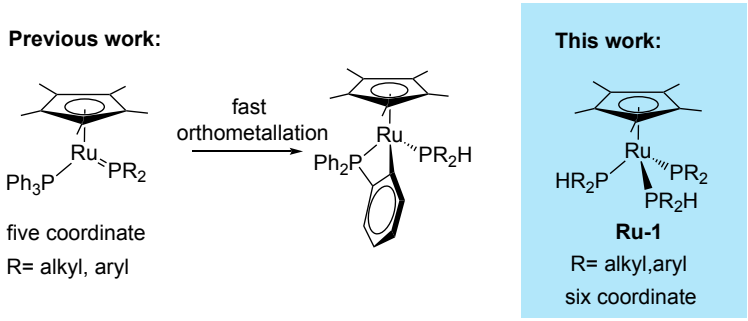

In this chapter, I present the design of new Ru(η^5-Cp*) phosphido complexes Ru(η^5-Cp*)(PR_2)(PR_2H)$_2$ (**Ru-1**, R= alkyl, aryl; Scheme 2.3, right), as catalysts for hydrophosphination. The investigations on **Ru-1** are consistent with the known chemistry of our indenyl catalysts, revealing similar outer-sphere, conjugate addition mechanisms, but show some specific differences.

2.2 Designing Cp*Ru phosphido catalysts for hydrophosphination.

In this section, I present the stepwise generation of new Ru(η^5-Cp*) phosphido complexes, Ru(η^5-Cp*)(PR_2)(PR_2H)$_2$ (**Ru-1(a-c)**, R = Ph (**a**), Tol^p (**b**), Et (**c**)) and Ru(η^5-Cp*)(PCy_2)(PCy_2H) (**Ru-2d**, R = Cy(**d**)) for catalytic hydrophosphination.

2.2.1 Ligand substitution reactions of Ru(η^5-Cp*)Cl(PPh$_3$)$_2$ (Ru-3) to generate Ru(η^5-Cp*)Cl(PR$_2$H)$_2$ (Ru-4)

I used the reaction of Ru(η^5-Cp*)Cl(PPh$_3$)$_2$ (**Ru-3**) with excess PR$_2$H to generate bis(phosphine) complexes Ru(η^5-Cp*)Cl(PR$_2$H)$_2$ (**Ru-4(a-d)**; R = Ph (**a**), Tol^p (**b**), Et (**c**) and Cy (**d**)); Scheme 2.4 and Table 2.1). These substitution reactions occur slowly at RT but much faster at 70 °C. A large excess of PR$_2$H is required for these ligand substitution reactions because it helps shift the equilibrium toward the side of **Ru-4** (Scheme 2.4, left). Except for bulky PCy$_2$H, complex **Ru-4d** is in equilibrium with Ru(η^5-Cp*)Cl(PCy$_2$H)(PPh$_3$) (**Ru-5d**, ~2%) and free PCy$_2$H (~2%), consistent with our previous report for this bulky phosphine (Scheme 2.4).[7] No **Ru-5(a-c)** and corresponding PR$_2$H are observed in the reaction mixtures of **Ru-4(a-c)** that contain smaller phosphines (R = Ph (**a**), Tol^p (**b**), Et (**c**)).

Scheme 2.4 Reactions of **Ru-3** with 10 equiv of PR$_2$H. The equilibrium is only spectroscopically observed for bulky PR$_2$H (R = Cy (d)); ^{31}P δ for **Ru-5d**: 49.6 (d, $^2J_{PP}$ = 40 Hz, PPh$_3$), 48.2 (d, PCy$_2$H).

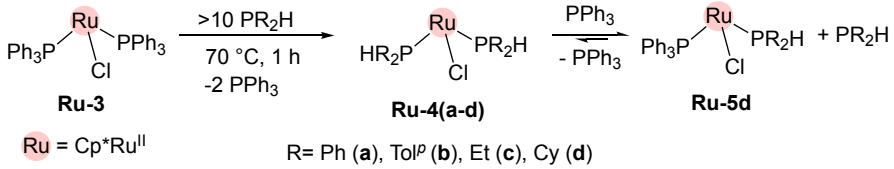

Table 2.1 ^{31}P{^{1}H} NMR (121.55 MHz, C$_6$D$_6$) data for complexes **Ru-4(a-d)**: δ (ppm) (multiplicity).

Complex		PR$_2$H
Ru(η^5-Cp*)Cl(PPh$_2$H)$_2$	**Ru-4a**	36.9 (s)
Ru(η^5-Cp*)Cl(PTol$^p_2$H)$_2$	**Ru-4b**	35.1 (s)
Ru(η^5-Cp*)Cl(PEt$_2$H)$_2$	**Ru-4c**	34.4 (s)
Ru(η^5-Cp*)Cl(PCy$_2$H)$_2$	**Ru-4d**	44.3 (s)

The high solubility of these complexes **Ru-4** in nonpolar solvents (e.g. pentane) makes isolation and purification difficult. For example, isolated **Ru-4a** (R = Ph) always contains free PPh_3 and PPh_2H. Although Lubian and Paz-Sandoval previously reported the purification of this **Ru-4a** using silica chromatography,[8] I have not used this method to isolate pure **Ru-4a**. I decided to generate **Ru-4a** *in situ* and then added a base to the mixture to obtain the desired new Cp*Ru phosphido complex as a potential catalyst (Scheme 2.5).

Scheme 2.5 Strategy of generating the Cp* complex **Ru-1**. Base = $NaN(SiMe_3)_2$ or $KOBu^t$.

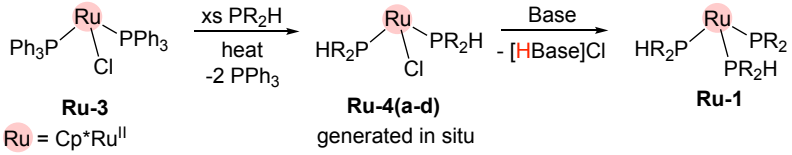

Ru-3

Ru = Cp^*Ru^{II}

Ru-4(a-d)

generated in situ

Ru-1

R= Ph (**a**), Tol^p (**b**), Et (**c**), Cy (**d**)

2.2.2 Attempted isolation of $Ru(\eta^5\text{-}Cp^*)(PPh_2)(PPh_2H)_2$ (Ru-1a)

Following the strategy shown in Scheme 2.5, I attempted to isolate phosphido complex **Ru-1a** (R = Ph (**a**)) with the help of Hayley Parkin. However, this complex is not stable in the absence of excess PPh_2H. We generated yellow $Ru(\eta^5\text{-}Cp^*)Cl(PPh_2H)_2$ (**Ru-4a**, not isolated) *via* ligand substitution of $Ru(\eta^5\text{-}Cp^*)Cl(PPh_3)_2$ (**Ru-3**) with 3 equiv of PPh_2H at 70 °C in toluene. After adding 1 equiv of base $NaN(SiMe_3)_2$ to the reaction mixture, it immediately changed colour from yellow to bright red. Although the NMR of an aliquot at this point revealed complete conversion to $Ru(\eta^5\text{-}Cp^*)(PPh_2)(PPh_2H)_2$ (**Ru-1a**), the complex decomposed to multiple species during workup. Scheme 2.6 illustrates a possible decomposition process: the PPh_3 in the mixture substitutes the PPh_2H ligands at **Ru-1a** to form $Ru(\eta^5\text{-}Cp^*)(PPh_2)(PPh_3)$, which further decomposes to an orthometallated complex.

Scheme 2.6 Attempted synthesis of complex **Ru-1a**, showing possible mechanisms for the undesired orthometallation.

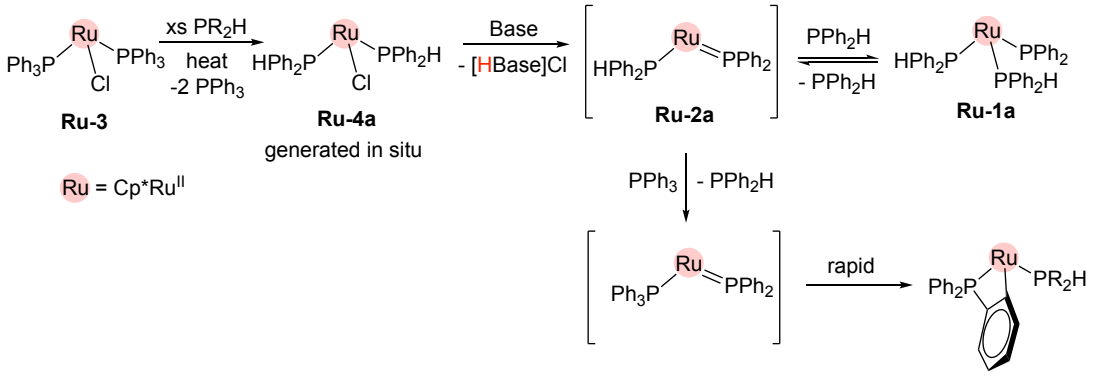

The proposed decomposition process above is consistent with the colour of the isolated mixture: phosphido **Ru-1a** is dark red, but the isolated mixture is orange (same colour of the orthometallated complex). Also, according to the $^{31}P\{^{1}H\}$ NMR spectrum (Figure 2.1), the isolated mixture contains the orthometallated complex (~50%), **Ru-1a** (~45%), free PPh_3, and some unidentified side products (~5%). Due to the challenge of isolating **Ru-1**, I decided to generate **Ru-1** *in situ* for further catalytic studies.

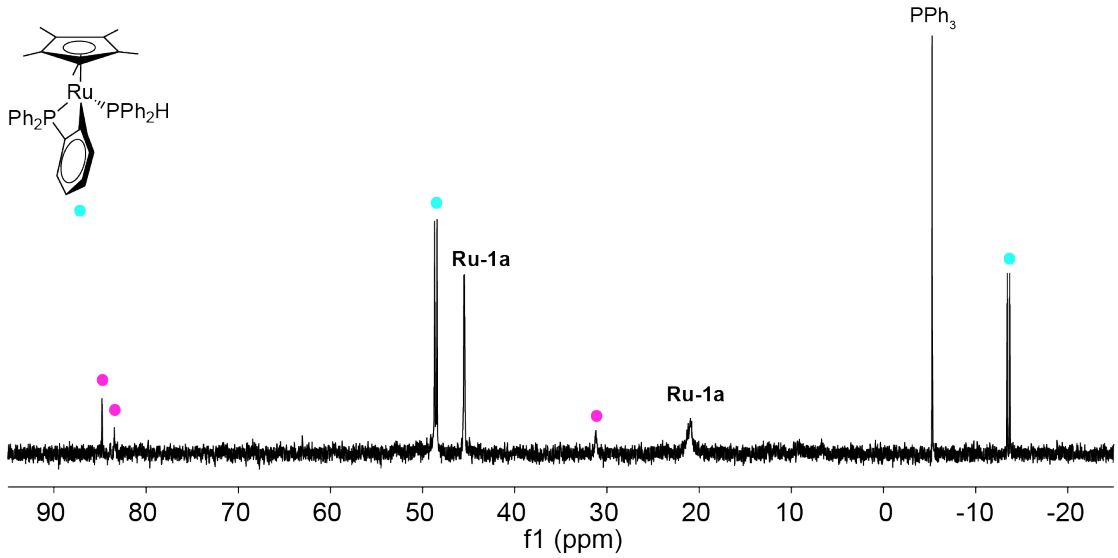

Figure 2.1 $^{31}P\{^{1}H\}$ NMR (121.55 MHz, C_6D_6) spectrum of the isolated mixture, including **Ru-1a**, the orthometallation product (●) and other impurities (●).

2.2.3 Dehydrohalogenation of Ru(η^5-Cp*)Cl(PR$_2$H)$_2$ (Ru-4) generated *in situ*

The reaction of **Ru-4(a-d)** with NaN(SiMe$_3$)$_2$ in the presence of excess PR$_2$H (10 equiv) gives phosphido complexes Ru(η^5-Cp*)(PR$_2$)(PR$_2$H)$_2$ (**Ru-1(a-c)**, R = Ph (**a**), Tol^p (**b**), Et (**c**)) and Ru(η^5-Cp*)(PCy$_2$)(PCy$_2$H) (**Ru-2d**) (Table 2.2).

Table 2.2 ^{31}P{^{1}H} NMR (121.55 MHz, C$_6$D$_6$) data for complexes **Ru-1(a-c)** and **Ru-2d** generated *in situ* in the presence of excess PR$_2$H: δ (ppm) (multiplicity, J or ω$_{1/2}$ in Hz).

Complex		PR$_2$	PR$_2$H
Ru(η^5-Cp*)(PPh$_2$)(PPh$_2$H)$_2$	**Ru-1a**	9.4 (br s, 164)	45.5 (d, 9)
Ru(η^5-Cp*)(PTol$^p_2$)(PTol$^p_2$H)$_2$	**Ru-1b**	11.0 (br s, 160)	44.1 (d, 8)
Ru(η^5-Cp*)(PEt$_2$)(PEt$_2$H)$_2$	**Ru-1c**	22.4 (t, 3)	43.2 (d)
Ru(η^5-Cp*)(PCy$_2$)(PCy$_2$H)	**Ru-2d**	198.8 (d, 65)	62.4 (d)

The size of the PR$_2$H ligand (Scheme 2.7) significantly affects the Ru phosphido species and its NMR behaviour (broad or sharp). According to Tolman cone angles,[9] phosphine ligand size increases in the order: PEt$_2$H (117°) < PPh$_2$H (126°) ≈ PTol$^p_2$H (126°) < PCy$_2$H (142°). No complex Ru(η^5-Cp*)(PCy$_2$)(PCy$_2$H)$_2$ (**Ru-1d**) is observed in the reaction mixture for the bulky PCy$_2$H. For the PR$_2$H of medium size (R = Ph or Tol^p), a significant broadening of the ^{31}P signal due to the PR$_2$ ligands is observed, most likely due to the reversible coordination of PR$_2$H (i.e. pyramidal PR$_2$ complex (δ 0–80 ppm) is in equilibrium with planar PR$_2$ complex (δ 150–200 ppm) and free PR$_2$H). Due to the smallest size of PEt$_2$H, this broadening is not detected in the reaction with PEt$_2$H.

Scheme 2.7 Impacts of the size of PR_2H on **Ru-1** and **Ru-2**.

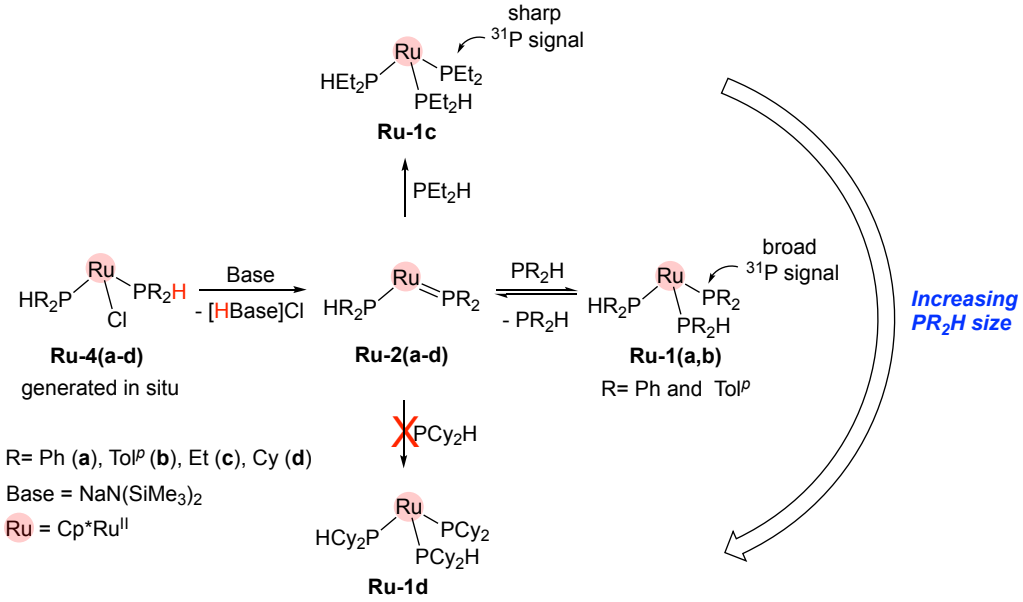

These in-situ-generated complexes **Ru-1(a-c)** and **Ru-2d** are fully characterized by NMR spectroscopy, described in Section 2.5.2. The ^{1}H and $^{13}C\{^{1}H\}$ NMR data for these complexes are summarized in Section 2.5.2, Table 2.3 and 2.4. ^{1}H, $^{31}P\{^{1}H\}$ and $^{13}C\{^{1}H\}$ NMR spectra of these complexes are presented in Appendix B.

2.2.4 Effect of the "free" base in catalytic hydrophosphination

As described above, $NaN(SiMe_3)_2$ is used to generate phosphido complexes **Ru-1(a-c)** and **Ru-2d**. However, this strong base can deprotonate free PPh_2H under catalytic conditions to form a free PPh_2^-. As a result, I conducted control experiments (Figure 2.2) to see if this anion could participate in hydrophosphination in the absence of Ru in catalytic reaction mixtures. If the free PPh_2^- does, I would need to avoid having any excess, unreacted base after the dehydrohalogenation of $Ru(\eta^5\text{-}Cp^*)Cl(PR_2H)_2$ (**Ru-4**).

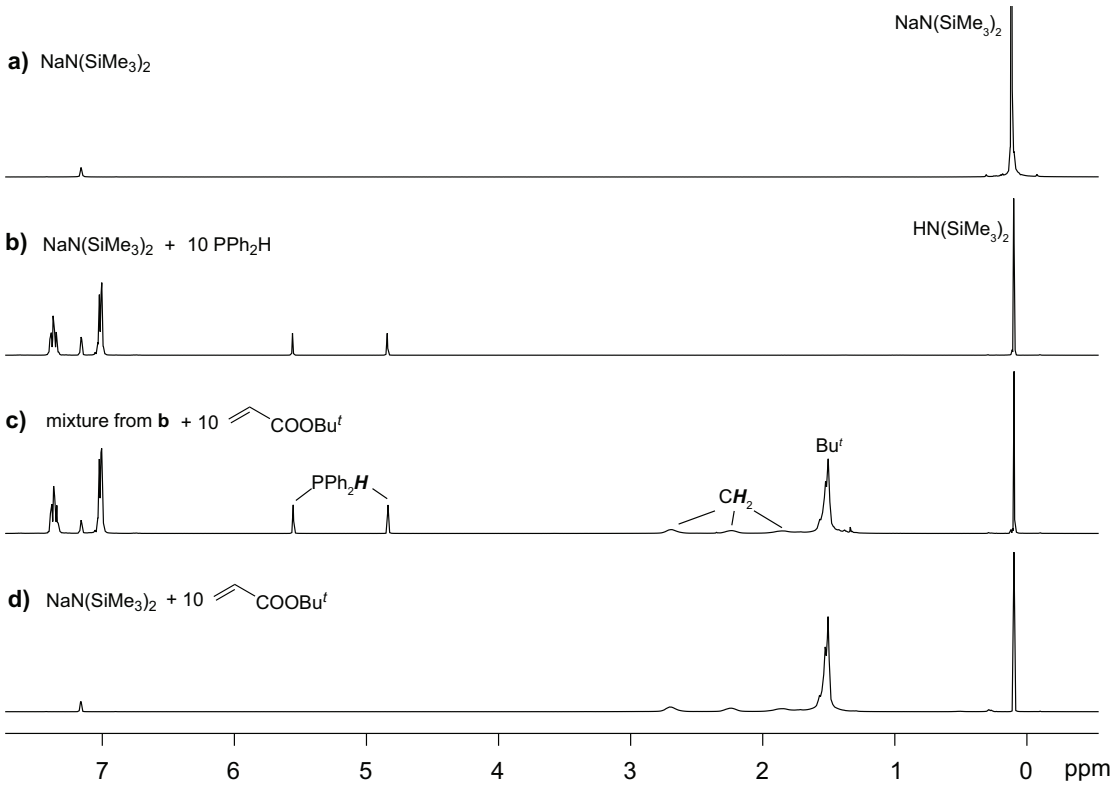

Figure 2.2 ^{1}H NMR spectra (300.13 MHz, C_6D_6) of: **a)** $NaN(SiMe_3)_2$; **b)** reaction of 1 equiv $NaN(SiMe_3)_2$ with 10 equiv PPh_2H (PPh_2^- generated *in situ*); **c)** reaction of 10 equiv *tert*-butyl acrylate with a previously prepared mixture of 1 equiv $NaN(SiMe_3)_2$ and 10 equiv PPh_2H (PPh_2^- generated *in situ*); **d)** the reaction of 1 equiv $NaN(SiMe_3)_2$ with 10 equiv *tert*-butyl acrylate.

I added 10 mol% $NaN(SiMe_3)_2$ to PPh_2H, producing an orange suspension in C_6D_6. The $^{31}P\{^{1}H\}$ and ^{1}H NMR (Figure 2.2b) spectra show only unreacted excess PPh_2H, suggesting that the resulting phosphido salt concentration in benzene is very low. The results are consistent with the known colour of $NaPPh_2$ and its low solubility in non-coordinating solvents.[10] For the next experiment (Figure 2.2c), I repeated the previous one first. Once the orange suspension had formed, *tert*-butyl acrylate was added. The reaction mixture showed the quick disappearance of the orange suspension and the formation of a clear, viscous solution. The ^{1}H NMR (Figure 2.2c) shows the total consumption of alkene and a large quantity of unreacted PPh_2H. Broad peaks in the alkyl region match closely the

shifts and broadenings of methylene and Bu^t signals previously observed for poly(*tert*-butyl acrylate).[11] The $^{31}P\{^1H\}$ NMR spectrum (Figure 2.3) reveals that the predominant species in this mixture (the reaction in Figure 2.2c) is unreacted PPh_2H, with trace quantities of the linear hydrophosphination product $Ph_2P(CH_2CHCO_2Bu^t)$ (**P**), and a minor amount of P-capped telomers. Finally, a control experiment with 10 mol% $NaN(SiMe_3)_2$ and *tert*-butyl acrylate gave a clear, viscous solution, and the ^1H NMR spectrum (Figure 2.2d) reveals complete alkene consumption and broad peaks in the alkyl region due to poly(*tert*-butyl acrylate).

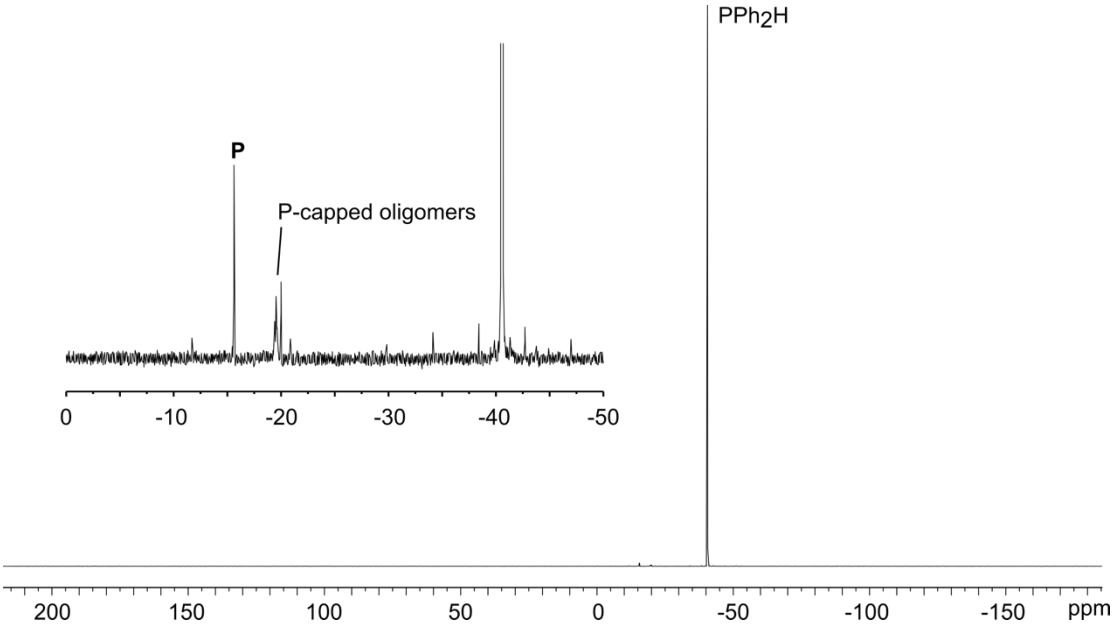

Figure 2.3 $^{31}P\{^1H\}$ NMR spectrum (121.55 MHz, C_6D_6) of a reaction where 10 equiv of *tert*-butyl acrylate was added to a premixed solution of 1 equiv $NaN(SiMe_3)_2$ and 10 equiv PPh_2H (10 mol% PPh_2^- generated *in situ*). **P** = $Ph_2P(CH_2CHCO_2Bu^t)$.

To avoid the side effect of the excess base, I chose to use 0.8 equiv of $NaN(SiMe_3)_2$, relative to Ru, to generate **Ru-1(a-c)** and **Ru-2d** for later hydrophosphination catalytic reactions (*vide infra*). Also, I let the sample sit overnight (before adding alkene) to ensure that no excess base is present that can deprotonate free PR_2H to give PR_2^- because the

dehydrohalogenation of bis(dialkylphosphine) complexes (e.g. **Ru-2c,d**) is slow (*vide infra*). Although this method ensures that only Ru phosphido will participate in hydrophosphination reactions, some unreacted Ru(η^5-Cp*)Cl(PR_2H)$_2$ (**Ru-4**) will also be observed in catalytic mixtures. The presence of 0.2 equiv of the Ru-Cl precursor does not affect the catalysis.

2.3 Investigation of Ru(η^5-Cp*)(PR_2)(PR_2H)$_2$ (Ru-1(a-c)) and Ru(η^5-Cp*)(PCy_2)(PCy_2H) (Ru-2d) in catalytic hydrophosphination

To study catalytic hydrophosphination, I generated the phosphido complexes Ru(η^5-Cp*)(PR_2)(PR_2H)$_2$ (**Ru-1(a-c)**, R = Ph (**a**), Tol^p (**b**), Et (**c**)) and Ru(η^5-Cp*)(PCy_2)(PCy_2H) (**Ru-2d**) as described above (Section 2.2.3). In this section, I compare catalytic behaviours of Ru(η^5-Cp*)(PPh_2)(PPh_2H)$_2$ (**Ru-1a**) to the indenyl analogue, Ru(η^5-indenyl)(PPh_2)(PPh_2H)(PPh_3).

2.3.1 Comparison of Ru(η^5-Cp*)(PPh_2)(PPh_2H)$_2$ (Ru-1a) with the indenyl analogue in hydrophosphination catalysis

Monitoring the hydrophosphination reactions of *tert*-butyl acrylate with PPh_2H using Ru(η^5-Cp*)(PPh_2)(PPh_2H)$_2$ (**Ru-1a**) shows its activity is much higher than the indenyl complex Ru(η^5-indenyl)(PPh_2)(PPh_2H)(PPh_3) for the same reaction. The catalytic reaction using 10 mol% **Ru-1a** was complete when the first NMR spectrum was collected, while it required 3 h using 10 mol% Ru(η^5-indenyl)(PPh_2)(PPh_2H)(PPh_3).[1] Reducing the catalyst loading to 1 mol% **Ru-1a** prolongs the reaction time to ~50 min, allowing reaction monitoring by ^{1}H NMR (Figure 2.4). Under these conditions, we observed a TOF (90% conversion) of 250 h^{-1}, representing a more than 30-fold increase in activity relative to 10

mol% the indenyl catalyst (TOF (90% conversion) = 7 h^{-1}). The catalysis using **Ru-1a** is fully selective to the linear product $Ph_2P(CH_2CH_2CO_2Bu^t)$ (**P**). The same reaction using the indenyl catalyst gives the linear product **P** as the major product along with 1% of the branched product $Ph_2PCH(CO_2Bu^t)CH_3$.

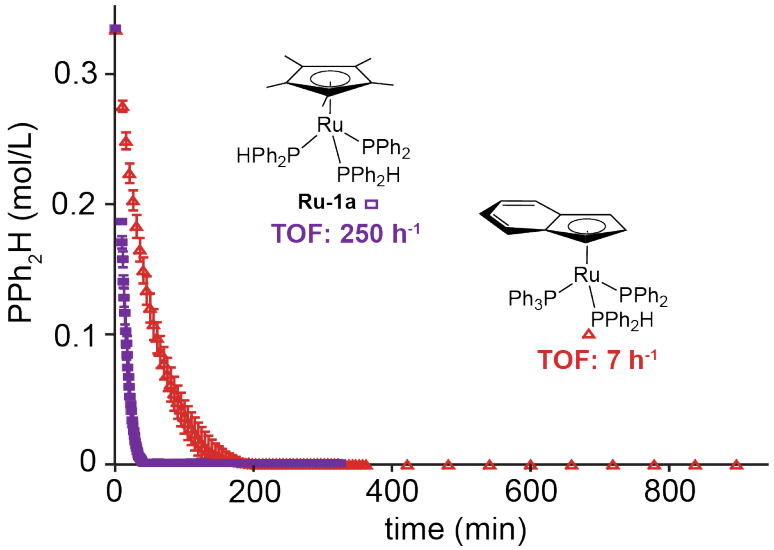

Figure 2.4 Rate profiles for the reaction of PPh_2H with *tert*-butyl acrylate catalyzed by **Ru-1a** (□) and Ru(η^5-indenyl)(PPh_2)(PPh_2H)(PPh_3) (Δ), as monitored by ^1H NMR (500.27 MHz, C_6D_6, RT). Conditions: 1 mol% Cp*Ru and 10 mol% indenyl Ru. Error bars show uncertainty over triplicate runs. The turnover frequencies (TOFs) shown were calculated for the 90% conversion.

^{31}P $\{^1H\}$ NMR monitoring of the hydrophosphination of *tert*-butyl acrylate with PPh_2H using 1 mol% **Ru-1a** exhibits a different catalyst resting state from that in the indenyl system. According to the $^{31}P\{^1H\}$ NMR spectra (Figure 2.5), only one Ru phosphine-containing species Ru(η^5-Cp*)(PPh_2)(PPh_2H)(**P**) (**Ru-6a**, **P** = $Ph_2P(CH_2CH_2CO_2Bu^t)$) is observed during catalysis. Within 15 min, **Ru-1a** completely converts to **Ru-6a**, which lasts till the end of catalysis. Thus, **Ru-6a** is the catalyst resting state for the Cp* system, whereas for the indenyl complex, Ru(η^5-indenyl)(PPh_2)(**P**)$_2$ is the catalyst resting state. The absence of signals due to a Cp* analogue Ru(η^5-Cp*)(PPh_2)(**P**)$_2$

indicates that the substitution of one product phosphine ligand by the less bulky PPh_2H (Scheme 2.1, step C) at the more crowded Cp*Ru center is extremely rapid and is not turnover-limiting as it is for the indenyl system.

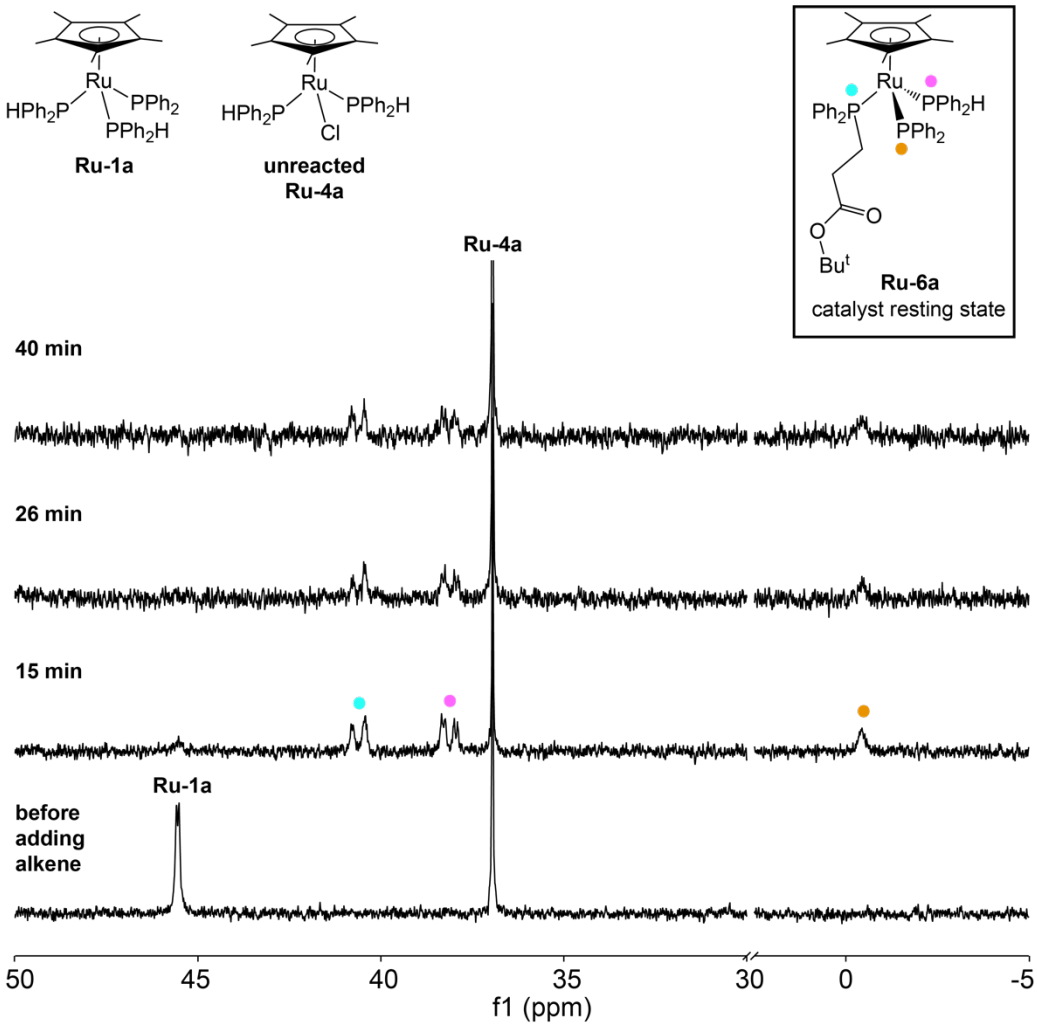

Figure 2.5 $^{31}P\{^{1}H\}$ NMR spectra (121.55 MHz, C_6D_6) of catalysis using 1 mol % **Ru-1a** showing the catalyst resting state **Ru-6a**. Note: unreacted **Ru-4a** in the catalytic mixture arises from the uncomplete dehydrohalogenation using less base (0.8 mol%) with respect to Ru (1 mol%).

I propose that the intramolecular P-H cleavage (Scheme 2.8, step B) is turnover-limiting. Evidence for this comes from my previous work,[7] monitoring the progress of dehydrohalogenation of Ru(η^5-Cp*)Cl(PCy_2H)(PPh_3) (**Ru-5d**) and analogous Ru(η^5-

indenyl)Cl(PCy_2H)(PPh_3). The indenyl complex is completely consumed within 1 h in the reaction with $KOBu^t$. However, **Ru-5d** reacts with $KOBu^t$ significantly more slowly, with only 40% consumption over 4 h. This result suggests that the P-H bond in the more electron-rich Cp* complex is less acidic. If the proton transfer is slow in the Cp* system, the zwitterionic complex should be the catalyst resting state. Since we observed no zwitterionic intermediate in the catalytic mixture, it suggests that the conjugate addition of **Ru-1a/Ru-6a** to a substrate alkene is fast and reversible, and this equilibrium lies at the side of **Ru-1a/Ru-6a** (Scheme 2.8, step A). Catalytic reactions using different PR_2H (i.e. different P-H acidities) also support that the turnover-limiting step is the intramolecular proton transfer (*vide infra*). However, I cannot rule out the possibility that the conjugate addition (Scheme 2.8, step A) and the intramolecular proton transfer (Scheme 2.8, step B) are concerted.

Scheme 2.8 Proposed relative rates of each step in the catalytic hydrophosphination of *tert*-butyl acrylate with PPh_2H using **Ru-1a**. **P** = $Ph_2P(CH_2CH_2CO_2Bu^t)$, R = CO_2Bu^t.

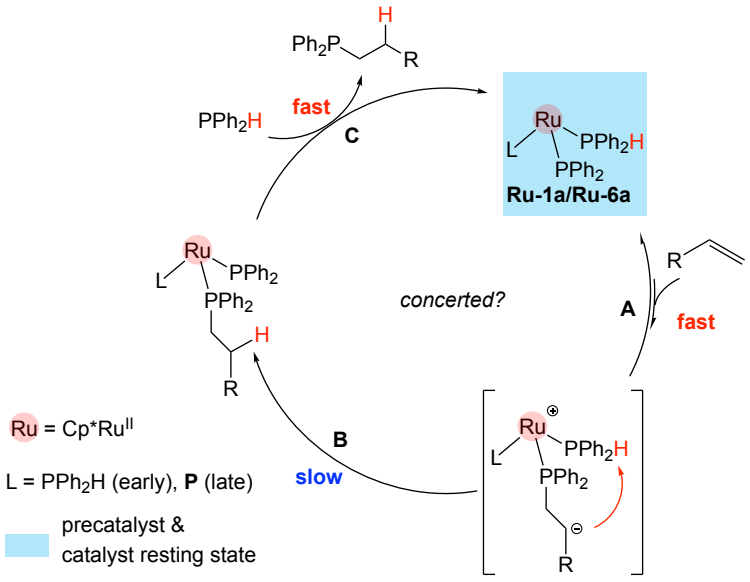

For this Cp* system, I also discovered that the rapid product substitution (Scheme 2.8, step C) could lead to catalyst deactivation in the absence of substrate PPh_2H (Scheme 2.9).

In-situ generation of **Ru-1a** requires 3 equiv of substrate PPh_2H (with respect to Ru), so the "free" substrate PPh_2H will be completely consumed before the alkene if the overall [PPh_2H] is equal to [alkene]. If excess alkene is present once the PPh_2H is consumed, **Ru-6a** converts to a metallacycle complex Ru(η^5-Cp*)(**P**)(κ^2-$Ph_2\underline{P}CH_2\underline{C}HCO_2Bu^t$ (**Ru-7a**), as determined by its diagnostic ^{31}P shifts (δ: 49.2 (br s) and -12.5 (br s) ppm). Adding more PPh_2H and *tert*-butyl acrylate to the catalytic mixture containing only **Ru-7a** (no Ru phosphido complex) shows no reaction, which suggests that the metallacycle is inactive for hydrophosphination. The analogue of **Ru-7a** is not observed in our indenyl system.

Scheme 2.9 Deactivation process of **Ru-7a** at the end of catalysis in the absence of PPh_2H. **P** = $Ph_2P(CH_2CH_2CO_2Bu^t)$, R = CO_2Bu^t.

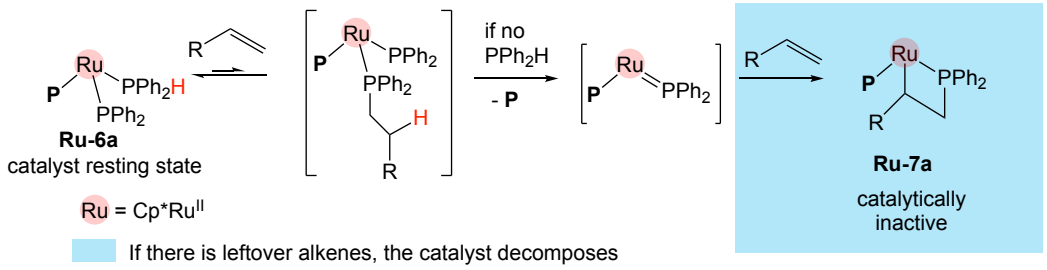

This potential catalyst deactivation can be simply addressed by using a very slight excess PPh_2H (1.01-1.02 equiv) with respect to the alkene in the catalysis. In the absence of alkene but with excess PPh_2H (Scheme 2.10), the regeneration of Ru(η^5-Cp*)(PPh_2)(PPh_2H)$_2$ (**Ru-1a**) occurs *via* substitution of the product phosphine at **Ru-6a** by substrate PPh_2H at the end of catalysis. The mixture containing **Ru-1a** or **Ru-6a** is still active for another hydrophosphination with comparable activity when more PPh_2H and alkenes are added.

Scheme 2.10 Regeneration of **Ru-1a** at the end of catalysis with a slight excess of PPh_2H with respect to the alkene. **P** = $Ph_2P(CH_2CH_2CO_2Bu^t)$, R = CO_2Bu^t.

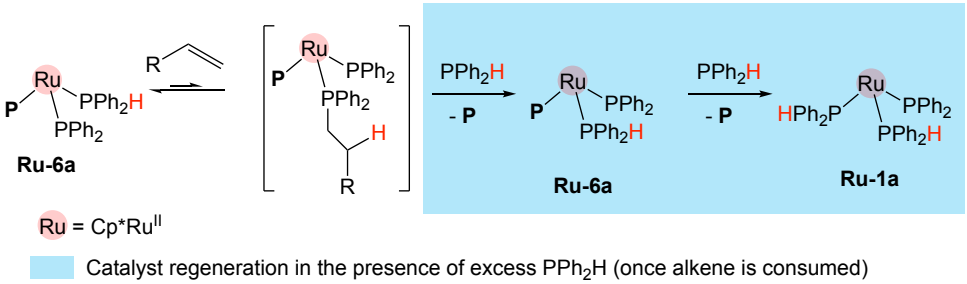

Overall, Cp* complex **Ru-1a** shows high activity in the hydrophosphination of *tert*-butyl acrylate with PPh_2H at RT, even with low catalyst loadings (~1 mol%). More importantly, using the Cp* catalyst addresses the issue of slow product substitution (i.e. two competing processes) observed for the indenyl catalyst Ru(η^5-indenyl)(PPh_2)(PPh_2H)(PPh_3) by changing the turnover-limiting step of the catalysis.

2.3.2 Substrate scope in Cp*Ru-catalyzed hydrophosphination

I assessed complexes **Ru-1(a-c)** and **Ru-2d** (generated *in situ*) in catalytic hydrophosphination of *tert*-butyl and methyl acrylate, respectively, with the corresponding substrate PR_2H (R = Ph (**a**), Tol^p (**b**), Et (**c**)) and Cy(**d**), Scheme 2.11). *tert*-Butyl acrylate is used in these reactions for consistency with our previous study on **Ru-1a**. The methyl acrylate reactions exhibit nearly identical results to those of *tert*-butyl acrylate. This part of the work was done with the help of Alexis Kellinghusen.

Scheme 2.11 Hydrophosphination of *tert*-butyl and methyl acrylate with various phosphines using Cp*Ru phosphido catalysts (generated *in situ*).[a]

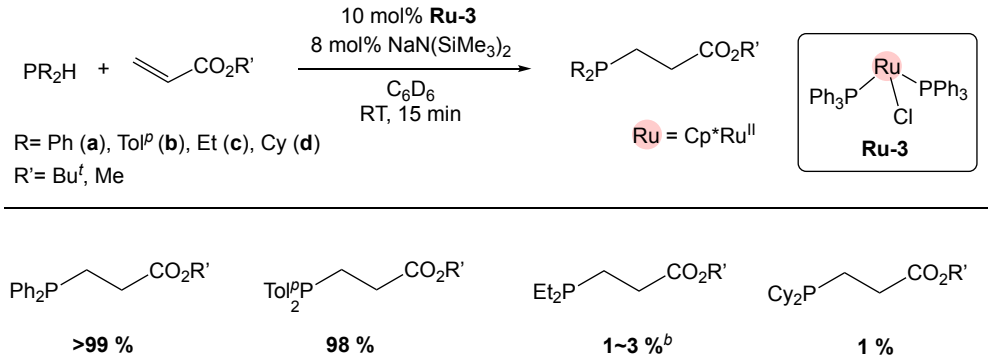

[a]0.37 M phosphine, 0.29 M *tert*-butyl acrylate. Conversions (%) determined by non-quantitative $^{31}P\{^{1}H\}$ NMR experiments (121.55 MHz) from relative integration of ^{31}P signals for products and free PR_2H. Conversions (%) for R' = Bu^t and Me are close. [b] Conversions (%) for P-capped telomers (Bu^t: 31%; Me: 7%), as determined as $^{31}P\{^{1}H\}$ NMR – the remainder of alkene was consumed to give alkene-terminated oligomers, as determined by ^{1}H NMR (300.27 MHz).

Scheme 2.11 shows that: only hydrophosphination product is formed in the hydrophosphination of acrylates with more acidic diarylphosphine (R = Ph or Tol^p); for less acidic dialkylphosphine (R = Et or Cy), only trace amounts of the hydrophosphination product are observed under identical conditions. The results suggest that the hydrophosphination activity highly correlates with the P-H acidity for the substrate phosphine (i.e. pK_a of PR_2H[12]). It provides evidence that intramolecular proton transfer is turnover-limiting (Scheme 2.8, step B). Additionally, alkene and phosphine-terminated acrylate oligomers are only observed for the reactions using small alkyl phosphido complex **Ru-1c** (R = Et), suggesting that the steric property of the Cp*Ru phosphido complex also plays a role in chemoselectivity of this catalysis (hydrophosphination vs oligomerization). As shown in Scheme 2.8, the conjugate addition of **Ru-1**/**Ru-6** to the substrate alkene occurs rapidly and reversibly; the intramolecular proton transfer occurs relatively slowly. Thus, no telomers will be observed if the intramolecular quenching process (e.g. more acidic PAr_2H) is sufficiently rapid (Scheme 2.12, right). However, if the intramolecular

quenching (e.g. less acidic, small PEt_2H) is slowed, and the relatively long-lived zwitterion undergoes fast conjugate addition at extra alkenes, leading to competitive telomerization (Scheme 2.12, bottom). For the reaction using complex Ru(η^5-Cp*)(PCy_2)(PCy_2H) (**Ru-2d**), the conjugate addition equilibrium tends to favor **Ru-2d** over the zwitterionic intermediate. Together with the slow intramolecular quenching owing to the low P-H acidity of PCy_2H, the reaction results in a trace amount of the hydrophosphination product and no oligomer.

Scheme 2.12 Two competitive processes depend on the P-H bond acidity of the coordinated PR_2H. R = Ph (**a**), Tol^p (**b**), Et (**c**); R' = CO_2Bu^t, CO_2Me. **P** = hydrophosphination product.

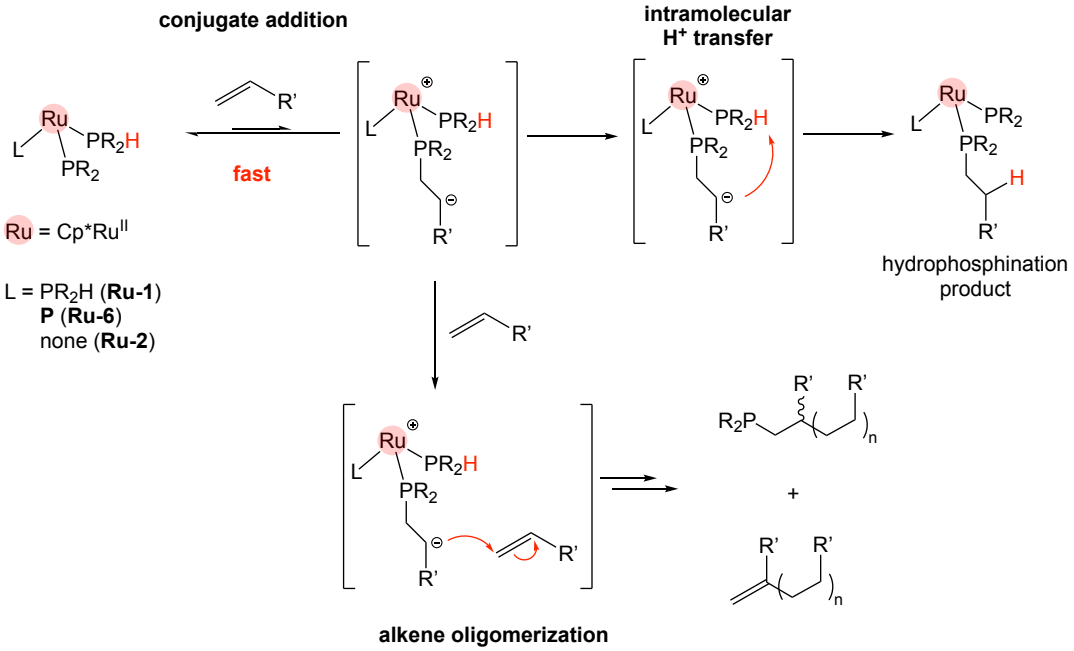

Complexes **Ru-1(a-c)** and **Ru-2d** exhibit no activity for the hydrophosphination of less activated alkenes (i.e. 2-vinyl pyridine and styrene) or the simple alkene 1-hexene. This result is consistent with our indenyl Ru catalysts. The fact that the Cp* system only works on electron-deficient alkenes supports the outer-sphere conjugate addition mechanism described above (Scheme 2.8).

2.3.3 Proposed mechanism for Cp*Ru-catalyzed hydrophosphination

Based on the above observations, Scheme 2.13 illustrates a proposed mechanism for the hydrophosphination of an activated alkene with PR_2H using **Ru-1** complexes. This cycle is nearly identical to the indenyl system (Scheme 2.1), which relies on an outer-sphere, conjugate addition mechanism.

Scheme 2.13 Proposed cycle for outer-sphere hydrophosphination catalyzed by **Ru-1** (R = Ph, Tol^p, Et), relying on conjugate addition. R' = electron withdrawing group (EWG).

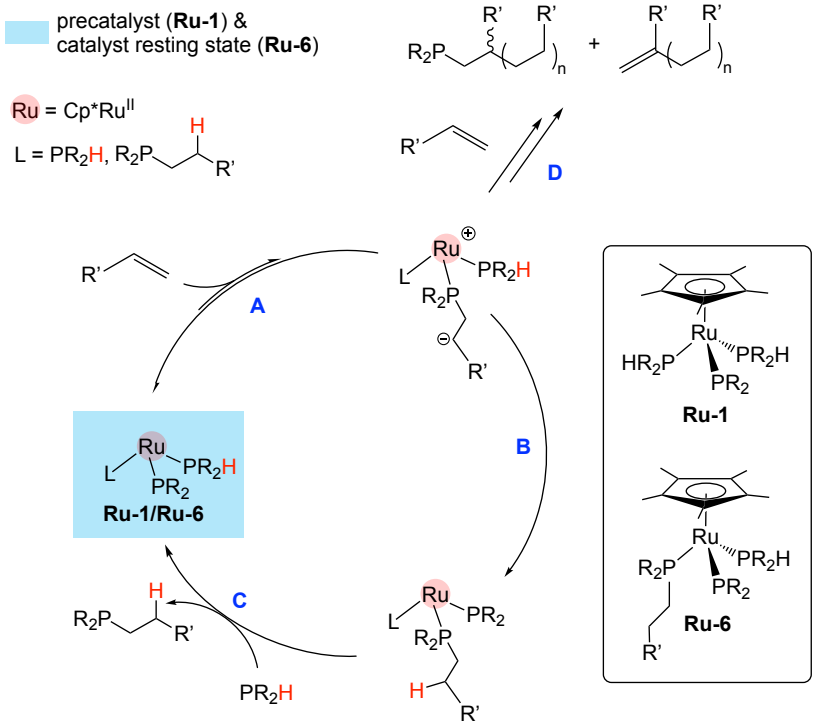

The conjugate addition of a phosphido ligand in **Ru-1** or **Ru-6** to the substrate alkene is quick and reversible (step A), resulting in an equilibrium favouring **Ru-1**/**Ru-6**. The intramolecular proton transfer step is apparently turnover-limiting (step B). The lifetime of the zwitterion is affected by the P-H acidity of the coordinated PR_2H, which determines the activity toward either hydrophosphination (step B) or telomerization (step D). Step B is sufficiently rapid for the most acidic PPh_2H to exclude off-cycle oligomerization (step D). However, for less acidic small PEt_2H, the zwitterion has a lifetime to react with extra

alkenes to give telomers and oligomers. Unlike the indenyl system, the substitution of the Ru-bound product phosphine with the substrate phosphine is fast (step C). Thus, it is improbable that the competing cycle shown on the left side of Scheme 2.1, which involves intermolecular proton transfer from free PR_2H, is operative in this Cp*Ru system.

2.4 Conclusion

Phosphido complexes Ru(η^5-Cp*)(PR_2)(PR_2H)$_2$ (**Ru-1(a,b)**) (R = Ph (**a**), Tol^p (**b**)), are competent catalysts for the hydrophosphination of electron-deficient alkenes. These Cp* catalysts, like our indenyl catalyst, apparently operate by an outer-sphere process that involves the conjugate addition of a phosphido ligand at an alkene. Complex **Ru-1a** is the most active catalyst for the hydrophosphination. The simple ligand switch from indenyl to Cp* changes the turnover-limiting step from the product substitution to the intramolecular P-H cleavage, which leads to a more than 30-fold increase in hydrophosphination activity.

However, this Cp* system shows limited substrate scope, especially phosphine. It is only highly active for sufficiently acidic diarylphosphine because of its turnover-limiting step. The next catalyst design targets expanding the phosphine scope in a half-sandwich metal system (see Chapter 4).

2.5 Experimental

2.5.1 General comments

Unless otherwise noted, the "General comments" described here are also applicable to the rest of the chapters. All reactions and manipulations were performed under nitrogen in a glovebox or using conventional Schlenk techniques. Deuterated solvents (Sigma-Aldrich) were stored over sodium/benzophenone (C_6D_6) or calcium hydride ($CDCl_3$,

CD_2Cl_2, CD_3CN) and then degassed using three freeze-pump-thaw cycles, and vacuum-transferred before use. Unless otherwise specified, reagents were purchased from Sigma-Aldrich Canada and used as received. Secondary or primary phosphines (neat or 10% hexane solution) were purchased from Strem Chemicals. The concentration of phosphines in hexanes was checked against a known concentration of triphenylphosphine oxide by quantitative $^{31}P\{^1H\}$ NMR (relaxation delay 55 s) before use.

NMR spectra were recorded on a Bruker Avance 300 spectrometer operating at 300.27 MHz for ^1H and 121.55 MHz for ^{31}P, a Bruker AMX 360 spectrometer operating at 360.13 MHz for ^1H and 145.78 MHz for ^{31}P and a Bruker NEO 500 spectrometer operating at 500.27 MHz for ^1H, 202.51 MHz for ^{31}P and 125.77 MHz for ^{13}C. Unless otherwise noted, chemical shifts are reported in ppm at RT. ^1H chemical shifts are referenced to residual proteo-solvent peak at 7.26 ppm ($CHCl_3$), 7.16 ppm (C_6D_5H) and 5.32 ppm ($CDHCl_2$). ^{13}C chemical shifts are referenced to C_6D_6 at 128.1 ppm, $CDCl_3$ at 77.5 ppm and CD_2Cl_2 at 54.0 ppm ^1H and ^{13}C chemical shifts are reported relative to tetramethylsilane, and ^{31}P chemical shifts are reported relative to 85% H_3PO_4 (aq).

2.5.2 In-situ generation of Ru-1 and Ru-2 for spectroscopic identification

$Ru(\eta^5\text{-}Cp^*)Cl(PPh_3)_2$ (0.023 mmol, 18 mg) and neat PR_2H (0.23 mmol, 10 equiv) were added into a J-Young NMR tube containing C_6D_6 (0.6 mL). The reaction mixture was heated in an oil bath at 70°C for 1 h, which caused the solution to change colour from orange to yellow. $NaN(SiMe_3)_2$ (0.027 mmol, 1.2 equiv) was added to the mixture, and the solution immediately changed to an intense red colour. NMR analysis of the mixture confirmed the formation of **Ru-1(a-c)** or **Ru-2d** in the presence of excess PR_2H.

Table 2.3 ^{1}H NMR (500.27 MHz, C_6D_6) data for complexes **Ru-1(a-c)** and **Ru-2d**: δ in ppm (multiplicity, J in Hz, RI).

Complex	η^5-Cp*	PR_2	PR_2H
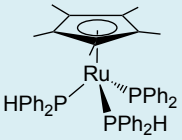 **Ru-1a**	1.55 (s, 15H)	7.12–6.96 (m, overlapping with H_m at PPh_2H, 10H)	**H-PPh₂** 6.50 (d, 352.8) **Hₒ** 7.26–7.16 (m, 8H) **Hₘ** 7.12–6.96 (m, overlapping with H from PPh_2, 8H) **Hₚ** 6.95 – 6.85 (m, 4H)
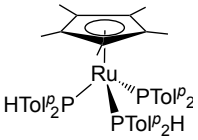 **Ru-1b**	1.66 (s, 15H)	**Hₒ** 7.26–7.17 (m, overlapping with H_o at $PTol^p_2H$, 4H), **CH₃** 2.19 (s, 6H) Other signals were not observed.	**H-PTol$^p_2$** 6.57 (d, 354, 2H) **Hₒ** 7.26–7.17 (m, overlapping with H_o at $PTol^p_2$, 8H), **Hₘ** 6.96 (d, 8, 4H), 6.80 (d, 8, 4H), **CH₃** 2.09 (s, 6H), 1.99 (s, 6H)
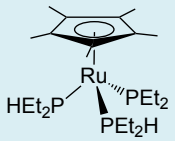 **Ru-1c**	1.70 (t, 2, 15H)	**CH₂** 1.74–1.67 (m, 2H,), 1.58–1.48 (m, 2H) **CH₃** 1.60–1.52 (m, 6H)	**H-PEt₂** 4.20 (d, 321, 2H), **CH₂** 1.86–1.74 (m, 2H), 1.66–1.60 (m, 2H), 1.52–1.31 (m, overlapping with CH_2 at free PEt_2H, 4H) **CH₃** 1.12–0.92 (m, overlapping with CH_3 at free PEt_2H, 12H)
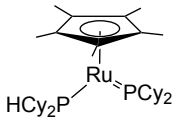 **Ru-2d**	1.93 (s, 15H)	**CH** 2.64–2.52 (m, 1H), 1.79–1.65 (m, 1H) **CH₂** 2.18–2.01 (m, 8H), 1.62–1.52 (m, 4H), 1.48–1.68 (m, 8H overlap with signals due to the free PCy_2H)	**H-PCy₂** 5.02 (d, 301.5, 2H) **CH** 2.25–2.07 (m, 2H) **CH₂** 1.33 (m, 14H, overlap with signals due to the free PCy_2H), 1.04–0.91 (m, 6H)

Table 2.4 $^{13}C\{^{1}H\}$ NMR (125.77 MHz, C_6D_6) data for complexes **Ru-1(a-c)** and **Ru-2d**: δ in ppm (multiplicity, J in Hz).

Compound	η^5-Cp*	PR_2	PR_2H
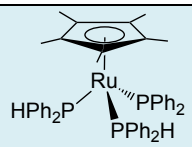 **Ru-1a**	**C_{ring}** 93.1 (s) **CH_3** 10.1 (d, 5).	**C_{ipso}** 137.7 (d, 21), 137.5 (d, 20), **C_{ortho}** 133.6 (d, 9) **C_{para}** 129.0 (s) **C_{meta}** 128.3 (t, 5)	**C_{ipso}** 136.8 (d, 21), 136.6 (d, 20) **C_{ortho}** 133.5 (d, 9) **C_{para}** 128.7 (s) **C_{meta}** 127.7 (t, 5)
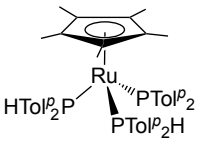 **Ru-1b**	**C_{ring}** 92.3 (s) **CH_3** 10.2 (d, 5)	**C_{ortho}** 133.6 (br s, overlapping with C_{ortho} at $PTol^p_2H$), **C_{meta}** 128.3 (t, 5) **C_{ipso}** and **C_{meta}** not observed. **CH_3** 21.3 (s)	**C_{ipso}** 145.8 (d, 39) **C_{para}** 138.6 (s) **C_{ortho}** 133.8–133.6 (m, overlapping with C_{ortho} at $PTol^p_2$) **C_{meta}** 128.2 (d, 5) **CH_3** 21.2 (s), 21.1 (s)
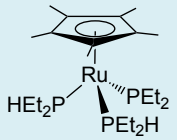 **Ru-1c**	**C_{ring}** 91.6 (s) **CH_3** 10.7 (d, 6).	**CH_2** 24.1 (dt, 34 5) **CH_3** 18.5 (d, 23)	**CH_2** 20.3 (dd, 14 6), 20.2 (dd, 14 6), 20.0 (dd, 12 5), 19.9 (dd, 14 5), **CH_3** 13.5 (dd, 5 4), 13.3 (dd, 5 4)
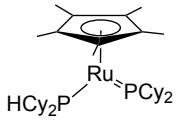 **Ru-2d**	**C_{ring}** 84.0 (s) **CH_3** 12.8 (s)	**CH** 55.4 (s), 48.9 (s), **CH_2** 32.5 (m), 31.7 (d, 10), 28.6–28.0 (m,), 27.1–26.4 (m)	**CH** and **CH_2** 36.5 (d, 21), 34.7 (d, 4), 33.1 (d, 8), 28.6–28.0 (m), 27.1-26.4 (m)

2.5.3 Monitoring catalytic reactions using Ru-1 or Ru-2

2.5.3.1 In-situ generation of Ru-1a for 1 mol% catalysis

Ru(η^5-Cp*)Cl(PPh_2H)(PPh_3) (**Ru-5a**, 10 μL, 0.1 M in C_6D_6) and neat PPh_2H (0.101 mmol, 18 μL, 101 equiv) were added into a J-Young NMR tube containing C_6D_6 (0.6 mL). The reaction mixture was heated in an oil bath at 70°C for 1 h, during which time the solution changed colour from orange to yellow. NMR spectra (^1H, $^{31}P\{^1H\}$, ^{31}P) of the sample after cooling to RT showed complete conversion to Ru(η^5-Cp*)Cl($PPh_2H)_2$ (**Ru-4a**). $NaN(SiMe_3)_2$ (8 μL, 0.1 M in C_6D_6, 0.8 equiv) was added to the mixture. The

generation of Ru(η^5-Cp*)(PPh_2)(PPh_2H)$_2$ (**Ru-1a**, 0.8 equiv) in the presence of excess PPh_2H and residual **Ru-4a** (0.2 equiv) was confirmed by NMR.

2.5.3.2 Probing the potential reactivity of uncoordinated PPh_2^- in hydrophosphination

The use of $NaN(SiMe_3)_2$ (0.8 equiv) to generate **Ru-1a** (Section 2.5.3.1) ensures that no excess base is present that could deprotonate free PPh_2H to give PPh_2^-, which causes competing telomerization of the activated alkene (*vide infra*). The presence of 0.2 equiv of the Ru-Cl precursor **Ru-4a** does not affect the catalysis.

Reaction of $NaN(SiMe_3)_2$ with PPh_2H

$NaN(SiMe_3)_2$ (0.016 mmol, 3.0 mg, 1 equiv) was added to excess PPh_2H (0.016 mmol, 28 μL, 10 equiv) in a vial containing C_6D_6 (~0.5 mL) with mixing. This gave an orange suspension that was then transferred to an NMR tube. The mixture was analyzed by ^1H and $^{31}P\{^1H\}$ NMR.

Reaction of $NaN(SiMe_3)_2$ with PPh_2H, then tert-butyl acrylate

$NaN(SiMe_3)_2$ (0.016 mmol, 3.0 mg, 1 equiv) was added to excess PPh_2H (0.016 mmol, 28 μL, 10 equiv) in a vial containing C_6D_6 (~0.5 mL). Following the formation of the orange suspension, *tert*-butyl acrylate (0.016 mmol, 24 μL, 10 equiv) was added with mixing. The resulting clear, viscous solution was then transferred to an NMR tube. The mixture was analyzed by ^1H and $^{31}P\{^1H\}$ NMR.

Reaction of $NaN(SiMe_3)_2$ with tert-butyl acrylate

$NaN(SiMe_3)_2$ (0.016 mmol, 3.0 mg, 1 equiv) was added to *tert*-butyl acrylate (0.016 mmol, 24 μL, 10 equiv) in a vial containing C_6D_6 (~0.5 mL). The resulting clear, viscous

solution was then transferred to an NMR tube. The mixture was analyzed by ^{1}H and $^{31}P\{^{1}H\}$ NMR.

2.5.3.3 Monitoring catalytic reaction using 1 mol% Ru

Quantitative ^{1}H NMR

The catalyst solution containing Ru(η^5-Cp*)(PPh_2)(PPh_2H)$_2$ (**Ru-1a**) was prepared in a J. Young NMR tube as described above. 100 equiv of *tert*-butyl acrylate (15 μL, 0.10 mmol) was added to this solution. Experiments were performed using a standard 5 mm NMR tube equipped with a coaxial tube containing 100 μL of a standard solution of $O(SiMe_3)_2$ (0.5 M in C_6D_6) as an internal standard. The mixture was transferred to the standard NMR tube equipped with the coaxial tube containing an internal standard. Conversion of PPh_2H and *tert*-butyl acrylate to $Ph_2P(CH_2CH_2CO_2Bu^t)$ catalyzed by **Ru-1a** was monitored by ^{1}H NMR (500.27 MHz) at RT using diagnostic signals due to the PPh_2H and the product phosphine. Each NMR experiment was a single scan with a delay of 5 min between each experiment for the first 6 h and a subsequent delay of 1 h between experiments. The first ^{1}H NMR spectrum (first data point) was collected within 10 min of mixing the catalytic solution. The reaction was performed in triplicate.

$^{31}P\{^{1}H\}$ NMR

The same procedures described above were followed to prepare the catalyst solution and perform a catalytic reaction with **Ru-1a,** except the reaction mixture was kept in the J Young tube. Ru(η^5-Cp*)Cl(PPh_2H)(PPh_3) (0.1 M, 20 μL), PPh_2H (0.20 mmol, 36 μL,), $NaN(SiMe_3)_2$ (0.1 M, 16 μL) and *tert*-butyl acrylate (0.20 mmol, 29 μL) were used. The mixture was analyzed by $^{31}P\{^{1}H\}$ NMR.

2.5.3.4 General procedure for catalytic reactions using 10 mol% Ru

The catalyst solution containing Ru(η^5-Cp*)(PR_2)(PR_2H)$_2$ (**Ru-1**) was prepared as described above, and each catalyst generation step was confirmed by NMR. Different from the 1 mol% reaction (Section 2.5.3.1), the pre-catalyst Ru(η^5-Cp*)Cl(PPh_3)$_2$ **Ru-3** (0.020 mmol,16 mg) was used instead, which was weighed and placed in a J. Young NMR tube. Neat PR_2H (0.260 mmol, 13 equiv) was added into the J-Young tube containing C_6D_6 (0.6 mL). The reaction mixture was heated in an oil bath at 70 °C for 1 h, then NaN($SiMe_3$)$_2$ (0.016 mmol, 3 mg, 0.8 equiv) was added to the mixture in the J-Young tube. After that, alkene (0.20 mmol, 10 equiv) was added to the reaction mixture, which was analyzed by ^{1}H and ^{31}P{^{1}H} NMR.

2.6 References

(1) Belli, R. G.; Yang, J.; Bahena, E. N.; McDonald, R.; Rosenberg, L. Mechanism and Catalyst Design in Ru-Catalyzed Alkene Hydrophosphination. *ACS Catal.* **2022**, *12*, 5247–5262.

(2) Scriban, C.; Glueck, D. S.; Zakharov, L. N.; Kassel, W. S.; DiPasquale, A. G.; Golen, J. A.; Rheingold, A. L. P-C and C-C Bond Formation by Michael Addition in Platinum-Catalyzed Hydrophosphination and in the Stoichiometric Reactions of Platinum Phosphido Complexes with Activated Alkenes. *Organometallics* **2006**, *25*, 5757–5767.

(3) Sarazin, Y.; Carpentier, J. F. Calcium, Strontium and Barium Homogeneous Catalysts for Fine Chemicals Synthesis. *Chem. Rec.* **2016**, *16*, 2482–2505.

(4) Webster, R. L. Room Temperature Ni(II) Catalyzed Hydrophosphination and Cyclotrimerization of Alkynes. *Inorganics* **2018**, *6*, 120.

(5) Costa, E.; G. Pringle, P.; Worboys, K. Chemoselective Platinum(0)-Catalysed Hydrophosphination of Ethyl Acrylate. *Chem. Commun.* **1998**, No. 1, 49–50.

(6) Costa, E.; G. Pringle, P.; B. Smith, M.; Worboys, K. Self-Replication of Tris(Cyanoethyl)Phosphine Catalysed by Platinum Group Metal Complexes. *J. Chem. Soc. Dalton Trans.* **1997**, No. 22, 4277–4282.

(7) Yang, J.; Langis-Barsetti, S.; Parkin, H. C.; McDonald, R.; Rosenberg, L. Terminal Phosphido Complexes of the Ru(η^5-Cp*) Fragment. *Organometallics* **2019**, *38*, 3257–3266.

(8) Lubián, R. T.; Paz-Sandoval, M. A. Synthesis, Properties and Crystal Structures of Pentamethylcyclopentadienyl- and Cyclopentadienyl-Ruthenium(II) Diphenylphosphine Complexes. *J. Organomet. Chem.* **1997**, *532*, 17–29.

(9) A. Tolman, C. Steric Effects of Phosphorus Ligands in Organometallic Chemistry and Homogeneous Catalysis. *Chem. Rev.* **1977**, *77*, 313–348.

(10) Wang, X.; Cao, K.; Liu, Y.; Tsang, B.; Liew, S. Migration Insertion Polymerization (MIP) of Cyclopentadienyldicarbonyldiphenylphosphinopropyliron (FpP): A New Concept for Main Chain Metal-Containing Polymers (MCPs). *J. Am. Chem. Soc.* **2013**, *135*, 3399–3402.

(11) Suchopárek, M.; Spěváček, J. Characterization of the Stereochemical Structure of Poly(Tert-Butyl Acrylate) by One- and Two-Dimensional NMR Spectroscopy. *Macromolecules* **1993**, *26*, 102–106.

(12) Li, J. N.; Liu, L.; Fu, Y.; Guo, Q. X. What Are the PKa Values of Organophosphorus Compounds? *Tetrahedron* **2006**, *62*, 4453–4462.

3. Synthesis and characterization of Cp*Co complexes

In this chapter, I describe the synthesis of Cp*Co(III) iodide complexes, including Co(η^5-Cp*)I_2(CO) (**Co-1**), Co(η^5-Cp*)$I_2(PR_2H)$ (**Co-2**), Co(η^5-Cp*)$I_2(PRH_2)$ (**Co-3**) and [Co(η^5-Cp*)$I(PR_2H)_2$]I (**Co-4**) and analogous dicationic complexes [Co(η^5-Cp*)$(NCCH_3)_3$][SbF_6]$_2$ (**Co-5**) and [Co(η^5-Cp*)$(NCCH_3)_2(PR_2H)$][SbF_6]$_2$ (**Co-6**) (R = alkyl and aryl, Section 3.2). Spectroscopic characterization of these complexes is presented in Section 3.3. In preliminary studies (Section 3.4), complexes **Co-1** and **Co-5** show catalytic activity for the hydrophosphination of *tert*-butyl acrylate with PPh_2H and dehydrocoupling of PPh_2H. Additionally, complexes **Co-1** and **Co-5** show an intriguing interaction (probably P-H activation) with excess PPh_2H. This chapter has contributions from Michelle Ting (a former M.Sc. student in the group of Prof. Scott McIndoe), Cameron Zheng and Elena Liles (previous undergraduate honours students), as well as Dr. Robert McDonald and Dr. Michael Ferguson (X-ray crystallography).

3.1 Introduction

In 1953, Fischer reported the first cyclopentadienyl cobalt(Co) compound, cobaltocene Co(η^5-Cp)$_2$.[1] Since then, many sandwich and half-sandwich cyclopentadienyl Co complexes and their derivatives have been reported for their use in various areas. The chemistry of CpCo(III) and Cp*Co(III) complexes has received considerable interest in the last decade, owing to their interesting activity in C-H functionalization reactions compared to other Group 9 metals (e.g. Rh, Ir).[2] C-H activation chemistry of Cp*Co(III) complexes has been summarized in recent reviews.[3–7] In these reviews, air-stable complex Co(η^5-Cp*)I_2(CO) (**Co-1**) and [Co(η^5-Cp*)$(NCCH_3)_3$][SbF_6]$_2$ (**Co-5**) are popular pre-catalysts for the C-H activation chemistry. However, most of these studies focus on the organic

transformations more than the catalytic behaviour of the Co catalysts. Moreover, none of them has been investigated for P-H activation reactions.

From a larger perspective, researches on 3d transition metals in catalysis have shown a rising trend in recent years. These earth-abundant metals are desirable candidates for catalysts in organic transformations. However, the fundamental reactivity of 3d metals may be distinct from those of well-established 4d and 5d metals. For example, 3d metals can react not just through two-electron processes but also *via* one-electron pathways, and their spin-states need to be considered carefully when proposing reaction mechanisms. Thus, understanding the physical properties of 3d metals is vital in developing and understanding first-row metal-mediated processes.

In this chapter, I present the synthesis of various Cp*Co(III) complexes, including $Co(\eta^5\text{-}Cp^*)I_2(L)$ (L = CO (**Co-1**), PR_2H (**Co-2**) and PRH_2 (**Co-3**), R = alkyl and aryl), $[Co(\eta^5\text{-}Cp^*)I(PR_2H)_2]I$ (**Co-4**), $[Co(\eta^5\text{-}Cp^*)(NCCH_3)_3][SbF_6]_2$ (**Co-5**) and $[Co(\eta^5\text{-}Cp^*)(NCCH_3)_2(PR_2H)][SbF_6]_2$ (**Co-6**, R = alkyl and aryl). These complexes are characterized by various techniques. Additionally, I describe preliminary investigations of P-H activation catalyses (i.e. hydrophosphination and dehydrocoupling) using **Co-1** and **Co-5**. The synthesis of these new phosphine complexes provides useful precursors for later mechanistic studies on these catalytic reactions.

3.2 Synthesis of Cp*Co(III) phosphine complexes

3.2.1 Iodide complexes Co(η⁵-Cp*)I₂(PR₂H) (Co-2), Co(η⁵-Cp*)I₂(PRH₂) (Co-3) and [Co(η⁵-Cp*)I(PR₂H)₂]I (Co-4)

I prepared the known complex Co(η⁵-Cp*)I₂(CO) (**Co-1**) by a literature procedure.[8] Mono(secondary phosphine) complexes Co(η⁵-Cp*)I₂(PR₂H) (**Co-2(a-d)**) can be isolated pure from the reaction of **Co-1** with ~1 equiv of secondary phosphine PR₂H (R = Ph (**a**), Tol^{p} (**b**), Cy (**c**) and Pr^{i} (**d**), Scheme 3.1), whereas the isolation of complexes Co(η⁵-Cp*)I₂(PRH₂) (**Co-3a,c**) requires almost 2 equiv of primary phosphine PRH₂ for completion of this substitution, likely due to the relatively poor donor ability of these phosphines.[9] The addition of 1 equiv of PEt₂H to **Co-1** results in an equilibrium mixture of mono(phosphine) complex **Co-2e**, bis(phosphine) complex [Co(η⁵-Cp*)I(PEt₂H)₂]I (**Co-4e**), and unreacted **Co-1** (R =Et (**e**)). The similar solubilities of these complexes prevented the isolation of pure **Co-2e**.

Scheme 3.1 Synthesis of complexes Co(η⁵-Cp*)I₂(PR₂H) (**Co-2**) and Co(η⁵-Cp*)I₂(PRH₂) (**Co-3**) from Co(η⁵-Cp*)I₂(CO) (**Co-1**).

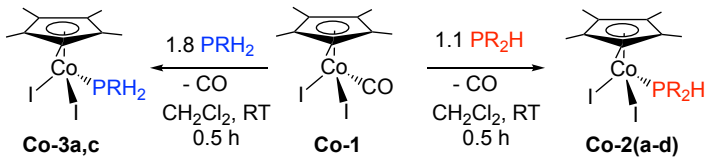

R = Ph (**a**), Tol^{p} (**b**), Cy (**c**), Pr^{i} (**d**)

Intrigued by the ease of PEt₂H coordination, I isolated pure bis(phosphine) complex **Co-4e** by adding ~2 equiv of PEt₂H to **Co-1**, as confirmed by NMR and ESI-MS (Section 3.6.4). The ability of I⁻ to move easily from inner to outer coordination sphere (Scheme 3.2) is known for other half sandwich Co systems.[10–12] A ligand redistribution equilibrium

(Scheme 3.2) poses challenges for isolating the other two bis(phosphine) complexes, [Co(η^5-Cp*)I(PR_2H)$_2$]I (**Co-4a,b**). The addition of PR_2H (R = Ph, Tol^p; 2~10 equiv) produces solutions containing complexes **Co-4a,b** as the major product (Figure 3.1a,b), from which brown solids could be obtained. NMR spectra (^{1}H, ^{31}P{^{1}H} and ^{13}C{^{1}H}) of these solids always reveal about 60% **Co-4** together with ~20% each of **Co-2** and free phosphine (Appendix C). This suggests that pure **Co-4** is probably isolated but it undergoes an equilibrium with **Co-2** and the free phosphine in a NMR sample. This phosphine lability (likely owing to steric crowding at the Cp*Co fragment) is unsatisfactory from a synthetic viewpoint but augurs well for hydrophosphination catalysis that depends on the rapid replacement of product phosphine at a metal center.

Scheme 3.2 Substitution chemistry of complex **Co-1** in the presence of excess PR_2H or PRH_2.

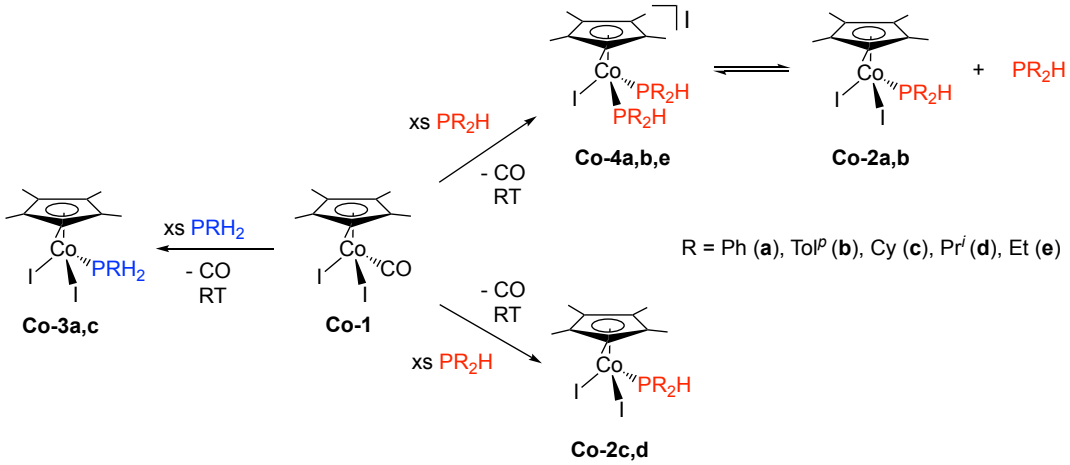

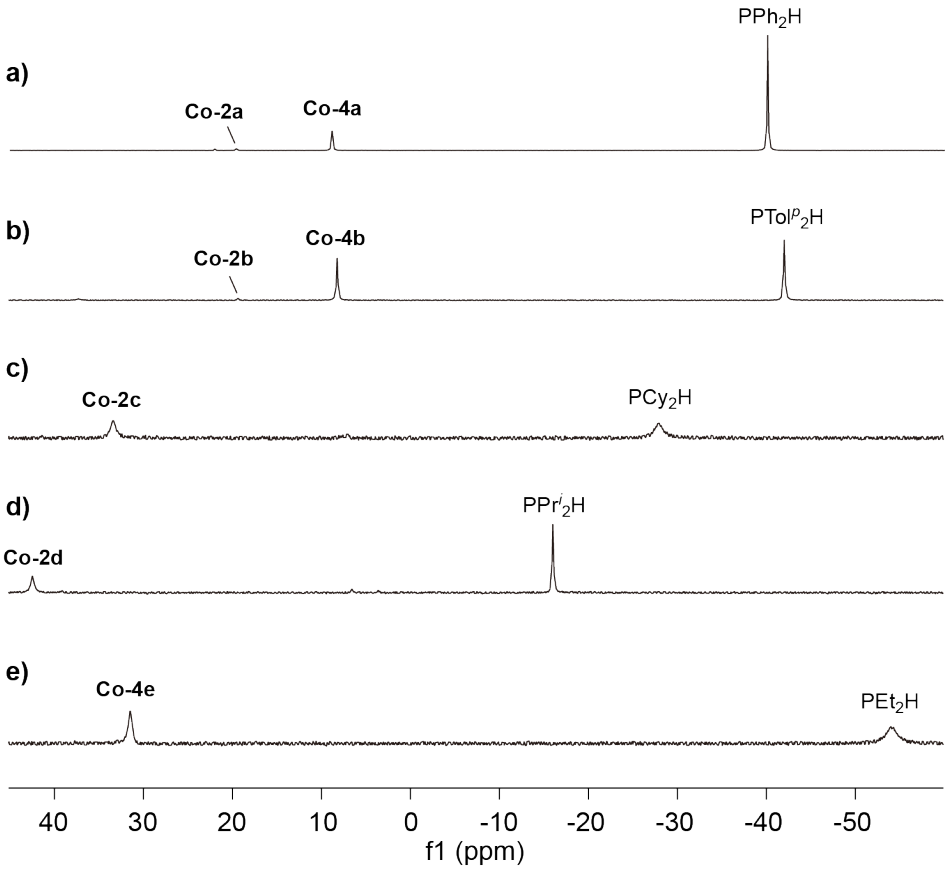

Figure 3.1 $^{31}P\{^{1}H\}$ NMR spectra (121.55 MHz, C_6D_6) of the mixture of **Co-1** and 10 equiv of PR_2H. R = (**a**) Ph, (**b**) Tol^p, (**c**) Cy, (**d**) Pr^i, (**e**) Et.

There is no formation of the bis(phosphine) complexes with either bulky PR_2H ligands (R = Cy, Pr^i) or PRH_2 ligands (R = Ph, Cy), as shown in Scheme 3.2. The addition of excess PCy_2H or PPr^i_2H to **Co-1** gives only the mono(phosphine) complex **Co-2c** or **Co-2d** (Figure 3.1c or d). This may be interpreted as the Co center being too crowded to bind two bulky PR_2H ligands.[9] The addition of excess PRH_2 to **Co-1** also generates only the mono(phosphine) complex **Co-3a,c** (Figure 3.2), which is consistent with the weaker donor ability of these ligands described above.[9]

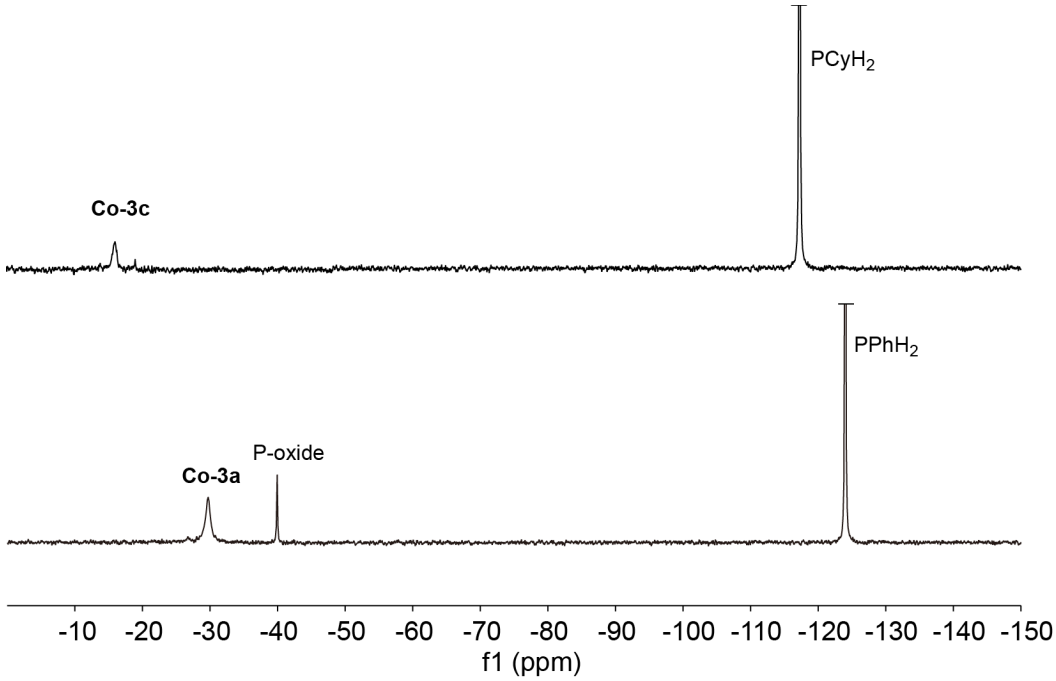

Figure 3.2 $^{31}P\{^{1}H\}$ NMR spectra (121.55 MHz, C_6D_6) of the mixture of **Co-1** and 10 equiv of PRH_2. R = Ph (**a**), Cy (**c**).

3.2.2 Dicationic phosphine complexes $[Co(\eta^5\text{-}Cp^*)(NCCH_3)_2(PR_2H)][SbF_6]_2$ (Co-6) and $[Co(\eta^5\text{-}Cp^*)(NCCH_3)(PR_2H)_2][SbF_6]_2$ (Co-7)

Complex $[Co(\eta^5\text{-}Cp^*)(NCCH_3)_3][SbF_6]_2$ (**Co-5**) was prepared using a literature procedure from $Co(\eta^5\text{-}Cp^*)I_2(CO)$ (**Co-1**).[13] The method and outcomes of synthesizing the secondary phosphine complexes $[Co(\eta^5\text{-}Cp^*)(NCCH_3)_2(PR_2H)][SbF_6]_2$ (**Co-6**) and $[Co(\eta^5\text{-}Cp^*)(NCCH_3)(PR_2H)_2][SbF_6]_2$ (**Co-7**) are quite similar to those described above for the iodide analogues, **Co-2** and **Co-4**. For mono(phosphine) complexes **Co-6(a-e)** (R = Ph (**a**), Tol^p(**b**), Cy(**c**) Pr^i (**d**) and Et (**e**)), only **Co-6c,d**, which contain bulky PR_2H ligands (R = Cy (**c**) and Pr^i (**d**)), can be isolated as pure solids (Scheme 3.3). It is challenging to isolate pure **Co-6a,b,e** containing smaller PR_2H ligands (R = Ph (**a**), Tol^p (**b**) and Et (**e**)) because of an equilibrium involving "over-substitution" by a second equivalent of PR_2H (Scheme 3.3 bottom). Attempts to isolate and purify either mono(phosphine) complexes

Co-6a,b,e or bis(phosphine) complexes **Co-7(a,b,e)**) always gives mixtures containing **Co-6** and **Co-7** even after multiple crystallizations.

Scheme 3.3 Synthesis of complex **Co-6** through the reaction of **Co-5** with 1 equiv PR_2H, highlighting an equilibrium involving **Co-6** and **Co-7** in CH_3CN solution (bottom box).

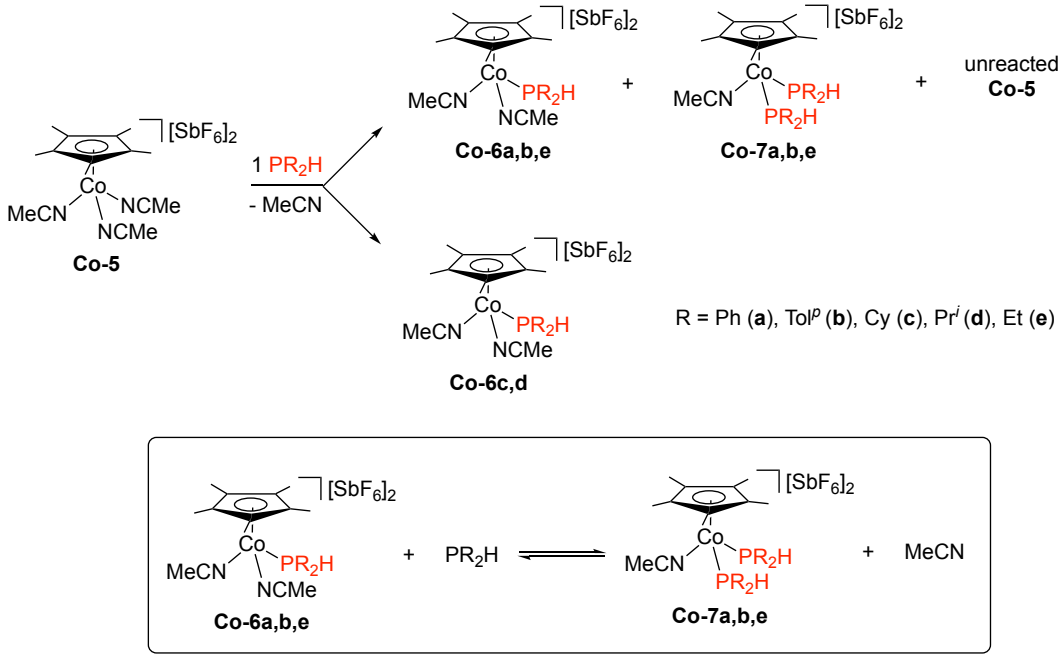

Solvation by CH_3CN plays an important role in dissolving dicationic complexes **Co-5** and **Co-6**; they are only soluble in acetonitrile (CH_3CN or CD_3CN). This is also consistent with the fact that the crystals of **Co-6a,c** (R = Ph (**a**) and Cy (**c**)) obtained for X-ray crystallography contain CH_3CN adducts (i.e. crystals analyzed are **Co-6a**•$2CH_3CN$ for and **Co-6c**•CH_3CN)

3.3 Characterization of Cp*Co(III) phosphine complexes

Phosphine complexes $Co(\eta^5\text{-}Cp^*)I_2(PR_2H)$ (**Co-2**), $Co(\eta^5\text{-}Cp^*)I_2(PRH_2)$ (**Co-3**), $[Co(\eta^5\text{-}Cp^*)I(PR_2H)_2]I$ (**Co-4**) and $[Co(\eta^5\text{-}Cp^*)(NCCH_3)_2(PR_2H)][SbF_6]_2$ (**Co-6**) (R = Ph (**a**), Tol^p (**b**), Cy (**c**), Pr^i (**d**), and Et (**e**)) were mostly characterized by NMR spectroscopy. Other types of characterization for some of these complexes included ESI-MS, IR

spectroscopy, CV, UV-vis, melting point determination and microanalysis. The microanalysis of **Co-6** is in progress. These experimental details are described in Section 3.5.

3.3.1 NMR characterization of Co-2, Co-3, Co-4, Co-6 and Co-7

The ^{31}P NMR data for complexes **Co-2**, **Co-3**, **Co-4**, **Co-6** and **Co-7** are shown in Table 3.1. Generally, ^{31}P signals for these Co complexes exhibit significant broadening ($\omega_{1/2}$ 40–102 Hz), attributable to the large quadrupole moment of ^{59}Co (I =7/2).[14] The ^{31}P shifts (δ 11–46 ppm) of iodide-containing secondary phosphine complexes **Co-2** and **Co-4** are similar to those for the dicationic complexes **Co-6** and **Co-7** (δ 17–47 ppm). There are surprisingly few reports of ^{31}P shifts for phosphine ligands at Co half-sandwich complexes, but the ^{31}P shifts for our Cp*Co(III) complexes are similar to those published (PR_3 and PR_2H: 7–50 ppm; PRH_2: –49 ppm).[15–18] The ^{1}H and ^{13}C{^{1}H} NMR data and assignments for these complexes are summarized in Section 3.5, Tables 3.4–3.7. ^{1}H, ^{31}P{^{1}H} and ^{13}C{^{1}H} NMR spectra of these complexes are presented in Appendix C.

Table 3.1 $^{31}P\{^{1}H\}$ NMR (202.51 MHz, solvent[a]) data for complexes **Co-2**, **Co-3**, **Co-4**, **Co-6** and **Co-7**.

Complex	δ (ppm)	$\omega_{1/2}$ (Hz)	Δδ (ppm)[b]
Co(η^5-Cp*)I$_2$(PPh$_2$H) (**Co-2a**)	22.7	75	62.7
Co(η^5-Cp*)I$_2$(PTol$^p_2$H) (**Co-2b**)	21.3	65	62.3
Co(η^5-Cp*)I$_2$(PCy$_2$H) (**Co-2c**)	36.9	71	63.9
Co(η^5-Cp*)I$_2$(PPr$^i_2$H) (**Co-2d**)	45.2	77	61.2
Co(η^5-Cp*)I$_2$(PEt$_2$H) (**Co-2e**)	37.1	60	92.1
Co(η^5-Cp*)I$_2$(PPhH$_2$) (**Co-3a**)	–30.0	90	90.0
Co(η^5-Cp*)I$_2$(PCyH$_2$) (**Co-3c**)	–9.5	102	90.5
[Co(η^5-Cp*)I(PPh$_2$H)$_2$]I (**Co-4a**)	11.5	60	51.5
[Co(η^5-Cp*)I(PTol$^p_2$H)$_2$]I (**Co-4b**)	15.4	62	49.9
[Co(η^5-Cp*)I(PEt$_2$H)$_2$]I (**Co-4e**)	36.9	61	91.9
[Co(η^5-Cp*)(NCCH$_3$)$_2$(PPh$_2$H)][SbF$_6$]$_2$ (**Co-6a**)	20.3	48	60.3
[Co(η^5-Cp*)(NCCH$_3$)$_2$(PTol$^p_2$H)][SbF$_6$]$_2$ (**Co-6b**)	17.9	44	58.9
[Co(η^5-Cp*)(NCCH$_3$)$_2$(PCy$_2$H)][SbF$_6$]$_2$ (**Co-6c**)	35.6	40	62.6
[Co(η^5-Cp*)(NCCH$_3$)$_2$(PPr$^i_2$H)][SbF$_6$]$_2$ (**Co-6d**)	46.4	47	62.4
[Co(η^5-Cp*)(NCCH$_3$)$_2$(PEt$_2$H)][SbF$_6$]$_2$ (**Co-6e**)	26.2	60	81.2
[Co(η^5-Cp*)(NCCH$_3$)(PPh$_2$H)$_2$][SbF$_6$]$_2$ (**Co-7a**)	19.6	46	59.6
[Co(η^5-Cp*)(NCCH$_3$)(PTol$^p_2$H)$_2$][SbF$_6$]$_2$ (**Co-7b**)	17.5	41	58.5
[Co(η^5-Cp*)(NCCH$_3$)(PEt$_2$H)$_2$][SbF$_6$]$_2$ (**Co-7e**)	26.6	54	81.6

[a] C_6D_6 for **Co-2** and **Co-3**, CD_2Cl_2 for **Co-4a**, $CDCl_3$ for **Co-4b,e**, CD_3CN for **Co-6** and **Co-7**.

[b] $\Delta\delta = \delta_{\text{coordinated phosphine}} - \delta_{\text{free phosphine}}$

3.3.2 X-ray analysis of Co-1, Co-2c, Co-3c, Co-4e and Co-6a,c

The structures of complexes **Co-1**, **Co-2c**, **Co-3c**, **Co-4e** and **Co-6a,c** were confirmed by X-ray crystallography (Figure 3.3 and Table 3.2). The Cp*-Co distances are consistent throughout this series of solid-state structures (1.70–1.72 Å). The bulk of the Cp* ligand and its closeness to the Co center increases the steric congestion in the Co coordination sphere, which is consistent with the observed variable Co-P bond distances (2.18–2.27 Å). This can be explained by the impact of phosphine size. For example, the Co-P distance in **Co-2c** (2.2319(8) Å) is longer than in **Co-3c** (2.1805(10) Å), which correlates with the order of cone angles of phosphine ligands (PCy_2H (142°) > PH_2Cy (117°)) and not the σ-donor ability (PCy_2H > $PCyH_2$).[9] Similarly, the Co-P distance in **Co-6c** (2.2784(6) Å) is longer than that for **Co-6a** (2.2330(7) Å) and correlates with decreasing phosphine cone angle: PCy_2H (142°) > PPh_2H (126°).

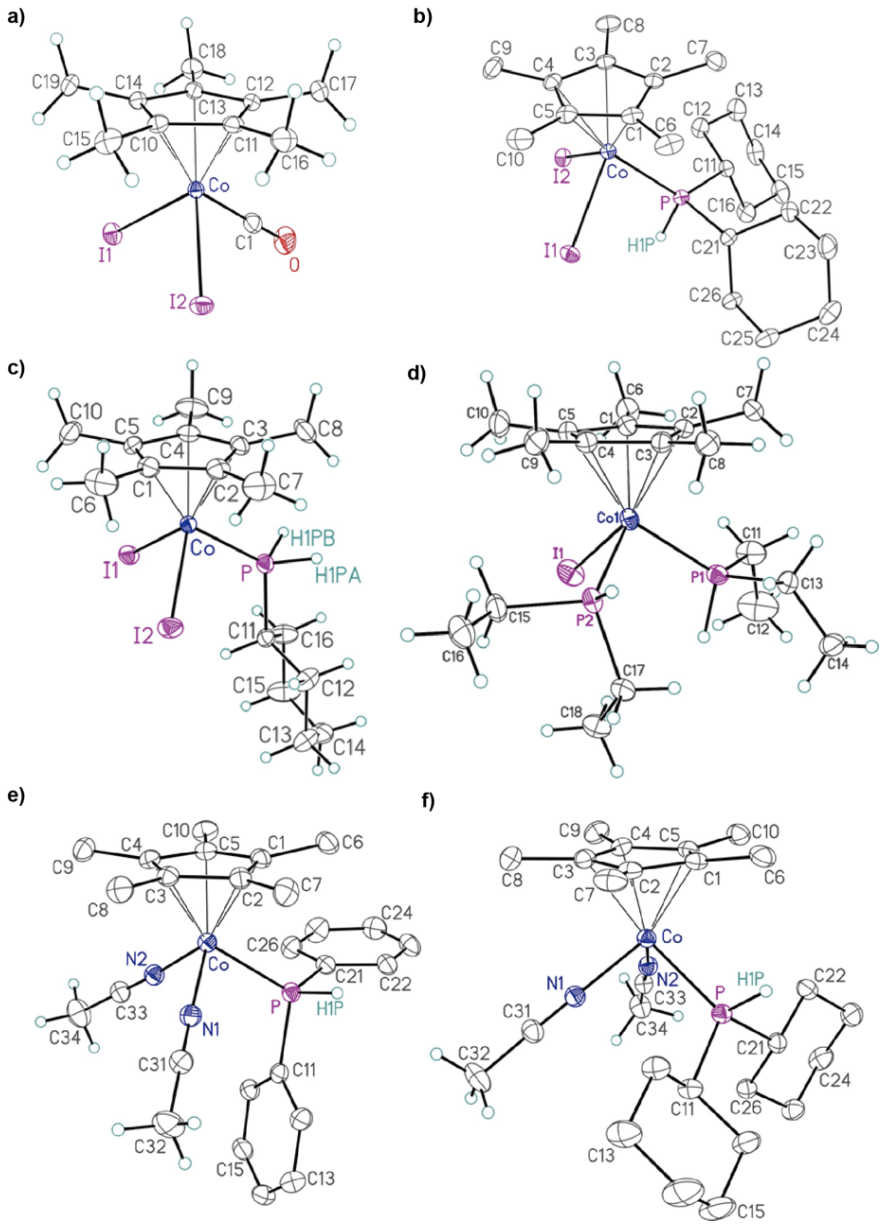

Figure 3.3 X-ray structures of: **a)** Co(η^5-Cp*)I_2(CO) **Co-1**; **b)** Co(η^5-Cp*)I_2(PCy_2H) **Co-2c**;[a] **c)** Co(η^5-Cp*)I_2($PCyH_2$) **Co-3c**; **d)** cation $[Co(\eta^5\text{-Cp*})I(PEt_2H)_2]^+$ in **Co-4e**; [b] **e)** cation $[Co(\eta^5\text{-Cp*})(NCCH_3)_2PPh_2H]^{2+}$ in **Co-6a**;[c] **f)** cation $[Co(\eta^5\text{-Cp*})(NCCH_3)_2PCy_2H]^{2+}$ in **Co-6c**;[c] showing the atom labeling. Non-hydrogen atoms are represented by Gaussian ellipsoids at the 30% probability level. Hydrogen atoms are shown with arbitrarily small thermal parameters.

[a]The phosphorus-bound hydrogen atom (H1P) is shown with an arbitrarily small thermal parameter; all other hydrogens are not shown.

[b]Only the major orientation of the two disordered ethyl groups is shown.

[c]The hydrogen atom attached to the phosphorus atom and the hydrogens of the acetonitrile ligands are shown with arbitrarily small thermal parameters; all other hydrogens are not shown.

Table 3.2 Selected interatomic distances (Å) and bond angles (°) in the structure of **Co-1**, **Co-2c**, **Co-3c**, **Co-4e** and **Co-6a,c**.[a]

	Co-1[b]		**Co-2c**
Co-C	1.798(3)	Co-P	2.2319(8)
Co-I1	2.5801(4)	Co-I1	2.6062(4)
Co-I2	2.5789(4)	Co-I2	2.5967(4)
Co-C_{cent}	1.708	Co-C_{cent}	1.718
C-O	1.114(4)	P-H	1.30(3)
C_{cent}-Co-C	126.8	C_{cent}-Co-P	132.0
C_{cent}-Co-I1	123.8	C_{cent}-Co-I1	122.2
C_{cent}-Co-I2	123.9	C_{cent}-Co-I2	122.9
C-Co-I1	88.17(10)	P-Co-I1	85.08(2)
C-Co-I2	90.02(10)	P-Co-I2	90.21(2)
I1-Co-I2	93.66(1)	I1-Co-I2	92.89(1)
	Co-3c[c]		**Co-4e**
Co-P	2.1805(10)	Co-I	2.5731(6)
Co-I1	2.5977(5)	Co-P1	2.1876(13)
Co-I2	2.5938(5)	Co-P2	2.2060(13)
Co-C_{cent}	1.707	Co-C_{cent}	1.721
P-H	1.30(5), 1.31(4)	P-H	1.33(4)
C_{cent}-Co-P	125.3	C_{cent}-Co-I	123.9
C_{cent}-Co-I1	123.5	C_{cent}-Co-P1	126.3
C_{cent}-Co-I2	124.1	C_{cent}-Co-P2	123.5
P-Co-I1	87.39(3)	I-Co-P1	88.77(4)
P-Co-I2	90.27(3)	I-Co-P2	90.72(4)
I1-Co-I2	96.13(2)	P1-Co-P2	93.29(5)
	Co-6a[b]		**Co-6c**[b]
Co-P	2.2330(7)	Co-P	2.2784(6)
Co-N1	1.924(2)	Co-N1	1.9257(18)
Co-N2	1.931(2)	Co-N2	1.9293(18)
Co-C_{cent}	1.700	Co-C_{cent}	1.710
P-H	1.23	P-H	1.28(2)
C_{cent}-Co-P	125.7	C_{cent}-Co-P	126.6
C_{cent}-Co-N1	122.5	C_{cent}-Co-N1	122.0
C_{cent}-Co-N2	123.6	C_{cent}-Co-N2	122.2
P-Co-N1	88.53(7)	P-Co-N1	91.82(6)
P-Co-N2	94.56(7)	P-Co-N2	94.41(5)
N1-Co-N2	92.30(9)	N1-Co-N2	90.39(7)

[a]C_{cent} denotes the centroid of the least-squares plane defined by C1–C2–C3–C4–C5.
[b]Obtained by Elena Liles and more details are shown in Appendixes G, K and L.
[c]Obtained by Cameron Zheng and more details are shown in Appendix I.

The secondary phosphine in the dicationic Cp*Co complexes **Co-6** coordinates to the Co center apparently less strongly than in the neutral analogues **Co-2** and **Co-4**. For instance, the Co-P bond length of **Co-6c** (2.28 Å) is longer than the corresponding bond length of the neutral analogue **Co-2c** (2.23 Å). The "hard-soft" theory can rationalize the variation of Co-P distances in the neutral **Co-2c** and dicationic **Co-6c**. Dicationic Co is considered "harder" than the neutral Co. Since phosphine is a soft ligand, I expect that phosphine ligands will form relatively poor bonds to the "harder" dicationic Co center.

3.3.3 UV-vis spectra of Co-1, Co-2(a-d), Co-3(a,c), Co-4(a,e), Co-5 and Co-6(a-d)

I obtained UV-vis spectra to gather information on electronic features of isolated complexes **Co-1**, **Co-2(a-d)**, **Co-3(a,c)**, **Co-4(a,e)**, **Co-5** and **Co-6(a-d)** (R = Ph (**a**), Tol^{p}(**b**), Cy(**c**), Pr^{i} (**d**) and Et (**e**)) (see in Figures 3.4–3.7 and detailed data in Table 3.8).

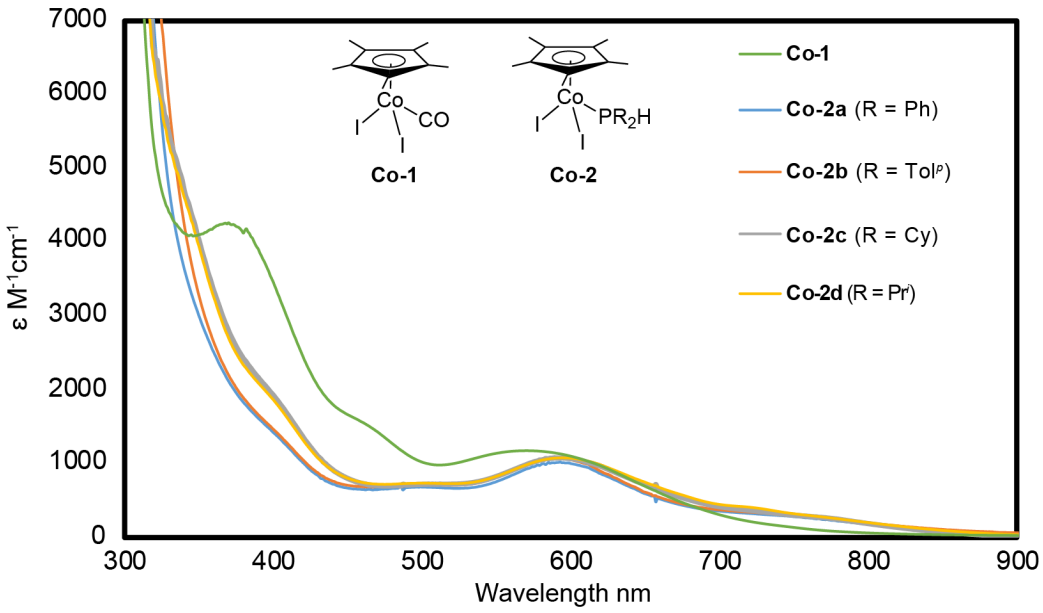

Figure 3.4 UV-vis absorption spectra of iodide complexes **Co-1** and **Co-2(a-d)** in CH_2Cl_2 at RT.

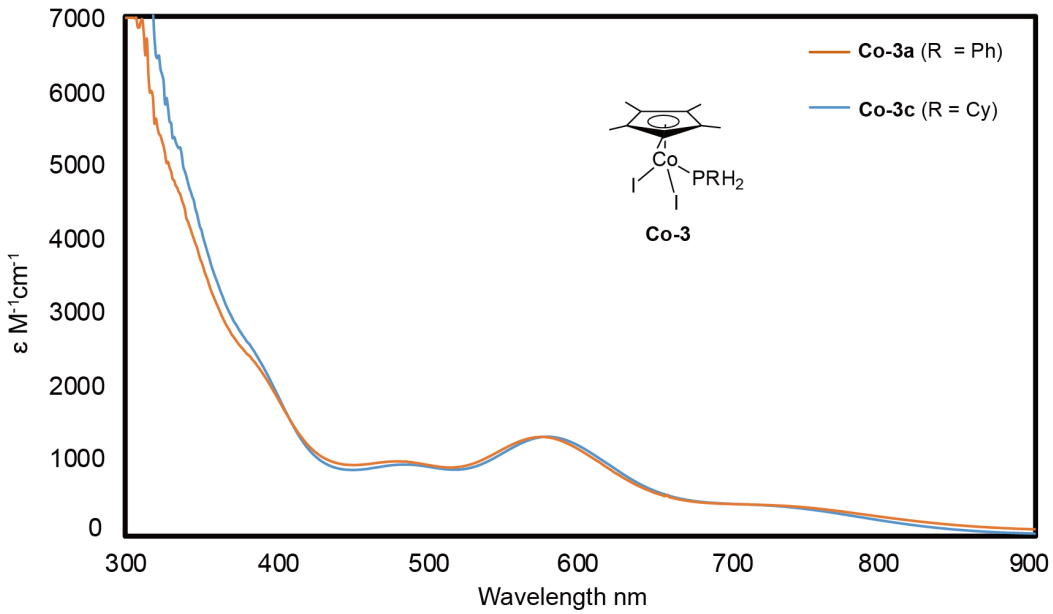

Figure 3.5 UV-vis absorption spectra of iodide complexes **Co-3(a,c)** in CH_2Cl_2 at RT.

The UV-vis spectrum of the purple Co(η^5-Cp*)I_2(CO) (**Co-1**) exhibits three absorbance peaks at 370, 461 and 570 nm (Figure 3.4). The peaks at 370 and 570 nm could be due to charge transfer (CT). The absorbance peak at 461 nm is tentatively assigned to *d–d* transition. The UV-vis spectra of green Co(η^5-Cp*)I_2(PR_2H) (**Co-2(a-d)**) are similar (Figure 3.4). The peaks at ~396 and ~ 593 nm are tentatively assigned to CT; the peaks at ~ 497 nm could be due to *d-d* transitions. Different from **Co-1**, extra broad, weak peaks (ε = ~ 3.2 x 10^2 M^{-1} cm^{-1}) centered around 726 nm are observed, which is assigned to *d-d* transition. In addition, the UV-vis spectra of purple Co(η^5-Cp*)I_2(PRH_2) (**Co-3a,c**) (Figure 3.5) are similar to those of **Co-2(a-d)**. The similarity of UV-vis spectra for these phosphine complexes **Co-2** and **Co-3** indicates that the type of phosphine ligands at Co(η^5-Cp*)I_2 fragment has no impact on their frontier orbitals. Except for these weak broad peaks at ~ 726 nm, all assigned peaks for **Co-2** and **Co-3** are red-shifted (to lower energy) than **Co-1**.

It suggests that replacing from CO to phosphine changes the frontier orbitals of the Cp*Co complexes.

The UV-vis spectra of cationic $[Co(\eta^5\text{-}Cp^*)I(PR_2H)_2]I$, **Co-4a** (R = Ph) and **Co-4e** (R = Et), exhibit three absorbance peaks (probably CT), but much more intense optical transitions compared to neutral **Co-1**, **Co-2** and **Co-3** (Figure 3.6). Different from **Co-2** and **Co-3**, different phosphine ligands (Ph vs. Et) significantly affect electronic transitions for bis(phosphine) complexes **Co-4a,e**. Compared to **Co-4a** (363 and 504 nm), the apparent CT peaks for **Co-4e** (345 and 454 nm) are more blue-shifted (to higher energy). Also, the *d-d* transition peaks for **Co-4a,e** are more blue-shifted than those for **Co-1**.

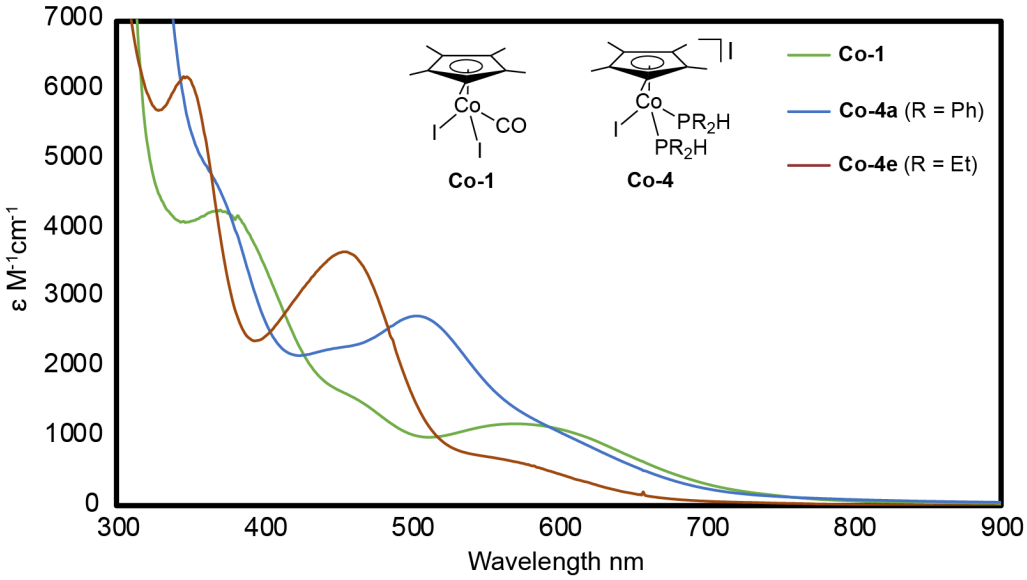

Figure 3.6 UV-vis absorption spectra of iodide complexes **Co-1** and **Co-4(a,e)** in CH_2Cl_2 at RT.

The UV-vis spectrum of purple $[Co(\eta^5\text{-}Cp^*)(NCCH_3)_3][SbF_6]_2$ (**Co-5**) shows two CT peaks at 316 and 511 nm (Figure 3.7), which are at the similar range reported for our iodide complexes but more intense. It also shows an absorbance peak at 381 nm possibly due to *d-d* transition. The UV-vis spectra of orange $[Co(\eta^5\text{-}Cp^*)(NCCH_3)_2(PR_2H)][SbF_6]_2$ (**Co-**

6(a-d)) all show an almost identical CT peaks at 468 nm, which is consistent with the observation for mono(phosphine) complexes **Co-2** and **Co-3**. Except for **Co-5**, this CT peak seems be to the only transition for **Co-6** in the UV-vis spectra, which could be explained by that other peaks are "swamped" by the more intense CT peak. Additionally, the λ_{max} values of **Co-6(a-d)** for charge transfer show more blue shifts than **Co-5**.

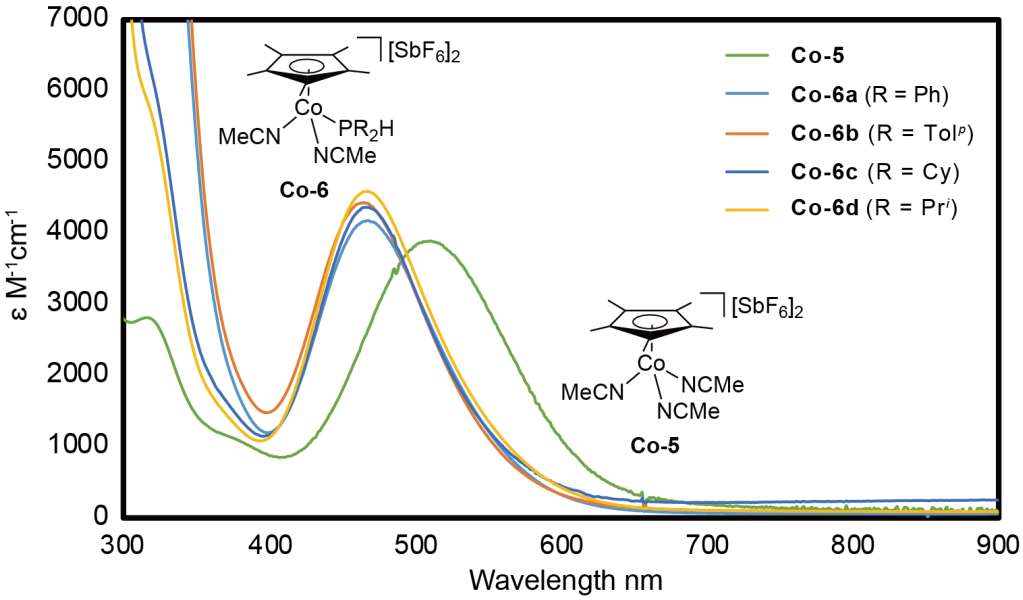

Figure 3.7 UV-vis absorption spectra of dicationic complexes **Co-5** and **Co-6(a-d)** in CH_3CN at RT.

In general, all transitions occurring at < 700 nm^{-1} in the spectra are attributable to metal to ligand or ligand to metal charge transfer (MLCT or LMCT; ε: 1 x 10^3 ~ 6 x 10^3 M^{-1} cm^{-1}) or *d-d* transition (ε: < 1.5 x 10^3 M^{-1} cm^{-1}). Additionally, broad weak peaks at > 700 nm^{-1} are observed in the spectra of mono(phosphine) complexes **Co-2** and **Co-3**, which probably originates from *d–d* transition (ε: 3 x 10^2 ~ 4 x 10^2 M^{-1} cm^{-1}). In the literature, detailed UV-vis absorbance assignments for CpCo or Cp*Co complexes are quite uncommon. To better understand or assign the UV-vis data, we may rely on our

computational collaborator, Dimitrios Pantazis, to identify the molecular orbitals participating in the transitions by using time-dependent DFT.

3.3.4 Electrochemical behaviour of Co-1, Co-2a, Co-4e, Co-5 and Co-6a.

I performed cyclic voltammetry (CV) experiments to understand the redox properties of the isolated complexes Co(η^5-Cp*)I_2(CO) (**Co-1**), Co(η^5-Cp*)I_2(PPh_2H) (**Co-2a**), [Co(η^5-Cp*)I(PEt_2H)$_2$]I (**Co-4e**), [Co(η^5-Cp*)($NCCH_3$)$_3$][SbF_6]$_2$ (**Co-5**) and [Co(η^5-Cp*)($NCCH_3$)$_2$(PPh_2H)][SbF_6]$_2$ (**Co-6a**). The CV results give some information on possible oxidation states of the Co during catalysis (*vide infra*). Electrochemical data obtained in CV experiments for these Co complexes is summarized in Table 3.3. More details for each complex are shown below in Figures 3.8–3.11.

Table 3.3 Selected peak potentials E_{pc}(red) and E_{pa}(ox) of complex **Co-1**, **Co-2a**, **Co-4e**, **Co-5** and **Co-6a** from cyclic voltammetry (CV) data.[a]

Entry	Co	potential (V vs Fc/Fc^+)				potential (V vs Fc/Fc^+)			
		E_{pc}	E_{pa}	$E_{1/2}$	ΔE	E_{pc}	E_{pa}	$E_{1/2}$	ΔE
1	**Co-1**	–0.82	–0.57	–0.70	0.25	-	-	-	-
2	**Co-2a**	–1.26	–0.32	-	-	-	-	-	-
3	**Co-4e**	–0.98	–0.91	–0.96	0.09	–1.35	–1.47	–1.41	0.12
4	**Co-5**	–0.64	–0.56	–0.60	0.08	–1.73	-	-	-
5	**Co-6a**	–0.67	–0.58	–0.63	0.09	–1.20	-	-	-

[a] 1 mM [Co] in CH_3CN, scan rate $\nu = 0.1$ V s^{-1}, 0.1 M supporting electrolyte Bu_4NPF_6. The voltammogram is referenced the Fc/Fc^+ redox couple. Fc/Fc^+ = ferrocene/ferrocenium.

Cp* or Cp Co complexes have a relatively wide range of redox potentials (Co(III)/Co(II): –0.26 ~ –1.65 V; Co(II)/Co(I): –0.93 ~ –2.25 V), which depend on the ancillary ligands attached to Co.[16,17,19–27] There is a lack of electrochemical research for Cp or Cp* Co (IV or V) complexes in the literature. The potentials I observe for our Cp*Co(III) complexes are within the range reported in the literature. Our complexes undergo reduction

from Co(III) to Co(II) (–0.64 ~ –0.98 V) and from Co(II) to Co(I) (–1.20 ~ –1.73 V). Because of the lack of literature reports for redox potentials (Co(IV) and Co(V)) of Cp* or Cp Co complexes, I could not explain most redox peaks above 0 V, explanations are only made for some peaks. Thus, I have no strong evidence for redox processes involving these higher Co oxidation states. Overall, the CV results presented below show that the reduction of Co(III) to Co(II) is mostly reversible and not difficult for our Cp*Co complexes under CV conditions. Although there is a difference between the electrochemical experiment setup and the solution environment in which the chemical reaction occurs, this suggests that Co(II) species could be formed in the Cp*Co(III)-catalyzed reactions (*vide infra*).

Details of CV results

The CV of precursor complex Co(η^5-Cp*)I_2(CO) (**Co-1**) is shown in Figure 3.8a. It exhibits an irreversible reduction peak at –0.70 V due to Co(III)/Co(II) and three irreversible oxidation peaks at 0.007, 0.24, and 0.96 V. The small oxidation peaks at 0.007 and 0.24 V are probably caused by the oxidation of a free iodide anion (I^-) based on the literature.[26,28] The free I^- could come from the dissociation of the iodide ligand at **Co-1** under CV conditions.

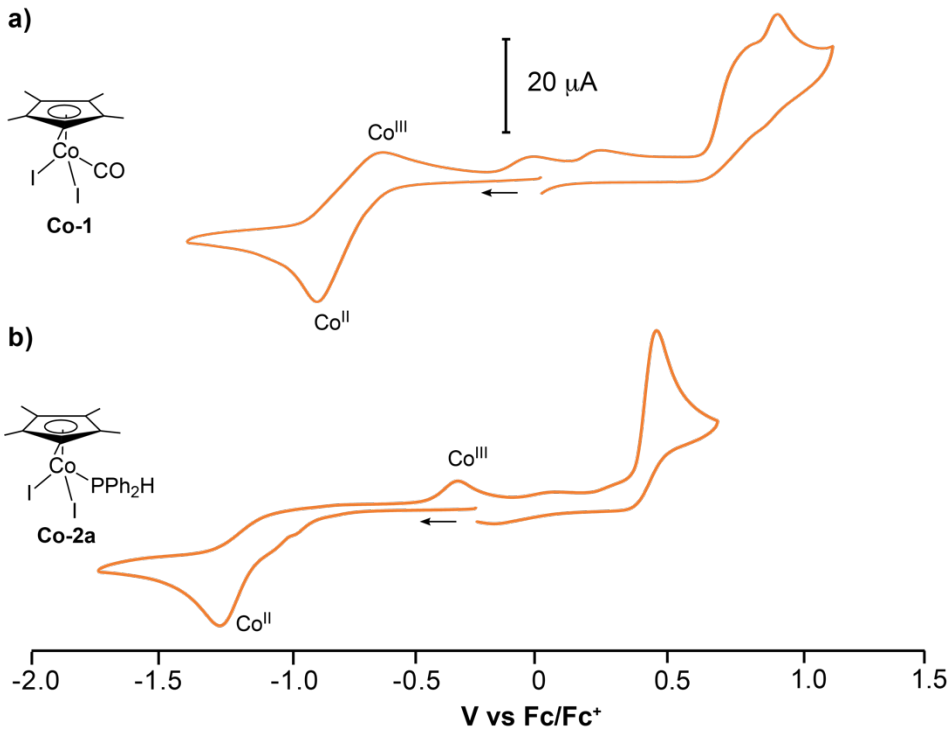

Figure 3.8 Cyclic voltammograms of complexes (**a**) **Co-1** and (**b**) **Co-2a**. 1 mM [Co] in CH_3CN, scan rate $\nu = 0.1$ V s^{-1}, 0.1 M supporting electrolyte Bu_4NPF_6. The voltammogram is referenced to the Fc/Fc^+ redox couple.

As shown in Figure 3.8b, the CV of **Co-2a** shows a small irreversible reduction peak at –0.96 V presumably due to ligand dissociation and a large irreversible reduction peak at –1.26 V assigned to Co(II)/Co(I). In addition, there are two major irreversible oxidation peaks at –0.32 and 0.44 V and some small oxidation peaks around 0 V in the CV. The peak at –0.32 V is tentatively assigned to the oxidation of Co(II) to Co(III).

To better understand why redox processes of **Co-2a** are irreversible, I performed CV experiments at different scan rates (Figure 3.9). One of the most common reasons for observing an irreversible redox process is an electron transfer reaction (E) followed by an irreversible chemical reaction (C), referred to as an EC mechanism. In other words, the Co(II) species generated at the electrode undergoes irreversible chemical decomposition. Scan rate experiments can help identify if there are irreversible chemical reactions under

CV conditions. With increasing scan rate, the time scale of the CV experiment competes with the time scale of the chemical reaction, leaving more Co(II) observable. Figure 3.9 shows a more intense peak at –0.32 V due to the oxidation of Co(II) back to Co(III) as the scan rate is increased, supporting the hypothesis that the reduced **Co-2a** decomposes under CV conditions. A possible decomposition is by loss of a ligand from the reduced Co complex. The preferences for coordination numbers vary based on the oxidation states of the metal.

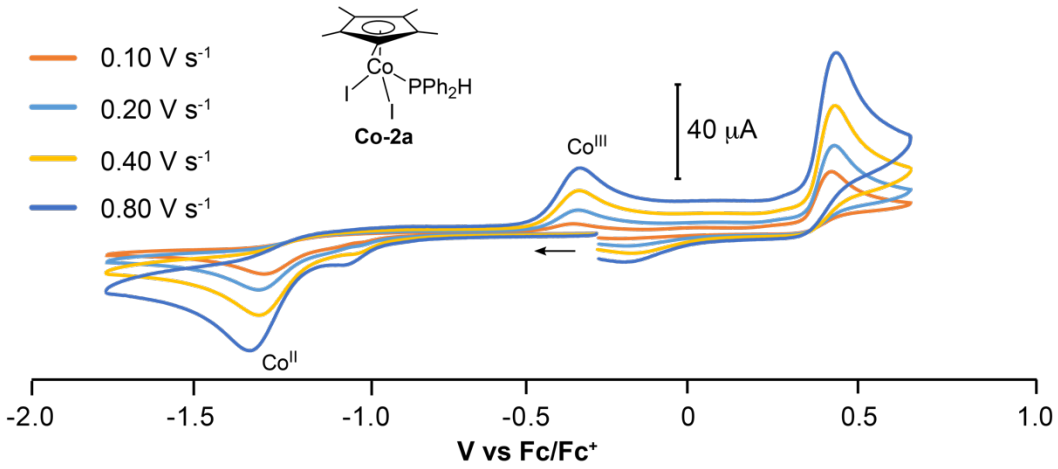

Figure 3.9 Effect of the scan rate (ν) on the CV of complex **Co-2a**. 1 mM [Co] in CH_3CN, 0.1 M supporting electrolyte Bu_4NPF_6. The voltammogram is referenced to the Fc/Fc^+ redox couple.

The CV of cationic bis(phosphine) complex **Co-4e** exhibits a more complicated CV than **Co-2a** and **Co-1** (Figure 3.10). It has two reversible peaks assigned to Co(III)/Co(II) ($E_{1/2}$ = –0.96 V) and Co(II)/Co(I) ($E_{1/2}$ = –1.41 V). An irreversible oxidation peak (E_{pa} = 0 V) and two quasi-reversible peaks ($E_{1/2}$ = 0.23 and 1.02 V) are possibly due to coordinated or free iodide oxidation. An irreversible reduction peak (E_{pc} = –0.49 V) and some tiny peaks were unidentified. The CV of **Co-4e** shows more reversible redox events than those of **Co-1** and **Co-2a**, presumably due to the less labile PEt_2H ligand. This is consistent with

the small size and high donor ability of PEt_2H, and my earlier scan rate experiment suggested that complex decomposition under the CV condition is most likely caused by ligand dissociation.

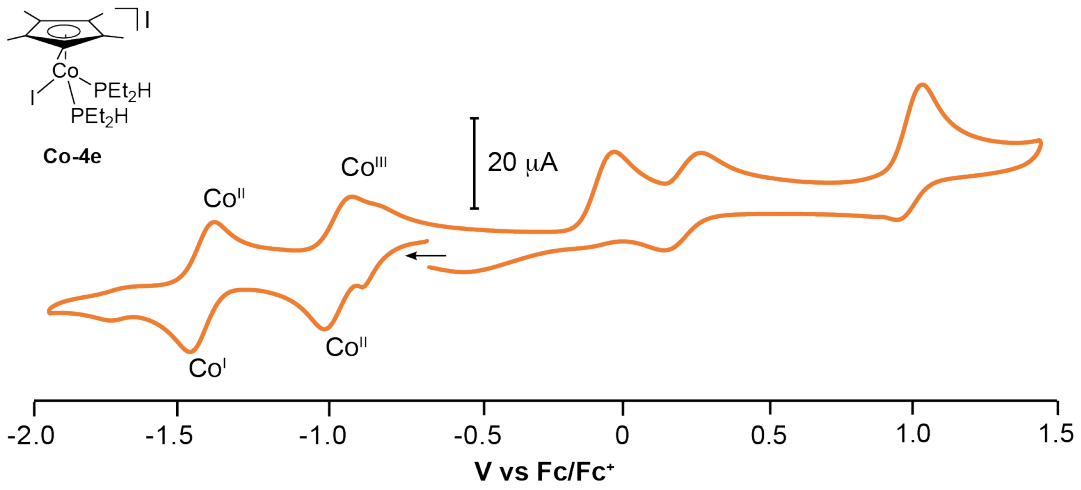

Figure 3.10 Cyclic voltammogram of complex **Co-4e**. 1 mM [Co] in CH_3CN, scan rate ν = 0.1 V s^{-1}, 0.1 M supporting electrolyte Bu_4NPF_6. The voltammogram is referenced to the Fc/Fc^+ redox couple.

The CV of **Co-5** shows a reversible peak ($E_{1/2}$ = –0.60 V) due to Co(III)/Co(II) (Figure 3.11a). For two major irreversible reduction peaks, one near –1.73 V is tentatively assigned to Co(II)/Co(I), and the other at –1.96 V is probably due to undefined chemical decomposition. The CV of **Co-6a** shows a nearly identical reversible peak ($E_{1/2}$ = –0.60 V) due to Co(III)/Co(II) (Figure 3.11b) relative to **Co-5**. This result suggests that the PPh_2H ligand at the Cp*Co(III) center does not affect the energy of the LUMO, which will receive the extra electron. However, more unidentified irreversible reduction and oxidation peaks were observed for **Co-6a**, suggesting that the PPh_2H ligand is not inert under the CV conditions (e.g. PPh_2H probably participates in chemical reactions like substitution by CH_3CN).

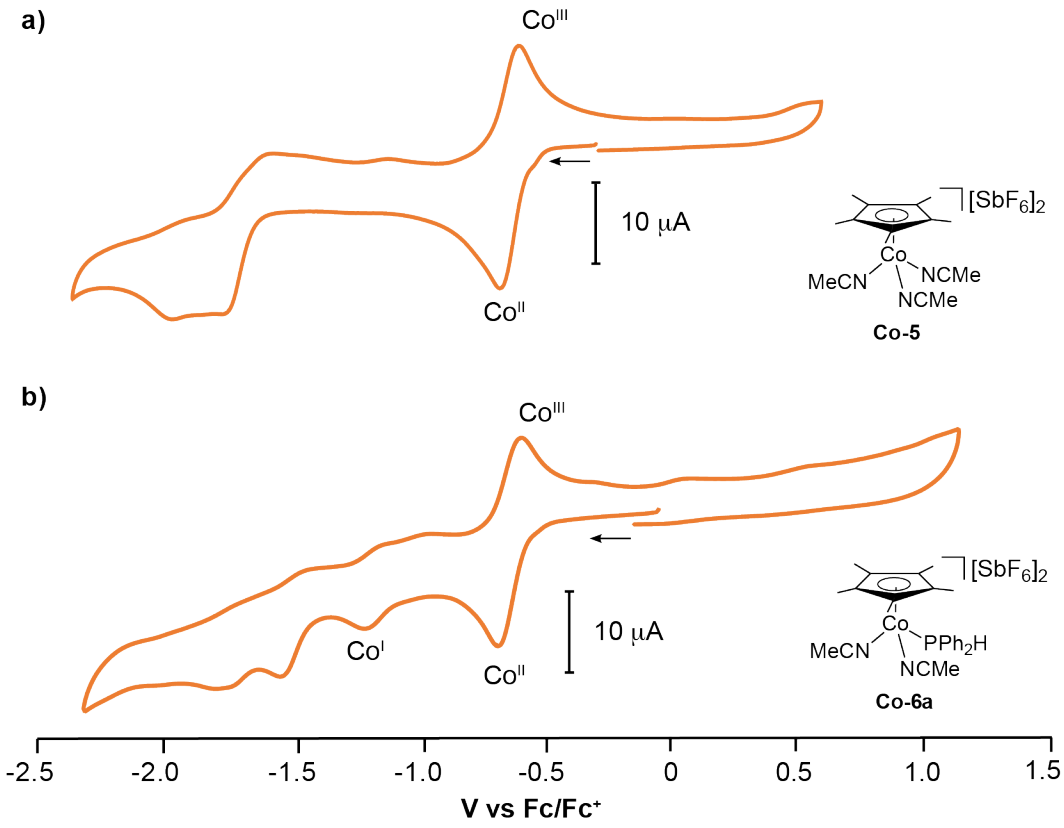

Figure 3.11 Cyclic voltammograms of **a) Co-5** and **b) Co-6a**. 1 mM [Co] in CH_3CN, scan rate $\nu = 0.1$ V s^{-1}, 0.1 M supporting electrolyte Bu_4NPF_6. The voltammogram is referenced to the Fc/Fc^+ redox couple.

3.4 Preliminary investigation of the participation of Cp*Co complexes in reactions involving P-H activation.

The activity of $Co(\eta^5\text{-}Cp^*)I_2(CO)$ (**Co-1**) and $[Co(\eta^5\text{-}Cp^*)(NCCH_3)_3][SbF_6]_2$ (**Co-5**) for catalytic hydrophosphination and dehydrocoupling has been assessed. Based on preliminary investigations (*vide infra*), complexes **Co-1** and **Co-5** show nearly identical activity. These complexes also exhibit an interesting dynamic process in the presence of excess phosphines. I chose to use PPh_2H as a model phosphine substrate for these investigations. The results indicate that ancillary ligands (i.e. I^- and CH_3CN) have comparable effect on the reaction products or processes in the Cp*Co system. The details

of Cp*Co(III)-catalyzed hydrophosphination using **Co-1** are presented in Chapter 4. The detailed investigations of dehydrocoupling of phosphine using **Co-1** are presented in Chapter 5. Detailed studies of the interesting dynamic process between **Co-5** and excess PPh_2H appear in Chapter 6.

3.4.1 Preliminary investigation of Cp*Co complexes in catalytic hydrophosphination of *tert*-butyl acrylate with PPh_2H

Complex $Co(\eta^5\text{-}Cp^*)I_2(CO)$ (**Co-1**) provides an entry point to test the catalytic viability of Cp*Co(III) complexes for hydrophosphination (Figure 3.12a). My preliminary assessments using 10 mol% **Co-1** show high catalytic activity for the hydrophosphination of *tert*-butyl acrylate with PPh_2H in the presence of at least a slight excess of a base (DBU, 1,8-diazabicyclo[5.4.0]undec-7-ene) with respect to **Co-1**. Total consumption of PPh_2H is achieved within 15 min, and the reaction gives a linear *anti*-Markovnikov product $Ph_2P(CH_2CH_2CO_2Bu^t)$ (~ 90%) and a byproduct $Ph_2P\text{-}PPh_2$ (~10%).

Phosphine complexes $Co(\eta^5\text{-}Cp^*)I_2(PPh_2H)$ (**Co-2a**) and $[Co(\eta^5\text{-}Cp^*)I(PPh_2H)_2]I$ (**Co-4a**) were also tested for the catalytic hydrophosphination (Figure 3.12b,c). These two catalytic reactions give identical results to that of **Co-1**. Since there is no discernible difference in performance among these catalysts, it is reasonable to assume that the formation of Co(III) phosphine complexes (i.e. **Co-2** or **Co-4**) is a precursor step to catalysis. Given that there is no difference between the reaction using **Co-2a** and **Co-4a**, the essential catalytic step appears to require at least one coordinated phosphine, which may be deprotonated by a base to generate a phosphido ligand, $Co\text{-}PPh_2$. This also explains why the base is required for this catalytic process. The specific basicity of the base is important for the catalysis. Mechanistic details are presented in Section 4.2.2.

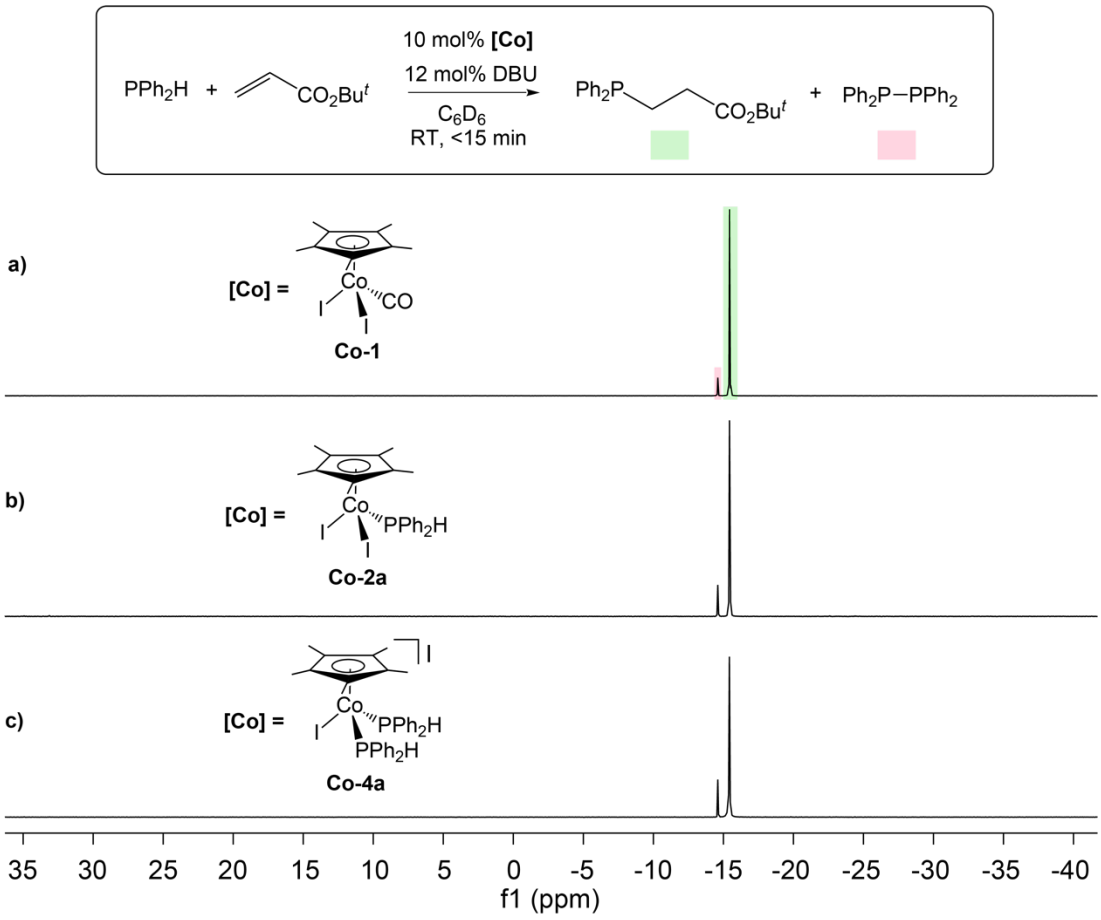

Figure 3.12 $^{31}P\{^{1}H\}$ NMR spectra (121.55 MHz, C_6D_6) of the hydrophosphination of *tert*-butyl acrylate with PPh_2H using 10 mol% **a) Co-1**, **b**) **Co-2a** or **c) Co-4a**.

I also performed a preliminary experiment to test the catalytic viability of $[Co(\eta^5\text{-}Cp^*)(NCCH_3)_3][SbF_6]_2$ (**Co-5**) for the hydrophosphination of *tert*-butyl acrylate with PPh_2H in the presence of a slight excess DBU (Scheme 3.4). The catalysis using **Co-5** gives a result similar to that of **Co-1** in terms of catalytic activity and product distributions. Because of the solubility issue of dicationic complex **Co-5** (Section 3.2.2), the catalytic reaction can be only performed in CD_3CN. Thus, the spectrum of the reaction mixture is similar to those for **Co-1** but slightly different chemical shifts for the products because of different solvents.

Scheme 3.4 Catalytic hydrophosphination using complex **Co-5** and DBU.

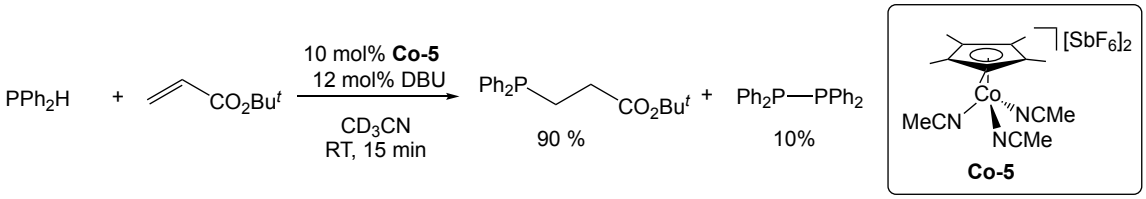

Although I observed modest hydrophosphination activity of Cp*Co complexes (TOF >36 h^{-1}; compared to that of our Cp*Ru catalyst described in Chapter 2, TOF 250 h^{-1}), I still need to answer two questions for this system: why does it require an excess of base (not just one equiv with respect to Co), and why does it produce the byproduct Ph_2P-PPh_2? These questions are answered by further investigations described in Chapter 4 (using **Co-1** as a model catalyst). Using **Co-1** instead of **Co-5** is mainly because of solubility consideration. Complex **Co-1** can be dissolved in polar and non-polar solvents, but **Co-5** is only soluble in CH_3CN.

Relevant to the future studies, I also tested the competitive coordination to complex **Co-1** between substrate PR_2H and alkene, showing that: in the presence of excess of both these reagents, $[Co(\eta^5\text{-}Cp^*)I(PPh_2H)_2]I$ (**Co-4a**) is the major Co species in the mixture. And the alkene does not bind to the Co(III) center at **Co-1**. More details are presented in Section 4.4.1, Chapter 4. The same result is found when complex **Co-5** are used under the identical condition.

3.4.2 Preliminary investigation of Cp*Co complexes in catalytic dehydrocoupling of PPh_2H

Since P-P bond formation occurred during the Co-catalyzed hydrophosphination described above, I assessed the catalytic activity of $Co(\eta^5\text{-}Cp^*)I_2(CO)$ (**Co-1**) and $[Co(\eta^5\text{-}Cp^*)(NCCH_3)_3][SbF_6]_2$ (**Co-5**) for dehydrocoupling of PPh_2H (Scheme 3.5). Both

complexes can catalyze dehydrocoupling of PPh_2H with or without cocatalyst DBU at a high temperature (i.e. 80 °C). Thus, unlike the hydrophosphination described above, adding DBU is not essential for the dehydrocoupling reaction but facilitates the reaction. This is consistent with the fact that the dehydrocoupling product conversion of DBU-mediated reaction is slightly higher than that of non-DBU-mediated. Another difference between the Co-mediated hydrophosphination and dehydrocoupling is that the catalytic dehydrocoupling requires high temperature (no catalysis at RT) while catalytic hydrophosphination occurs rapidly at RT.

Scheme 3.5 Preliminary assessments of dehydrocoupling of PPh_2H using **Co-1** and **Co-5**.

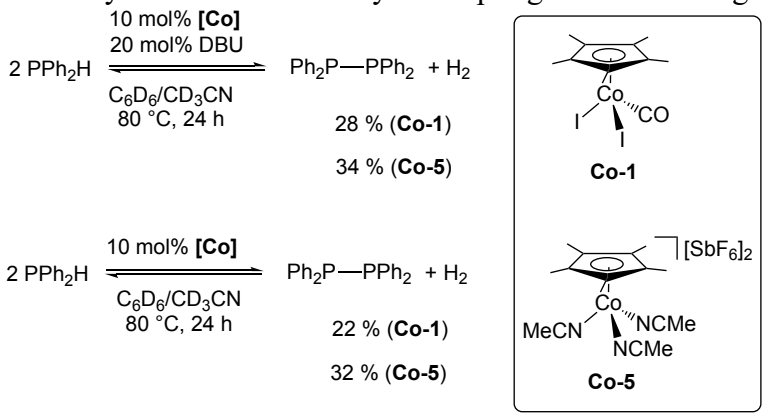

As shown in Scheme 3.5, **Co-5** shows slightly higher activity than **Co-1** under identical conditions. This slightly higher activity is partially relevant to the solvent (C_6D_6 vs. CD_3CN). Our preliminary investigation shows the conjugate acid (i.e. $[HDBU]^+$), which results from the deprotonation of Co phosphine complex, plays a role in the base-mediated dehydrocoupling reaction (see Chapter 5). I chose **Co-1** to study the dehydrocoupling of phosphines further, which is presented in Chapter 5. The reason of using **Co-1** as the model catalyst is described above.

3.4.3 Reactions of Co-1 and Co-5 with excess PPh_2H involving an interesting dynamic process

As described above (Figure 3.1 and 3.2, Section 3.2.1), I explored the substitution chemistry of complex Co(η^5-Cp*)I_2(CO) (**Co-1**) in the presence of excess phosphine, which gives a varied amounts of mono- and/or bis(phosphine) complexes, Co(η^5-Cp*)$I_2(PR_2H)$ (**Co-2**) and/or [Co(η^5-Cp*)$I(PR_2H)_2$]I **(Co-4)** (Scheme 3.2). The relative amounts of these complexes that appear in the reaction mixture vary with relative size and donor ability of phosphines. In addition, both ^{1}H and ^{31}P signals due to the free phosphine are broadened and lose the $^1J_{PH}$ coupling in the NMR spectra (see a PPh_2H example in Scheme 3.6 top and Figure 3.13). This indicates some dynamic process occurs in the mixtures, which could be a fast exchange of PPh_2H (i.e. coordination to Co) or reversible P-H activation of free PPh_2H. The ^{31}P NMR spectrum of a mixture of [Co(η^5-Cp*)$(NCCH_3)_3$][SbF_6]$_2$ (**Co-5**) in the presence of excess PPh_2H (Scheme 3.6 bottom and Figure 3.14) shows similar features to what was seen with **Co-1**: the free PPh_2H signal gets broad, and the P-H coupling disappears.

Scheme 3.6 Reactions of complex **Co-1** (top) and **Co-5** (bottom) with excess PPh_2H, showing the formation of corresponding bis(phosphine) complexes as major products.

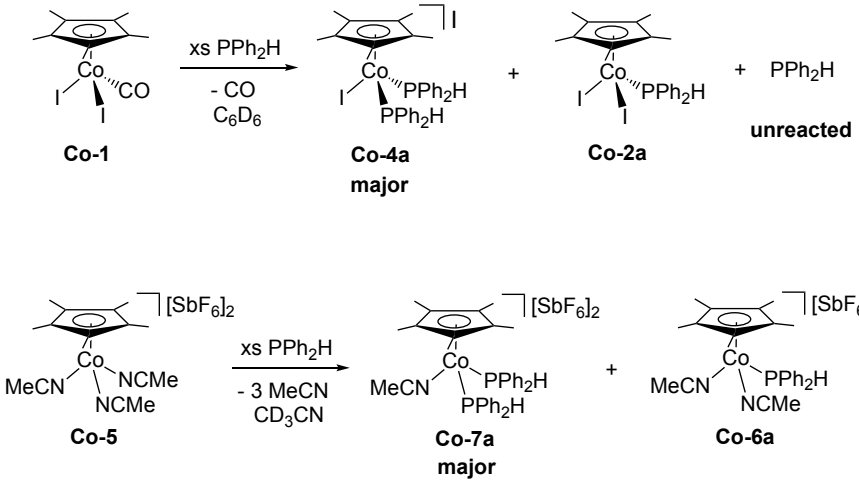

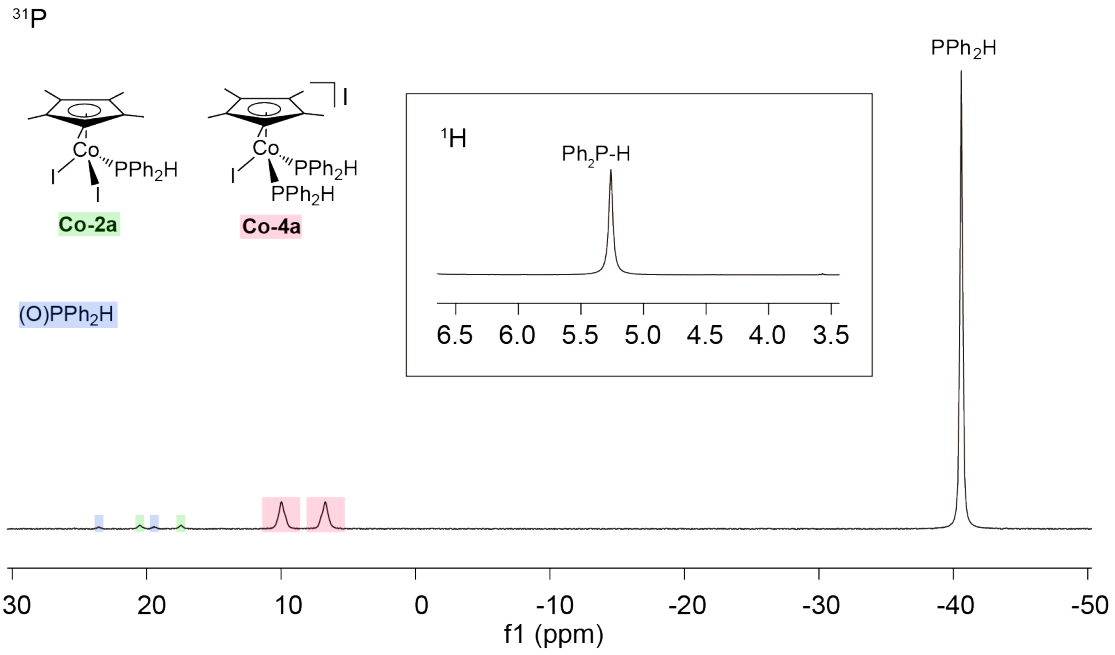

Figure 3.13 ^{31}P NMR (121.55 MHz, C_6D_6) spectrum of the reaction of **Co-1** with 10 equiv of PPh_2H, showing the absence of $^{1}J_{PH}$ coupling in free PPh_2H. Inset: P-H region of the ^{1}H NMR (300.27 MHz, C_6D_6) spectrum of the mixture.

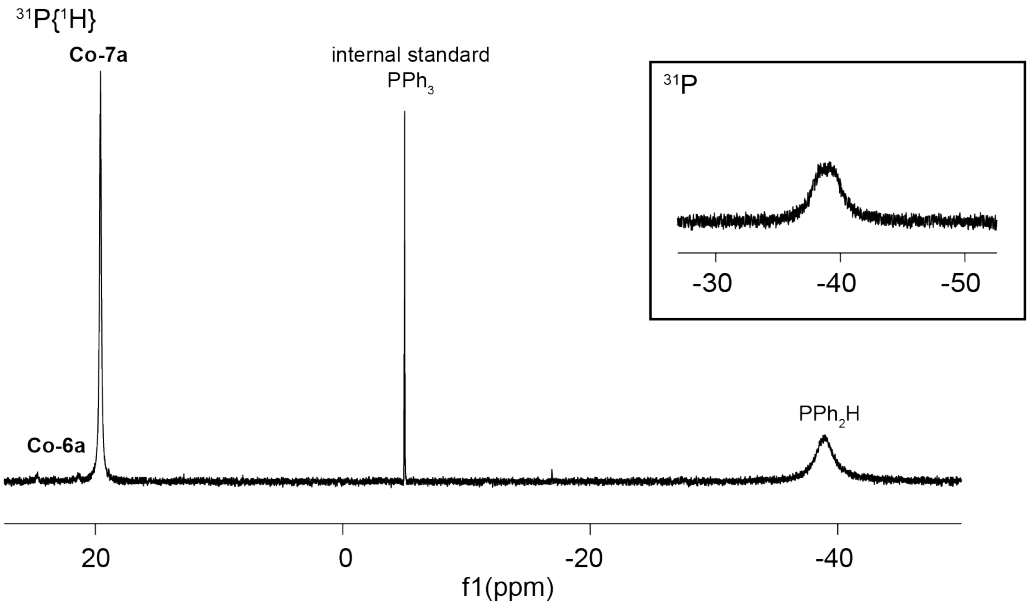

Figure 3.14 $^{31}P\{^{1}H\}$ NMR (202.51 MHz, CD_3CN) spectrum of the mixture of **Co-5** with 3 equiv of PPh_2H, showing the broadening of signal due to free PPh_2H. Note: the internal standard PPh_3 is in a sealed capillary. Inset: partial ^{31}P NMR of the mixture.

According to the "base-free" dehydrocoupling reaction mediated by Co(η^5-Cp*)I_2(CO) (**Co-1**) and [Co(η^5-Cp*)$(NCCH_3)_3$][SbF_6]$_2$ (**Co-5**) described above, P-H activation of substrate PPh_2H must occur, at least at high temperatures. My detailed investigations of this solution behaviour of Cp*Co(III) complexes are described in Chapter 6.

3.5 Conclusion

In this chapter, I described the synthesis and characterization of various Cp*Co(III) complexes, including Co(η^5-Cp*)I_2(CO) (**Co-1**), Co(η^5-Cp*)$I_2(PR_2H)$ (**Co-2(a-d)**), Co(η^5-Cp*)$I_2(PRH_2)$ (**Co-3a,c**), [Co(η^5-Cp*)$I(PR_2H)_2$]I (**Co-4a,b,e**), [Co(η^5-Cp*)$(NCCH_3)_3$][SbF_6]$_2$ (**Co-5**) and [Co(η^5-Cp*)$(NCCH_3)_2(PR_2H)$][SbF_6]$_2$ (**Co-6(a-d)**, R = Ph (**a**), Tol^p(**b**), Cy(**c**), Pr^i (**d**) and Et(**e**)). These complexes are relevant to my investigations of P-H activation reactions in the next three chapters.

Based on preliminary studies, complexes **Co-1** and **Co-5** are active in the catalytic hydrophosphination of *tert*-butyl acrylate with PPh_2H and the catalytic dehydrocoupling of PPh_2H. According to the substitution chemistry of **Co-1** and **Co-5**, the phosphine complexes **Co-3**, **Co-4**, **Co-6** and **Co-7** are probably precursors for these catalyses and lead to Co phosphido complexes that are important for the hydrophosphination and dehydrocoupling as described in Chapter 1. In addition, complexes **Co-1** and **Co-5** exhibit an intriguing interaction with excess PPh_2H, probably involving a P-H activation process.

This study broadens the chemistry of the Cp*Co(III) complex beyond the area of C-H activation. The study also includes NMR, UV-vis, and electrochemical data for Cp*Co(III) complexes with secondary phosphine ligands, contributing to the scant

literature on the physical properties of half sandwich Co complexes. In the following three chapters, I investigate these Co-mediated P-H activation reactions in detail.

3.6 Experimental

See Chapter 2, Section 2.5.1 for general experimental details**.** Melting/decomposition temperatures were recorded using a Gallenkamp apparatus and are uncorrected. Microanalysis was performed using the Perkin Elmer 2400 Series II CHNO/S analyzer in the Mass Spectrometry Laboratory at the University of Windsor, Windsor, ON, Canada. IR spectra were recorded for KBr pellets on a PerkinElmer FTIR Spectrum 1000 spectrophotometer. Electrospray ionization mass spectrometry (ESI-MS) was carried out on Waters QTOF Micromass and QTOF II instruments in the group of Prof. Scott McIndoe at the University of Victoria by Michelle Ting. Routine UV-vis spectra were acquired for samples in dry CH_2Cl_2 at RT on a Varian Cary-100 spectrophotometer or a Perkin-Elmer Lambda 1050 spectrometer.

3.6.1 Modified synthesis of Co(η^5-Cp*)I_2(CO) (Co-1)

The literature method was slightly modified.[8] A round bottom Schlenk flask was charged with $Co_2(CO)_8$ (14 mmol, 5.0 g) and CH_2Cl_2 (100 mL). Pentamethylcyclopentadiene (Cp*H, 36 mmol, 5.6 mL, 2.5 equiv) was added by syringe and allowed to reflux over 6 h. The resulting brown solution was cooled, and the solvent was removed under vacuum. Et_2O (50 mL) was added to the remaining solid *via* cannula transfer, and a solution of I_2 (36 mmol, 9.1 g, 2.5 equiv) in Et_2O (50 mL) was added dropwise from an addition funnel (Note: the I_2 needs to be finely ground to dissolve completely in Et_2O). The resulting brown solution was allowed to stir for 1 h. The solvent

was removed under vacuum from the resulting purple solution to yield a dark purple solid. The solid was then purified through a silica column (CH_2Cl_2: hexane = 4: 1). The solvent was removed from the resulting purple fractions by rotary evaporation to yield a dark purple solid (13 mmol, 12 g, 90%). Crystals were obtained from a concentrated CH_2Cl_2 solution (5 mL) layered with hexane or from slow evaporation of a concentrated CH_3CN solution (1 mL) (used to prepare crystals of X-ray quality).

^{1}H NMR (300.27 MHz, $CDCl_3$) δ 2.23 (s, 15H, Cp*). This is consistent with the literature.[8]

^{1}H NMR (300.27 MHz, C_6D_6) δ 1.61 (s, 15H, Cp*)

3.6.2 General procedure for the synthesis of Co(η^5-Cp*)I$_2$(PR$_2$H) (Co-2)

To a solution of complex **Co-1** (0.42–0.56 mmol) in CH_2Cl_2 (10 mL) in a Schlenk flask, PR_2H was added directly or as a hexane solution (0.46–0.61 mmol, 1.1 equiv). After 1 h stirring at RT, the resulting green solution was concentrated to 2 mL and layered with Et_2O (30 mL). The supernatant was removed by cannula, and the resulting dark green crystals were washed with pentane (3 x 10 mL) and dried under vacuum. Dark green crystals were obtained (0.18–0.46 mmol, 38–87 %).

3.6.2.1 Co(η^5-Cp*)I$_2$(PPh$_2$H) (Co-2a)

Complex **Co-1** (0.56 mmol, 0.27 g) and neat PPh_2H (0.58 mmol, 0.11 g, 1.1 equiv) were used. Dark green powder (0.46 mmol, 0.29 g, 82 %) was obtained. **Melting point:** 210–211 °C. **IR** (KBr, cm^{-1}): 2326 (w, ν_{PH}). **Anal.** found (calcd for $C_{22}H_{26}I_2PCo$): C, 41.32 (41.67); H, 3.92 (4.13).

3.6.2.2 Co(η^5-Cp*)I_2(PTol$^p_2$H) (Co-2b)

Complex **Co-1** (0.53 mmol, 0.25 g) and neat PTol$^p_2$H (0.58 mmol, 0.12 g, 1.1 equiv) were used. Dark green solid (0.46 mmol, 0.30 g, 87 %) was obtained. **Melting point**: 211–212 °C. **IR** (KBr, cm^{-1}): 2324 (w, ν_{PH}). **Anal.** found (calcd for $C_{24}H_{30}I_2PCo$): C, 43.32 (43.53); H, 4.34 (4.57).

3.6.2.3 Co(η^5-Cp*)I_2(PCy_2H) (Co-2c)

Complex **Co-1** (0.53 mmol, 0.25 g) and PCy_2H (0.58 mmol, 0.11 g, 1.1 equiv) were used. Dark green solid (0.45 mmol, 0.29 g, 86 %) was obtained. **Melting point**: 165–167 °C. **IR** (KBr, cm^{-1}): 2318 (w, ν_{PH}). **Anal.** found (calcd for $C_{22}H_{38}I_2PCo$): C, 40.43 (40.89); H, 5.76 (5.93).

3.6.2.4 Co(η^5-Cp*)I_2(PPr$^i_2$H) (Co-2d)

To a solution of **Co-1** (0.48 mmol, 0.23 g,) in CH_2Cl_2 (10 mL) in a Schlenk flask, a solution of PPr$^i_2$H in hexanes (0.53 mmol, 0.30 M, 1.8 mL, 1.1 equiv) was added. After 1 h stirring at RT, the green solution was concentrated to 2 mL and layered with pentane (20 mL). The supernatant was removed from the dark slurry by cannula. The solvent was removed from this supernatant under vacuum, and a dark green solid was obtained (0.18 mmol, 0.10 g, 38 %). **Melting point:** 123–125 °C. **IR (KBr, cm^{-1}):** 2320 (w, ν_{PH}). **Anal.** found (calcd for $C_{16}H_{30}I_2PCo$): C, 30.98 (33.95); H, 4.79 (5.34).

The unsatisfactory elemental analysis may be attributed to the instability of this complex under vacuum: even in the solid-state, complex **Co-2d** slowly releases PPr$^i_2$H to give [Co(η^5-Cp*)I(μ-I)]$_2$ (calcd C, 26.81; H, 3.38)[29] and other decomposition products at RT, as determined by ^{1}H NMR (Figure 3.15).

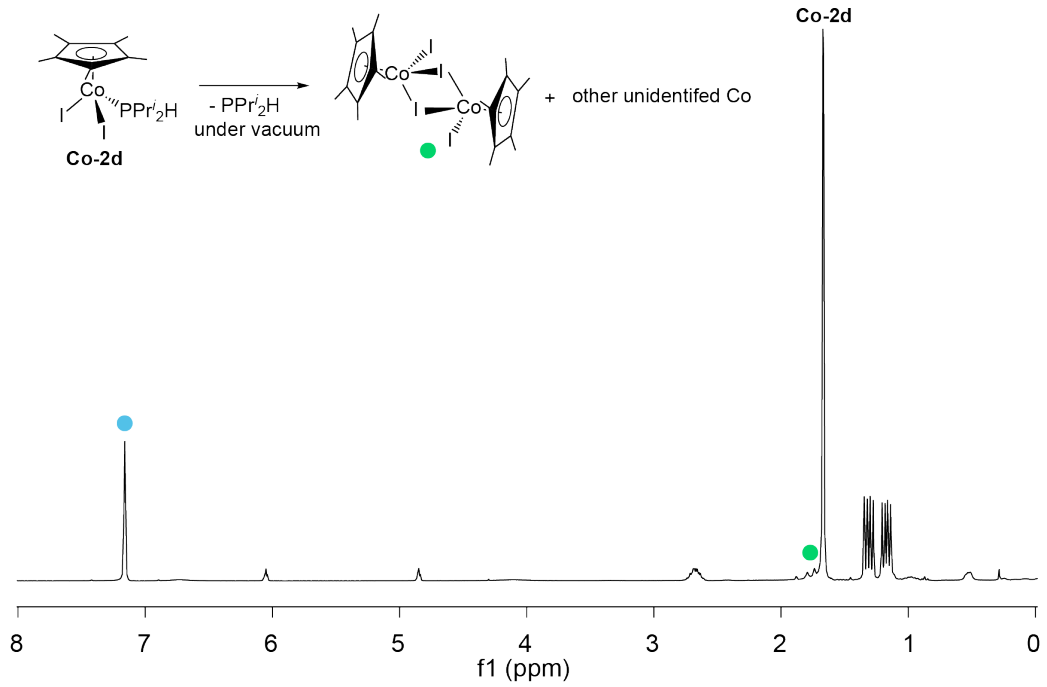

Figure 3.15 ^{1}H NMR (300.27 MHz, C_6D_6) spectrum of complex **Co-2d** dried under vacuum for 1 h, showing its decomposition to several Co-containing species. Residual proteo-solvent is marked with •.

3.6.3 General procedure for the synthesis of Co(η^5-Cp*)I$_2$(PRH$_2$) (Co-3)

To a solution of complex **Co-1** (2.1 mmol) in CH_2Cl_2 (20 mL) in a Schlenk flask, a solution of PH_2R in hexanes (3.7–3.8 mmol, 1.8 equiv) was added. After stirring for 1 h at RT, the purple solution was concentrated to 5 mL, layered with pentane (40 mL), and then stored in a freezer (–14 °C) over 48 h. The supernatant was removed by cannula, and the resulting shiny purple crystals were washed with pentane (3 x 10 mL) and dried under vacuum. Dark purple crystals were obtained (1.6–1.7 mmol, 76–81 %).

3.6.3.1 Co(η^5-Cp*)I$_2$(PPhH$_2$) (Co-3a)

Complex **Co-1** (2.1 mmol, 1.0 g) and $PPhH_2$ in hexanes (3.9 mmol, 1.1 M, 3.6 mL, 1.8 equiv) were used. Dark purple crystals (1.7 mmol, 0.95 g, 81 %) were obtained.

Melting point: 180–183 °C. **IR** (KBr, cm^{-1}): 2363, 2352 (w, ν_{PH}). **Anal.** found (calcd for $C_{16}H_{22}I_2PCo$): C, 34.75 (34.44); H, 3.70 (3.97).

3.6.3.2 Co(η^5-Cp*)I_2($PCyH_2$) (Co-3c)

Complex **Co-1** (2.1 mmol, 1.0 g) and $PCyH_2$ in hexanes (3.7 mmol, 0.78 M, 4.7 mL, 1.8 equiv) were used. Purple crystals were obtained (1.6 mmol, 0.90 g, 76 %). **Melting point**: 190–194 °C. **IR** (KBr, cm^{-1}): 2338, 2321 (w, ν_{PH}). **Anal.** found (calcd for $C_{16}H_{28}I_2PCo$): C, 33.43 (34.07); H, 4.61 (5.00). The unsatisfactory elemental analysis for **Co-3c** may be instability of this complex under vacuum as described for **Co-2d**.

3.6.4 General procedure for the synthesis of [Co(η^5-Cp*)I(PR_2H)$_2$]I (Co-4)

To a solution of complex **Co-1** (1.0–1.3 mmol) in CH_2Cl_2 (10 mL) in a Schlenk flask, a solution of PR_2H in hexane (2.0–2.9 mmol, 2.2 equiv) was added. After stirring for 1 h at RT, the solvent in the resulting dark brown solution was removed under vacuum to afford a deep brown oil. The oil was triturated with pentane (5 x 10 mL) and dried under vacuum to afford a dark brown powder. Dark brown powder was obtained (0.70–1.2 mmol, 70–89 %).

3.6.4.1 Attempted isolation of [Co(η^5-Cp*)I(PR_2H)$_2$]I (Co-4) (R = Ph (a), Tol^p (b))

Complex **Co-1** (**Ph:** 1.3 mmol, 0.62 g; **Tol^p:** 1.2 mmol, 0.59 g,) and neat PR_2H (**Ph:** 2.0 mmol, 0.53 g, 2.2 equiv; **Tol^p:** 2.9 mmol, 0.43 g, 2.2 equiv) were used. Dark brown powder (**Ph:** 0.95 g, 1.2 mmol, 89 %; **Tol^p:** 1.0 mmol, 0.9 g, 82 %) was obtained. The isolated **Co-4** undergoes a ligand redistribution to give variable amounts of **Co-2** and PR_2H in solution (*vide infra*).

3.6.4.2 Evidence for the equilibrium of Co-4a in solution

Brown powder isolated as described above (**Co-4a**, 20 mg) was dissolved in $CDCl_3$ (0.6 mL). The intense golden solution was transferred to a J. Young NMR tube. ^{1}H, $^{31}P\{^{1}H\}$ and ^{31}P spectra were initially collected at 293 K. After that, additional spectra were collected at 323 K. Final spectra were collected again at 293 K.

The equilibrium for **Co-4a** is supported by VT $^{31}P\{^{1}H\}$ NMR spectroscopy (Figure 3.16). When the solution of the isolated **Co-4a** (R = Ph) was heated to 50 °C, $^{31}P\{^{1}H\}$ NMR signals due to **Co-2a** and free PPh_2H increase in intensity while **Co-4a** decreases, all species returned to the original concentration as the mixture is cooled to RT.

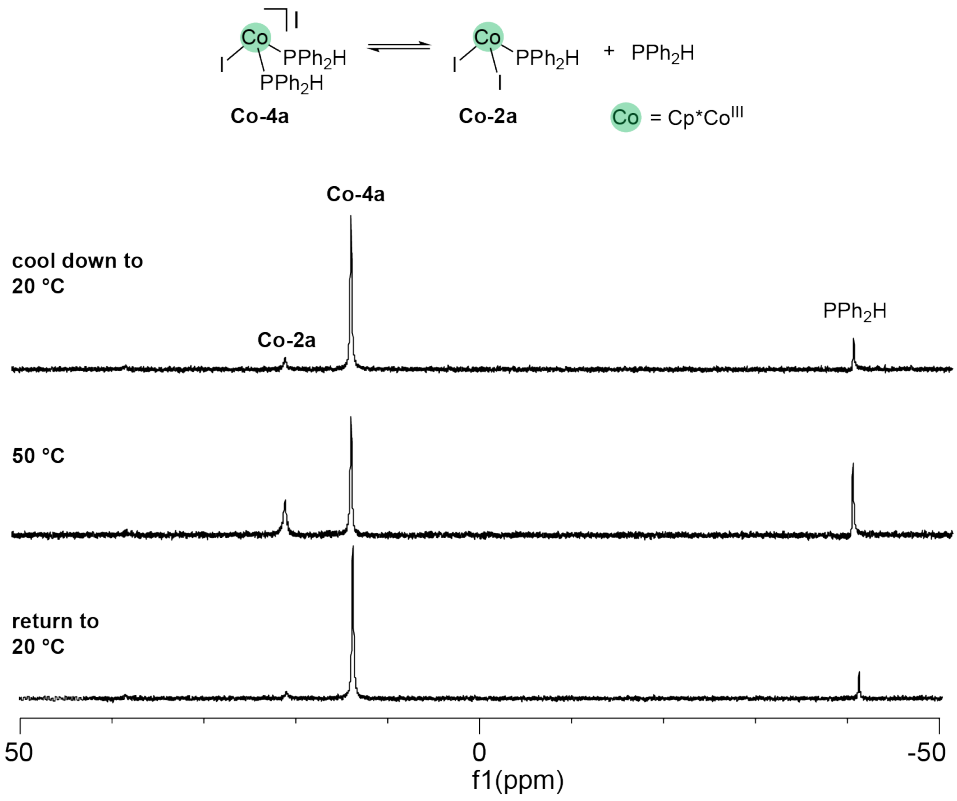

Figure 3.16 VT $^{31}P\{^{1}H\}$ NMR (145.78 MHz, $CDCl_3$) spectra of the isolated **Co-4a**, showing a ligand redistribution in the solution.

3.6.4.3 [Co(η^5-Cp*)I(PEt$_2$H)$_2$]I (Co-4e)

Complex **Co-1** (1.0 mmol, 0.48 g) and PEt_2H in a hexane solution (2.1 mmol, 0.75 M, 2.8 mL, 2.2 equiv) were used. Dark brown powder (0.70 mmol, 0.48 g, 70 %) was obtained. **Melting point**: 138–140 °C. **IR** (KBr, cm^{-1}): 2360 cm^{-1} (w, ν_{PH}). **ESI-MS** (CH_3CN, *m/z*, relative intensity): 501.30 (M^+, 501.07 calcd, 100%). **Anal.** found (calcd for $C_{18}H_{37}I_2Co_1P_2$): C, 31.92 (34.42); H, 4.86 (5.94).

The unsatisfactory elemental analysis may be attributed to instability: this bis(phosphine) complex slowly releases PEt_2H, giving Co(η^5-Cp*)I_2PEt_2H (**Co-2e**) in solution or under vacuum (Figure 3.18).

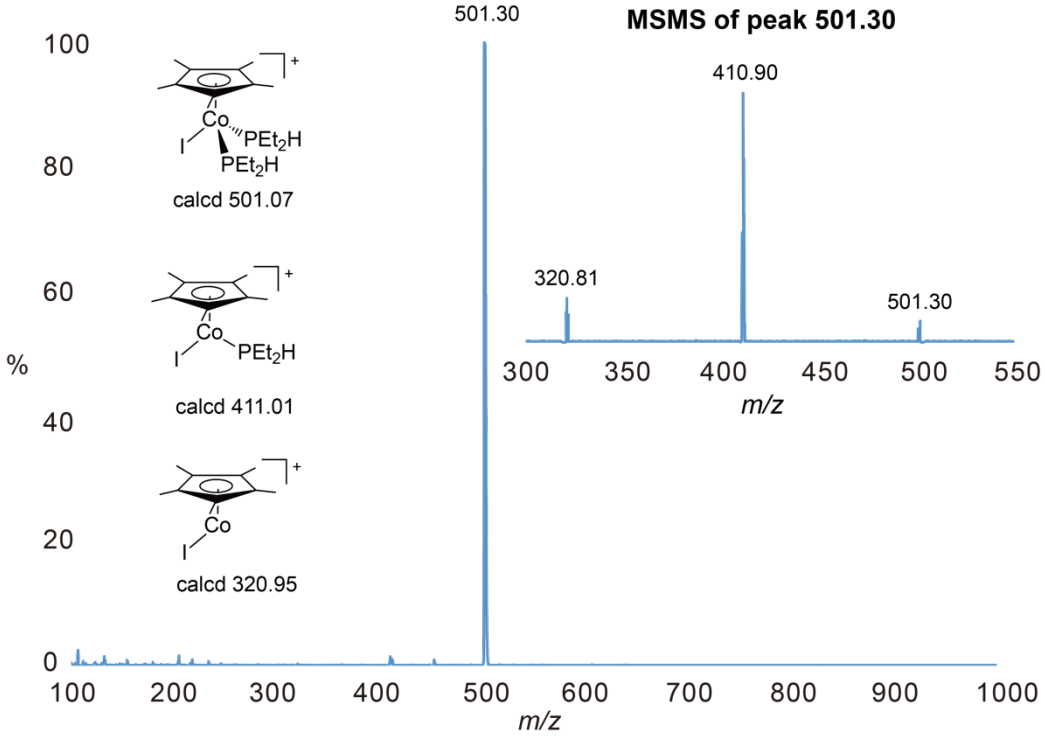

Figure 3.17 ESI-MS spectrum of **Co-4e** in CH_2Cl_2 and MS/MS of the peak at *m/z* = 501.30 (inset). Other unidentified peaks could be due to the decomposition of this reactive Co complex. Conditions: a solution of **Co-4e** (0.02 mmol) in CH_2Cl_2 (0.6 mL) was further diluted 20 times for the ESI-MS experiments.

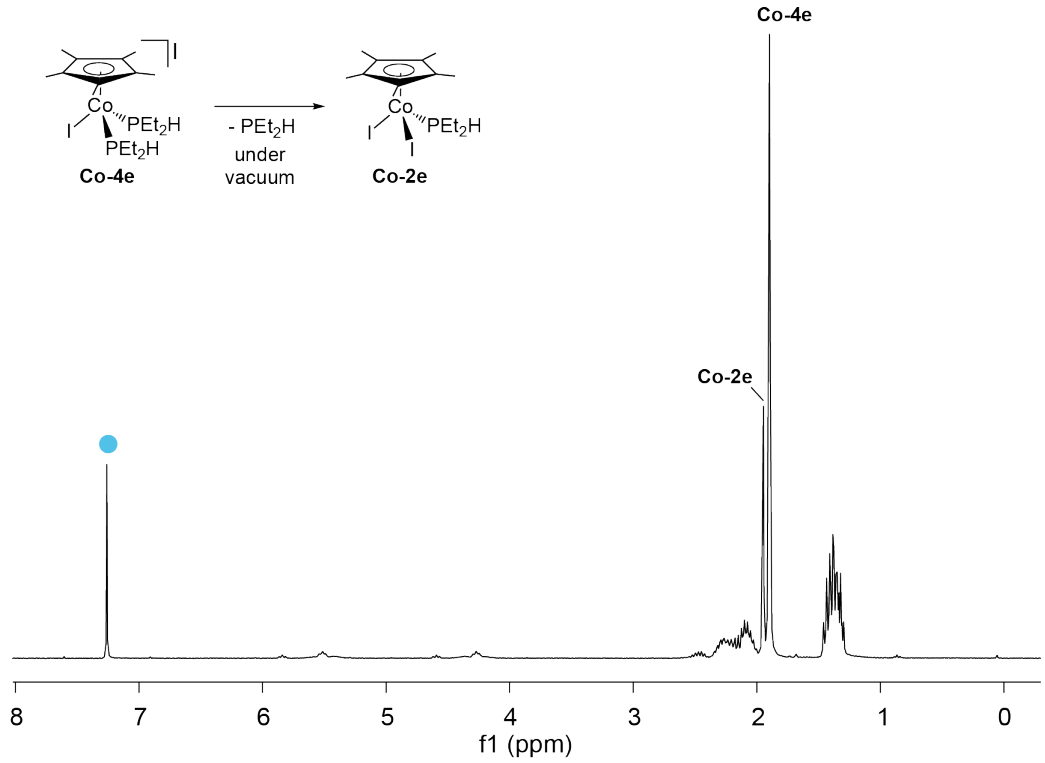

Figure 3.18 ^{1}H NMR (300.27 MHz, C_6D_6) spectrum of complex **Co-4e** dried under vacuum for 1h, showing its decomposition to **Co-2e**. Residual proteo-solvent (•).

3.6.5 Modified synthesis of $[Co(\eta^5\text{-}Cp^*)(NCCH_3)_3][SbF_6]_2$ (Co-5)

The literature method was slightly modified.[13] $Co(\eta^5\text{-}Cp^*)I_2(CO)$ (**Co-1**, 3.6 mmol, 1.7 g) and $AgSbF_6$ (7.5 mmol, 2.6 g, 2.1 equiv) were placed in a Schlenk flask and CH_3CN (15 mL) was added. A white solid immediately precipitated. This suspension was stirred at RT for 3 h and filtered through Celite (1 x 3 cm). After filtration, the resulting purple solution was concentrated to 5 mL, which caused the white solid to precipitate (Note: Best results are obtained if the concentrated purple solution is left to stand overnight before filtration to allow complete precipitation of the white solid). This white solid was removed by filtration. The addition of Et_2O (50 mL) to the filtrate caused the precipitation of a purple solid. The purple solid was isolated by filtration, rinsed with Et_2O (50 mL) on a filter frit, and dried under vacuum (2.1 mmol, 1.7 g, 58 %).

The ^{1}H NMR spectrum (Figure 3.19) of isolated **Co-5** obtained in CD_3CN shows rapid substitution of CH_3CN ligand by CD_3CN. As shown in the ^{1}H NMR spectrum (Figure 3.19), 3 equiv of free CH_3CN with respect to Co can be quantified. As a result, an anticipated stoichiometric amount of free CH_3CN (3 equiv) is observed in the ^{1}H NMR spectrum. As described above, this solvation plays an important role in dissolving the isolated **Co-5**; hence it is only soluble in acetonitrile (CH_3CN or CD_3CN).

^{1}H NMR (300.27 MHz, CD_3CN): δ 1.96 (s, 9H, CH_3CN), 1.39 (s, 15H, CH_3 in Cp*).

ESI-MS (CH_3CN, *m/z*): 158.21 [M^{2+}], 137.50 [$(M - CH_3CN)^{2+}$].

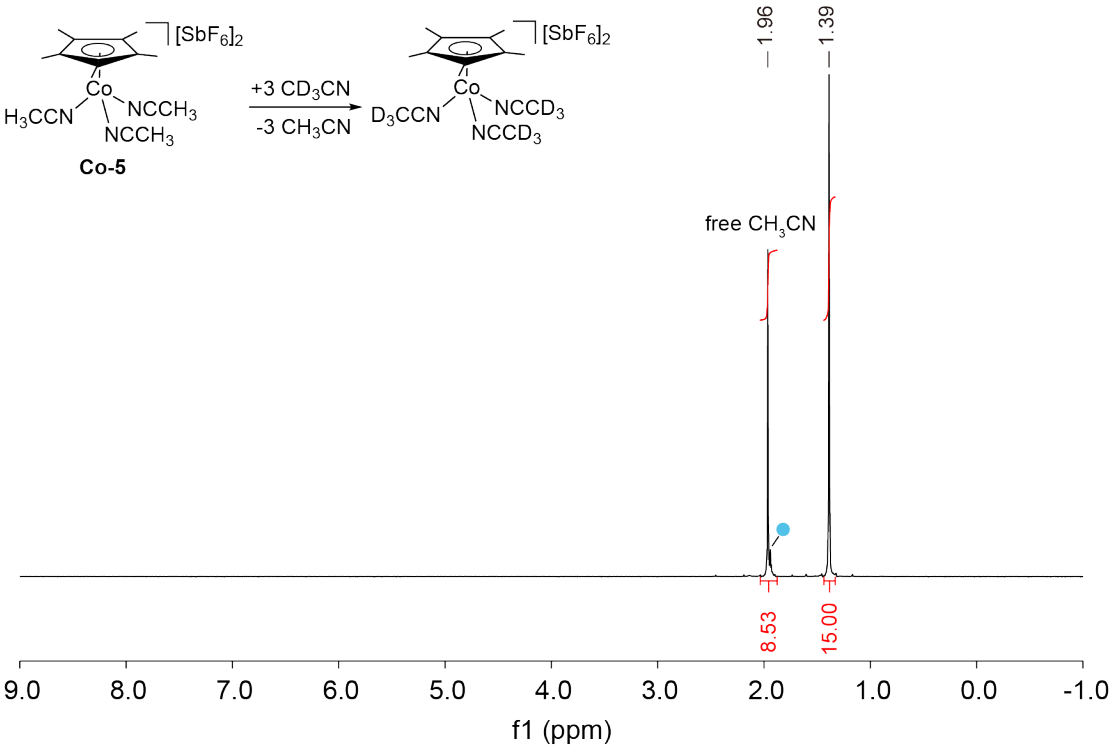

Figure 3.19 ^{1}H NMR (300.27 MHz, CD_3CN) spectrum of isolated complex **Co-5** in CD_3CN and scheme illustrating substitution of CH_3CN ligand by CD_3CN. Residual proteo-solvent (•).

3.6.6 General procedure for the synthesis of $[Co(\eta^5\text{-}Cp^*)(NCCH_3)_2(PR_2H)][SbF_6]_2$ (Co-6)

To a solution of $[Co(\eta^5\text{-}Cp^*)(NCCH_3)_3][SbF_6]_2$ (**Co-5**, 0.62-0.74 mmol) in CH_3CN (10 mL) in a Schlenk flask, PR_2H or PR_2H was added (0.87–1.2 mmol, 1.3–1.7 equiv). After 1 h stirring at RT, the dark red solution was concentrated to 1 mL and layered with Et_2O (30 mL). The supernatant was removed by cannula, and the resulting dark red crystals were washed with pentane (3 x 10 mL) and dried under vacuum. Dark red solids (0.42–0.50 mmol, 67–74 %) were obtained.

3.6.6.1 $[Co(\eta^5\text{-}Cp^*)(NCCH_3)_2(PPh_2H)][SbF_6]_2$ (Co-6a)

Complex **Co-5** (0.62 mmol, 0.49 g) and neat PPh_2H (1.1 mmol, 0.20 g, 1.7 equiv) were used. Dark red solid (0.42 mmol, 0.39 g, 67 %) was obtained after 3 recrystallizations. **Melting point:** 208–209 °C. **IR** (KBr, cm^{-1}): 2324 (w, ν_{PH}), 2295 (w, ν_{CN}). **ESI-MS** (CH_3CN, *m/z*, relative intensity): 231.20 [M^{2+}, 231.08 calcd, 100%]. The isolated **Co-6a** always contains various amount of $[Co(\eta^5\text{-}Cp^*)(NCCH_3)(PPh_2H)_2][SbF_6]_2$ (**Co-7a**).

3.6.6.2 $[Co(\eta^5\text{-}Cp^*)(NCCH_3)_2(PTol^p{}_2H)][SbF_6]_2$ (Co-6b) generated *in situ*

Complex **Co-5** (0.74 mmol, 0.58 g) and neat $PTol^p{}_2H$ (1.3 mmol, 0.27 g, 1.7 equiv) were used. Dark red solid (0.49 mmol, 0.48 g, 67 %) was obtained, which contains 52% **Co-7b** and 48% $[Co(\eta^5\text{-}Cp^*)(NCCH_3)(PTol^p{}_2H)_2][SbF_6]_2$ (**Co-7b**) even after three recrystallizations. **Melting point**: 200–210°C. **IR** (KBr, cm^{-1}): 2326 (w, ν_{PH}), 2290 (w, ν_{CN}). **ESI-MS** (CH_3CN, *m/z*, relative intensity): 246.12 [M^{2+}, 246.10 calcd, 100%] (Note: Peaks due to the cationic disubstituted compound **Co-7b** was not observed.)

3.6.6.3 [Co(η^5-Cp*)(NCCH$_3$)$_2$(PCy$_2$H)][SbF$_6$]$_2$ (Co-6c)

Complex **Co-5** (0.70 mmol, 0.55 g) and neat PCy$_2$H (0.91 mmol, 0.18 g, 1.3 equiv) were used. Dark red solid was obtained (0.48 mmol, 0.45 g, 69 %). **Melting point**: 211–212 °C. **IR** (KBr, cm^{-1}): 2328 (w, ν_{PH}), 2302 (w, ν_{CN}). **ESI-MS** (CH$_3$CN, *m/z*, relative intensity): 237.07 [M^{2+}, 237.13 calcd, 100%].

3.6.6.4 [Co(η^5-Cp*)(NCCH$_3$)$_2$(PPr$^i_2$H)][SbF$_6$]$_2$ (Co-6d)

Complex **Co-5** (0.67 mmol, 0.53 g) and PPr$^i_2$H in hexane (0.87 mmol, 0.30 M, 2.9 mL, 1.3 equiv) were used. Dark red solid (0.50 mmol, 0.43 g, 74 %) was obtained. **Melting point**: 220–221°C. **IR** (KBr, cm^{-1}): 2325 (w, ν_{PH}), 2297 (w, ν_{CN}). **ESI-MS** (CH$_3$CN, *m/z*, relative intensity): 628.97 [(M^{2+} + SbF$_6^-$)$^+$, 629.09 calcd, 100%], 197.01 [M^{2+}, 197.10 calcd, 48%], 176.62 [(M – CH$_3$CN)$^{2+}$, 176.58 calcd, 6%].

3.6.7 ^{1}H and ^{13}C{^{1}H} NMR data for Cp*Co phosphine complexes

Table 3.4 ^{1}H NMR (500.27 MHz, solvent) data for complexes **Co-2**, **Co-3** and **Co-4**: δ in ppm (multiplicity, J or $\omega_{1/2}$ in Hz, RI,)

Complex	Cp*	PR$_2$H or PH$_2$R
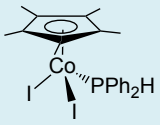 **Co-2a** **C$_6$D$_6$**	1.60 (d, 2.1, 15H)	**H-PPh$_2$** 7.40 (d, 370.5, 1H) **Ph:** **H$_o$** 7.95 (ddd, 10.2 7.3 2.1, 4H) **H$_{m,p}$** 7.01–6.93 (m, 6H)
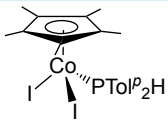 **Co-2b** **C$_6$D$_6$**	1.64 (d, 2.1, 15H)	**H-PTol$^p_2$** 7.45 (d, 370.4, 1H) **H$_o$** 7.91 (dd, 10.5 8.0, 4H) **H$_m$** 6.85 (dd, 8.1 2.1, 4H) **CH$_3$ in Tol** 1.96 (s, 6H)
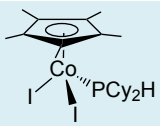	1.71 (s, 15H)	**H-PCy$_2$** 5.41 (dt, 362.1 3.6, 1H) **Cy:** **CH** 2.69–2.51 (m, 2H)

Co-2c **C_6D_6**		**CH_2** 2.29 (d, J 12.6, 2H), 2.06 (d, 10.7, 4H), 1.83–1.10 (m, 8H, overlaps with Cp*), 1.54 (d, 13.0, 2H), 1.46–1.33 (m, 2H), 1.31–1.14 (m, 3H), 1.12–0.97 (m, 1H)
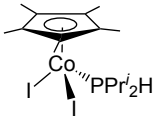 **Co-2d** **C_6D_6**	1.65 (d, 1.7, 15H)	**H-PPr$^i_2$** 5.45 (dt, 361.1 3.4, 1H) **Pr^i:** **CH** 2.67 (tdp, 10.7 7.2 3.7, 2H) **CH_3** 1.30 (dd, 14.1 7.4, 6H), 1.16 (dd, 13.2, 7.1, 6H)
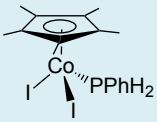 **Co-3a** **C_6D_6**	1.53 (d, 2.7, 15H)	**H_2-PPh** 6.58 (d, 383.5, 2H) **Ph:** **H_o** 7.98 –7.83 (m, 2H) **H_p** 7.06 (td, 7.3 1.9, 1H) **H_m** 6.98 (td, 7.8 2.0, 2H)
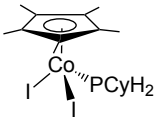 **Co-3c** **C_6D_6**	1.61 (d, 2.9, 15H)	**H_2-PCy** 5.24 (dd, 331.8 4.2, 2H) **Cy:** **CH** 2.41 (m, 1H) **CH_2** 2.26 (m, 2H), 1.67–1.58 (m, 1H, overlaps with Cp*), 1.51 (m, 2H), 1.43–1.33 (m, 1H), 1.30–0.79 (m, 4H)
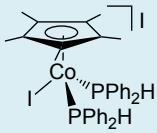 **Co-4a** **CD_2Cl_2**	1.66 (t, 1.9, 15H)	**H-PPh$_2$** 7.51 (d, 393.1, 2H) **Ph:** **H_o** 7.95–7,84 (m, 4H), 7.76–7.68 (m, 4H) **$H_{m,p}$** 7.01–6.93 (m, 6H) **H_p** 7.41–7.30 (m, 2H) **H_m** 7.24 (dd, 7.8 3.9, 4H)
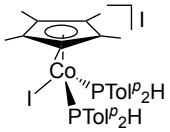 **Co-4b** **$CDCl_3$**	1.66 (t, 2.0, 15H)	**H-PTol$^p_2$** 7.47 (d, 392.8, 2H) **H_o** 7.81–7.74 (m, 4H), 7.65–7.59 (m, 4H) **H_m** 7.30–7.27 (m, 4H), 7.04–7.00 (m, 4H) **CH_3 in Tol** 2.35 (s, 6H), 2.26 (s, 6H)
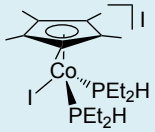 **Co-4e** **$CDCl_3$**	1.94 (t, 1.7, 15H)	**H-PEt$_2$** 4.94 (dt, 372.6 7.5, 2H) **Et:** **CH_2** 2.38–2.19 (m, 4H), 2.19–2.05 (m, 4H) **CH_3** 1.43 (dt,15.6 7.5, 6H), 1.36 (dt, 15.9 7.5, 6H)

Table 3.5 $^{13}C\{^{1}H\}$ NMR (125.77 MHz, solvent) data for complexes **Co-2**, **Co-3** and **Co-4**: δ in ppm (multiplicity, J or $\omega_{1/2}$ in Hz).

Complex	Cp*	PR_2H or PH_2R
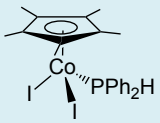 **Co-2a** **C_6D_6**	**C_{ring}** 93.9 (s) **CH_3** 11.1 (s)	**Ph:** **C_o** 135.2 (d, 7) **C_{ipso}** 132.8 (d, 43) **C_p** 130.5 (s) **C_m** 128.0 (d, 10)
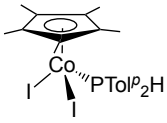 **Co-2b** **C_6D_6**	**C_{ring}** 93.8 (s) **CH_3** 11.1 (s)	**Tol^p:** **C_p** 140.6 (s) **C_o** 135.2 (d, 7) **C_{ipso}** 129.6 (d, 46) **C_m** 128.9 (d, 10) **CH_3** 21.2 (s)
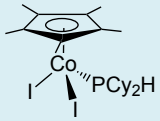 **Co-2c** **C_6D_6**	**C_{ring}** 93.1 (s) **CH_3** 11.7 (s)	**Cy:** **CH** 38.8 (d, 20) **CH_2** 36.3 (d, 6), 31.8 (d, 5), 28.1 (d, 9), 27.7 (d, 9), 26.2 (s)
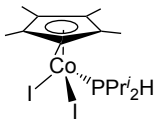 **Co-2d** **C_6D_6**	**C_{ring}** 93.1 (s) **CH_3** 11.8 (s)	**Pr^i:** **CH** 28.2 (d, 21) **CH_3** 25.8 (d, 5), 21.3 (d, 4)
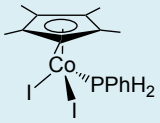 **Co-3a** **C_6D_6**	**C_{ring}** 93.7 (d, 3) **CH_3** 10.9 (s)	**Ph:** **C_o** 134.7 (d, 7) **C_p** 131.3 (s) **C_m** 128.6 (d, 9) **C_{ipso}** not observed
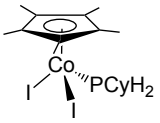 **Co-3c** **C_6D_6**	**C_{ring}** 93.2 (d, 3) **CH_3** 10.7 (s)	**Cy:** **CH** 36.2 (d, 34) **CH_2** 35.2 (d, 7), 27.0 (d, 11), 26.0 (s)

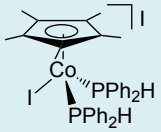 **Co-4a** **CD_2Cl_2**	**C_{ring}** 100.3 (s) **CH_3** 11.1 (s)	**Ph:** **C_o** 134.9 (d, 5), 134.2 (d, 5) **C_p** 132.2 (s), 131.8 (s) **C_m** 129.8 (d, 5), 129.0 (d, 5) **C_{ipso}** 127.9 (d, 60), 127.7 (d, 62)
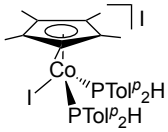 **Co-4b** **$CDCl_3$**	**C_{ring}** 99.6 (s) **CH_3** 11.1 (s)	**Tol^p:** **C_p** 142.2 (s), 141.8 (s) **C_o** 134.6 (dd, 6 3), 134.1 (dd, 6 3) **C_m** 130.1 (dd, 6 5), 129.4 (dd, 6 5) **C_{ipso}** 124.5 (d, 47), 124.0 (d, 53) **CH_3** 21.6 (s), 21.5 (s)
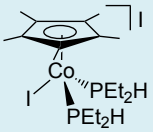 **Co-4e** **$CDCl_3$**	**C_{ring}** 98.3 (t, 2) **CH_3** 11.3 (s)	**Et:** **CH_2** 21.0 (dd, 15 13), 18.6 (dd, 19 18) **CH_3** 14.4 (dd, 5 5), 14.4 (dd, 6 5)

Table 3.6 ^{1}H NMR (500.27 MHz, CD_3CN) data for complexes **Co-6**: δ in ppm (multiplicity, J or $\omega_{1/2}$ in Hz, RI)[a]

Complex	Cp*	PR_2H
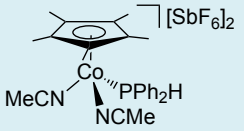 **Co-6a**	1.42 (d, 3.2, 15H)	**H-PPh$_2$** 7.07 (d, 387.2, 1H) **H$_{o,p}$** 7.70–7.61 (m, 6H) **H$_m$** 7.60–7.54 (m, 4H)
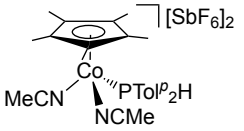 **Co-6b**	1.41 (d, 3.2, 15H)	**H-PTol$^p_2$** 7.01 (d, 388.0, 1H) **H$_o$** 7.57–7.49 (m, 4H) **H$_m$** 7.41–7.36 (m, 4H) **CH$_3$ in Tol** 2.38 (s, 6H)
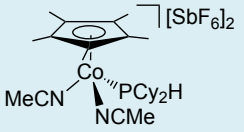 **Co-6c**	1.45 (d, 2.7, 15H)	**H-PCy$_2$** 4.86 (dt, 354.5 4.7, 1H) **CH** 2.23 (tdd, 12.4 8.7 4.5, 2H) **CH$_2$** 1.95–1.88 (m, 4H), 1.87–1.76 (m, 6H), 1.77–1.70 (m, 2H), 1.55–1.47 (m, 2H), 1.42–1.32 (m, 4H), 1.28 (tt, 12.7 3.3, 2H)
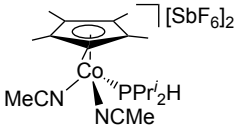 **Co-6d**	1.46 (d, 2.8, 15H)	**H-PPr$^i_2$** 5.00 (dt, 354.2 4.8, 1H) **CH** 2.58–2.45 (m, 2H) **CH$_3$** 1.36–1.23 (m, 12H)

[a] Signals due to free CH_3CN are observed for all complexes, similar to our observation for **Co-5** (Figure 3.19).

Table 3.7 $^{13}C\{^1H\}$ NMR (125.77 MHz, CD_3CN) data for complexes **Co-6**: δ in ppm (multiplicity, J or $\omega_{1/2}$ in Hz).[a]

Complex	Cp*	CD_3CN	PR_2H or PH_2R
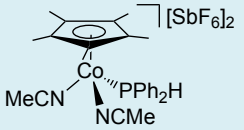 **Co-6a**	**C_{ring}** 103.7 (s) **CH_3** 10.0 (s)	**CN** 135.1 (s) **CD_3** 5.3–4.2 (m)	**C_o** 134.0 (d, 9) **C_p** 133.6 (d, 3) **C_m** 130.9 (d, 11) **C_{ipso}** 125.4 (d, 48)
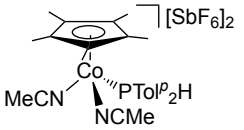 **Co-6b**	**C_{ring}** 103.4 (s) **CH_3** 9.9 (s)	Not observed	**C_p** 144.6 (s) **C_o** 134.1–133.7 (m) **C_m** 131.7–131.3 (m) **C_{ipso}** 122.4–121.7 (m) **CH_3** 21.6 (s)
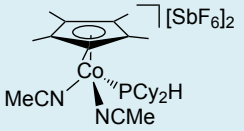 **Co-6c**	**C_{ring}** 103.3 (s) **CH_3** 10.4 (s)	**CN** 135.5 (s) **CD_3** 5.6–4.5 (m)	**CH** 34.1 (d, 21) **CH_2** 32.0 (d, 3), 30.8 (d, 4), 27.7 (d, 12), 27.5 (d, 11), 26.4 (d, 1)
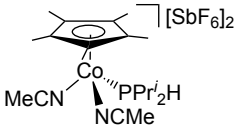 **Co-6d**	**C_{ring}** 103.4 (s) **CH_3** 10.3 (s)	**CN** 136.3 (s) **CD_3** not observed	**CH** 24.3 (d, 22) **CH_3** 21.2 (d, 2), 20.0 (d, 3)

[a] Signals due to free CH_3CN are observed for all complexes, similar to our observation for **Co-5** (Figure 3.19).

3.6.8 UV-vis spectroscopy of Cp*Co complexes

The data is presented in Table 3.8. Dry CH_2Cl_2/CH_3CN solutions of the isolated Co complexes (**Co-1**, **Co-2(a-d)**, **Co-3a,c**, **Co-4(a,e)**, **Co-5** and **Co-6(a-d)**) were prepared in sealed UV-vis cuvettes (Figure 3.20), in which concentrations of the Co range from 0.00015 to 0.00057 M.

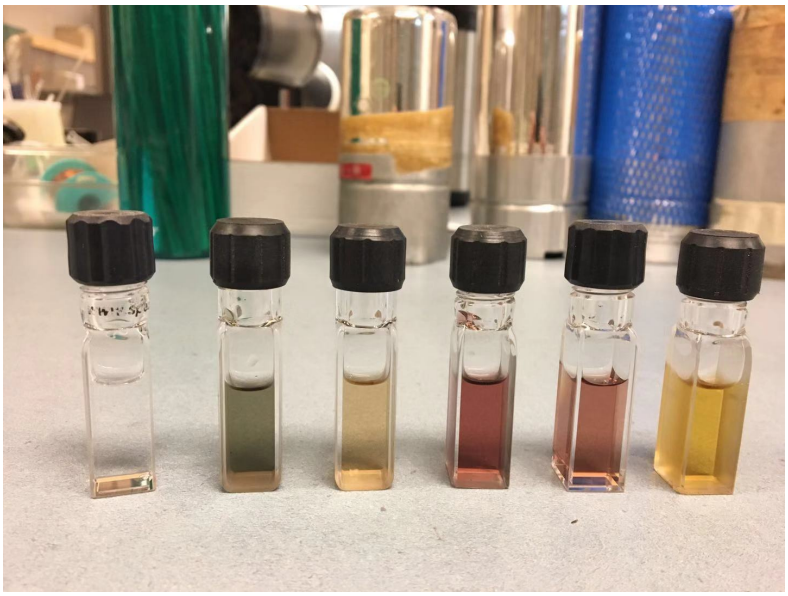

Figure 3.20 Photograph of UV-vis samples (from left to right): blank, **Co-2**, **Co-4**, **Co-5**, **Co-1** and **Co-6**.

Table 3.8 UV-vis data for complexes **Co-1**, **Co-2(a-d)** and **Co-4(a,e)** in CH_2Cl_2 and **Co-5** and **Co-6(a-d)** in CH_3CN.

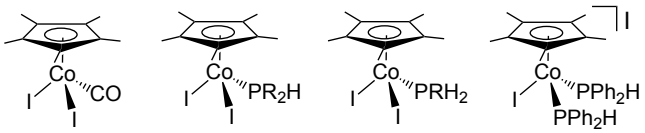

Co-1 **Co-2** **Co-3** **Co-4a**

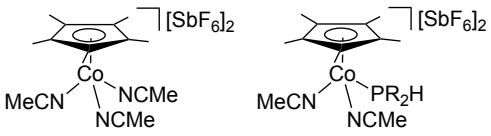

Co-5 **Co-6**

R = Ph (**a**), Tol^p (**b**), Cy (**c**), Pr^i (**d**) and Et (**e**)

Complex	λ_{max}, nm (ε, L mol^{-1} cm^{-1})
Co-1	570 (1.1 x 10^3), 461 (1.5 x 10^3), 370 (4.3 x 10^3)
Co-2a	726 (3.2 x 10^2), 593 (1.1 x 10^3), 497 (6.8 x 10^2), 397 (1.5 x 10^3)
Co-2b	726 (3.3 x 10^2), 592 (1.1 x 10^3), 497 (7.2 x 10^2), 397 (1.5 x 10^3)
Co-2c	726 (3.5 x 10^2), 594 (1.1 x 10^3), 498 (7.2 x 10^2), 396 (2.1 x 10^3)
Co-2d	726 (4.0 x 10^2), 594 (1.1 x 10^3), 497 (7.3 x 10^2), 396 (2.0 x 10^3)
Co-3a	729 (3.9 x 10^2), 583 (1.3 x 10^3), 458 (5.9 x 10^2), 391 (2.1 x 10^3)
Co-3c	740 (3.9 x 10^2), 580 (1.3 x 10^3), 483 (9.9 x 10^2), 390 (2.3 x 10^3)
Co-4a	595 (1.0 x 10^3), 504 (2.7 x 10^3), 445 (2.3 x 10^3), 363 (4.8 x 10^3)
Co-4e	564 (6.5 x 10^2), 454 (3.7 x 10^3), 345 (6.5 x 10^3)
Co-5	511 (3.9 x 10^3), 381 (1.0 x 10^3), 316 (2.8 x 10^3)
Co-6a	468 (4.2 x 10^3)
Co-6b	465 (4.4 x 10^3)
Co-6c	468 (4.4 x 10^3), 365 (1.8 x 10^3), 316 (6.5 x 10^3)
Co-6d	468 (4.6 x 10^3), 370 (1.5 x 10^3), 313 (6.0 x 10^3)

3.6.9 General procedure for preliminary catalytic hydrophosphination reactions using Cp*Co complexes

Complex **Co-1**, **Co-2a**, **Co-4a** or **Co-5** (0.021 mmol), was weighed into a small glass vial, and 0.5 mL of C_6D_6 or CD_3CN (for **Co-5** only) was added. (Note: Catalysts **Co-1**, **Co-2a** and **Co-4a** need approximately 30 min to dissolve in C_6D_6 completely, especially for **Co-4a**.) After the precatalyst was dissolved, neat PPh_2H (0.21 mmol, 39 mg), *tert*-butyl acrylate (0.21 mmol, 27 mg) and DBU (0.025 mmol, 3.8 μL) were added to get a final volume of 0.7 mL. The reaction mixture was transferred to a J. Young NMR tube, and loaded into the NMR spectrometer. Initial ^1H and $^{31}P\{^1H\}$ NMR spectra could be obtained at RT within ~15 min. Conversions and product ratios were determined from the relative integrations of all products using non-quantitative $^{31}P\{^1H\}$ NMR. All reactions were performed in triplicate.

3.6.10 General procedure for preliminary dehydrocoupling reactions using Co-1 or Co-5

Complex **Co-1** or **Co-5** (0.021 mmol) was accurately weighed into a small glass vial containing C_6D_6 or CD_3CN (0.5 mL). After the precatalyst was dissolved for ~30 min, neat PPh_2H (0.21 mmol, 39 mg) was added to get a total volume of 0.7 mL. DBU (0.042 mmol, 6.3 μL) was added for the base-mediated reactions. The reaction mixture was transferred to a J. Young NMR tube, and placed in an oil bath with a thermometer for heating at 80 °C. Initial ^1H and $^{31}P\{^1H\}$ NMR spectra could be obtained at RT within ~15 min. Conversions and product ratios were determined from the relative integrations of all products using non-quantitative $^{31}P\{^1H\}$ NMR. All reactions were performed in triplicate.

3.6.11 Reaction of Co-1 or Co-5 with excess phosphine.

Complex **Co-1** or **Co-5** (0.021 mmol) was dissolved in C_6D_6 or CD_3CN (0.6 ml) in a small vial for 0.5 h, then phosphine, PPh_2H, $PTol^p_2H$, PCy_2H, PPr^i_2H, PEt_2H, $PPhH_2$ or $PCyH_2$ (0.210 mmol, 10 equiv) was added. The mixture was analyzed by ^1H and ^{31}P NMR spectroscopy.

3.6.12 Reaction of Co-1 or Co-5 with excess *tert*-butyl acrylate

Complex **Co-1** or **Co-5** (0.021 mmol) was dissolved in C_6D_6 or CD_3CN (0.6 ml) in a small vial for 0.5 h, then *tert*-butyl acrylate (0.210 mmol, 10 equiv) was added. The mixture was analyzed by ^1H and ^{31}P NMR spectroscopy.

3.7 References

(1) Fischer, E. O.; Jira, R. Notizen: Di-Cyclopentadienyl-Kobalt (II). *Z. Naturforsch. B* **1953**, *8*, 327–328.

(2) Loginov, D. A.; Shul'pina, L. S.; Muratov, D. V.; Shul'pin, G. B. Cyclopentadienyl Cobalt(III) Complexes: Synthetic and Catalytic Chemistry. *Coord. Chem. Rev.* **2019**, *387*, 1–31.

(3) Yoshino, T.; Matsunaga, S. Chiral Carboxylic Acid Assisted Enantioselective C-H Activation with Achiral Cp^xM^{III}(M = Co, Rh, Ir) Catalysts. *ACS Catal.* **2021**, *11*, 6455–6466.

(4) Sunny, S.; Karvembu, R. Recent Advances in Cobalt-Catalyzed, Directing-Group-Assisted C−H Bond Amidation Reactions. *Adv. Synth. Catal.* **2021**, *363*, 4309–4331.

(5) Lukasevics, L.; Cizikovs, A.; Grigorjeva, L. C-H Bond Functionalization by High-Valent Cobalt Catalysis: Current Progress, Challenges and Future Perspectives. *Chem. Commun.* **2021**, *57*, 10827–10841.

(6) Yoshino, T.; Satake, S.; Matsunaga, S. Diverse Approaches for Enantioselective C−H Functionalization Reactions Using Group 9 Cp^xM^{III} Catalysts. *Chem. – Eur. J.* **2020**, *26*, 7346–7357.

(7) Yoshikai, N. Cobalt-Catalysed C-H Functionalisation. In *Cobalt Catalysis in Organic Synthesis: Methods and Reactions*; Wiley, 2019; pp 89–161.

(8) Sun, B.; Yoshino, T.; Matsunaga, S.; Kanai, M. Air-Stable Carbonyl(Pentamethylcyclopentadienyl)Cobalt Diiodide Complex as a Precursor for Cationic (Pentamethylcyclopentadienyl)Cobalt(Iii) Catalysis: Application for Directed C-2 Selective C-H Amidation of Indoles. *Adv. Synth. Catal.* **2014**, *356*, 1491–1495.

(9) Tolman, C. A. Steric Effects of Phosphorus Ligands in Organometallic Chemistry and Homogeneous Catalysis. *Chem. Rev.* **1977**, *77*, 313–348.

(10) Fairhurst, G.; White, C. Syntheses of Pentamethylcyclopentadienylcobalt(III) Compounds and Reactions of $[Co(C_5Me_5)(Solvent)_3]X_2$ (Solvent = Acetonitrile or Acetone, X = BF_4 or PF_6). *J. Chem. Soc. Dalton Trans.* **1979**, No. 10, 1524–1530.

(11) Brunner, H.; Jablonski, C. R.; Jones, P. G. Optically Active Transition-Metal Compounds. Preparation, Structure, Absolute Configuration, and Conformational Analysis of Chiral Pseudooctahedral Cobalt(III) Phosphonato and Phosphinato Complexes. Optical Induction in the Transition-Metal Arbuzov Reacti. *Organometallics* **1988**, *7*, 1283–1292.

(12) Powell, E. W.; Mays, M. J. π-Cyclopentadienyl—Cobalt Complexes Containing Isocyanide Ligands. *J. Organomet. Chem.* **1974**, *66*, 137–147.

(13) Yu, D. G.; Gensch, T.; De Azambuja, F.; Vásquez-Céspedes, S.; Glorius, F. Co(III)-Catalyzed C-H Activation/Formal SN-Type Reactions: Selective and Efficient Cyanation, Halogenation, and Allylation. *J. Am. Chem. Soc.* **2014**, *136*, 17722–17725.

(14) Quin, L. D. *A Guide to Organophosphorus*; Wiley: New York, 2000.

(15) Werner, H.; Scheller, L. Synthesis and Reactivity of Half-Sandwich Type Cobalt, Rhodium and Iridium Complexes Containing Trithiocarbonate, Dithiocarbonate, N-Cyanodithiocarbimate, 1,1-Dicyanoethylene-2,2-Dithiolate and 1,1-Dicyanoethylene-2,2-Diselenolate as Chelating Ligands. *Polyhedron* **2012**, *34*, 13–23.

(16) Nomura, M.; Takayama, C.; Sugiyama, T.; Yokoyama, Y.; Kajitani, M. Electrochemistry and Reactivity of Cobaltadithiolene Complexes Having Sulfilimine Structures: Effect of Phosphorus Ligand Basicity and Cone Angle on the Electrochemical Behavior and on the Imido Migration to the Cp Ring. *Organometallics* **2004**, *23*, 1305–1312.

(17) Kim, B. Y.; Lee, C.; Chung, S. W.; Lee, Y. J.; Pak, J. Y.; Ko, J.; Kang, S. O. Electrochemical Behavior of the Cp*(Dithiolato)Co(III) Complex [(η^5-Cp*)Co(1,2-$S_2C_2B_{10}H_{10}$-S,S′)] and Its Derivatives: The Effect of the Ligand on Half-Sandwich Cobalt(III) Complexes. *J. Organomet. Chem.* **2003**, *688*, 236–245.

(18) T. Termaten, A.; Aktas, H.; Schakel, M.; W. Ehlers, A.; Lutz, M.; L. Spek, A.; Lammertsma, K. Terminal Phosphinidene Complexes CpR(L)MPAr of the Group 9 Transition Metals Cobalt, Rhodium, and Iridium. Synthesis, Structures, and Properties. *Organometallics* **2003**, *22*, 1827–1834.

(19) Nagasawa, T.; Nagata, T. Synthesis and Electrochemistry of Co(III) and Co(I) Complexes Having C5Me5 Auxiliary. *Biochim. Biophys. Acta - Bioenerg.* **2007**, *1767*, 666–670.

(20) Zhang, S.; Zhai, X.; Song, Y.; Feng, L.; Tung, C. H.; Wang, W. Insertion of BH3 into a Cobalt-Aryl Bond: Synthetic Routes to Arylborohydride and Borane-Amino Hydride Complexes. *Organometallics* **2021**, *40*, 1692–1698.

(21) Kurtz, D. A.; Dhar, D.; Elgrishi, N.; Kandemir, B.; McWilliams, S. F.; Howland, W. C.; Chen, C. H.; Dempsey, J. L. Redox-Induced Structural Reorganization Dictates Kinetics of Cobalt(III) Hydride Formation via Proton-Coupled Electron Transfer. *J. Am. Chem. Soc.* **2021**, *143*, 3393–3406.

(22) Kurtz, D. A.; Dempsey, J. L. Proton-Coupled Electron Transfer Kinetics for the Photoinduced Generation of a Cobalt(III)-Hydride Complex. *Inorg. Chem.* **2019**, *58*, 16510–16517.

(23) Lee, J. P.; Latendresse, T. P.; Henson, K. R.; Dean, P. A.; Mehne, L. F. Synthetic, Electrochemical, Spectroscopic, and Structural Studies of Mixed Sandwich Co(III) Complexes Involving Cp or Cp* with Tridentate N-Donor and S-Donor Macrocycles. *Inorg. Chim. Acta* **2019**, *485*, 200–208.

(24) Waldie, K. M.; Kim, S. K.; Ingram, A. J.; Waymouth, R. M. Cyclopentadienyl Cobalt Complexes as Precatalysts for Electrocatalytic Hydrogen Evolution. *Eur. J. Inorg. Chem.* **2017**, *2017*, 2755–2761.

(25) Fang, M.; Wiedner, E. S.; Dougherty, W. G.; Kassel, W. S.; Liu, T.; Dubois, D. L.; Bullock, R. M. Cobalt Complexes Containing Pendant Amines in the Second Coordination Sphere as Electrocatalysts for H_2 Production. *Organometallics* **2014**, *33*, 5820–5833.

(26) Nomura, M.; Imamura, F.; Ba Tuyet Nga, N.; Fujita-Takayama, C.; Sugiyama, T.; Kajitani, M. Synthesis and Electrochemistry of Organometallic Cobaltadithiaazulenes. *Inorg. Chem.* **2012**, *51*, 10695–10703.

(27) Nomura, M.; Fourmigué, M. Isostructural Diamagnetic Cobalt(III) and Paramagnetic Nickel(III) Dithiolene Complexes with an Extended Benzenedithiolate Core [CpM^{III}(Bdtodt)] (M = Co and Ni). *J. Organomet. Chem.* **2007**, *692*, 2491–2499.

(28) Zhang, Y.; Zheng, J. Bin. Investigation on the Electro-Oxidation of Iodide in the Room Temperature Ionic Liquid, 1-Butyl-3-Methylimidazolium Tetrafluoroborate at Platinum Electrode. *Electrochim. Acta* **2007**, *52*, 4082–4086.

(29) Sun, B.; Yoshino, T.; Matsunaga, S.; Kanai, M. A Cp*CoI_2-Dimer as a Precursor for Cationic Co(iii)-Catalysis: Application to C–H Phosphoramidation of Indoles. *Chem. Commun.* **2015**, *51*, 4659–4661.

4. Investigation of Cp*Co-catalyzed hydrophosphination

As described in Chapter 3, a two-component catalyst, Co(η^5-Cp*)I_2(CO) (**Co-1**) and base (1,8-Diazabicyclo[5.4.0]undec-7-ene, DBU), is active for the hydrophosphination of *tert*-butyl acrylate with PPh_2H (TOF >36 h^{-1}, Section 3.4.1). In this chapter, I describe the optimization of the catalytic hydrophosphination using this model reaction (Section 4.2). Using the optimized conditions, I investigated the alkene and phosphine substrate scope for this Co system (Section 4.3). Finally, I performed a series of control experiments and preliminary kinetic studies to gain insights into the participation of this Cp*Co system in hydrophosphination (Section 4.4). This chapter includes contributions from Dr. Charles Walsby (EPR spectroscopy, SFU).

4.1 Introduction

Early investigations of metal-catalyzed hydrophosphination focused on noble metals and lanthanides (see Chapter 1 and reference therein). First-row transition metal-catalyzed hydrophosphination has gained attention over the last two decades (Appendix A), especially for late first-row metals. However, there is still limited precedent for Co-catalyzed hydrophosphination (Scheme 4.1)[1–4] and hydrophosphinylation.[5,6]

Scheme 4.1 Literature examples of Co-catalyzed hydrophosphination.

Hydrophosphination of alkyne catalyzed by **Co(II)**, Oshima 2005[1]

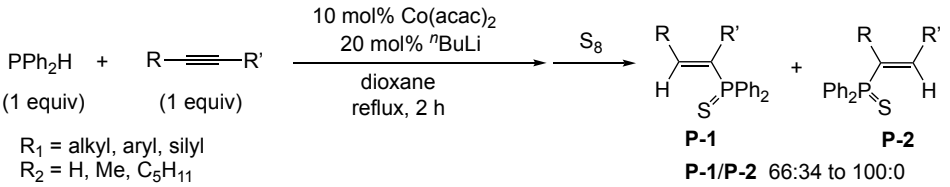

R_1 = alkyl, aryl, silyl
R_2 = H, Me, C_5H_{11}

Hydrophosphination of alkyne catalyzed by **Co(0)**, Shanmugam & Shanmugam 2018[2]

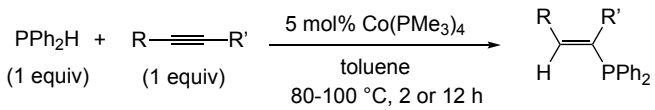

R = alkyl, aryl,
R' = H, aryl, Me

Hydrophosphination of activated alkenes catalyzed by **Co(I or II),** Kays & Geer 2020[3]

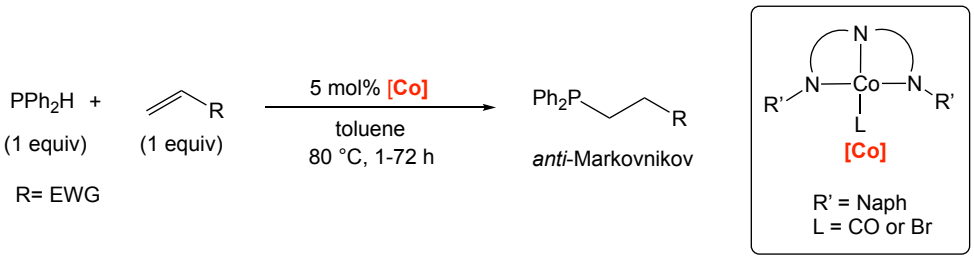

Hydrophosphination of alkyne catalyzed by **Co(I and II**), Shanmugam & Rajaraman 2022[4]

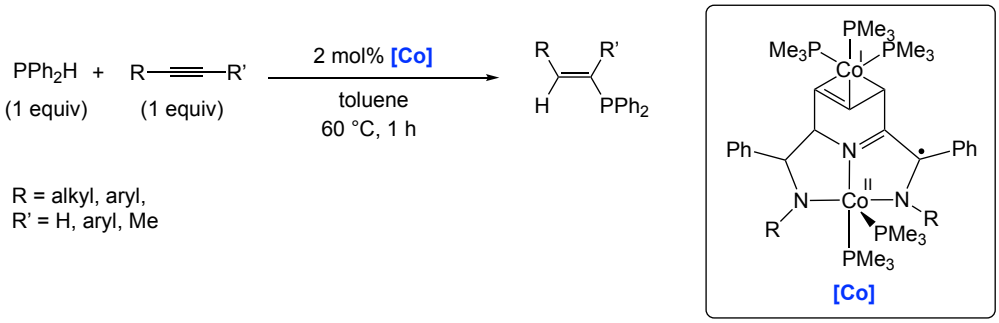

R = alkyl, aryl,
R' = H, aryl, Me

Proposed mechanisms for Co-catalyzed hydrophosphination vary in P-H bond activation and P-C bond formation steps. For example, Shanmugam and coworkers proposed a catalytic cycle involving Co(0)/Co(II) (Scheme 4.2).[2] Spectroscopic analysis (NMR, EPR, and UV-vis) reveals that the Co(0) complex undergoes oxidative addition of PPh_2H to give a catalytically competent Co(II) phosphido hydride complex, $Co(H)(PPh_2)(PMe_3)_3$ (step A). Then, a substrate alkyne coordinates to the Co center (step

B) and inserts to the Co-H bond (step C), generating a Co(II) alkenyl phosphido intermediate. The final P-C reductive elimination (step D) gives the product phosphine and regenerates the active Co(0) species. In the absence of alkynes, $Co(H)(PPh_2)(PMe_3)_3$ reacts with another equiv of PPh_2H, forming the byproduct $Ph_2P\text{-}PPh_2$ and the catalytically inactive Co(II) bis(hydride) complex $Co(H)_2(PMe_3)_4$.

Scheme 4.2 Proposed cycle for the Co-catalyzed hydrophosphination involving Co(0)/Co(II).

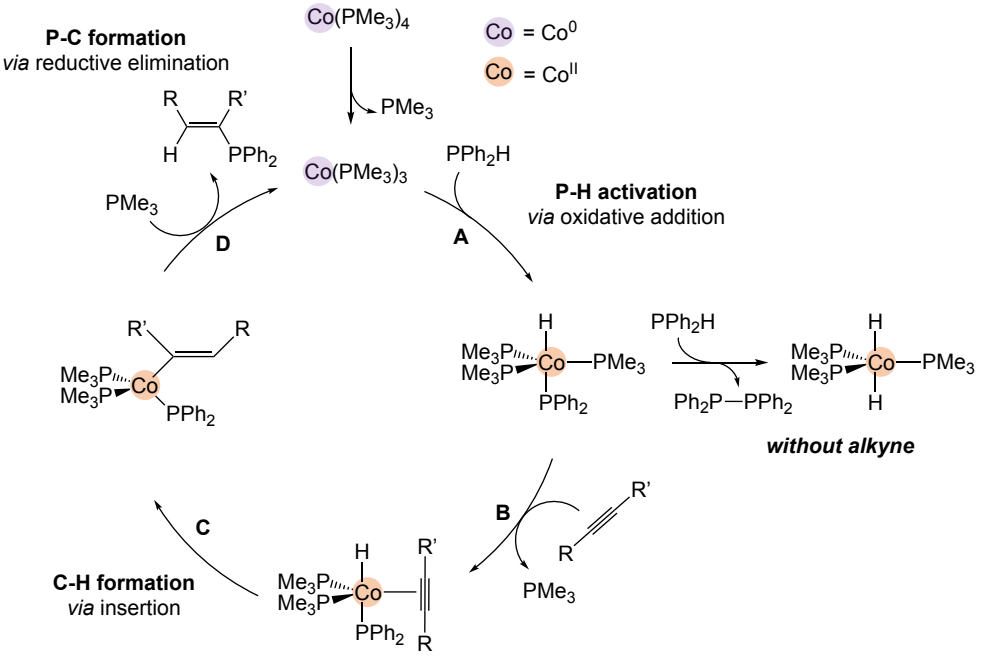

Kays and Geer, unlike Shanmugam, proposed a catalytic cycle for Co(I) or Co(II) pincer complexes that includes no change in the Co oxidation state (Scheme 4.3).[3] The coordination of the activated alkene is a critical step in the catalytic cycle (step A). The free substrate PPh_2H undergoes conjugate addition at the coordinated olefin (step B), followed by a 1,3-proton shift to give the coordinated product (step C). A final ligand substitution regenerates the active metal-alkene complex (step D). As described in Chapter 1, such conjugate addition of free PPh_2H to a metal-coordinated unsaturated substrate (step B) is uncommon. Additionally, in the absence of alkenes, the Co(I) pincer complex reacts

with PPh_2H to stoichiometrically form Ph_2P-PPh_2 (Scheme 4.3), which is consistent with the finding reported by Shanmugam (the off-cycle step in Scheme 4.2).

Scheme 4.3 Proposed cycle for the Co-catalyzed hydrophosphination involving conjugate addition of substrate PPh_2H at metal-alkene complexes.

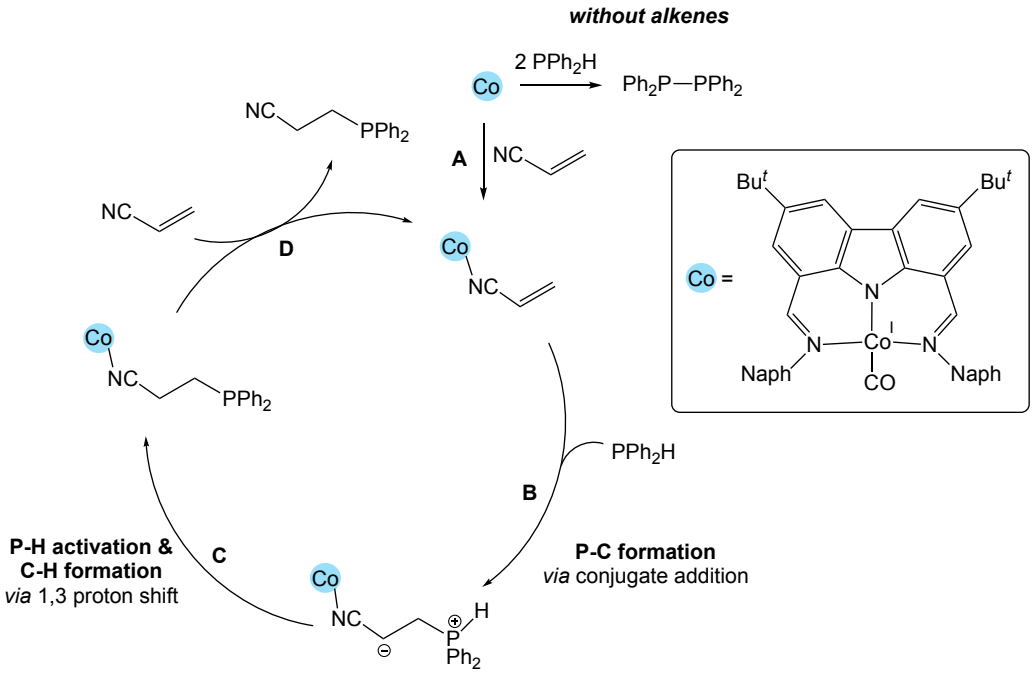

In this Co pincer system (Scheme 4.3), the Co(I) complex with a CO ligand shows much better activity and selectivity than the Co(II) analogue with a bromide ligand. Under identical conditions, the hydrophosphination of acrylonitrile with PPh_2H using the Co(I) catalyst gives the complete conversion to the linear hydrophosphination product within 1.5 h, whereas the hydrophosphination using the Co(II) catalyst gives 74% the linear hydrophosphination product, 3% the branched product and 11% Ph_2P-PPh_2 after 18 h. The authors explained this difference in activity by stating that the Co(I) carbonyl complex is a more effective Lewis acid than the Co(II) bromo complex (i.e. alkene coordination is more favourable for the Co(I) complex).

However, there are still gaps in understanding these catalytic mechanisms thoroughly. For the example reported by Oshima, the role of a strong base, *n*-BuLi, is unclear.[1] The

stoichiometric formation of Ph_2P-PPh_2 is observed in the systems reported by Kay and Shanmugam, but how this byproduct forms is not described. As described in Section 3.4.1, I also observed Ph_2P-PPh_2 as a minor product in the preliminary hydrophosphination reactions.

The formation of diphosphine is also common in other first-row metal-catalyzed hydrophosphination reactions.[7–11] In some examples as above,[8,12] diphosphines are formed exclusively in the absence of alkene/alkyne. The formation of the diphosphine is required in particular systems to initiate catalytic hydrophosphination.[10] In some cases, the P-P bond formation results in the deactivation of the catalyst.[2] Diphosphine formation occurs less often with second- or third-row metal catalysts for hydrophosphination. Understanding the mechanism of the formation of diphosphine is a non-negligible aspect of further developing first-row metal catalysts for hydrophosphination.

In this chapter, I present the optimization of catalytic conditions and exploration of substrate scope for the precatalyst Co(η^5-Cp*)I_2(CO) (**Co-1**). I also present mechanistic studies for this system, mainly answering two questions. One question is how diphosphine is formed in the Cp*Co(III)-catalyzed hydrophosphination – an aspect rarely studied for the first-row metal systems. The other question is why excess base, relative to Co, is required for the catalysis.

4.2 Optimizing conditions for Co-catalyzed hydrophosphination

Complex Co(η^5-Cp*)I_2(CO) (**Co-1**) is active for the catalytic hydrophosphination of *tert*-butyl acrylate with PPh_2H in the presence of excess base co-catalyst DBU, giving exclusively the linear, *anti*-Markovnikov product. In this section, I optimize the catalytic conditions (*vide infra*) by screening different catalyst loadings (Co:base ratio), base types

and solvents. The results demonstrate the optimal reaction conditions: **Co-1** (2 mol%) and DBU (4 mol%) in C_6D_6 at RT.

4.2.1 Optimizing the Co:base ratio for catalytic hydrophosphination

My preliminary assessment using 10 mol% Co(η^5-Cp*)I_2(CO) (**Co-1**, entries 1-4, Table 4.1) showed that DBU (the choice of this base shown in Section 4.2.2) is necessary for hydrophosphination activity and this co-catalyst must be present in an at least modest excess over **Co-1**. In Table 4.1, entries 1 and 2 (>1 equiv base added with respect to **Co-1**) show high hydrophosphination product conversions (i.e. the reactions are complete within 15 min), whereas entries 3 and 4 (≤1 equiv base added) show low hydrophosphination product conversions over 24 h. Under these circumstances (entries 3 and 4), the only hydrophosphination reaction occurring is the slow, background thermal hydrophosphination reaction (see entry 5). Entry 6 shows that catalysis can be mediated by DBU alone, but that it is slower than the Co/DBU-catalyzed process (*vide infra*).

Table 4.1 Screening the catalytic activity of complex **Co-1** and DBU for the hydrophosphination of *tert*-butyl acrylate with PPh_2H.[a]

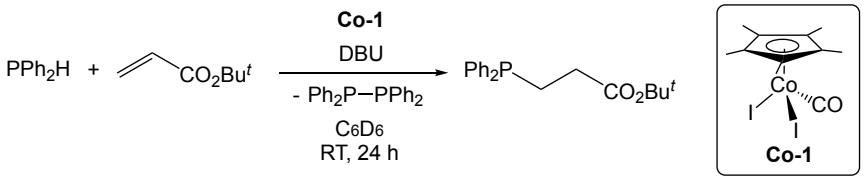

			% Conversion[b]	
Entry	**Co-1** (mol %)	DBU (mol%)	HP	Ph_2P-PPh_2
1	10	20	90(2)[c]	10(2)[c]
2	10	12	90(1)[c]	10(1)[c]
3	10	10	12(2)	10(2)[c]
4	10	0	11(3)	9(1)
5	0	0	11(2)	0
6	0	10	38(0)	0
7[d]	0.5	0.6	54(4)	0(1)
8[d]	1	1.2	84(1)	1(1)
9[d]	2	2.4	93(4)	2(1)
10[d]	5	6	93(2)	5(1)

[a]0.3 M PPh_2H, *tert*-butyl acrylate. [b]Conversions (%) determined by ^1H NMR (300.27 MHz), with respect to PPh_2H consumed; standard deviations for triplicate runs in parentheses. [c]Conversion observed after 15 min and unchanged after 24 h. [d]Co:base ratio maintained at 1:1.2, as for entry 2, for this initial screening.

Ph_2P-PPh_2 is formed, corresponding to ~10% substrate PPh_2H consumption, in all hydrophosphination reactions utilizing 10 mol% **Co-1** for entries 1–4 in Table 4.1. However, the diphosphine formation occurs significantly more slowly in entry 4 (no base) than in entries 1–3 (≥1 equiv of base added). After 15 min, $^{31}P\{^1H\}$ NMR shows ~1% diphosphine formation for entry 4, whereas conversion to the diphosphine is complete by this time for entries 1–3. This rapid Ph_2P-PPh_2 formation seen for entries 1–3 is consistent with its stoichiometric formation from a Co(III)-PPh_2 intermediate, presumably formed by deprotonation of Co-bound PPh_2H; it appears to be essential to the hydrophosphination catalysis (details in Section 4.4). The slower diphosphine formation for entry 4 is consistent

with the Co-mediated dehydrocoupling of PPh_2H (described in Section 3.4.2; it is faster at high temperatures, as described in Chapter 5). Change of the **Co-1** loading in the presence of a slight excess base (entries 7–10) under these conditions (24 h, RT, C_6D_6) indicates that 2 mol% of **Co-1** is optimal for maximizing the hydrophosphination product while minimizing the diphosphine byproduct. Thus, I utilized this Co loading for further optimization and the examination of substrate scope.

Figure 4.1 illustrates the results of experiments aiming to optimize the **Co-1**:DBU ratio necessary for catalytic hydrophosphination and to evaluate the role of excess DBU in the mixture. Monitoring hydrophosphination reactions over 2 h as a function of increasing the concentration of DBU relative to **Co-1** (Figure 4.1a) reveals the dramatic effect of excess base: a jump from trace product in the thermal background reaction (i.e. **Co-1**:DBU = 2:2) to ~35% conversion for the reaction using just 0.1 mol% DBU in excess (**Co-1**:DBU = 2:2.1). The optimal conversion (~70% in 2 h) is reached with a 2:4 **Co-1**:DBU ratio, and a bigger excess base does not result in a substantial improvement in product conversion. Figure 4.1b illustrates the hydrophosphination activity of DBU at concentrations corresponding to the excess, with respect to **Co-1**, utilized in Figure 4.1a (0–4 mol%). This demonstrates the low activity of DBU by itself compared to the enhanced activity produced by the action of excess DBU in the presence of **Co-1**. This apparent cooperative action of Co and the excess base is explored in Section 4.4.4. In short, the base is a key component of this catalytic system.

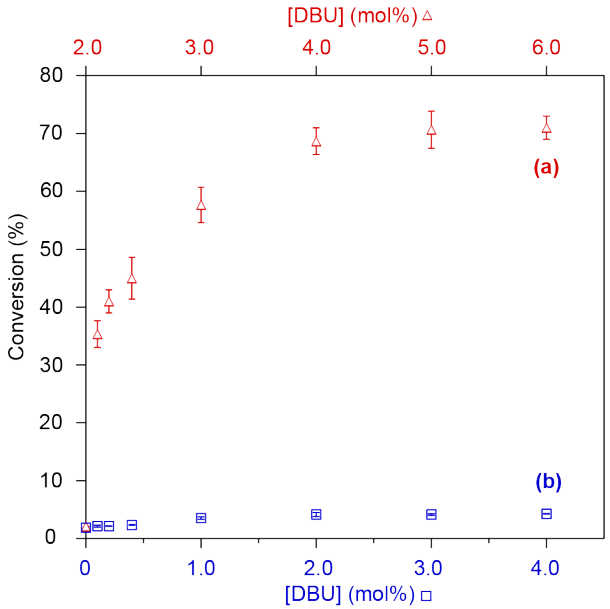

Figure 4.1 Conversion to hydrophosphination product after 2 h, as a function of DBU loading. (**a**) Reactions using 2 mol% **Co-1** and the DBU loading shown on the top axis, Δ; (**b**) reactions using the DBU loading shown on the bottom axis (corresponds to DBU in excess of 2 mol% used in (**a**)), □. Error bars represent standard deviation over triplicate runs.

4.2.2 Screening different bases for the catalytic hydrophosphination

I screened four bases for their participation as co-catalysts for the hydrophosphination of *tert*-butyl acrylate with PPh_2H using $Co(\eta^5\text{-}Cp^*)I_2(CO)$ (**Co-1**). Figure 4.2 depicts the results of screening studies demonstrating that the intermediate basicity of DBU is essential to the success of this reaction. My experiments show that catalysis only proceeds in the presence of a base sufficiently strong to deprotonate Co-PR_2H (i.e. to form a Co-PR_2 intermediate). In all cases when the unreacted substrate PPh_2H is in the catalytic mixture, its signal is significantly broad. As will be discussed in Section 4.4.4, this is consistent with the coordination of the substrate PPh_2H to paramagnetic Co intermediates.

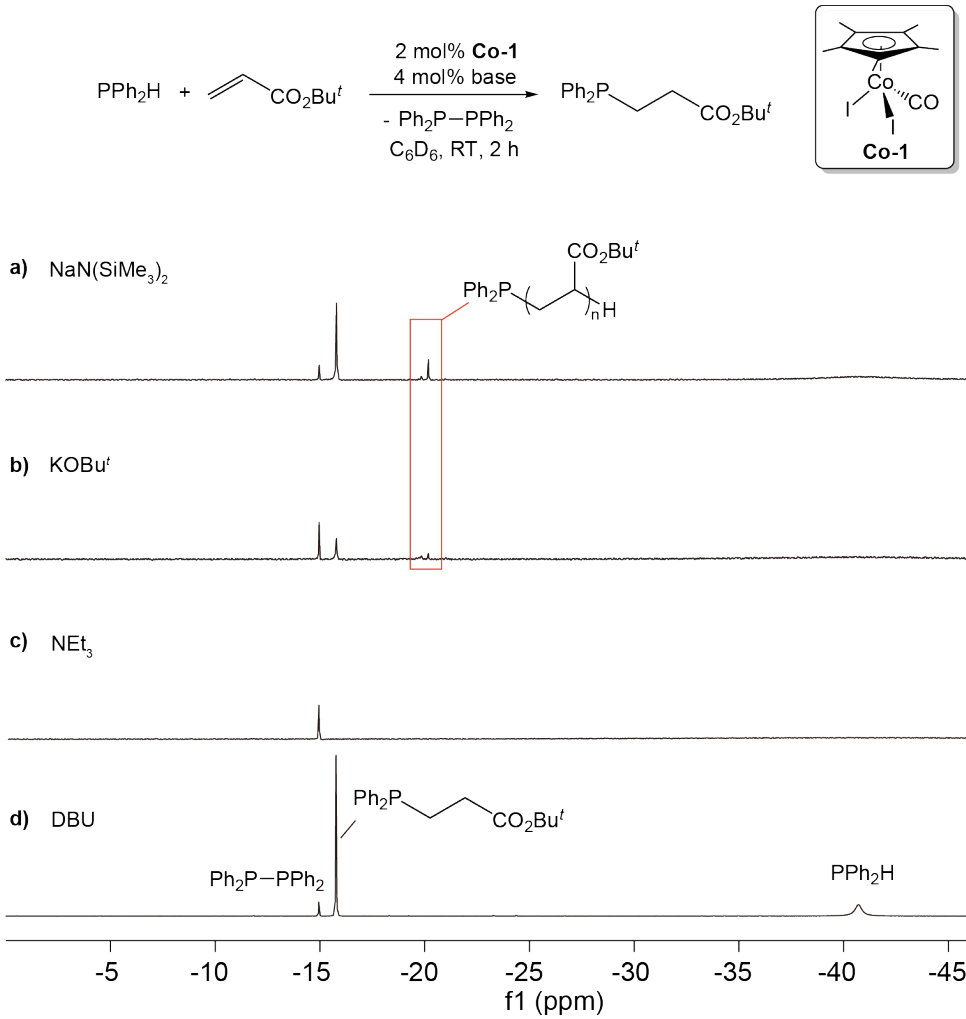

Figure 4.2 $^{31}P\{^{1}H\}$ NMR (202.51 MHz, C_6D_6) spectra of the hydrophosphination of *tert*-butyl acrylate with PPh_2H using 2 mol% **Co-1** and 4 mol% base after 2 h.

Two very strong bases, $NaN(SiMe_3)_2$ (pK_a $HN(SiMe_3)_2$ = 25.8 (THF))[13] and $KOBu^t$ (pK_a Bu^tOH = 19.2 (H_2O)[14]) facilitate the hydrophosphination reaction when used at the optimized Co:base ratio (**Co-1**:base = 1:2, Section 4.2.1). However, in both cases, extra $^{31}P\{^{1}H\}$ signals due to telomers are observed (Figure 4.2a,b), suggesting that these bases deprotonate free PPh_2H, in addition to Co-bound PPh_2H, to generate reactive free PPh_2^- (Section 2.2.4).[15] I also see relative levels of diphosphine, Ph_2P-PPh_2, that exceed the 2% anticipated for simple stoichiometric production of this P-P bond through intermediary Co-PPh_2 complexes (see Section 4.4), indicating that these strong bases also promote the

catalytic dehydrocoupling of PPh_2H. The weakest base I examined is NEt_3 (pK_a $[HNEt_3]Cl$ = 10.7 (H_2O)[16]). The reaction using 1:2 Co/base loading gives ~2% Ph_2P-PPh_2 as a minor product but no hydrophosphination product (Figure 4.2c). The reaction using 2 mol% **Co-1** and 4 mol% intermediate base DBU (pK_a $[HDBU]^+$ = 13.5 (H_2O)[17]) generates only the hydrophosphination product and ~2% diphosphine under the conditions shown in Figure 4.2.

To understand why the intermediate basicity of DBU is important for this catalysis, I performed two sets of control experiments. According to these control experiments, DBU is optimal because it has sufficient basicity to deprotonate Co-bound PPh_2H but insufficient to deprotonate the free substrate PPh_2H. First, I conducted a reaction of free PPh_2H with a base ($NaN(SiMe_3)_2$, $KOBu^t$, NEt_3 or DBU, respectively). For the reactions of $NaN(SiMe_3)_2$ and $KOBu^t$, the solutions turn to an orange suspension, consistent with the known colour and poor solubility of $NaPPh_2$ in non-coordinating solvents.[18] Similar deprotonation of PPh_2H using $KOBu^t$ or $NaN(SiMe_3)_2$ to generate free PPh_2^- was reported in the literature.[15,19] For the reactions using NEt_3 and DBU, no deprotonation of PPh_2H occurs: the resulting solution remains clear and colourless, and no signal broadening of PPh_2H is detected by NMR (Figure 4.3).

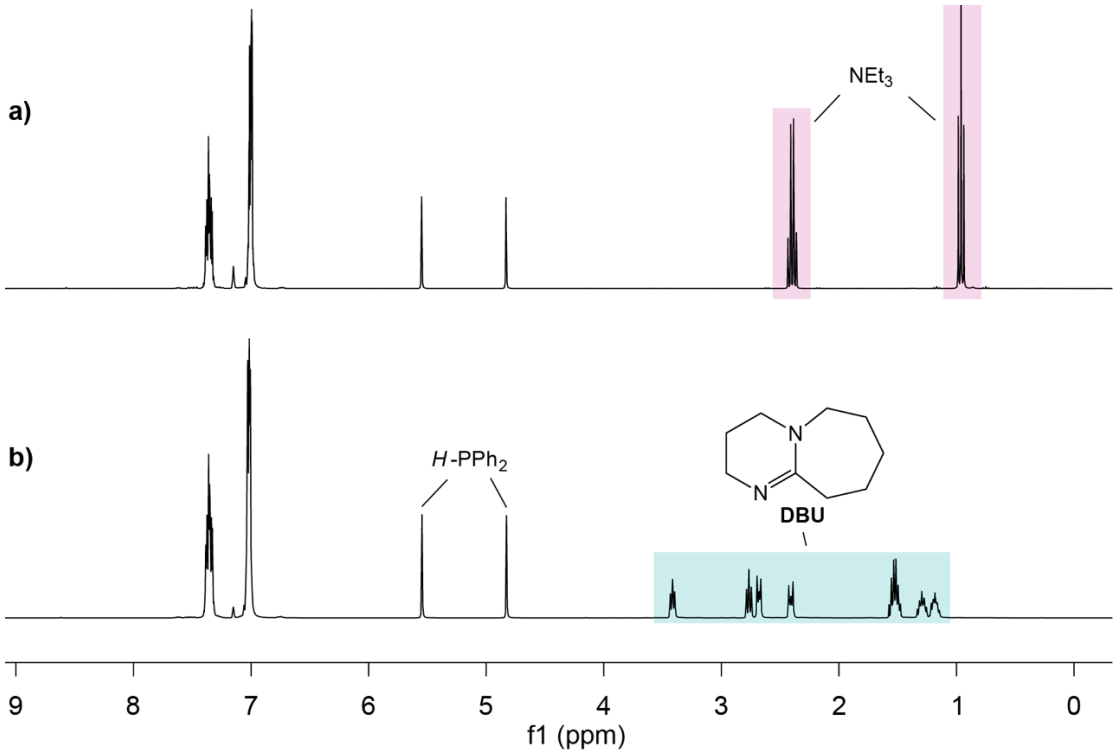

Figure 4.3 ^{1}H NMR (500.27 MHz, C_6D_6) spectra of the reaction of PPh_2H with 4 mol% of base ((**a**) NEt_3 or (**b**) DBU), showing that no deprotonation occurs.

Second, I added 1 equiv of base (NEt_3, DBU, $KOBu^t$ or $NaNSi(Me_3)_2$) to the mono(phosphine) complex $Co(\eta^5\text{-}Cp^*)I_2(PPh_2H)$ (**Co-2a**), to see if the base is capable of deprotonating the Co-bound PPh_2H. Generally, metal coordination makes the PR_2H more acidic.[20] The results show all bases except the weakest, NEt_3, can deprotonate the PPh_2H ligand at **Co-2a** (see details in Section 4.6.2).

4.2.3 Optimizing the solvent for catalytic hydrophosphination

To test the solvent effect on the catalytic activity, I performed the hydrophosphination of *tert*-butyl acrylate with PPh_2H in a different solvent, CD_2Cl_2, instead of C_6D_6. When CD_2Cl_2 is used as a solvent, the reaction using 2 mol% $Co(\eta^5\text{-}Cp^*)I_2(CO)$ (**Co-1**) and 4 mol% DBU gives just a trace amount of the hydrophosphination product (that is due to the

thermal hydrophosphination product) after 24 h. Additionally, by ^{31}P NMR, I observed a catalytic amount of Ph_2P-PPh_2 (i.e. ~10% PPh_2H consumption), along with unreacted PPh_2H (~74%) and some P-containing species (~16%).

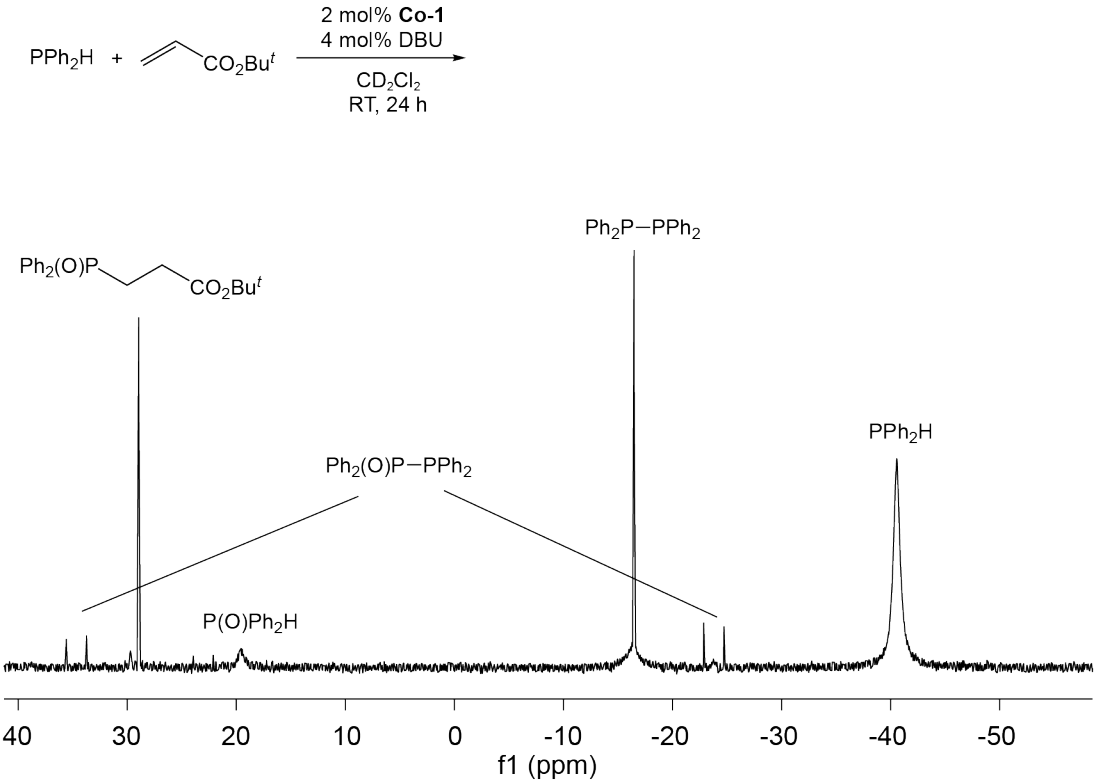

Figure 4.4 $^{31}P\{^1H\}$ NMR (121.55 MHz, CD_2Cl_2) spectrum of the hydrophosphination of *tert*-butyl acrylate with PPh_2H catalyzed by 2 mol% of **Co-1** and 4 mol% of DBU, after 24 h. Note: the oxidized product arises from using insufficiently dried CD_2Cl_2 or slowly oxidized substrate PPh_2H.

The loss of catalytic hydrophosphination activity and a relatively messy reaction mixture in CD_2Cl_2 could be due to the decomposition of important Cp*Co phosphido intermediates in the solution. Support for this comes from a previous study of the dimeric phosphido complex $[Co(\eta^5\text{-}Cp)(\mu\text{-}PMe_2)]_2$ showing that it reacts with halogenated solvents.[21] Solvent-dependent PPh_2H reactivity in hydrophosphination and dehydrocoupling has also been reported for a β-diketiminate Fe(II) catalyst.[12] However, in that example, the solvent polarity has the opposite effect from ours: dehydrocoupling

occurs in C_6D_6 but not in CD_2Cl_2, and hydrophosphination of a variety of alkenes occurs in CD_2Cl_2.

4.3 Investigating substrate scope for Co-catalyzed hydrophosphination

With the optimized conditions in hand, I assessed a variety of alkene and phosphine substrates in hydrophosphination reactions catalyzed by Co(η^5-Cp*)I_2(CO) (**Co-1**) and DBU, which is described in this section.

4.3.1 Alkene scope

I performed the hydrophosphination of various alkene substrates with a model phosphine PPh_2H using 2 mol% **Co-1** and 4 mol% DBU. Scheme 4.4 shows this Co system is limited to electron-deficient alkenes (i.e. activated alkenes). Methyl acrylate and *tert*-butyl acrylate show the highest activity in the reactions, followed by acrylonitrile. Methyl methacrylate and cyclohexanone, which are more hindered and less activated alkenes, exhibit significantly decreased activity. Aryl alkenes and 1-hexene are inert to hydrophosphination in this system (only thermal hydrophosphination occurs), but they seem to operate as hydrogen acceptors for catalytic dehydrocoupling of PPh_2H because I observe diphosphine concentrations over the stoichiometric 2% in these reaction mixtures (Scheme 4.4).

Scheme 4.4 Alkene scope for Co-catalyzed hydrophosphination with PPh_2H.[a]

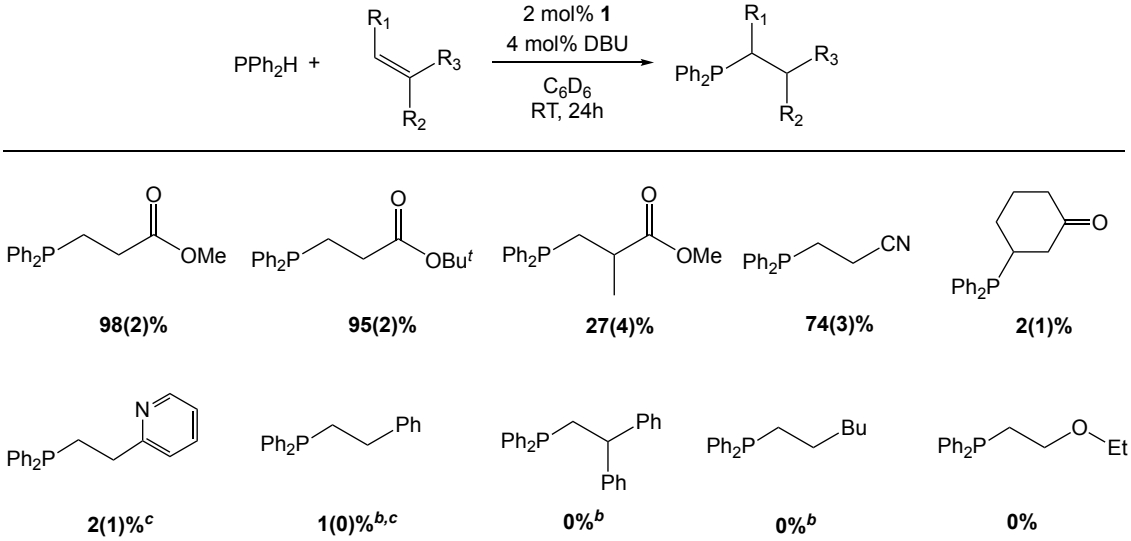

[a]0.3 M PPh_2H, alkene. Conversions (%) determined by ^1H NMR (300.27 MHz); standard deviations for triplicate runs are shown in parentheses. Stoichiometric Ph_2P-PPh_2 (2% PPh_2H consumed) observed unless otherwise noted. [b]12-20% Ph_2P-PPh_2 observed. [c]Observed trace hydrophosphination product is due to the thermal background reaction.

The fact that the catalysis only works for activated alkenes implies that P-C bond formation relies on an outer-sphere mechanism involving conjugate addition of Co phosphido species at the unsaturated substrate. This essential step has been proposed for hydrophosphination catalysts as an alternative to a "classic" mechanism that depends on alkene insertion chemistry. The initial catalytic activities of methyl acrylate and *tert*-butyl acrylate are high: these reactions reach 90% and 72% conversion, respectively, within 3 h (TOFs = 15 and 12 h^{-1}, respectively). However, their activity starts to level out after 3 hours, and the full 24 h are required to obtain the greater conversions illustrated in Scheme 4.4. This observation suggests that catalyst deactivation is occurring (see Section 4.4.6). Remarkably, the catalytic activity of highly activated and sterically unrestricted acrylonitrile is much lower than that of methyl- and *tert*-butyl acrylates. However, a similar trend in activity for these Michael acceptor substrates was recently reported for a highly

active Rh hydrophosphination catalyst that also operates through a conjugate addition mechanism.[22]

4.3.2 Phosphine scope

I evaluated the activity of this Co system for the catalytic hydrophosphination of *tert*-butyl acrylate by different phosphine substrates (Scheme 4.5). The catalytic activity of secondary phosphines PR_2H (Scheme 4.5, top) correlates with the steric properties of the phosphines. Catalysis slows with increasing phosphine steric bulk as described by Tolman cone angles for these phosphines: PEt_2H (117°) > PPh_2H (126°) ≅ $PTol^p_2H$ (126°) > PCy_2H (142°).[23] Given that the vast majority of hydrophosphination catalyses reported in the literature use only secondary aryl phosphine substrates (PAr_2H), it is noteworthy that I found such high activity with the small alkyl phosphine PEt_2H for this Co system.

Scheme 4.5 Phosphine scope for Co-catalyzed hydrophosphination of *tert*-butyl acrylate.[a]

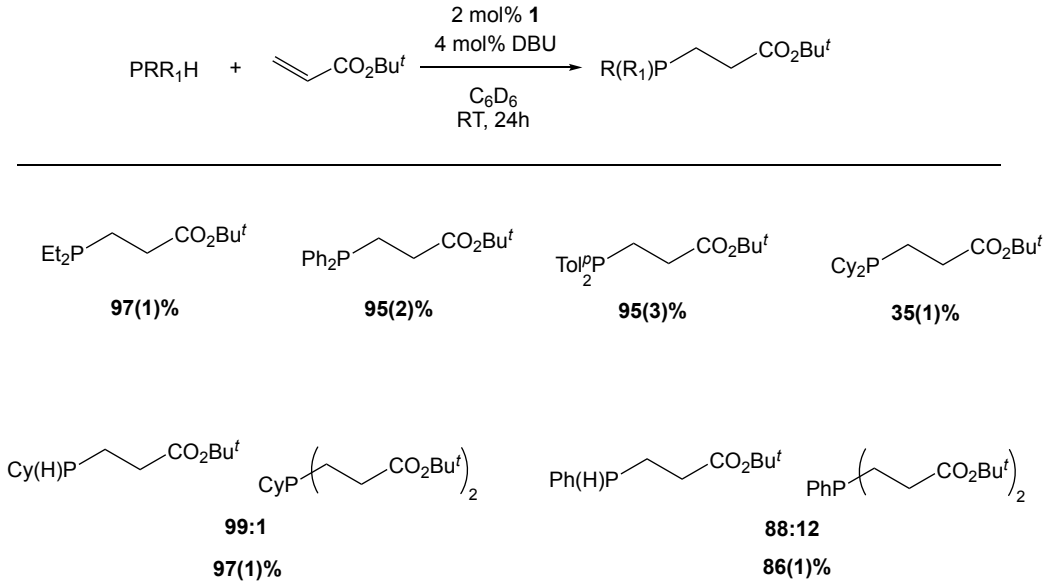

[a]0.3 M phosphine, *tert*-butyl acrylate. Conversions (%) determined by ^{1}H NMR (300.27 MHz), with standard deviations for triplicate runs shown in parentheses. Stoichiometric diphosphine (2% conversion) was observed for all reactions, including 1:1 rac/meso mixtures of diphosphines HRP-PRH (R = Cy, Ph).

Unlike the secondary phosphine results, the activity of the two primary phosphines PRH_2 in the hydrophosphination of *tert*-butyl acrylate has no correlation with the phosphine size (Scheme 4.5, bottom). $PCyH_2$ (115°) and $PPhH_2$ (106°) have much smaller Tolman cone angles than the smallest (and most reactive) secondary phosphine, PEt_2H (117°). However, high activity is observed for the slightly bulkier, more electron-rich $PCyH_2$. The 97% conversion shown in Scheme 4.5 is achieved in 3 h, while for the smaller PPh_2H, the 86% product conversion takes 24 h. This is surprising because the $PPhH_2$ seems to be a more reactive substrate than $PCyH_2$ in two other metal systems for which hydrophosphination (of styrene or 1,3-butadiene) with primary phosphine has been reported.[24,25] The inverted activity for these primary phosphine reactions in our Co system could be explained by different mechanisms for these metal systems. In the reported Zr system, protonolysis of the Zr-C bond by substrate PRH_2 seems to be turnover-limiting.[25] Thus, in this case, it is reasonable that $PPhH_2$ is more active than $PCyH_2$ due to its higher acidity (pK_a values: $PPhH_2$ (22.4) < $PCyH_2$ (29.6)).[26] For our Co system, the result suggests that a conjugate addition step is important in the catalytic cycle and could be the turnover-limiting step. Thus, the catalytic reactions proceed faster for a more nucleophilic Co phosphido intermediate. This is consistent with the highest activity observed for the smallest, electron-rich secondary phosphine PEt_2H (Scheme 4.5, top).

The high activity I observe for $PCyH_2$ is notable because PRH_2 substrates are less commonly used in catalytic hydrophosphination than PR_2H, and it is unusual to see activity reported for primary alkylphosphines.[27] Our Co system has the potential to produce either secondary or tertiary alkylphosphine from primary phosphines by modifying the reaction conditions slightly. For example, the reaction of *tert*-butyl acrylate with $PCyH_2$ (1 equiv)

yields mostly the single hydrophosphination product $P(CH_2CH_2CO_2Bu^t)(Cy)H$ and only trace quantities of the double hydrophosphination product $P(CH_2CH_2CO_2Bu^t)_2Cy$. Complete conversion to $P(CH_2CH_2CO_2Bu^t)_2Cy$ may be accomplished by adding a subsequent equiv of the alkene, which takes 6 h for completion. However, double hydrophosphination of *tert*-butyl acrylate (2 equiv) with $PPhH_2$ (1 equiv) is much slower than that of $PCyH_2$, which produces 88% of desired $P(CH_2CH_2CO_2Bu^t)_2Ph$ and 12% of unreacted $P(CH_2CH_2CO_2Bu^t)(Ph)H$.

4.4 Investigating the mechanism of Co-catalyzed hydrophosphination

The fact that hydrophosphination activity of $Co(\eta^5\text{-}Cp^*)I_2(CO)$ (**Co-1**) is restricted to activated alkene substrates is compatible with a mechanism involving conjugate addition of a Co phosphido (Co-PR_2) fragment at an alkene. The need for a base is also consistent with the importance of a Co-PR_2 fragment, which would result from the deprotonation of a Co-bound substrate phosphine. Thus, in this section, mechanistic studies focus on revealing the formation of Co-PR_2 intermediates (Section 4.4.1–4.4.5). I also present preliminary kinetic experiments to show that catalyst deactivation occurs for this system (Section 4.4.6). Further kinetic and stoichiometric control experiments suggest the participation of a monomeric Co(II)-PR_2 intermediate in conjugate addition (Section 4.4.7).

4.4.1 Substitution chemistry of complex Co-1 with substrate phosphines and *tert*-butyl acrylate

As described in Section 3.4.1, I used complex **Co-1** and its PPh_2H derivative (i.e. **Co-2a** and **Co-4a**) to study the catalytic process for the reaction of *tert*-butyl acrylate and

PPh_2H, finding no discernible performance difference among these three catalysts. Also, I found that *tert*-butyl acrylate does not compete with PPh_2H for the coordination to the Cp*Co(III) fragment. It is reasonable to assume that the formation of Co(III) phosphine complexes is a precursor step for catalysis for all phosphine substrates, and the resulting Co phosphine complexes are deprotonated by a base to generate a Co-PR_2 intermediate for hydrophosphination.

Before attempting to make a Co-PR_2 complex, I initially examined the generation of Co phosphine complexes using excess substrate phosphine to mimic catalytic conditions. The addition of excess secondary phosphine (PR_2H) to Co(η^5-Cp*)I_2(CO) (**Co-1**) results in the formation of the mono- and bis(phosphine) complexes Co(η^5-Cp*)I_2(PR_2H) (**Co-2**) and [Co(η^5-Cp*)I(PR_2H)$_2$]I (**Co-4**) (Scheme 4.6a), for which preparation and characterization are described in Chapter 3. The ratio of these complexes is determined by the relative size of PR_2H. For the smallest PEt_2H, only bis(phosphine) complex **Co-4e** is observed in the reaction mixtures. The addition of excess PR_2H (R = Ph, Tol^p) of modest size gives solutions containing mainly Co complexes **Co-4a,d** and some **Co-2a,d**, respectively. This is consistent with my observation that the isolated **Co-4a,d** undergoes ligand redistribution in the NMR sample (see Chapter 3). For the very bulky phosphines PCy_2H and PPr^i_2H, only mono(phosphine) complexes **Co-2c,d** are observed. The addition of excess primary phosphine (PRH_2) to **Co-1** also produces the mono(phosphine) complex Co(η^5-Cp*)I_2(PRH_2) (**Co-3**) (Scheme 4.6b). As noted in Chapter 3, this is somewhat unexpected, considering the smaller size of primary phosphines; nevertheless, it may be explained by the weaker donor ability of these ligands.[23]

Scheme 4.6 Reactions of complex **Co-1** with excess **a)** secondary phosphine or **b)** primary phosphine. R = Ph (**a**), Tol^{p} (**b**), Cy (**c**), Pr^{i} (**d**) and Et (**e**).

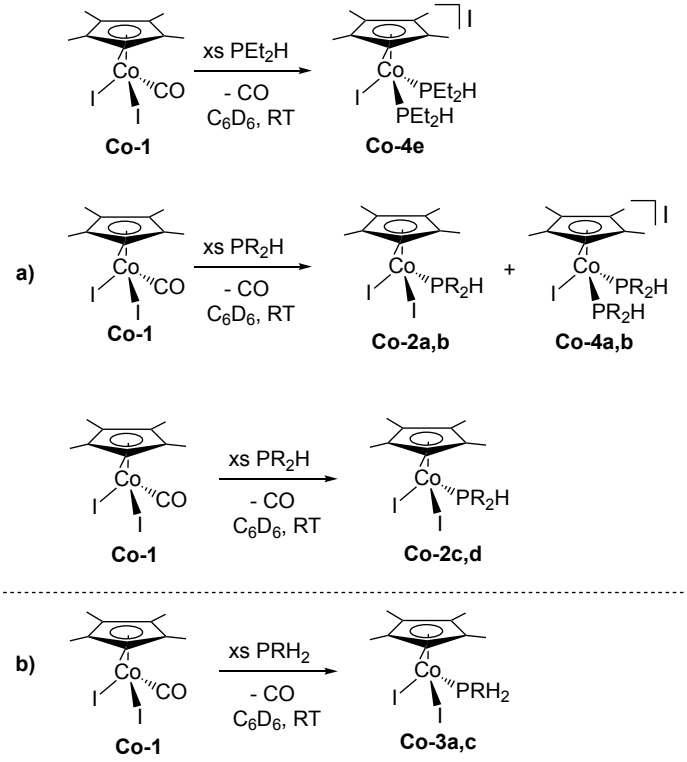

Most importantly, the substitution chemistry presented here shows that the degree of phosphine substitution at the Co(III) (i.e. forming mono- or bis(phosphine) complexes) is not important for the overall catalytic process. The important catalytic first step requires at least one coordinated phosphine, which may be deprotonated by base to provide a phosphido ligand. The mono(diphenylphosphine) complex **Co-2a** was used as a model catalyst precursor in subsequent mechanistic studies.

4.4.2 Identifying Co intermediates in the catalytic mixture by NMR

I scrutinized the catalytic mixture through NMR monitoring experiments. Initially, the hydrophosphination of *tert*-butyl acrylate with PPh_2H using 10 mol% Co(η^5-Cp*)I_2(CO) (**Co-1**) and 20 mol% DBU was monitored by ^{1}H and $^{31}P\{^{1}H\}$ NMR. The reaction was complete within 15 min (i.e. first spectrum was obtained). I identified Co-P-

containing intermediates with very weak signals in the $^{31}P\{^{1}H\}$ NMR spectrum of this catalytic mixture (Figure 4.5). A signal at 47.8 ppm shows a $^{1}J_{PH}$ coupling (~343 Hz) in the ^{31}P NMR spectrum, suggesting that it could be due to Co-PPh_2H. Thus, the signal is tentatively assigned as Co(I) phosphine complex Co(η^5-Cp*)(PPh_2H)$_2$ (**Co-8**, ~11% with respect to **Co-1**). The ^{31}P shift for **Co-8** is close to those for Cp'Co(I) analogues with PPh_3 ligand.[28–30] The signal is also more downfield than that due to the Cp*Co(III) secondary phosphine complex (10-20 ppm, Table 3.1 in Chapter 3), which may be explained by PPh_2H being coordinated to Co in a different oxidation state. The signal at 127 ppm is close to ^{31}P shifts reported for bridging CpCo phosphido complexes in the literature (δ 112.8–133.4 ppm).[31,32] So, the signal is tentatively assigned as Co(II) bridging phosphido complex [Co(η^5-Cp*)(μ-PPh_2)]$_2$ (**Co-9**, ~5 % with respect to **Co-1**). $^{1}H/^{31}P\{^{1}H\}$ HMBC also supports the identities of these two Co complexes, as shown in Figure 4.6. The quantity of observable Co intermediates is substantially less than the amount of complex **Co-1** used (i.e. ~80% Co(III) signals disappear in the NMR), which suggests that the Co(III) complexes have been converted to paramagnetic species that cannot be detected by NMR.

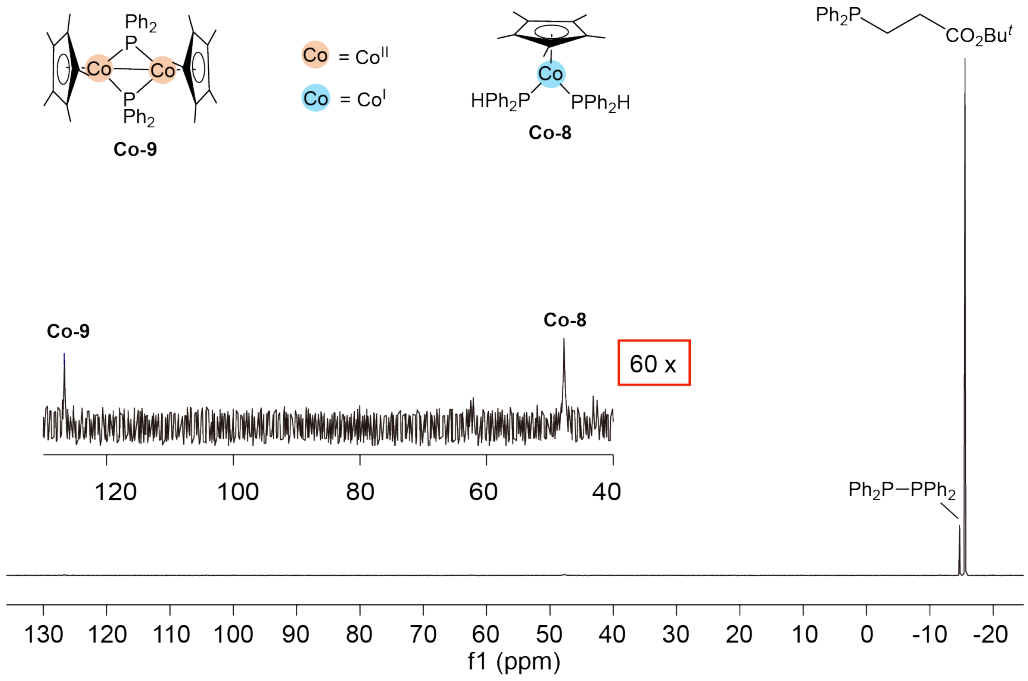

Figure 4.5 $^{31}P\{^{1}H\}$ NMR (202.51 MHz, C_6D_6) spectrum of the reaction of *tert*-butyl acrylate with PPh_2H catalyzed by 10 mol% **Co-1** and 20 mol% DBU. Inset shows trace amounts of complexes **Co-8** and **Co-9** in the catalytic mixture.

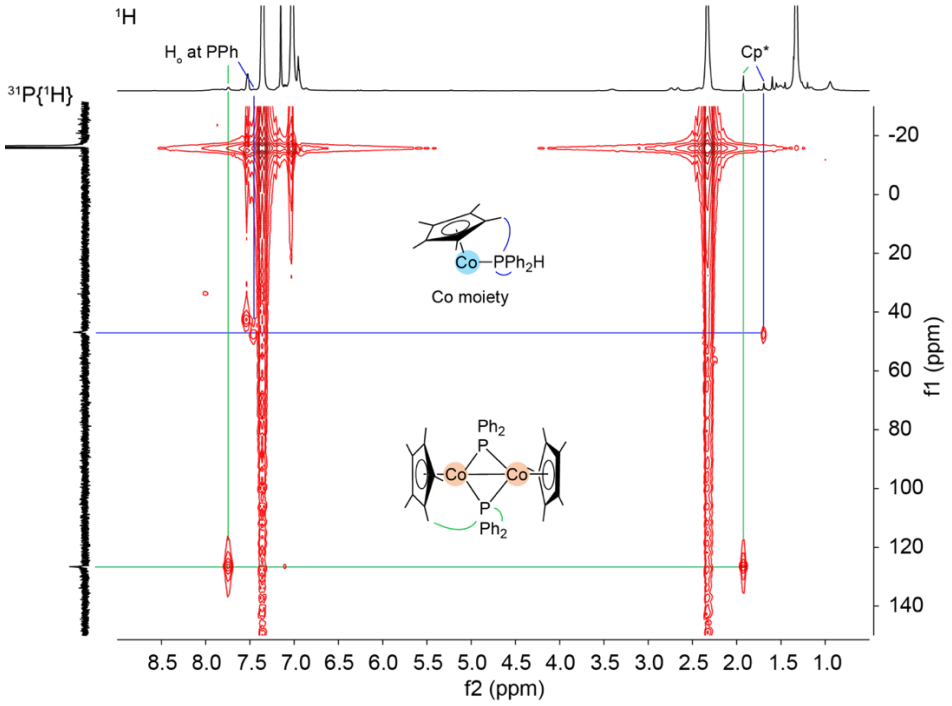

Figure 4.6 $^{1}H/^{31}P\{^{1}H\}$ HMBC (500.27 MHz, C_6D_6) spectrum of the reaction of 10 equiv of *tert*-butyl acrylate and PPh_2H catalyzed by **Co-1**, showing correlations of the ^{31}P signals in Co-P species with their Cp* signals and phenyl *ortho*-H signals.

After the first catalytic run was complete, *tert*-butyl acrylate and PPh_2H were added to this mixture for a second run, with a decrease in catalytic activity (i.e. the reaction was complete in 30 min). Thus, the mixture is still catalytically active. However, this decreased activity suggests that some catalyst deactivation at this high Co loading. The observed Co(I) complex **Co-8** could be relevant to the catalyst deactivation, and bridging phosphido complex **Co-9** may be important for catalysis.

4.4.3 Investigating the reduction of Co(III) phosphido to Co(II) and diphosphine

I next investigated how the Co(III) precursor is activated to give a catalytically active mixture containing ~80% paramagnetic Co species. I hypothesized that Co(III)-PR_2 must form at some stages during catalysis, probably through dehydrohalogenation of a Co(III) phosphine complex by a base (see example in Scheme 4.7).

Scheme 4.7 Dehydrohalogenation of **Co-2a** by DBU, showing the formation of Ph_2P-PPh_2 and a paramagnetic Co(II) complex.

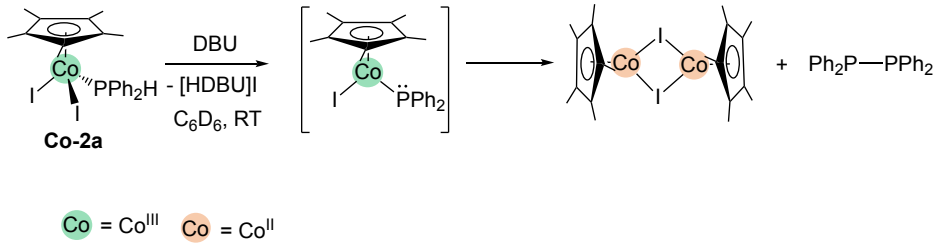

The addition of 1 equiv of DBU to a solution of **Co-2a** results in an instantaneous change in colour from green to dark brown, with the formation of a white precipitate [HDBU]I (Scheme 4.7). The identity of the [HDBU]I is confirmed by NMR and ESI-MS (see Section 4.6.8). This indicates that the dehydrohalogenation does occur, producing Co(III)-PPh_2. However, this species is not observed by NMR even when the dehydrohalogenation reaction is conducted at –70 °C. The $^{31}P\{^1H\}$ NMR spectrum of the reaction shows only one signal at about –14 ppm due to Ph_2P-PPh_2. Even when the ^{31}P

NMR spectral width is increased to 2000 ppm, there are no observable Co-P signals (Figure 4.7). The absence of Co-P signals in the NMR indicates that Co(III)-PPh_2 undergoes binuclear reductive elimination to give diphosphine and one or more paramagnetic Co species. One paramagnetic Co species, Co(II) iodide dimer $[Co(\eta^5\text{-}Cp^*)(\mu\text{-}I)]_2$, can be detected by ^1H NMR. The ^1H NMR spectrum (Figure 4.8) shows a broad signal at 56.7 ppm, which is consistent with methyl protons on a Cp* ligand in dimeric Co(II) sandwich complexes with bridging chloride (δ 38.5–41 ppm).[33] The instability of $[Co(\eta^5\text{-}Cp^*)(\mu\text{-}I)]_2$ precludes the isolation of this compound (see Section 4.6.8 for attempted synthesis). This is also consistent with the literature report on this Co(II) iodide dimer.[34]

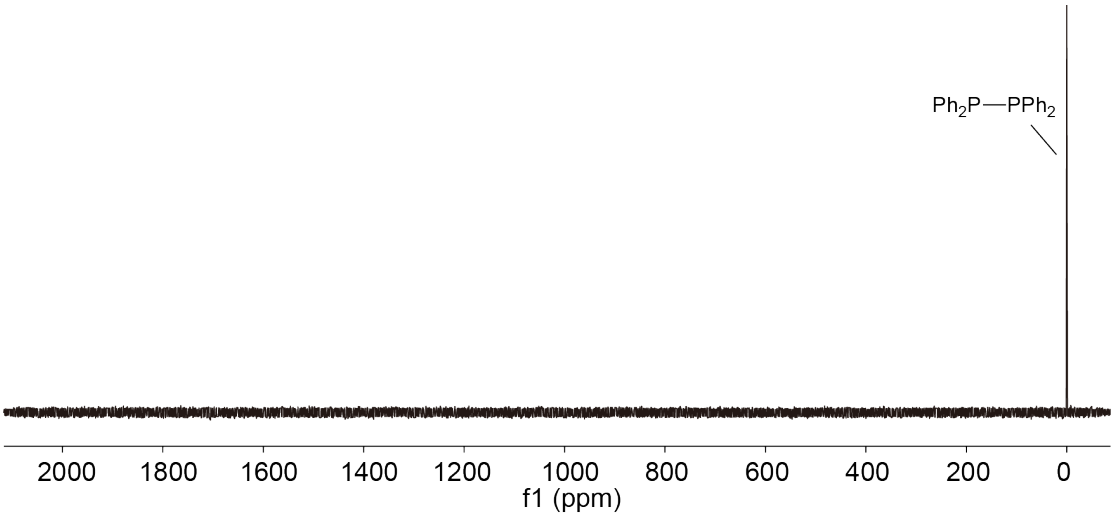

Figure 4.7 Wide $^{31}P\{^1H\}$ NMR (121.55 MHz, C_6D_6, up to 2000 ppm) spectrum of the reaction of complex **Co-2a** with DBU, showing no Co-PPh_2 observed in the mixture.

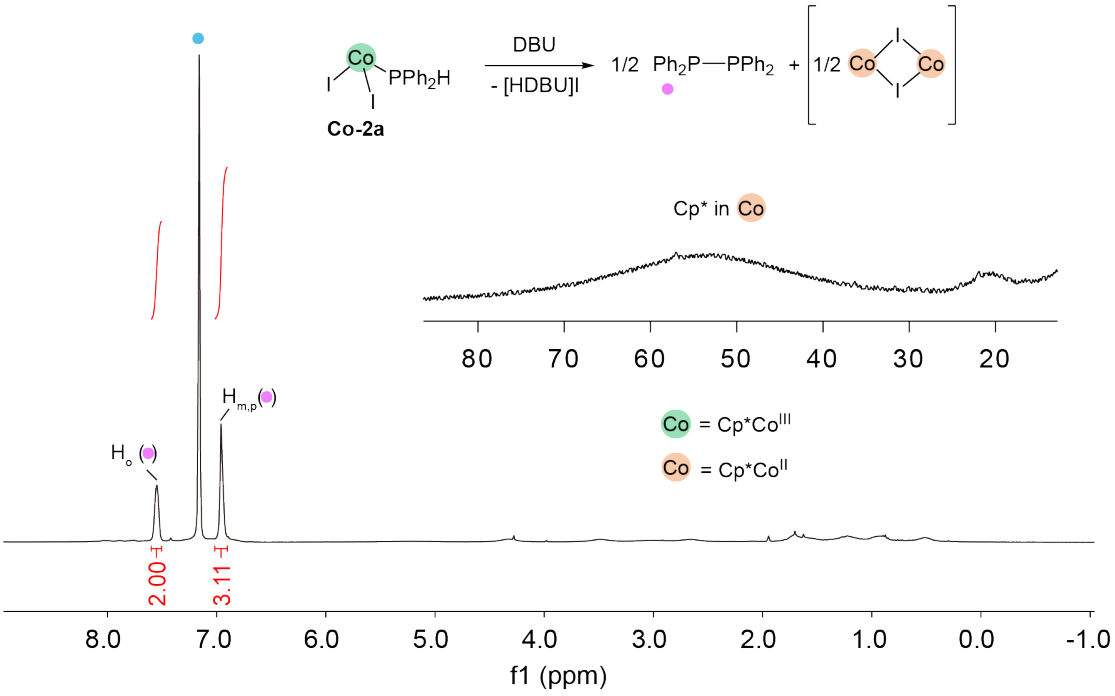

Figure 4.8 ^{1}H NMR (300.27 MHz, C_6D_6) spectrum of the reaction of **Co-2a** with DBU, showing the broad paramagnetic ^{1}H signals. Note: deuterated solvent (•).

Overall, dehydrohalogenation of the Co(III) phosphine complex by a base leads to the reduction of Co(III) to Co(II). Probably, overall binuclear reductive elimination of the Co(III)-PR_2 intermediate occurs in the reaction.

I performed EPR experiments to gather further information on the presence and identity of paramagnetic Co species generated by this stoichiometric dehydrohalogenation reaction (Scheme 4.7). The EPR spectrum shows a rhombic spin system consistent with low-spin Co(II) $S = 1/2$ species (Figure 4.9).[33] Ideally, the rhombic g tensor with the three components should split into octets due to hyperfine coupling to single Co (I =7/2), but not all hyperfine couplings to Co(II) are detected in our case. This might be explained by the fact that the mixture contains multiple paramagnetic species (that could be in equilibrium or overlapping spectra). Further evidence for the presence of several paramagnetic species may come from the discrepancy between my preliminary EPR spectral simulation of a

single Co(II) species (refinement is ongoing) and the actual experimental spectrum. Although the EPR studies do not reveal how many Co(II) species are present in a mixture, at least one major species, monomeric complex Co(η^5-Cp*)I(PPh_2-PPh_2), is identified based on diagnostic Co(II)-P hyperfine couplings. A signal with clear octet hyperfine coupling to the Co(II) as well as the coupling to Ph_2P-PPh_2 ligand (doublet of doublet) is observed in the EPR spectrum (Figure 4.9). The EPR observation of the monomeric diphosphine complex and the NMR observation of the dimeric [Co(η^5-Cp*)(μ-I)]$_2$ described above suggests monomer/dimer equilibrium occurs in the mixture (Scheme 4.8). This is consistent with previous reports of solution behaviour of dimeric Co(II) complexes [Co(η^5-Cp*)(μ-X)]$_2$.[33,34]

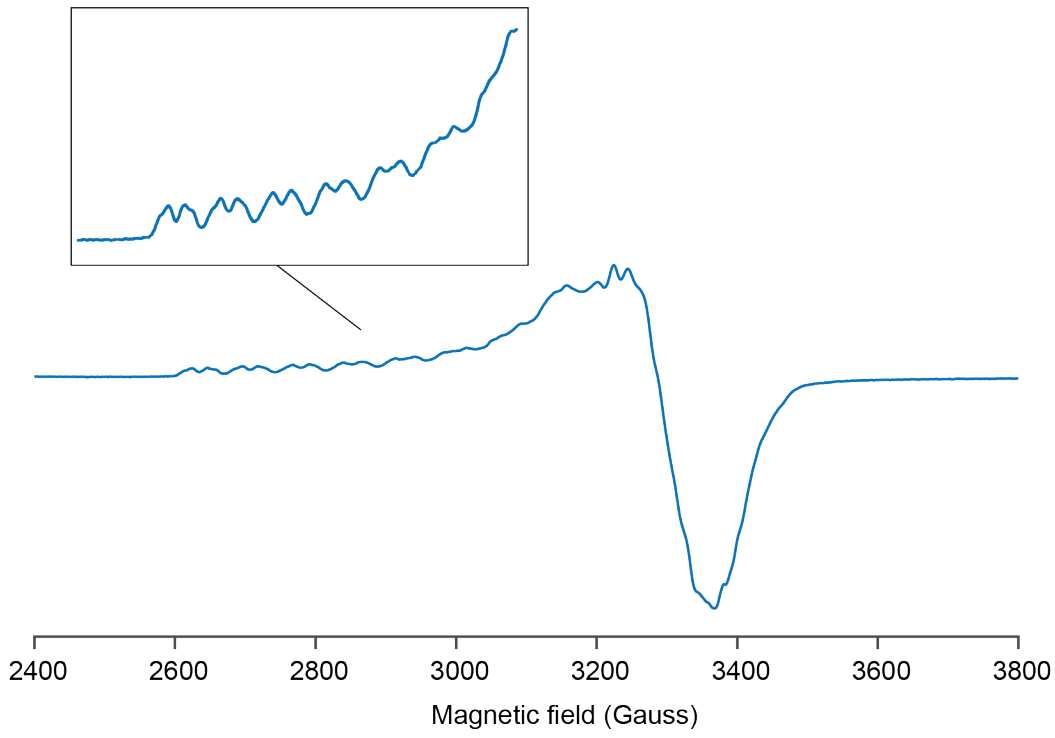

Figure 4.9 X-band EPR spectrum of the reaction of **Co-2a** with DBU measured in d_8-toluene at ~20 mM concentration at 100 K with a microwave frequency of 9.39 GHz. Parameters used in preliminary simulation in EasySpin: $g_1 = 2.348$, $g_2 = 2.039$, $g_3 = 2.001$, $A_1(^{59}Co) = 74$ G, $A_3(^{59}Co) = 16$ G, $A_1(^{31}P) = 39$ G, 1G.

Scheme 4.8 Proposed equilibria of Co(II) complexes in the reaction mixture of **Co-2a** and DBU.

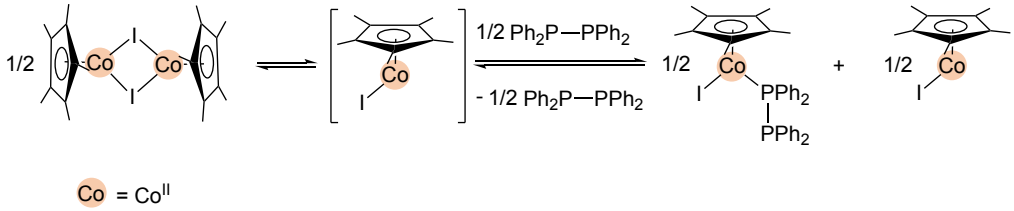

I want to understand how P-P bond formation is correlated to the Co(III) reduction in the dehydrohalogenation reaction of **Co-2a**. The above evidence confirms that the reactive Co(III)-PPh_2 is formed initially in the reaction. The decomposition of the Co(III)-PPh_2 to some Co(II) species and Ph_2P-PPh_2 could possibly involve valence tautomerism (Scheme 4.9a). Metal-centered redox chemistry (e.g., oxidative addition/reductive elimination) is central to organotransition metal chemistry, but in some examples, the ligands undergo redox state changes, resulting in a dramatic extension of the chemistry of transition metal complexes.[35–40] When ligand-centered redox events occur, the oxidation state of the metal center often changes in lockstep. Thus, the term "valence tautomerism" has been coined to refer to this phenomenon involving redox-active ligands. Valence tautomers or electromers are identical structures but vary in electron density distribution between the metal and the ligand (Scheme 4.9a). An example is the cobalt bis(dioxolene)(bpy) complex (Scheme 4.9b), which exists in two states depending on temperature: Co(III)(cat)(sq)(bpy) and Co(II)$(sq)_2$(bpy) (cat = catecholate, sq = semiquinone).[41] Notably, nearly all redox-active ligands that have been reported are N-, O-, and C-based. Although no detailed proposal for redox-active phosphido ligands has been made, they may have been present in some metal-catalyzed hydrophosphination reactions. This is most likely the primary explanation for forming the byproduct diphosphine in some first-row metal-catalyzed hydrophosphination systems (Section 4.1).

Scheme 4.9 **a)** Representation of valence tautomerism/electromerism (M = transition metal, L = ligand). **b)** An example of valence tautomerism in a cobalt bis(dioxolene) complex.

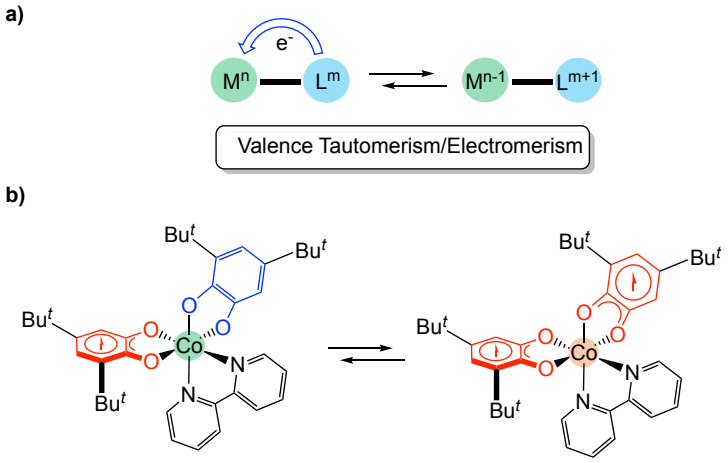

I performed an experiment using TEMPO (2,2,6,6-tetramethylpiperidin-1-yl)oxyl) to see if the "non-innocent" Co(III) phosphido complex undergoes valence tautomerism to give a Co(II)-bound phosphinyl radical (could also be Co(II) and free •PPh_2). As shown in Scheme 4.10, no reaction of TEMPO with **Co-2a** occurs. The addition of DBU to a mixture of 1:1 **Co-2a** and TEMPO gives ~ 50% Ph_2P-PPh_2 and ~50% other phosphine oxides. The result indicates that •PPh_2 is trapped by TEMPO; these PPh_2-containing species are consistent with literature report of the reaction of PPh_2H with TEMPO involving a phosphinyl radical (•PPh_2).[42] In a possible mechanism (Scheme 4.10 bottom), the deprotonation of **Co-2a** by DBU yields a highly reactive Co(III)-PPh_2 intermediate, which subsequently undergoes single electron transfer (SET) to give a Co(II) phosphinyl complex. The phosphinyl ligand could directly couple to TEMPO or itself in the mixture, and these resulting coupling products dissociate from the Co(II) center. Alternatively, the PPh_2 radical could dissociate from the Co(II) phosphinyl intermediate initially, and then react with TEMPO or itself to generate the observed trapping products.

Scheme 4.10 Dehydrohalogenation of **Co-2a** by DBU in the presence of TEMPO (top), showing phosphinyl trapping products. Box inset shows possible valence tautomerism of Co(III)-PPh_2. Plausible mechanisms of the phosphinyl trapping (bottom).

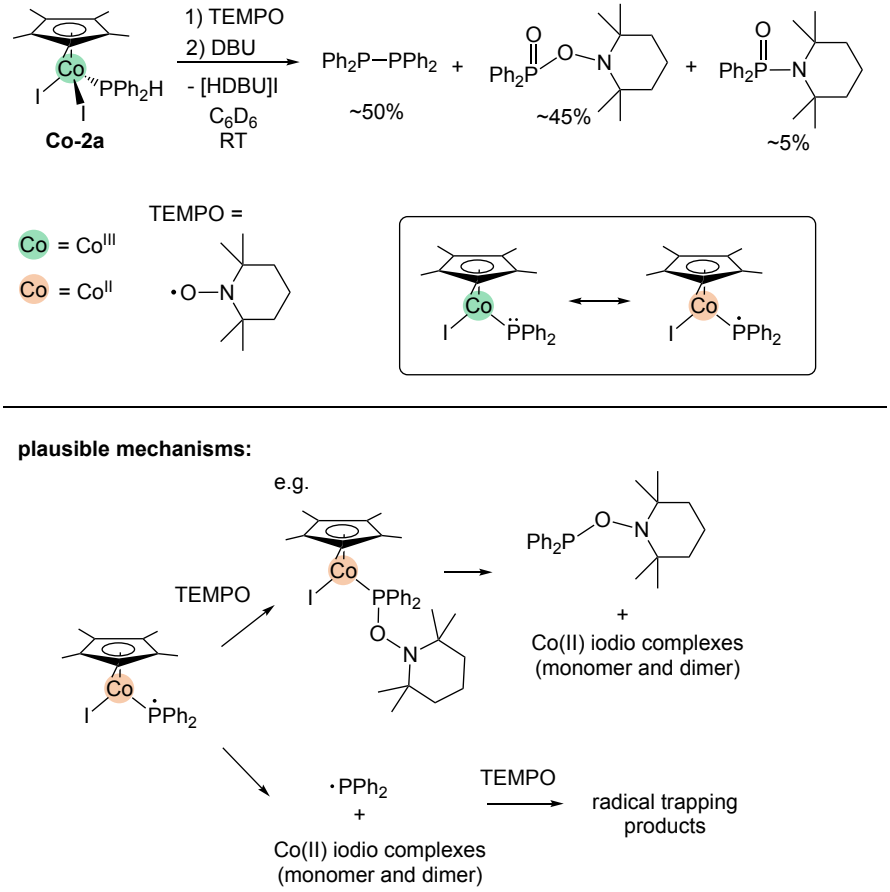

I also assessed how easily the PPh_2 ligand at Co(III) is oxidized by estimating its reduction potential (E_{ox}). Given the short lifetime of the Co(III)-PPh_2 generated from the stoichiometric reaction (Scheme 4.7), it is challenging to use cyclic voltammetry (CV) to determine this redox potential directly. Thus, I used a well-established thermochemical cycle technique[43] to estimate the redox potential of Co(III)-PPh_2 (Scheme 4.12). The thermochemical cycle method is primarily used to determine the bond dissociation free energies (BDFEs) of metal-coordinated O-H and N-H bonds.[43] As shown in Scheme 4.12, if the pK_a and BDFE values of the Co(III)-PR_2H are known, I will be able to calculate the $E_{1/2}$ of the Co(III)-PPh_2 using the Bordwell equation.[44] Using my base screening

experiments (Section 4.2.2), the pK_a value for complex Co(η^5-Cp*)I_2(PPh_2H) (**Co-2a**) can be estimated (Scheme 4.13 top): it is between 18.82 (pK_a ($HNEt_3^+$) in CH_3CN) and 24.34 (pK_a($HDBU^+$) in CH_3CN).[45] I estimated BDFEs of the P-H bond at **Co-2a** by attempting to abstract a hydrogen atom from the Co-bound P-H using hydrogen atom transfer (HAT) reagents: these experiments suggest a BDFE in the range of 66.5 to 77.1 kcal/mol in CH_3CN (Scheme 4.13 bottom).[43] I substituted these ranges into the Bordwell equation using $C_{G,CH3CN}$ of 52.6 kcal/mol.[43] This gave me an $E_{1/2}(PPh_2^-/PPh_2\bullet)$ value for the Co(III)-PPh_2 complex between –0.05 and –0.84 V. Based on this estimated E_{ox} range, the phosphido ligand at the Co(III) center is apparently easier to be oxidized than Co(III) fragment (E_{ox} of Co(III) to Co(IV) is not determined since, probably, the oxidized Co(IV) is unstable under CV condition; see Chapter 3). Collectively, the result provides some information on the oxidation of the phosphido ligand in a Co(III) complex to a phosphinyl ligand, which is apparently not difficult.

Scheme 4.11 Thermochemical cycle used for measuring $E_{1/2}(PPh_2^-/PPh_2\bullet)$ of the Co(III)-PPh_2. C_G is the constant used to convert reduction potentials and pK_a values into bond dissociation free energies (BDFEs), which varies in different solvents.

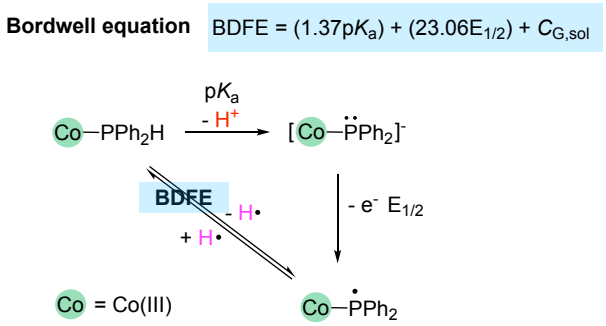

Scheme 4.12 Estimations of pK_a and bond dissociation free energies (BDFE) for complex **Co-2a**.

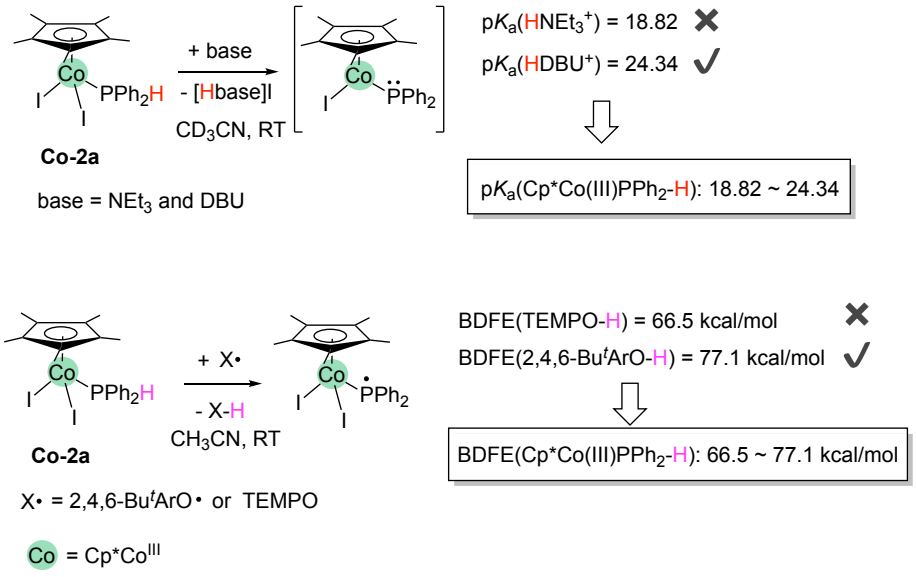

4.4.4 Investigating the participation of Co(II) species in catalytic hydrophosphination

In the previous section, I elucidated how Co(II) species were generated from the stoichiometric reaction of mono(phosphine) complex Co(η^5-Cp*)I_2(PPh_2H) (**Co-2a**) with the addition of 1 equiv of DBU. In this section, I generate this Co(II) mixture *in situ* to study how it participates in the actual catalysis.

Initially, I investigated the substitution chemistry of substrate *tert*-butyl acrylate and PPh_2H at the Co(II) fragment generated *in situ*. The addition of 1 equiv of *tert*-butyl acrylate to the paramagnetic Co(II) mixture leads to the loss of ~67% signals due to the free alkene, as determined by ^{1}H NMR (Figure 4.10). The result suggests that some Co(II)-alkene complexes are probably formed in the mixture. Further evidence for the formation of Co(II)-alkene complexes comes from the observation of some broad ^{1}H signals (δ ~1 ppm). The broad signals are presumably due to methyl protons at the coordinated alkene.

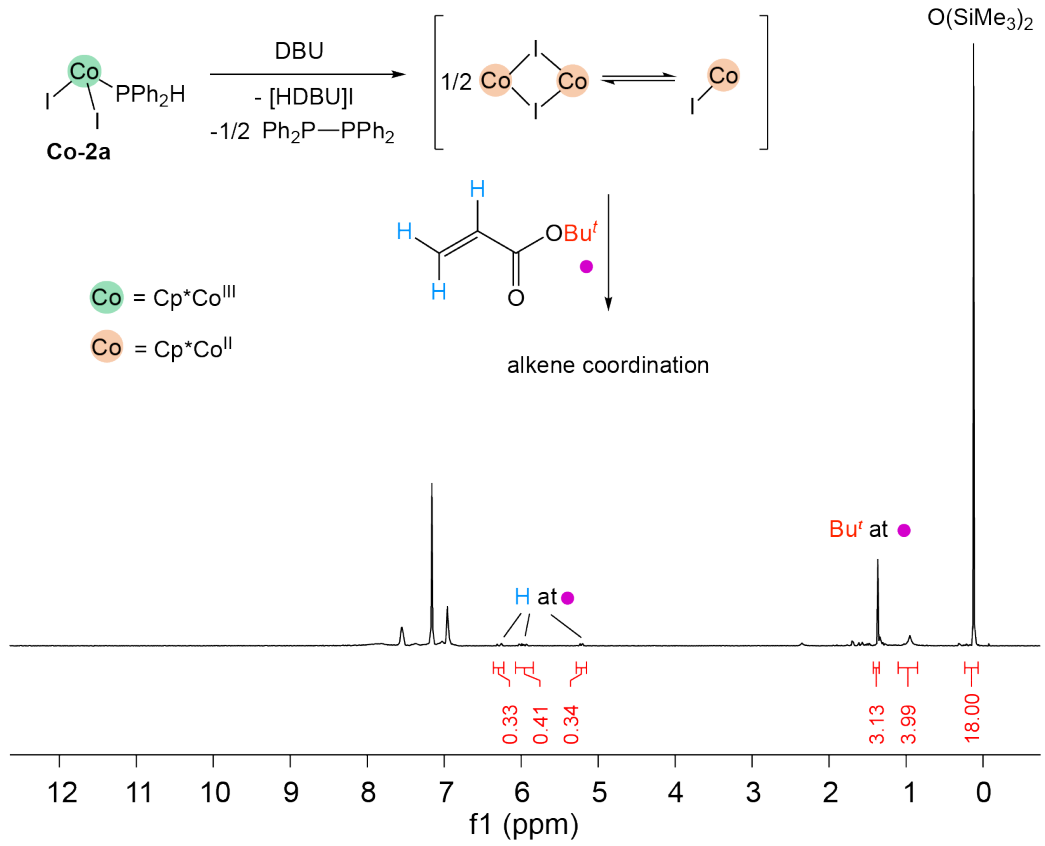

Figure 4.10 ^{1}H NMR (300.27 MHz, C_6D_6, 1 scan) spectrum of the reaction of [**Co-2a** +DBU] with 1 equiv of *tert*-butyl acrylate and internal standard $O(SiMe_3)_2$, showing the possible coordination of *tert*-butyl acrylate to the resulting paramagnetic Co species.

To mimic catalytic conditions, I added both substrate *tert*-butyl acrylate and PPh_2H (10 equiv each) to the Co(II) mixture generated *in situ* (Figure 4.11a,b and Scheme 4.13). The signals of free PPh_2H disappear in the ^{1}H NMR, suggesting the coordination of the substrate PPh_2H to the paramagnetic Co(II) center occurs. However, the signals due to *tert*-butyl acrylate are sharp in the ^{1}H NMR spectrum; ^{1}H NMR shows that there is no coordination of the alkene to the Co(II) fragment. These results demonstrate that the *tert*-butyl acrylate can coordinate to the Co(II) in the absence of the substrate PPh_2H, but that the PPh_2H outcompetes the *tert*-butyl acrylate in coordinating to the Co(II) center at actual catalytic concentrations. Some unidentified broad signals (trace) are observed in the mixture, which is probably due to the thermal hydrophosphination product. Nevertheless,

the absence of metal-alkene complexes in the catalytic mixture suggests that mechanisms involving either alkene insertion into a Co-PPh_2 bond or nucleophilic attack of free phosphine at a Co-bound alkene are unlikely. No catalytic conversion was observed under these conditions (Figure 4.11a,b).

Scheme 4.13 Addition of *tert*-butyl acrylate and PPh_2H to the mixture containing Co(II) complexes.

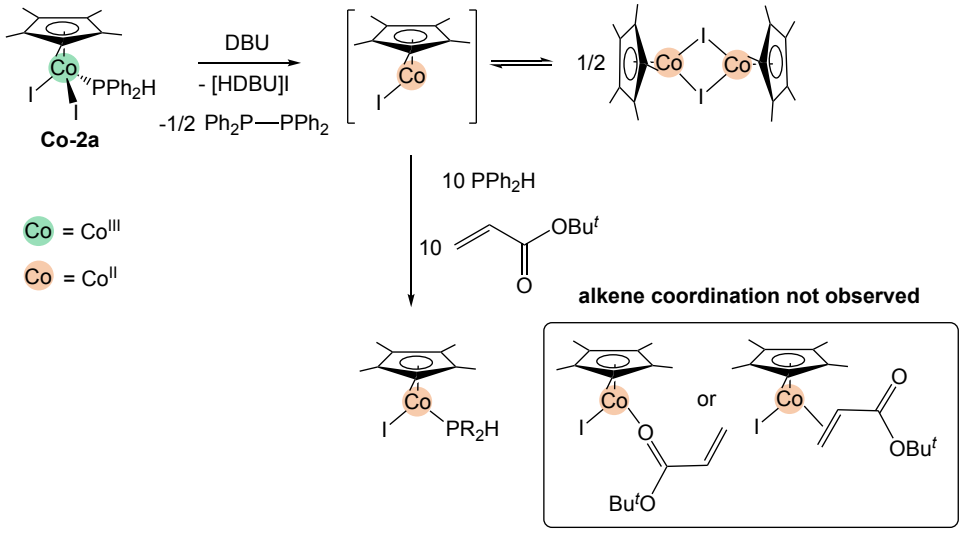

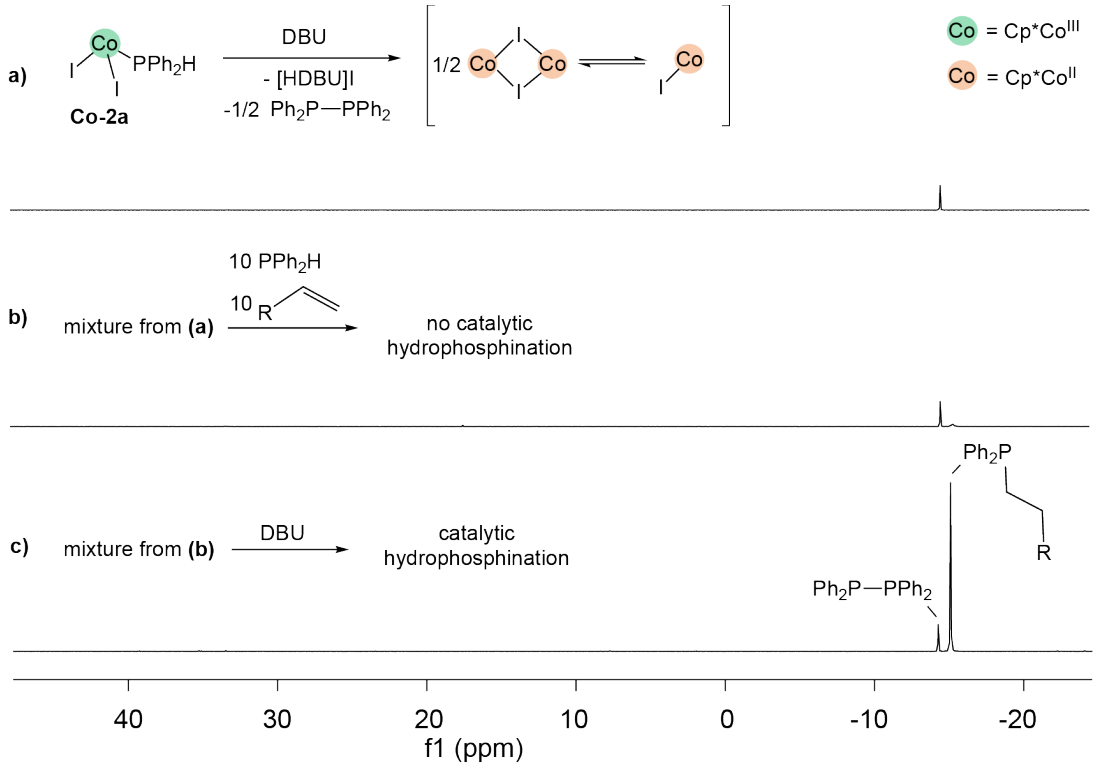

Figure 4.11 $^{31}P\{^{1}H\}$ NMR (121.55 MHz, C_6D_6) spectra of **a**) the reaction of complex **Co-2a** with 1 equiv of DBU; **b**) the reaction of the mixture generated in (**a**) with 10 equiv each of *tert*-butyl acrylate and PPh_2H; **c**) the reaction of the mixture generated from (**b**) with 1 equiv of DBU, showing catalytic activity.

Notably, the addition of 1 equiv of DBU to the above reaction mixture leads to rapid hydrophosphination that is complete within 15 min (Figure 4.11c). This suggests that the resulting Co(II) mixture and the second equiv of DBU play an important role in catalytic hydrophosphination. The critical step is probably the deprotonation of substrate phosphine bound to the Co(II) fragment. More white precipitate [HDBU]I precipitates form the mixture at this step. I also quantified the amount of the [HDBU]I precipitated during the catalysis, which is approximately equal to the amount of DBU used (2 equiv with respect to Co). Indirect evidence for the presence of a Co(II)-PR_2 intermediate comes from an EPR experiment designed for investigating the Co-catalyzed dehydrocoupling of PPh_2H, in the absence of reactive alkene (see Chapter 5).

4.4.5 Proposed steps for the reduction of Co(III) to a catalytically active Co(II) phosphido complex

Based on the high instability of the Co(III)-PPh_2 intermediate (Section 4.4.3) and the evidence for Co(II)-PPh_2 participating in catalysis (Section 4.4.4), I propose the active catalyst must be a Co(II) phosphido complex (see Scheme 4.14).

Scheme 4.14 Proposed formation of Co(II)-PR_2 intermediates for catalysis.

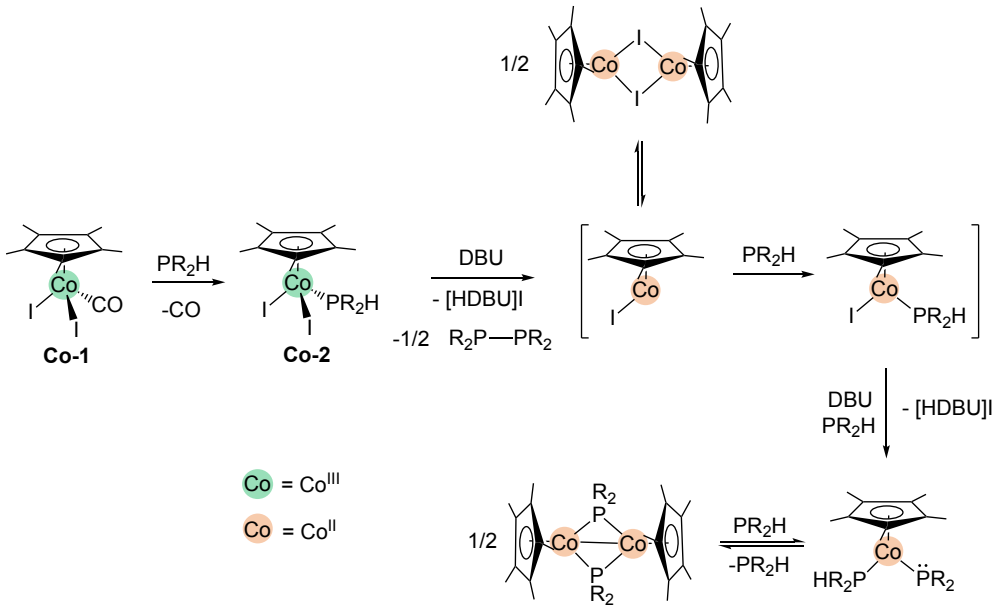

As shown in Scheme 4.14, a Co(III) phosphido complex is generated by adding 1 equiv of base to Co(III) phosphine complex Co(η^5-Cp*)I_2(PPh_2H) (**Co-2a**), giving diphosphine and the reduced Co(II) species. Another equiv of base deprotonates coordinated PR_2H at the Co(II) complex, generating the active Co(II)-PPh_2. This proposed process is consistent with the stoichiometric formation of Ph_2P-PPh_2 (equal to the amount of the Co used) and the optimized Co:base ratio (1:2) in the catalytic reactions (Section 4.2.1). As mentioned in Section 4.4.4 (described in more detail in Chapter 5), EPR analysis of the mixture of Co(η^5-Cp*)I_2(CO) (**Co-1**) and DBU (1:2) in the presence of 10 equiv of PPh_2H provides some evidence for the existence of a monomeric Co(II)-PPh_2 intermediate.

A proposed equilibrium between monomeric phosphido and bridging phosphido complexes is consistent with our observation of the trace amount of bridging Co(II) phosphido dimer [Co(η^5-Cp*)(μ-PPh_2)]$_2$ (**Co-9**) by NMR in the catalytic mixture (Section 4.4.2). I proposed a monomeric phosphido complex Co(η^5-Cp*)(PPh_2)(PPh_2H) is the active catalyst. This phosphido complex is similar to our Ru phosphido catalyst for hydrophosphination.

Despite having only indirect evidence for the formation of [Co(η^5-Cp*)(PPh_2)(PPh_2H)] in the catalytic mixture, the proposed Co(II)-PPh_2 fragment must be more stable (with respect to reduction) than the Co(III)-PR_2 fragment, enabling it to participate in the catalytic reaction. I cannot observe Co(III)-PPh_2 even at low temperatures, but I can observe Co(II)-PR_2 in the catalytic mixture at least by EPR, and indirectly by NMR (i.e. bridging phosphido dimer). Additionally, as shown in Appendix E for a survey of literature examples of Co-PR_2 complexes, most of the isolable Co phosphido complexes in the literature are Co(I or II). There are a few examples of Co(III) but they contain specialized phosphido ligands. As described in Section 4.1, current examples of Co-catalyzed hydrophosphination also use Co complexes in low oxidation states (0, I and II). For example, Shanmugam and coworkers proposed a Co(II) phosphido complex as a critical intermediate (Scheme 4.15 top). Although Oshima and coworkers proposed no intermediate for their Co(II)-catalyzed hydrophosphination, they found that the reaction results in no or little conversion in the absence of either Co(acac)$_2$ or butyllithium. The butyllithium could deprotonate the substrate PPh_2H to generate $LiPPh_2$ (Scheme 4.15 bottom), which could undergo a salt metathesis reaction with Co(acac)$_2$ to form a potential intermediate Co(II)-PPh_2. Although one or more Co(II)-PR_2 complexes may be critical

intermediates in these catalytic reactions, no one has yet isolated them. I also faced a similar challenge. The proposed monomeric phosphido complex Co(η^5-Cp*)(PPh_2)(PPh_2H) is a 17-electron complex (Scheme 4.14), which is inherently unstable and may decompose during catalysis (*vide infra*).

Scheme 4.15 Possible pathways for the formation of Co(II)-PPh_2 from the literature about Co-catalyzed hydrophosphination.

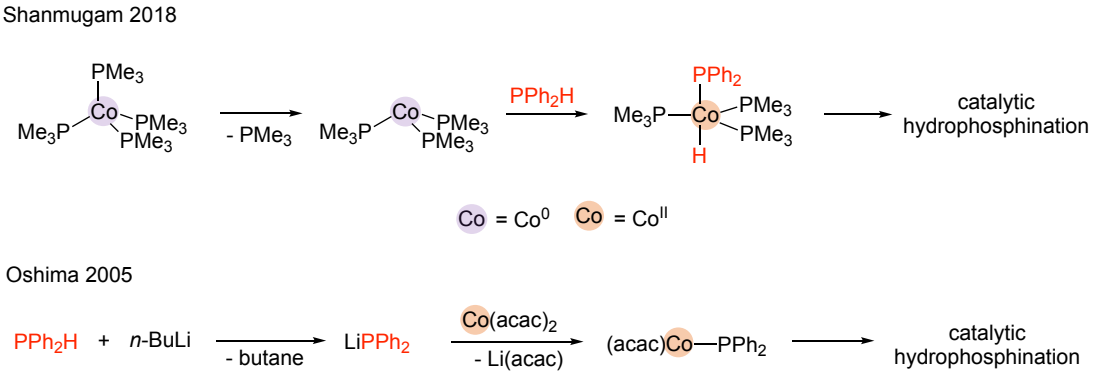

4.4.6 Preliminary kinetic studies of Co-catalyzed hydrophosphination

I performed preliminary kinetic experiments to gather more mechanistic information for the Co system. Reaction profiles (Figure 4.12) were obtained from ^{1}H NMR monitoring of the hydrophosphination of *tert*-butyl acrylate with PPh_2H using Co(η^5-Cp*)I_2(CO) (**Co-1**). Figure 4.12 shows that the amount of Ph_2P-PPh_2 produced (corresponding to ~2% substrate PPh_2H consumption) remains nearly steady throughout the catalysis after a rapid increase within 15 min. This is consistent with my previous observations in Section 4.2.1, and further confirms that the formation of diphosphine is a stoichiometric step related to catalyst activation. Closer inspection of the reaction profile in Figure 4.12 shows the reaction rate diminishes substantially with time, suggesting that product inhibition or catalyst deactivation occurs in the catalytic system.

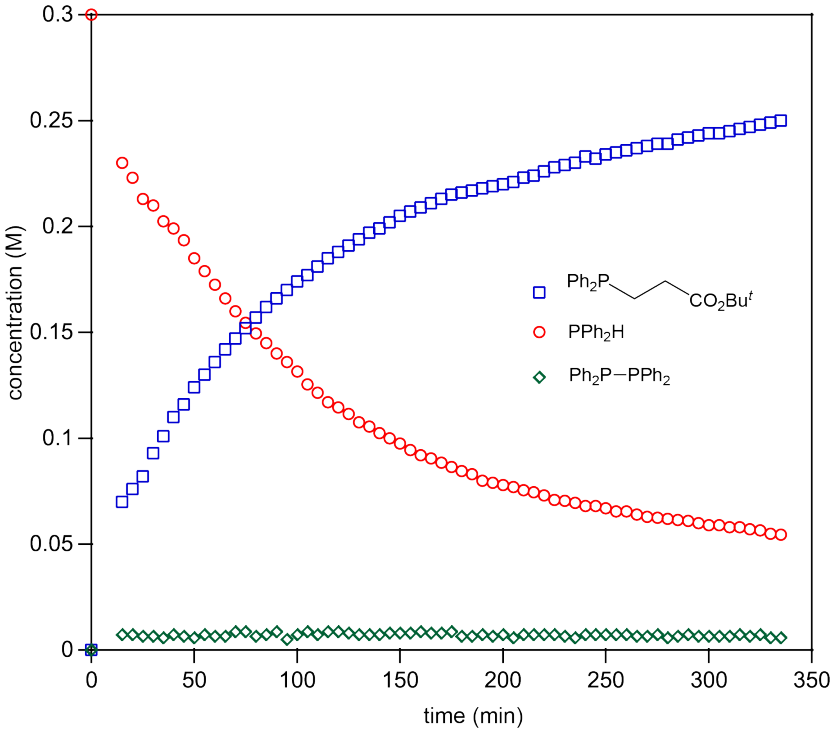

Figure 4.12 Monitoring the hydrophosphination of *tert*-butyl acrylate by PPh_2H catalyzed by 2 mol% **Co-1** and 4 mol% DBU by ^1H NMR (500.27 MHz, C_6D_6) spectra.

I used the "same excess" method[46] for the hydrophosphination catalysis using **Co-1** to show that our system is vulnerable to catalyst deactivation (Figure 4.13). In this method, the concentration difference between the reactants is held constant over several experiments. In our case, I used equal amounts of the two reactants, PPh_2H and *tert*-butyl acrylate, throughout the experiments (i.e. $[PPh_2H] - [\text{alkene}] = 0$). Two reactions (**R-a** and **R-b)** were performed initially. Reaction **R-a** (green) was run under normal catalytic conditions, while reaction **R-b** (red) was run under the same condition (i.e. original amount of Co/DBU used) of **R-a** but using only 50% substrates. The reaction profile of **R-b** was time-adjusted to the half-life time ($t_{1/2}$) of **R-a** (Figure 4.13 right); I observed no overlap of the two profiles, indicating that either the product is inhibiting the catalysis, or the catalyst is being deactivated. Thus, a third reaction **R-c** was performed. Reaction **R-c** (blue) was identical to **R-b**, except that 50% product phosphine (relative to the reactants used in **R-a**)

was added. In other words, the **R-c** mimics exactly the conditions of **R-a** at its $t_{1/2}$ if no catalyst deactivation occurs. After a similar time adjustment to **R-b**, the reaction profiles of **R-b** and **R-c** closely overlapped, with neither overlapping the profile for **R-a**. This indicates that the drop in catalytic activity over time is due to catalyst deactivation, not product inhibition. If the **R-c** profile overlapped with **R-a**, the activity loss would be due to product inhibition.

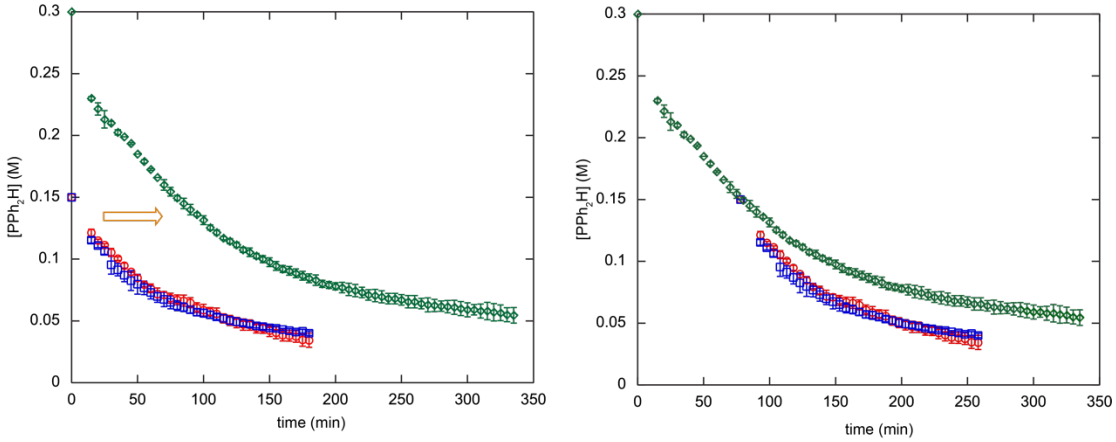

Figure 4.13 Reaction profiles for the hydrophosphination of *tert*-butyl acrylate by PPh_2H following the "same excess" protocol. Profile **R-a** (green) and **R-b** (red) have different initial concentrations of *tert*-butyl acrylate and PPh_2H. Profile **R-c** (blue) has the same initial concentrations as **R-b** and added the product phosphines to match the initial concentration of PPh_2H in **R-b**. Error bars represent standard deviation over triplicate runs.

I performed a series of hydrophosphination reactions of *tert*-butyl acrylate with PPh_2H under identical conditions using various concentrations of **Co-1** to determine the rate dependence on the Co catalyst. Initial reaction rates were calculated using the conversion in 15 min. The initial rates method[47] (Figure 4.14) indicates a first-order rate dependence on the Co catalyst concentration for the hydrophosphination of *tert*-butyl acrylate with PPh_2H catalyzed by **Co-1**.

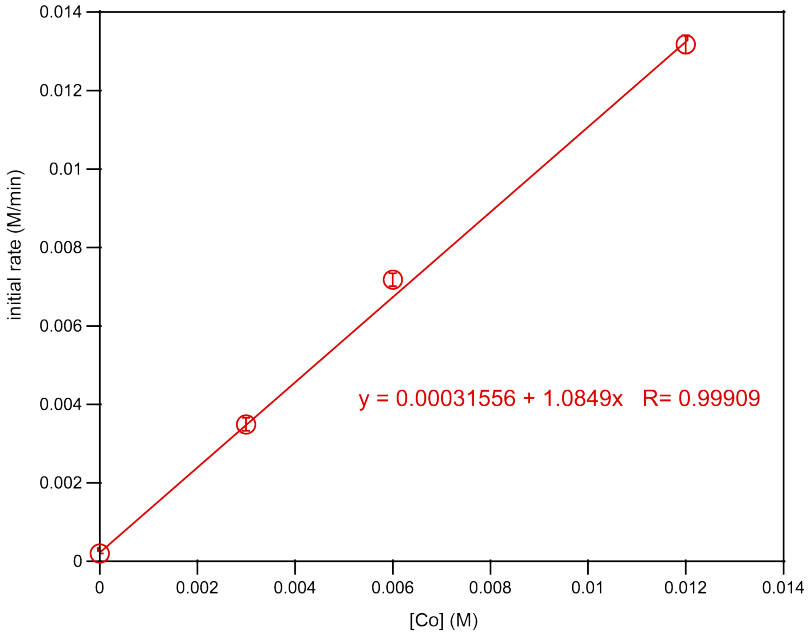

Figure 4.14 Reaction rate dependence on [cat] (cat = **Co-1**) determined by the initial rate method. Conditions: [**Co-1**] 0.003 M (1 mol%), 0.006 M (2 mol%), 0.012 M (4 mol%). Error bars represent standard deviation over triplicate runs. Initial rates = % conversion/15 min.

An alternative method for determining reaction orders, Variable Time Normalization Analysis (VTNA)[48], was not suitable for our system to estimate the reaction rate dependency. This visual analysis method requires that the overall catalyst concentration remains unchanged during the reaction, but catalyst deactivation occurs in our system. Thus, I only used the initial rates method to determine rate dependence on the Co catalyst concentrations.

The first-order rate dependence on [**Co-1**] suggests that a monomeric Co(II)-PR_2 intermediate is important for catalysis. It rules out the possibility of the Co dimers, e.g. $[Co(\eta^5\text{-Cp*})(\mu\text{-I})]_2$ and $[Co(\eta^5\text{-Cp*})(\mu\text{-PPh}_2)]_2$ (**Co-9**), being the active catalysts, e.g. involving a binuclear conjugate addition mechanism.

4.4.7 Proposed mechanism for Co-catalyzed hydrophosphination

I propose an outer-sphere conjugate addition mechanism for Cp*Co-catalyzed hydrophosphination shown in Scheme 4.16. The overall process of catalytic hydrophosphination consists of two parts: 1) catalyst activation by the reduction of diamagnetic Co(III) to paramagnetic Co(II) and the formation of a Co(II) phosphido complex (steps A-D); 2) participation of the Co(II) phosphido intermediate in a conjugate addition pathway (steps E-F). Notably, regardless of whether mono(phosphine) complex **Co-2** or bis(phosphine) complex **Co-4** is deprotonated (steps A and B), a 17-electron Co(II)-PR_2H complex (in step C) will ultimately form (i.e. would lose a second PPh_2H ligand from a 19-electron complex). The Co(II)-PR_2H complex is deprotonated by the second equivalent of base to give the catalytically active Co(II)-PR_2 intermediates (step D). Overall, 2 equiv of base, with respect to the **Co-1**, are needed for the catalysis, and the base works as an initiator rather than a co-catalyst. The catalytic steps (steps E-G) in this mechanism are identical to those proposed for our Ru system (Chapter 2) because catalysis only works for electron-deficient substrates.

Scheme 4.16 Proposed catalyst activation and mechanism for the hydrophosphination of an electron-deficient alkene with PR_2H using **Co-1** and DBU. R = alkyl and aryl, R' = CO_2Bu^t.

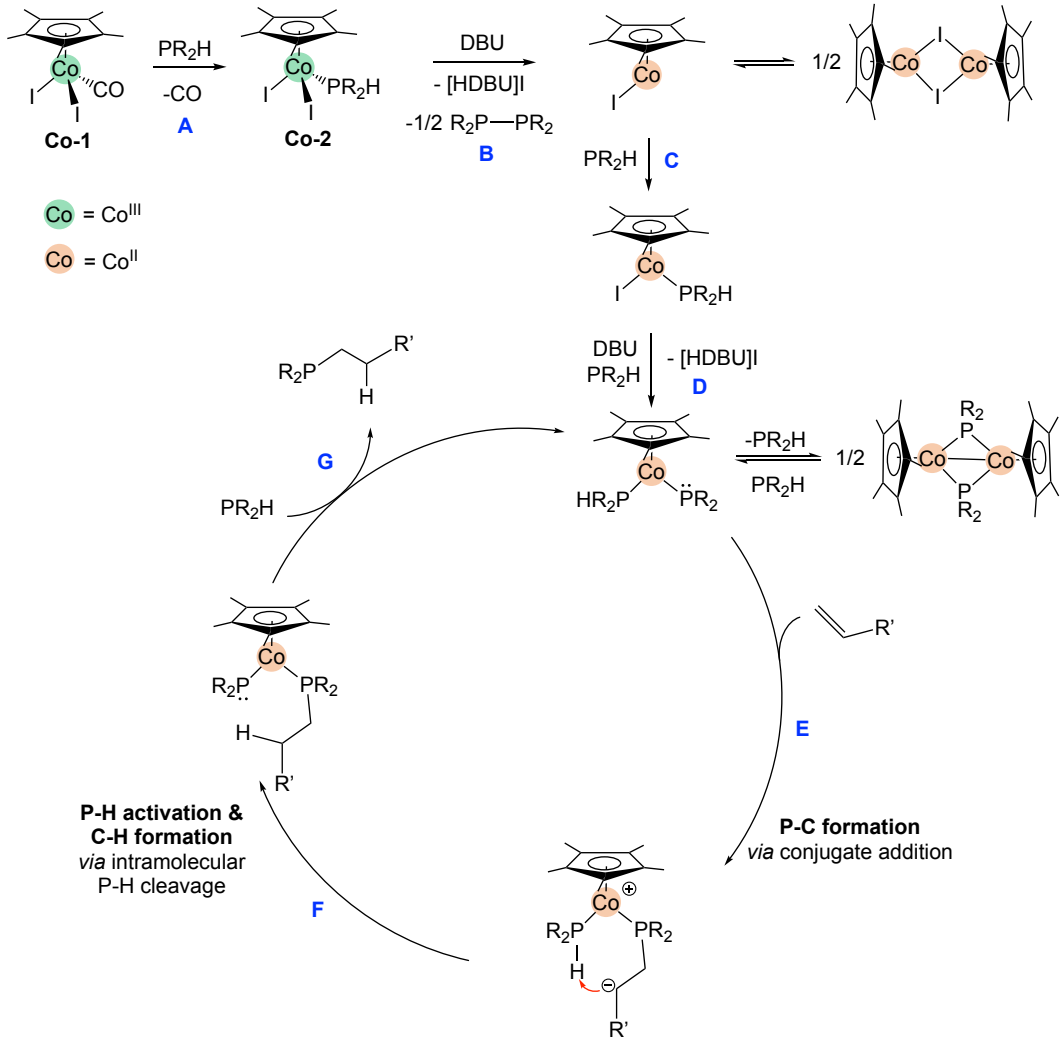

Although this proposed catalytic cycle is similar to the Cp*Ru system, the Cp*Co system has two distinct features. First, the Co system operates for a much wider phosphine scope. This could be explained by a change of the turnover-limiting step. The intramolecular P-H cleavage step (step F) is turnover-limiting for my Cp*Ru system. In contrast, the conjugate addition step (step E) is apparently turnover-limiting for this Cp*Co system. Evidence comes from the fact that small, alkyl phosphines have the highest hydrophosphination activity, which suggests that intramolecular P-H cleavage (step F) is

not so critical. More support for that comes from that no alkene oligomerization is observed in the Co system (even for less acidic phosphine substrates). This suggests that the intramolecular P-H cleavage step (step F) is sufficiently fast (i.e. the zwitterion has a short lifetime).

Compared to the Ru system (Chapter 2), the Co system apparently speeds the intramolecular proton transfer from Co-PR_2H to the zwitterionic intermediate (step F) and slows the conjugate addition of Co-PR_2 (step E). These two features point out that the Co-PR_2 is a worse nucleophile than the Ru-PR_2. Evidence comes from that the P-H bonds of the Co(III)- or Co(II)-bound phosphines are more acidic than those for the Ru(II)-bound phosphines (i.e. DBU can deprotonate the Co-bound phosphines but not the Ru-bound one). Thus, the corresponding Co phosphido complexes should be less nucleophilic relative to the Ru ones. There is also a steric argument in the kinetics of nucleophilic attack. According to the X-ray analyses of Cp*Co (Chapter 3) and Cp*Ru phosphine complexes[49], the Cp*-Co distances (1.70–1.72 Å) are significantly shorter than the Cp*-Ru distances (1.87–1.88 Å). Therefore, conjugate addition of the phosphido ligand at the more crowded Co center should be slower than that at the Ru center.

4.5 Conclusion

In this chapter, I showed that complex Co(η^5-Cp*)I_2(CO) (**Co-1**) works as a catalyst for the hydrophosphination of activated alkenes. The catalysis operates for an unusually wide range of phosphine substrates, including primary, secondary, alkyl, and aryl phosphines, despite of the limited alkene substrate scope. The alkene substrate scope implies an outer-sphere conjugate addition mechanism for this Co system.

I investigated P-H bond activation at these Co phosphine complexes using base, finding the facile formation of a Co(III)-PR_2 intermediate that rapidly decomposes to a diphosphine and a paramagnetic Co(II) species. Clearly, this reductive P-P bond formation occurs for the Co(III)-PR_2 complex. A more stable, paramagnetic Co(II)-PR_2 complex, generated by deprotonation of a Co(II)-bound phosphine, is the active catalyst for hydrophosphination based on preliminary mechanistic and kinetic analyses. Despite the wider substrate scope this catalyst provides, catalyst deactivation is a drawback that needs to be addressed.

4.6 Experimental

See Chapter 2, Section 2.5.1 for general experimental details**.** See Chapter 3, Section 3.6 for general instrumental/spectroscopic details**.** EPR measurements were carried out in the X-band (9.4-9.8 GHz) using a Bruker EMXplus spectrometer equipped with a Premium X microwave bridge and HS resonator in the group of Prof. Charles Walsby, Simon Fraser University, Burnaby, BC, Canada. Low-temperature measurements were performed using a Bruker ER 4112HV temperature control system and a liquid nitrogen-cooled continuous-flow cryostat. EasySpin,[50] a Matlab-based application, was used to produce all simulations. The NMR data for hydrophosphination products are summarized in Section 4.6.5. ^{1}H, $^{31}P\{^{1}H\}$ and $^{13}C\{^{1}H\}$ NMR spectra of these products are found in Appendix D. Conversions and product ratios were determined from relative integrals of product and internal standard signals in ^{1}H NMR spectra (single scan).

4.6.1 General procedure for Co-catalyzed hydrophosphination

Complex Co(η^5-Cp*)I_2(CO) (**Co-1**, 0.0021–0.021 mmol, 1–10 mol%) was weighed into a glass vial and dissolved in the appropriate amount of C_6D_6 to give a volume of 0.6 mL (wait for 30 min). Neat alkene (0.21 mmol), neat phosphine (0.21 mmol), DBU (0.0025–0.042 mmol, 1.2–20 mol%) and $O(SiMe_3)_2$ (0.018 mmol, internal standard) were then added to give a total volume of 0.7 mL. The reaction mixture was transferred to a J. Young NMR tube, and loaded into the NMR spectrometer (~15 min to get the initial NMR spectra). Each quantitative ^{1}H NMR monitoring of catalysis consisted of an initial experiment after first 15 min and a 5-minute delay between each subsequent experiment for the first 6 h (see example in Figure 4.15). The optimal reaction conditions to be used for the substrate scope studies: **Co-1** (2 mol%) and DBU (4 mol%) in C_6D_6 at RT. Base (NEt_3, DBU, $KOBu^t$ or $NaNSi(Me_3)_2$, 0.084 mmol, 4 mol%) were used in the base screening experiments.

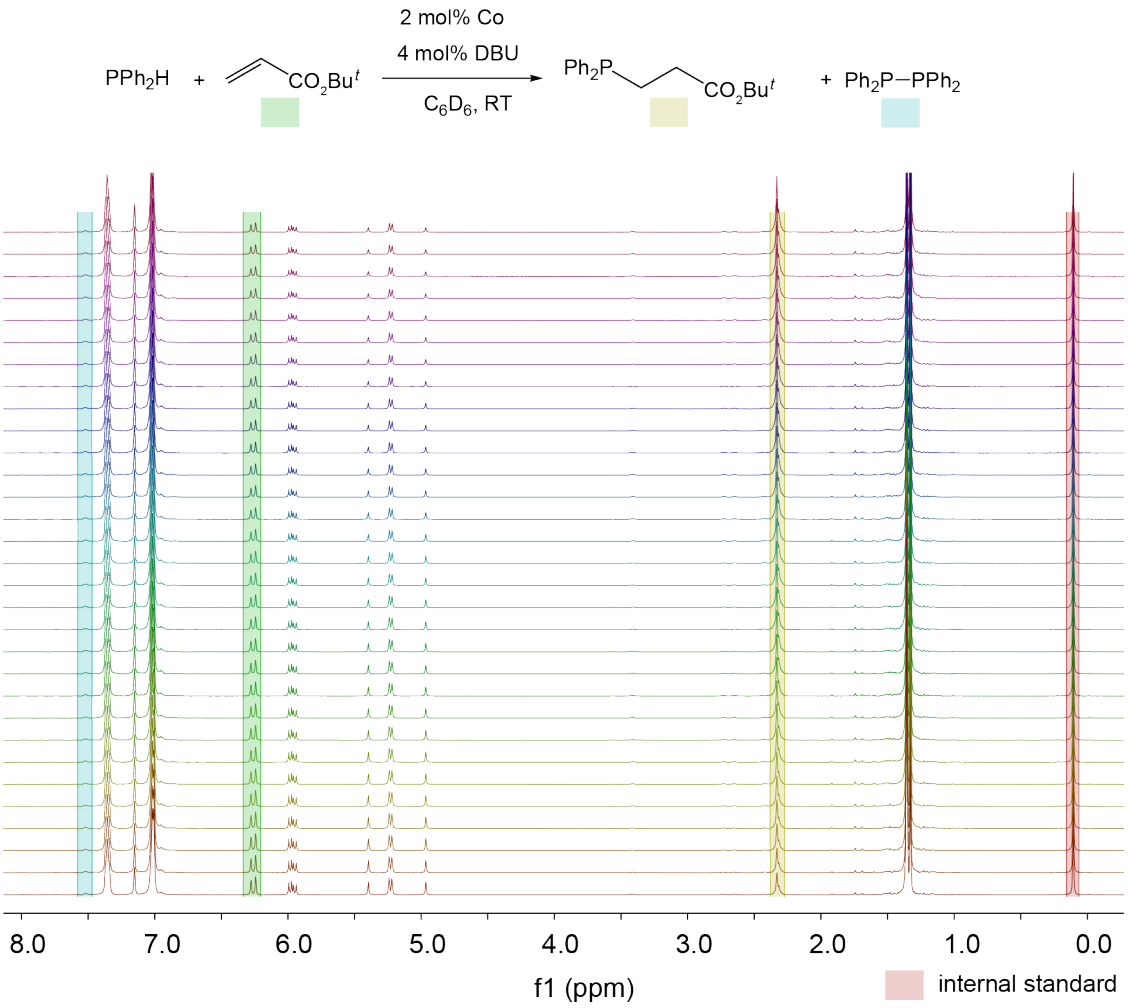

Figure 4.15 Representative ^{1}H NMR (500.27 MHz, C_6D_6) spectra of the reaction of *tert*-butyl acrylate with PPh_2H catalyzed by **Co-1** (2 mol%) and DBU (4 mol%). The first spectrum (first data point) was collected within 15 minutes of mixing the catalytic solution (bottom). The remaining spectra were with a delay of 5 minutes between each (from bottom to up).

4.6.2 Reactions of complex Co-2a with different bases

A small vial was loaded with the dark green complex $Co(\eta^5\text{-}Cp^*)I_2(PPh_2H)$ (**Co-2a**) (0.016 mmol), and then C_6D_6 (0.5 mL) was added. After 30 min, a base (NEt_3, DBU, $KOBu^t$ or $NaNSi(Me_3)_2$, 0.016 mmol) was added to the solution. The resulting mixture was transferred to a J. Young NMR tube, and loaded into the NMR spectrometer (~15 min to

get the first ^{1}H and $^{31}P\{^{1}H\}$ NMR spectra, Figure 4.16). Except for the mixture using NEt_3, the colour of the reaction mixture after adding the base changed from dark green to brown.

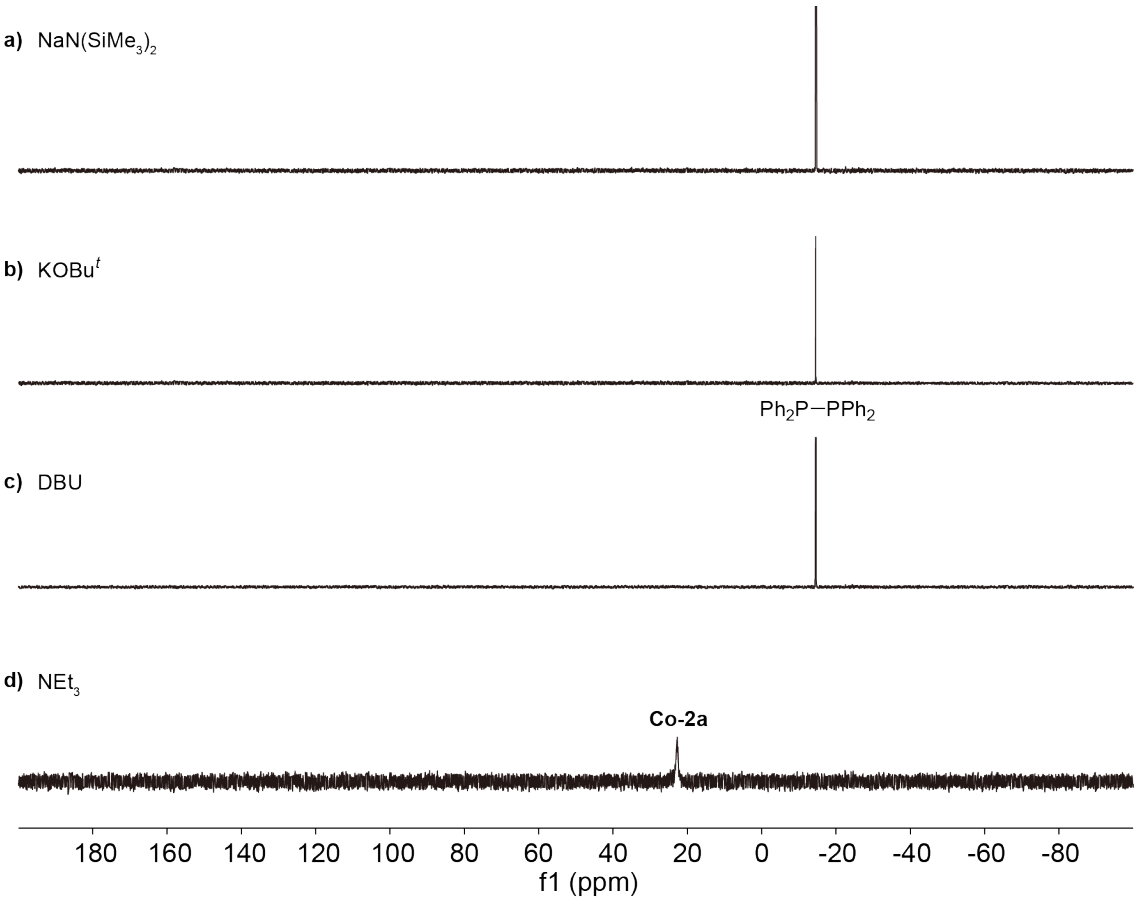

Figure 4.16 $^{31}P\{^{1}H\}$ NMR (121.55 MHz, C_6D_6) spectra of the reaction of complex **Co-2a** with 1 equiv of **a**) $NaN(SiMe_3)_2$, **b**) $KOBu^t$, **c**) DBU or **d**) NEt_3.

4.6.3 Reactions of PPh_2H with different bases

A small vial was loaded with a base (NEt_3, DBU, $KOBu^t$ or $NaNSi(Me_3)_2$, 0.016 mmol) before adding C_6D_6 (0.7 mL) and neat PPh_2H (0.40 mmol, 74 mg). The resulting mixtures were analyzed by ^{1}H and $^{31}P\{^{1}H\}$ NMR.

4.6.4 Optimization of Co:base ratio

Following the general procedure for catalytic hydrophosphination described in Section 4.6.1, complex **Co-1** (0.0042 mmol, 2 mol%) and a corresponding amount of DBU

(0.0042–0.013 mmol, 2–6 mol%) were used for the Co-mediated hydrophosphination reactions (Figure 4.1, red triangles). For the non-Co-mediated hydrophosphination reactions (Figure 4.1, blue squares), variable amounts of DBU (0–0.0084 mmol, 0–4 mol%) were used. All reactions were performed in triplicate.

4.6.5 NMR characterization of hydrophosphination products

All the Co-catalyzed hydrophosphination reactions were performed using the optimized conditions (section 4.6.1), neat alkene (0.21 mmol) and neat phosphine (0.21 mmol). Unless otherwise specified, hydrophosphination products in the resulting mixture after 24 h were characterized by NMR spectroscopy without further isolation/purification. $^{13}C\{^1H\}$ NMR spectra were not obtained for known hydrophosphination products. Full NMR characterization was performed for all new hydrophosphination products.

$Ph_2P{-}CH_2CH_2CO_2Me$

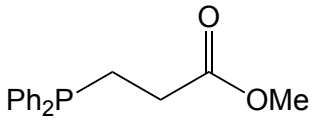

^{1}H NMR (300.27 MHz, C_6D_6) δ: 7.42–7.28 (m, 4H, H_{ortho} at PPh), 7.11–6.99 (m, 6H, H_{meta} & H_{para} at PPh), 3.28 (s, 3H, OMe), 2.30 (m, 4H, CH_2CH_2).

^{31}P{^{1}H} NMR (121.55 MHz, C_6D_6) δ: –15.7 (s).

The ^{1}H and ^{31}P{^{1}H} NMR data are consistent with that reported in the literature.[22]

$Ph_2P{-}CH_2CH_2CO_2Bu^t$

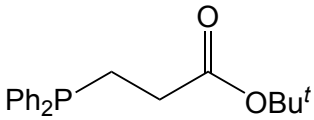

^{1}H NMR (300.27 MHz, C_6D_6) δ: 7.42–7.32 (m, 4H, H_{ortho} at PPh), 7.08–6.97 (m, 6H, H_{meta} & H_{para} at PPh), 2.41–2.27 (s, 4H, CH_2CH_2), 1.34 (m, 9H, Bu^t).

^{31}P{^{1}H} NMR (121.55 MHz, C_6D_6) δ: –15.4 (s).

The ^{1}H and ^{31}P{^{1}H} NMR data are consistent with that reported in the literature.[15,51]

$Ph_2P-CH_2CH(Me)CO_2Me$

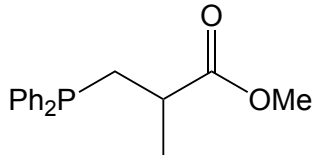

^{1}H NMR (300.27 MHz, C_6D_6) δ: 7.45–7.37 (m, 4H, H_{ortho} at PPh), 7.10–7.00 (m, 6H, H_{meta} & H_{para} at PPh), 3.29 (s, 3H, OMe), 2.62–2.46 (m, 2H, PCH_2 & CHMe), 2.13–1.98 (m, 1H, PCH_2), 1.22 (d, $^3J_{HH}$ = 6.7 Hz, 3H, Me).

$^{31}P\{^1H\}$ NMR (121.55 MHz, C_6D_6) δ: –19.3 (s).

The ^{1}H and $^{31}P\{^1H\}$ NMR data are consistent with that reported in the literature.[22]

$Ph_2P-CH_2CH_2CN$

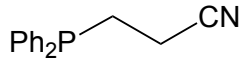

^{1}H NMR (300.27 MHz, C_6D_6) δ: 7.21–7.11 (m, 4H, H_{ortho} at PPh), 7.08–6.98 (m, 6H, H_{meta} & H_{para} at PPh), 1.83–1.70 (m, 2H, P-CH_2), 1.68–1.57 (m, 2H, CH_2CN).

$^{31}P\{^1H\}$ NMR (121.55 MHz, C_6D_6) δ: –16.0 (s).

The ^{1}H and $^{31}P\{^1H\}$ NMR data are consistent with that reported in the literature.[22]

$Ph_2P-C_6H_9O$

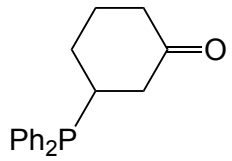

$^{31}P\{^1H\}$ NMR (121.55 MHz, C_6D_6) δ: –3.6 (s).

^{1}H NMR was not obtained because the conversion to this product is low conversion even after 7 days (~2%).

The $^{31}P\{^1H\}$ NMR data is consistent with that reported in the literature.[22]

$Ph_2P-CH_2CH_2Ph$

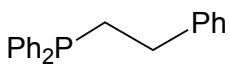

$^{31}P\{^1H\}$ NMR (121.55 MHz, C_6D_6) δ: –15.0 (s).

^{1}H NMR was not obtained because of low conversion of this product (~1%).

The $^{31}P\{^1H\}$ NMR data is consistent with that reported in the literature.[52]

$Ph_2P-CH_2CH_2Py$ (Py = 2-Pyridyl)

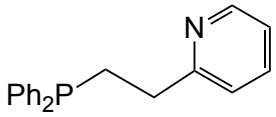

$^{31}P\{^1H\}$ NMR (121.55 MHz, C_6D_6) δ: −15.8 (s).

^1H NMR was not obtained because of low conversion of this product (~2%).

The $^{31}P\{^1H\}$ NMR data is consistent with that reported in the literature.[52]

$Et_2P-CH_2CH_2CO_2Bu^t$

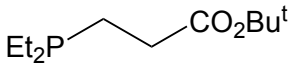

^1H NMR (500.27 MHz, C_6D_6) δ: 2.29 (td, $^3J_{HH}$= 8.3 Hz, $^3J_{HP}$ = 8.1 Hz, 2H, CH_2CO), 1.65−1.59 (m, 2H, CH_2P), 1.39 (s, 9H, Bu^t), 1.19−1.11 (m, 2H, CH_2 at PEt), 0.91 (dt, $^3J_{PH}$= 14.8 Hz, $^3J_{HH}$ = 7.7 Hz, 3H, CH_3 at PEt).

$^{31}P\{^1H\}$ NMR (202.51 MHz, C_6D_6) δ: −22.1 (s).

$^{13}C\{^1H\}$ NMR (125.77 MHz, C_6D_6) δ: 172.4 (d, $^3J_{CP}$= 11 Hz, C=O), 79.7 (s, C at Bu^t), 32.4 (d, $^2J_{CP}$ = 17 Hz, CH_2CO), 28.2 (s, CH_3 at Bu^t), 21.8 (d, $^1J_{CP}$= 15 Hz, CH_2P), 19.2 (d, $^1J_{CP}$ = 13 Hz, CH_2 at PEt), 9.8 (d, $^2J_{CP}$ = 13 Hz, CH_3 at PEt).

$Tol^p{}_2P-CH_2CH_2CO_2Bu^t$

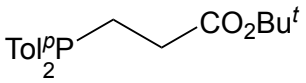

^1H NMR (500.27 MHz, C_6D_6) δ: 7.36 (dd, $^3J_{HH}$ = 7.7 Hz, $^3J_{HP}$ = 7.5 Hz, 4H, H_{ortho} at $PTol^p$), 6.91 (d, $^3J_{HH}$ = 7.7 Hz, 2H, H_{meta} at $PTol^p$), 2.43−2.33 (m, 4H, CH_2CH_2), 2.04 (s, 6H, CH_3 at $PTol^p$), 1.34 (s, 9H, Bu^t).

$^{31}P\{^1H\}$ NMR (202.51 MHz, C_6D_6) δ: −17.8 (s).

$^{13}C\{^1H\}$ NMR (125.77 MHz, C_6D_6) δ: 172.15 (d, $^3J_{CP}$ = 15 Hz, C=O), 138.5 (s, C_{para} at $PTol^p$), 135.7 (d, $^1J_{CP}$ = 13 Hz, C_{ipso} at $PTol^p$), 133.1 (d, $^2J_{CP}$ = 19 Hz, C_{ortho} at $PTol^p$), 129.6 (d, $^3J_{CP}$ = 7 Hz, C_{meta} at $PTol^p$), 79.9 (s, C at Bu^t), 32.3 (d, $^2J_{CP}$ = 19 Hz, $\underline{C}H_2CO$), 28.1 (s, CH_3 at Bu^t), 23.9 (d, $^3J_{CP}$ = 12 Hz, CH_2P), 21.2 (CH_3 at $PTol^p$).

$Cy_2P-CH_2CH_2CO_2Bu^t$

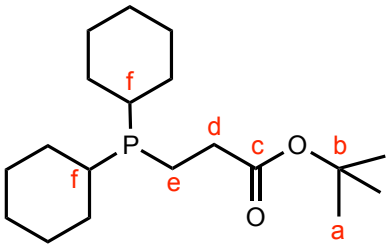

^{1}H NMR (500.27 MHz, C_6D_6) δ: 1.82–1.73 (4H, CH_2 at PCy), 1.76–1.67 (m, 2H, H_e), 1.70–1.62 (m, 6H, CH_2 at PCy),1.61–1.55 (m, 2H, CH_2 at PCy), 1.46–1.38 (m, 2H, H_f), 1.41 (s, 9H, H_a), 1.20–1.05 (m, 8H, CH_2 at PCy)

^{31}P{^{1}H} NMR (202.51 MHz, C_6D_6) δ: –3.8 (s).

^{13}C{^{1}H} NMR (125.77 MHz, C_6D_6) δ: 172.5 (d, $^3J_{CP}$ = 13 Hz, C_c), 79.8 (s, C_b), 34.9 (d, $^1J_{CP}$ = 24 Hz, C_d), 33.9 (d, $^1J_{CP}$ = 14 Hz, C_f), 30.7 (d, J_{CP} = 15 Hz, CH_2 at PCy), 29.3 (d, J_{CP} = 9 Hz, CH_2 at PCy), 28.2 (s, C_a), 27.7 (d, J_{CP} = 11 Hz, CH_2 at PCy), 27.6 (d, J = 7.2 Hz, CH_2 at PCy), 26.9 (s, CH_2 at PCy),17.0 (d, $^1J_{CP}$ = 19 Hz, C_e)

Note: This product also contains ~1% of Markovnikov phosphine isomer (branched product) detected by ^{31}P{^{1}H} NMR spectroscopy. Since the Co-catalyzed hydrophosphination is relatively slow, this trace amount of branched product could be due to the competing background thermal hydrophosphination (it is also slow).

$Cy_2P-CH(CH_3)CO_2Bu^t$

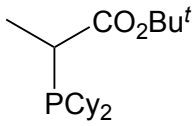

^{31}P{^{1}H} NMR (202.51 MHz, C_6D_6) δ: –9.8 (s).

$Cy(H)P-CH_2CH_2CO_2Bu^t$

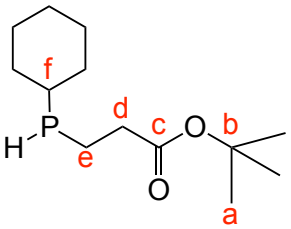

^{1}H NMR (500.27 MHz, C_6D_6) δ: 2.98 (dq, $^1J_{PH}$ = 194.4 Hz, $^3J_{HH}$ = 6.9 Hz, 1H, HP), 2.30 (td, $^3J_{HH}$ = 8.2 Hz, $^3J_{HP}$ = 6.9 Hz, 2H, H_d), 1.92–1.83 (m, 1H, H_e), 1.71–1.68 (m, 1H, CH_2

at PCy), 1.68–1.62 (m, 3H, H_e & CH_2 at PCy), 1.62–1.54 (m, 2H, CH_2 at PCy), 1.53–1.50 (m, 2H, CH_2 at PCy), 1.50–1.44 (m, 1H, H_f), 1.38 (s, 9H, H_a), 1.11–1.03 (m, 2H, CH_2 at PCy), 1.09–1.05 (m, 1H, CH_2 at PCy).

$^{31}P\{^1H\}$ NMR (202.51 MHz, C_6D_6) δ: –49.3 (s).

$^{13}C\{^1H\}$ NMR (125.77 MHz, C_6D_6) δ: 172.0 (d, $^3J_{CP}$ = 9 Hz, C_c), 79.8 (s, C_b), 34.7 (d, $^2J_{CP}$ = 13 Hz, C_d), 32.7 (d, J_{CP} = 7 Hz, CH_2 at PCy), 32.0 (d, J_{CP} = 17 Hz, CH_2 at PCy), 31.5 (d, $^1J_{CP}$ = 8 Hz, C_f), 28.2 (s, C_a), 27.3 (d, J_{CP} = 7 Hz, CH_2 at PCy), 27.2 (d, J_{CP} = 11 Hz, CH_2 at PCy), 26.5 (s, CH_2 at PCy), 14.2 (d, $^1J_{CP}$ = 13 Hz, C_e).

CyP–(CH$_2$CH$_2$CO$_2$Bu^t)$_2$

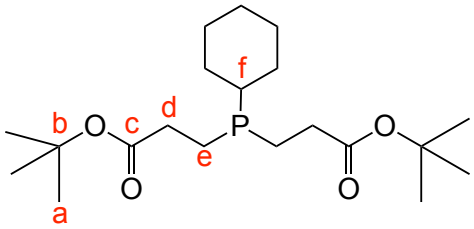

^1H NMR (500.27 MHz, C_6D_6) δ: 2.31 (td, $^3J_{HH}$ = 8.6 Hz, $^3J_{HP}$ = 7.1 Hz, 4H, H_d), 1.73–1.66 (m, 2H, H_e), 1.65–1.55 (m, 4H, CH_2 at PCy), 1.61–1.55 (m, 2H, H_e), 1.54–1.48 (m, 2H, CH_2 at PCy), 1.38 (s, 18H, H_a), 1.21–1.14 (m, 1H, H_f), 1.09–0.98 (m, 4H, CH_2 at PCy).

$^{31}P\{^1H\}$ NMR (202.51 MHz, C_6D_6) δ: –16.0 (s).

$^{13}C\{^1H\}$ NMR (125.77 MHz, C_6D_6) δ: 172.4 (d, $^3J_{CP}$ = 11 Hz, C_c), 79.8 (s, C_b), 35.5 (d, $^1J_{CP}$ = 12 Hz, C_f), 32.8 (d, $^2J_{CP}$ = 18, C_d), 29.4 (d, J_{CP} = 12 Hz, CH_2 at PCy), 28.2 (s, C_a), 27.3 (d, J_{CP} = 9 Hz, CH_2 at PCy), 26.7 (s, CH_2 at PCy), 19.5 (d, $^1J_{CP}$ = 17, C_e).

Ph(H)P–CH$_2$CH$_2$CO$_2$Bu^t

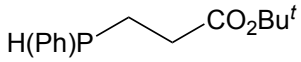

^1H NMR (500.27 MHz, C_6D_6) δ: 7.32–7.27 (m, 2H, H_{ortho} at PPh), 7.06–6.97 (m, 3H, H_{meta} & H_{para} at PPh), 4.05 (ddd, $^1J_{HP}$ = 207.3 Hz, $^3J_{HP}$ = 8.3 Hz, $^3J_{HP}$ = 5.9 Hz, 1H, HP), 2.31–2.12 (m, 2H, CH_2CO), 2.00–1.83 (m, 2H, CH_2P), 1.33 (s, 9H, Bu^t).

$^{31}P\{^1H\}$ NMR (202.51 MHz, C_6D_6) δ: –51.6 (s).

$^{13}C\{^1H\}$ NMR (125.77 MHz, C_6D_6) δ: 171.8 (d, $^3J_{CP}$ = 8 Hz, C=O), 135.4 (d, $^1J_{PC}$ = 12 Hz, C_{ipso} at PPh), 134.0 (d, $^2J_{CP}$ = 16 Hz, C_{ortho} at PPh), 128.7 (d, $^3J_{CP}$ = 6 Hz, C_{meta} at PPh),

128.4 (s, C_{para} at PPh), 79.9 (s, C at Bu^t), 34.3 (d, $^2J_{CP}$ = 8 Hz, $\underline{C}H_2CO$), 28.1 (s, CH_3 at Bu^t), 19.0 (d, $^1J_{CP}$ = 13 Hz, CH_2P).

PhP−(CH$_2$CH$_2$CO$_2$Bu^t)$_2$

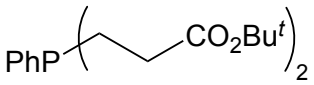

^{1}H NMR (500.27 MHz, C_6D_6) δ: 7.39–7.34 (m, 2H, H_{ortho} at PPh), 7.08–7.01 (m, 3H, H_{meta} & H_{para} at PPh), 2.30–2.11 (m, 4H, CH_2CO), 1.97–1.82 (m, 4H, CH_2P), 1.34 (s, 18H, Bu^t)

^{31}P{^{1}H} NMR (202.51 MHz, C_6D_6) δ: –23.5 (s).

^{13}C{^{1}H} NMR (125.77 MHz, C_6D_6) δ: 172.0 (d, $^3J_{CP}$ = 13 Hz, C=O), 138.0 (d, $^1J_{PC}$ = 16 Hz, C_{ipso} at PPh), 132.8 (d, $^2J_{CP}$ = 20 Hz, C_{ortho} at PPh), 129.2 (s, C_{para} at PPh), 128.8 (d, $^3J_{CP}$ = 7 Hz, C_{meta} at PPh), 79.8 (s, C at Bu^t), 32.2 (d, $^2J_{CP}$ = 17 Hz, $\underline{C}H_2CO$), 28.1 (s, CH_3 at Bu^t), 23.4 (d, $^1J_{CP}$ = 13 Hz, CH_2P).

4.6.6 Reaction of Co-1 with excess phosphine or *tert*-butyl acrylate

See Sections 3.6.11 and 3.6.12 in Chapter 3.

4.6.7 Reaction of Co-2a with DBU in the presence of TEMPO.

Complex **Co-2a** (0.019 mmol, 12 mg) and TEMPO (0.019 mmol, 3.0 mg) were dissolved in C_6D_6 (0.6 ml) in a small vial for 0.5 h before adding base. ^{1}H and ^{31}P{^{1}H} NMR at this point indicated that no reaction has occurred. DBU (0.019 mmol, 2.8 μL) was added to this solution, and the mixture was transferred to an NMR tube. The colour of the mixture changed from dark green to brown.

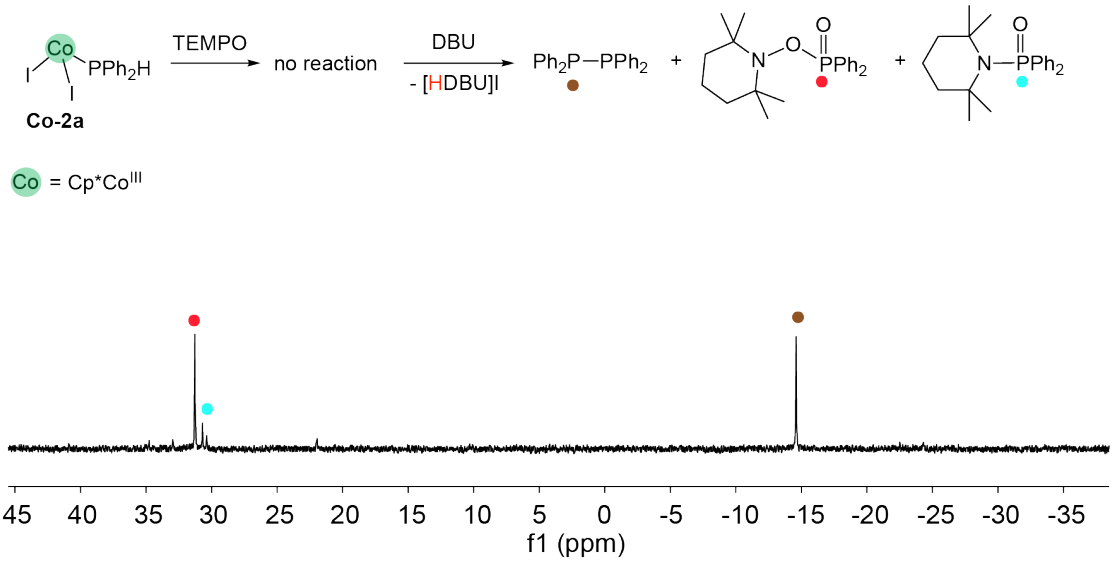

Figure 4.17 $^{31}P\{^{1}H\}$ NMR (121.55 MHz, C_6D_6) spectra of the reaction of complex **Co-2a** with DBU in the presence of TEMPO, showing the different species. Note: some small signals are not identified.

4.6.8 Attempted isolation of Co(II) complex $[Co(\eta^5\text{-}Cp^*)(\mu\text{-}I)]_2$

To a solution of complex **Co-2a** (0.173 mmol, 110 mg) in toluene (10 mL) in a Schlenk flask, neat DBU (0.208 mmol, 31.0 µL) was added. The colour of the mixture changed from dark green to brown. After 1 h stirring at ambient temperature, some white solid, [HDBU]I, precipitated from the brown solution. The resulting brown mixture was filtered through a frit to remove [HDBU]I. The white solid was washed with toluene (2 x 5 mL) and dried under vacuum. The solvent from the combined filtrate was removed under vacuum, and the resulting brown paste was triturated with pentane (5 ×10 mL). The pentane was removed under vacuum to give an oily brown paste. ^{1}H NMR of this oily brown mixture showed that the broad signal due to $[Co(\eta^5\text{-}Cp^*)(\mu\text{-}I)]_2$ disappeared, suggesting the decomposition of this product. The instability of $[Co(\eta^5\text{-}Cp^*)(\mu\text{-}I)]_2$ is consistent with the literature.[53] The white solid was identified as the conjugate acid [HDBU]I by ^{1}H NMR (Figure 4.18) and ESI-MS (Figure 4.19).

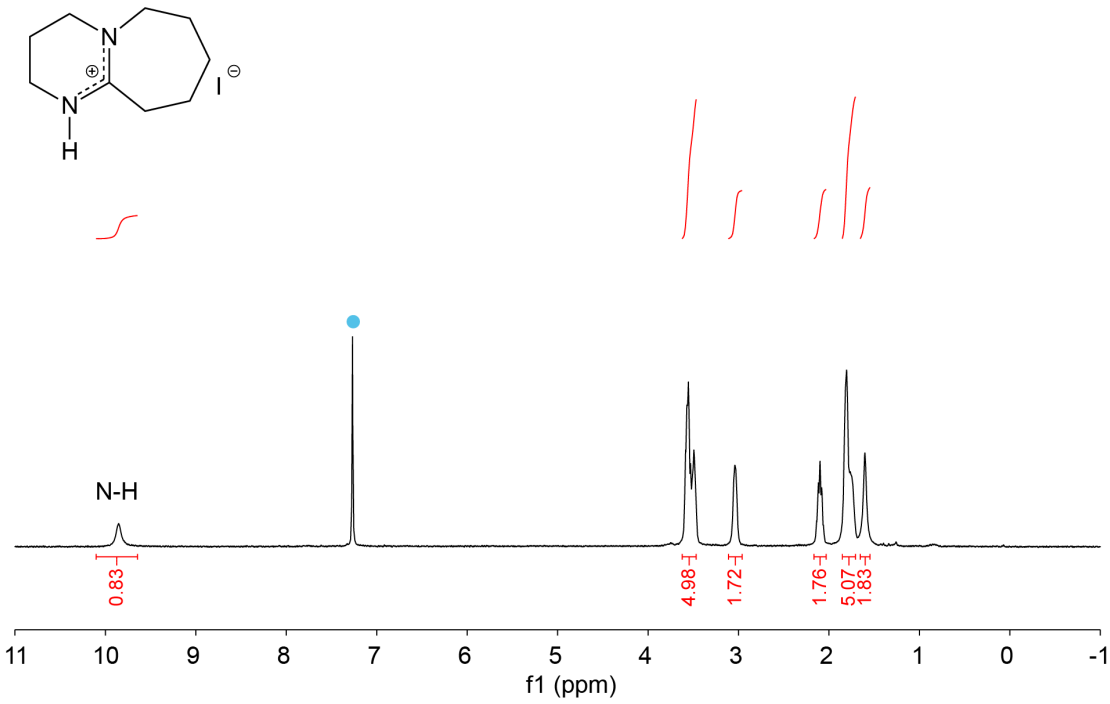

Figure 4.18 ^{1}H NMR (300.27 MHz, $CDCl_3$) spectrum of isolated [HDBU]I. Residual proteo-solvent (•).

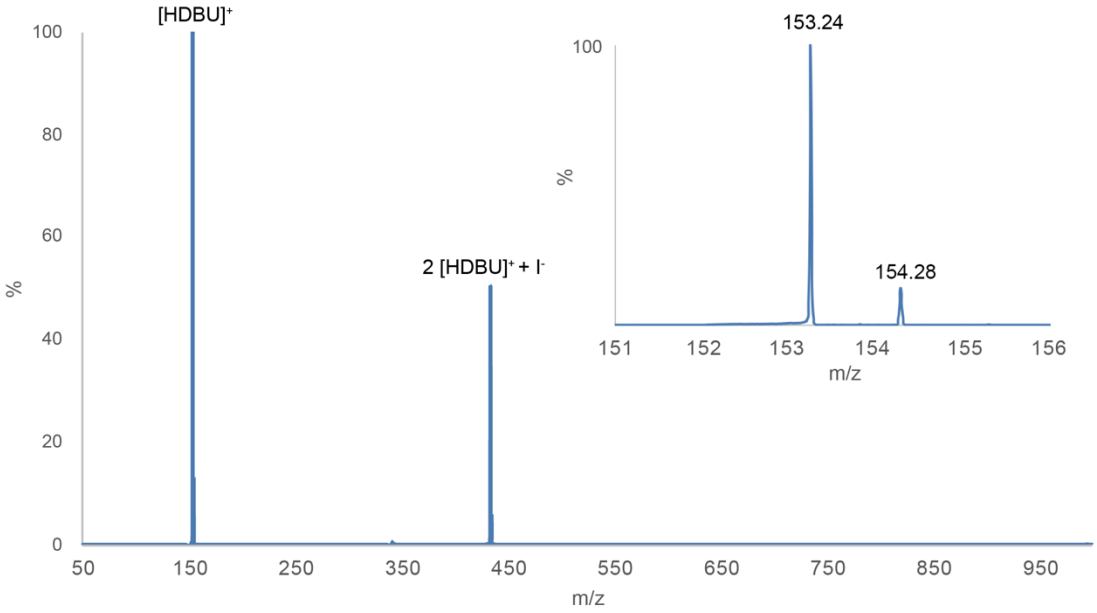

Figure 4.19 ESI-MS spectrum of isolated [HDBU]I, showing *m/z* 153.24 (M^+, 153.14 calcd, 100%) and *m/z* 433.30 ($2M^+ + I^-$, 433.18 calcd, 50%). Conditions: a solution of [HDBU]I (0.02 mmol) in (CH_3CN) (0.6 mL) was further diluted 20 times for the ESI-MS experiments.

4.6.9 Reaction of in-situ-generated Co(II) species with *tert*-butyl acrylate and PPh_2H.

A small vial was loaded with Co(η^5-Cp*)I_2(PPh_2H) (**Co-2a**, 0.016 mmol) and C_6D_6 (0.5 mL). After 30 min, DBU (0.016 mmol) was added to the dark green solution, giving a brown mixture. *tert*-Butyl acrylate (0.210 mmol, 10 equiv) and PPh_2H (0.210 mmol, 10 equiv) were added. The resulting mixture was analyzed by ^1H and $^{31}P\{^1H\}$ NMR.

4.6.10 Reactions of complex Co-2a with hydrogen atom abstraction agents

A small vial was loaded with Co(η^5-Cp*)I_2(PPh_2H) (**Co-2a**, 0.016 mmol) and C_6D_6 (0.5 mL). After 30 min, a hydrogen atom transfer (HAT) reagent (TEMPO or 2,4,6-$Bu^t_3C_6H_2O$ (Mes*O), 0.016 mmol) was added to the dark green solution. The resulting mixtures were analyzed by ^1H and $^{31}P\{^1H\}$ NMR (Figure 4.20). TEMPO was obtained from Sigma-Aldrich, and Mes*O was synthesized by a literature procedure.[54]

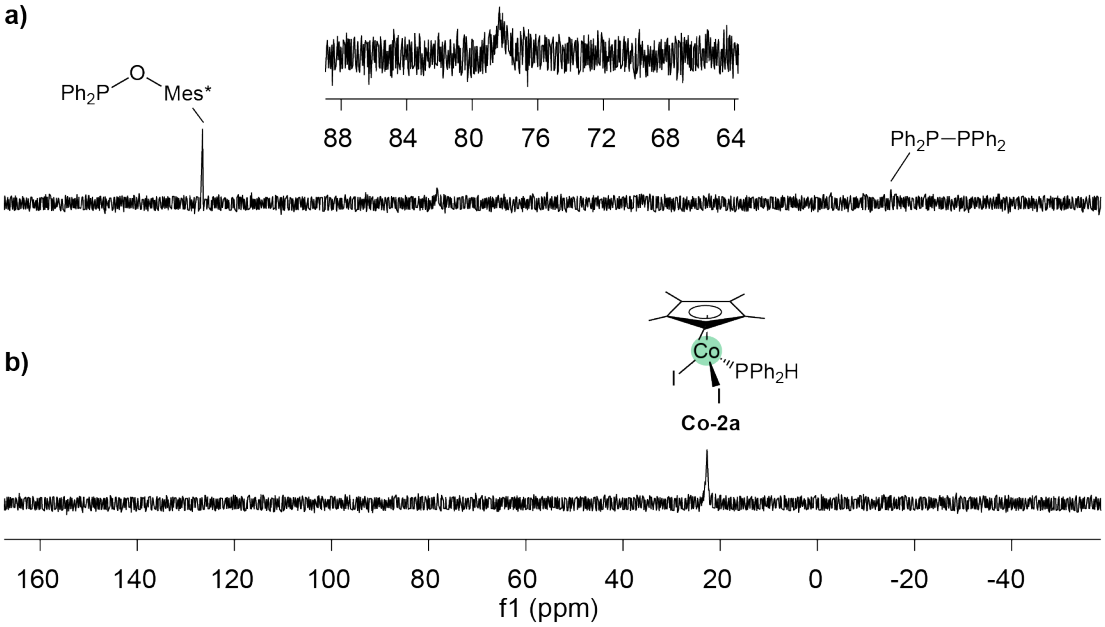

Figure 4.20 $^{31}P\{^1H\}$ NMR (121.55 MHz, C_6D_6) spectra of experiments using complex **Co-2a** and (**a**) Mes*O or (**b**) TEMPO.

For the reaction with Mes*O radical (Figure 4.20a), the signals due to **Co-2a** disappear, but signals due to Mes*OH are observed in the ^{1}H NMR. In the $^{31}P\{^{1}H\}$ NMR, trace amounts of Ph_2P-PPh_2 and the P-O coupling product Ph_2POMes^*, as well as an unidentified species (δ 78 ppm), are observed. The observation of these products by NMR indicates that the hydrogen atom has been abstracted from the coordinated PPh_2H in the Co(III) complex. In addition, the loss of Co-P signals in the NMR spectra suggests the formation of some paramagnetic Co products. Although I have not identified the paramagnetic species, it is reasonable that homolytic P-H cleavage occurs at **Co-2a**. Figure 4.20b shows that no reaction occurs using TEMPO. Thus, the BDFE of the P-H bond at **Co-2a** must be between 66.5 and 77.1 kcal/mol, based on the BDFEs of TEMPOH and Mes*OH, respectively.[43]

4.6.11 The "same excess" experiment

For all three reactions, solutions of **Co-1** and DBU with concentrations of 0.00600 M and 0.0120 M were used, with an internal standard $O(SiMe_3)_2$ (0.0180 mmol). Substrate concentrations: neat alkene (0.30 M) and neat PPh_2H (0.30 M) were used in the **R-a**; neat alkene (0.15 M) and neat PPh_2H (0.15 M) were used in the **R-b**; neat alkene (0.15 M), neat PPh_2H (0.15 M) and the product phosphine (0.15 M) were used in the **R-c**.

Synthesis of $Ph_2P(CH_2CH_2CO_2Bu^t)$

The product phosphine, $Ph_2P(CH_2CH_2CO_2Bu^t)$, was synthesized under catalyst-free conditions: PPh_2H (1.00 mmol, 186 mg) and *tert*-butyl acrylate (1.00 mmol, 128 mg) were mixed in toluene (5 mL). The reaction was stirred for one week, and the solvent was removed under vacuum. White solids were obtained (0.860 mmol, 270 mg, 86.0 %). The ^{1}H and $^{31}P\{^{1}H\}$ NMR data are consistent with that reported in the literature.[55]

4.6.12 The initial rates method

Following the general procedure for catalytic hydrophosphination described in Section 4.6.1, **Co-1** (0.00210 mmol, 0.00420 mmol and 0.00840 mmol) and DBU (0.00420 mmol, 0.00840 mmol and 0.0168 mmol) were employed. Neat alkene (0.210 mmol), neat secondary phosphine (0.210 mmol) and internal standard $O(SiMe_3)_2$ (0.018 mmol) were added to give a total volume of 0.7 mL. The initial rates were calculated from ^1H NMR conversions over 15 min.

4.7 References

(1) Ohmiya, H.; Yorimitsu, H.; Oshima, K. Cobalt-Catalyzed Syn Hydrophosphination of Alkynes. *Angew. Chem. Int. Ed.* **2005**, *44*, 2368–2370.

(2) Rajpurohit, J.; Kumar, P.; Shukla, P.; Shanmugam, M.; Shanmugam, M. Mechanistic Investigation of Well-Defined Cobalt Catalyzed Formal E-Selective Hydrophosphination of Alkynes. *Organometallics* **2018**, *37*, 2297–2304.

(3) Nolla-Saltiel, R.; Geer, A. M.; Taylor, L. J.; Churchill, O.; Davies, E. S.; Lewis, W.; Blake, A. J.; Kays, D. L. Hydrophosphination of Activated Alkenes by a Cobalt(I) Pincer Complex. *Adv. Synth. Catal.* **2020**, *362*, 3148–3157.

(4) Kumar, P.; Sen, A.; Rajaraman, G.; Shanmugam, M. An Unusual Mixed-Valence Cobalt Dimer as a Catalyst for the Anti-Markovnikov Hydrophosphination of Alkynes. *Inorg. Chem. Front.* **2022**, 32–34.

(5) Wu, Z. H.; Cheng, A. Q.; Yuan, M.; Zhao, Y. X.; Yang, H. L.; Wei, L. H.; Wang, H. Y.; Wang, T.; Zhang, Z.; Duan, W. L. Cobalt-Catalysed Asymmetric Addition and Alkylation of Secondary Phosphine Oxides for the Synthesis of P-Stereogenic Compounds. *Angew. Chem. Int. Ed.* **2021**, *60*, 27241–27246.

(6) Liu, W. Q.; Lei, T.; Zhou, S.; Yang, X. L.; Li, J.; Chen, B.; Sivaguru, J.; Tung, C. H.; Wu, L. Z. Cobaloxime Catalysis: Selective Synthesis of Alkenylphosphine Oxides under Visible Light. *J. Am. Chem. Soc.* **2019**, *141*, 13941–13947.

(7) King, A. K.; Buchard, A.; Mahon, M. F.; Webster, R. L. Facile, Catalytic Dehydrocoupling of Phosphines Using β-Diketiminate Iron(II) Complexes. *Chem. – Eur. J.* **2015**, *21*, 15960–15963.

(8) Webster, R. L. Room Temperature Ni(II) Catalyzed Hydrophosphination and Cyclotrimerization of Alkynes. *Inorganics* **2018**, *6*, 120.

(9) Yuan, J.; Zhu, L.; Zhang, J.; Li, J.; Cui, C. Sequential Addition of Phosphine to Alkynes for the Selective Synthesis of 1,2-Diphosphinoethanes under Catalysis. Well-Defined NHC-Copper Phosphides vs in Situ $CuCl_2$/NHC Catalyst. *Organometallics* **2017**, *36*, 455–459.

(10) Dannenberg, S. G.; Waterman, R. A Bench-Stable Copper Photocatalyst for the Rapid Hydrophosphination of Activated and Unactivated Alkenes. *Chem. Commun.* **2020**, *56*, 14219–14222.

(11) Shulyupin, M. O.; Kazankova, M. A.; Beletskaya, I. P. Catalytic Hydrophosphination of Styrenes. *Org. Lett.* **2002**, *4*, 761–763.

(12) King, A. K.; Buchard, A.; Mahon, M. F.; Webster, R. L. Facile, Catalytic Dehydrocoupling of Phosphines Using β-Diketiminate Iron(II) Complexes. *Chem. – Eur. J.* **2015**, *21*, 15960–15963.

(13) Fraser, R. R.; Mansour, T. S.; Savard, S. Acidity Measurements on Pyridines in Tetrahydrofuran Using Lithiated Silylamines. *J. Org. Chem.* **1985**, *50*, 3232–3234.

(14) Eaborn, C. The Proton: Applications to Organic Chemistry. *J. Organomet. Chem.* **1986**, *308*, C33.

(15) Belli, R. G.; Yang, J.; Bahena, E. N.; McDonald, R.; Rosenberg, L. Mechanism and Catalyst Design in Ru-Catalyzed Alkene Hydrophosphination. *ACS Catal.* **2022**, *12*, 5247–5262.

(16) Kolthoff, I. M.; Chantooni, M. K.; Bhowmik, S. Dissociation Constants of Uncharged and Monovalent Cation Acids in Dimethyl Sulfoxide. *J. Am. Chem. Soc.* **1968**, *90*, 23–28.

(17) Kaupmees, K.; Trummal, A.; Leito, I. Basicities of Strong Bases in Water: A Computational Study. *Croat. Chem. Acta* **2014**, *87*, 385–395.

(18) Wang, X.; Cao, K.; Liu, Y.; Tsang, B.; Liew, S. Migration Insertion Polymerization (MIP) of Cyclopentadienyldicarbonyldiphenylphosphinopropyliron (FpP): A New Concept for Main Chain Metal-Containing Polymers (MCPs). *J. Am. Chem. Soc.* **2013**, *135*, 3399–3402.

(19) Wu, L.; Annibale, V. T.; Jiao, H.; Brookfield, A.; Collison, D.; Manners, I. Homo- and Heterodehydrocoupling of Phosphines Mediated by Alkali Metal Catalysts. *Nat. Commun.* **2019**, *10*, 2786.

(20) Sues, P. E.; Lough, A. J.; Morris, R. H. Reactivity of Ruthenium Phosphido Species Generated through the Deprotonation of a Tripodal Phosphine Ligand and Implications for Hydrophosphination. *J. Am. Chem. Soc.* **2014**, *136*, 4746–4760.

(21) Werner, H.; Hofmann, W.; Zolk, R.; Dahl, L. F.; Kocal, J.; Kühn, A. Synthesis and Reactions of a Nucleophilic Bis(μ-Dimethylphosphido)Dicobalt Complex. The Crystal and Molecular Structure of $[C_5H_5Co(\mu\text{-}PMe_2)]_2$ and $[(C_5H_5Co)_2(\mu\text{-}H)(\mu\text{-}PMe_2)_2]$BPh4. *J. Organomet. Chem.* **1985**, *289*, 173–188.

(22) Varela-Izquierdo, V.; Geer, A. M.; Navarro, J.; López, J. A.; Ciriano, M. A.; Tejel, C. Rhodium Complexes in P-C Bond Formation: Key Role of a Hydrido Ligand. *J. Am. Chem. Soc.* **2021**, *143*, 349–358.

(23) A. Tolman, C. Steric Effects of Phosphorus Ligands in Organometallic Chemistry and Homogeneous Catalysis. *Chem. Rev.* **1977**, *77*, 313–348.

(24) Cibuzar, M. P.; Dannenberg, S. G.; Waterman, R. A Commercially Available Ruthenium Compound for Catalytic Hydrophosphination. *Isr. J. Chem.* **2020**, *60*, 446–451.

(25) Ghebreab, M. B.; Bange, C. A.; Waterman, R. Intermolecular Zirconium-Catalyzed Hydrophosphination of Alkenes and Dienes with Primary Phosphines. *J. Am. Chem. Soc.* **2014**, *136*, 9240–9243.

(26) Li, J. N.; Liu, L.; Fu, Y.; Guo, Q. X. What Are the PKa Values of Organophosphorus Compounds? *Tetrahedron* **2006**, *62*, 4453–4462.

(27) Bange, C. A.; Waterman, R. Challenges in Catalytic Hydrophosphination. *Chem. – Eur. J.* **2016**, *22*, 12598–12605.

(28) Bunker, K. D.; Rheingold, A. L.; Moore, C. E.; Aubrey, M.; O'Connor, J. M. Synthesis of the Cobalt-Alkyne Complex $(\eta^5\text{-}C_5H_5)(PPh_3)Co\{\eta^2\text{-}(Me_3Si)CC(CO_2Et)\}$ and Structural Characterization of Trimethylsilyl Substituted Cobaltacyclopentadiene Complexes Derived Therefrom. *J. Organomet. Chem.* **2014**, *749*, 100–105.

(29) Connor, J. M.; Baldridge, K. K.; Velez, C. L.; Rheingold, A. L.; Moore, C. E. Chemistry at the Alkyne − Carbene Intersection : A. *J. Am. Chem. Soc.* **2013**, 8826–8829.

(30) Song, L. C.; Liu, P. C.; Hu, Q. M.; Lu, G. L.; Wang, G. F. Synthesis, Characterization and Properties of New Organocobalt Complexes Containing H5-Functionally Substituted Cyclopentadienyl and [60]Fullerene Ligands. *J. Organomet. Chem.* **2003**, *681*, 264–268.

(31) Chen, L.; Kountz, D. J.; Meek, D. W. New Bimetallic Cobalt(II) Complexes of Chelated, Bridged Phosphido Ligands. *Organometallics* **1985**, *4*, 598–601.

(32) Hayter, R. G.; Williams, L. F. Phosphorus- and Arsenic-Bridged Complexes of Metal Carbonyls-VIII. Cyclopentadienylcobalt and -Manganese Complexes. *J. Inorg. Nucl. Chem.* **1964**, *26*, 1977–1983.

(33) Koelle, U.; Fuss, B.; Raabe, E. Pentamethylcyclopentadlenyl Transition Metal Complexes. 9.1 Reactions and Solid-State and Solution Behavior of Dinuclear Cobalt(II) Complexes $[C_5Me_5Co(\mu\text{-}X)]_2$. *Organometallics* **1986**, *5*, 980–987.

(34) Kölle, U.; Khouzami, F.; Fuss, B. Bridged $C_5Me_5Co^{II}$ Complexes— Reactive Intermediates in the Cyclopentadienylation of Cobalt(II) Halides. *Angew. Chem. Int. Ed. English* **1982**, *21*, 131–132.

(35) Kaim, W. The Shrinking World of Innocent Ligands: Conventionaland Non-Conventional Redox-Active Ligands. *Eur. J. Inorg. Chem.* **2012**, *2012*, 343–348.

(36) Kaim, W. Manifestations of Noninnocent Ligand Behavior. *Inorg. Chem.* **2011**, *50*, 9752–9765.

(37) Chirik, P. J. Preface: Forum on Redox-Active Ligands. *Inorg. Chem.* **2011**, *50*, 9737–9740.

(38) Chirik, P. J.; Wieghardt, K. Radical Ligands Confer Nobility on Base-Metal Catalysts. *Science* **2010**, *327*, 794–795.

(39) Evangelio, E.; Ruiz-Molina, D. Valence Tautomerism: More Actors than Just Electroactive Ligands and Metal Ions. *C. R. Chim.* **2008**, *11*, 1137–1154.

(40) Tezgerevska, T.; Alley, K. G.; Boskovic, C. Valence Tautomerism in Metal Complexes: Stimulated and Reversible Intramolecular Electron Transfer between Metal Centers and Organic Ligands. *Coord. Chem. Rev.* **2014**, *268*, 23–40.

(41) Buchanan, R. M.; Pierpont, C. G. Tautomeric Catecholate-Semiquinone Interconversion via Metal-Ligand Electron Transfer. Structural, Spectral, and Magnetic Properties of (3,5-Di-Tert-Butylcatecholato)- (3,5-Di-Tert-Butylsemiquinone)(Bipyridyl)Cobalt(III), a Complex Containing Mixed-Valence Organic Ligands. *J. Am. Chem. Soc.* **1980**, *102*, 4951–4957.

(42) Heurich, T.; Qu, Z. W.; Nožinović, S.; Schnakenburg, G.; Matsuoka, H.; Grimme, S.; Schiemann, O.; Streubel, R. Synthesis and Rearrangement of P-Nitroxyl-

Substituted PIIIand PVPhosphanes: A Combined Experimental and Theoretical Case Study. *Chem. – Eur. J.* **2016**, *22*, 10102–10110.

(43) Warren, J. J.; Tronic, T. A.; Mayer, J. M. Thermochemistry of Proton-Coupled Electron Transfer Reagents and Its Implications. *Chem. Rev.* **2010**, *110*, 6961–7001.

(44) G. Bordwell, F. Equilibrium Acidities in Dimethyl Sulfoxide Solution. *Acc. Chem. Res.* **2002**, *21*, 456–463.

(45) Sooväli, L.; Kaljurand, I.; Kütt, A.; Leito, I. Uncertainty Estimation in Measurement of PKa Values in Nonaqueous Media: A Case Study on Basicity Scale in Acetonitrile Medium. *Anal. Chim. Acta* **2006**, *566*, 290–303.

(46) Blackmond, D. G. Reaction Progress Kinetic Analysis: A Powerful Methodology for Mechanistic Studies of Complex Catalytic Reactions. *Angew. Chem. Int. Ed.* **2005**, *44*, 4302–4320.

(47) Casado, J.; López-Quintela, M. A.; Lorenzo-Barral, F. M. The Initial Rate Method in Chemical Kinetics: Evaluation and Experimental Illustration. *J. Chem. Educ.* **1986**, *63*, 450–452.

(48) Burés, J. A Simple Graphical Method to Determine the Order in Catalyst. *Angew. Chem. Int. Ed.* **2016**, *55*, 2028–2031.

(49) Yang, J.; Langis-Barsetti, S.; Parkin, H. C.; McDonald, R.; Rosenberg, L. Terminal Phosphido Complexes of the Ru(η^5-Cp*) Fragment. *Organometallics* **2019**, *38*, 3257–3266.

(50) Stoll, S.; Schweiger, A. EasySpin, a Comprehensive Software Package for Spectral Simulation and Analysis in EPR. *J. Magn. Reson.* **2006**, *178*, 42–55.

(51) Scriban, C.; Kovacik, I.; Glueck, D. S. A Protic Additive Suppresses Formation of Byproducts in Platinum-Catalyzed Hydrophosphination of Activated Olefins. Evidence for P-C and C-C Bond Formation by Michael Addition. *Organometallics* **2005**, *24*, 4871–4874.

(52) Gallagher, K. J.; Espinal-Viguri, M.; Mahon, M. F.; Webster, R. L. A Study of Two Highly Active, Air-Stable Iron(III)-μ-Oxo Precatalysts: Synthetic Scope of Hydrophosphination Using Phenyl- and Diphenylphosphine. *Adv. Synth. Catal.* **2016**, *358*, 2460–2468.

(53) Kölle, U.; Fuss, B. Pentamethylcyclopentadienyl-Übergangsmetall-π-Komplexe, V1). (Pentamethylcyclopentadienyl)Cobalt(III)-Halogeno- Und -Amido-Komplexe. *Chem. Ber.* **1984**, *117*, 743–752.

(54) Manner, V. W.; Markle, T. F.; Freudenthal, J. H.; Roth, J. P.; Mayer, J. M. The First Crystal Structure of a Monomeric Phenoxyl Radical: 2,4,6-Tri-Tert-Butylphenoxyl Radical. *Chem. Commun.* **2008**, 256–258.

(55) Bissessar, D.; Egly, J.; Achard, T.; Steffanut, P.; Bellemin-Laponnaz, S. Catalyst-Free Hydrophosphination of Alkenes in Presence of 2-Methyltetrahydrofuran: A Green and Easy Access to a Wide Range of Tertiary Phosphines. *RSC Adv.* **2019**, *9*, 27250–27256.

5. Investigation of Cp*Co-catalyzed dehydrocoupling

As described in Chapter 3, complexes Co(η^5-Cp*)I_2(CO) (**Co-1**) and [Co(η^5-Cp*)$(NCCH_3)_3$][SbF_6]$_2$ (**Co-5**) show catalytic activity for dehydrocoupling of PPh_2H. In this chapter, I perform detailed investigations on catalytic dehydrocoupling of primary and secondary phosphines using **Co-1**. This chapter includes contributions from Dr. Charles Walsby (EPR spectroscopy, SFU).

5.1 Introduction

Molecular compounds containing P-P bonds have practical applications in coordination and synthetic chemistry (references in Chapter 1). For example, diphosphines (R_2P-PR_2), as the simplest compounds containing P-P bonds, readily react with alkenes and alkynes to form bidentate phosphine ligands.[1] Historically, diphosphines have been synthesized *via* Wurtz-type reductive coupling of a halophosphine, PR_2X, with metals (e.g., M = Li, Na, K, Mg) or *via* salt metathesis of a metal phosphido (M-PR_2) with PR_2X.[2,3] Alternatively, catalytic routes to form P-P bonds are known, primarily *via* dehydrocoupling reactions of phosphines. Transition metal and main group compounds are known to catalyze dehydrocoupling reactions (see Chapter 1). However, most of these catalysts have poor activities (TOFs < 2 h^{-1}) and low product conversion (see Chapter 1). The activity and conversion are limited by a low K_{eq} for a dehydrocoupling equilibrium (Scheme 5.1). According to a recently reported computational study, the direct dehydrocoupling of PPh_2H to Ph_2P-PPh_2 and H_2 is endergonic by 2.64 kcal/mol; the thermodynamic equilibrium lies heavily toward the side of PPh_2H.[4]

Scheme 5.1 Equilibrium of dehydrocoupling of PPh_2H, showing the reaction heavily lies on the left side.

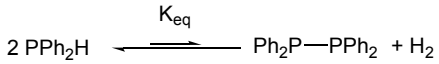

In this chapter, I initially probed mechanisms of catalytic dehydrocoupling of PPh_2H using Co(η^5-Cp*)I_2(CO) (**Co-1**) under conditions allowing the equilibrium to establish (Scheme 5.1). Two different conditions (base-mediated, non-base-mediated) were explored. Then, I explored using hydrogen acceptors (HAs) to push the equilibrium toward the dehydrocoupling product.

5.2 Investigating catalytic dehydrocoupling of PPh_2H using Co-1

In this section, I first attempted to improve Ph_2P-PPh_2 conversion by optimizing catalytic conditions (Section 5.2.1). In addition, I carefully identified Co intermediates in the catalytic mixture mainly using NMR spectroscopy, thus deducing the role of Co and co-catalyst base in the dehydrocoupling reaction.

5.2.1 Screening catalytic conditions for dehydrocoupling of PPh_2H using Co-1

I investigated the catalytic activity of Co(η^5-Cp*)I_2(CO) (**Co-1**) for dehydrocoupling of PPh_2H by screening different Co:base ratios, temperatures and solvents (Table 5.1). These conditions are based on those for the Co-catalyzed hydrophosphination that used base. PPh_2H was selected because it is the most common substrate for catalytic dehydrocoupling systems (see Appendix A).

Table 5.1 Assessing catalytic activity of **Co-1** for catalytic dehydrocoupling of PPh_2H.[a]

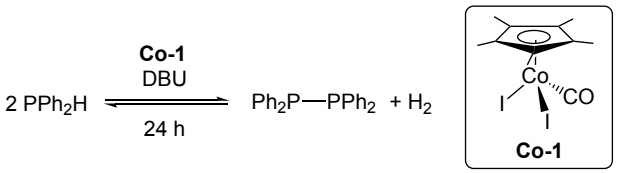

Entry	**[Co-1]** (mol%)	[DBU] (mol%)	Solvent	T (°C)	Ph_2P-PPh_2 (%)
1	10	0	C_6D_6	20	0
2	0	10	C_6D_6	20/80	0
3	10	10	C_6D_6	20	10(1)
4	10	20	C_6D_6	20	13(2)
5	10	0	C_6D_6	80	22(1)
6	10	20	C_6D_6	80	28(2)
7	10	20	CD_3CN	80	33(3)
8	10	10	C_6D_6	80	20(1)

[a]0.3 mM PPh_2H. Conversions (%) determined by non-quantitative $^{31}P\{^1H\}$ NMR experiments (121.55 MHz, RT) from relative integration of ^{31}P signals for Ph_2P-PPh_2 and free PPh_2H. Standard deviations for triplicate runs are shown in parentheses. Other signals appeared in the region due to Co-P-containing complexes.

The Co-catalyzed dehydrocoupling reaction is slow at RT. In the presence of only 10 mol% **Co-1** or DBU, no reaction occurs at RT (entries 1 and 2, Table 5.1). Using 10 mol% **Co-1** and equal or higher amounts of DBU (10 mol% or 20 mol%, respectively), the catalytic reaction at RT (entries 3 and 4) gives 10 % product conversion within 15 min, which is attributed to the rapid stoichiometric reaction described in Chapter 4. After that, both reactions (entries 3 and 4) become slow, giving 10 % to 13 % product conversion after 24 h (0–3% additional, catalytic dehydrocoupling).

Higher product conversions are mostly possible at higher temperatures. Using 10 mol% **Co-1** alone at 80 °C after 24 h (entry 5) gives 22% Ph_2P-PPh_2 but using 10 mol% DBU alone at 80 °C gives no dehydrocoupling activity (entry 2). Also, at 80 °C, using 10 mol% **Co-1** and 20 mol% DBU (entry 6) slightly increases the Ph_2P-PPh_2 conversion

(28%) after 24 h compared to using only 10 mol% **Co-1** (entry 5). These results suggest that adding DBU to Co is not essential for the dehydrocoupling reaction but facilitates the reaction.

Switching the solvent from C_6D_6 to CD_3CN, the reaction using 10 mol% **Co-1** and 20 mol% DBU at 80 °C (entry 7) slightly increases the conversion to Ph_2P-PPh_2 after 24 h (33%). This variation could be due to the relative solubility of the conjugate acid (i.e. [HDBU]I) in these solvents. [HDBU]I precipitates from the reaction in C_6D_6 while it stays dissolved in CD_3CN. This conjugate acid may play a role in the formation of H_2 in the catalytic reaction (*vide infra*). Therefore, an increase in solubility of [HDBU]I in CD_3CN might affect the Ph_2P-PPh_2 conversion.

Regardless of varying reaction conditions shown in Table 5.1, the amount of Ph_2P-PPh_2 produced does not significantly change. This indicates that a low K_{eq} limits the product conversion in the reaction (Scheme 5.2 and described in Section 5.1).

Scheme 5.2 Equilibrium of dehydrocoupling of PPh_2H using **Co-1**.

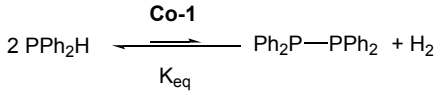

5.2.2 Identifying Co intermediates in catalytic dehydrocoupling

Although this Co catalytic system gives a low conversion to Ph_2P-PPh_2, I am still curious about the roles of Co species in the dehydrocoupling process. In this section, I focus on elucidating the fate of the precatalyst Co(η^5-Cp*)I_2(CO) (**Co-1**) during catalysis to understand better the mechanism. According to Table 5.1, the reaction involving **Co-1** and base DBU (entry 6) slightly differs from the non-base mediated reaction (entry 5).

Thus, I examined both reactions (Scheme 5.3) more closely, focusing on identifying Co intermediates.

Scheme 5.3 Catalytic dehydrocoupling of PPh_2H using **Co-1** in the presence of (**a**) base or (**b**) not.

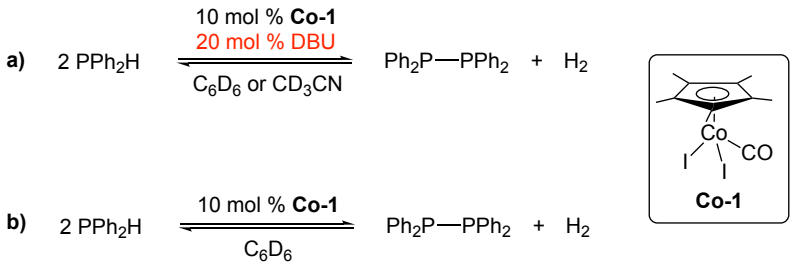

I identified possible Co intermediates in the catalytic mixtures mainly using ^{1}H and ^{31}P NMR monitoring experiments, as well as EPR and ESI-MS analyses. For each reaction shown in Scheme 5.3, I assessed speciation in the catalytic mixture in a stepwise fashion. I first examined Co intermediates present at RT and then heated the mixtures to detect the changes of the original Co intermediates. This enabled the detection of as many Co intermediates as feasible (e.g. some Co species could disappear rapidly during heating). Unless otherwise noted, NMR experiments described in this section were run at RT.

5.2.2.1 Dehydrocoupling of PPh_2H using 10 mol% Co-1 and 20 mol% DBU

Co intermediates in the catalytic mixture before heating

The $^{31}P\{^{1}H\}$ NMR spectrum (Figure 5.1) of the reaction mixture (Scheme 5.3a) at RT (before heating) shows signals assigned to Co(I) phosphine complex $Co(\eta^5\text{-}Cp^*)(PPh_2H)_2$ (**Co-8**) and Co(II) bridging phosphido complex $[Co(\eta^5\text{-}Cp^*)(\mu\text{-}PPh_2)]_2$ (**Co-9**), which is comparable to the catalytic mixture previously observed for hydrophosphination (Section 4.4.2, Chapter 4). Possible mechanisms for forming these two intermediates are shown in Scheme 5.4.

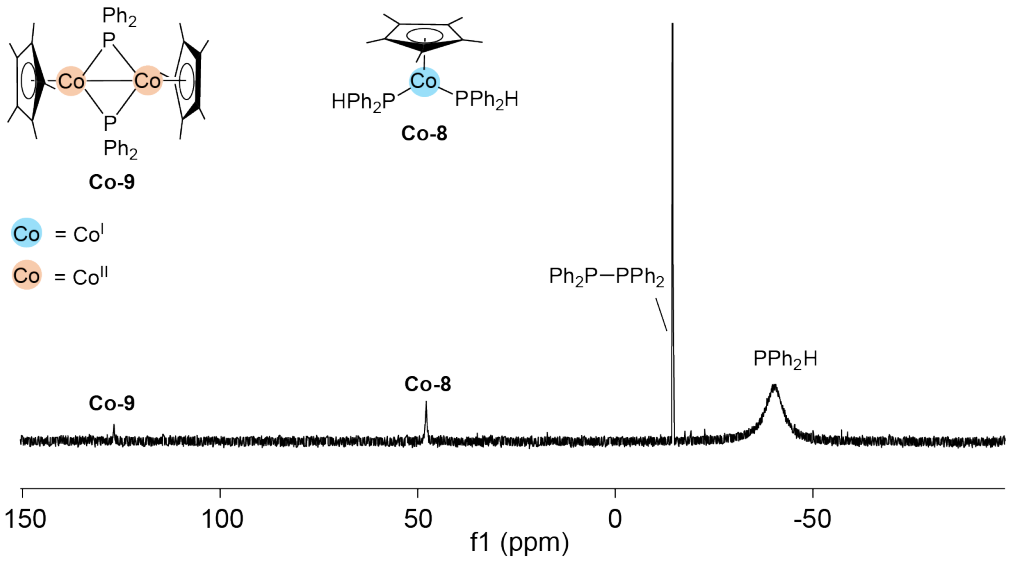

Figure 5.1 $^{31}P\{^{1}H\}$ NMR (121.55 MHz, C_6D_6) spectrum of the dehydrocoupling reaction of PPh_2H using 10 mol% **Co-1** and 20 mol% DBU at RT after 15 min (before heating).

Scheme 5.4 Proposed process for the formation of **Co-8** and **Co-9** in the base-mediated dehydrocoupling reaction of PPh_2H using **Co-1** in C_6D_6, before heating. R = Ph.

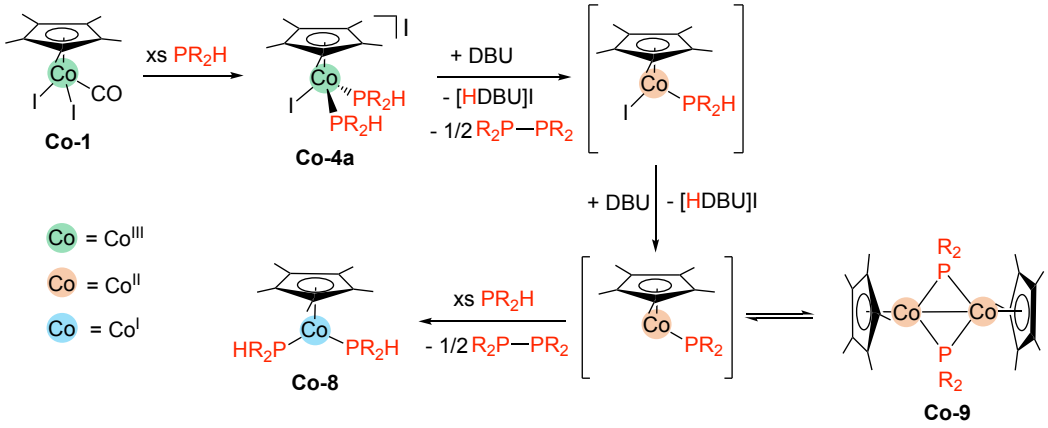

Compared to the reaction performed in C_6D_6 (Figure 5.1), the reaction performed in CD_3CN shows only a weak signal due to complex **Co-8** (no signal due to **Co-9**) in the $^{31}P\{^{1}H\}$ spectrum before heating. The absence of **Co-9** could result from coordination of solvent CD_3CN to the Co(II) center (Scheme 5.5, blue box). The proposed monomeric Cp*Co(II) phosphido species, Co(η^5-Cp*)(PPh_2)($NCCD_3$), was identified by EPR analysis of the mixture containing **Co-1**, DBU (2 equiv) and PPh_2H (10 equiv). The EPR spectrum

of the mixture at 100 K reveals diagnostic rhombic low-spin Co(II) signals (Figure 5.2), as well as hyperfine couplings to Co(II) and P. Due to the lack of hyperfine coupling to H, it is likely that this signal is due to the proposed Co(II)-PPh_2 rather than Co(II)-PPh_2H). Nonetheless, I cannot rule out the possibility that hyperfine couplings to H in a possible complex are too weak to detect. In addition, I cannot rule out that multiple Co(II) intermediates in the mixture analyzed by EPR and have no direct evidence for the formation of the complex Co(η^5-Cp*)(PPh_2)(PPh_2H).

Scheme 5.5 Proposed process for the formation of the Co species observed by NMR (red) and EPR (blue) in the catalytic mixture in CD_3CN, before heating. R = Ph.

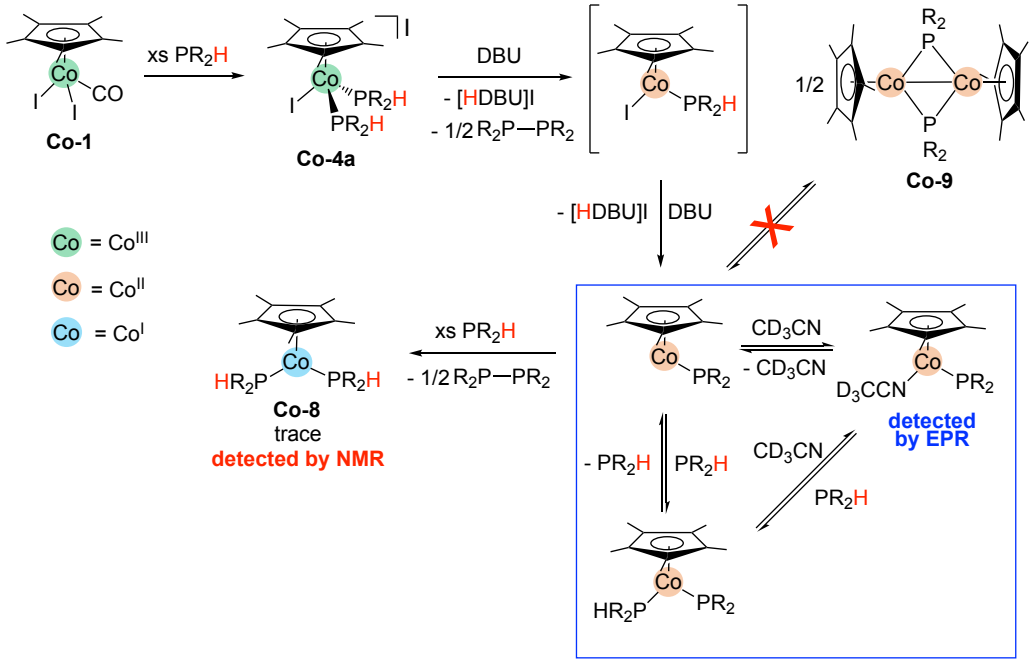

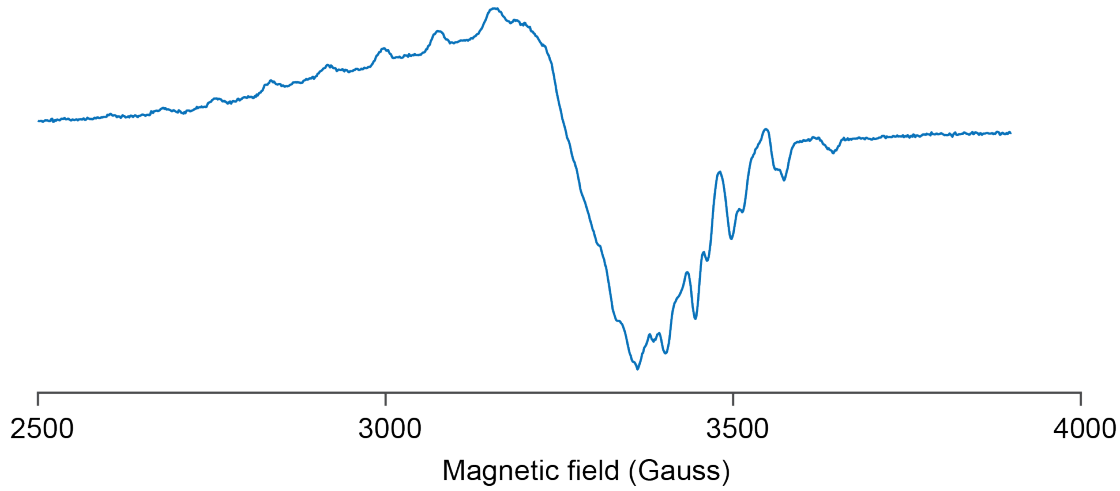

Figure 5.2 X-band EPR spectrum of the reaction of complex **Co-1** with 2 equiv of DBU in the presence of 10 equiv of PPh_2H. Measured in CD_3CN at ~20 mM concentration at 100 K with a microwave frequency of 9.39 GHz. Parameters used in preliminary simulation in EasySpin: $g_1 = 2.351$, $g_2 = 2.065$, $g_3 = 1.979$, $A_1(^{59}Co) = 80$ G, $A_3(^{59}Co) = 72$ G, $A_1(^{31}P) = 6$ G.

Co intermediates in the catalytic mixture after heating

After heating the mixture (in C_6D_6) at 80 °C for 1 h, the ^{31}P signals due to[Co(η^5-Cp*)(μ-PPh_2)]$_2$ (**Co-9**) disappeared in the ^1H and $^{31}P\{^1H\}$ NMR spectra, and the signals due to Co(η^5-Cp*)(PPh_2H)$_2$ (**Co-8**) and Ph_2P-PPh_2 slightly increased their intensity in the $^{31}P\{^1H\}$ NMR spectrum. This is consistent with the proposed binuclear reductive elimination (a similar process was described in Chapter 4) of the Cp*Co(II)-PPh_2 complex to give Ph_2P-PPh_2 and **Co-8** (Scheme 5.4, bottom left), which could shift the equilibrium (Scheme 5.4, bottom right) away from **Co-9**. After heating at 80 °C for 3 h, the signal due to **Co-8** disappeared; instead, the ^1H NMR spectrum (Figure 5.3) shows a set of diagnostic shifts assigned to a η^4-Cp*H ligand.[5–10] The new Co complex was tentatively assigned as [Co(η^4-Cp*H)(η^6-C_6D_6)]I (**[Co-10]I**). The assignment is mainly derived from the following evidence. First, there is no signal due to Co-P complexes observed in the $^{31}P\{^1H\}$

NMR spectrum. Second, sandwich Co analogues are well-established complexes in the literature.[11]

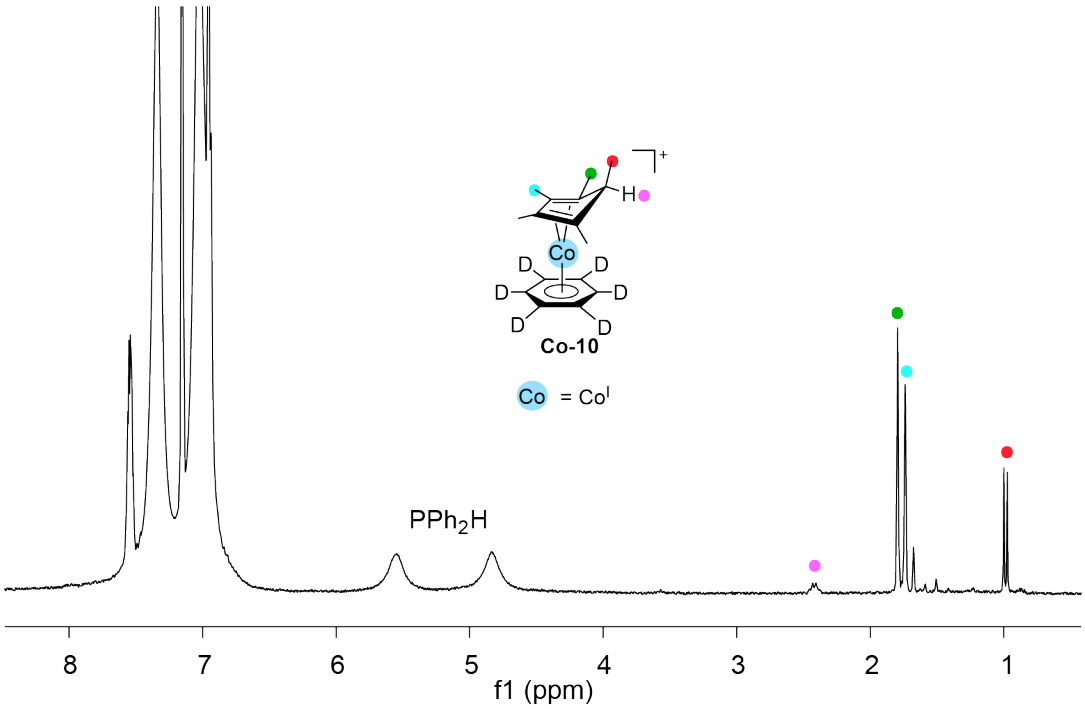

Figure 5.3 ^{1}H NMR (300.27 MHz, C_6D_6) spectrum of the dehydrocoupling reaction of PPh_2H using 10 mol% **Co-1** and 20 mol% DBU after heating 3 h, showing the formation of cationic **Co-10** fragment.

Heating the mixture (in CD_3CN) at 80 °C for 3 h gives a similar Co(I) complex Co(η^4-Cp*H)I(PPh_2H)$_2$ (**Co-11**, major) to **Co-10** and a new Co(III) hydride complex tentatively assigned as [Co(η^5-Cp*)H(PPh_2H)$_2$]I (**[Co-12]I**, minor), detected by ^{31}P{^{1}H} NMR (Figure 5.4). The identity of **Co-11** is confirmed by diagnostic signals due to the η^4-Cp*H ligand in the ^{1}H NMR spectrum (Figure 5.5). ESI-MS of an aliquot of this mixture also supports the assignment for **Co-11**. The *m/z* value (567.60) corresponds to a formula that is consistent with the fragment [Co(η^4-Cp*H)(PPh_2H)$_2$]$^+$ (calcd *m/z* 567.55). Complex **[Co-12]I** shows a diagnostic triplet (due to Co-H, couples to two P at PPh_2H ligands) at −14.0 ppm in the ^{1}H NMR spectrum (Figure 5.4 inset) due to the Co-H.

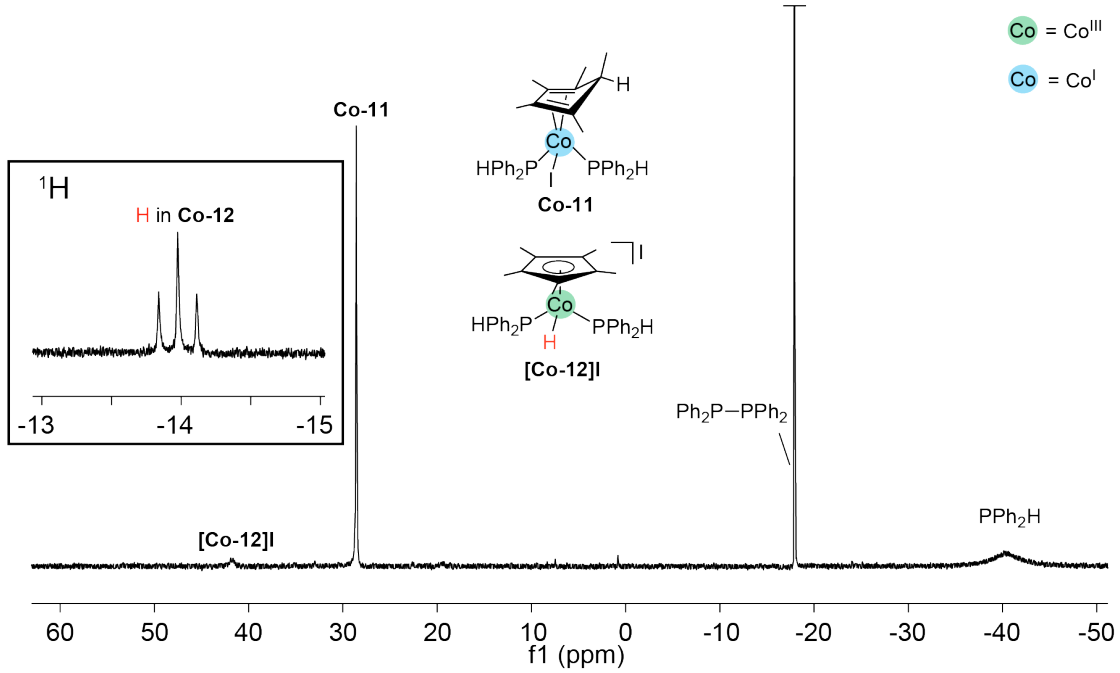

Figure 5.4 $^{31}P\{^{1}H\}$ NMR (121.55 MHz, CD_3CN) spectrum and partial ^{1}H NMR (300.27 MHz, CD_3CN, inset) spectrum of the dehydrocoupling reaction of PPh_2H using 10 mol% **Co-1** and 20 mol% DBU, after heating 3 h.

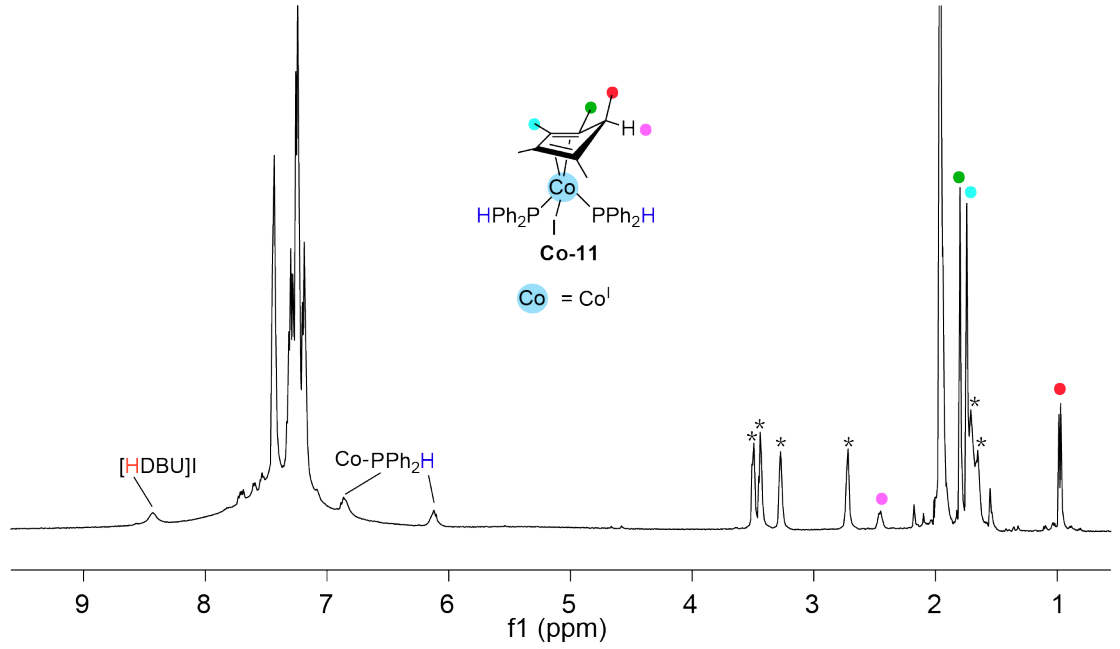

Figure 5.5 ^{1}H NMR (300.27 MHz, CD_3CN) spectrum of the dehydrocoupling reaction of PPh_2H using 10 mol% **Co-1** and 20 mol% DBU, after heating 3 h. Note: ⋆ signals due to [HDBU]I.

More evidence for the formation of the cation $[Co(\eta^5\text{-}Cp^*)H(PPh_2H)_2]^+$ (**Co-12**) comes from the dehydrocoupling reaction of PPh_2H using 10 mol% $[Co(\eta^5\text{-}Cp^*)(NCCH_3)_3][SbF_6]_2$ (**Co-5**) and 20 mol% DBU (Chapter 3). Unlike using **Co-1** as a catalyst, the catalytic mixture using **Co-5** shows a Co(III) hydride complex **[Co-12][SbF$_6$]** as the major Co species at RT, detected by ^1H and $^{31}P\{^1H\}$ NMR. Taking advantage of this long-lived hydride complex, I deliberately heated the catalytic mixture at 80 °C (Figure 5.6). This caused the irrevocable conversion of **[Co-12][SbF$_6$]** to a Co(I) complex $[Co(\eta^4\text{-}Cp^*H)(NCCH_3)(PPh_2H)_2][SbF_6]$, which is an analogue to **Co-11**.

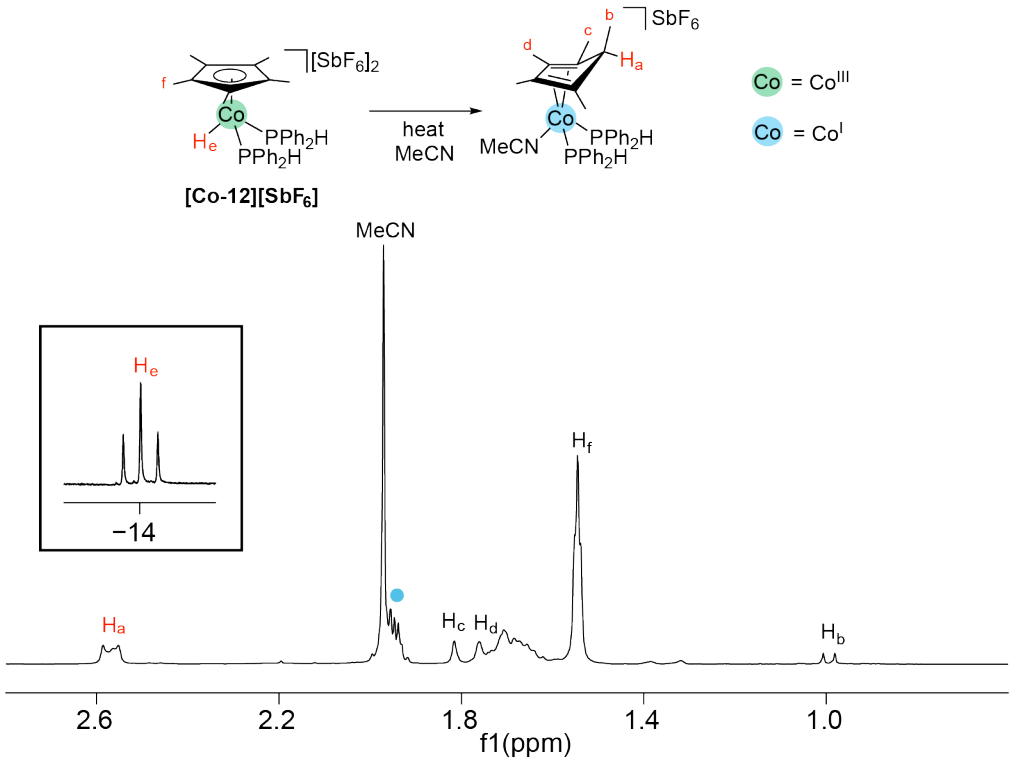

Figure 5.6 $^{31}P\{^1H\}$ NMR (121.55 MHz, CD_3CN) spectrum of the dehydrocoupling of PPh_2H using 10 mol% **Co-5** and 20 mol% DBU, after heating at 80 °C for 2 h. Residual proteo-solvent (•).

The fate of the Co complex in the catalytic mixture

Based on the Co intermediates identified above, I have proposed mechanisms for the dehydrocoupling reaction. In Chapter 4 (also shown in Scheme 5.6), I described a stepwise mechanism to give a Co(II)-PR_2 intermediate (for catalytic hydrophosphination) and a half equiv of diphosphine with respect to Co, from adding base to a Co(III)-PR_2H complex. In this section, I have evidence that this catalytic mixture for hydrophosphination is also important for the Co-catalyzed dehydrocoupling. The monomeric Co(II)-PR_2 was identified by EPR, which undergoes further binuclear reductive elimination to produce Ph_2P-PPh_2 and the Co(I) species (**Co-8** in the presence of PPh_2H). Complex **Co-8** is responsible for dehydrocoupling. As shown in Scheme 5.6, catalyst activation (to generate **Co-8**) produces a full equiv of Ph_2P-PPh_2 (corresponds to 20% PPh_2H consumption with 10 mol% Co loading) stoichiometrically in the base-mediated reaction.

Scheme 5.6 Stepwise mechanism for the formation of **Co-8** and **Co-9** in the base-mediated dehydrocoupling reaction of PPh_2H using **Co-1**. R = Ph.

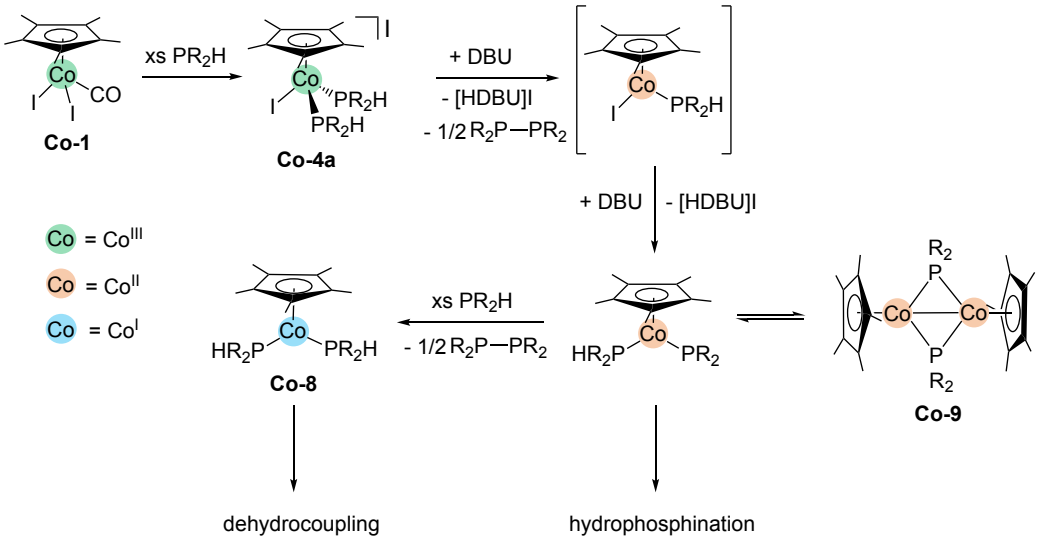

As shown in Scheme 5.7 step A, I propose that the protonation of complex **Co-8** *via* a proton (H^+) source could occur to form a monocationic Co(III) hydride intermediate (e.g. **[Co-12]X**, **X** = I or SbF_6). This is consistent with my observation of such intermediate in

the mixture. The origin of the H^+ in the proposed process may be from substrate PPh_2H or conjugate acid [HDBU]I. The reported pK_a(PPh_2H) vary from 21.7 (THF)[12] and 22.9 (calcd for DMSO),[13] to 38± 4 (THF).[14] The reported pK_a([HDBU]$^+$) range from 13.5 (H_2O)[15] and 16.9 (THF)[16] to 24.3 (CH_3CN).[17] Given that [HDBU]I appears to be more acidic than PPh_2H, it seems likely that the [HDBU]I serves as the primary H^+ source for this reaction ([HDBU]I is slightly more soluble in C_6D_6 at high temperatures than at RT).

Scheme 5.7 Proposed process for the formation of Co species involving protonation of the Co(I) fragment and subsequent proton transfer.

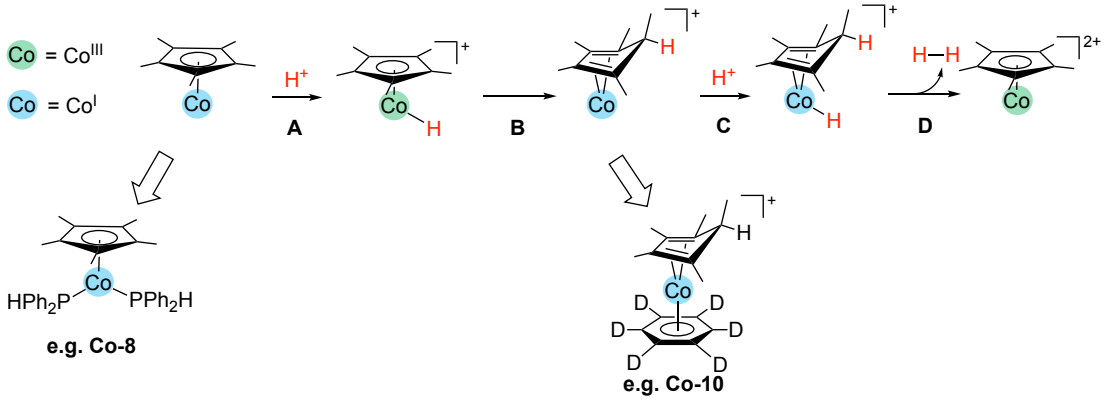

Co-C protonolysis *via* a Co(III)-H moiety occurs subsequently (Scheme 5.7, step B), which is supported by my control experiment above (Figure 5.6) and literature examples (Cp*-mediated proton transfer reported for Cp*Rh complexes[5–10]). This also explains the formation of the (η^4-Cp*H)Co complex (i.e. **[Co-10]I** or **Co-11**) in the reaction mixture. Such complex is analogous to that reported for a similar Rh species active for dehydrocoupling dimethylamine-borane.[5] It is also the only Co intermediate in the catalytic reaction because its amount is nearly identical to the quantity of precatalyst **Co-1** used. Thus, the (η^4-Cp*H)Co complex is proposed as the catalyst resting state. Thus, I propose that this complex undergoes a similar protonation pathway to produce H_2 (Scheme 5.7, steps C and D). Briefly, Co(I) is the source of electrons to turn two H^+ into one H_2.

5.2.2.2 Proposed mechanism for dehydrocoupling using Co-1 and DBU

Building on the steps proposed above, I propose a generic mechanism for the catalytic dehydrocoupling of PPh_2H using a Cp*Co(III) moiety and DBU (Scheme 5.8). The proposed cycle contains only the Cp*Co fragment rather than complete complex structures because: 1) I have no evidence that other ancillary ligands (e.g. I^-, solvent) participate directly in P-P bond and H-H bond formation, other than by filling empty coordination sites at Co; 2) it is unclear which ancillary ligand binds to the Co center during catalysis; those ligands are probably in equilibrium with each other; 3) using the simplified Cp*Co fragment helps focus on the actual impacts of the Cp*Co moiety on bond formation.

Scheme 5.8 Proposed catalytic cycle for dehydrocoupling PPh_2H using Cp*Co(III) and DBU.

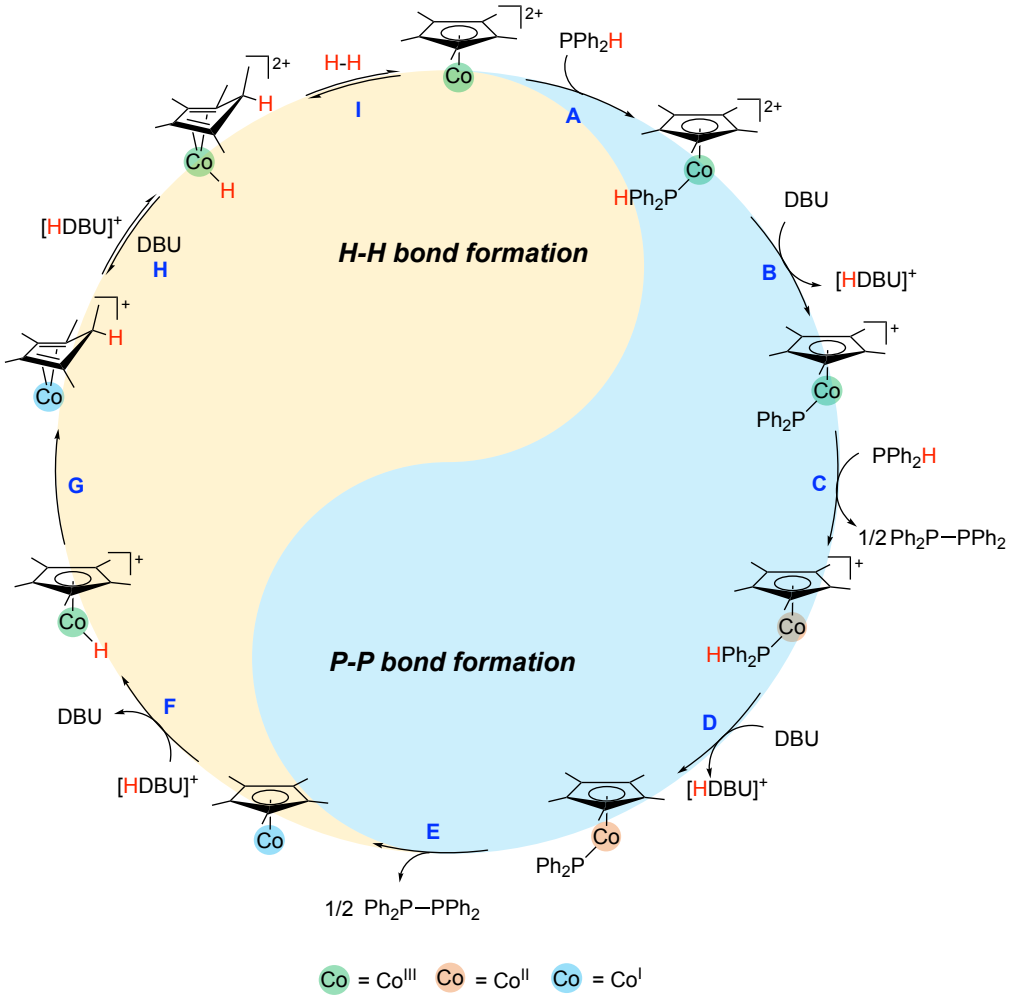

Steps A–E show that 1 equiv of Ph_2P-PPh_2 (i.e. 2 equiv of PPh_2H consumed) and 2 equiv of $[HDBU]^+$, with respect to Co, are produced by deprotonating coordinated PPh_2H twice with DBU while the Co(III) is reduced twice down to the Co(I). Steps A–D are consistent with the steps proposed for the Co-catalyzed hydrophosphination described in Chapter 4. In step E, the Co(II)-PPh_2 complex undergoes a binuclear reductive elimination to produce Ph_2P-PPh_2 and a Co(I) species.

The formation of H_2 in steps F–I is mainly based on literature examples of H-H bond formation proposed for other dehydrocoupling reactions (references see Section 5.2.2.1). The H^+ source in these steps is probably the conjugate acid (i.e. [HDBU]I) generated from

the previous deprotonations (steps B and D). Protonation of $[HDBU]^+$ (steps F and H) allows the formation of H_2 and regeneration of the base DBU and the original Co(III) catalyst. In short, DBU works as a "proton shuttle" for this reaction.

5.2.2.3 Dehydrocoupling of PPh_2H using 10 mol% of Co-1 alone

In Scheme 5.3b, the reaction without DBU shows $[Co(\eta^5\text{-}Cp^*)I(PPh_2H)_2]I$ (**Co-4a**) and $Co(\eta^5\text{-}Cp^*)I_2(PPh_2H)$ (**Co-2a**) are the major Co intermediates before heating, which is different from the reaction in the presence of DBU described above.

After the mixture is heated at 80 °C for 3 h, the $^{31}P\{^1H\}$ NMR spectrum of the catalytic mixture shows decreased intensity for signals due to **Co-2a** and **Co-4a** relative to the mixture before heating. After 24 h heating, most signals due to the Co disappeared in the ^1H and $^{31}P\{^1H\}$ NMR spectra, suggesting the formation of paramagnetic Co species in the catalytic mixture. Only a small amount of signals due to diamagnetic Co complexes is observed by NMR, which includes those due to $[Co(\eta^4\text{-}Cp^*H)(\eta^6\text{-}C_6D_6)]^+$ (**Co-9**) and **Co-4a**.

This non-base-mediated dehydrocoupling reaction shows more unidentified paramagnetic Co species than the base-mediated reaction. Thus, the catalytic cycle for this "base-free" reaction is not proposed. However, this reaction indicates that P-H activation must occur between Cp*Co(III) complexes and free substrate PPh_2H. Detailed investigations of this possible P-H activation mechanism are presented in Chapter 6.

5.3 Using hydrogen acceptors (HAs) in catalytic dehydrocoupling using Co-1

5.3.1 Screening for the optimal HA for Co-catalyzed dehydrocoupling of PPh_2H

Considering the thermodynamic issue for dehydrocoupling described above, I explored the impact of using hydrogen acceptors (HAs) to facilitate dehydrocoupling reactions (Scheme 5.9). These HAs have been employed in catalytic dehydrocoupling systems. Most HAs are unsaturated species that can potentially undergo hydrophosphination with PPh_2H and hydrogenation of the generated H_2. I chose the non-base mediated reaction (Scheme 5.3b) for the screening reactions with HAs because: 1) including both DBU and HA in the mixture would complicate the investigation; 2) Co(η^5-Cp*)I_2(CO) (**Co-1**) exhibits catalytic activity at high temperatures without DBU. Notably, DBU cannot act as an HA for the catalytic dehydrocoupling reaction. This result is consistent with the proposed cycle for the base-mediated dehydrocoupling (Scheme 5.8), in which DBU works as a proton shuttle rather than an HA.

Scheme 5.9 Screening of different hydrogen acceptors (HAs) in the dehydrocoupling reactions of PPh_2H using 10 mol % **Co-1**.[a]

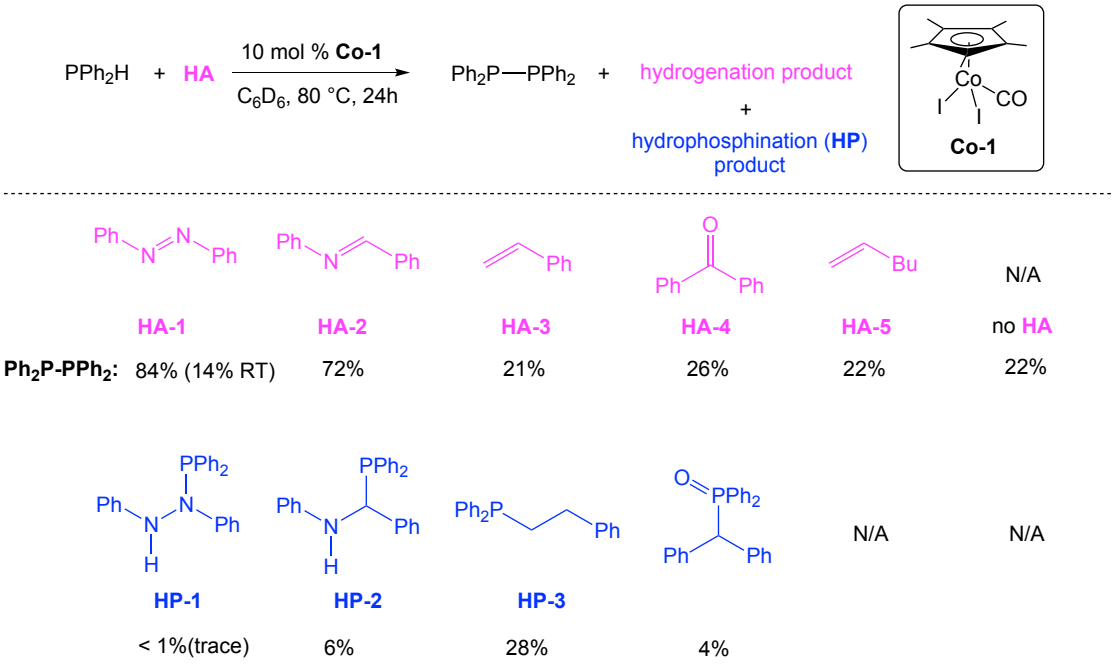

[a]0.3 M [PPh_2H], [**HA**]. Conversions (%) determined by non-quantitative $^{31}P\{^1H\}$ NMR experiments (121.55 MHz, RT) from relative integration of ^{31}P signals for Ph_2P-PPh_2 and free PPh_2H. Other signals appeared in the region due to Co-P-containing complexes.

The tested HAs exhibit markedly varied behaviours in this catalytic reaction. Azobenzene (**HA-1**) and *N*-benzylideneaniline **(HA-2**) are more effective than other HAs in the dehydrocoupling reaction. Scheme 5.9 shows that azobenzene (**HA-1**) is the most effective HA for the reaction at 80 °C. **HA-1** also remains effective at RT, but at a much slower rate. *N*-benzylideneaniline **(HA-2**) is quite effective, but it results in more hydrophosphination products (i.e. Ph_2P-CHPh-NHPh) than **HA-1**. A hydrophosphination product observed in the reaction of styrene (**HA-3**) comes from a thermal background hydrophosphination reaction at high temperatures, which is confirmed by the control experiment of just styrene and PPh_2H under the same conditions. Along with the hydrophosphination product, ethylbenzene is detected by ^1H NMR, demonstrating that styrene does function as an HA. Benzophenone (**HA-4**) only slightly facilitates the

dehydrocoupling reaction. In addition, a phosphine oxide $P(O)Ph_2(CH(Ph)_2)$ (^{31}P δ 30.7 ppm) is observed in the reaction with **HA-4**. The assignment for this phosphine oxide is based on its comparable ^{31}P shift reported in the literature.[18] The formation of phosphine oxide could result from a rearrangement of the hydrophosphination product $Ph_2P\{OC(H)Ph_2\}$. 1-Hexene (**HA-5**) does not act as a HA for this reaction.

5.3.2 Phosphine substrate scope in catalyzed dehydrocoupling using 10 mol% Co-1 in the presence of HA-1

I chose to employ the more efficient azobenzene (**HA-1**) to investigate the substrate phosphine scope for our Co-mediated dehydrocoupling system. As shown in Scheme 5.10, complex $Co(\eta^5\text{-}Cp^*)I_2(CO)$ (**Co-1**) acts as a catalyst, whereas **HA-1** is a stoichiometric additive to the substrate phosphine (**HA-1**: phosphine = 1: 1). **Co-1** is active for dehydrocoupling reactions of secondary and primary phosphines (PR_2H and PRH_2) with **HA-1** (Scheme 5.10).

Scheme 5.10 Substrate phosphine scope for the dehydrocoupling reactions using 10 mol % **Co-1** in the presence of **HA-1**.[a]

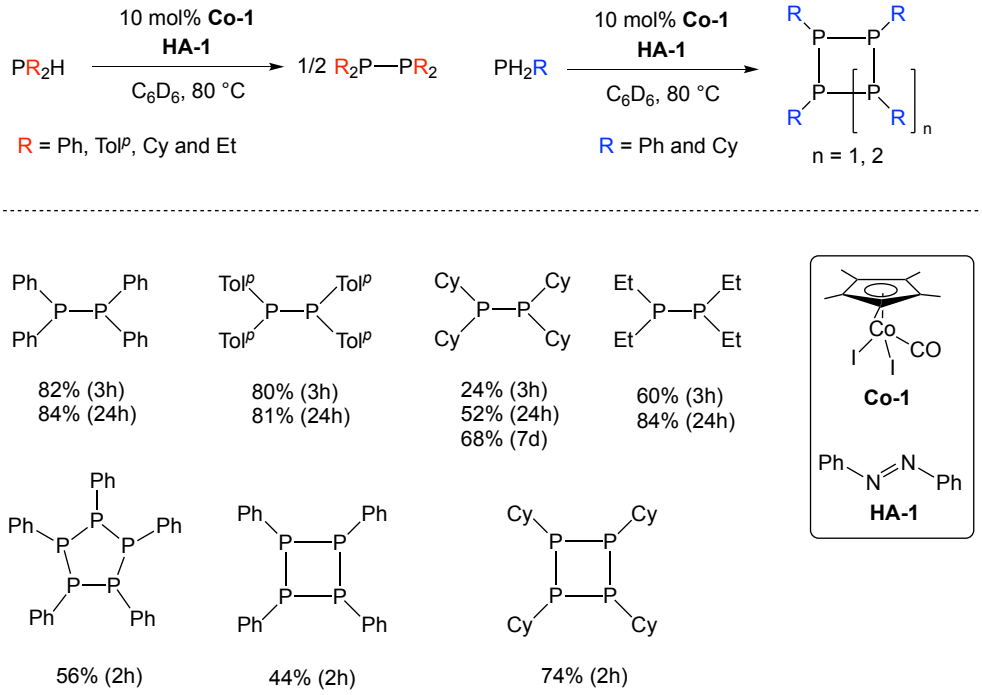

[a]0.3 M [PPh_2H], [**HA-1**]. Conversions (%) determined by non-quantitative $^{31}P\{^1H\}$ NMR experiments (121.55 MHz, RT) from relative integration of ^{31}P signals for the dehydrocoupling products and free substrate phosphines. Other signals appeared in the region due to Co–P-containing complexes and minor byproducts (details in Appendix F).

In general, high activity is observed for substrate phosphines with aryl substituents (R = Ph, Tol^p) than those with alkyl substituents (R = Cy, Et) in these dehydrocoupling reactions (Scheme 5.10). The size of PR_2H also impacts the catalytic activity in our system. The reactions of $PTol^p{}_2H$ and PEt_2H give the corresponding R_2P-PR_2 in a comparable yield (R = Tol^p, Et, with cone angle 126° and 117° respectively) to PPh_2H after 24 h. However, under identical conditions, the reaction of bulky PCy_2H (cone angle 142°) only yields 52% of Cy_2P-PCy_2 after 24 h.

Compared to PR_2H, this Co system exhibits greater activity for PRH_2 (Scheme 5.10). The primary phosphines (R = Ph and Cy) are consumed completely in the dehydrocoupling reactions of PRH_2 in less than 2 h at 80 °C, giving some cyclic dehydrocoupling products.

For the reaction of $PPhH_2$, the cyclic products include $(PPh)_4$ and $(PPh)_5$. $(PCy)_4$ is the major product in the reaction of $PCyH_2$. Other transition metal catalysts are known to give these cyclic products,[19–22] but in these cases, prolonged reaction periods (1.5–4 days) and elevated temperatures (80–120 °C) are required to accomplish good conversions. Thus, our **Co-1** combined with an HA offers a rapid and straightforward method for synthesizing cyclopolyphosphines.

5.4 Conclusion

In this chapter, I showed that $Co(\eta^5\text{-}Cp^*)I_2(CO)$ (**Co-1**) is a competent catalyst for dehydrocoupling of PPh_2H with or without base (DBU) at a high temperature. For the base-mediated reaction, the observed product and catalyst speciation in the catalytic mixture suggests a mechanism involving Co(III), Co(II), and Co(I) species, along with requiring the participation of the Cp* ligand in the dihydrogen formation. One full equiv of diphosphine, with respect to Co, is formed stoichiometrically to give the active catalyst Co(I) complex. In the absence of base, the observed dehydrocoupling activity of **Co-1** indicates that P-H activation of substrate phosphines must occur at the Cp*Co(III) fragment. The investigation of this P-H activation is presented in Chapter 6.

Although a low K_{eq} for reversible dehydrocoupling of phosphines limits the product conversion, using hydrogen acceptors (HA), such as azobenzene (**HA-1**) and imines (i.e. **HA-2**), significantly facilitates the reactions.

5.5 Experimental

See Chapter 2, Section 2.5.1 for general experimental details**.** See Chapter 3, Section 3.6 for general instrumental/spectroscopic details**.** Complexes $[Co(\eta^4\text{-}Cp^*H)(\eta^6\text{-}C_6D_6)]I$

(**[Co-10]I**) and Co(η^4-Cp*H)I(PPh_2H)$_2$ (**Co-11**) were fully characterized by NMR spectroscopy. The ^{1}H, ^{31}P{^{1}H} and ^{13}C{^{1}H} NMR data for these complexes are summarized in Tables 5.2, 5.3 and 5.4. ^{1}H, ^{31}P{^{1}H} and ^{13}C{^{1}H} NMR spectra of these complexes are found in Appendix F. The dehydrocoupling products are known compounds, and their formation was confirmed based on the diagnostic ^{1}H and ^{31}P NMR shifts reported in the literature (*vide infra*). Conversions and product ratios were determined from the relative integrations of all products using non-quantitative ^{31}P{^{1}H} NMR. ^{1}H and ^{31}P{^{1}H} NMR spectra of the dehydrocoupling of different phosphines using 10 mol% Co(η^5-Cp*)I_2(CO) (**Co-1**) in the presence of azobenzene (**HA-1**) are presented in Appendix F.

5.5.1 General procedure for Co-catalyzed dehydrocoupling of PPh_2H.

Complex Co(η^5-Cp*)I_2(CO) (**Co-1**, 0.010–0.042 mmol, 5–20 mol%) was weighed into a glass vial and dissolved in the appropriate amount of solvent (C_6D_6 or CD_3CN) to give a volume of 0.5 mL (30 min). Neat PPh_2H (0.21 mmol, 39 mg) and DBU (0.021–0.084 mmol) were added to get a total volume of 0.7 mL. The reaction mixture was transferred to a J. Young NMR tube, and placed in an oil bath with a thermometer for heating at 80 °C (if needed). Initial ^{1}H and ^{31}P{^{1}H} NMR spectra could be obtained at RT within ~15 min.

NMR data for the product Ph_2P-PPh_2:

^{1}H NMR (500.27 MHz, CD_3CN) δ: 7.47–7.40 (m, 8H, H_{ortho}), 7.33–7.28 (m, 4H, H_{para}), 7.21–7.16 (m, 8H, H_{meta}).

^{31}P{^{1}H} NMR (202.51 MHz, CD_3CN) δ: –17.9 (s).

^{13}C{^{1}H} NMR (125.77 MHz, CD_3CN) δ: 136.5 (d, $^1J_{CP}$ = 5 Hz, C_{ipso}), 136.4 (d, $^1J_{CP}$ = 5 Hz, C_{ipso}), 135.0 (d, $^2J_{CP}$ = 13 Hz, C_{ortho}), 134.9 (d, $^2J_{CP}$ = 13 Hz, C_{ortho}), 129.8 (s, C_{para}), 129.2 (d, $^3J_{CP}$ = 3 Hz, C_{meta}) 129.1 (d, $^3J_{CP}$ = 3 Hz, C_{meta}).

These NMR data are consistent with the literature.[23,24]

5.5.2 General procedure for Co-catalyzed dehydrocoupling of phosphines in the presence of hydrogen acceptors (HAs)

Complex Co(η^5-Cp*)I_2(CO) (**Co-1**, 0.021 mmol, 10 mg) was accurately weighed into a small glass vial, and C_6D_6 (0.5 mL) was added. Neat primary or secondary phosphine (0.21 mmol) and the corresponding hydrogen acceptor (0.21 mmol) were added to give a total volume of 0.7 mL. The reaction mixture was transferred to a J. Young NMR tube, and placed in an oil bath with a thermometer for heating at 80 °C (if needed). Initial ^{1}H and ^{31}P{^{1}H} NMR spectra could be obtained at RT within ~15 min.

5.5.3 NMR data for Co complexes Co-10, Co-11 and [Co-12]I

Table 5.2 ^{1}H NMR (500.27 MHz, C_6D_6 or CD_3CN) data of complexes **Co-10**, **Co-11** and **[Co-12]I**: δ in ppm (multiplicity, J or $\omega_{1/2}$ in Hz, RI)

Complex	Cp*H and/or Cp*Co-H	PPh_2H
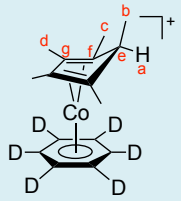 **Co-10** C_6D_6	**H_a** 2.42 (t, 7.6, 1H), **H_c** 1.80 (s, 6H), **H_d** 1.74 (s, 6H), **H_b** 0.99 (d, 7.6, 3H)	N/A
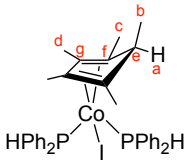 **Co-11** CD_3CN	**H_a** 2.46 (t, 8.2, 1H), **H_c** 1.80 (s, 6H,), **H_d** 1.74 (s, 6H), **H_b** 0.99 (d, 7.6, 3H).	**H-PPh_2** 6.49 (d, 367.9, 2H) **Ph:** 7.37–7.14 (m, overlapping with signal due to PPh_2H and PPh_2-PPh_2, 20H).
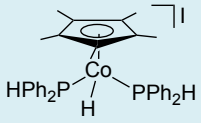 **[Co-12]I** CD_3CN	**CH_3** 1.55 (s, 15H) **Co-H** −13.97 (t, 68.2, 1H)	Not observed. [a]

[a]Since only a trace amount of **Co-8** was observed in the reaction mixture, I was able to assign only some signals due to it.

Table 5.3 $^{31}P\{^{1}H\}$ NMR (202.51 MHz, C_6D_6 or CD_3CN) data of complexes **Co-10**, **Co-11** and **[Co-12]I**: δ in ppm (multiplicity).

Complex	δ ^{31}P
Co-10 C_6D_6	N/A
Co-11 CD_3CN	28.6(s)
[Co-12]I CD_3CN	41.6 (s)

Table 5.4 $^{13}C\{^{1}H\}$ NMR (125.77 MHz, C_6D_6 or CD_3CN) data of complexes **Co-10**, **Co-11** and **[Co-12]I**: δ in ppm (multiplicity, J or $\omega_{1/2}$ in Hz).

Complex	Cp*H	PPh_2H
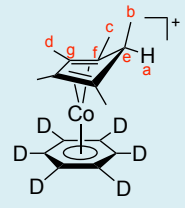 **Co-10** C_6D_6	**C_f** 137.5 (s), **C_g** 134.2 (s, overlapping with signal due to PPh_2H), **C_g** 128.2 (t, 24, overlapping with signal due to solvent), **C_e** 51.8 (s), **C_b** 14.3 (s), **C_c** 11.8 (s), **C_d** 11.3 (s)	N/A
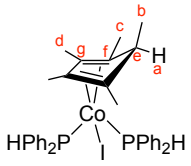 **Co-11** CD_3CN	**C_f** 138.4 (s), **C_g** 134.8 (s), **C_e** 52.0 (s), **C_b** 14.2 (s), **C_c** 11.5 (s), **C_d** 11.0 (s)	**C_o** 133.4 (d, 5), 133.3 (d, 5), **C_p** 131.6 (s), **C_m** 129.9 (d, 3), 129.8 (d, 3), **C_{ipso}** not observed.
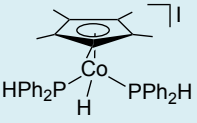 **[Co-12]I** CD_3CN	**C_{ring}** 98.2 (s), **CH_3** 9.8 (s)	Not observed. [a]

[a]Since only a trace amount of **Co-8** was observed in the reaction mixture, I was able to assign some signals due to it.

5.5.4 $^{31}P\{^{1}H\}$ NMR data for diphosphines and other P-containing products.

The dehydrocoupling products are known compounds with identical NMR data in the literature (see references in Table 5.5). For these compounds, I did not perform complete spectroscopic characterization of them. Only partial NMR characterization was possible

for trace amounts of other products resulting from the dehydrocoupling reactions in the presence of HA (Table 5.6) because of their low concentration in the reaction mixtures.

Table 5.5 $^{31}P\{^{1}H\}$ NMR (121.55 MHz, C_6D_6) data for P-P coupling products (diphosphines and polyphosphines): δ (ppm) (multiplicity, J in Hz).

Entry	P-P coupling products	δ ^{31}P	Reference
1	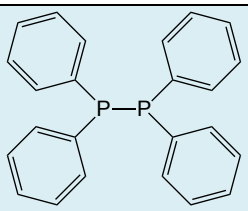	–14.6 (s)	Neumüller 1999[24] Brookhart 2001[23] Webster 2015[19]
2	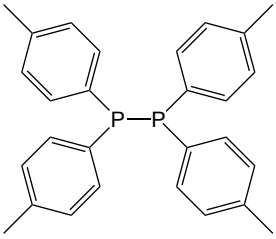	–17.6 (s)	Webster 2015[19]
3	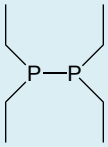	–33.2 (s)	Binder 1967[25] Zarkadas 1972[26] Brookhart 2001[23]
4	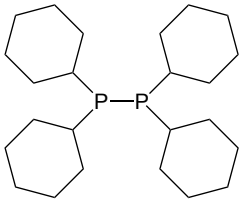	–21.7 (s)	Erker 2009[27]
5	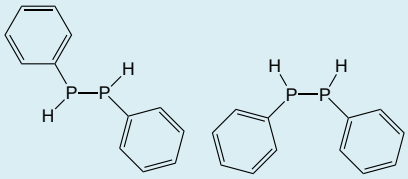	–66.9 (s, *rac*), –66.4 (s, *meso*)	Brookhart 2001[23] Waterman 2007[20]
6	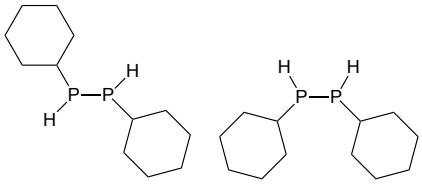	–88.1 (s, *rac*), –84.9 (s, *meso*)	Waterman 2007[20] Wright 2010[28]
7	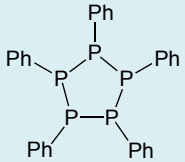	–1.4 ~ –6.2 (m)	Manners 2019[4] Webster 2021[29]

8	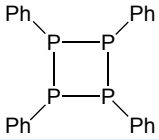	–48.2 (s)	Webster 2021[29]
9	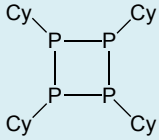	–68.0 (s)	Manners 2019[4] Webster 2021[29]
10	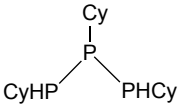	31.9 (t, $^{1}J_{PP}$ 139 , PCy), –54.3 (d, $^{1}J_{PP}$ 139, PCyH)	N/A (weak intensity in the NMR, not fully characterized)

Table 5.6 $^{31}P\{^{1}H\}$ NMR (121.55 MHz, C_6D_6) data for products containing P-N and P-C bonds observed in the catalytic dehydrocoupling reactions in the presence of HAs: δ (ppm) (multiplicity).

Entry	Coupling products	δ ^{31}P	Reference
1	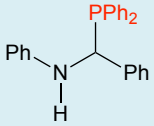	5.1 (s)	Manners 2019[4]
2	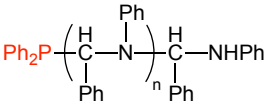 n = 1, 2, …	–1.5 ~ –10.4 (m)	Tentative assignment based on similar Δ^{31}P shift between HP product and P-capped telomers
3	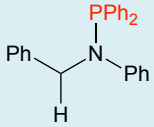	35.5 (s)	Walker 1970[30] (no ^{31}P shift reported)
4	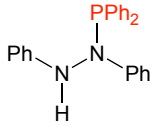	61.9 (s)	Kornev 2004[31] Manners 2019[4]
5	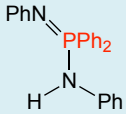	–6.6 (s)	Kornev 2004[31]
6	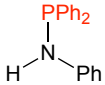	28.4 (s)	Manners 2019[4]
7	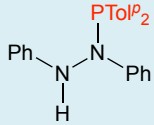	61.9 (s)	Based on entry 4 (comparable ^{31}P shift for Ph analogue)
8	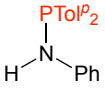	26.5 (s)	Based on entry 6 (comparable ^{31}P shift for Ph analogue)

9	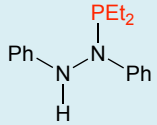	67.9 (s)	Based on entry 4 (comparable ^{31}P shift for Ph analogue)
10	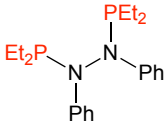	90.0(s)	based on the analogous products reported by Kornev 2009[32]
11	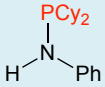	41.2(s)	Based on entry 6 (comparable ^{31}P shift for Ph analogue)
12	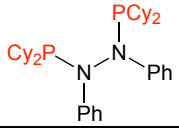	101.4(s)	See entry 10

5.7 References

(1) Hirano, K.; Miura, M. Recent Advances in Diphosphination of Alkynes and Alkenes. *Tetrahedron Lett.* **2017**, *58*, 4317–4322.

(2) John Emsley; Dennis Hall. *The Chemistry of Phosphorus.*; London, 1976.

(3) Cowley, A. H. The Chemistry of the Phosphorus-Phosphorus Bond. *Chem. Rev.* **1965**, *65*, 617–634.

(4) Wu, L.; Annibale, V. T.; Jiao, H.; Brookfield, A.; Collison, D.; Manners, I. Homo- and Heterodehydrocoupling of Phosphines Mediated by Alkali Metal Catalysts. *Nat. Commun.* **2019**, *10*, 2786.

(5) Pal, S.; Kusumoto, S.; Nozaki, K. Dehydrogenation of Dimethylamine-Borane Catalyzed by Half-Sandwich Ir and Rh Complexes: Mechanism and the Role of Cp* Noninnocence. *Organometallics* **2018**, *37*, 906–914.

(6) Peng, Y.; Ramos-Garcés, M. V.; Lionetti, D.; Blakemore, J. D. Structural and Electrochemical Consequences of [Cp∗] Ligand Protonation. *Inorg. Chem.* **2017**, *56*, 10824–10831.

(7) Johnson, S. I.; Gray, H. B.; Blakemore, J. D.; Goddard, W. A. Role of Ligand Protonation in Dihydrogen Evolution from a Pentamethylcyclopentadienyl Rhodium Catalyst. *Inorg. Chem.* **2017**, *56*, 11375–11386.

(8) Quintana, L. M. A.; Johnson, S. I.; Corona, S. L.; Villatoro, W.; Iii, W. A. G.; Takase, M. K.; Vandervelde, D. G.; Winkler, J. R.; Gray, H. B.; Blakemore, J. D. Proton-Hydride Tautomerism in Hydrogen Evolution Catalysis. *Proc. Natl. Acad. Sci. U. S. A.* **2016**, *113*, 6409–6414.

(9) Pitman, C. L.; Finster, O. N. L.; Miller, A. J. M. Cyclopentadiene-Mediated Hydride Transfer from Rhodium Complexes. *Chem. Commun.* **2016**, *52*, 9105–9108.

(10) Lo, H. C.; Leiva, C.; Buriez, O.; Kerr, J. B.; Olmstead, M. M.; Fish, R. H. Bioorganometallic Chemistry. 13. Regioselective Reduction of NAD+ Models, 1-Benzylnicotinamde Triflate and B-Nicotinamide Ribose-5′-Methyl Phosphate, with in Situ Generated $[Cp^*Rh(Bpy)H]^+$: Structure-Activity Relationships, Kinetics, and Mechanistic Aspect. *Inorg. Chem.* **2001**, *40*, 6705–6716.

(11) Loginov, D. A.; Shul'pina, L. S.; Muratov, D. V.; Shul'pin, G. B. Cyclopentadienyl Cobalt(III) Complexes: Synthetic and Catalytic Chemistry. *Coord. Chem. Rev.* **2019**, *387*, 1–31.

(12) Issleib, K.; Kümmel, R. Alkali-Phosphorverbindungen Und Ihr Reaktives Verhalten: XXX. Zur P-H- Und As-H-Acidität Primärer Und Sekundärer Phosphine Bzw. Arsine. *J. Organomet. Chem.* **1965**, *3*, 84–91.

(13) Li, J. N.; Liu, L.; Fu, Y.; Guo, Q. X. What Are the PKa Values of Organophosphorus Compounds? *Tetrahedron* **2006**, *62*, 4453–4462.

(14) Sues, P. E.; Lough, A. J.; Morris, R. H. Reactivity of Ruthenium Phosphido Species Generated through the Deprotonation of a Tripodal Phosphine Ligand and Implications for Hydrophosphination. *J. Am. Chem. Soc.* **2014**, *136*, 4746–4760.

(15) Kaupmees, K.; Trummal, A.; Leito, I. Basicities of Strong Bases in Water: A Computational Study. *Croat. Chem. Acta* **2014**, *87*, 385–395.

(16) Kaljurand, I.; Rodima, T.; Pihl, A.; Mäemets, V.; Leito, I.; Koppel, I. A.; Mishima, M. Acid-Base Equilibria in Nonpolar Media. 4. Extension of the Self-Consistent Basicity Scale in THF Medium. Gas-Phase Basicities of Phosphazenes. *J. Org. Chem.* **2003**, *68*, 9988–9993.

(17) Kaljurand, I.; Kütt, A.; Sooväli, L.; Rodima, T.; Mäemets, V.; Leito, I.; Koppel, I. A. Extension of the Self-Consistent Spectrophotometric Basicity Scale in Acetonitrile to a Full Span of 28 PKa Units: Unification of Different Basicity Scales. *J. Org. Chem.* **2005**, *70*, 1019–1028.

(18) Sha, S. C.; Zhang, J.; Carroll, P. J.; Walsh, P. J. Raising the p K a Limit of "Soft" Nucleophiles in Palladium-Catalyzed Allylic Substitutions: Application of Diarylmethane Pronucleophiles. *J. Am. Chem. Soc.* **2013**, *135*, 17602–17609.

(19) King, A. K.; Buchard, A.; Mahon, M. F.; Webster, R. L. Facile, Catalytic Dehydrocoupling of Phosphines Using β-Diketiminate Iron(II) Complexes. *Chem. – Eur. J.* **2015**, *21*, 15960–15963.

(20) Waterman, R. Selective Dehydrocoupling of Phosphines by Triamidoamine Zirconium Catalysts. *Organometallics* **2007**, *26*, 2492–2494.

(21) Masuda, J. D.; Hoskin, A. J.; Graham, T. W.; Beddie, C.; Fermin, M. C.; Etkin, N.; Stephan, D. W. Catalytic P-H Activation by Ti and Zr Catalysts. *Chem. – Eur. J.* **2006**, *12*, 8696–8707.

(22) Fermin, M. C.; Stephan, D. W. Catalytic Oligomerization of Primary Phosphines by the Anionic Zirconocene Trihydride: $[Cp^*_2ZrH_3]^-$. *J. Am. Chem. Soc.* **1995**, *117*, 12645–12646.

(23) Böhm, V. P. W.; Brookhart, M. Dehydrocoupling of Phosphanes Catalyzed by a Rhodium(I) Complex. *Angew. Chem. Int. Ed.* **2001**, *40*, 4694–4696.

(24) Dashti-Mommertz, A.; Neumüller, B. Gallium and Indium Arsanido Metalates: Compounds Derived from the Zinc Blende and Wurtzite Structure. *Z. Anorg. Allg. Chem.* **1999**, *625*, 954–960.

(25) Fluck, E.; Binder, H. Chemische Reaktionen Der Perthiophosphonsäureanhydride. *ZAAC - J. Inorg. Gen. Chem.* **1967**, *354*, 113–129.

(26) Baudler, M.; Zarkadas, A. Beiträge Zur Chemie Des Phosphors, 48 Darstellung von Tetraorganyldiphosphanen Und Quecksilber-bis(Di-tert-butylphosphid). *Chem. Ber.* **1972**, *105*, 3844–3849.

(27) Spannhoff, K.; Kuhl, N.; Kehr, G.; Fröhlich, R.; Erker, G. Remarkable Product Diversity in the "Self-Organized" Reaction of Deprotonated Acetonitrile with Chlorophosphines. *J. Am. Chem. Soc.* **2009**, *131*, 17836–17842.

(28) Naseri, V.; Less, R. J.; Mulvey, R. E.; McPartlin, M.; Wright, D. S. Stoichiometric and Catalytic Sn-Mediated Dehydrocoupling of Primary Phosphines. *Chem. Commun.* **2010**, *46*, 5000–5002.

(29) Barrett, A. N.; Woof, C. R.; Goult, C. A.; Gasperini, D.; Mahon, M. F.; Webster, R. L. Hydrogen/Halogen Exchange of Phosphines for the Rapid Formation of Cyclopolyphosphines. *Inorg. Chem.* **2021**, *60*, 16826–16833.

(30) Nelson, J.; Spratt, R.; Walker, B. J. The Effect of Phosphorus Lone Pair Orientation on P-N-C-H Coupling Constants in Aminophosphines. *J. Chem. Soc. D Chem. Commun.* **1970**, No. 22, 1509–1510.

(31) Fedotova, Y. V.; Kornev, A. N.; Sushev, V. V.; Kursky, Y. A.; Mushtina, T. G.; Makarenko, N. P.; Fukin, G. K.; Abakumov, G. A.; Zakharov, L. N.; Rheingold, A. L. Phosphinohydrazines and Phosphinohydrazides M(-N(R)-N(R) -PPh_2)n of Some

Transition and Main Group Metals: Synthesis and Characterization. Rearrangement of Ph_2P-NR-NR- Ligands into Aminoiminophosphorane, RN=PPh_2-NR-, and Related Chemistry. *J. Organomet. Chem.* **2004**, *689*, 3060–3074.

(32) Kornev, A. N.; Belina, N. V.; Sushev, V. V.; Fukin, G. K.; Baranov, E. V.; Kurskiy, Y. A.; Poddelskii, A. I.; Abakumov, G. A.; Lönneeke, P.; Hey-Hawkins, E. The First Structurally Characterized Metal (κ^2 N, P)-Phosphinohydrazides: The Key to Understanding the Intramolecular Rearrangement R_2P-NR′-NR′-M → R′N = PR_2-NR′-M. Metalloderivatives of Diisopropylphosphinohydrazines: Synthesis and Properties. *Inorg. Chem.* **2009**, *48*, 5574–5583.

6. Investigation of Cp*Co(III) complexes in non-base-mediated P-H activation

As described in Chapter 3, complexes Co(η^5-Cp*)I_2(CO) (**Co-1**) and [Co(η^5-Cp*)$(NCCH_3)_3$][SbF_6]$_2$ (**Co-5**) exhibit an intriguing interaction with excess PPh_2H (without base), probably involving a P-H activation process. This P-H activation could also be relevant to the activity of **Co-1** for catalytic dehydrocoupling of phosphines (Chapter 5). Complex **Co-5** is considered as a simplified $[Cp^*Co(III)]^{2+}$ fragment relative to **Co-1**, which allows us to investigate this P-H activation of PPh_2H at the Cp*Co(III) center more easily. In this chapter, I use various analytic techniques to gather evidence for the Cp*Co(III) mediated P-H activation at **Co-5** in the presence of excess PPh_2H (Section 6.2). Based on these results, two proposed mechanisms involving paramagnetic Co intermediates are presented in Section 6.3. This chapter includes contributions from Dr. Anuj Joshi (a former Ph.D. student in the group of Prof. Scott McIndoe) and Dr. Charles Walsby (EPR spectroscopy, SFU).

6.1 Introduction

Catalytic routes to new carbon-element (C-E, E = main group element) bonds play an important role in state-of-the-art synthetic organic chemistry. They often involve E-H activation of the substrates. Examples include E-H hydroboration (E = B), hydrosilylation (E = Si), hydroamination (E = N) and hydrophosphination (E = P). E-H activation is also important in catalytic dehydrocoupling of first- and second-row main group elements (E = B, N, Al, Si, P, S) to give main group E-E and E-E' bonds. Using dehydrocoupling for synthesizing main group molecules and materials with homo or hetero element-element

(E-E or E-E′) bonds has a substantial recent impact in some areas, such as hydrogen storage and transfer, and the synthesis of functional inorganic polymers.[1]

A mechanistic study is important since it can guide us to discover and use transition metal-mediated E-H activation reactions more effectively. For example, transition metal-mediated P-H bond activation is essential in metal-catalyzed transformations involving P-C and P-P bond formation, such as hydrophosphination[2] and dehydrocoupling.[3–5] However, P-H activation is less studied than other E-H activations (E = Si, N and O). For example, well-established catalytic hydrosilylation is a common synthetic technique,[6] but catalytic hydrophosphination is still not routinely used in phosphine synthesis.[7]

The great majority of transition metal-mediated P-H activation includes the generation of M-PR_2 (metal phosphido) intermediates in which the phosphido ligands serve as nucleophilic and basic anions (PR_2^-). The standard mechanisms of forming metal phosphido have been described in Chapter 1 (shown again in Scheme 6.1).

Scheme 6.1 Transition metal-mediated P-H activation giving a metal phosphido intermediate.

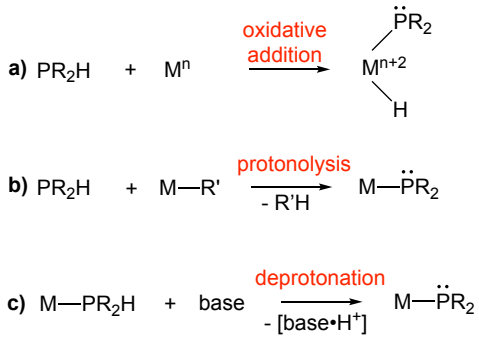

However, transition metal-mediated P-H activation could also occur through hydride (H^-) or hydrogen atom (H•) abstraction, owing to the comparable Pauling electronegativities of hydrogen and phosphorus (2.20 and 2.19, respectively).[8] For example, a notable example of reversible hydride abstraction from the coordinated PR_2H

was reported (Scheme 6.2a).[9] Our group also reported the synthesis of novel molybdenum phosphenium complexes *via* hydride abstraction (Scheme 6.2b).[10]

Scheme 6.2 Transition metal-mediated P-H activation *via* hydride (H^-) abstraction.

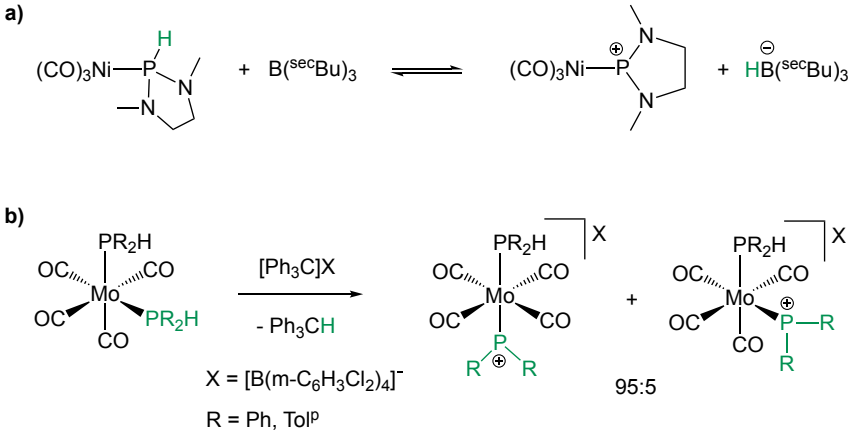

Another fascinating area is transition metal-mediated homolytic P-H cleavage. Transition metal-mediated E-H homolytic cleavage (E = O, N) is well established in the context of proton-coupled electron transfer (PCET) in the physical organic and bioinorganic chemistry communities.[11] Although metal-free homolytic P-H cleavage has been known since the early 1950s (see Chapter 1),[12] there are just a few transition metal-mediated examples (Scheme 6.3).[13,14] Scheme 6.3a shows an example of H-atom abstraction from a coordinated phosphine.[13] When a hydrogen atom transfer (HAT) reagent TEMPO was added to a tungsten complex $W(CO)_5(PPh_2H)$, a metal phosphinyl intermediate formed quickly in solution, but this reactive species subsequently rapidly coupled with unreacted TEMPO to form the P-O bound adduct. An apparent example of transition metal-mediated homolytic P-H cleavage is shown in Scheme 6.3b: a Ni(I) dimer reacts with $PPhH_2$ to form a Ni(II) hydride (PNP)Ni-H and a Ni(II) phosphido (PNP)Ni-PHPh, referred to as a binuclear oxidation addition that may involve radical intermediates.[14]

Scheme 6.3 Examples of transition metal-mediated homolytic P-H cleavage.

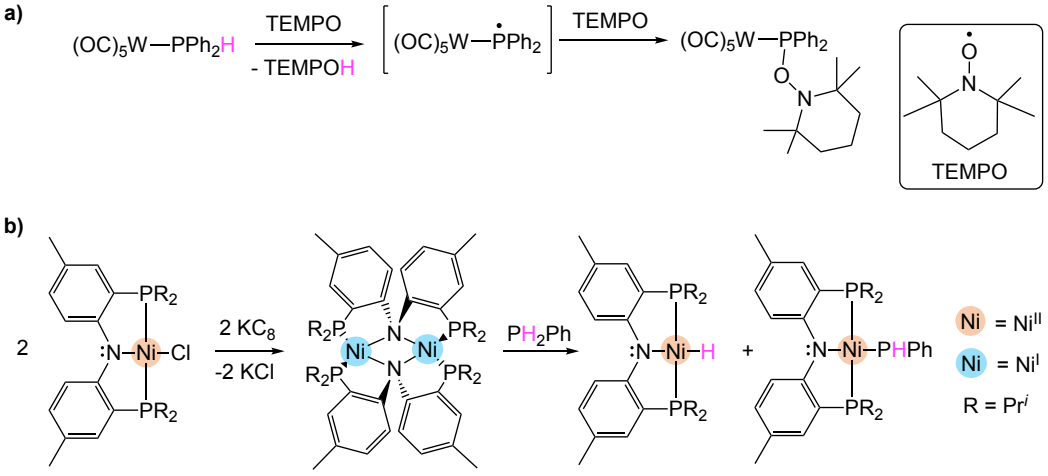

As mentioned in Chapter 3, NMR spectra reveal an odd phenomenon in mixtures of Co(η^5-Cp*)I_2(CO) (**Co-1**) or [Co(η^5-Cp*)$(NCCH_3)_3$][SbF_6]$_2$ (**Co-5**) in the presence of excess PPh_2H (see an example in Figure 6.1): the ^{31}P signals due to the free PR_2H are broad at RT. Notably, the $^1J_{PH}$ coupling (normally >200 Hz) for free PR_2H is absent in ^{1}H and ^{31}P NMR spectra. These features suggest that reversible P-H activation of free PPh_2H occurs rapidly on the NMR time scale. As shown in Scheme 6.1a, oxidative addition of the P-H bond increases the metal oxidation state by two units (+2). However, the Cp*Co(III) fragment seems to be incompatible with oxidation to Cp*Co(V), as evidenced by the absence of oxidation to Co(V) species observed in CV experiments (Section 3.4.4, Chapter 3). Thus, the behaviour of this mixture is of interest since it appears to involve some new type of reversible P-H bond cleavage.

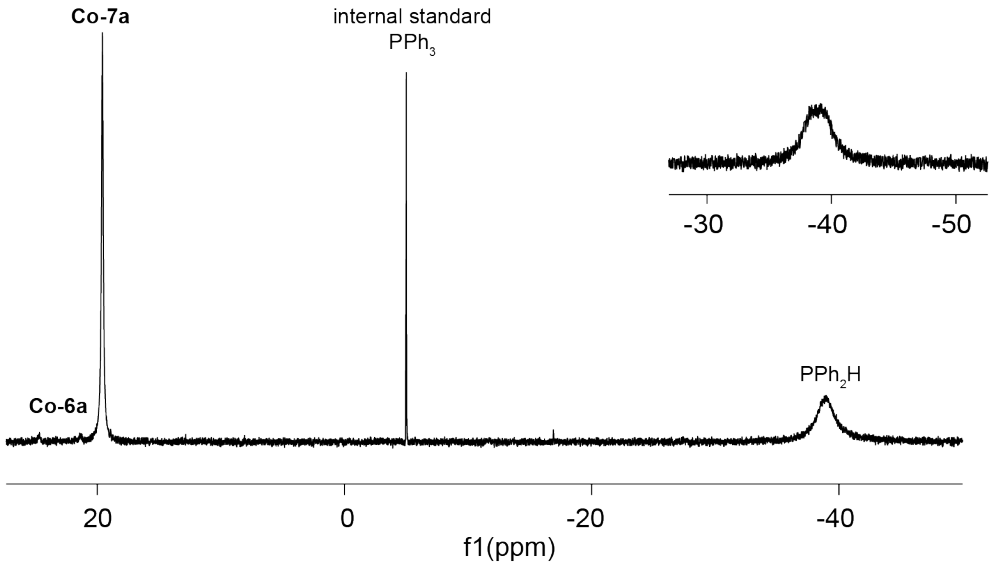

Figure 6.1 $^{31}P\{^{1}H\}$ NMR (202.51 MHz, CD_3CN) and partial ^{31}P NMR (inset) spectra of a mixture of **Co-5** with 3 equiv of PPh_2H, showing the broadening of signal due to free PPh_2H. Internal standard PPh_3 is in a sealed capillary.

In this chapter, I use the simple dicationic complex $[Co(\eta^5\text{-}Cp^*)(NCCH_3)_3][SbF_6]_2$ (**Co-5**) to study this apparent P-H activation with excess PPh_2H in solution. I present substantial spectroscopic evidence revealing a novel radical-mediated P-H activation mechanism involving our Cp*Co(III) system. These findings may be relevant to the mechanism of Cp*Co(III)-catalyzed dehydrocoupling reactions (non-base mediated) described in Chapter 5.

6.2 Spectroscopic evidence for reversible P-H activation of PPh_2H by Cp*Co(III) complexes

In this section, I demonstrate that the Cp*Co(III) fragment participates in an unusual reversible P-H activation process involving some paramagnetic species, using variable temperature (VT) NMR, the Evans method,[15] EPR, ESI-MS, VT-UV-vis and deuterium labelling experiments.

6.2.1 Investigating the dynamic process using VT-NMR

I performed VT-NMR experiments for the reaction of $[Co(\eta^5\text{-}Cp^*)(NCCH_3)_3][SbF_6]_2$ (**Co-5**) and 3 equiv of PPh_2H to understand the dynamic process that probably involves P-H cleavage of PPh_2H (Figure 6.2). The results indicate that the broadening of the free PPh_2H signal is caused by equilibria involving some paramagnetic species.

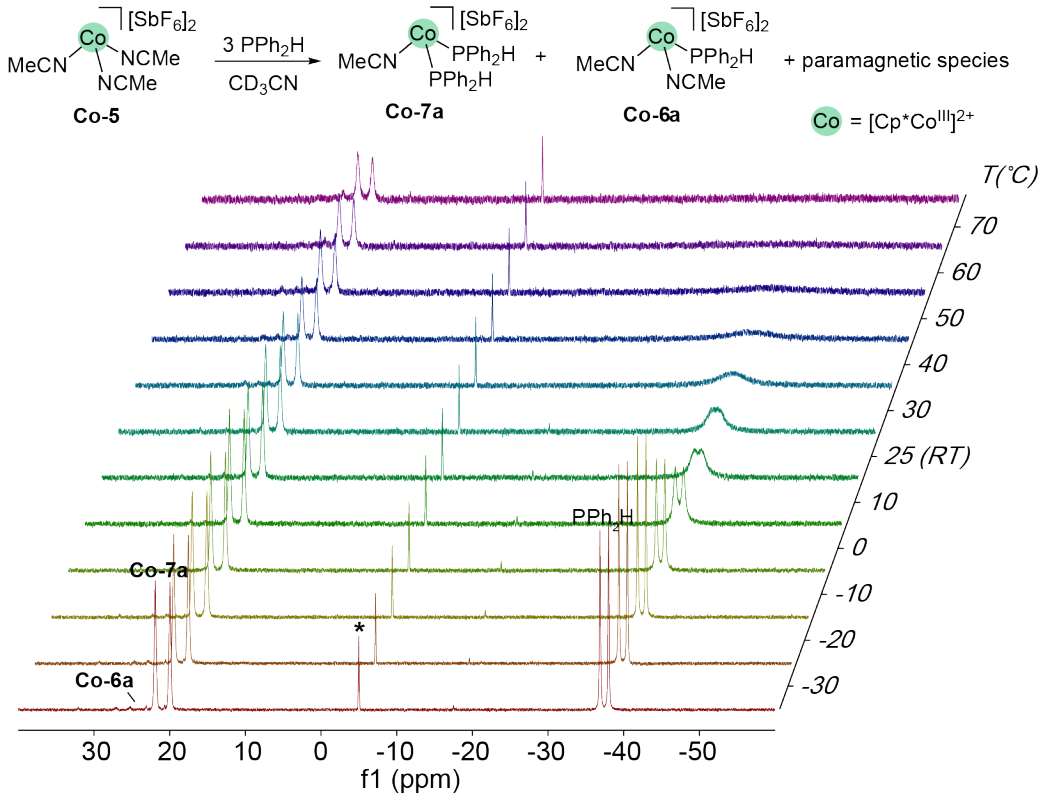

Figure 6.2 VT ^{31}P NMR (202.51 MHz, CD_3CN) spectra of the reaction of **Co-5** with 3 equiv of PPh_2H, showing variable broadening of the free PPh_2H signal at different temperatures. Internal standard PPh_3 (∗) is in a sealed capillary; a tiny peak at ~ –14 ppm is due to $Ph_2P\text{-}PPh_2$.

As shown in Figure 6.2, cooling the sample from 25 °C to –30 °C causes the PPh_2H signal to sharpen and regain $^1J_{PH}$ coupling. Heating the sample above 25 °C causes increased broadening of the PPh_2H signal, and the signal is lost in the baseline at 70 °C. Cooling the sample back down to 25 °C leads to a return to the original spectrum obtained.

At elevated temperatures, the signals due to diamagnetic **Co-6a** and **Co-7a** lose their intensities compared to 25 °C (Figure 6.2). This may indicate their participation in the conversion at high temperatures to some paramagnetic species. In addition to the signals due to diamagnetic Co species, the ^{31}P NMR spectra show a tiny signal (~ –14 ppm) due to Ph_2P-PPh_2, indicating that Ph_2P-PPh_2 could be a part of the dynamic process.

6.2.2 Evidence for paramagnetic species by the Evans method

Given that our VT-NMR experiments imply that paramagnetic species might be produced in the mixture of $[Co(\eta^5\text{-Cp*})(NCCH_3)_3][SbF_6]_2$ (**Co-5**) and excess of PPh_2H (≥ 3 equiv), I used the Evans method to confirm the presence of paramagnetic species in this mixture (Figure 6.3). The Evans method was firstly developed in 1959 to measure magnetic susceptibility in solution.[15] The technique takes advantage of the difference in the NMR chemical shifts generated by the presence of a paramagnetic species in solution. The experiment requires an NMR tube inset – a coaxial tube that physically separates two solutions: one chamber contains a reference solvent, while the other chamber has a solution of the paramagnetic analyte in the reference solvent. The chemical shift(s) of the reference solvent resonances in the resulting NMR spectrum will be different for these two chambers. Typically, the reference solvent is just one solvent, but the situation becomes more complicated when the solvent used can potentially coordinate to the analyte (especially for transition metals). In this case, it is difficult to determine if the chemical shift change is due to the coordination of the solvent or the paramagnetic impact of the analyte. For the experiments presented in this section, I used a 4:1 mixture of CD_2Cl_2 and CD_3CN as the solvent. CD_3CN is the only solvent capable of dissolving **Co-5**, but it is a coordinating solvent incompatible with the Evans method. Thus, I used CD_2Cl_2 as a reference solvent

with a small amount of CD_3CN that allows the Co complex to dissolve in the mixed solvents.

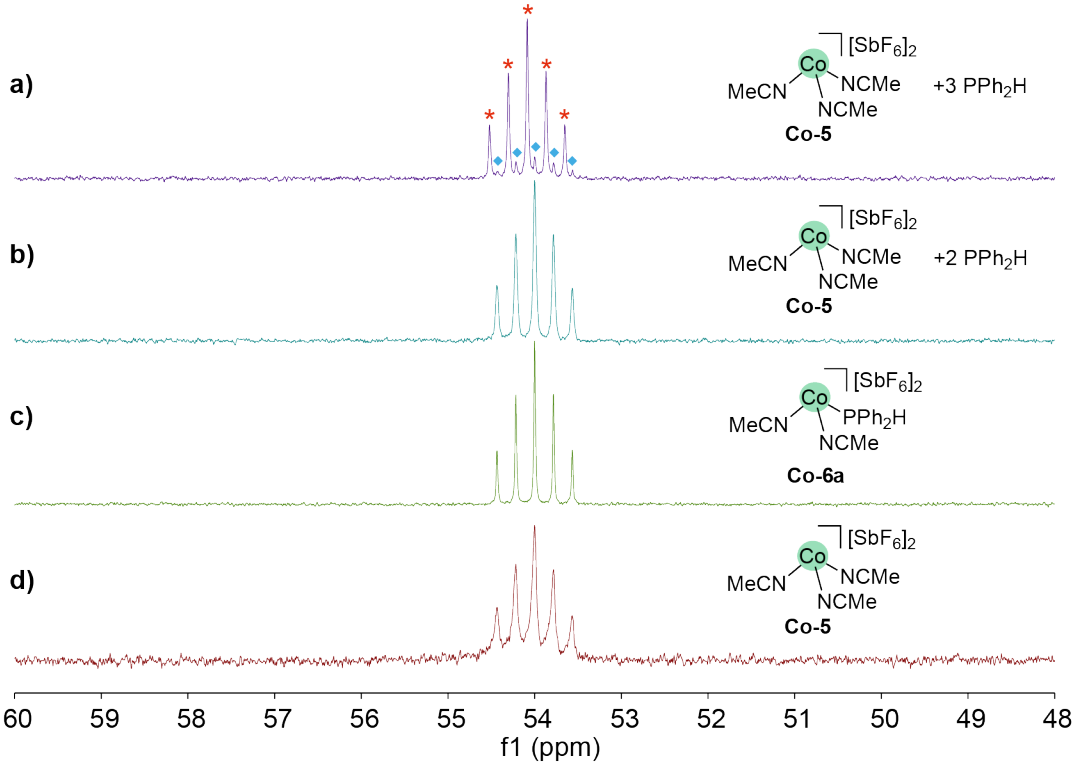

Figure 6.3 Partial $^{13}C\{^1H\}$ NMR (121.55 MHz, CD_2Cl_2/CD_3CN = 4:1, ✱) spectra of samples in CD_2Cl_2/CD_3CN (4:1) containing inserted coaxial tubes containing just the identical solvent (CD_2Cl_2 : CD_3CN = 4:1, ◆). Samples: **a) Co-5** and 3 equiv of PPh_2H, **b) Co-5** and 2 equiv of PPh_2H, **c) Co-6a**, **d) Co-5**.

The NMR experiments using the Evans method (Figure 6.3) confirm that there are paramagnetic species in the mixture of **Co-5** and 3 equiv of PPh_2H. The $^{13}C\{^1H\}$ NMR spectrum reveals a minor downfield shift (~10 Hz) for the CD_2Cl_2 (Figure 6.3a). Other Co species or species mixtures exhibit no comparable frequency shift (Figure 6.3b–d). For reactions shown in Figure 6.3b, $^{31}P\{^1H\}$ NMR spectra shows an equilibrium mixture of $[Co(\eta^5\text{-}Cp^*)(NCCH_3)_2(PPh_2H)][SbF_6]_2$ (**Co-6a**), bis(phosphine) complex $[Co(\eta^5\text{-}Cp^*)(NCCH_3)(PPh_2H)_2][SbF_6]_2$ (**Co-7a**), and free PPh_2H. These results indicate that the

formation of the unidentified paramagnetic species requires excess PPh_2H (> 2 equiv) with respect to **Co-5**.

6.2.3 Identifying paramagnetic species using EPR spectroscopy

The Evans method experiments described above confirm the existence of paramagnetic species in the mixture of $[Co(\eta^5\text{-}Cp^*)(NCCH_3)_3][SbF_6]_2$ (**Co-5**) and 3 equiv of PPh_2H. I performed EPR experiments to identify these paramagnetic species in the mixture. Briefly, the EPR spectrum (Figure 6.4) shows that there are paramagnetic Co(II) species and an unidentified organic radical (probably phosphinyl radical) in the reaction mixture, and these species could be in equilibria.

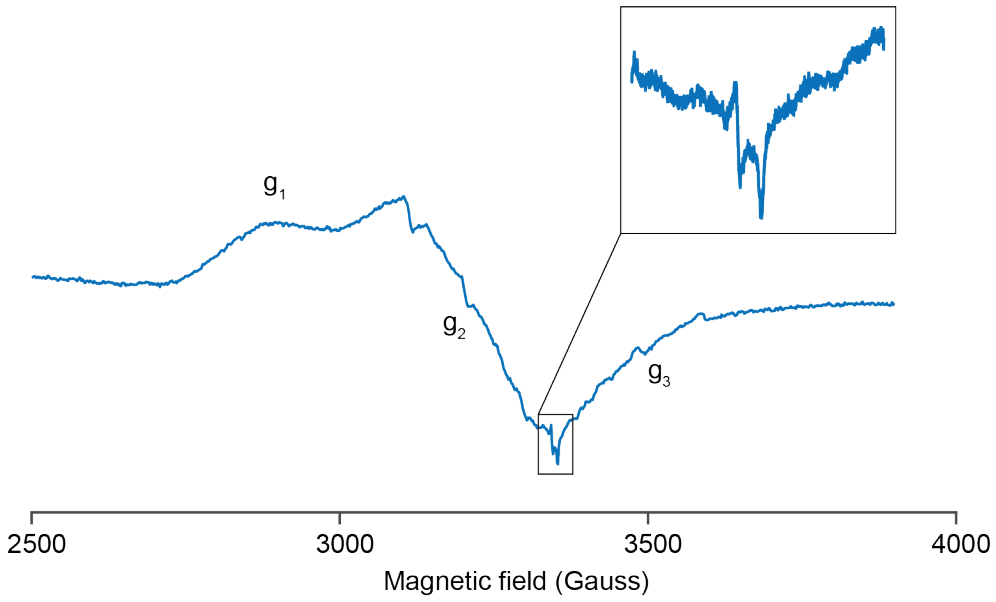

Figure 6.4 X-band EPR spectrum of the reaction of complex **Co-5** in the presence of 3 equiv of PPh_2H. Measured in CD_3CN at ~20 mM concentration, at 100 K, with a microwave frequency of 9.39 GHz. Inset shows an extra tiny signal due to an organic radical. Parameters used for preliminary simulation in EasySpin: $g_1 = 2.271$, $g_2 = 2.090$, $g_3 = 1.970$, $A_1(^{59}Co) = 30$ G, $A_2(^{59}Co) = 20$ G, $A_3(^{59}Co) = 50$ G.

The EPR spectrum (Figure 6.4) at 100 K shows a rhombic spin system consistent with at least one low-spin Co(II) ($S = 1/2$) species.[16] Typically, measuring low-spin metal in the

range of 100 K is relatively simple. However, detecting high-spin metal is usually difficult at 100 K, it requires temperatures below 20 K. Due to the absence of analogous Co(IV) systems reported in the literature, this rhombic signal is probably due to the Co(II), but I cannot completely rule out the presence of Co(IV), in addition to Co(II), in the mixture.

Regardless of low-spin Co(II) or Co(IV), the three components of the expected rhombic g tensor should split into octets (8-line patterns) due to hyperfine coupling to a single Co (I =7/2). Although I observe the rhombic g tensor, no hyperfine coupling is seen for g_1, and the octet coupling is barely observable for g_2 and g_3 in the experimental spectrum (Figure 6.4). The loss of the apparent observable octet coupling could be because the Co(II) species is in equilibrium with other species. In addition, a small doublet signal seems to overlap with the signal due to the Co(II) in the EPR spectrum (Figure 6.4 inset). The signal is tentatively assigned to an organic radical $[\bullet PPh_2H]^+$ or $\bullet PPh_2$ (normally, an organic radical is around g tensor ~2, ~3430 Gauss). The refinement of the simulation is ongoing.

6.2.4 Identifying charged species using ESI-MS

I used ESI-MS to look for charged species in a mixture of $[Co(\eta^5\text{-}Cp^*)(NCCH_3)_3][SbF_6]_2$ (**Co-5**) and PPh_2H (3 equiv), as shown in Figure 6.5. Although MS does not provide direct structural information about a complex, it could give some valuable information that helps for identifying the species.

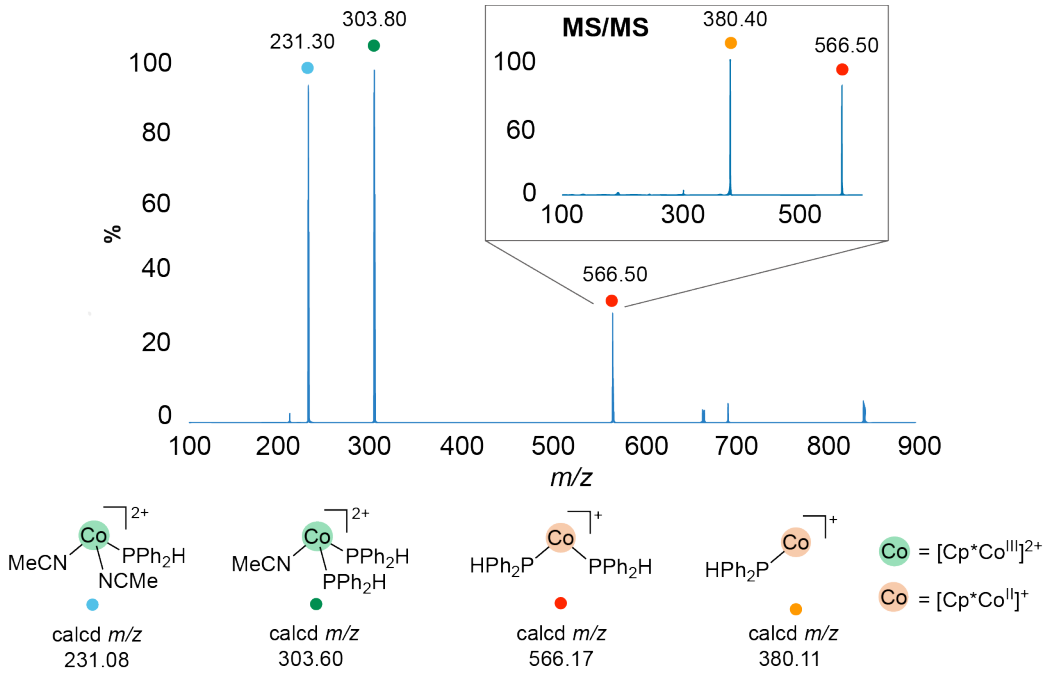

Figure 6.5 ESI-MS spectrum of the reaction mixture of complex **Co-5** in the presence of 3 equiv of PPh_2H. Inset: MS/MS spectrum of the peak at *m/z* = 566.17. Other unidentified peaks could be due to the decomposition of highly reactive Co species. Peaks at higher *m/z* could be due to unidentified dimeric Co species after the decomposition.

As shown in Figure 6.5, the ESI-MS spectrum of an aliquot of the mixture of **Co-5** and 3 equiv of PPh_2H shows two major peaks at *m/z* = 231.30 and 303.80, which correspond to the formulas of $[Co(\eta^5\text{-Cp*})(NCCH_3)_2(PPh_2H)]^{2+}$ (**Co-6a** dication, calcd *m/z* 231.08) and $[Co(\eta^5\text{-Cp*})(NCCH_3)(PPh_2H)_2]^{2+}$ (**Co-7a** dication calcd *m/z* 303.60). Additionally, the spectrum has a peak at *m/z* = 566.50, which is consistent with the formula of the monocation $[Co(\eta^5\text{-Cp*})(PPh_2H)_2]^{+}$ (calcd *m/z* 566.17). In this formula, the oxidation state of Co is 2+, but how the Co(II) species forms is unclear. It is difficult to know if the Co(II) species was formed during the ionization process (prior to MS analysis) or if it originates from the reaction mixture itself. Alternatively, the peak at *m/z* = 566.50 could be due to the monocation $[Co(\eta^5\text{-Cp*})H(PPh_2H)_2]^{+}$ (calcd *m/z* 567.17). I prefer this peak corresponding to the Co(II) species since the instrument resolution is usually ≤ 0.4

m/z. Nevertheless, the MS/MS experiment for this new peak (Figure 6.5 inset) shows a daughter peak at *m/z* = 380.40, which is consistent with the formula of monocation $[Co(\eta^5\text{-}Cp^*)(PPh_2H)]^+$ (calcd *m/z* 380.11). This fragment probably results from the loss of a PPh_2H ligand from the $[Co(\eta^5\text{-}Cp^*)(PPh_2H)_2]^+$. Despite the lack of direct structural information on the species, MS results indicate the possible formation of paramagnetic Co species in this mixture

6.2.5 Investigating the dynamic process using UV-vis spectroscopy

As for the VT-NMR experiments described in Section 6.2.1, I used VT-UV-vis experiments to gather more evidence for new Co species present in an equilibrium mixture of $[Co(\eta^5\text{-}Cp^*)(NCCH_3)_3][SbF_6]_2$ (**Co-5**) and excess PPh_2H, as a complement to the NMR experiments.

A critical issue for the VT-UV-vis experiments is the concentration difference in NMR and UV-vis experiments. As described in Section 6.2.1, NMR experiments suggest that at least two chemical equilibria exist in the mixture of **Co-5** and excess PPh_2H (Scheme 6.4). The relative concentrations of **Co-5** and PPh_2H substantially affect the direction of the chemical equilibria. Typically, the concentrations of reactants are several orders of magnitude lower in a UV-vis experiment than in an NMR experiment. With the higher dilution of the UV-vis sample in CH_3CN, the equilibria are expected to shift toward the **Co-6a** side (Scheme 6.4). Thus, increasing the PPh_2H concentration while maintaining a relatively low concentration of the Co species appears to be a feasible strategy to detect the formation of paramagnetic species using UV-vis spectroscopy.

Scheme 6.4 Possible equilibria in the mixture of complex **Co-5** and excess PPh_2H.

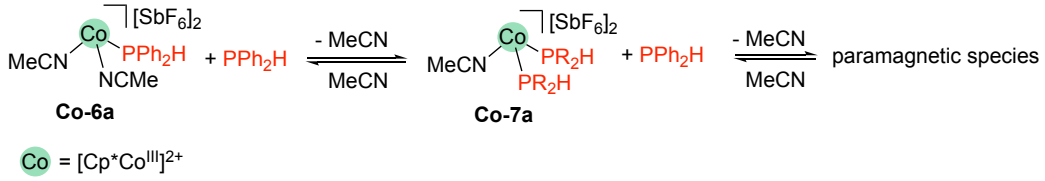

I performed a series of UV-vis experiments on **Co-5** using varying concentrations of PPh_2H (2, 3, 25, 500 and 1500 equiv, Figure 6.6) to determine the actual concentrations of PPh_2H required for detecting the right equilibrium shown in Scheme 6.4. As described in Chapter 3, UV-vis spectra of isolated complex **Co-5** and **Co-6a** were obtained. It is challenging to isolate pure **Co-7a** because of the equilibrium (Scheme 6.4 left). Herein, when 2 or 3 equiv of PPh_2H is added to a solution with a sufficiently low concentration of **Co-5** (~ 1.5 x 10^{-4} M) for obtaining an electronic spectrum, the equilibrium does not significantly shift toward the **Co-7a** side (Scheme 6.4), since the UV-vis spectrum of the reaction mixture is almost identical to that of the isolated **Co-6a** (Figure 6.6 and Chapter 3). However, the UV-vis spectra of **Co-5** in the presence of higher PPh_2H concentrations (25, 500 and 1500 equiv) all show a new signal at 445 nm that replaced the peak at 468 nm. The signal is more blue-shifted than that for **Co-6a** (468 nm), which is tentatively assigned to the peak due to **Co-7a**. Increasing the quantity of PPh_2H from 25 to 1500 equiv does not affect further shifting the absorbance bands toward higher energy. Thus, I conducted VT UV-vis experiments using a mixture of **Co-5** and 25 equiv of PPh_2H as a model system for studying the equilibria shown in Scheme 6.4 right.

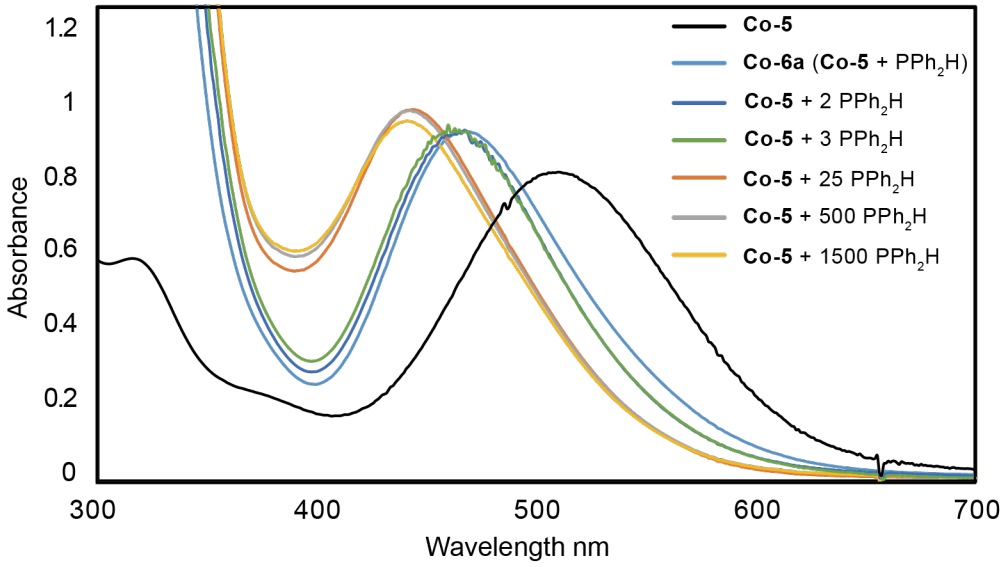

Figure 6.6 UV-vis absorption spectra of **Co-5**, **Co-6a** and the mixtures of **Co-5** with 2, 3, 25, 500, and 1500 equiv of PPh_2H in CH_3CN at RT.

The VT UV-vis spectra of the mixture of **Co-5** in the presence of 25 equiv of PPh_2H (Figure 6.7) demonstrate that bis(phosphine) complex **Co-7a** participates in another temperature-sensitive equilibrium process. In Figure 6.7a, the absorbance peak around 445 nm due to **Co-7a** diminishes and shifts to slightly higher wavelengths as the temperature rises. This is consistent with the formation of a new species generated at high temperatures; there is an isosbestic point in the UV-vis spectra (Figure 6.7a). When the sample is cooled back down to RT, the resulting spectrum almost returns to the original RT spectrum (Figure 6.7b). However, the mismatching of two spectra suggests this temperature-dependent process is not completely reversible (i.e. some decomposition/dehydrocoupling of phosphines might occur at high temperatures). These UV-vis results are aligned with our initial observations in the VT-NMR experiments (Section 6.2.1). In addition to the "disappearance" of the peak (445 nm) due to **Co-7a**, as the temperature increases, a peak at > 500 nm appears to increase in intensity in the VT-UV-vis spectrum (Figure 6.7a). This

new peak may be due to the new Co species (probably paramagnetic). However, the new signal observed as the temperature rises is less intense and broader than the strong signal at 445 nm. These results indicate the participation of complex **Co-7a** in the conversion at high temperatures to some new species, and this process is mostly reversible.

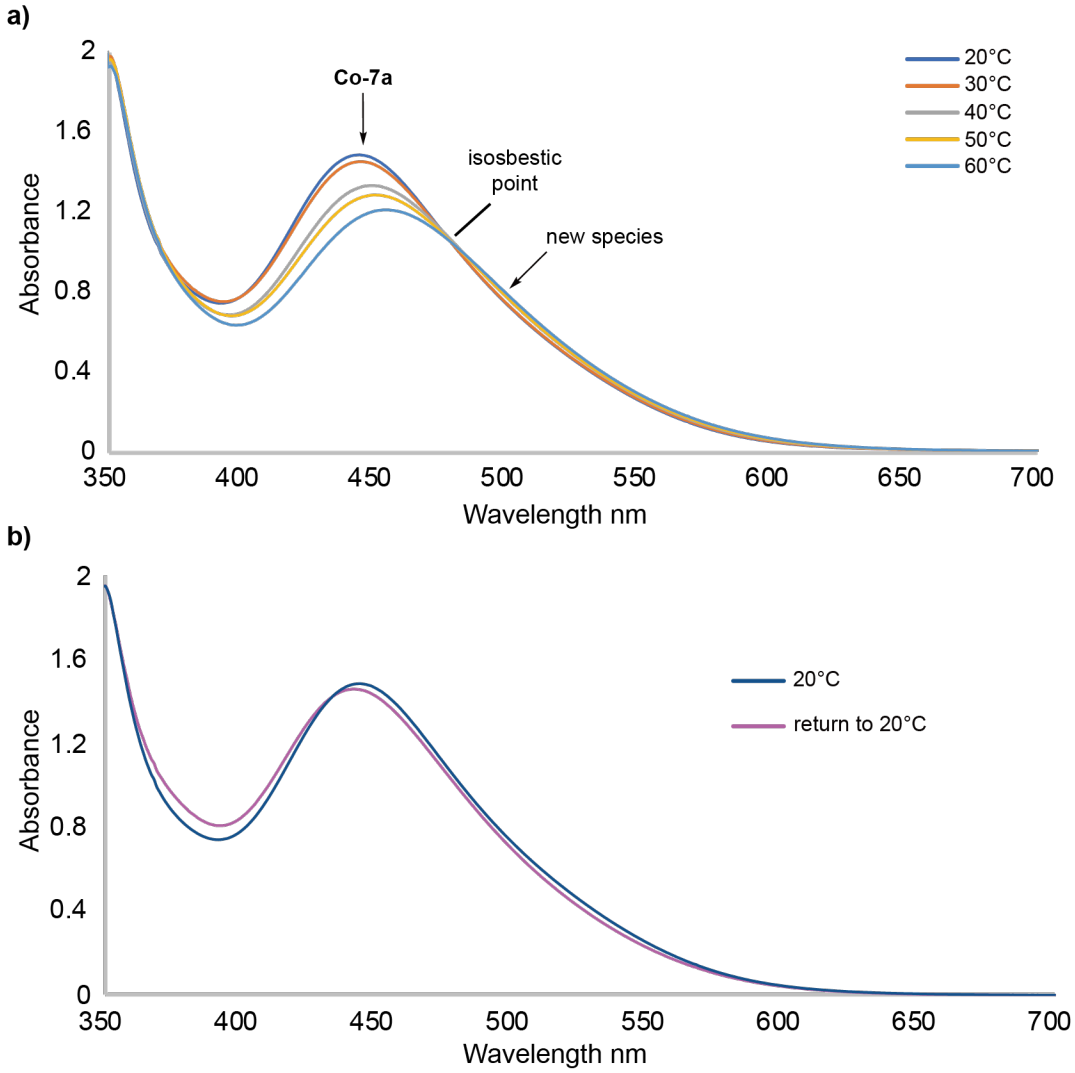

Figure 6.7 **a**) VT-UV-vis absorption spectra of the mixture of **Co-5** in the presence of 25 equiv of PPh_2H in CH_3CN; **b**) original and post-VT spectra recorded at 20 °C.

6.2.6 Investigating the reversible P-H activation using deuterium labelling experiments

I performed deuterium labelling experiments using PPh_2D to probe the apparent reversible P-H activation in mixtures of $[Co(\eta^5\text{-}Cp^*)(NCCH_3)_3][SbF_6]_2$ (**Co-5**) and $Co(\eta^5\text{-}Cp^*)I_2(CO)$ (**Co-1**), respectively, with excess PPh_2H. Experiments using PPh_2D and **Co-1**, rather than **Co-5**, are presented in this section. The results support my hypothesis that reversible P-H activation occurs in the mixture of the Cp*Co(III) complex **Co-1** and excess PPh_2H.

As shown in Figure 6.8, the reaction of **Co-5** with PPh_2D (10 equiv, 93% deuterated) in CD_3CN results in a rather complicated mixture, which may arise from the participation of solvent CD_3CN in competing for bond activation and exchange. The labelling experiments with the neutral analogue **Co-1** in C_6D_6 showed much simpler results. As described above (Section 6.1 and Chapter 3), **Co-1** and **Co-5** show similar "free" PPh_2H peak broadening and loss of $^1J_{PH}$ coupling in the presence of PPh_2H. Thus, the labelling experiment using **Co-1** can also give credible evidence for the generic interaction between a Cp*Co(III) complex and excess phosphines.

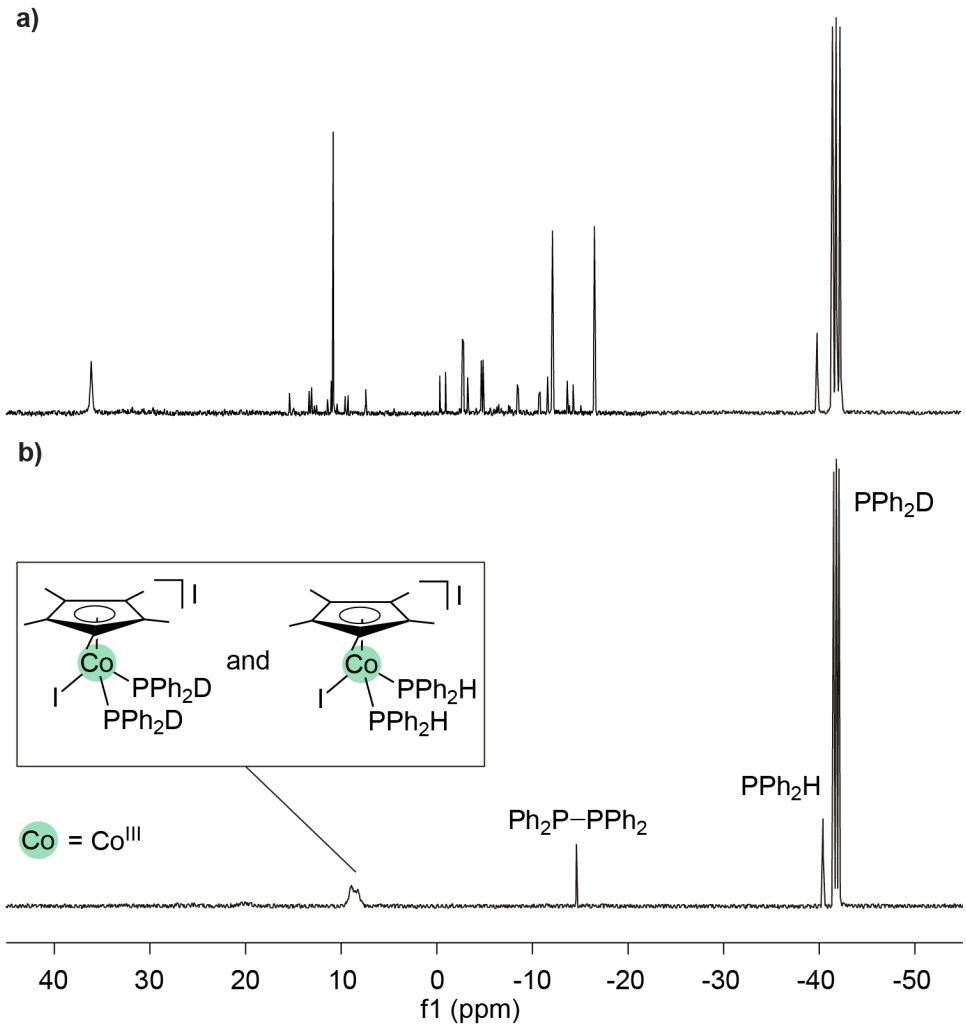

Figure 6.8 **a**) $^{31}P\{^{1}H\}$ NMR (121.55 MHz, CD_3CN) spectrum of the mixture of **Co-5** and PPh_2D (10 equiv), showing the multiple unidentified species in the reaction. **b)** $^{31}P\{^{1}H\}$ NMR (121.55 MHz, C_6D_6) spectrum of the mixture of **Co-1** and PPh_2D (10 equiv).

The addition of excess PPh_2D (10 equiv, 93% deuterated) to **Co-1** in C_6D_6 at RT gives ~2% Ph_2P-PPh_2, detected by ^{31}P NMR (Scheme 6.5a and Figure 6.8b). No PPh_2-PPh_2 is observed under the identical reaction with PPh_2H instead of PPh_2D (Scheme 6.5b). This suggests that reversible P-H activation occurs rapidly in the mixture, but this process is slower after introducing deuterium (D), allowing for coupling of the resulting phosphorus species. What is more intriguing is that this P-P bond formation (Scheme 6.5a) seems to be reversible: the resulting Ph_2P-PPh_2 disappears after 24 h. The result suggests that P-P

formation does occur for diphenylphosphine in the Co-mediated reaction (Scheme 6.5a,b), but the H allows faster reversibility than the D.

Scheme 6.5 Deuterium labelling experiments using **Co-1**: **a)** reaction of **Co-1** with 10 equiv of PPh_2D; **b)** reaction of **Co-1** with 10 equiv of PPh_2H; **c)** reaction of **Co-1** with 5 equiv of PPh_2D and 5 equiv of $PTol^p_2H$; **d)** the mixture of PPh_2D and $PTol^p_2H$ (1:1).

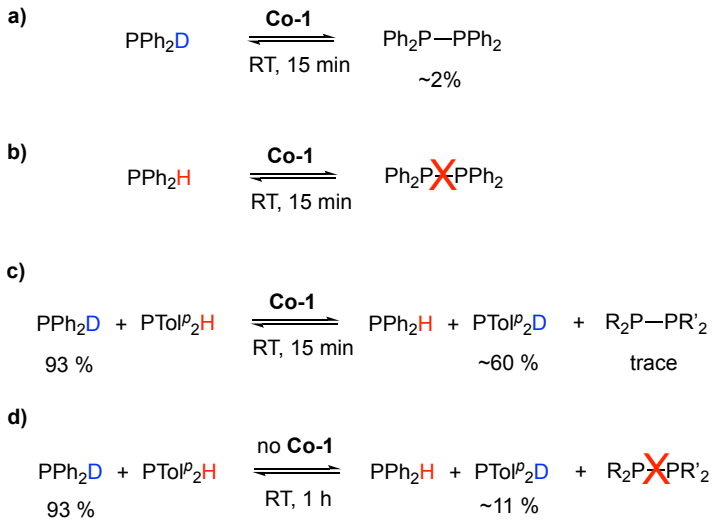

I performed a crossover experiment using **Co-1** and a 1:1 mixture of PPh_2D/$PTol^p_2H$ (5 equiv of each, Scheme 6.5c). I observed four different secondary phosphines in the reaction by $^{31}P\{^1H\}$ NMR spectroscopy (Figure 6.9), including PPh_2H, PPh_2D, $PTol^p_2H$ and $PTol^p_2D$. This H/D exchange at secondary phosphine demonstrates that reversible P-H activation occurs in the reaction mixture. Similar to the reaction with just PPh_2D (Scheme 6.5a), diphosphines (Ph_2P-PPh_2, Tol^p_2P-$PTol^p_2$ and Tol^p_2P-PPh_2) are produced initially and then disappear after 24 h. Additionally, I conducted a control experiment using just PPh_2D and $PTol^p_2H$ (Scheme 6.5d), showing that there is a slow spontaneous H/D exchange occurring even without Co. However, complex **Co-1** does play a role in facilitating the H/D-scrambling processes. The control experiment (Scheme 6.5d) results in 11% of $PTol^p_2D$ after 1 h at RT, while the reaction involving **Co-1** generates 60% of $PTol^p_2D$ within 15 min under identical conditions (Scheme 6.5c).

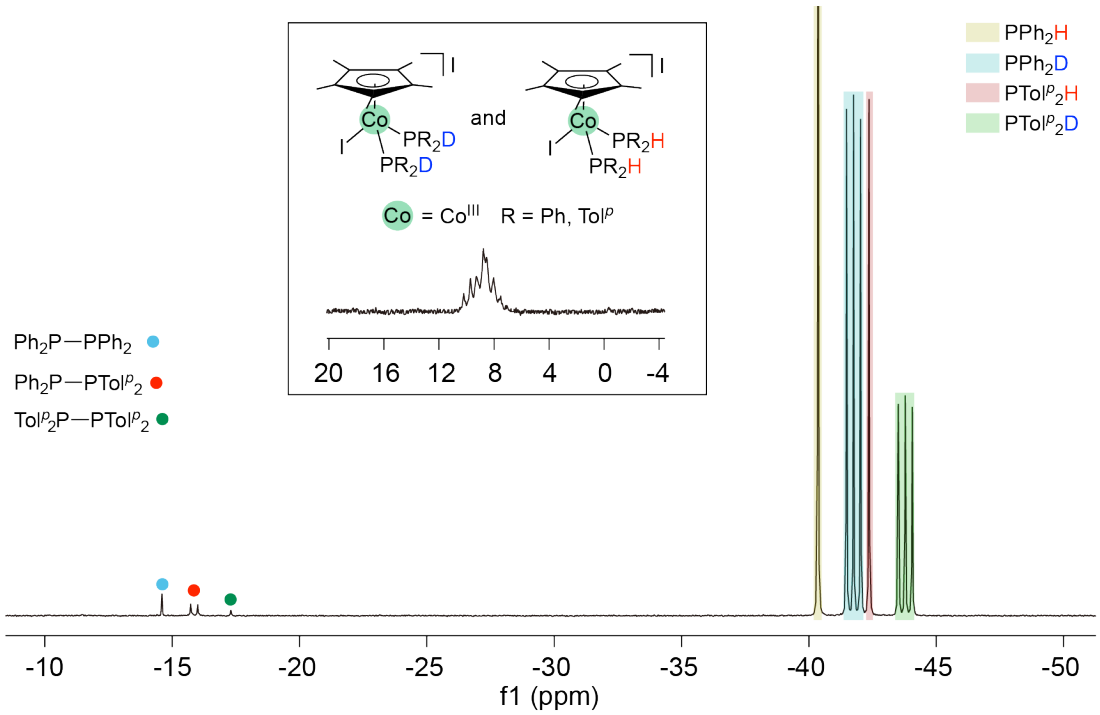

Figure 6.9 $^{31}P\{^{1}H\}$ NMR (121.55 MHz, C_6D_6) spectrum of the reaction of complex **Co-1** with 5 equiv of PPh_2D and 5 equiv of $PTol^p{}_2H$ after 15 min. Inset: Co phosphine complex region of the $^{31}P\{^{1}H\}$ NMR spectrum.

6.3 Two proposed mechanisms for P-H activation at Cp*Co(III)

Collectively, the above experimental evidence supports a plausible mechanism in which bis(phosphine) complex $[Co(\eta^5\text{-}Cp^*)(NCCH_3)(PPh_2H)_2][SbF_6]_2$ (**Co-7a**) abstracts the H-atom from PPh_2H in these reaction mixtures (Scheme 6.6). The proposed transition state involving an η^1-H-PPh_2 at the Co center is mainly based on the steric congestion at Co, which is reinforced by the fact that no trisubstituted PPh_2H complex $[Co(\eta^5\text{-}Cp^*)(PPh_2H)_3][SbF_6]_2$ has ever been seen (for PPh_2H).

Scheme 6.6 Proposed mechanism (#1) for reversible homolytic P-H bond cleavage by complex **Co-7a**.

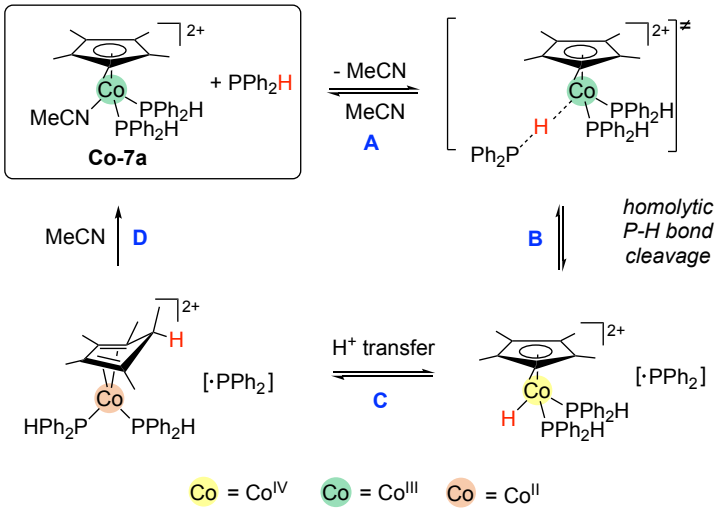

As shown in Scheme 6.6, free PPh_2H approaches the Co(III) center to form an end-on, η^1-H-PPh_2 complex initially (might be just a transition state, step A). Then, the P-H bond is activated homolytically to generate a Co(IV) hydride complex and a phosphinyl radical (•PPh_2) that is probably closely associated with the Co complex (step B). Since the free •PPh_2 is not stable, it readily couples each other to give Ph_2P-PPh_2. The literature indicates that the weak hydrogen atom transfer (HAT) reagent TEMPO can abstract an H-atom from a PPh_2H.[17] The bond dissociation free energy (BDFE) of the O-H bond in TEMPOH is 66.5 kcal/mol in CH_3CN or 65.2 kcal/mol in C_6H_6.[11] Thus, the BDFE of the P-H bond at PPh_2H is lower than that of TEMPOH (~66 kcal/mol), indicating that the P-H bond is sufficiently weak and could participate in H-atom transfer. This is also known from thermal hydrophosphination (see Chapter 1). The literature is sparse regarding the homolytic cleavage of the P-H bond by transition metal complexes, but one example involving binuclear oxidative addition of the P-H bond could be relevant (Scheme 6.3b).[14]

Considering that the "associated" phosphinyl radical is probably still rather reactive, it likely gives a diphosphine Ph_2P-PPh_2. This is consistent with our observation of the

formation of small amounts of Ph_2P-PPh_2 in the mixture of $[Co(\eta^5\text{-}Cp^*)(NCCH_3)_3][SbF_6]_2$ (**Co-5**) and excess PPh_2H. Perhaps, the "associated" $\bullet PPh_2$ is less active than the free one. This could be important for the reversibility of these proposed steps. The diphosphine formation seems to be reversible in this case. According to literature, the presence of sterically demanding and electron-withdrawing substituents on the P-atoms enhances the tendency for the P-P bond to break homolytically, and equilibrium is found between the radical and dimer forms in solution.[18] The phenyl group (Ph) may be seen as medium-sized, modest electron-withdrawing substituents at Ph_2P-PPh_2, which indicates that Ph_2P-PPh_2 may dissociate into $\bullet PPh_2$ spontaneously in solution and then closely associate with the Co complex. Nevertheless, it is unclear to me what interaction would allow this associated complex to form the diphosphine.

Alternatively, my experimental observations could be explained by a frustrated Lewis pair (FLP) participating in a single electron transfer (SET) (Scheme 6.7). An FLP is a combination comprising a Lewis acid and a Lewis base that cannot combine due to steric hindrance.[19] Although most FLPs contain only main group Lewis acids and bases, some metal-containing FLPs are also known.[20] Notably, Stephan and coworkers identified SET from Cp^*_2Fe to a Lewis acid ($E(C_6F_5)_3$, E = B or Al) [21] In our system, the Cp*Co(III) complex **Co-7a** is the Lewis acid, and PPh_2H is the Lewis base in a proposed transition metal/main group molecule FLP.

Scheme 6.7 Proposed mechanism (#2) for reversible P-H activation by a Cp*Co(III) complex with an FLP adduct.

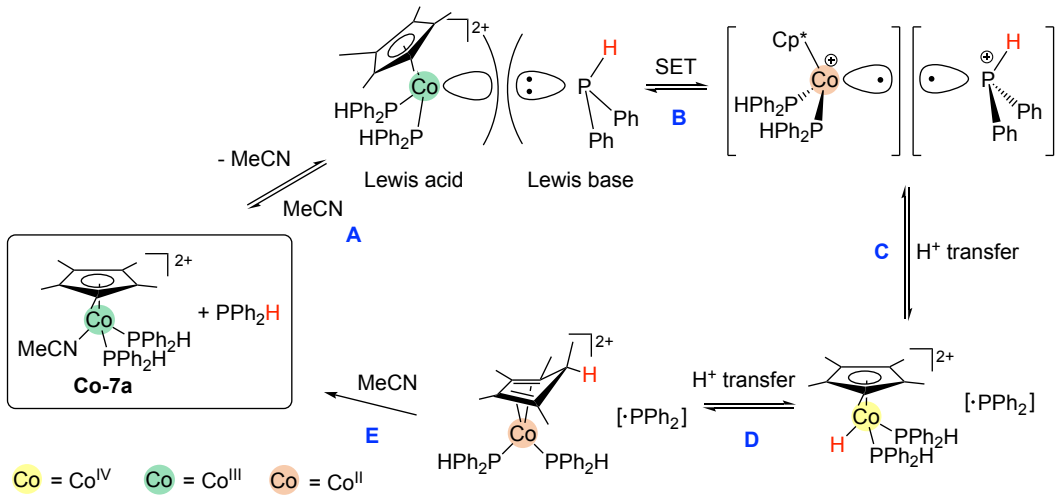

As shown in Scheme 6.7, the proposed P-H activation proceeds *via* an initial approach of the PPh_2H to the Co(III) center (step A), followed by SET to make a radical pair consisting of the phosphinyl radical cation (i.e. $[\bullet PPh_2H]^+$) and the Co(II) complex (step B). The resulting Co(II) species in the radical pair is consistent with our observation in ESI-MS (Section 6.2.4). Also, the $[\bullet PPh_2H]^+$ is anticipated to be very acidic. A rapid intramolecular H^+ transfer could occur in the FLP, generating a new pair, including phosphinyl radical ($\bullet PPh_2$) and a Co(IV) hydride complex (step C). The rest of the proposed steps (steps D and E) are similar to the previous mechanism (Scheme 6.6).

Collectively, both hypotheses (Scheme 6.6 and 6.7) imply the reversible production of Co(IV)-H and $\bullet PPh_2$. No observation or isolation of Co(IV)-H related compounds has been reported so far, suggesting Co(IV)-H complexes are generally very reactive. This is consistent with my previous CV results (Chapter 3): no redox potential of Co(IV) is determined. In light of our past findings (Chapter 5) and a literature example, I assume that the $[(\eta^5\text{-Cp*})\text{Co(IV)-H}]^{2+}$ would further irreversibly convert to the more stable $[(\eta^4\text{-}$

Cp*H)Co(II)]$^{2+}$. This is consistent with our EPR results: only Co(II) species is detected (Section 6.3.4). EPR experiments reported in the literature demonstrated the instability of free •PPh_2 even at 77 K; the unstable species quickly couples to form Ph_2P-PPh_2.[22] However, our EPR experiments show signals possibly due to the •PPh_2 or [•PPh_2H]$^+$) (presumably associated with Co). Further computational studies are required to help us better understand the mechanism of this exchange process.

6.4 Conclusion

Based on various spectroscopic evidence, I demonstrate a new reversible P-H activation of substrate PPh_2H, involving paramagnetic Co(II) species and possible •PPh_2, in the mixture of [Co(η^5-Cp*)($NCCH_3$)$_3$][SbF_6]$_2$ (**Co-5**) and excess PPh_2H. In the short term, this P-H activation discovery establishes a new conceptual framework for interacting transition metals with phosphines containing P-H bonds. Its application could be useful in the long term, particularly for synthesizing a broad range of organophosphines (with P-P or P-C bonds) *via* a homolytic P-H cleavage route.

6.5 Experimental

See Chapter 2, Section 2.5.1. for general experimental details. See Chapter 3, Section 3.6 and Chapter 4, Section 4.6 for general spectroscopic information.

6.5.1 VT-NMR

Complex [Co(η^5-Cp*)($NCCH_3$)$_3$][SbF_6]$_2$ (**Co-5**, 0.025 mmol, 20 mg) and PPh_2H (0.076 mmol, 13 μL, 3 equiv) were dissolved in CD_3CN (0.6 mL). The intense golden solution was transferred to a J. Young NMR tube. ^1H, $^{31}P\{^1H\}$ and ^{31}P spectra were initially collected at RT (298 K). After that, additional spectra were collected at various

temperatures ranging from 243 to 353 K (Figure 6.2). Final spectra were collected again at RT, which replicated the first 298 K spectra.

6.5.2 The Evans method

Complex $[Co(\eta^5\text{-}Cp^*)(NCCH_3)_3][SbF_6]_2$ (**Co-5**, 0.025 mmol, 20 mg) and PPh_2H (0.076 mmol, 13 μL, 3 equiv) were mixed in a 4: 1 ratio of CD_2Cl_2/CD_3CN solvent (0.6 mL). The same solvent mixture (0.1 mL) was added to the coaxial tube immediately after mixing. The $^{13}C\{^1H\}$ NMR spectrum was obtained at ~15 min. Note: All procedures were completed as quickly as possible to avoid evaporation of CD_2Cl_2, which would change the solution composition, and affect the results.

6.5.3 EPR

See Section 4.6, Chapter 4 for general experimental details. Complex $[Co(\eta^5\text{-}Cp^*)(NCCH_3)_3][SbF_6]_2$ (**Co-5**, 0.020 mmol, 16 mg) and PPh_2H (0.060 mmol, 10 μL, 3 equiv) were dissolved in dry CD_3CN (1 mL) in a J. Young EPR tube.

6.5.4 ESI-MS

Complex $[Co(\eta^5\text{-}Cp^*)(NCCH_3)_3][SbF_6]_2$ (**Co-5**, 0.025 mmol, 20 mg) and PPh_2H (0.076 mmol, 13 μL, 3 equiv) were dissolved in CH_3CN (0.6 mL), and then a 20-fold dilution of this solution was prepared for the ESI-MS experiments. ESI source parameters were as follows: capillary voltage was held at 3.0 kV, cone voltage at 15.0 V, and extraction cone at 2 V.

6.5.5 UV-vis spectroscopy

6.5.5.1 Routine experiments

For experiments using different concentrations of PPh_2H, neat PPh_2H (0.00060–0.45 mmol) was added to a solution of **Co-5** while maintaining a 2 mL total volume of the resultant solution ([**Co-5**] = 0.00015 M).

6.5.5.2 VT experiments

A stock solution of $[Co(\eta^5\text{-}Cp^*)(NCCH_3)_3][SbF_6]_2$ (**Co-5**, 0.003 M, 1 mL) was prepared. The Co stock solution (0.0003 mmol, 0.1 mL) and PPh_2H (0.0075 mmol, 1.3 μL, 25 equiv) were added to give a total volume of 2 mL in CH_3CN. The initial spectrum was collected at 293 K. Additional spectra were collected at 303, 313, 323 and 333 K. Final spectra were collected again at 293, which closely replicated the first spectrum.

6.5.6 Deuterium labelling experiments

6.5.6.1 Synthesis of PPh_2D

Diphenylphosphine-*d* (PPh_2D) was prepared using a literature method.[23] *n*-BuLi (10 mmol, 1.4 M in cyclohexane, 2.0 equiv) was added dropwise to a solution of PPh_2H (5.0 mmol, 1.0 equiv) in dry THF (3 mL) in an ice bath (0 °C). After stirring for 1 h, a yellow solution (i.e. $LiPPh_2$) formed, and then D_2O (11 mmol, 2.2 equiv) was added, and the mixture was stirred for 10 min. Finally, anhydrous $MgSO_4$ was added to quench the reaction. The resulting mixture was decanted *via* cannula, and the solvent was removed under vacuum to yield the desired product (3.1 mmol, 62%). The product was obtained as

a colourless oil (93% PPh_2D and 7% PPh_2H as determined by ^{31}P NMR). The NMR measurements are consistent with published data.[23]

^{1}H NMR (300.27 MHz, C_6D_6): δ 7.41−7.32 (m, 4H, H_o), 7.04−6.98 (m, 6H, H_m and H_p)

$^{31}P\{^1H\}$ NMR (121.55 MHz, C_6D_6): δ – 42.0 (t, $^1J_{PD}$ 33.4 Hz).

6.5.6.2 Reaction of Co-1 or Co-5 with PPh_2D

Complex $[Co(\eta^5\text{-}Cp^*)(NCCH_3)_3][SbF_6]_2$ (**Co-5**, 0.020 mmol, 16 mg) or $Co(\eta^5\text{-}Cp^*)I_2(CO)$ (**Co-1**, 0.020 mmol, 10 mg) was dissolved in CD_3CN (0.5 mL) or C_6D_6 (0.5 mL), respectively, and PPh_2D (0.20 mol, 36 μL, 10 equiv) was added. The mixture was analyzed by ^1H and $^{31}P\{^1H\}$ NMR.

6.5.6.4 Reaction of $PTol^p_2H$ and PPh_2D

$PTol^p_2H$ (0.10 mol, 21 μL, 5 equiv) and PPh_2D (0.10 mol, 18 μL, 5 equiv) were dissolved in C_6D_6 (0.5 mL). The mixture was analyzed by ^1H and $^{31}P\{^1H\}$ NMR.

6.6 References

(1) Leitao, E. M.; Jurca, T.; Manners, I. Catalysis in Service of Main Group Chemistry Offers a Versatile Approach to P-Block Molecules and Materials. *Nat. Chem.* **2013**, *5*, 817–829.

(2) Rosenberg, L. Mechanisms of Metal-Catalyzed Hydrophosphination of Alkenes and Alkynes. *ACS Catal.* **2013**, *3*, 2845–2855.

(3) Greenberg, S.; Stephan, D. W. Stoichiometric and Catalytic Activation of P–H and P–P Bonds. *Chem. Soc. Rev.* **2008**, *37*, 1482–1489.

(4) Waterman, R. Mechanisms of Metal-Catalyzed Dehydrocoupling Reactions. *Chem. Soc. Rev.* **2013**, *42*, 5629–5641.

(5) Waterman, R. Dehydrogenative Bond-Forming Catalysis Involving Phosphines: Updated Through 2010. *Curr. Org. Chem.* **2012**, *16*, 1313–1331.

(6) Clarson, S. J. *Bogdan Marciniec, Hydrosilylation: A Comprehensive Review on Recent Advances*; Springer: Berlin, 2009; Vol. 1.

(7) Bange, C. A.; Waterman, R. Challenges in Catalytic Hydrophosphination. *Chem. – Eur. J.* **2016**, *22*, 12598–12605.

(8) Haynes, W. M. *CRC Handbook of Chemistry and Physics, 94th Edition*; 100 Key Points; CRC Press, 2016.

(9) Snow, S. S.; Jiang, D. X.; Parry, R. W. Formation of a Nickel Carbonyl Cation Containing a Cyclophosphenium Ligand by Hydride Abstraction. *Inorg. Chem.* **1987**, *26*, 1629–1631.

(10) Belli, R. G.; Pantazis, D. A.; McDonald, R.; Rosenberg, L. Reversible Silylium Transfer between P-H and Si-H Donors. *Angew. Chem. Int. Ed.* **2021**, *60*, 2379–2384.

(11) Warren, J. J.; Tronic, T. A.; Mayer, J. M. Thermochemistry of Proton-Coupled Electron Transfer Reagents and Its Implications. *Chem. Rev.* **2010**, *110*, 6961–7001.

(12) Stiles, A. R.; Rust, F. F.; Vaughan, W. E. The Preparation of Organo-Phosphines by the Addition of Phosphine to Unsaturated Compounds. *J. Am. Chem. Soc.* **1952**, *74*, 3282–3284.

(13) Heurich, T.; Nesterov, V.; Schnakenburg, G.; Qu, Z. W.; Grimme, S.; Hazin, K.; Gates, D. P.; Engeser, M.; Streubel, R. Strong Evidence of a Phosphanoxyl Complex: Formation, Bonding, and Reactivity of Ligated Phosphorus Analogues of Nitroxides. *Angew. Chem. Int. Ed.* **2016**, *55*, 14439–14443.

(14) Adhikari, D.; Mossin, S.; Basuli, F.; Dible, B. R.; Chipara, M.; Fan, H.; Huffman, J. C.; Meyer, K.; Mindiola, D. J. A Dinuclear Ni(I) System Having a Diradical Ni_2N_2 Diamond Core Resting State: Synthetic, Structural, Spectroscopic Elucidation, and Reductive Bond Splitting Reactions. *Inorg. Chem.* **2008**, *47*, 10479–10490.

(15) Evans, D. F. The Determination of the Paramagnetic Susceptibility of Substances in Solution by Nuclear Magnetic Resonance. *J. Chem. Soc.* **1959**, 2003–2005.

(16) Koelle, U.; Fuss, B.; Raabe, E. Pentamethylcyclopentadlenyl Transition Metal Complexes. 9.1 Reactions and Solid-State and Solution Behavior of Dinuclear Cobalt(II) Complexes $[C_5Me_5Co(\mu\text{-}X)]_2$. *Organometallics* **1986**, *5*, 980–987.

(17) Heurich, T.; Qu, Z. W.; Nožinović, S.; Schnakenburg, G.; Matsuoka, H.; Grimme, S.; Schiemann, O.; Streubel, R. Synthesis and Rearrangement of P-Nitroxyl-Substituted PIIIand PVPhosphanes: A Combined Experimental and Theoretical Case Study. *Chem. – Eur. J.* **2016**, *22*, 10102–10110.

(18) Szynkiewicz, N.; Ponikiewski, Ł.; Grubba, R. Symmetrical and Unsymmetrical Diphosphanes with Diversified Alkyl, Aryl, and Amino Substituents. *Dalton Trans.* **2018**, *47*, 16885–16894.

(19) Stephan, D. W. "frustrated Lewis Pairs": A Concept for New Reactivity and Catalysis. *Org. Biomol. Chem.* **2008**, *6*, 1535–1539.

(20) Stephan, D. W. Diverse Uses of the Reaction of Frustrated Lewis Pair (FLP) with Hydrogen. *J. Am. Chem. Soc.* **2021**, *143*, 20002–20014.

(21) Liu, L. L.; Stephan, D. W. Radicals Derived from Lewis Acid/Base Pairs. *Chem. Soc. Rev.* **2019**, *48*, 3454–3463.

(22) Fullam, B. W.; Mishra, S. P.; Symons, M. C. R. Unstable Intermediates. Part CXLIX. An Electron Spin Resonance Study of Various Phosphinyl Radicals Formed by Solid-State Radiolysis. *J. Chem. Soc. Dalton Trans.* **1974**, No. 20, 2145–2148.

(23) Moglie, Y.; González-Soria, M. J.; Martín-García, I.; Radivoy, G.; Alonso, F. Catalyst- and Solvent-Free Hydrophosphination and Multicomponent Hydrothiophosphination of Alkenes and Alkynes. *Green Chem.* **2016**, *18*, 4896–4907.

7. Future work

The studies detailed in my thesis shed light on the hydrophosphination of alkenes and the dehydrocoupling of phosphines catalyzed by Cp*M complexes. This chapter outlines the work required to publish the projects mentioned in Chapters 2-6 (short-term work) and the future directions for the hydrophosphination projects (long-term work).

7.1 Short-term work

7.1.1 Investigation of highly active Cp*Ru catalysts for hydrophosphination of activated alkenes

As detailed in Chapter 2, complexes Ru(η^5-Cp*)(PR_2)(PR_2H)$_2$ (**Ru-1**, R = aryl or alkyl) can catalyze the hydrophosphination of electron-deficient alkenes. The preliminary investigations of **Ru-1a** (R = Ph (**a**)) reveals that it is extraordinarily active (TOF ~250 h^{-1} at 90% conversion). Additionally, I showed that the active catalyst operates by a similar mechanism to our indenyl catalyst Ru(η^5-indenyl)(PPh_2)(PPh_2H)(PPh_3), which entails conjugate addition of the phosphido ligand to an alkene (Scheme 7.1, step A) and subsequent intramolecular H^+ transfer from the coordinated PPh_2H (Scheme 7.1, step B). Meanwhile, the electronic and steric characteristics of the Cp* ligand change the general conjugate addition mechanism considerably. In particular, the turnover-limiting step for Cp*Ru-catalyzed hydrophosphination is the intramolecular H^+ transfer (Scheme 7.1, step B) instead of the product substitution (Scheme 7.1, step C). The work described above has been published recently.[1]

Scheme 7.1 Proposed mechanism for outer-sphere hydrophosphination catalyzed by **Ru-1**. (R = Ph; R' = CO_2Bu^t)

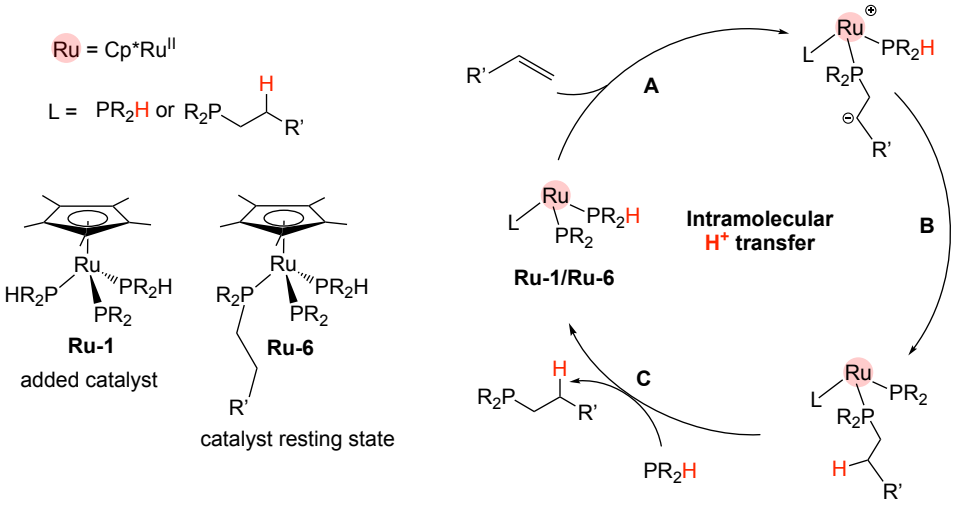

Unpublished substrate scope studies in Chapter 2 will be turned into a new publication. The main selling point of the article will be the utilization of highly reactive Cp*Ru catalysts to produce racemic mixtures of chiral phosphines (Scheme 7.2). Short-term experiments include the exploration of phosphine and alkene substrate scopes. Alexis Kellinghusen (an undergraduate summer student) and I are currently working on this project. A preliminary study of a new complex Ru(η^5-Cp*)(PRH)(PRH_2)$_2$ generated *in situ* shows that this complex is highly active for the hydrophosphination of methyl acrylate with primary phosphines, such as $PPhH_2$ and $PCyH_2$. This additional experimental work will be included in the publication. The paper will help us set up the future development of a highly reactive half-sandwich metal catalyst for asymmetric hydrophosphination (long-term goal).

Scheme 7.2 Proposed Cp*Ru-catalyzed hydrophosphination reactions using primary phosphine or methyl methacrylate (prochiral alkene) giving chiral phosphine products. R = Ph and Cy, R' = Me, Bu^t.

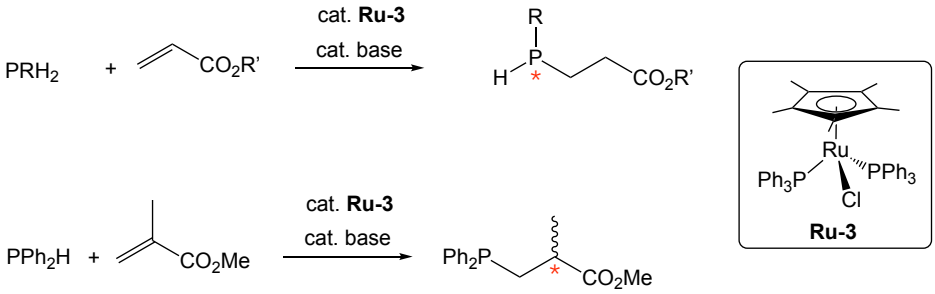

7.1.2 Publication on synthesis and physical properties of Cp*Co(III) complexes

In Chapter 3, I presented the synthesis and physical properties of Cp*Co(III) complexes, including Co(η^5-Cp*)I_2(CO) (**Co-1**), Co(η^5-Cp*)I_2(PR_2H) (**Co-2**), Co(η^5-Cp*)I_2(PRH_2) (**Co-3**), [Co(η^5-Cp*)I(PR_2H)$_2$]I (**Co-4**) and [Co(η^5-Cp*)($NCCH_3$)$_3$][SbF_6]$_2$ (**Co-5**) and [Co(η^5-Cp*)($NCCH_3$)$_2$(PR_2H)][SbF_6]$_2$ (**Co-6**) (R = alkyl and aryl). In this early research, I demonstrate the catalytic activity of **Co-1** and **Co-5** for hydrophosphination and dehydrocoupling. In addition, these complexes exhibit a fascinating interaction (likely P-H activation) with excess PPh_2H. This work will be published as an article.

According to reactivity studies of **Co-1** and **Co-5**, these Co(III) complexes do not react with alkene but show diverse phosphine coordination chemistry. This highlights the importance of the phosphine complexes **Co-2**, **Co-3**, **Co-4** and **Co-6**. First, these complexes are relevant to catalytic or other interesting reactivity. Second, there are few physical properties of Cp*Co secondary phosphine complexes reported in the literature. In addition, although complexes **Co-1** and **Co-5** have been widely used in C-H activation chemistry,[2–5] none of these Cp*Co(III) complexes has been investigated for their activities for P-H activation. This will be another selling point for this paper.

This paper will lay the groundwork for our future publication on the comprehensive research of these catalytic reactions. I have finished most of the characterization of these Cp*Co complexes except the microanalysis of dicationic complexes **Co-6**. The short-term goal for completing this paper is to prepare pure **Co-6** for microanalysis.

7.1.3 Publication on Cp*Co-catalyzed hydrophosphination

In Chapter 4, I described the investigation of the hydrophosphination of alkenes using Co(η^5-Cp*)I_2(CO) (**Co-1**) as a catalyst, and mechanistic studies. I am currently writing the manuscript on this work. This paper will include two major selling points. First, there are only a few examples of Co-catalyzed hydrophosphination in the literature (references see Section 4.1). Additionally, the phosphine substrate scope in our Co system includes primary and secondary, and alkyl and aryl, phosphines, despite catalysis being limited to activated alkenes. This broad substrate scope is intriguing because most catalyses use PPh_2H as the only phosphine substrate. In addition, 3d metals may have both two-electron and one-electron reactivities, which highlights that their oxidation states need to be considered in catalyses. Our Co-catalyzed hydrophosphination provides an example of reducing Co(III) to Co(II), which then catalyzes the hydrophosphination process.

In the short term, the priority is to refine my preliminary EPR simulations for the experiment in which complex Co(η^5-Cp*)I_2(PPh_2H) (**Co-2a**) reacts with DBU to generate a paramagnetic mixture (Scheme 7.3). According to an initial rates experiment (Section 4.4.6), the catalytic reaction shows first-order dependence on the concentration of Co, suggesting that monomeric Co-PR_2 is probably the active catalytic component. Thus, I want to use EPR to probe the reaction mixture of **Co-1** and DBU (2 equiv) in the presence of excess PPh_2H (10 equiv) in C_6D_6 or C_7D_8. A similar experiment described in Chapter 5

was carried out in CD_3CN instead of C_6D_6, which was not directly relevant. Ideally, we will observe the proposed intermediate Co(η^5-Cp*)(PPh_2)(PPh_2H).

Scheme 7.3 Paramagnetic species resulting from the reaction of **Co-2a** with DBU.

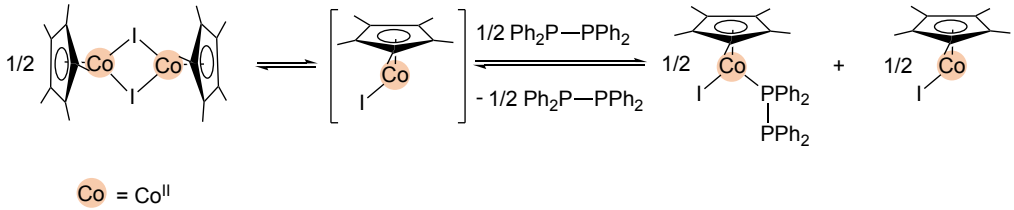

I want to deliberately isolate the binuclear complex [Co(η^5-Cp*)(μ-I)]$_2$ that has been proposed as the critical intermediate to form the active Co(II) phosphido complex. However, according to the literature, this complex is too reactive to isolate.[6] Thus, I plan to synthesize a relatively stable analogue [Co(η^5-Cp*)(μ-Cl)]$_2$ through a literature procedure (Scheme 7.4) [7] and test its activity for hydrophosphination. Using this Co(II) complex as a catalyst can avoid the formation of a byproduct, diphosphine.

Scheme 7.4 Synthesis of binuclear Co(II) complex [Co(η^5-Cp*)(μ-Cl)]$_2$.

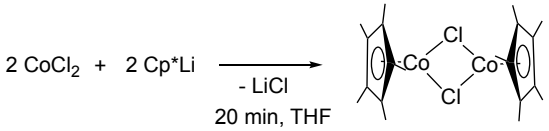

7.1.4 Publication based on Chapters 5 and 6

In Chapter 5, complex Co(η^5-Cp*)I_2(CO) (**Co-1**) can catalyze dehydrocoupling of PR_2H and PRH_2 in the presence of hydrogen acceptors (HAs). While the addition of HA facilitates the catalytic reaction, a quantity of byproducts was produced, including some P-N coupling products. This work could be published as a communication.

In Chapter 6, in a mixture of [Co(η^5-Cp*)($NCCH_3$)$_3$][SbF_6]$_2$ (**Co-5**) and excess PPh_2H, I show a novel reversible P-H activation of free PPh_2H involving paramagnetic Co(II) species and a possible PPh_2 radical. This work is suitable for publication as a

communication. For both potential papers, short-term work is that my preliminary EPR simulations need refinement.

7.2 Long-term work: developing chiral metal catalysts for asymmetric hydrophosphination

Given that our Cp*Ru and Cp*Co systems work for diverse phosphine substrates, the future project is to develop chiral metal catalysts for asymmetric hydrophosphination. One approach is to build a metal catalyst with a chiral half-sandwich ligand. The synthesis and use of chiral Cp ligands (Cp^x) have developed as a fascinating area of enantioselective catalysis, especially for Rh(III) catalyzed C-H functionalizations.[8–12] Some half-sandwich chiral Ru[12] and Co[11] complexes might be probed as potential catalyst candidates. For example, trisubstituted chiral Cp^xCo(III) complexes could be prepared (Scheme 7.5). These complexes are known catalysts that demonstrate their outstanding efficacy in asymmetric C-H bond functionalization.[8] As shown in Scheme 7.5, the desired complexes are prepared by mixing Cp^xH with Co_2CO_8 and then oxidizing with I_2, a procedure similar to that used to synthesize **Co-1**. The chirality of the Cp^x moieties enables the incorporation of chirality into the catalyst while leaving at least two open coordination sites for substrate binding, as shown previously with the comparable **Co-1**. In addition, this similar class of chiral Cp^x ligands can be used to make chiral Cp^xRu(II) complexes,[12] such as [Ru(η^5-Cp^x)(η^6-C_6H_6)][PF_6] and [Ru(η^5-Cp^x)($NCCH_3$)$_3$][PF_6]. Given the high activity of our Cp*Ru-catalyzed hydrophosphination, I proposed these chiral Cp^xRu complexes could be potential candidates for asymmetric hydrophosphination.

Scheme 7.5 Synthesis of chiral $Cp^xCo(III)$ complexes.

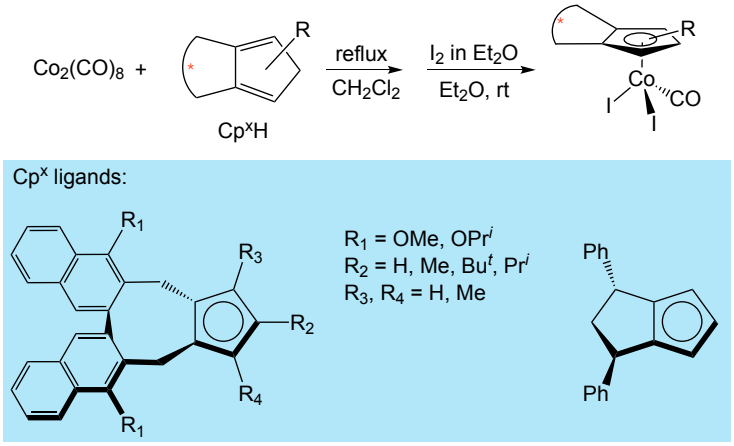

With a chiral half-sandwich Co or Ru catalyst in hand, our primary objective would be to investigate the enantioselective synthesis of P-chiral phosphines through prochiral substrates PRH_2. Notably, the barrier to inversion at phosphorus is often significantly lower for the key intermediates, metal phosphido (M-PRH).[13] With a chiral metal catalyst, it is possible to capture these intermediates stereoselectively (i.e. one chiral M-PRH dominate over the other) through the formation of P-C bonds (dynamic kinetic resolution). For example, some exceptional enantioselectivities (er as high as 99%) have been reported for some recent first-row metal-catalyzed hydrophosphination (e.g. Ni catalyst with chiral ligands[14]).

7.3 References

(1) Belli, R. G.; Yang, J.; Bahena, E. N.; McDonald, R.; Rosenberg, L. Mechanism and Catalyst Design in Ru-Catalyzed Alkene Hydrophosphination. *ACS Catal.* **2022**, *12*, 5247–5262.

(2) Loginov, D. A.; Shul'pina, L. S.; Muratov, D. V.; Shul'pin, G. B. Cyclopentadienyl Cobalt(III) Complexes: Synthetic and Catalytic Chemistry. *Coord. Chem. Rev.* **2019**, *387*, 1–31.

(3) Prakash, S.; Kuppusamy, R.; Cheng, C. H. Cobalt-Catalyzed Annulation Reactions via C−H Bond Activation. *ChemCatChem* **2018**, *10*, 683–705.

(4) Yoshino, T.; Matsunaga, S. High-Valent Cobalt-Catalyzed C–H Bond Functionalization. *Adv. Organomet. Chem.* **2017**, *68*, 197–247.

(5) Yoshino, T.; Matsunaga, S. (Pentamethylcyclopentadienyl)Cobalt(III)-Catalyzed C–H Bond Functionalization: From Discovery to Unique Reactivity and Selectivity. *Adv. Synth. Catal.* **2017**, *359*, 1245–1262.

(6) Kölle, U.; Fuss, B. Pentamethylcyclopentadienyl-Übergangsmetall-π-Komplexe, V1). (Pentamethylcyclopentadienyl)Cobalt(III)-Halogeno- Und -Amido-Komplexe. *Chem. Ber.* **1984**, *117*, 743–752.

(7) Koelle, U.; Fuss, B.; Raabe, E. Pentamethylcyclopentadlenyl Transition Metal Complexes. 9.1 Reactions and Solid-State and Solution Behavior of Dinuclear Cobalt(II) Complexes $[C_5Me_5Co(\mu\text{-}X)]_2$. *Organometallics* **1986**, *5*, 980–987.

(8) Ozols, K.; Onodera, S.; Woźniak, Ł.; Cramer, N. Cobalt(III)-Catalyzed Enantioselective Intermolecular Carboamination by C−H Functionalization. *Angew. Chem. Int. Ed.* **2021**, *60*, 655–659.

(9) Ozols, K.; Jang, Y. S.; Cramer, N. Chiral Cyclopentadienyl Cobalt(III) Complexes Enable Highly Enantioselective 3d-Metal-Catalyzed C-H Functionalizations. *J. Am. Chem. Soc.* **2019**, *141*, 5675–5680.

(10) Duchemin, C.; Smits, G.; Cramer, N. RhI, IrIII,and CoIII Complexes with Atropchiral Biaryl Cyclopentadienyl Ligands: Syntheses, Structures, and Catalytic Activities. *Organometallics* **2019**, *38*, 4014–4021.

(11) Herraiz, A. G.; Cramer, N. Cobalt(III)-Catalyzed Diastereo- And Enantioselective Three-Component C-H Functionalization. *ACS Catal.* **2021**, *11*, 11938–11944.

(12) Wang, S. G.; Park, S. H.; Cramer, N. A Readily Accessible Class of Chiral Cp Ligands and Their Application in RuII-Catalyzed Enantioselective Syntheses of Dihydrobenzoindoles. *Angew. Chem. Int. Ed.* **2018**, *57*, 5459–5462.

(13) Gallant, S. K.; Tipker, R. M.; Glueck, D. S. Copper-Catalyzed Asymmetric Alkylation of Secondary Phosphines via Rapid Pyramidal Inversion in P-Stereogenic Cu–Phosphido Intermediates. *Organometallics* **2022**, *41*, 1721–1730.

(14) Liu, X. T.; Han, X. Y.; Wu, Y.; Sun, Y. Y.; Gao, L.; Huang, Z.; Zhang, Q. W. Ni-Catalyzed Asymmetric Hydrophosphination of Unactivated Alkynes. *J. Am. Chem. Soc.* **2021**, *143*, 11309–11316.

Appendix A – Survey of first-row transition metal-catalyzed hydrophosphination and metal-catalyzed dehydrocoupling of phosphines

This section describes the examples (from 2000 to early 2022) of first-row metal-catalyzed hydrophosphination in terms of activity and selectivity (Table A.1).

Table A.1 Reactivity currently available on some first-row metal-catalyzed hydrophosphination reactions.

Catalyst	Selectivity	Substrate scope		TOF (h^{-1})[a]	Ref
		phosphine	alkenes/alkynes		
22 Ti 5.56 x 10^3 Titanium					
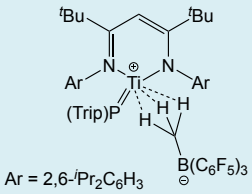 Ar = 2,6-^{i}Pr$_2$C$_6$H$_3$ Trip = 2,4,6-^{i}Pr$_3$C$_6$H$_2$	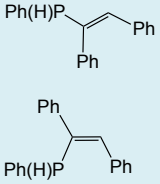 No specific selectivity	PH_2Ph	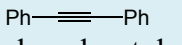 diphenylacetylene	0.6	1
$Ti(NMe_2)_4$/ $LiN(SiMe_3)_2$/ N-heterocyclic carbene	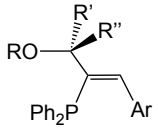 *Z*-selective	PPh_2H	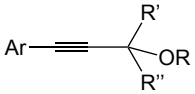 propargylic ethers (alkynes)	120	2
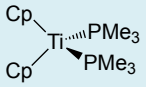 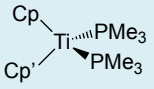 Cp' = $C_5H_4(CH_2)_2PPh_2$ *n*-BuLi cocatalyst	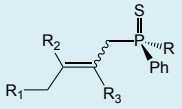 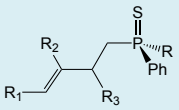 *anti*-Markovnikov	PPh_2H	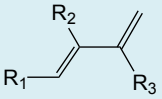 diene  styrene	3.2	3
25 Mn 950 Manganese					
$MnCl_2•4H_2O$	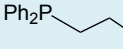 *anti*-Markovnikov	PPh_2H	 styrene derivatives	0.2	4

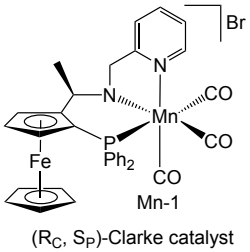 (R$_C$, S$_P$)-Clarke catalyst *t*-PentOK cocatalyst	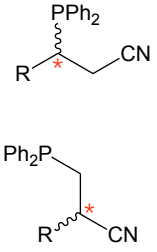 *anti*-Markovnikov, enantioselective	PPh_2H	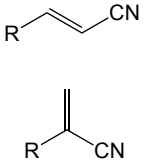 activated alkenes	50.0	5
Same catalyst above	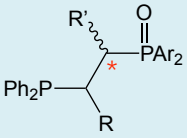 *anti*-Markovnikov, enantioselective	PPh_2H	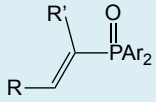 Vinyl phosphine oxide	2.4	6
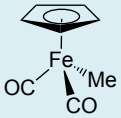	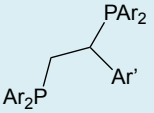	PAr_2H	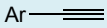 terminal aryl acetylenes	0.3	7
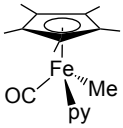	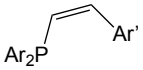 *anti*-Markovnikov, *Z*-selective	PAr_2H	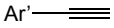 terminal aryl acetylenes	0.2	8
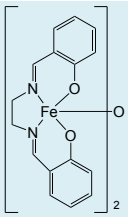	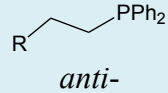 *anti*-Markovnikov	PPh_2H	 activated alkenes	8.3	9
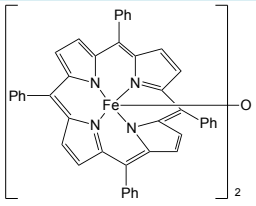	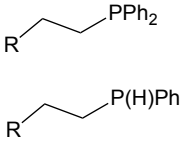 *anti*-Markovnikov	PPh_2H $PPhH_2$	 activated alkenes	8.3	10
	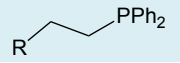	PPh_2H		0.8	11

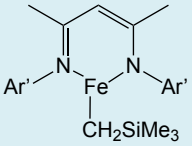	*anti*-Markovnikov		activated alkenes & aryl alkenes		
	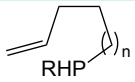 vinyl primary phosphines	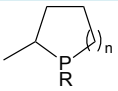 vinyl primary phosphine s	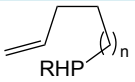 vinyl primary phosphines	0.7	12
	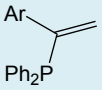 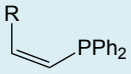 regioselective; Markovnikov (Solvent-dependent)	PPh$_2$H	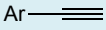 terminal aryl acetylenes	6.7	13
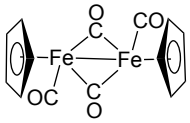	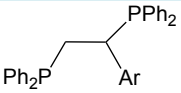	PPh$_2$H	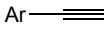 terminal aryl acetylenes	9.6	14
					
Co(acac)$_2$ *n*-BuLi cocatalyst	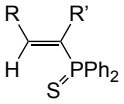 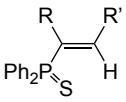 regioselective (*syn*-addition)	PPh$_2$H	 alkyl and aryl alkynes	5.0	15
Co(PMe$_3$)$_4$	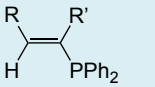 regioselective (*syn*-addition)	PPh$_2$H	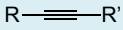 alkyl and aryl alkynes	16.8	16

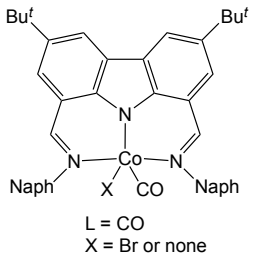 L = CO X = Br or none	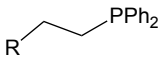 *anti*-Markovnikov	PPh_2H	 activated alkenes & imine	20.0	17
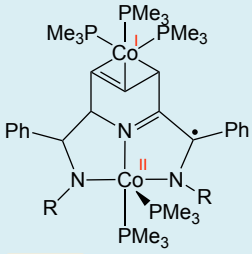	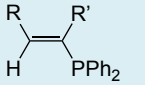 regioselective (*syn*-addition)	PPh_2H	 alkyl and aryl alkynes	45	18
28 Ni 84 Nickel					
$Ni[P(OEt)_3]_4$ *et al*	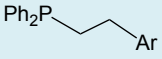 *anti*-Markovnikov	PPh_2H	 aryl alkene	1.0	19
$NiBr_2$ *et al*	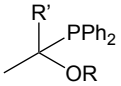 Markovnikov	PPh_2H	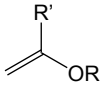 alkenyl alkyl ethers	25.0	20
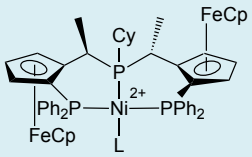	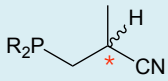 *anti*-Markovnikov, enantioselective	Alkyl and aryl PR_2H	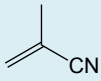 methacrylonitrile	12.5 (R = Ph)	21
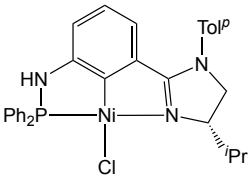	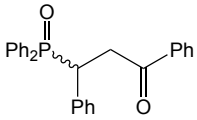 regioselective	PPh_2H	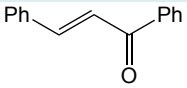 activated internal alkenes (chalcone)	0.75	22
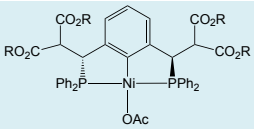	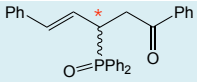 enantioselective (poor)	PPh_2H	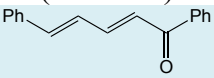 activated alkenes	0.3	23

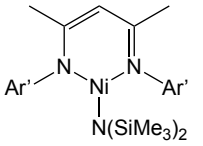	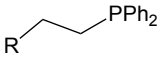 *anti*-Markovnikov	PPh_2H	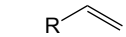 activated alkenes, aryl alkynes	1.1	24
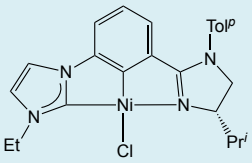	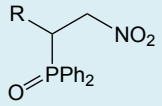 *anti*-Markovnikov	PPh_2H	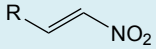 internal activated alkenes	0.8	25
$Ni(COD)_2$/ chiral P-ligand/ $P(O)(OPh)_2OH$	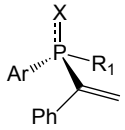 Markovnikov, enantioselective	PPh_2H, chiral PRR'H	 aryl alkynes	0.3	26
29 Cu 60 Copper					
CuI/Cs_2CO_3	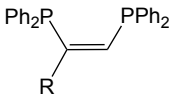 Z-selective	PPh_2H	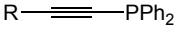 alkynyl phosphines	24.8	27
$(CuOTf)_2$	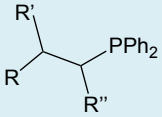 *anti*-Markovnikov	PPh_2H, （PCy_2H ）	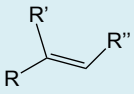 styrene derivatives	0.5	4
$CuCl_2$/ *N*-heterocyclic carbene	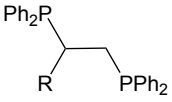	PPh_2H	 alkyl and aryl terminal alkynes	19.2	28
$Cu(acac)_2$	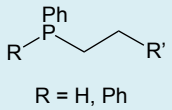 R = H, Ph *anti*-Markovnikov (for alkene)	PPh_2H, $PPhH_2$	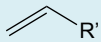 activated and unactivated alkenes/alkynes	118	29
$[Cu(CH_3CN)]PF_6$/ chiral P-ligand/ Barton's base	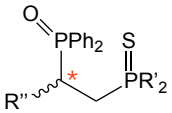 enantioselective	PPh_2H, chiral PRR'H	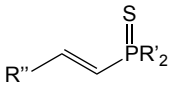 vinyl phosphines	0.8	30

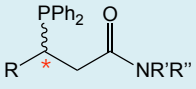 *anti*-Markovnikov, enantioselective	PPh_2H, chiral PRR'H	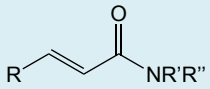 activated alkenes	0.4	31

[a]TOF = (mol substrate converted)/(mol. Cat x time) = (% conversion/%loading)/time; the presented TOF is the highest value for the reaction.

References:

(1) Zhao, G.; Basuli, F.; Kilgore, U. J.; Fan, H.; Aneetha, H.; Huffman, J. C.; Wu, G.; Mindiola, D. J. Neutral and Zwitterionic Low-Coordinate Titanium Complexes Bearing the Terminal Phosphinidene Functionality. Structural, Spectroscopic, Theoretical, and Catalytic Studies Addressing the Ti-P Multiple Bond. *J. Am. Chem. Soc.* **2006**, *128*, 13575–13585.

(2) Sakae, R.; Yamamoto, Y.; Komeyama, K.; Takaki, K. Hydrophosphination of Propargylic Ethers with Diphenylphosphine in the Presence of LiHMDS, N-Heterocyclic Carbene, and Ti(NMe2)4. *Chem. Lett.* **2010**, *39*, 276–277.

(3) Perrier, A.; Comte, V.; Moïse, C.; Le Gendre, P. First Titanium-Catalyzed 1,4-Hydrophosphination of 1,3-Dienes. *Chem. – Eur. J.* **2010**, *16*, 64–67.

(4) Leyva-Pérez, A.; Vidal-Moya, J. A.; Cabrero-Antonino, J. R.; Al-Deyab, S. S.; Al-Resayes, S. I.; Corma, A. Copper(I)-Catalyzed Hydrophosphination of Styrenes. *J. Organomet. Chem.* **2011**, *696*, 362–367.

(5) Pérez, J. M.; Postolache, R.; Castiñeira Reis, M.; Sinnema, E. G.; Vargová, D.; De Vries, F.; Otten, E.; Ge, L.; Harutyunyan, S. R. Manganese(I)-Catalyzed H-P Bond Activation via Metal-Ligand Cooperation. *J. Am. Chem. Soc.* **2021**, *143*, 20071–20076.

(6) Ge, L.; Harutyunyan, S. R. Manganese(i)-Catalyzed Access to 1,2-Bisphosphine Ligands. *Chem. Sci.* **2022**, *13*, 1307–1312.

(7) Kamitani, M.; Itazaki, M.; Tamiya, C.; Nakazawa, H. Regioselective Double Hydrophosphination of Terminal Arylacetylenes Catalyzed by an Iron Complex. *J. Am. Chem. Soc.* **2012**, *134*, 11932–11935.

(8) Itazaki, M.; Katsube, S.; Kamitani, M.; Nakazawa, H. Synthesis of Vinylphosphines and Unsymmetric Diphosphines: Iron-Catalyzed Selective Hydrophosphination

Reaction of Alkynes and Vinylphosphines with Secondary Phosphines. *Chem. Commun.* **2016**, *52*, 3163–3166.

(9) Gallagher, K. J.; Webster, R. L. Room Temperature Hydrophosphination Using a Simple Iron Salen Pre-Catalyst. *Chem. Commun.* **2014**, *50*, 12109–12111.

(10) Gallagher, K. J.; Espinal-Viguri, M.; Mahon, M. F.; Webster, R. L. A Study of Two Highly Active, Air-Stable Iron(III)-μ-Oxo Precatalysts: Synthetic Scope of Hydrophosphination Using Phenyl- and Diphenylphosphine. *Adv. Synth. Catal.* **2016**, *358*, 2460–2468.

(11) King, A. K.; Buchard, A.; Mahon, M. F.; Webster, R. L. Facile, Catalytic Dehydrocoupling of Phosphines Using β-Diketiminate Iron(II) Complexes. *Chem. – Eur. J.* **2015**, *21*, 15960–15963.

(12) Espinal-Viguri, M.; King, A. K.; Lowe, J. P.; Mahon, M. F.; Webster, R. L. Hydrophosphination of Unactivated Alkenes and Alkynes Using Iron(II): Catalysis and Mechanistic Insight. *ACS Catal.* **2016**, *6*, 7892–7897.

(13) King, A. K.; Gallagher, K. J.; Mahon, M. F.; Webster, R. L. Markovnikov versus Anti-Markovnikov Hydrophosphination: Divergent Reactivity Using an Iron(II) β-Diketiminate Pre-Catalyst. *Chem. – Eur. J.* **2017**, *23*, 9039–9043.

(14) Ackley, B. J.; Pagano, J. K.; Waterman, R. Visible-Light and Thermal Driven Double Hydrophosphination of Terminal Alkynes Using a Commercially Available Iron Compound. *Chem. Commun.* **2018**, *54*, 2774–2776.

(15) Ohmiya, H.; Yorimitsu, H.; Oshima, K. Cobalt-Catalyzed Syn Hydrophosphination of Alkynes. *Angew. Chem. Int. Ed.* **2005**, *44*, 2368–2370.

(16) Rajpurohit, J.; Kumar, P.; Shukla, P.; Shanmugam, M.; Shanmugam, M. Mechanistic Investigation of Well-Defined Cobalt Catalyzed Formal E-Selective Hydrophosphination of Alkynes. *Organometallics* **2018**, *37*, 2297–2304.

(17) Nolla-Saltiel, R.; Geer, A. M.; Taylor, L. J.; Churchill, O.; Davies, E. S.; Lewis, W.; Blake, A. J.; Kays, D. L. Hydrophosphination of Activated Alkenes by a Cobalt(I) Pincer Complex. *Adv. Synth. Catal.* **2020**, *362*, 3148–3157.

(18) Kumar, P.; Sen, A.; Rajaraman, G.; Shanmugam, M. An Unusual Mixed-Valence Cobalt Dimer as a Catalyst for the Anti-Markovnikov Hydrophosphination of Alkynes. *Inorg. Chem. Front.* **2022**, 32–34.

(19) Kazankova, M. A.; Shulyupin, M. O.; Borisenko, A. A.; Beletskaya, I. P. Synthesis of Alkyl(Diphenyl)Phosphines by Hydrophosphination of Vinylarenes Catalyzed by Transition Metal Complexes. *Russ. J. Org. Chem.* **2002**, *38*, 1479–1484.

(20) Kazankova, M. A.; Shulyupin, M. O.; Beletskaya, I. P. Catalytic Hydrophosphination of Alkenylalkyl Ethers. *Synlett* **2003**, No. 14, 2155–2158.

(21) Sadow, A. D.; Togni, A. Enantioselective Addition of Secondary Phosphines to Methacrylonitrile: Catalysis and Mechanism. *J. Am. Chem. Soc.* **2005**, *127*, 17012–17024.

(22) Yang, M. J.; Liu, Y. J.; Gong, J. F.; Song, M. P. Unsymmetrical Chiral PCN Pincer Palladium(II) and Nickel(II) Complexes with Aryl-Based Aminophosphine-Imidazoline Ligands: Synthesis via Aryl C-H Activation and Asymmetric Addition of Diarylphosphines to Enones. *Organometallics* **2011**, *30*, 3793–3803.

(23) Yang, X. Y.; Tay, W. S.; Li, Y.; Pullarkat, S. A.; Leung, P. H. Asymmetric 1,4-Conjugate Addition of Diarylphosphines to α,β,γ,δ-Unsaturated Ketones Catalyzed by Transition-Metal Pincer Complexes. *Organometallics* **2015**, *34*, 5196–5201.

(24) Webster, R. L. Room Temperature Ni(II) Catalyzed Hydrophosphination and Cyclotrimerization of Alkynes. *Inorganics* **2018**, *6*, 120.

(25) Yan, J.; Wang, Y. B.; Hou, S.; Shi, L.; Zhu, X.; Hao, X. Q.; Song, M. P. NCC Pincer Ni (II) Complexes Catalyzed Hydrophosphination of Nitroalkenes with Diphenylphosphine. *Appl. Organomet. Chem.* **2020**, *34*, e5954.

(26) Liu, X. T.; Han, X. Y.; Wu, Y.; Sun, Y. Y.; Gao, L.; Huang, Z.; Zhang, Q. W. Ni-Catalyzed Asymmetric Hydrophosphination of Unactivated Alkynes. *J. Am. Chem. Soc.* **2021**, *143*, 11309–11316.

(27) Kondoh, A.; Yorimitsu, H.; Oshima, K. Copper-Catalyzed Anti-Hydrophosphination Reaction of 1-Alkynylphosphines with Diphenylphosphine Providing (Z)-1,2-Diphosphino-1-Alkenes. *J. Am. Chem. Soc.* **2007**, *129*, 4099–4104.

(28) Yuan, J.; Zhu, L.; Zhang, J.; Li, J.; Cui, C. Sequential Addition of Phosphine to Alkynes for the Selective Synthesis of 1,2-Diphosphinoethanes under Catalysis. Well-Defined NHC-Copper Phosphides vs in Situ $CuCl_2$/NHC Catalyst. *Organometallics* **2017**, *36*, 455–459.

(29) Dannenberg, S. G.; Waterman, R. A Bench-Stable Copper Photocatalyst for the Rapid Hydrophosphination of Activated and Unactivated Alkenes. *Chem. Commun.* **2020**, *56*, 14219–14222.

(30) Yue, W.; Xiao, J.; Zhang, S.; Yin, L. Rapid Synthesis of Chiral 1,2-Bisphosphine Derivatives through Copper(I)-Catalyzed Asymmetric Conjugate Hydrophosphination. *Angew. Chem. Int. Ed.* **2020**, *59*, 7057–7062.

(31) Li, Y. B.; Tian, H.; Yin, L. Copper(I)-Catalyzed Asymmetric 1,4-Conjugate Hydrophosphination of α,β-Unsaturated Amides. *J. Am. Chem. Soc.* **2020**, *142*, 20098–20106.

A significant impediment to accurate comparisons of the activity of transition metal-catalyzed dehydrocoupling reactions is the absence of quantitative data such as TOF, and the wide variety of solvents and conditions used, which can vary significantly between reactions. The activity reported in the literature is often given as a % conversion/yield (semiquantitative) during a specific time period. Table A.2 summarizes reaction details on the most known transition metal catalysts and transforms them into estimated TOF values. Since all cases include PPh_2H or PH_2Ph, they are used as representative substrates for secondary or primary phosphine.

Table A.2 Reactivity currently available on metal-catalyzed dehydrocoupling of phosphines.

Catalyst	Substrate	Product	Time (h)	T (°C)	TOF (h^{-1})[a]	Ref.[b]
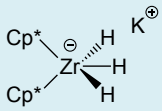	$PPhH_2$	$(PPh)_5$	72	120	1.4	Stephan 1995
	PPh_2H	$(PPh_2)_2$	24	95	0.4	Stephan 2006
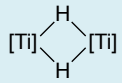	$PPhH_2$	$(PHPh)_2$		40-50	n/a	Harrod 1997
[Ti] = (EBTHI)Ti						

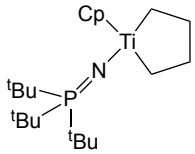	PPh_2H	$(PPh_2)_2$	168	75	0.06	Stephan 2006
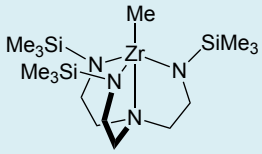	$PPhH_2$	$(PHPh)_2$	168	90	0.1	Waterman 2007
	PPh_2H	$(PPh_2)_2$	288	90	0.06	
	$PPhH_2$	$(PHPh)_2$ $(PPh)_n$	36	120	0.5	
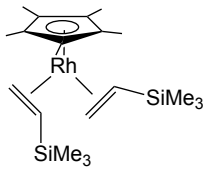	$PPhH_2$	$(PHPh)_2$	18	145	0.3	Brookhart 2001
	PPh_2H	$(PPh_2)_2$	16	140	2.3	
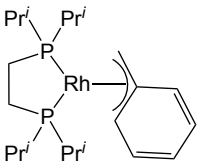	$PPhH_2$	$(PHPh)_2$	20	20	0.4	Tilley 2006
	PPh_2H	$(PPh_2)_2$	8	70	2.3	
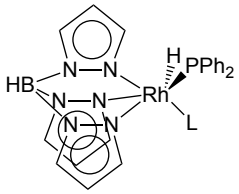 L = PMe_3 (**a**), PPh_2H (**b**)	PPh_2H	$(PPh_2)_2$	13	80	0.8	Tejel 2015
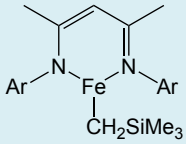	PPh_2H	$(PPh_2)_2$	24	70	0.8	Webster 2015
	PH_2Ph	$(PHPh)_2$	24	100	0.5	
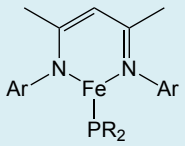	PPh_2H	$(PPh_2)_2$	24	120	0.7	Grubba 2018
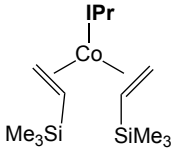	PH_2Ph	$(PHPh)_2$	10	80	0.5	Deng 2018
	PPh_2H	$(PPh_2)_2$	10	80	0.07	
	$PArH_2$	$(PHAr)_2$	10	80	0.6	
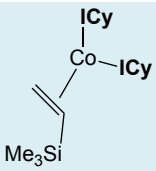	$PArH_2$	$(PHAr)_2$	10	80	0.6	Deng 2018

[a]TOF = (mol substrate converted)/(mol. Cat x time) = (% conversion/%loading)/time; the presented TOF is the highest value for the reaction.

According to the examples described above, the poor product conversion and low activity (TOF) is probably due to the thermodynamic issue (see Introduction). Harrod and colleagues discovered that several of the dehydrocoupling reactions involving a range of main-group elements were almost thermoneutral.[1] For example, the P-H bond dissociation energy (BDE) is 318 kJ/mol, and the BDE of the P-P bond is 214 kJ/mol. Based on a value of 435 kJ/mol for the H-H bond, the bond enthalpy changes (ΔH) for the dehydrocoupling could be estimated as -13 kJ/mol, which is expected to be close to the reaction enthalpy. This suggests that reaction enthalpy for the dehydrocoupling of phosphine is slightly exothermic. In addition, the BDEs of substituted phosphines might vary due to their substituted group, i.e. the substantial difference in P–H BDEs are possible. The most important finding from these data is that the driving force of the dehydrocoupling is predominantly determined by the entropic advantage of eliminating H_2 from the system rather than the strength of the resulting P-P bond. If the H_2 is not removed from the system efficiently, the dehydrocoupling of phosphine would be thermodynamically unfavourable, which is consistent with the computational study reported by Manners and coworkers (see Introduction).

Reference:

(1) Gauvin, F.; Harrod, J. F.; Woo, H. G. Catalytic Dehydrocoupling: A General Strategy for the Formation of Element-Element Bonds. In *Advances in Organometallic Chemistry*; 1998; Vol. 42, pp 363–405.

Appendix B – NMR spectra of Cp*Ru phosphido complexes generated *in situ*

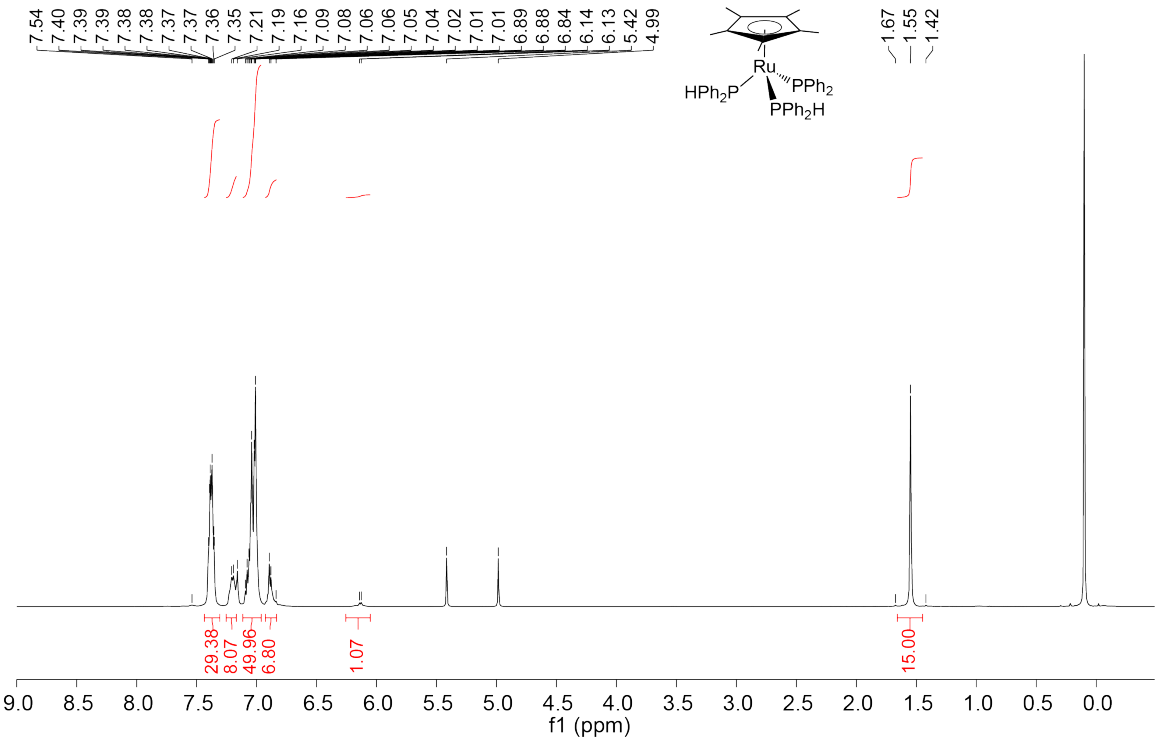

Figure B.1 ^{1}H NMR (500.27 MHz, C_6D_6) spectrum of complex **Ru-1a**.

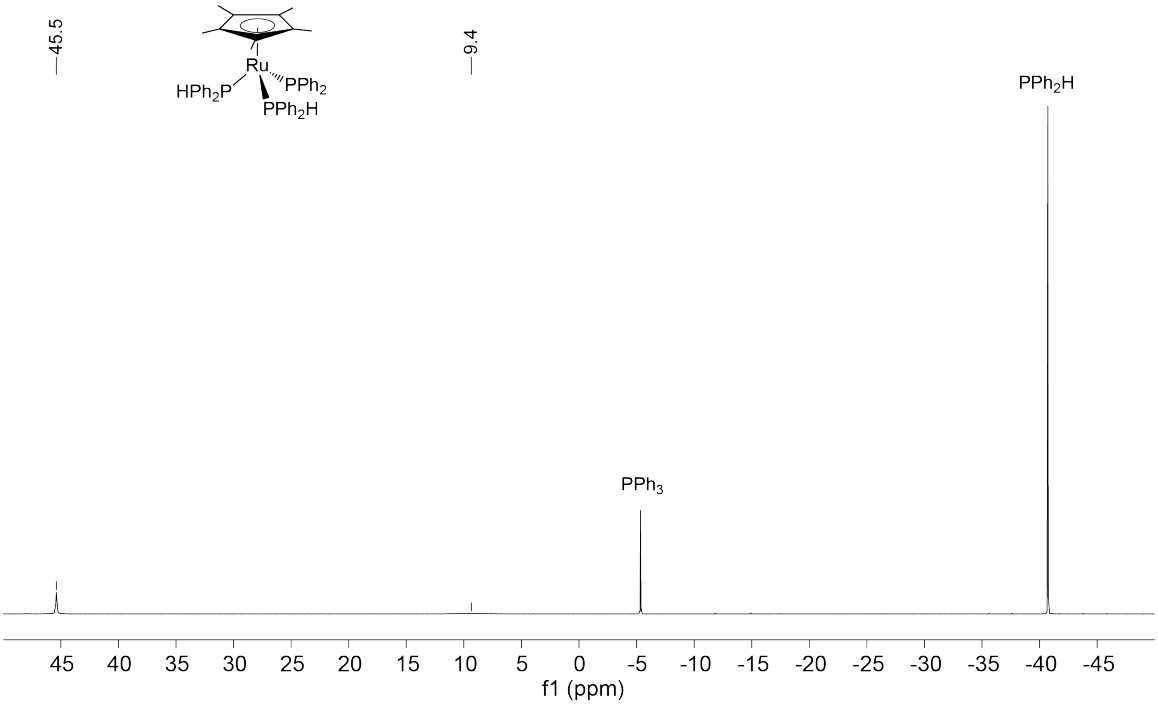

Figure B.2 $^{31}P\{^{1}H\}$ NMR (202.51 MHz, C_6D_6) spectrum of complex **Ru-1a**.

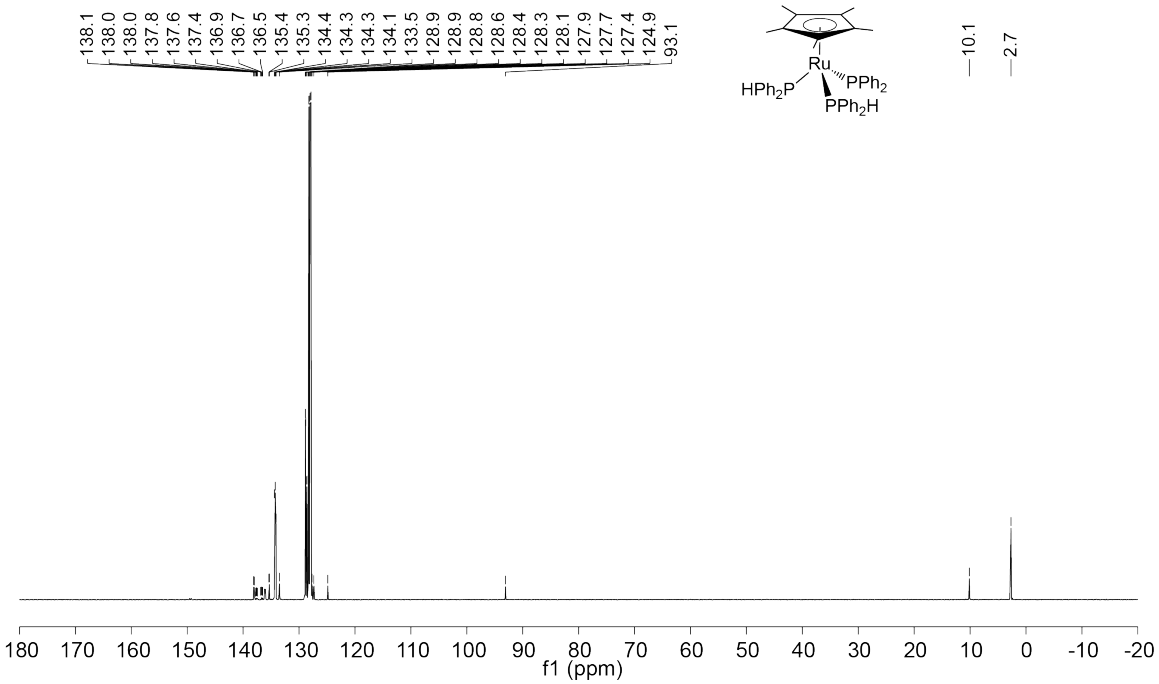

Figure B.3 $^{13}C\{^{1}H\}$ NMR (125.77 MHz, C_6D_6) spectrum of complex **Ru-1a**.

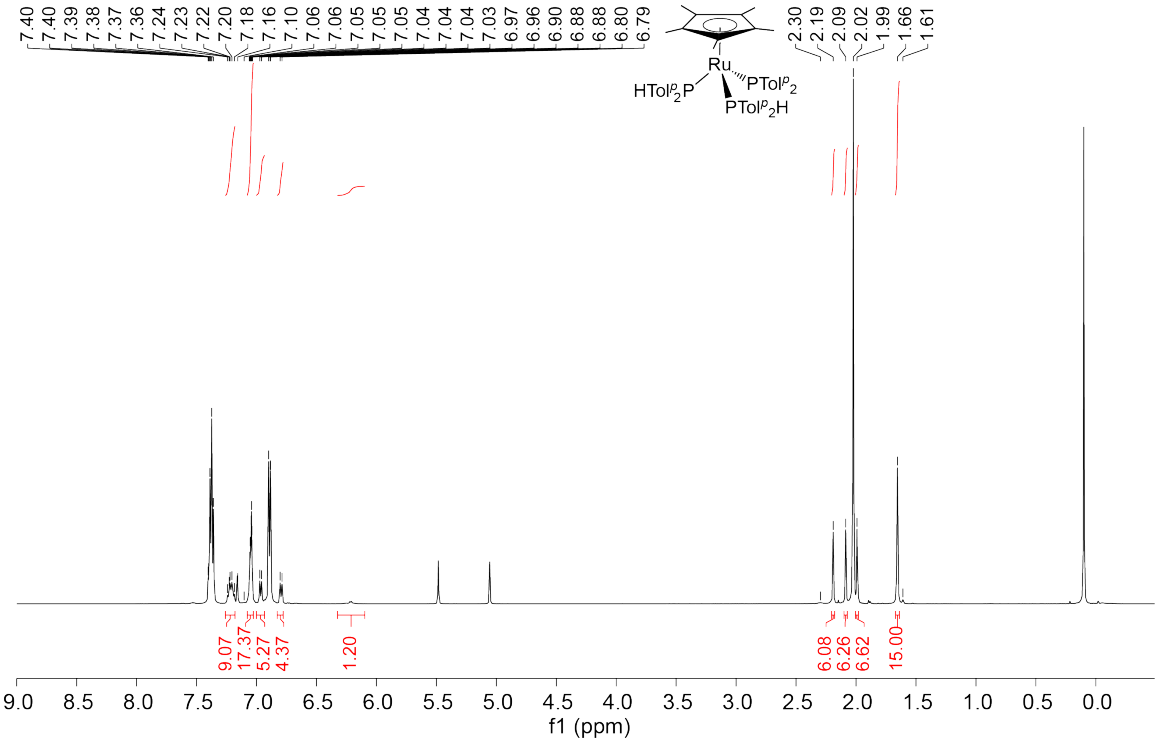

Figure B.4 ^{1}H NMR (500.27 MHz, C_6D_6) spectrum of complex **Ru-1b**.

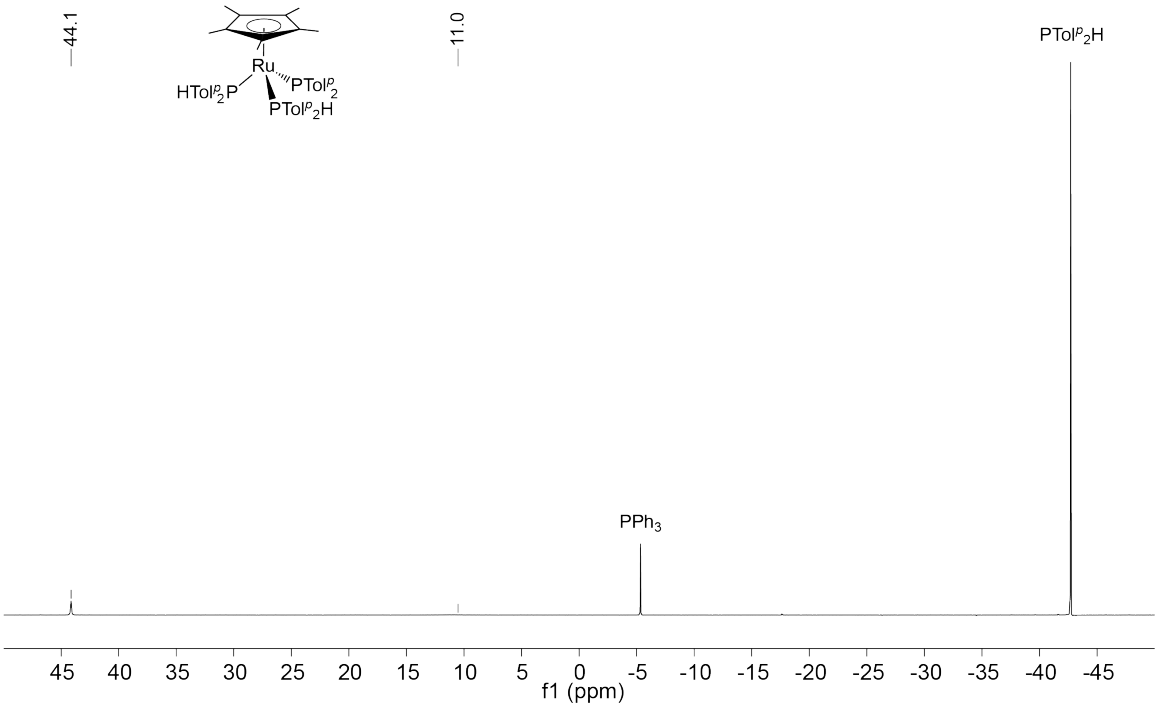

Figure B.5 $^{31}P\{^1H\}$ NMR (202.51 MHz, C_6D_6) spectrum of complex **Ru-1b**.

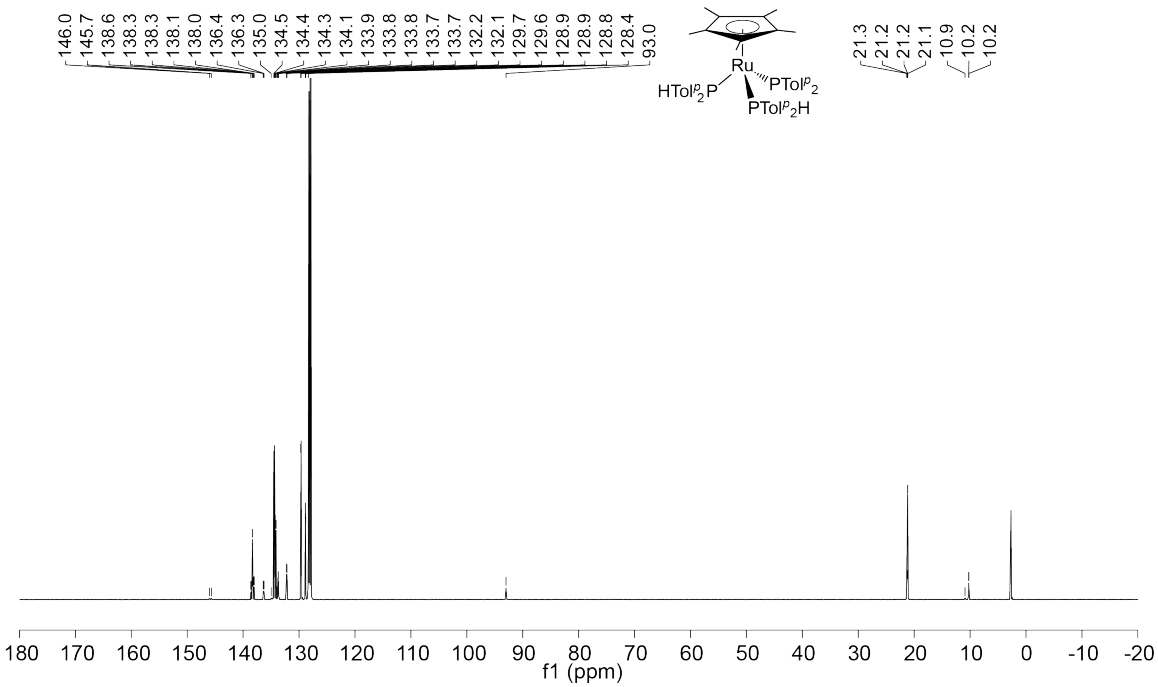

Figure B.6 $^{13}C\{^1H\}$ NMR (125.77 MHz, C_6D_6) spectrum of complex **Ru-1b**.

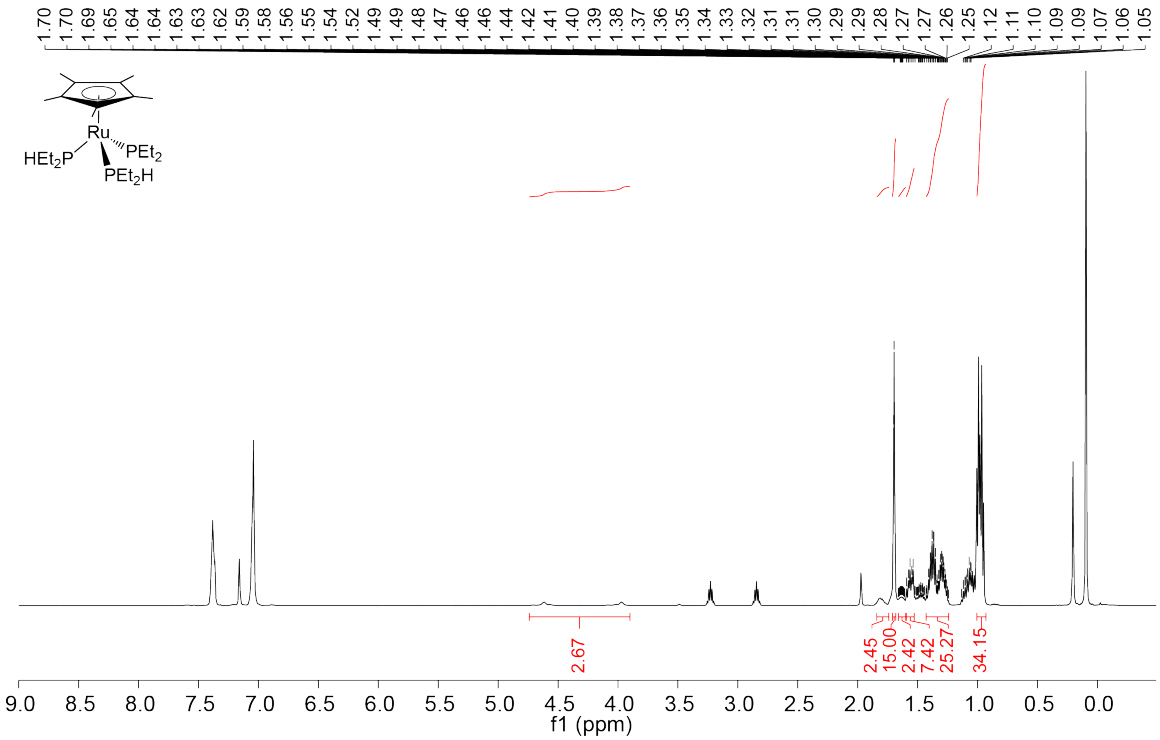

Figure B.7 ^{1}H NMR (500.27 MHz, C_6D_6) spectrum of complex **Ru-1c**.

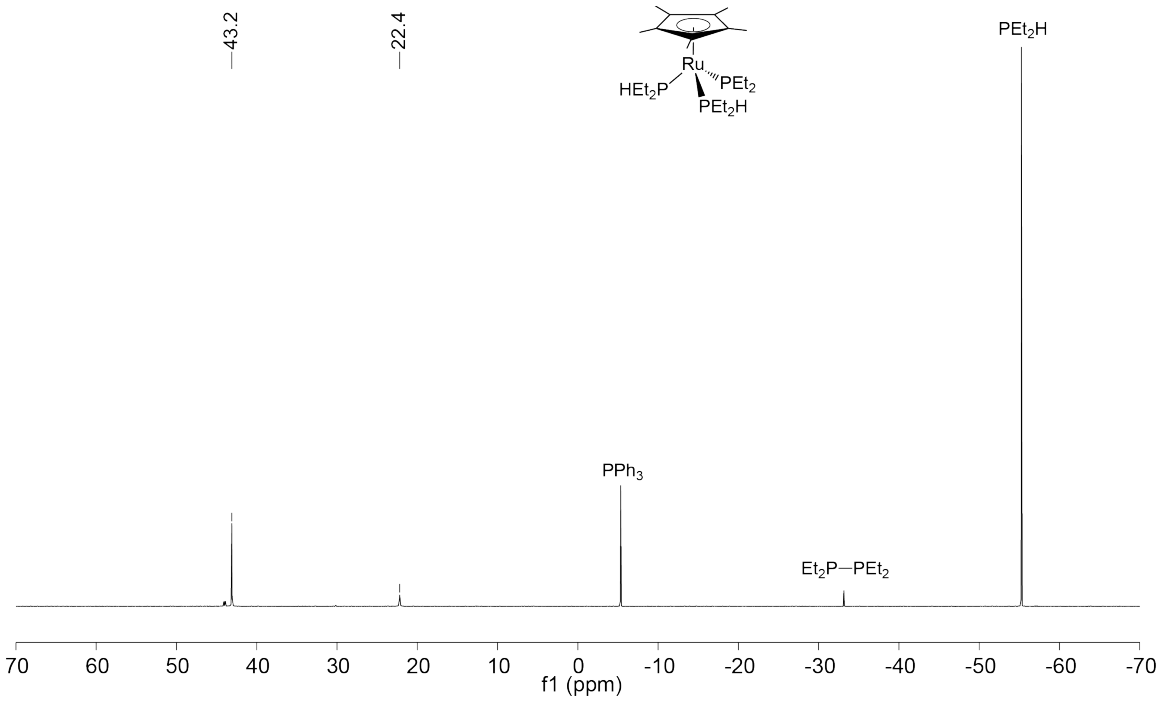

Figure B.8 ^{31}P{^{1}H} NMR (202.51 MHz, C_6D_6) spectrum of complex **Ru-1c**.

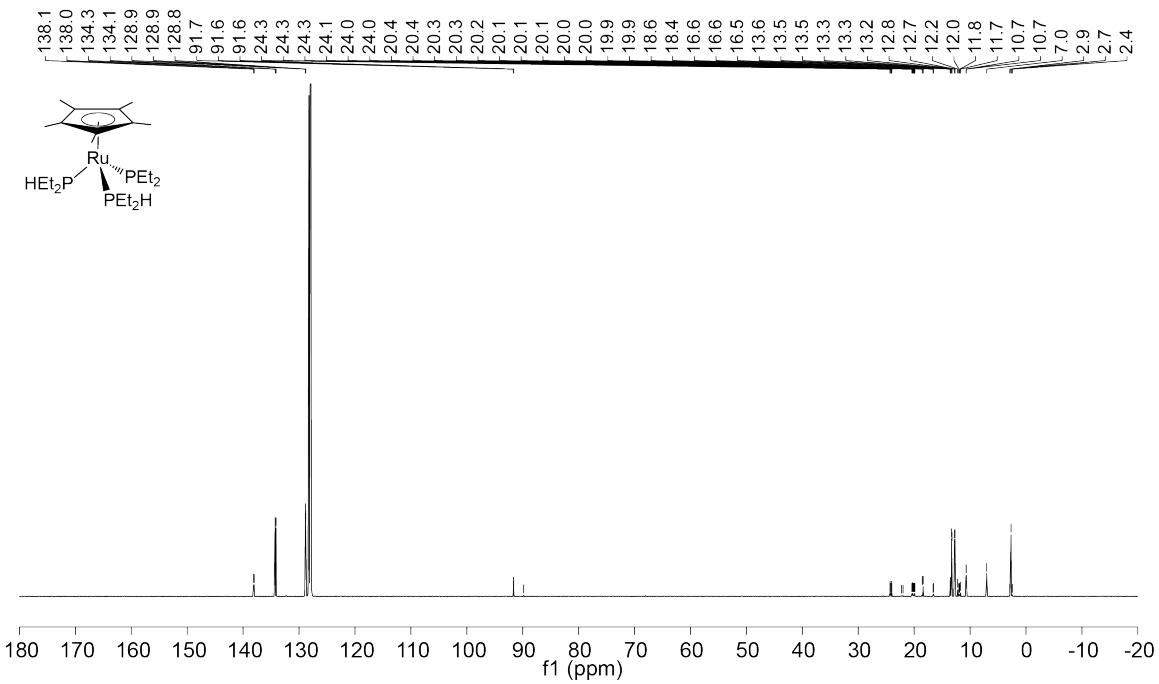

Figure B.9 $^{13}C\{^{1}H\}$ NMR (125.77 MHz, C_6D_6) spectrum of complex **Ru-1c**.

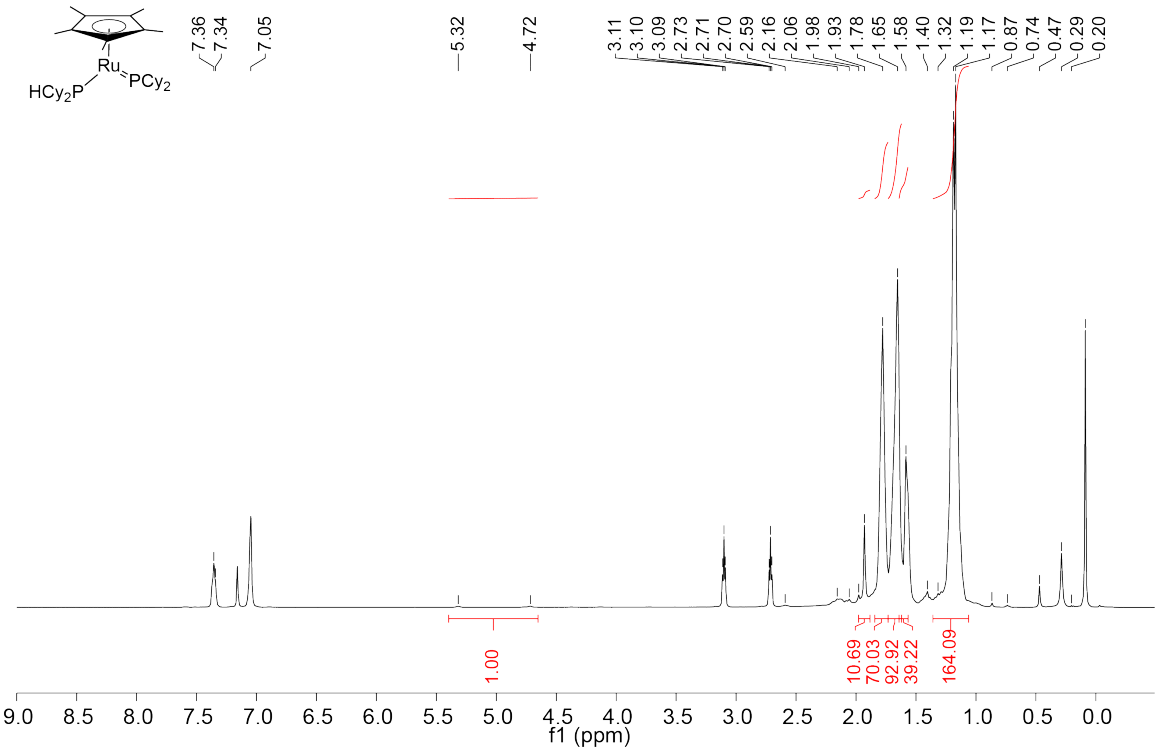

Figure B.10 ^{1}H NMR (500.27 MHz, C_6D_6) spectrum of complex **Ru-2d**.

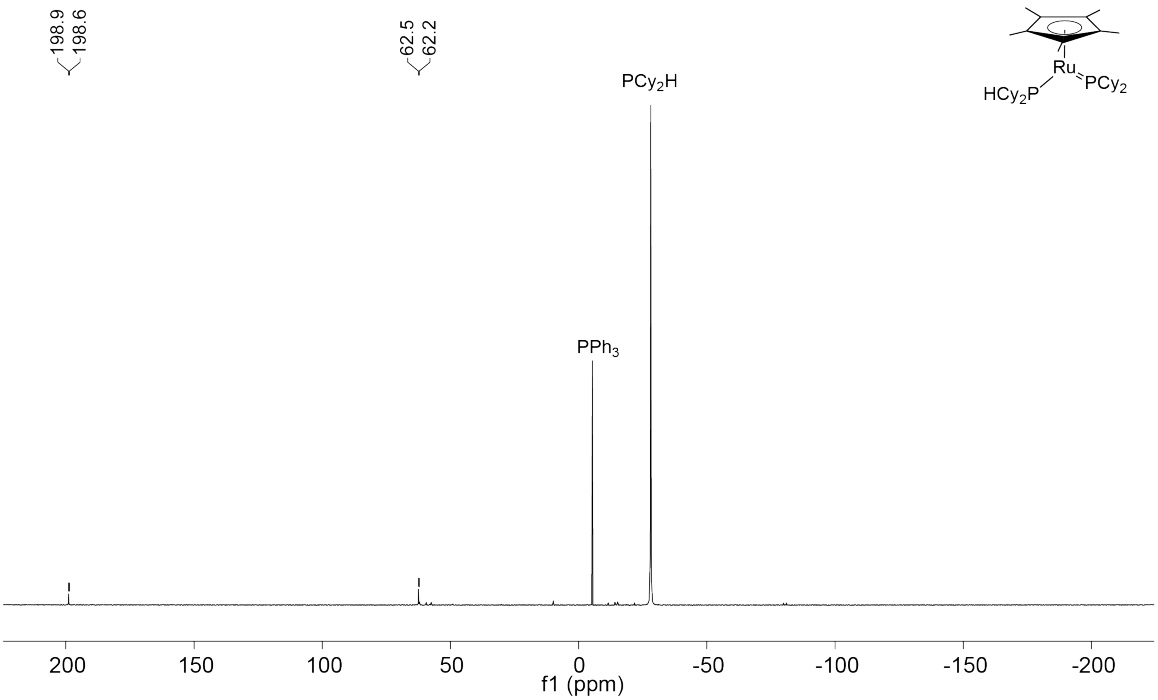

Figure B.11 $^{31}P\{^{1}H\}$ NMR (202.51 MHz, C_6D_6) spectrum of complex **Ru-2d**.

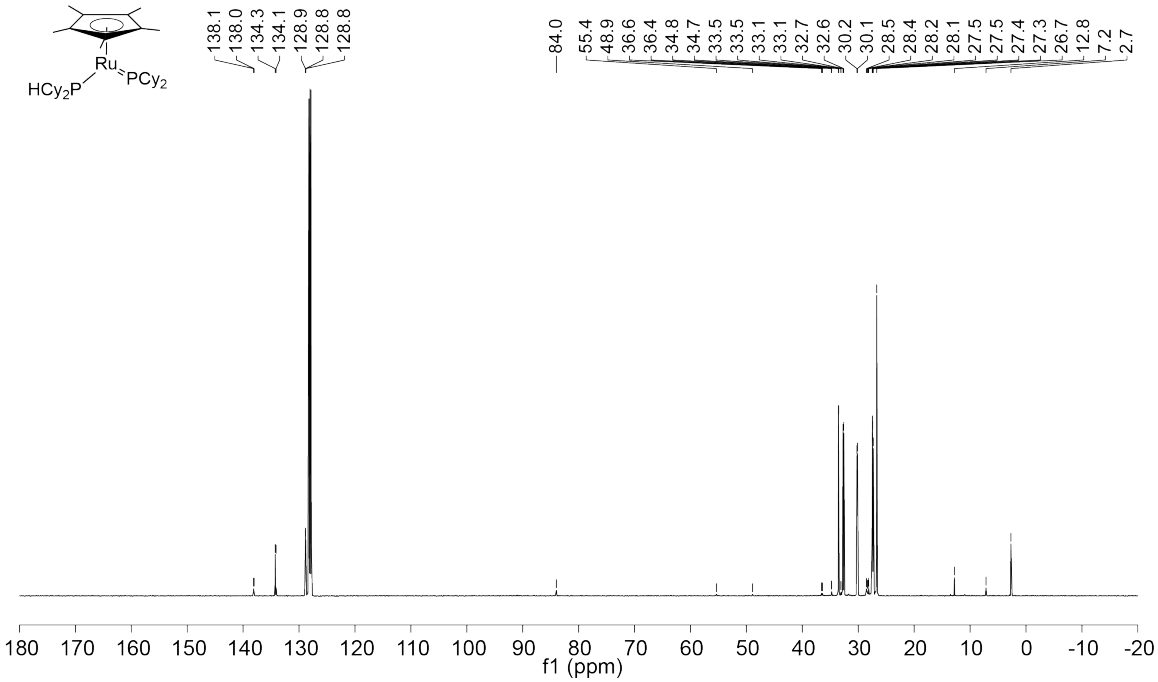

Figure B.12 $^{13}C\{^{1}H\}$ NMR (125.77 MHz, C_6D_6) spectrum of complex **Ru-2d.**

Appendix C – NMR spectra of isolated Cp*Co compounds

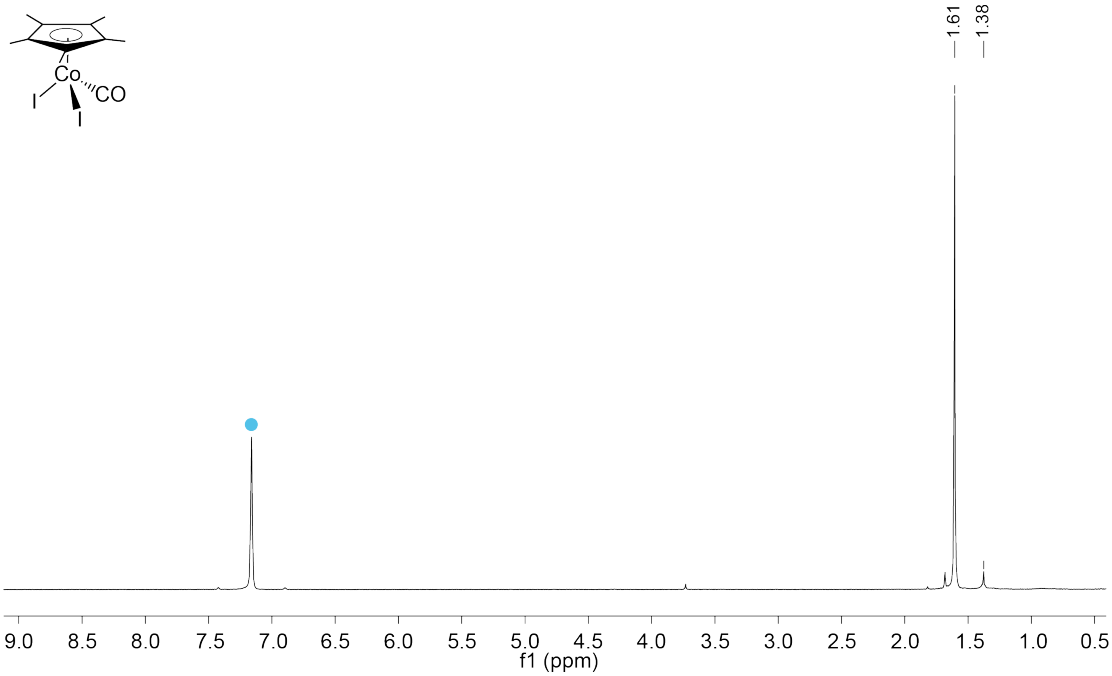

Figure C.1 ^{1}H NMR (300.27 MHz, C_6D_6) spectrum of complex **Co-1**. Small amounts of impurity result from the thermal dissociation of CO ligand to generate a dimer $[Cp^*CoI_2]_2$; residual proteo-solvent (•).

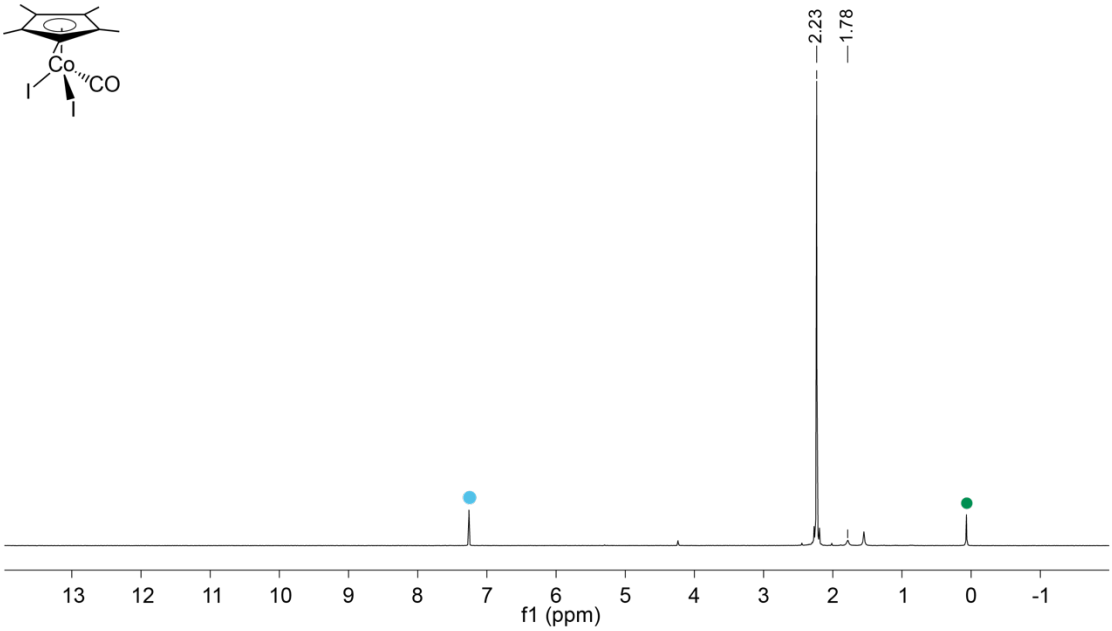

Figure C.2 ^{1}H NMR (300.27 MHz, $CDCl_3$) spectrum of complex **Co-1**. Small amounts of impurity result from the thermal dissociation of CO ligand to generate a dimer $[Cp^*CoI_2]_2$; residual proteo-solvent (•), grease (green).

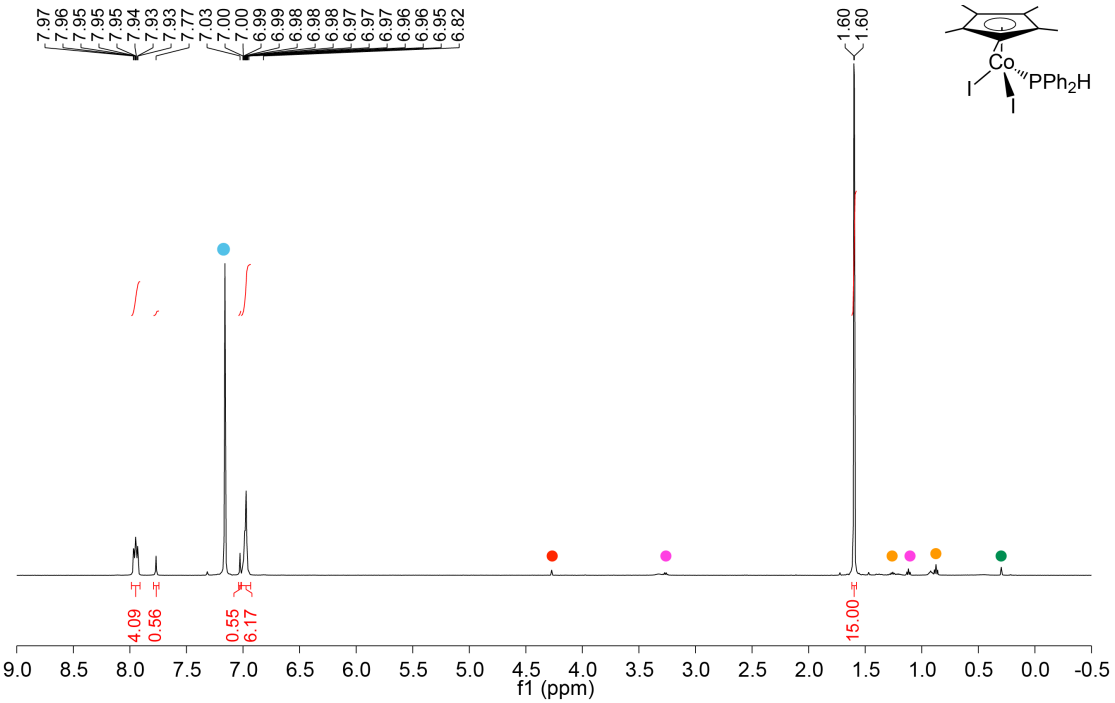

Figure C.3 ^{1}H NMR (500.27 MHz, C_6D_6) spectrum of complex **Co-2a**. Grease (green), pentane (orange), Et_2O (pink), CH_2Cl_2 (red) and residual proteo-solvent (•).

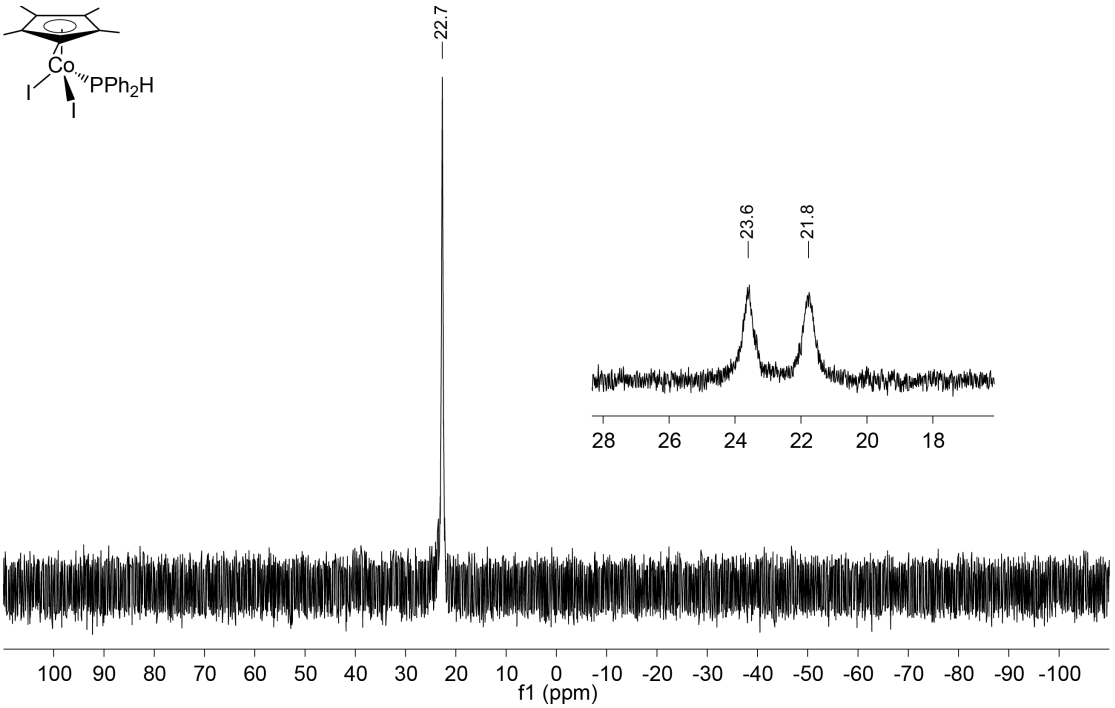

Figure C.4 ^{31}P{^{1}H} and ^{31}P (inset) NMR (202.51 MHz, C_6D_6) spectra of complex **Co-2a**.

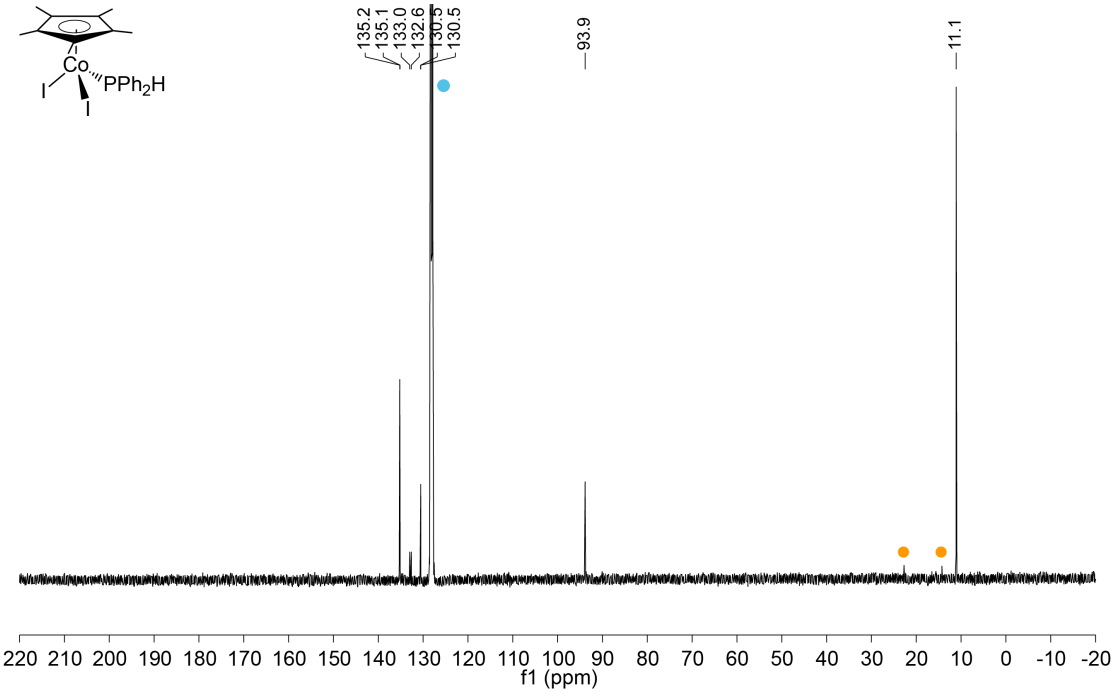

Figure C.5 $^{13}C\{^{1}H\}$ NMR (125.77 MHz, C_6D_6) spectrum of complex **Co-2a**. Pentane (orange) and deuterated solvent (•).

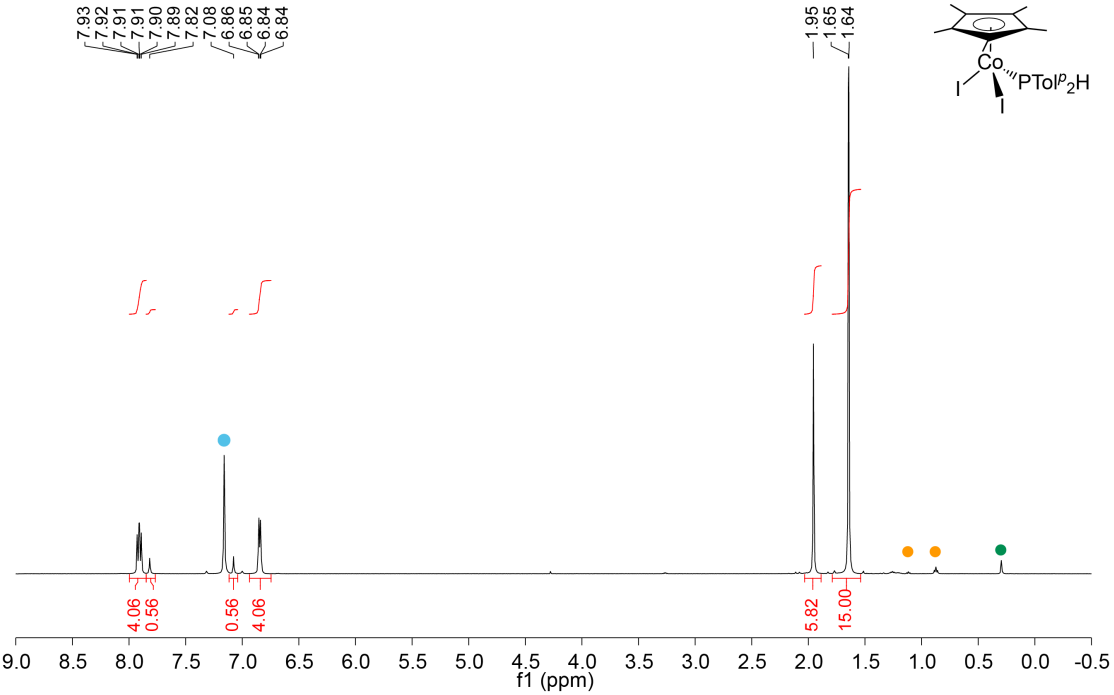

Figure C.6 ^{1}H NMR (500.27 MHz, C_6D_6) spectrum of complex **Co-2b**. Grease (green), pentane (orange) and residual proteo-solvent (•).

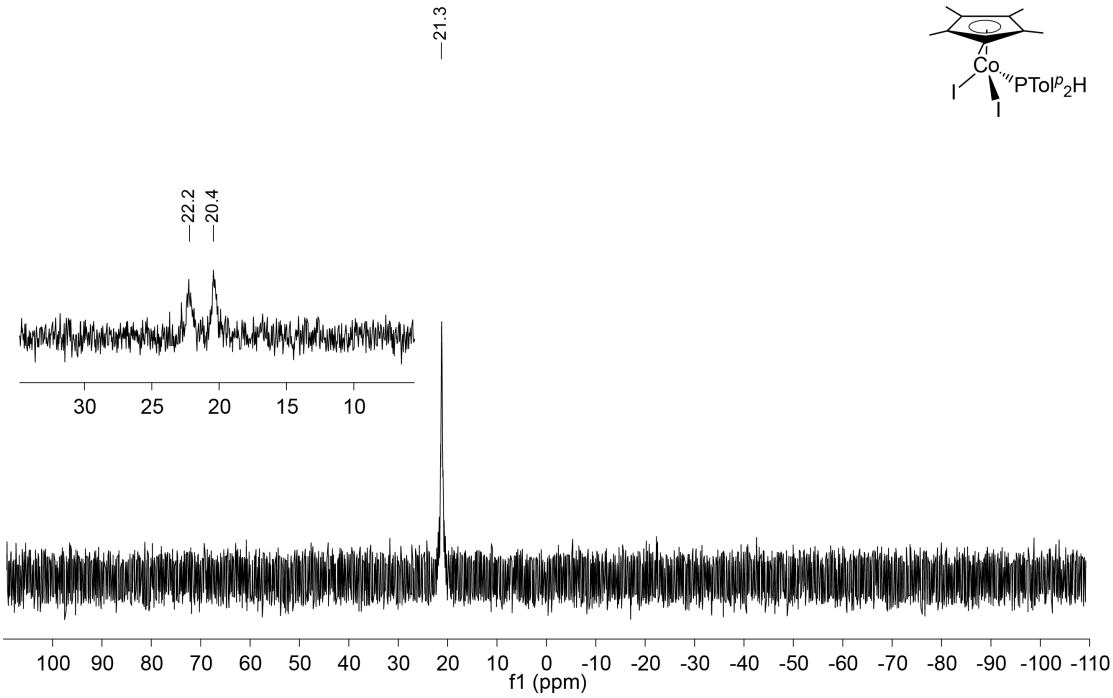

Figure C.7 $^{31}P\{^1H\}$ and ^{31}P (inset) NMR (202.51 MHz, C_6D_6) spectra of complex **Co-2b**.

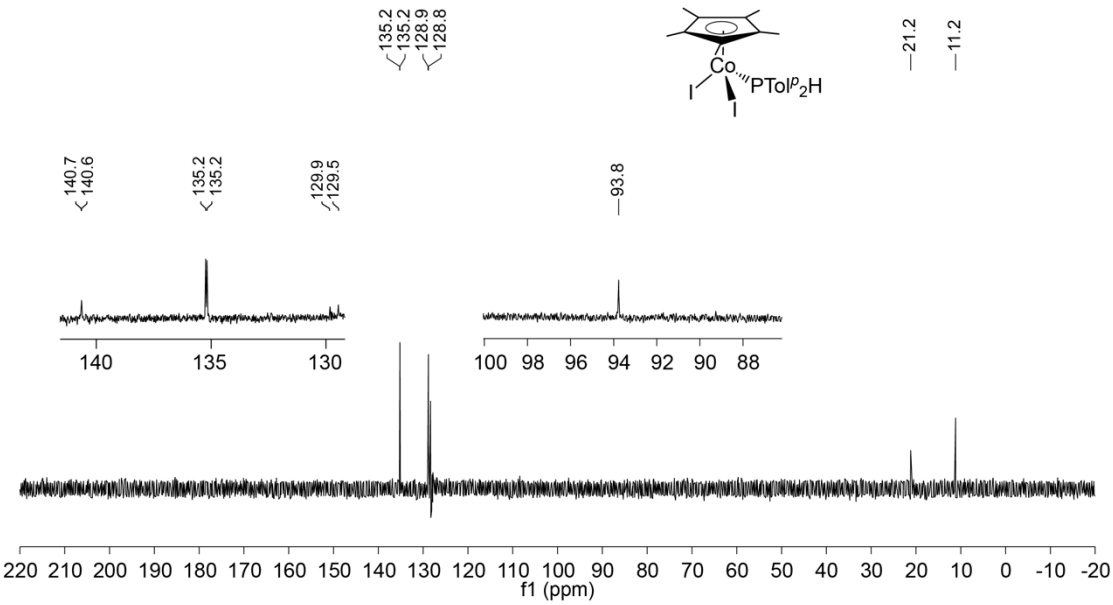

Figure C.8 ^{13}C DEPT 135 and $^{13}C\{^1H\}$ (inset) NMR (125.77 MHz, C_6D_6) spectra of complex **Co-2b.**

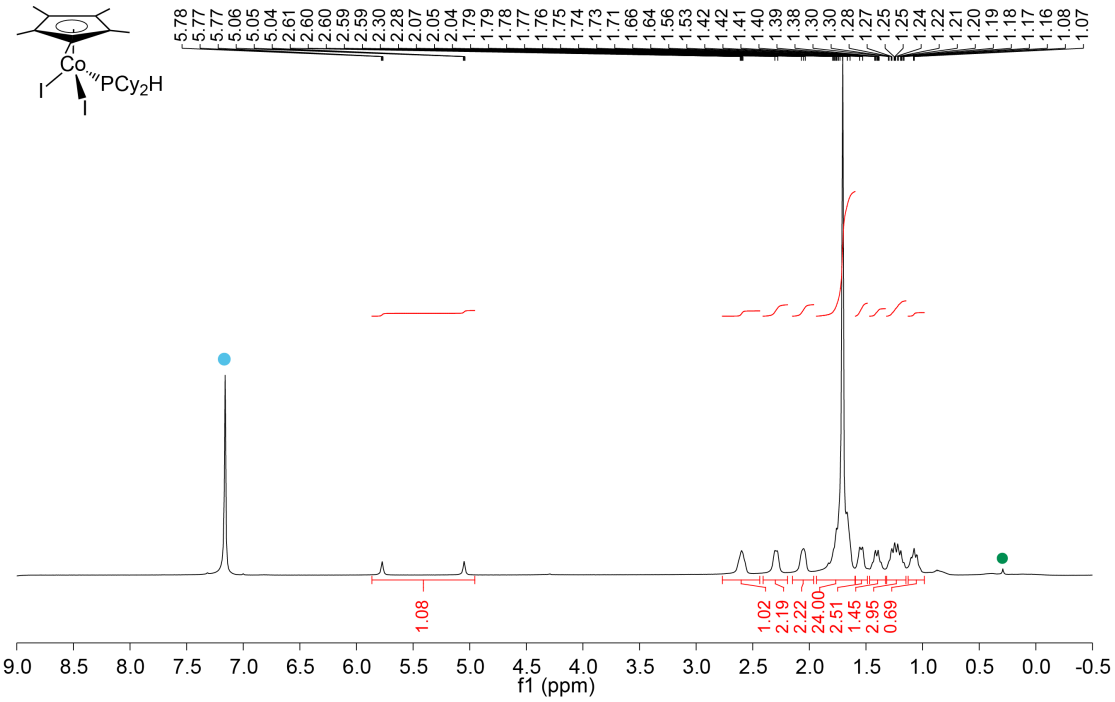

Figure C.9 ^{1}H NMR (500.27 MHz, C_6D_6) spectrum of complex **Co-2c**. Grease (green) and residual proteo-solvent (•).

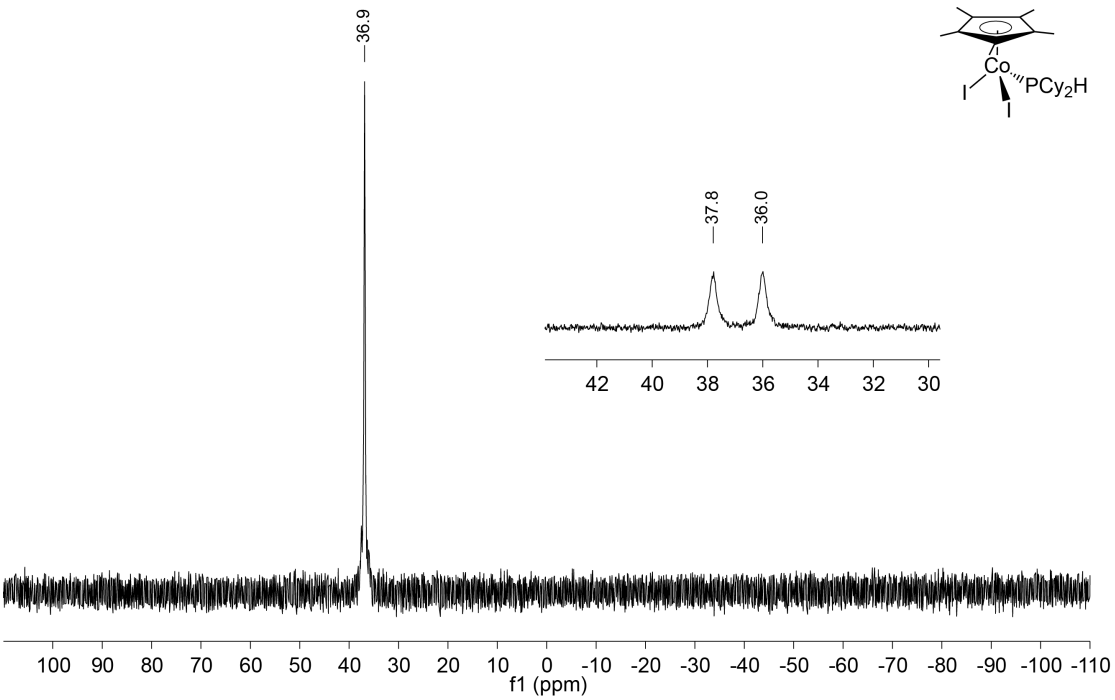

Figure C.10 ^{31}P{^{1}H} and ^{31}P (inset) NMR (202.51 MHz, C_6D_6) spectra of complex **Co-2c**.

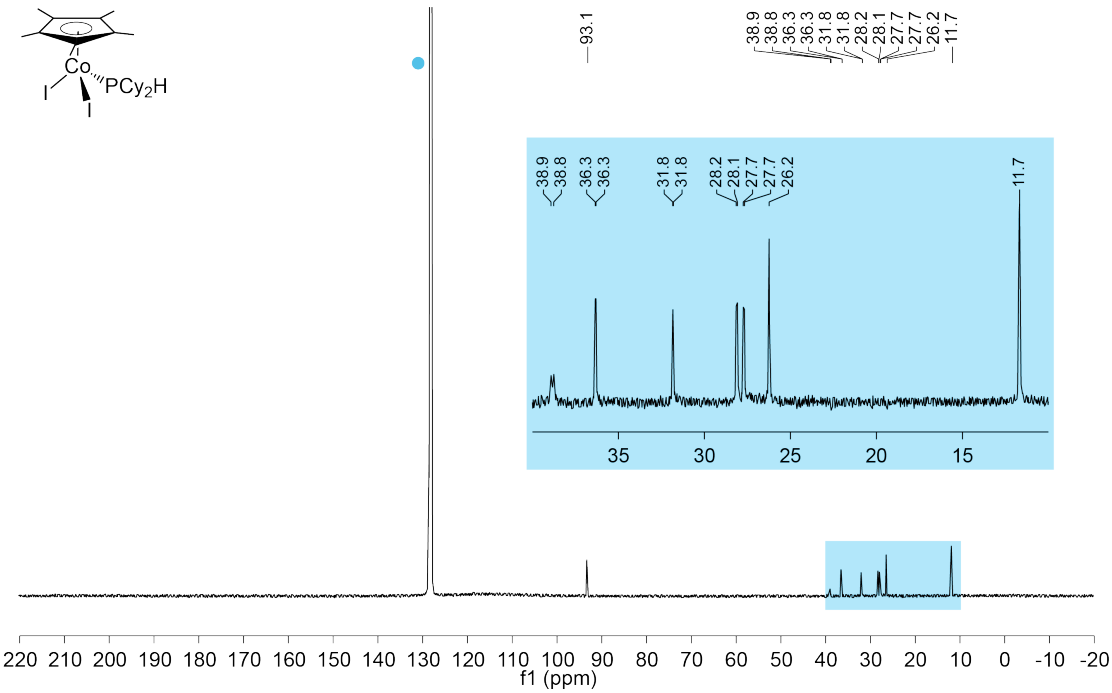

Figure C.11 $^{13}C\{^{1}H\}$ NMR (125.77 MHz, C_6D_6) spectrum of complex **Co-2c**. Deuterated solvent (•).

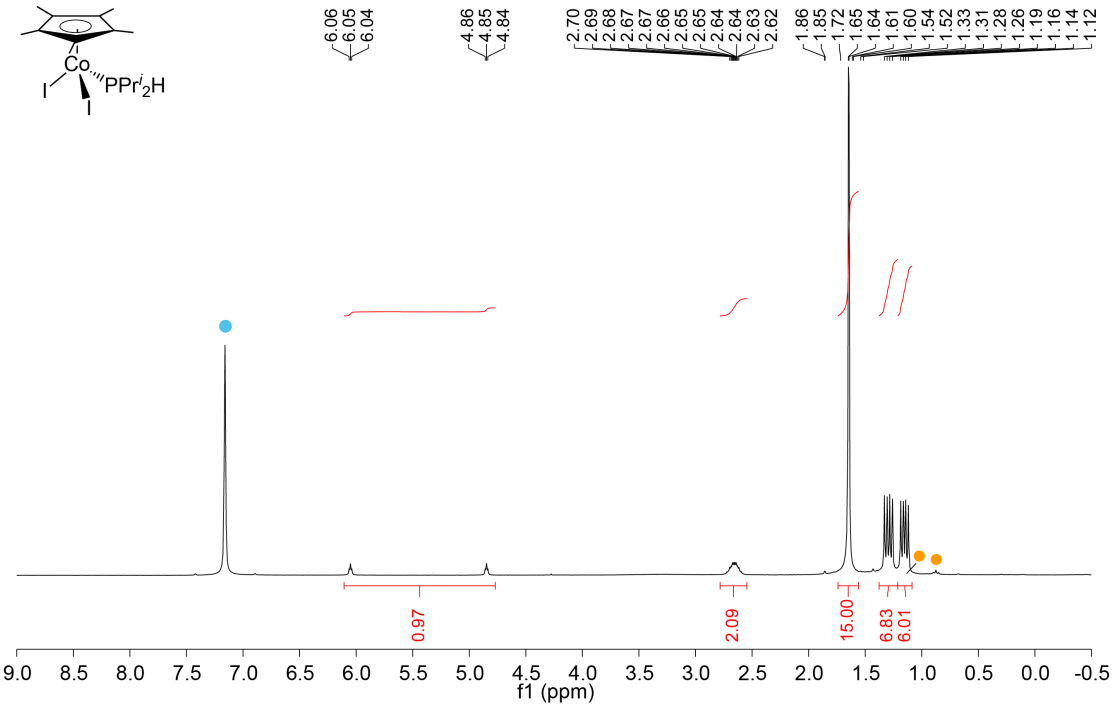

Figure C.12 ^{1}H NMR (500.27 MHz, C_6D_6) spectrum of complex **Co-2d**. Pentane (orange) and residual proteo-solvent (•).

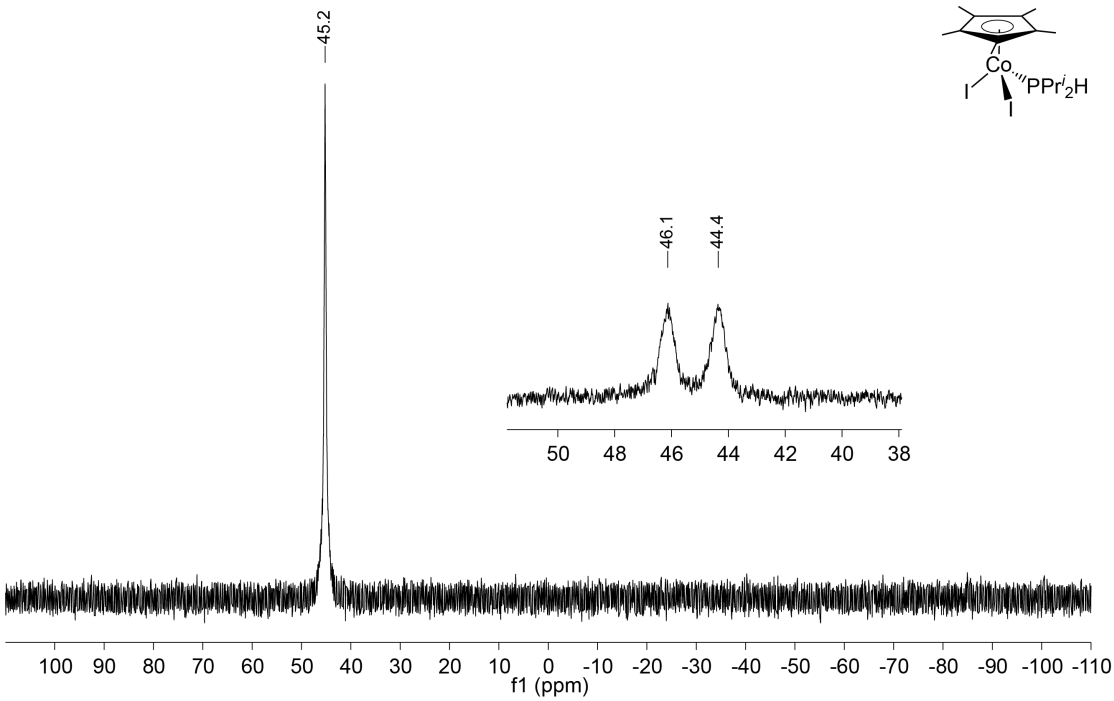

Figure C.13 $^{31}P\{^{1}H\}$ and ^{31}P (inset) NMR (202.51 MHz, C_6D_6) spectra of complex **Co-2d**.

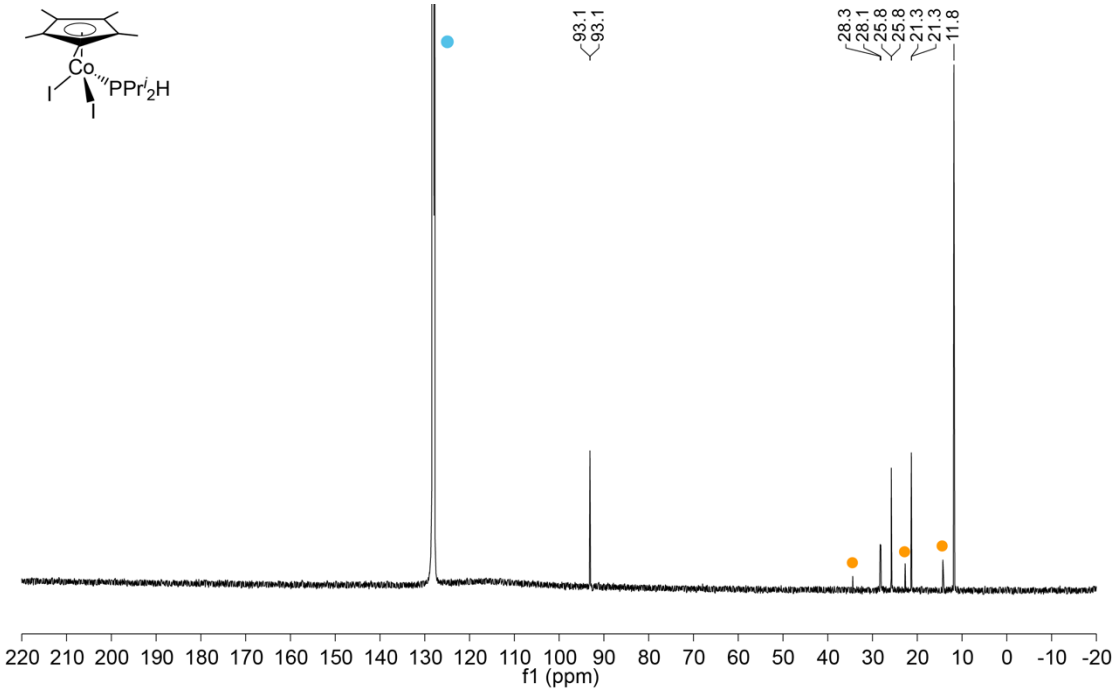

Figure C.14 $^{13}C\{^{1}H\}$ NMR (125.77 MHz, C_6D_6) spectrum of complex **Co-2d**. Pentane (orange) and deuterated solvent (•).

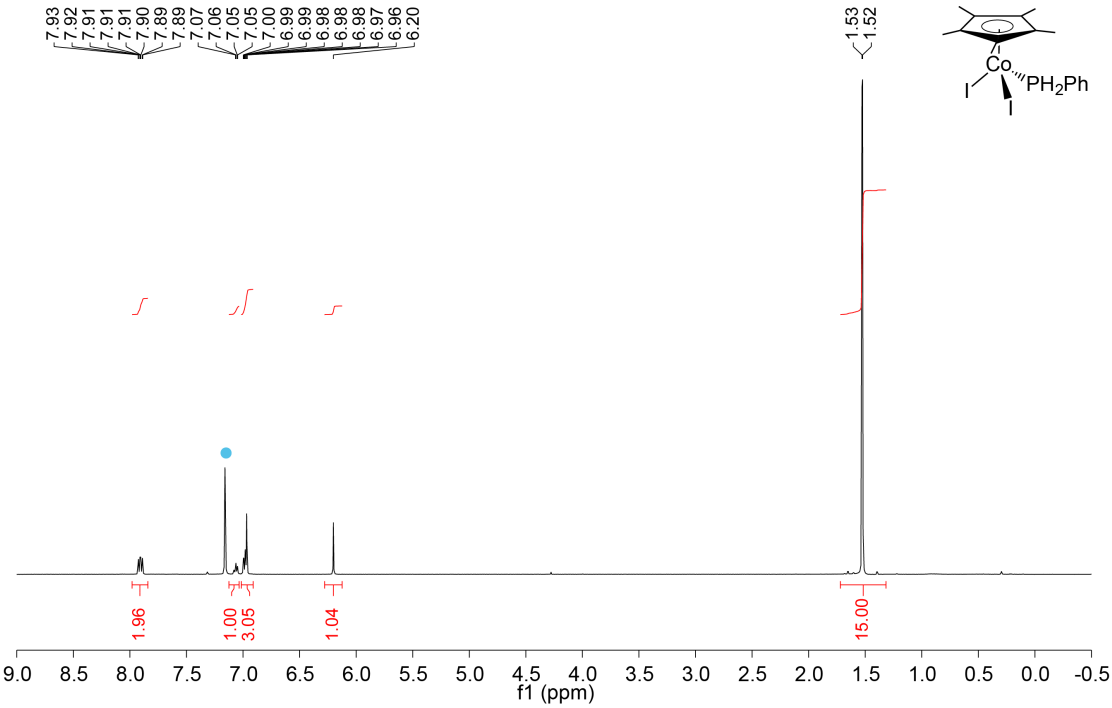

Figure C.15 ^{1}H NMR (500.27 MHz, C_6D_6) spectrum of isolated **Co-3a**. Residual proteo-solvent (•).

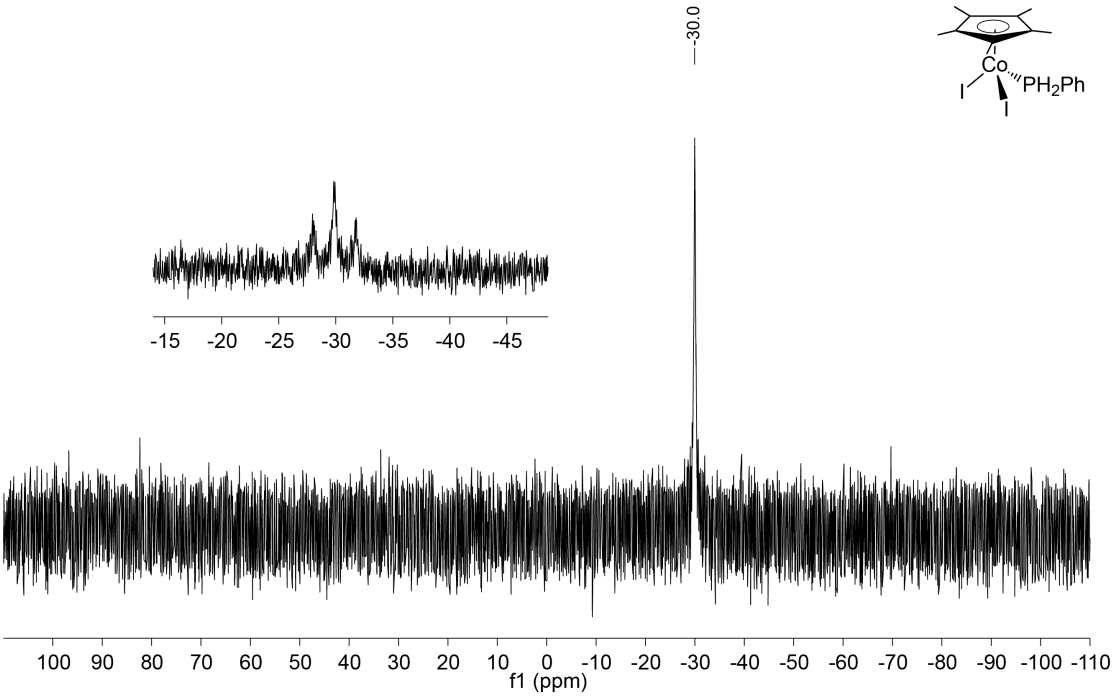

Figure C.16 ^{31}P{^{1}H} and ^{31}P (inset) NMR (202.51 MHz, C_6D_6) spectra of complex **Co-3a**.

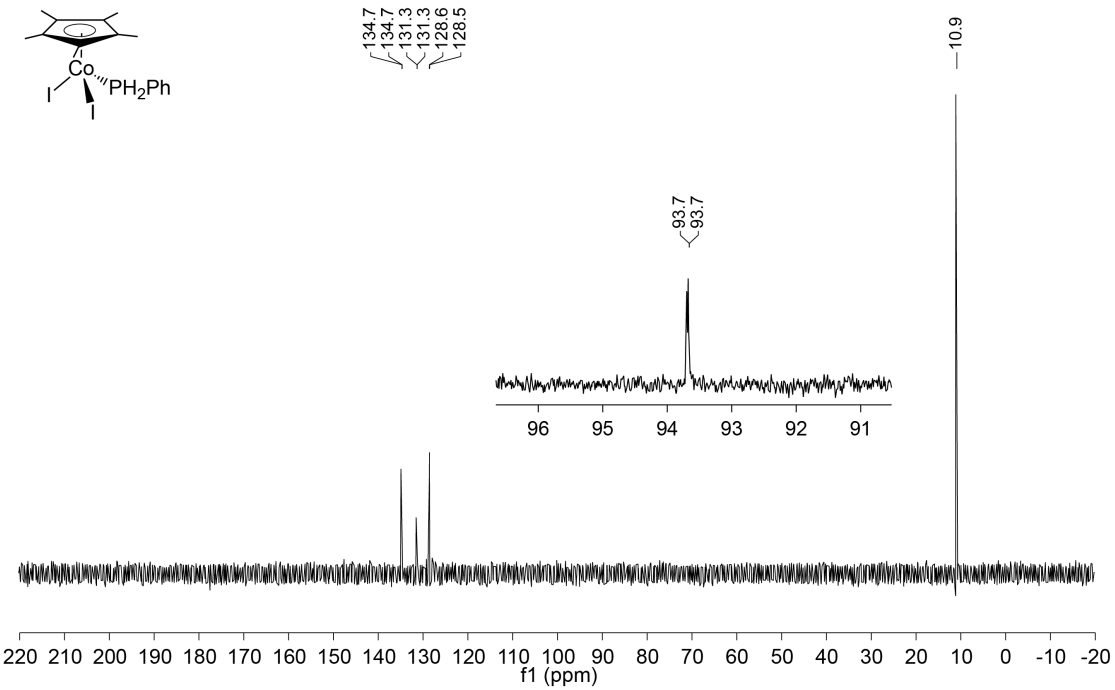

Figure C.17 ^{13}C DEPT 135 and $^{13}C\{^{1}H\}$ (inset) NMR (125.77 MHz, C_6D_6) spectra of complex **Co-3a.**

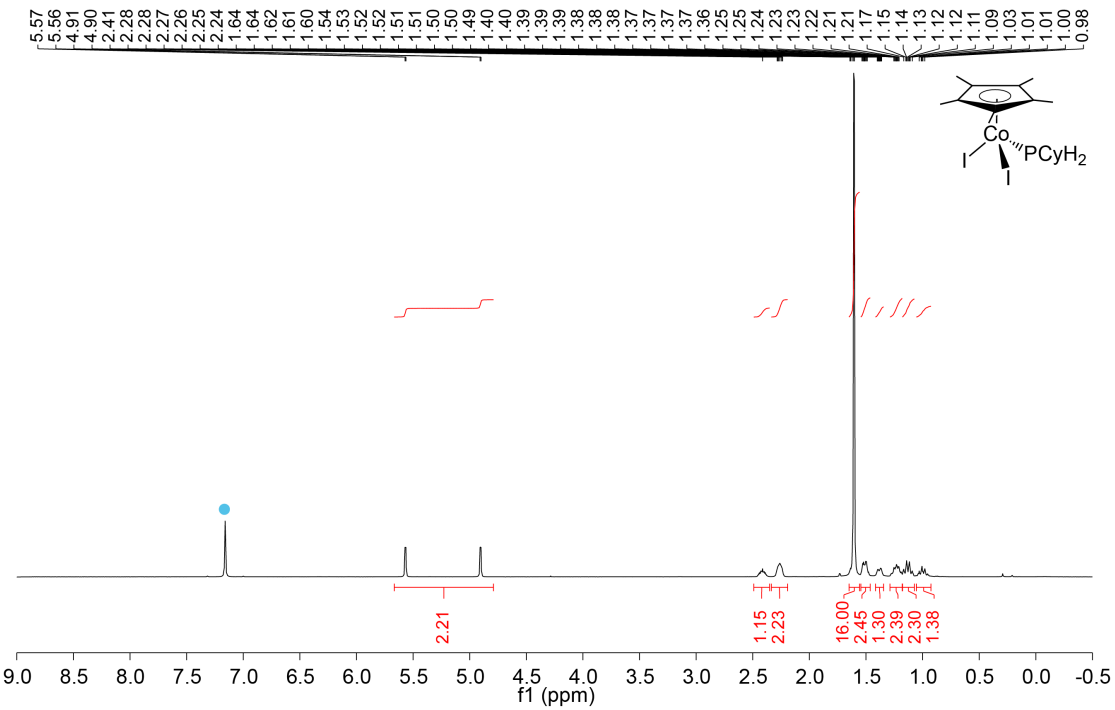

Figure C.18 ^{1}H NMR (500.27 MHz, C_6D_6) spectrum of complex **Co-3c**. Residual proteo-solvent (•).

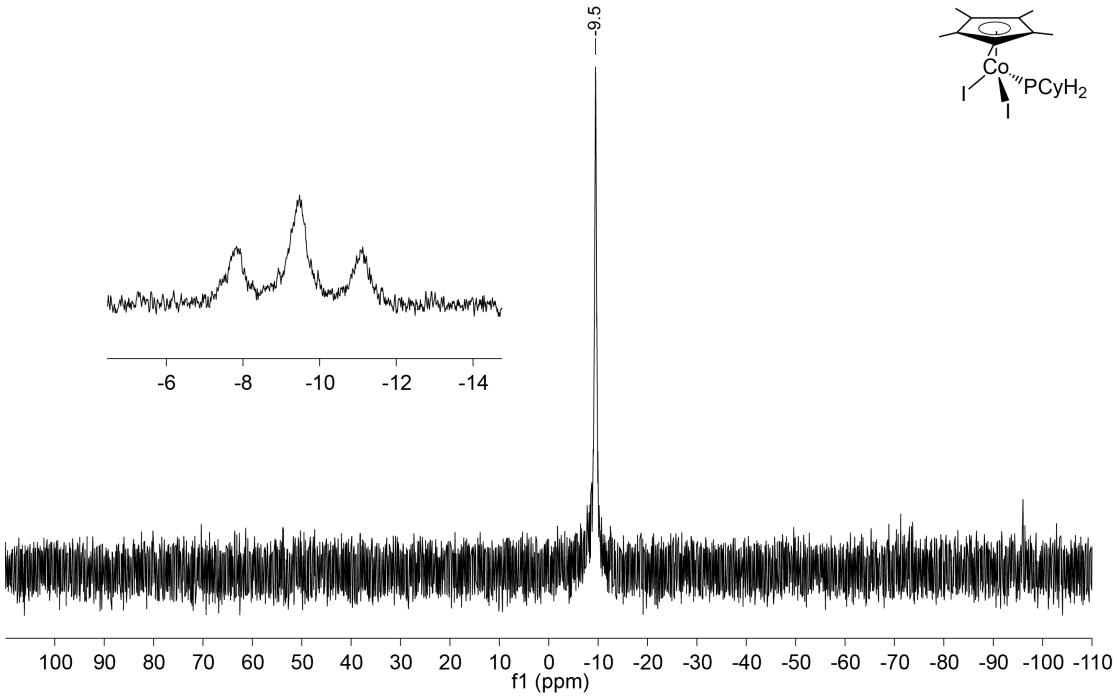

Figure C.19 $^{31}P\{^{1}H\}$ and ^{31}P (inset) NMR (202.51 MHz, C_6D_6) spectra of complex **Co-3c**.

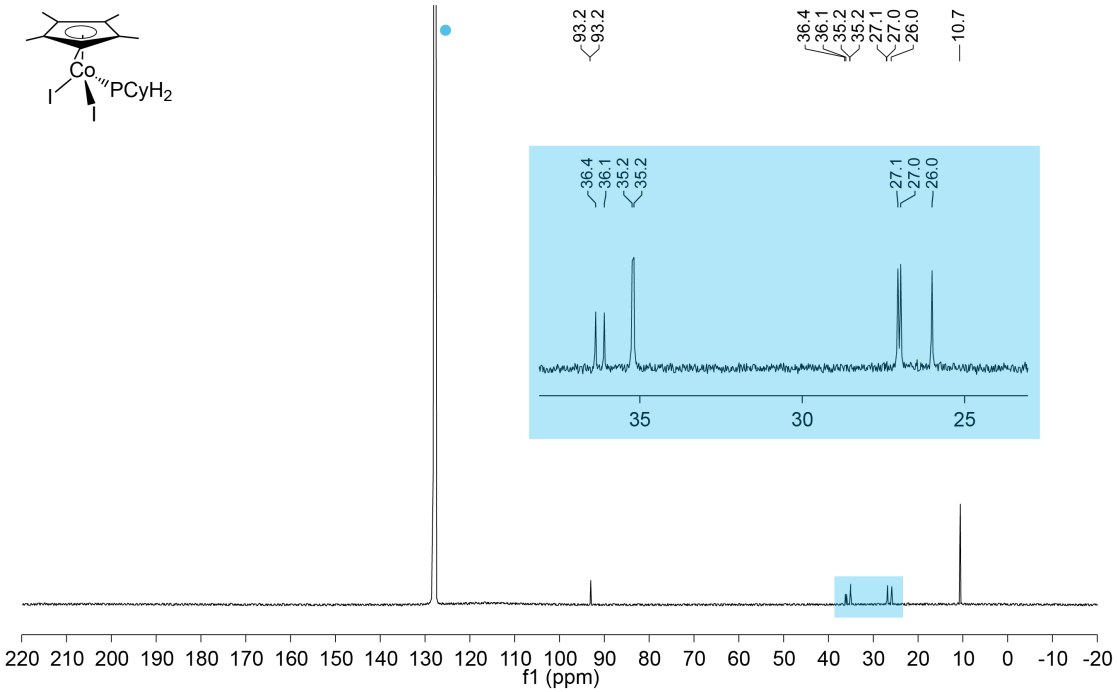

Figure C.20 $^{13}C\{^{1}H\}$ NMR (125.77 MHz, C_6D_6) spectrum of complex **Co-3c**. Deuterated solvent (•).

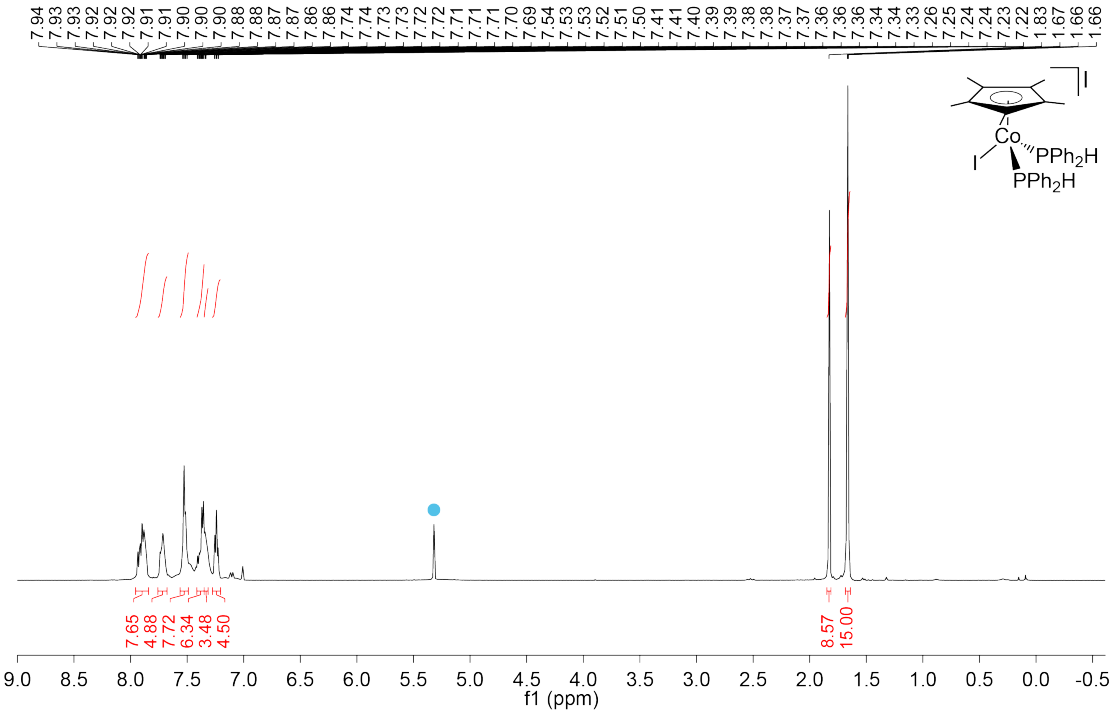

Figure C.21 ^{1}H NMR (500.27 MHz, CD_2Cl_2) spectrum of complex **Co-4a**. Pentane (orange) and residual proteo-solvent (•).

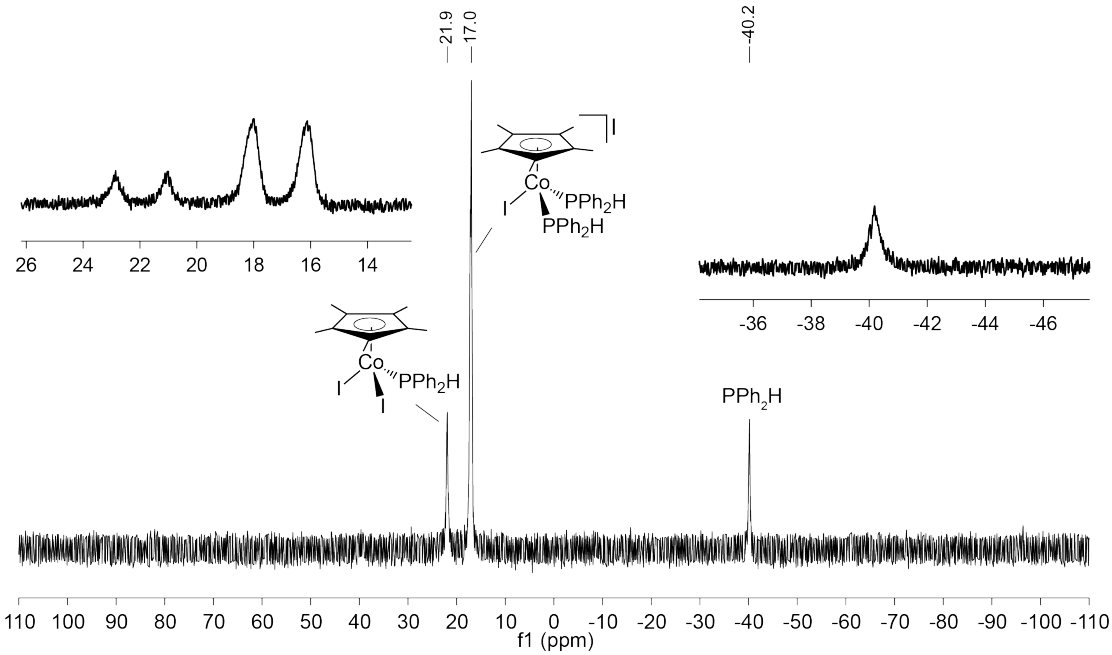

Figure C.22 $^{31}P\{^{1}H\}$ and ^{31}P (inset) NMR (202.51 MHz, CD_2Cl_2) spectra of complex **Co-4a**.

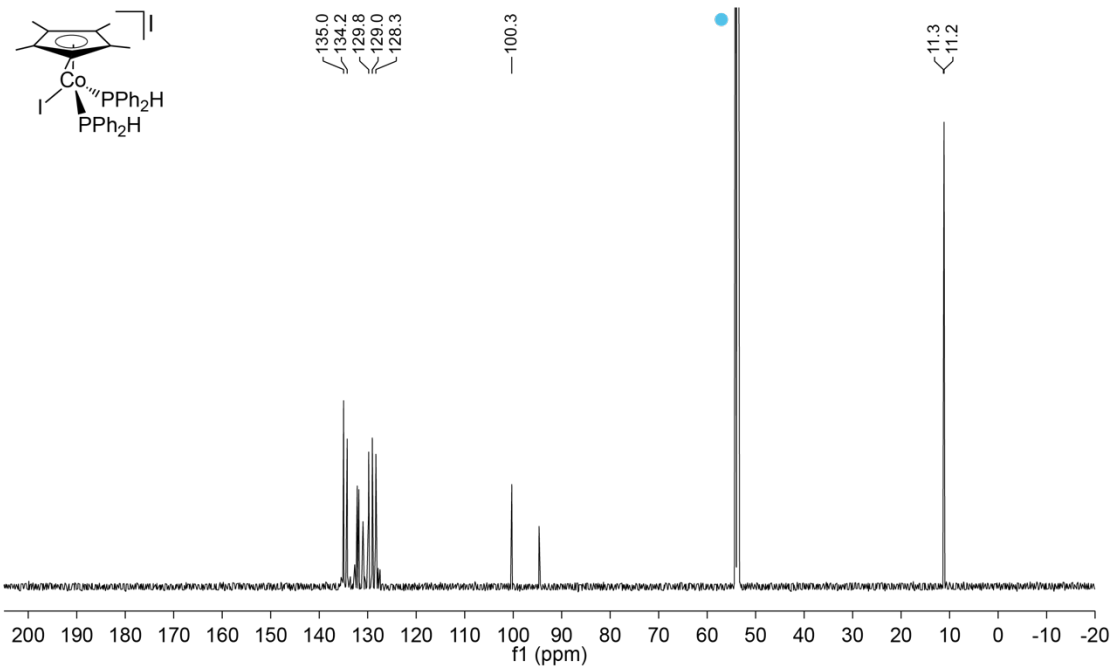

Figure C.23 $^{13}C\{^{1}H\}$ NMR (125.77 MHz, CD_2Cl_2) spectrum of complex **Co-4a**. Deuterated solvent (•).

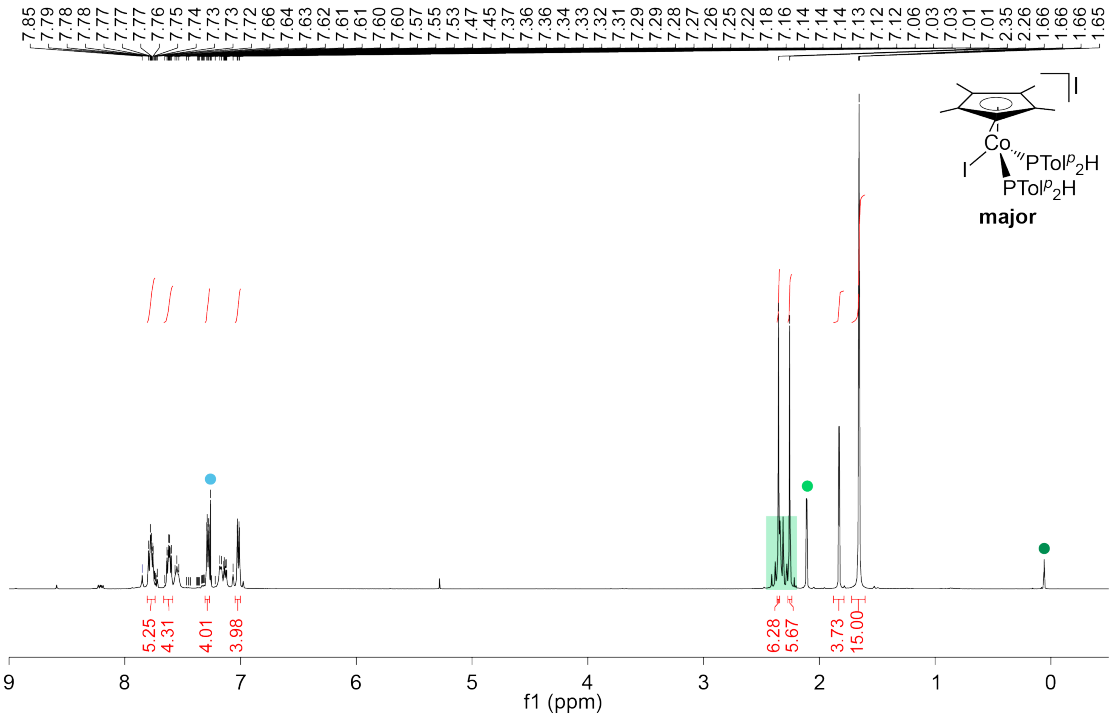

Figure C.24 ^{1}H NMR (500.27 MHz, $CDCl_3$) spectrum of complex **Co-4b** and unidentified impurities (bright green). Grease (green) and residual proteo-solvent (•).

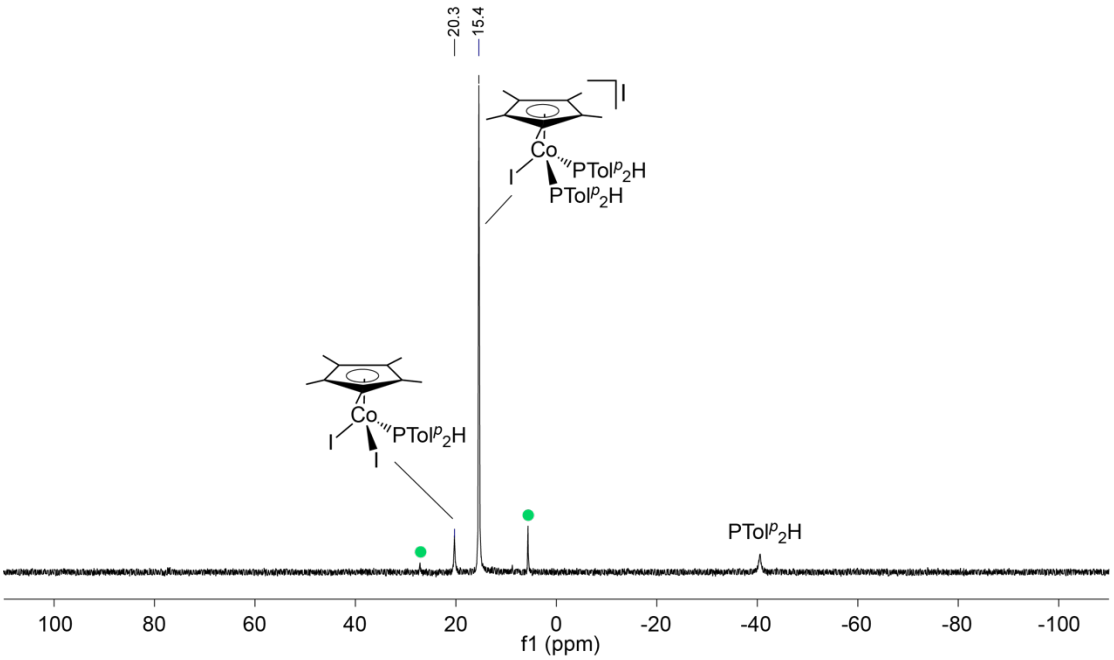

Figure C.25 $^{31}P\{^1H\}$ NMR (202.51 MHz, $CDCl_3$) spectrum of complex **Co-4b** and unidentified impurities (bright green).

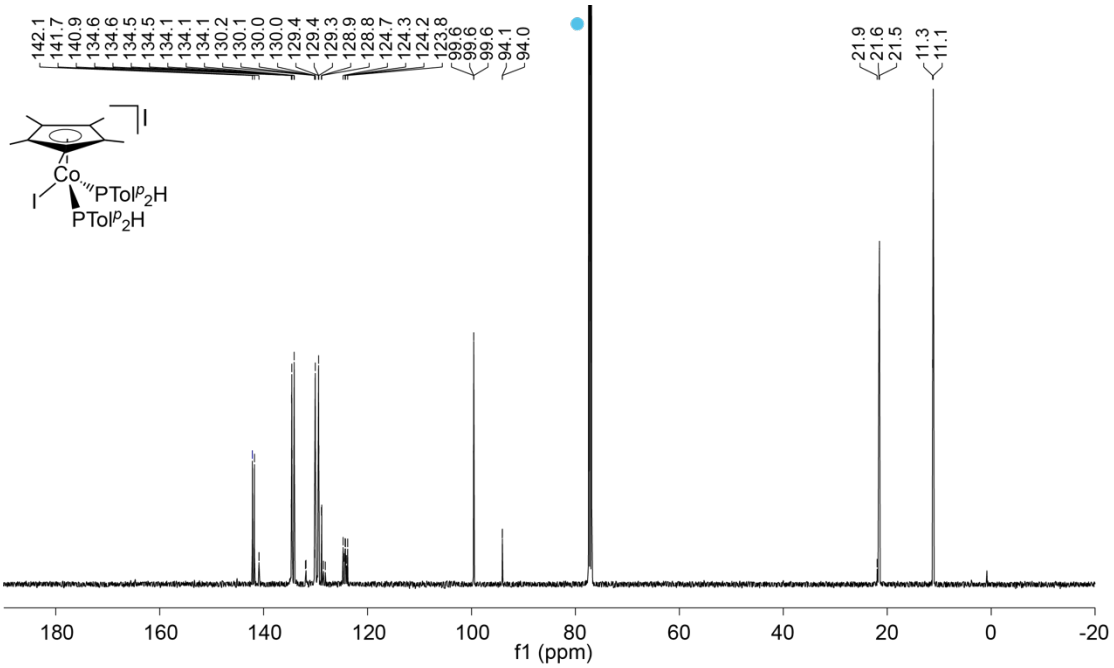

Figure C.26 $^{13}C\{^1H\}$ NMR spectrum (125.77 MHz, $CDCl_3$) of complex **Co-4b** and unidentified impurities (bright green). Deuterated solvent (•).

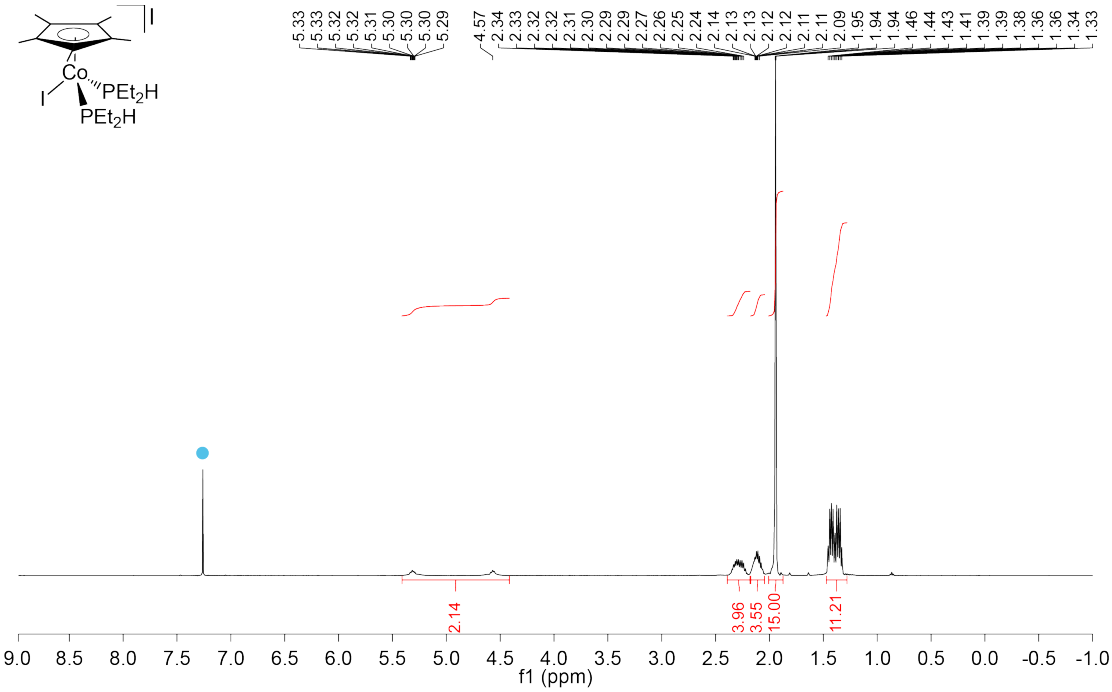

Figure C.27 ^{1}H NMR (500.27 MHz, $CDCl_3$) spectrum of complex **Co-4e**. Residual proteo-solvent (•).

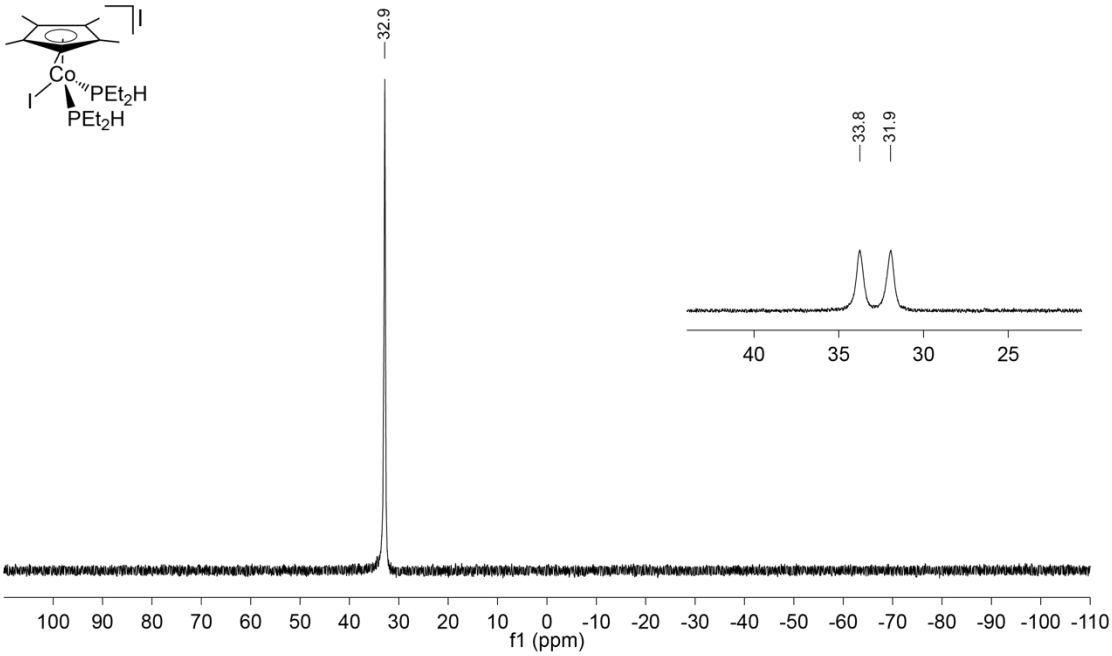

Figure C.28 $^{31}P\{^{1}H\}$ and ^{31}P (inset) NMR (202.51 MHz, $CDCl_3$) spectra of isolated **Co-4e**.

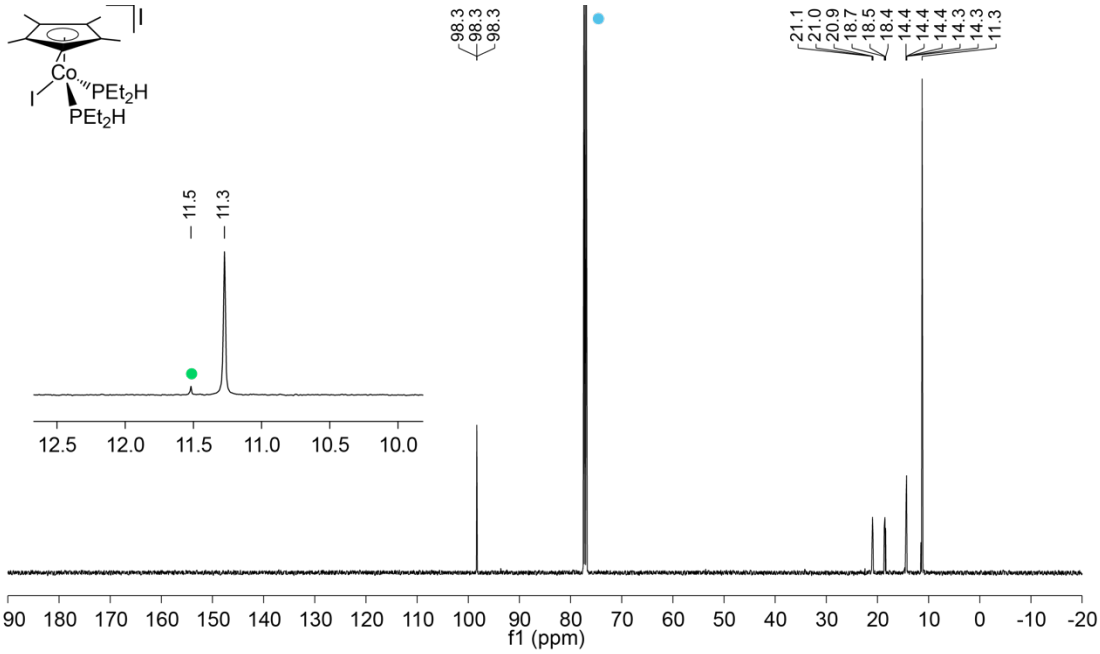

Figure C.29 $^{13}C\{^{1}H\}$ NMR (125.77 MHz, $CDCl_3$) spectrum of complex **Co-4e**. Methyl carbon at Cp* group due to the slow decomposition of **Co-4e** to **Co-2e** (bright green); deuterated solvent (•).

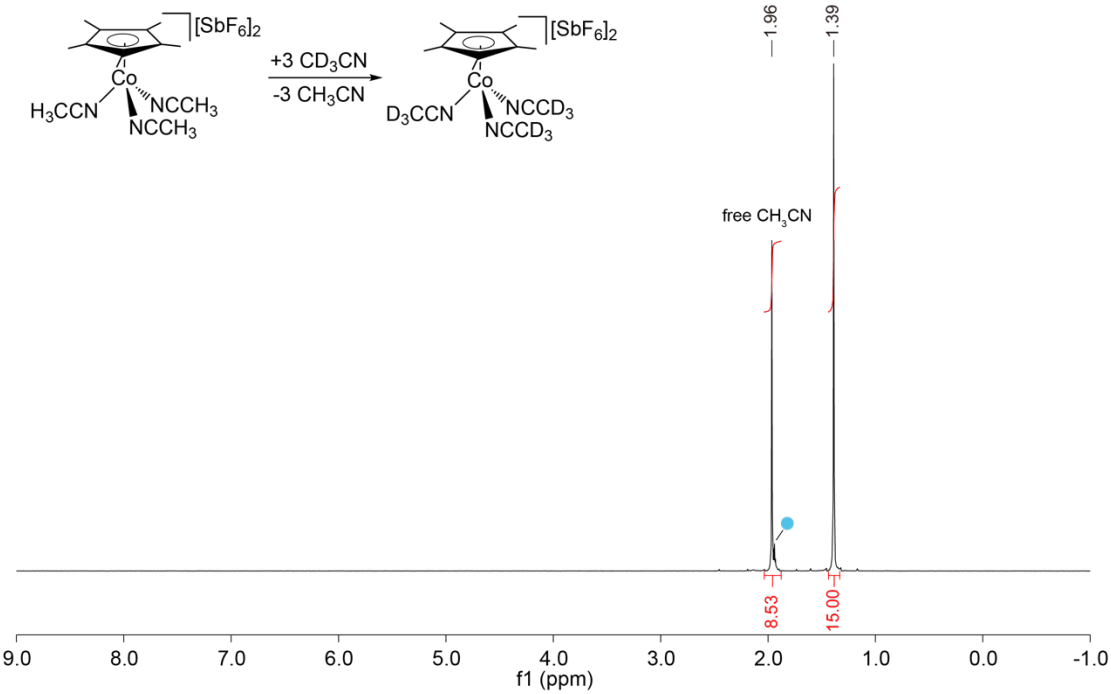

Figure C.30 ^{1}H NMR (300.27 MHz, CD_3CN) spectrum of complex **Co-5**. Scheme illustrating substitution of CH_3CN ligand by CD_3CN. Residual proteo-solvent (•).

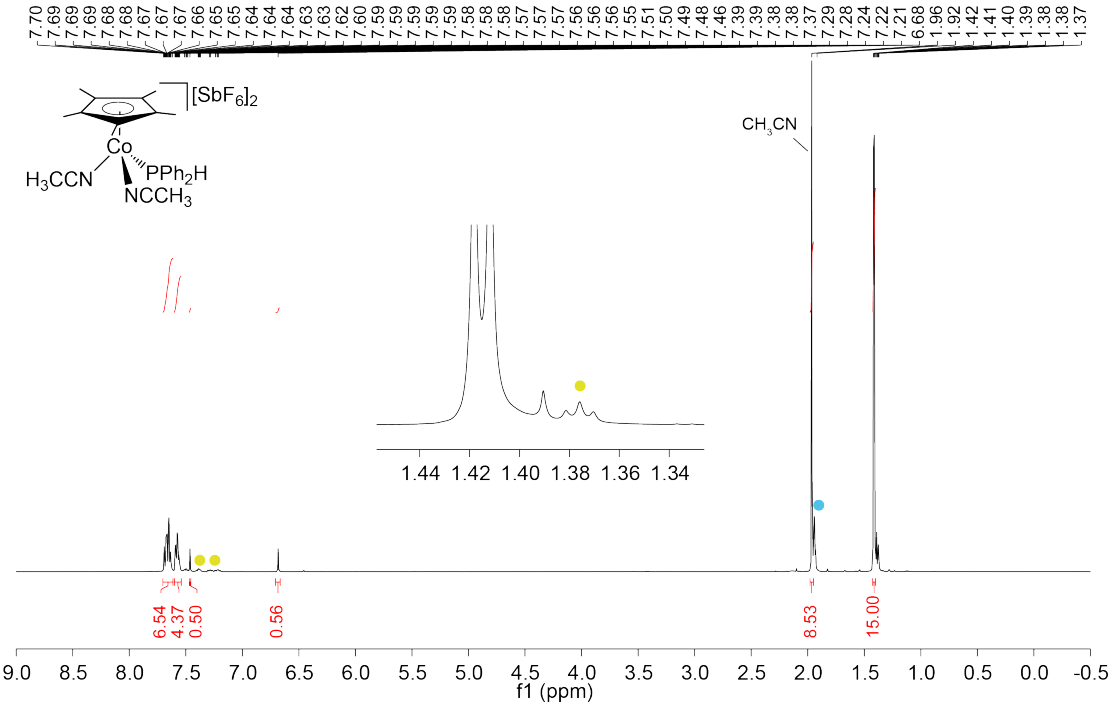

Figure C.31 ^{1}H NMR (500.27 MHz, CD_3CN) spectrum of the mixture containing **Co-6a** with a small amount of **Co-7a** (yellow). Residual proteo-solvent (•).

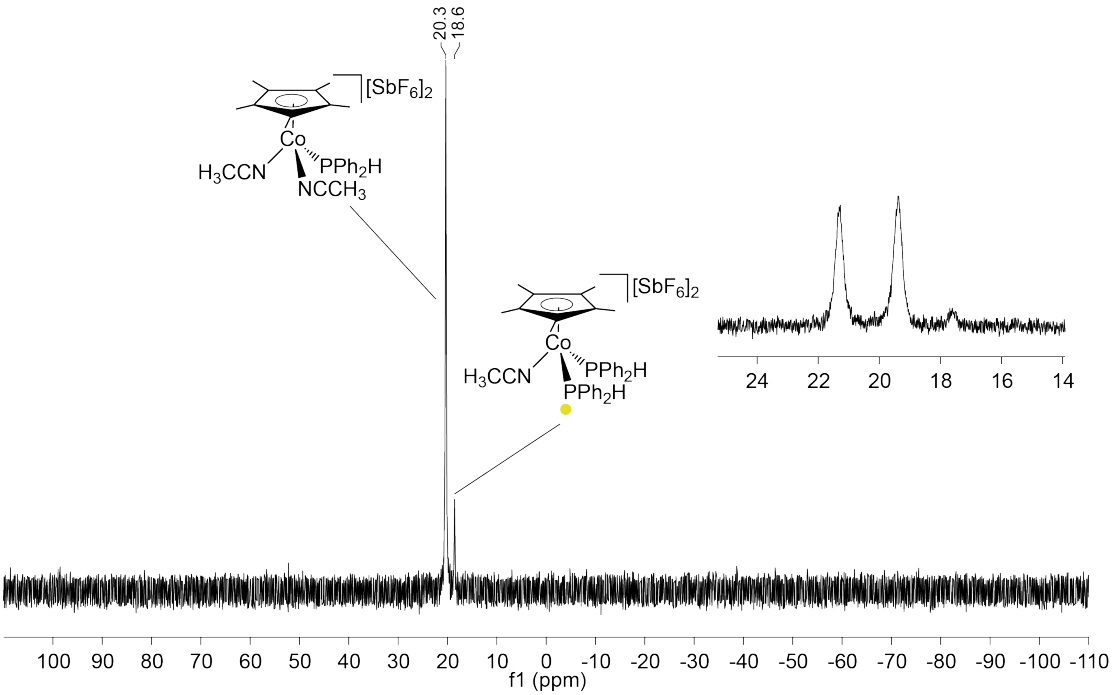

Figure C.32 ^{31}P{^{1}H} and ^{31}P (inset) NMR (202.51 MHz, CD_3CN) spectra of the mixture containing **Co-6a** with a small amount of **Co-7a** (yellow).

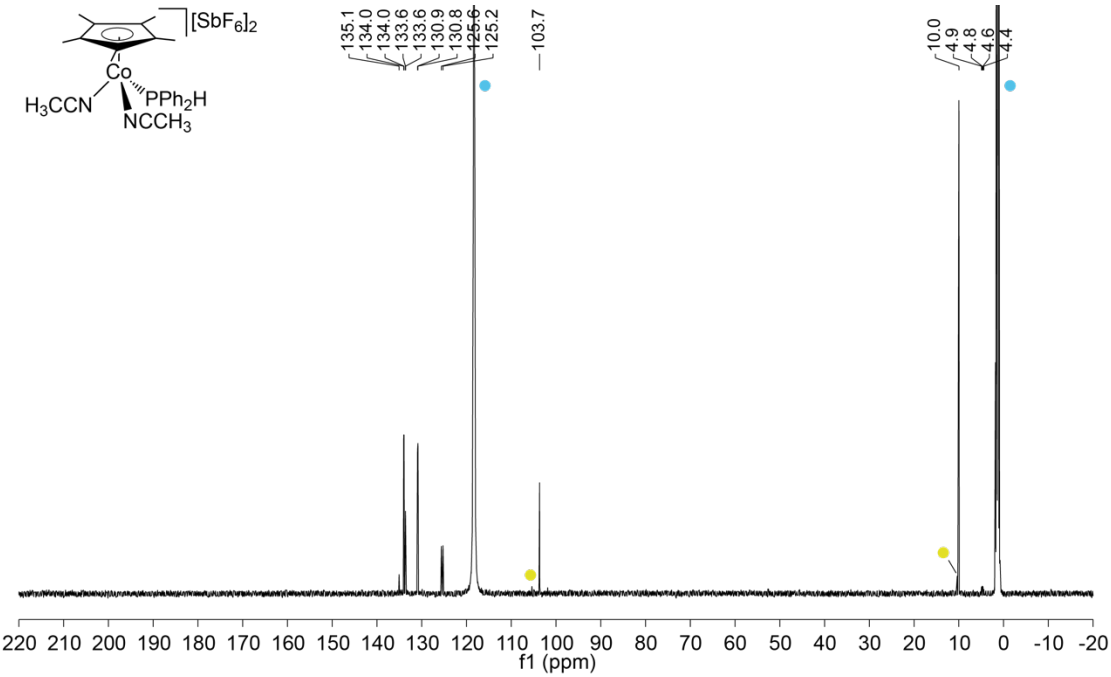

Figure C.33 $^{13}C\{^{1}H\}$ NMR (125.77 MHz, CD_3CN) spectrum of the mixture containing **Co-6a** with a small amount of **Co-7a** (yellow). Deuterated solvent (•).

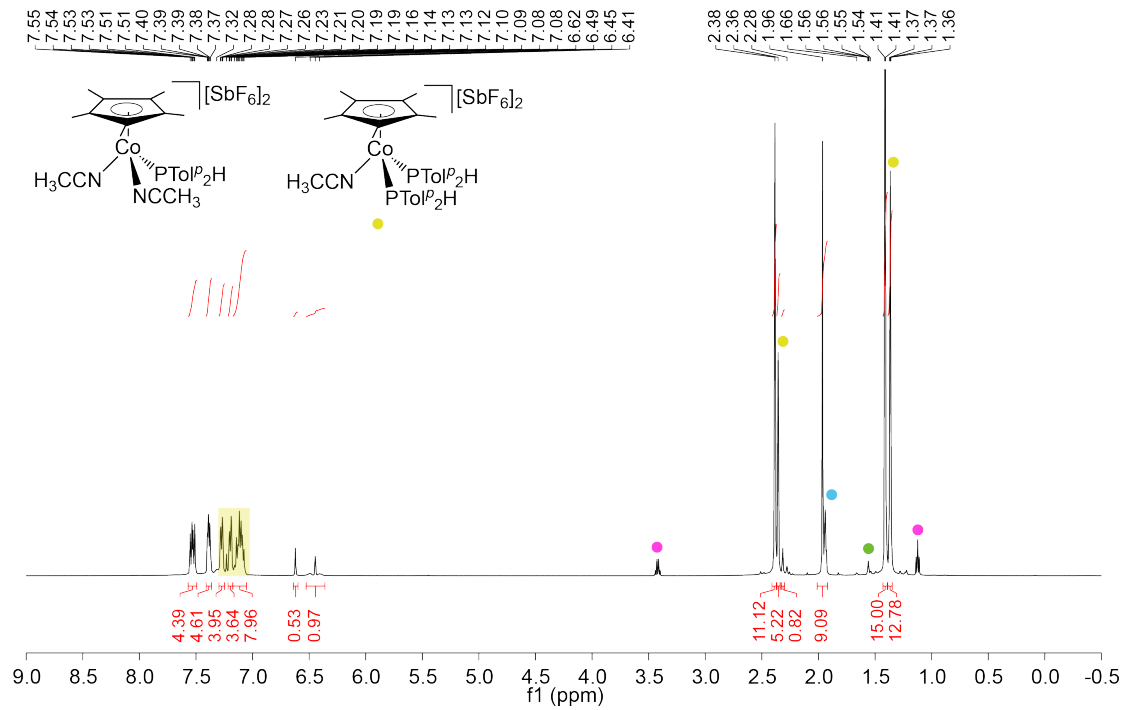

Figure C.34 ^{1}H NMR (500.27 MHz, CD_3CN) spectrum of the mixture containing **Co-6b** and **Co-7b** (yellow). Diethyl ether (pink), unidentified impurities (bright green) and residual proteo-solvent (•).

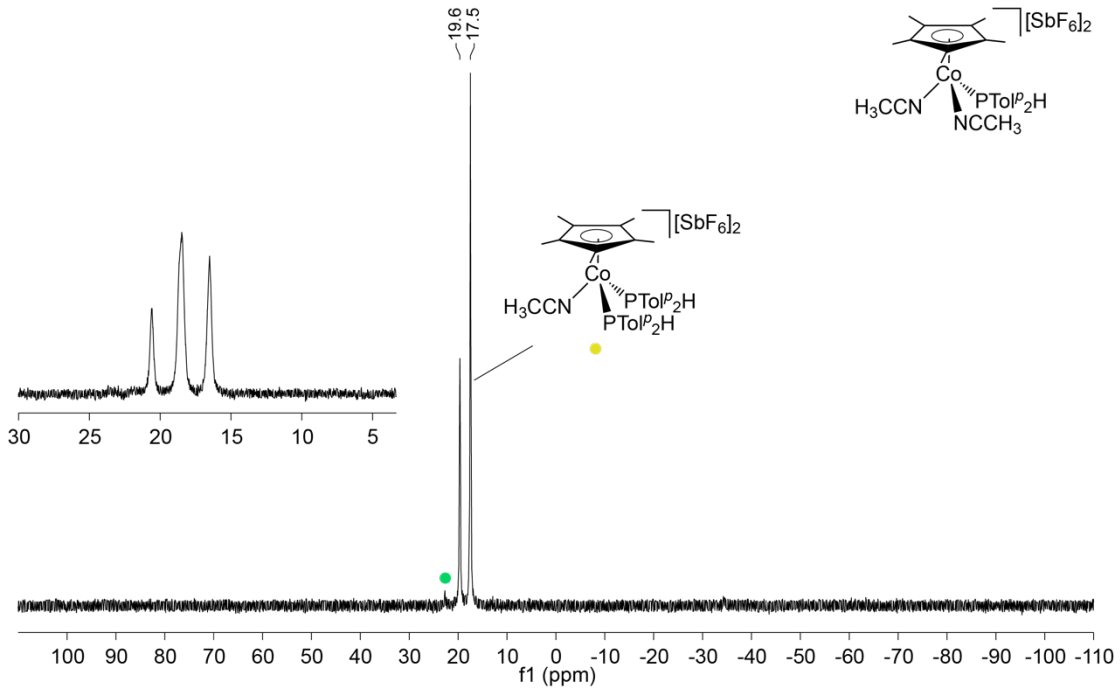

Figure C.35 $^{31}P\{^{1}H\}$ and ^{31}P (inset) NMR (202.51 MHz, CD_3CN) spectra of the mixture containing **Co-6b** and **Co-7b** (yellow) with a small amount of unidentified species (bright green).

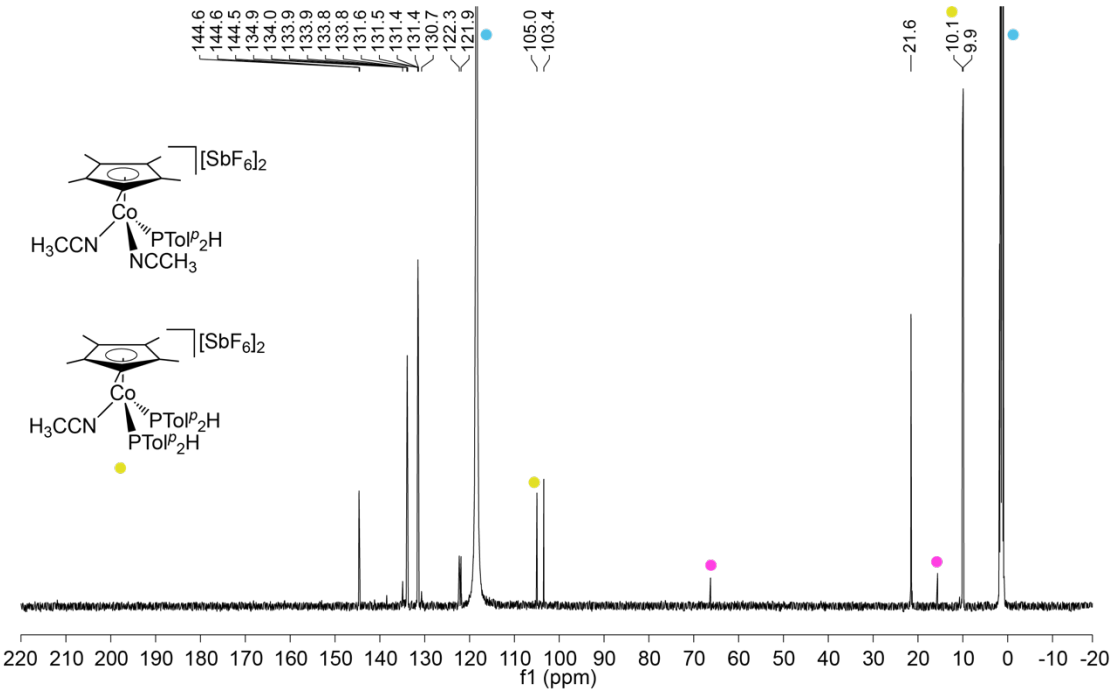

Figure C.36 $^{13}C\{^{1}H\}$ NMR (125.77 MHz, CD_3CN) spectrum of the mixture containing **Co-6b** and **Co-7b** (yellow). Diethyl ether (pink) and deuterated solvent (•).

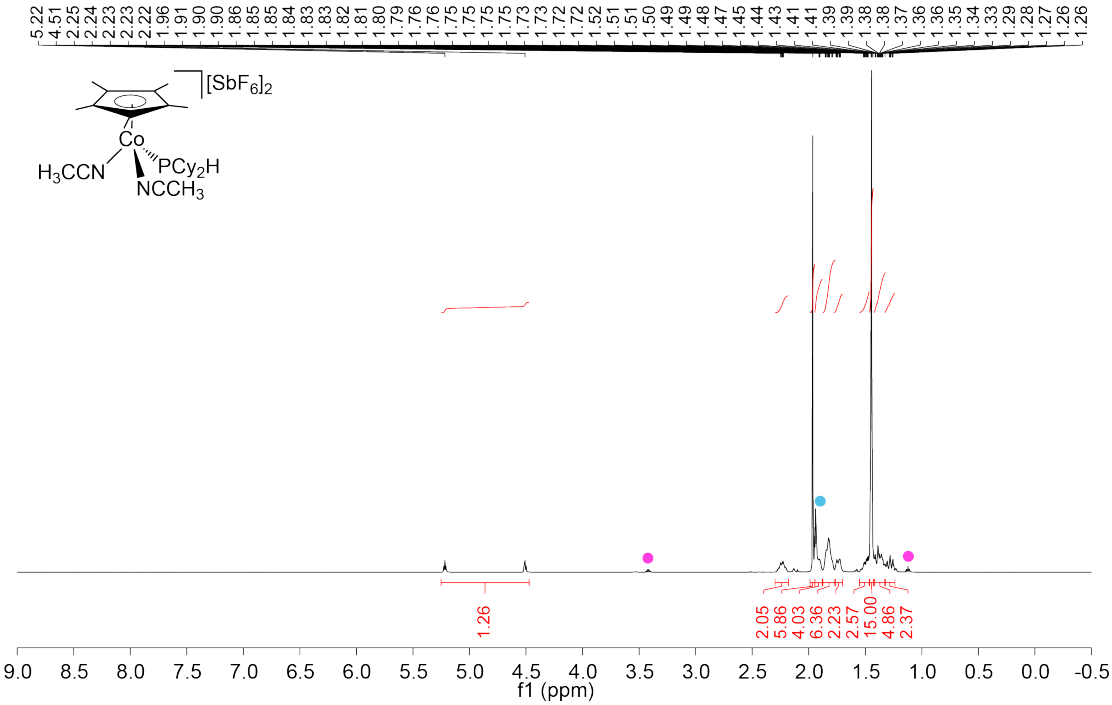

Figure C.37 ^{1}H NMR (500.27 MHz, CD_3CN) spectrum of complex **Co-6c**. Diethyl ether (pink) and residual proteo-solvent (•).

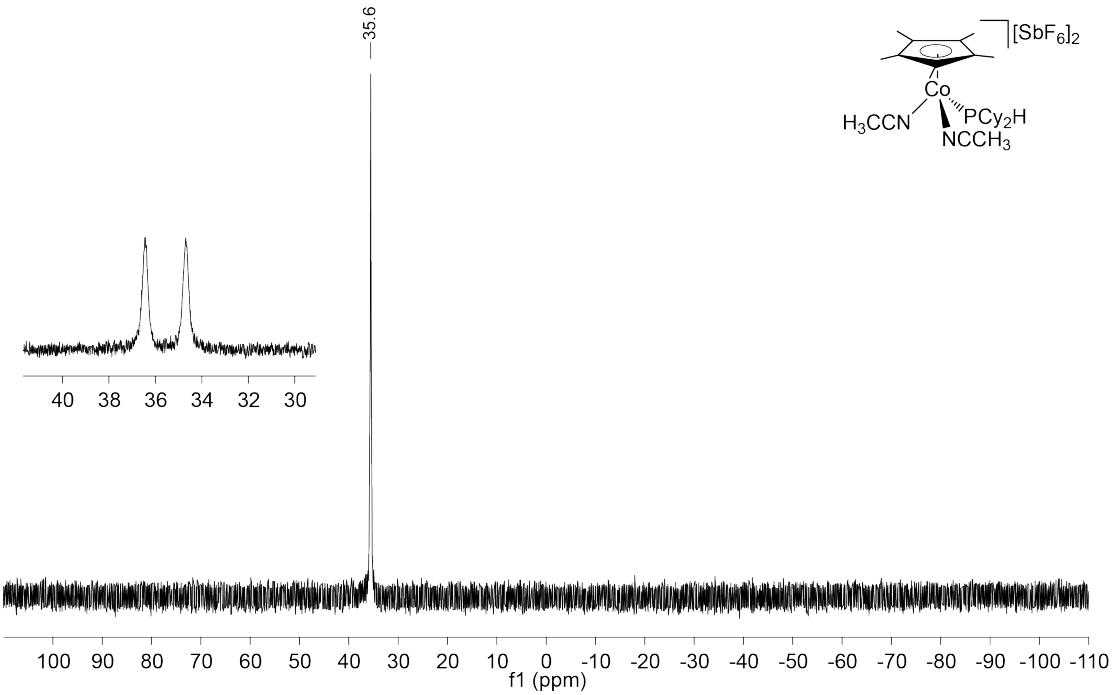

Figure C.38 ^{31}P{^{1}H} and ^{31}P (inset) NMR (202.51 MHz, CD_3CN) spectra of complex **Co-6c.**

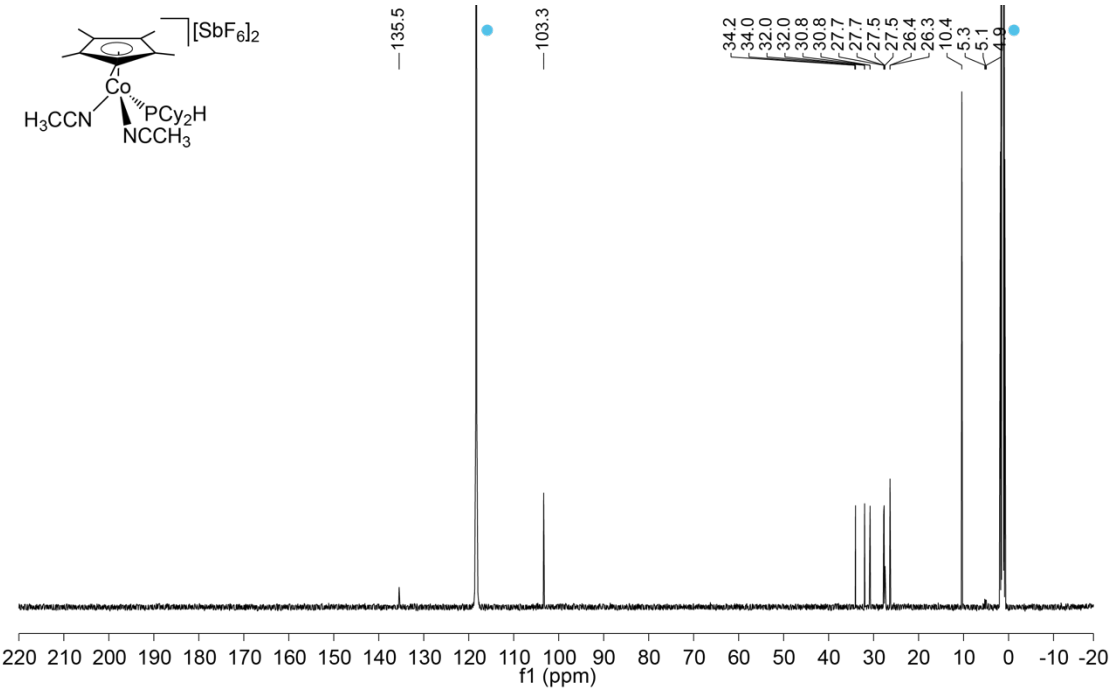

Figure C.39 $^{13}C\{^{1}H\}$ NMR (125.77 MHz, CD_3CN) spectrum of complex **Co-6c**. Deuterated solvent (•).

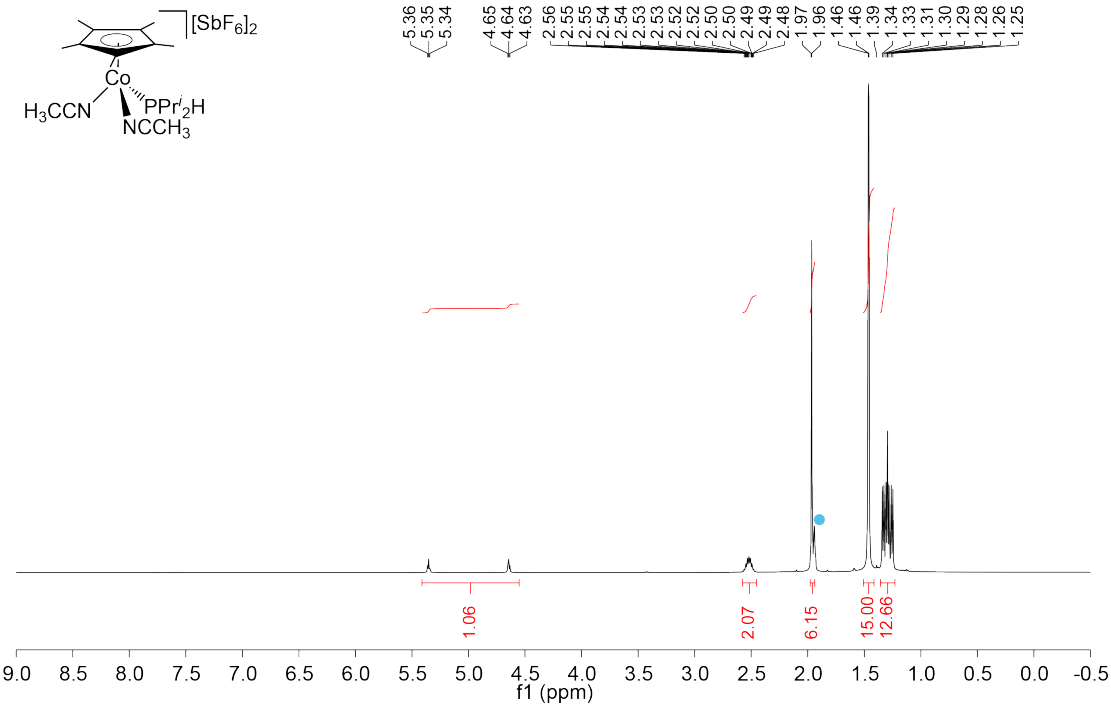

Figure C.40 ^{1}H NMR (500.27 MHz, CD_3CN) spectrum of complex **Co-6d**. Residual proteo-solvent (•).

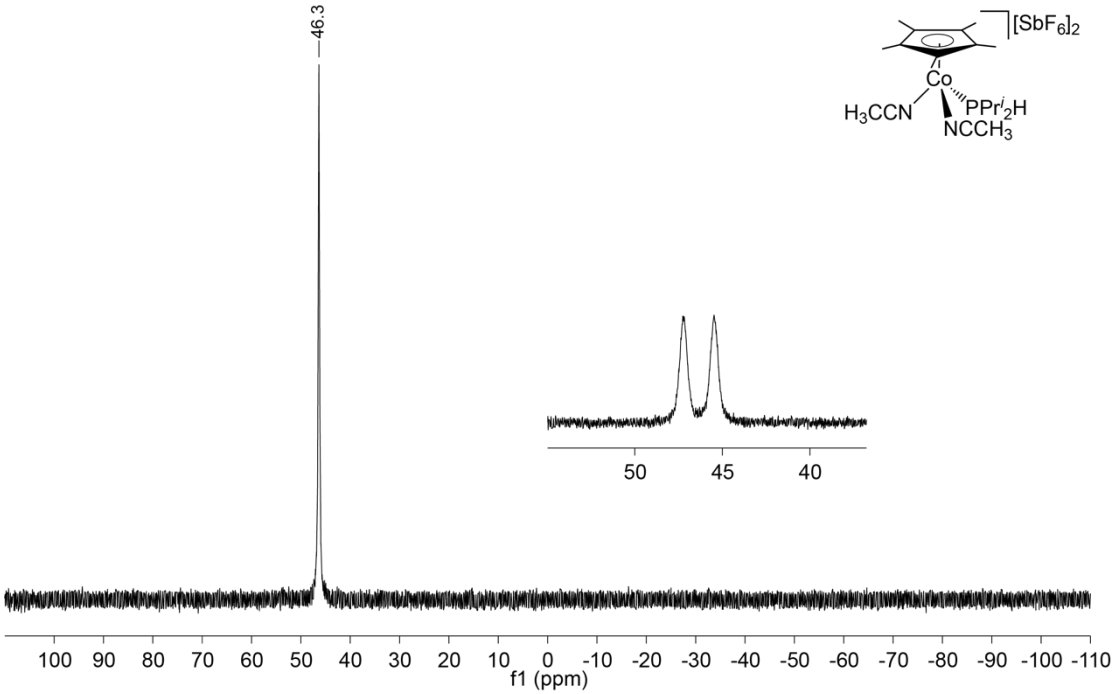

Figure C.41 $^{31}P\{^{1}H\}$ and ^{31}P (inset) NMR (202.51 MHz, CD_3CN) spectra of complex **Co-6d.**

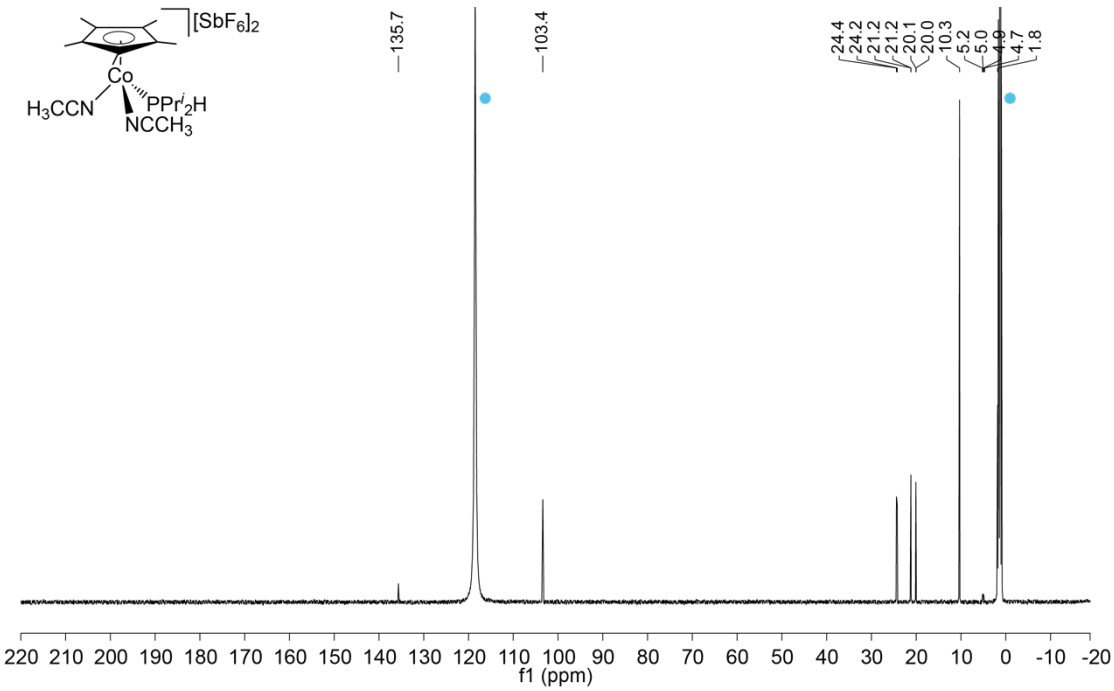

Figure C.42 $^{13}C\{^{1}H\}$ NMR (125.77 MHz, CD_3CN) spectrum of complex **Co-6d**. Deuterated solvent (•).

Appendix D – NMR spectra of hydrophosphination products

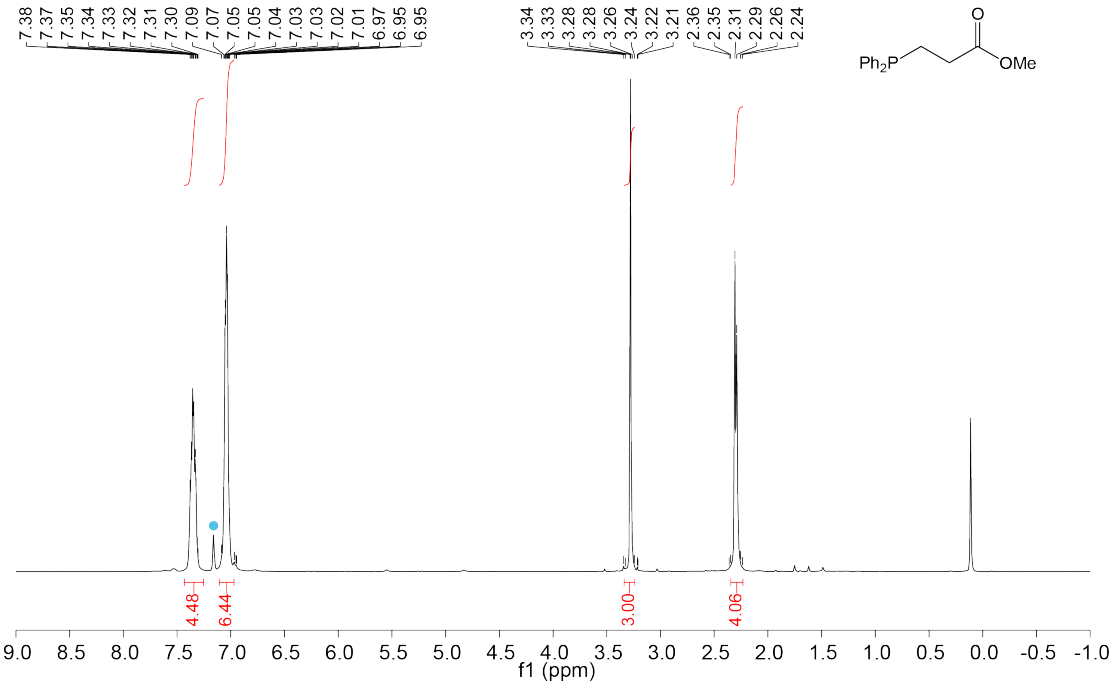

Figure D.1 ^{1}H NMR (300.27 MHz, C_6D_6) spectrum of $Ph_2P(CH_2CH_2CO_2Me)$. Residual proteo-solvent (•).

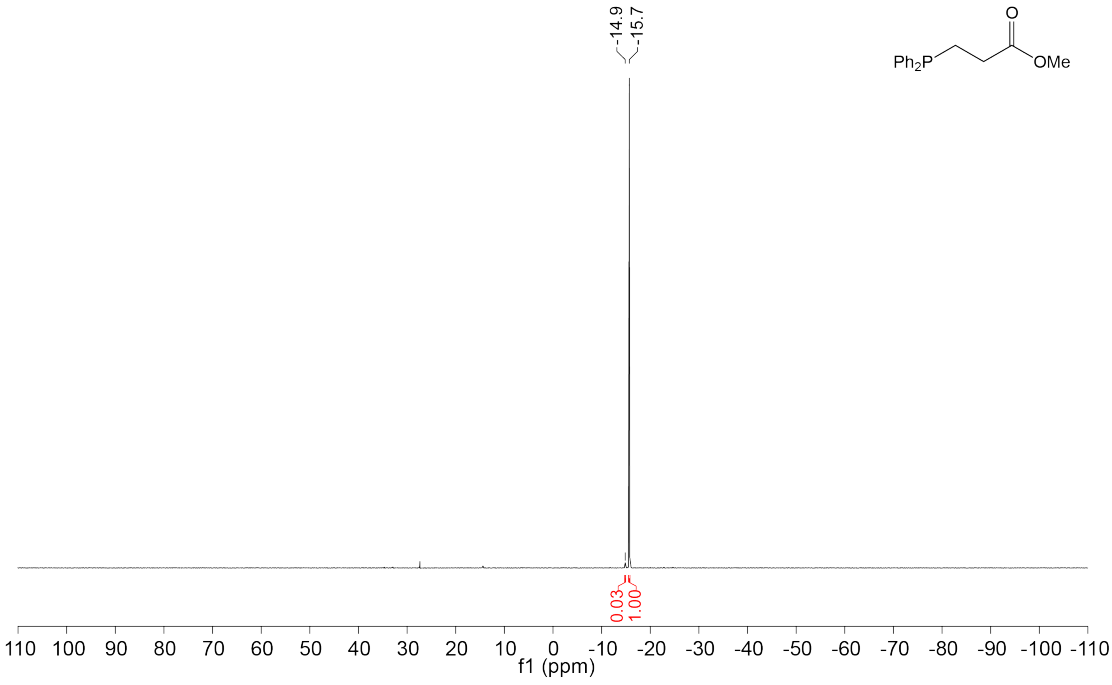

Figure D.2 $^{31}P\{^{1}H\}$ NMR (121.55 MHz, C_6D_6) spectrum of $Ph_2P(CH_2CH_2CO_2Me)$.

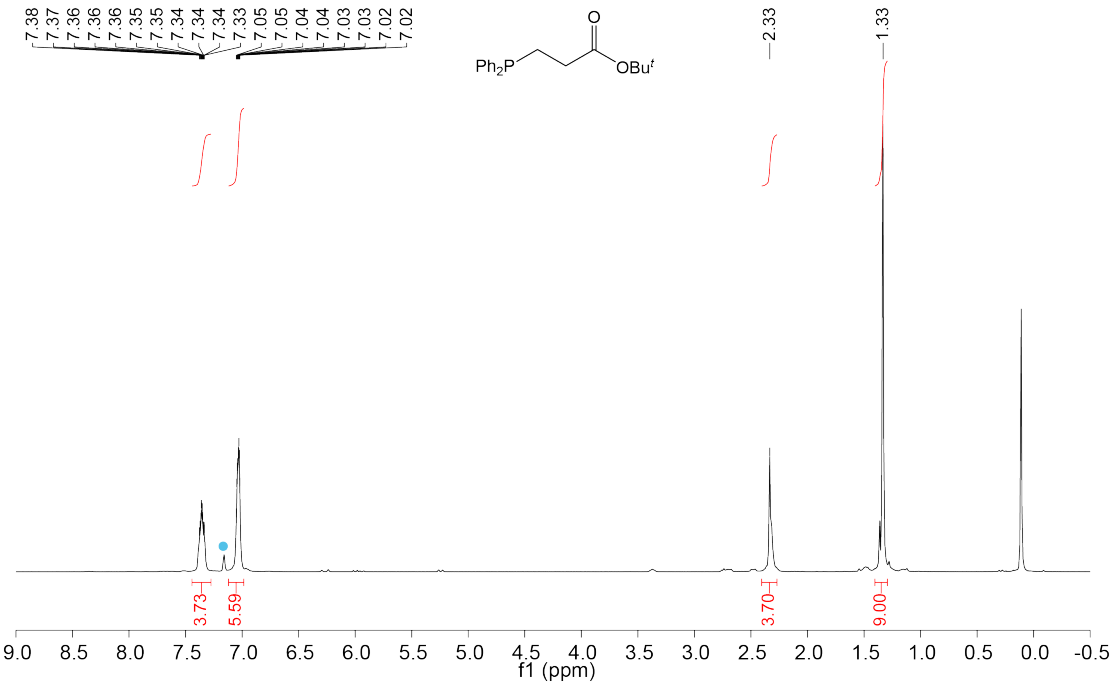

Figure D.3 ^{1}H NMR (300.27 MHz, C_6D_6) spectrum of $Ph_2P(CH_2CH_2CO_2Bu^t)$. Residual proteo-solvent (•).

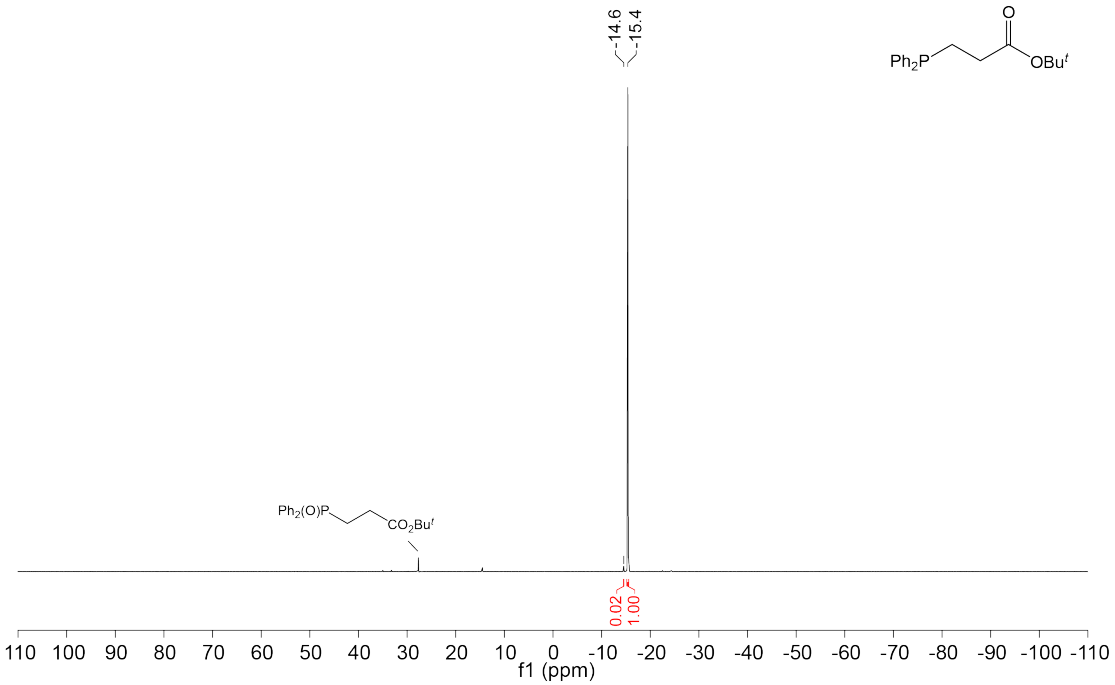

Figure D.4 ^{31}P{^{1}H} NMR (121.55 MHz, C_6D_6) spectrum of $Ph_2P(CH_2CH_2CO_2Bu^t)$.

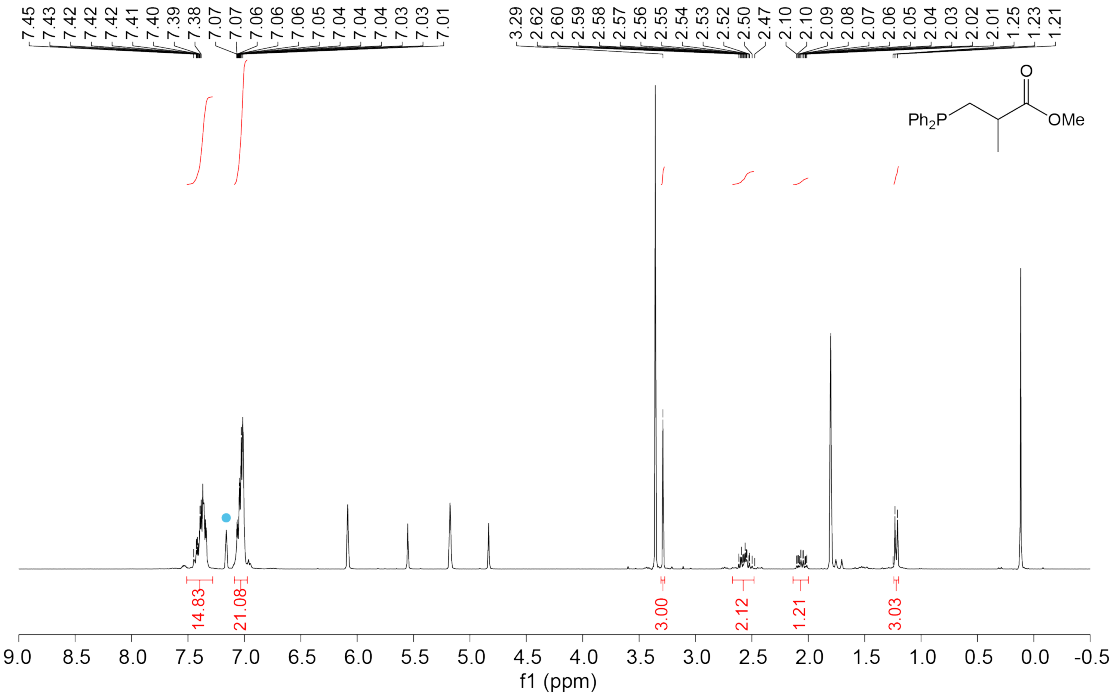

Figure D.5 ^{1}H NMR (300.27 MHz, C_6D_6) spectrum of $Ph_2P\{CH_2CH(Me)CO_2Me\}$. Residual proteo-solvent (•).

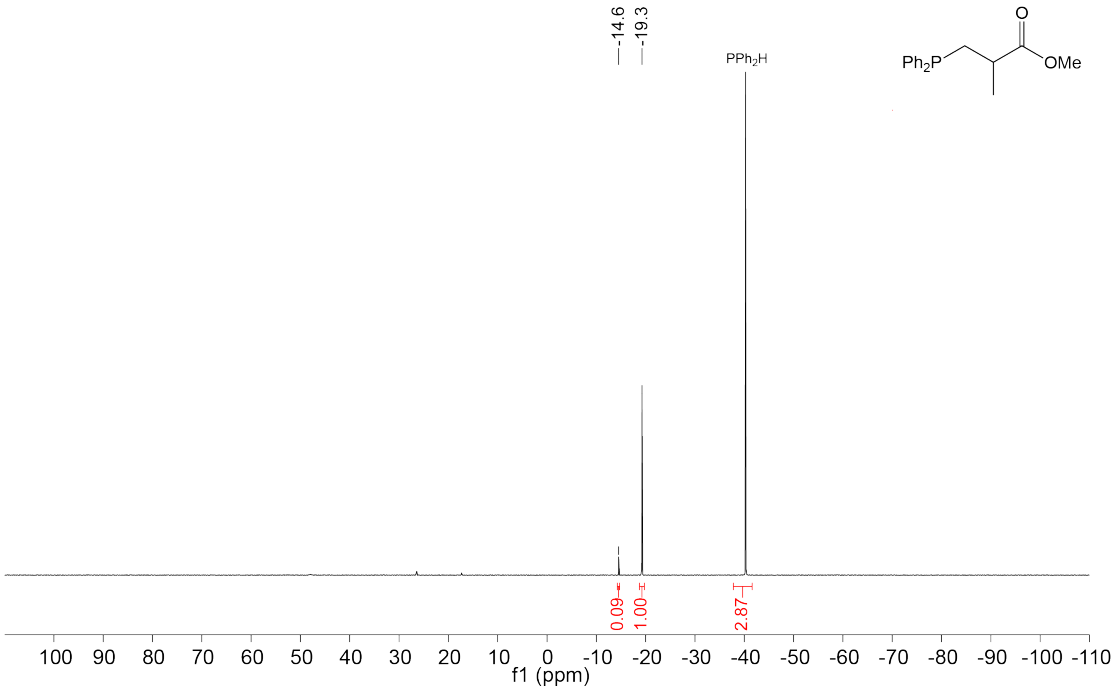

Figure D.6 $^{31}P\{^{1}H\}$ NMR (121.55 MHz, C_6D_6) spectrum of $Ph_2P\{CH_2CH(Me)CO_2Me\}$.

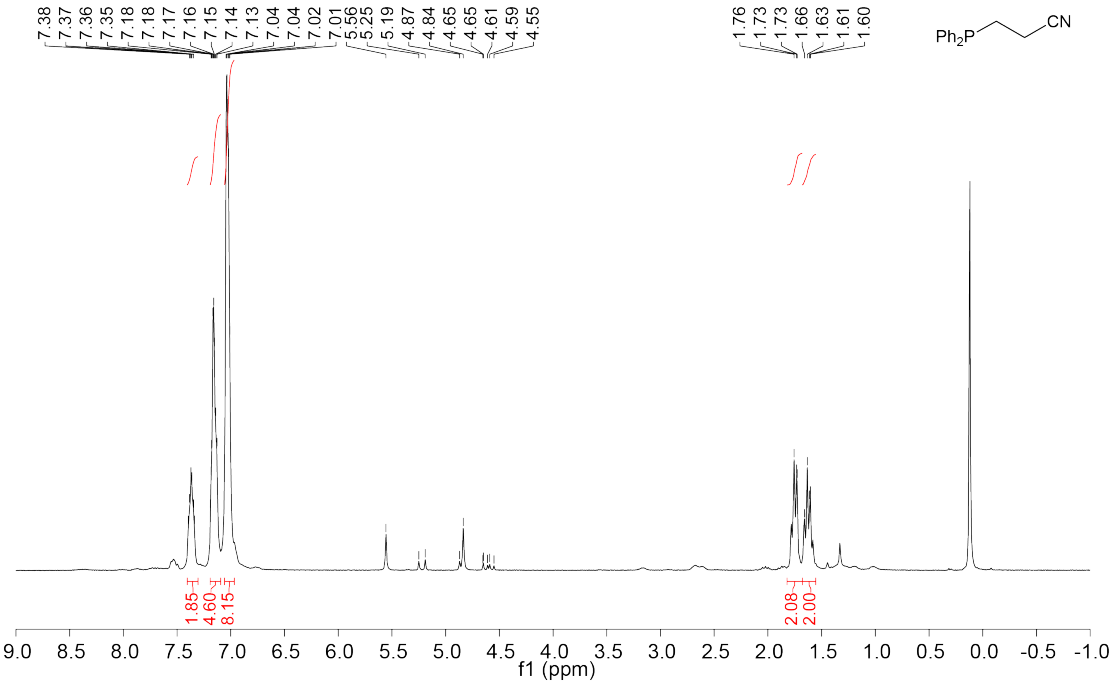

Figure D.7 ^{1}H NMR (300.27 MHz, C_6D_6) spectrum of $Ph_2P(CH_2CH_2CN)$.

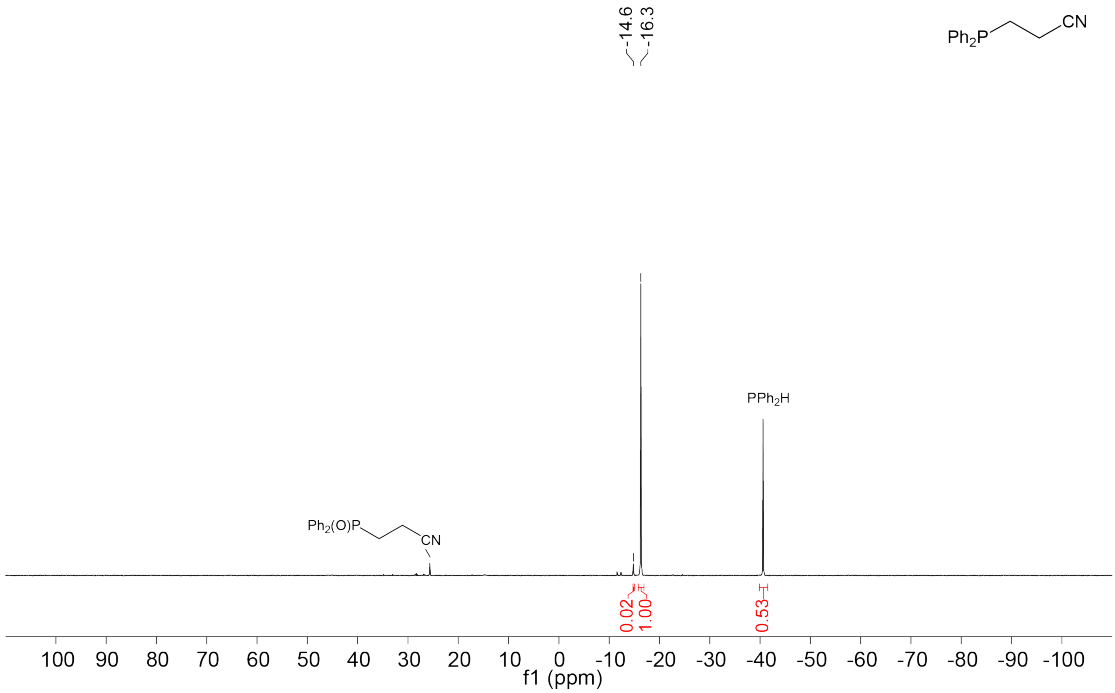

Figure D.8 $^{31}P\{^{1}H\}$ NMR (121.55 MHz, C_6D_6) spectrum of $Ph_2P(CH_2CH_2CN)$.

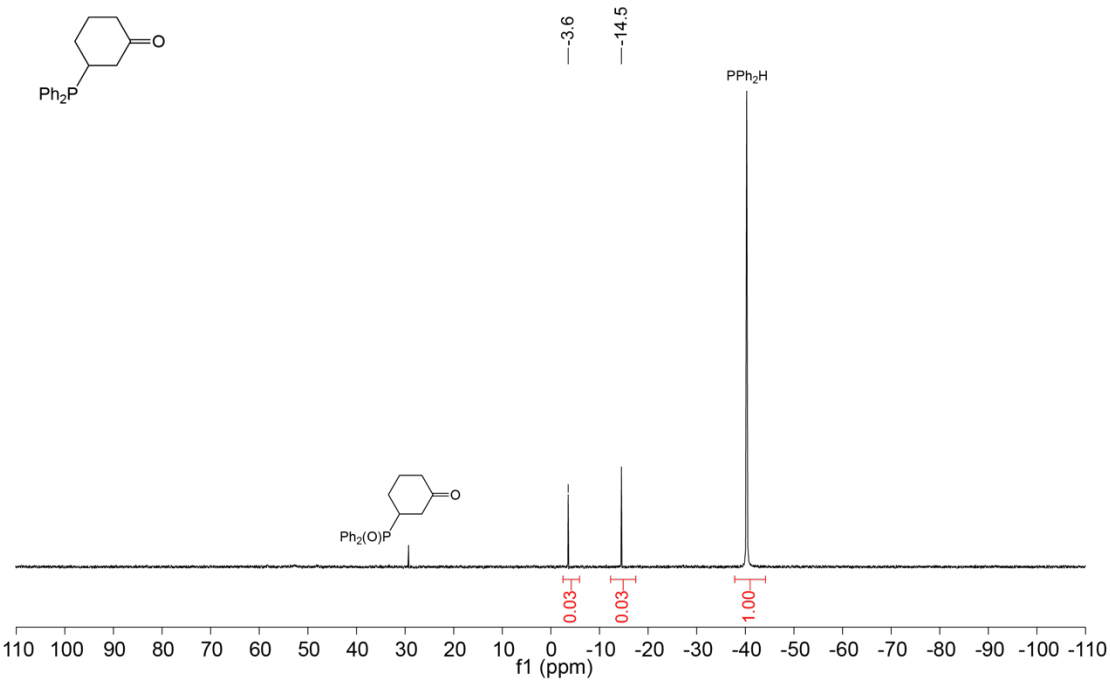

Figure D.9 $^{31}P\{^{1}H\}$ NMR (121.55 MHz, C_6D_6) spectrum of $Ph_2P(C_6H_9O)$.

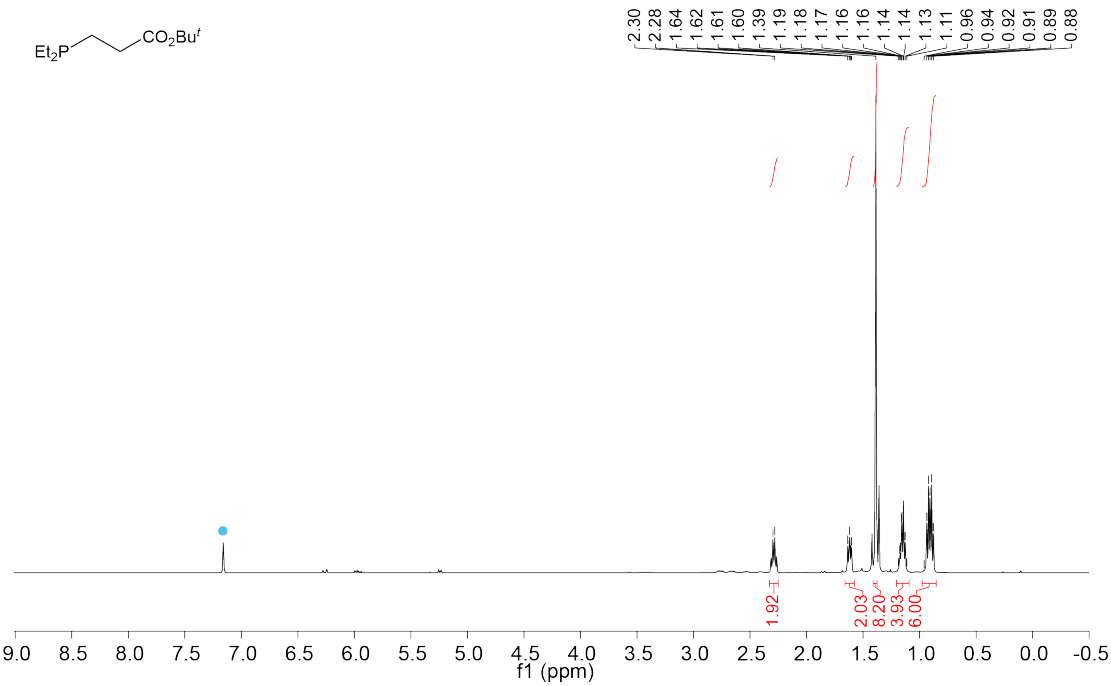

Figure D.10 ^{1}H NMR (500.27 MHz, C_6D_6) spectrum of $Et_2P(CH_2CH_2CO_2Bu^t)$. Residual proteo-solvent (•).

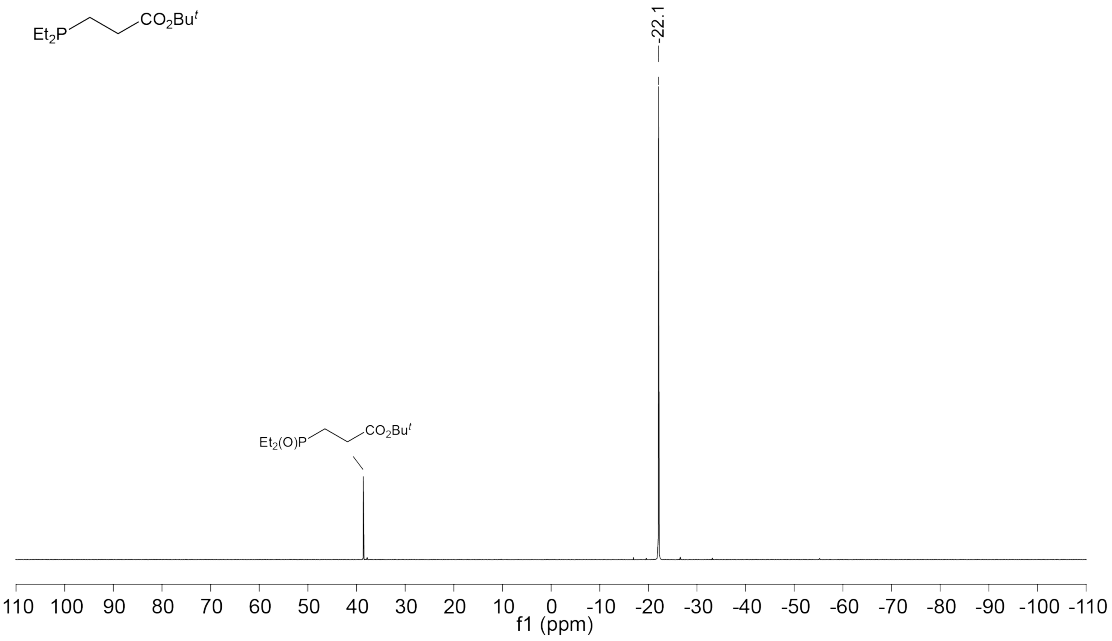

Figure D.11 $^{31}P\{^{1}H\}$ NMR (202.51 MHz, C_6D_6) spectrum of $Et_2P(CH_2CH_2CO_2Bu^t)$.

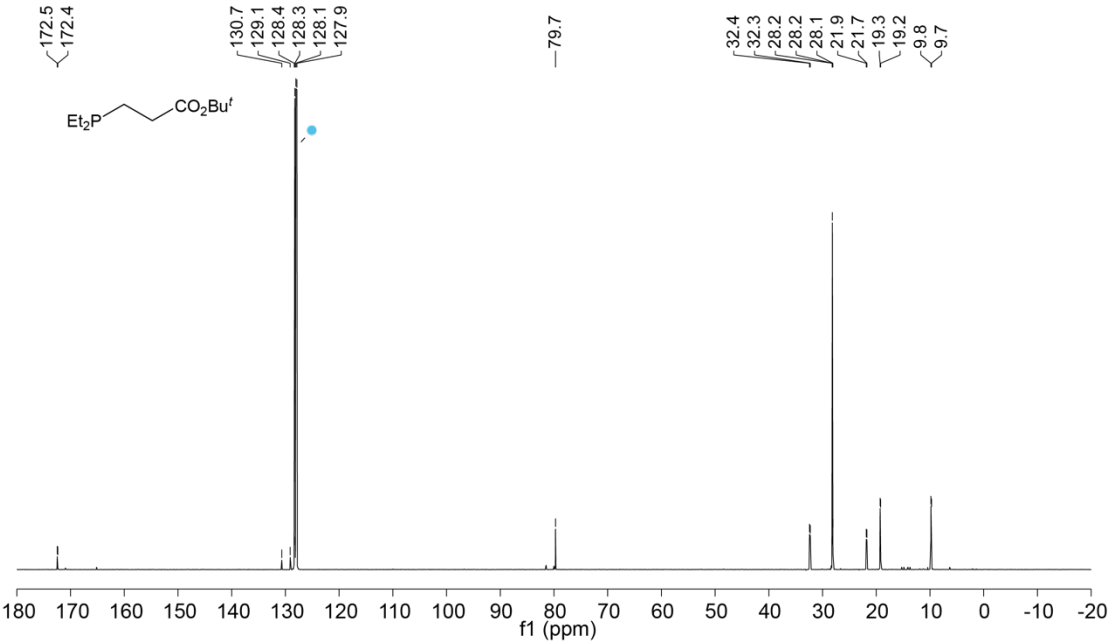

Figure D.12 $^{13}C\{^{1}H\}$ NMR (125.77 MHz, C_6D_6) spectrum of $Et_2P(CH_2CH_2CO_2Bu^t)$. Deuterated solvent (•).

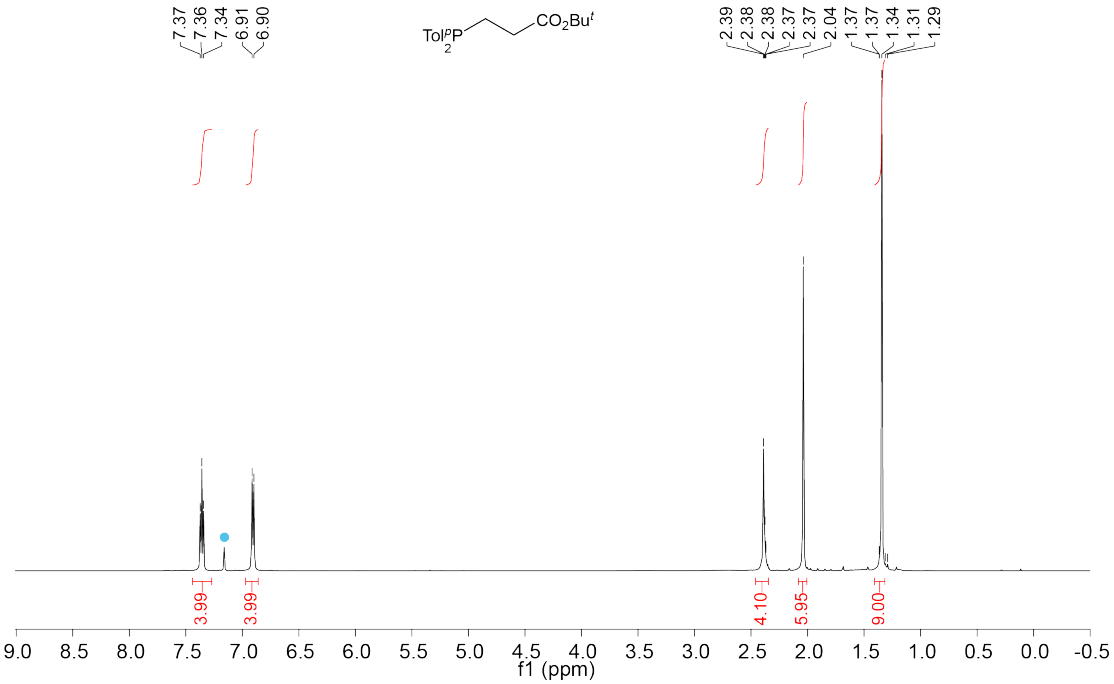

Figure D.13 ^{1}H NMR (500.27 MHz, C_6D_6) spectrum of Tol$^p_2$P($CH_2CH_2CO_2Bu^t$). Residual proteo-solvent (•).

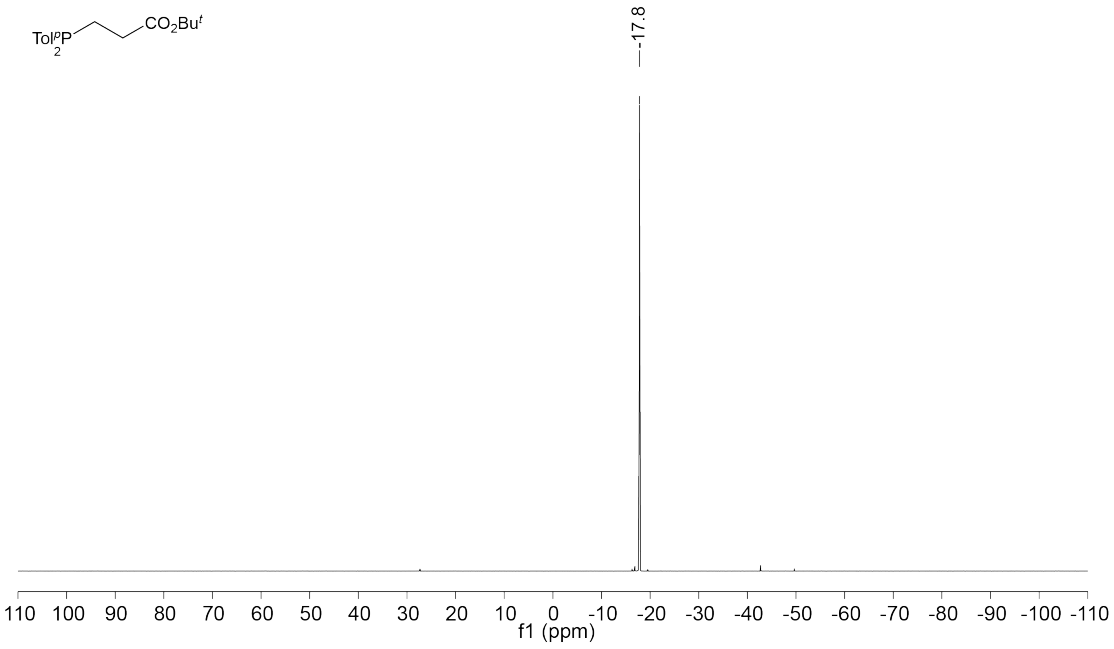

Figure D.14 ^{31}P{^{1}H} NMR (202.51 MHz, C_6D_6) spectrum of Tol$^p_2$P($CH_2CH_2CO_2Bu^t$).

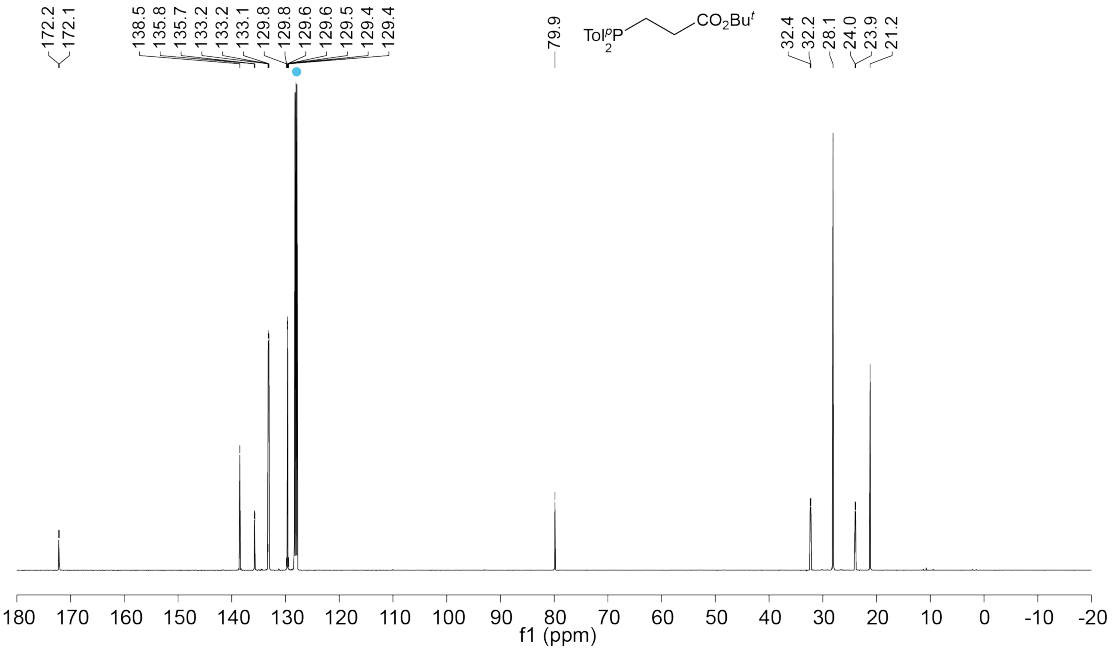

Figure D.15 $^{13}C\{^{1}H\}$ NMR (125.77 MHz, C_6D_6) spectrum of $Tol^{p}_2P(CH_2CH_2CO_2Bu^t)$. Deuterated solvent (•).

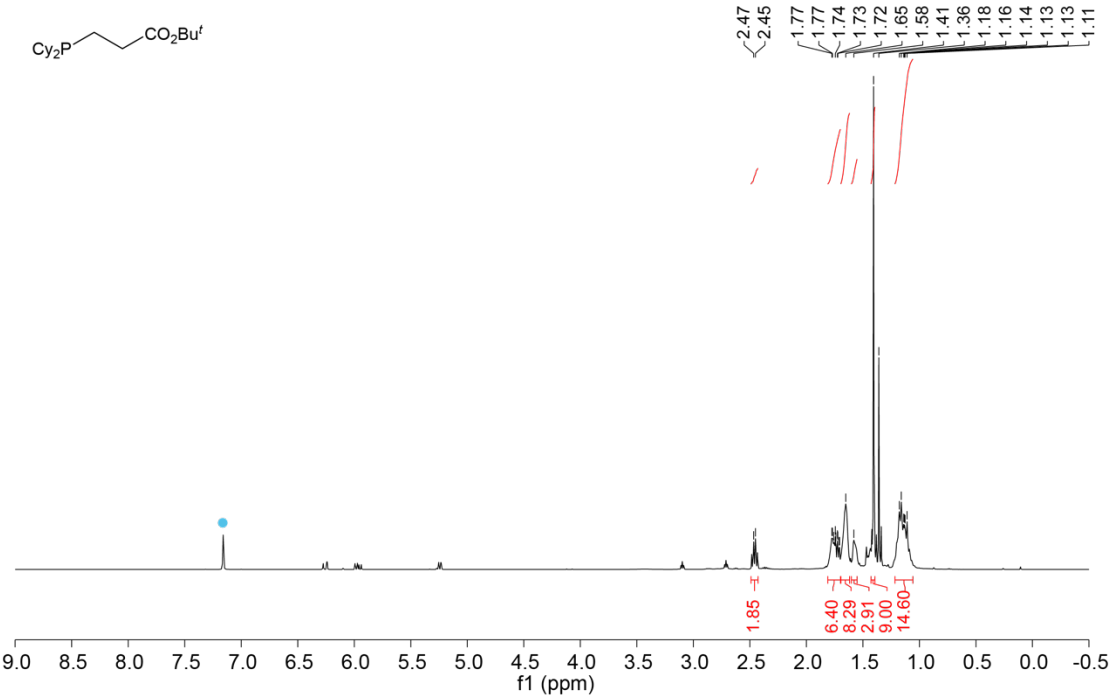

Figure D.16 ^{1}H NMR (500.27 MHz, C_6D_6) spectrum of $Cy_2P(CH_2CH_2CO_2Bu^t)$ (3 days reaction). Residual proteo-solvent (•).

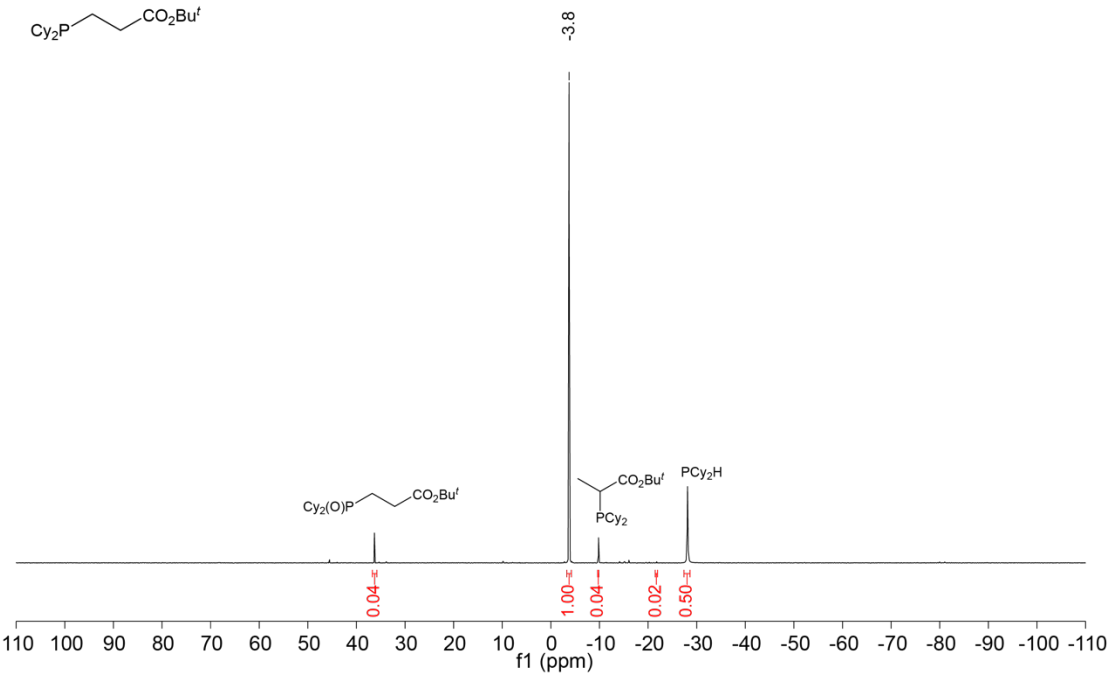

Figure D.17 $^{31}P\{^{1}H\}$ NMR (202.51 MHz, C_6D_6) spectrum of $Cy_2P(CH_2CH_2CO_2Bu^t)$ (3 days reaction).

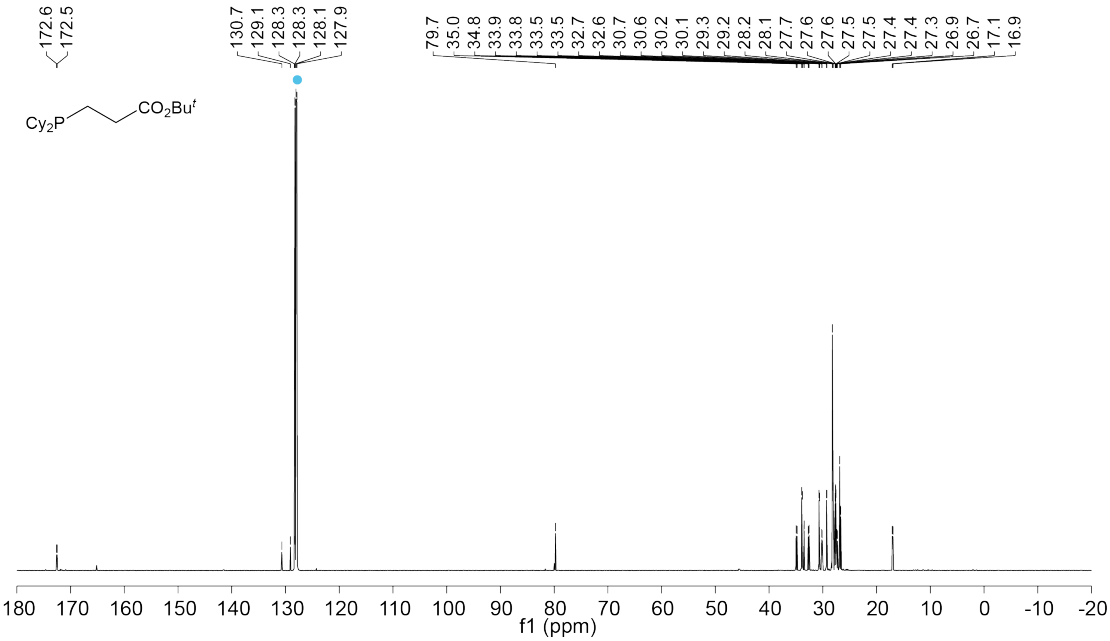

Figure D.18 $^{13}C\{^{1}H\}$ NMR (125.77 MHz, C_6D_6) spectrum of $Cy_2P(CH_2CH_2CO_2Bu^t)$ (3 days reaction). Deuterated solvent (•).

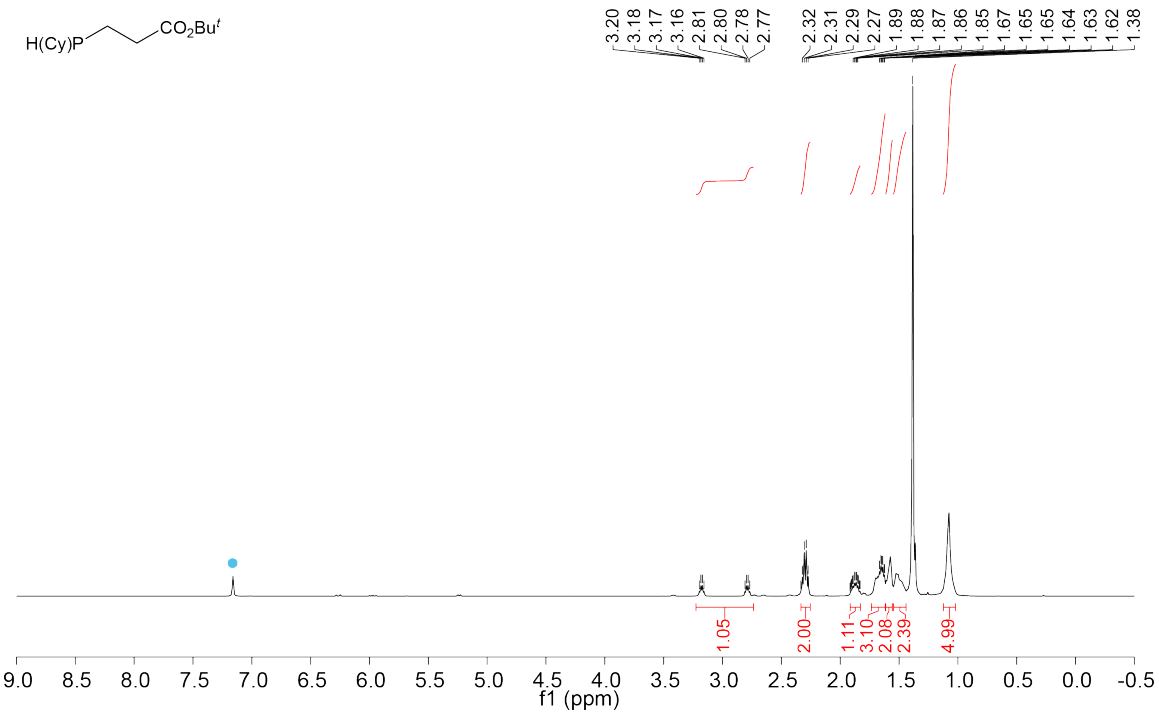

Figure D.19 ^{1}H NMR (500.27 MHz, C_6D_6) spectrum of P(Cy)(H)($CH_2CH_2CO_2Bu^t$). Residual proteo-solvent (•).

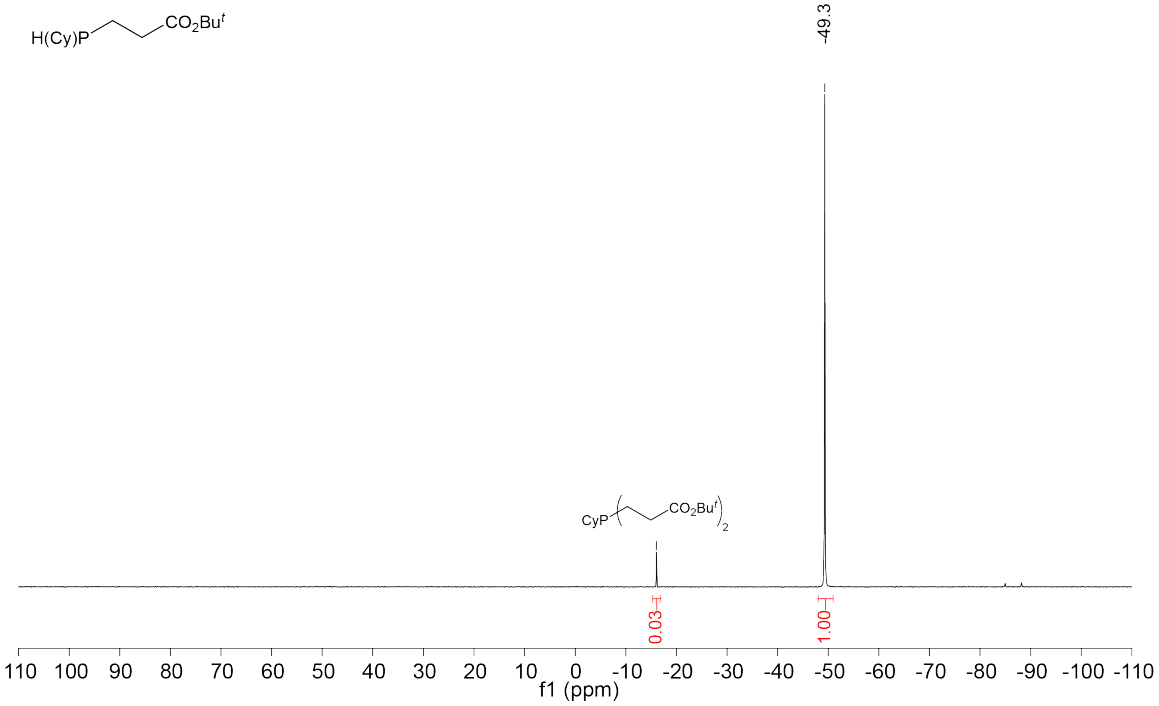

Figure D.20 ^{31}P{^{1}H} NMR (202.51 MHz, C_6D_6) spectrum of P(Cy)(H)($CH_2CH_2CO_2Bu^t$).

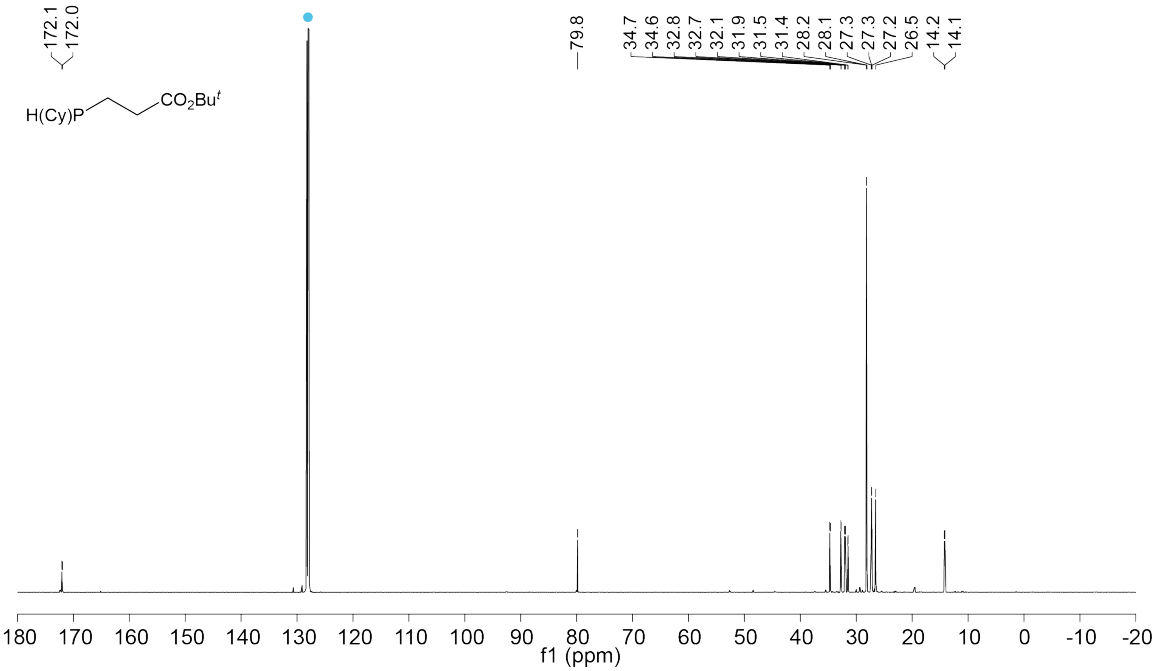

Figure D.21 $^{13}C\{^{1}H\}$ NMR (125.77 MHz, C_6D_6) spectrum of $P(Cy)(H)(CH_2CH_2CO_2Bu^t)$. Deuterated solvent (•).

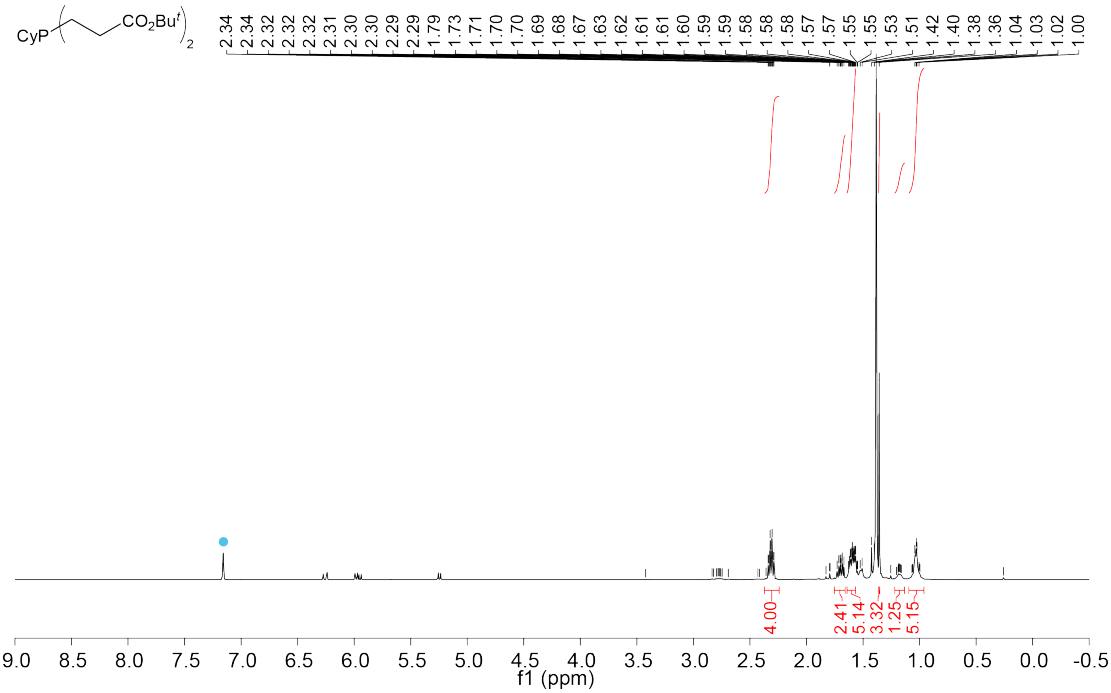

Figure D.22 ^{1}H NMR (500.27 MHz, C_6D_6) spectrum of $CyP(CH_2CH_2CO_2Bu^t)_2$. Residual proteo-solvent (•).

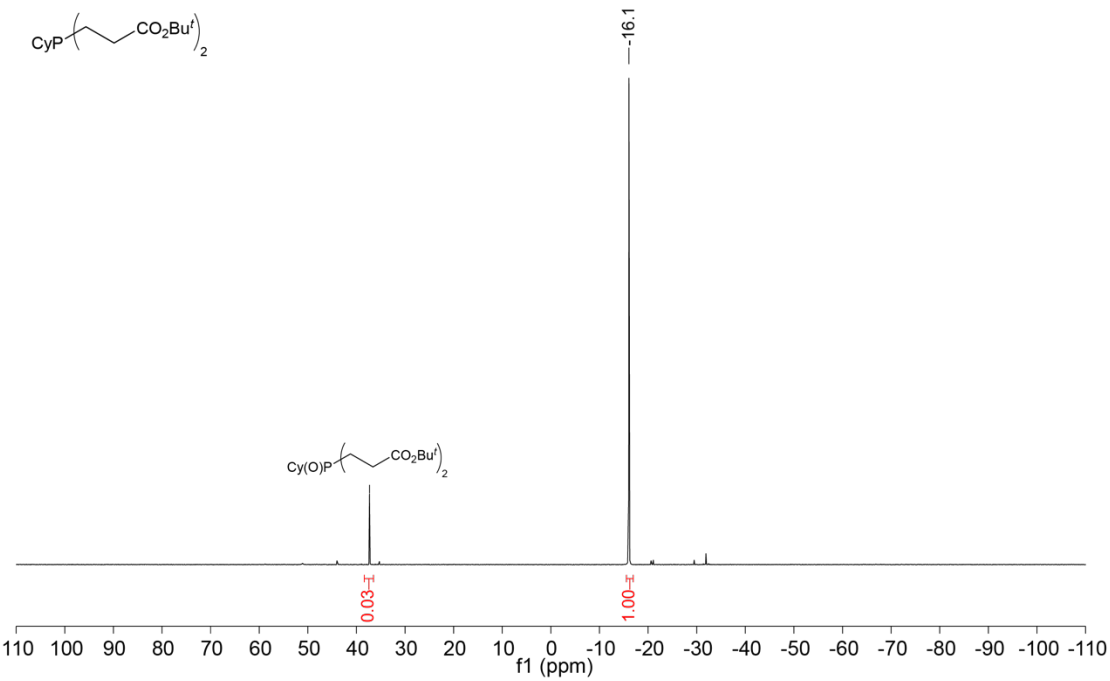

Figure D.23 $^{31}P\{^{1}H\}$ NMR (202.51 MHz, C_6D_6) spectrum of $CyP(CH_2CH_2CO_2Bu^t)_2$.

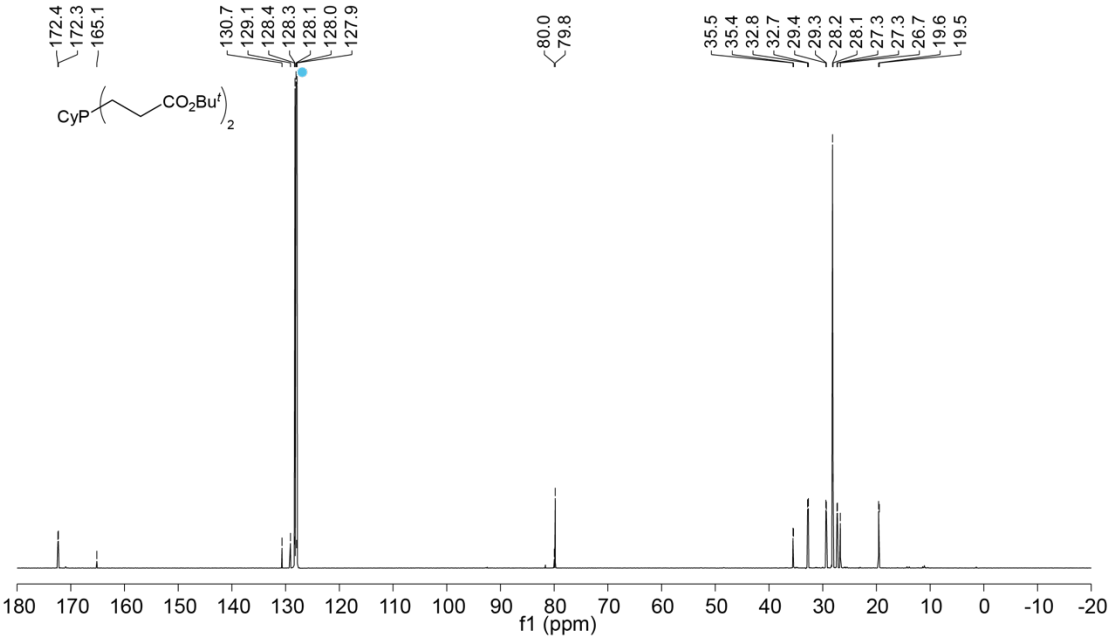

Figure D.24 $^{13}C\{^{1}H\}$ NMR (125.77 MHz, C_6D_6) spectrum of $CyP(CH_2CH_2CO_2Bu^t)_2$. Deuterated solvent (•).

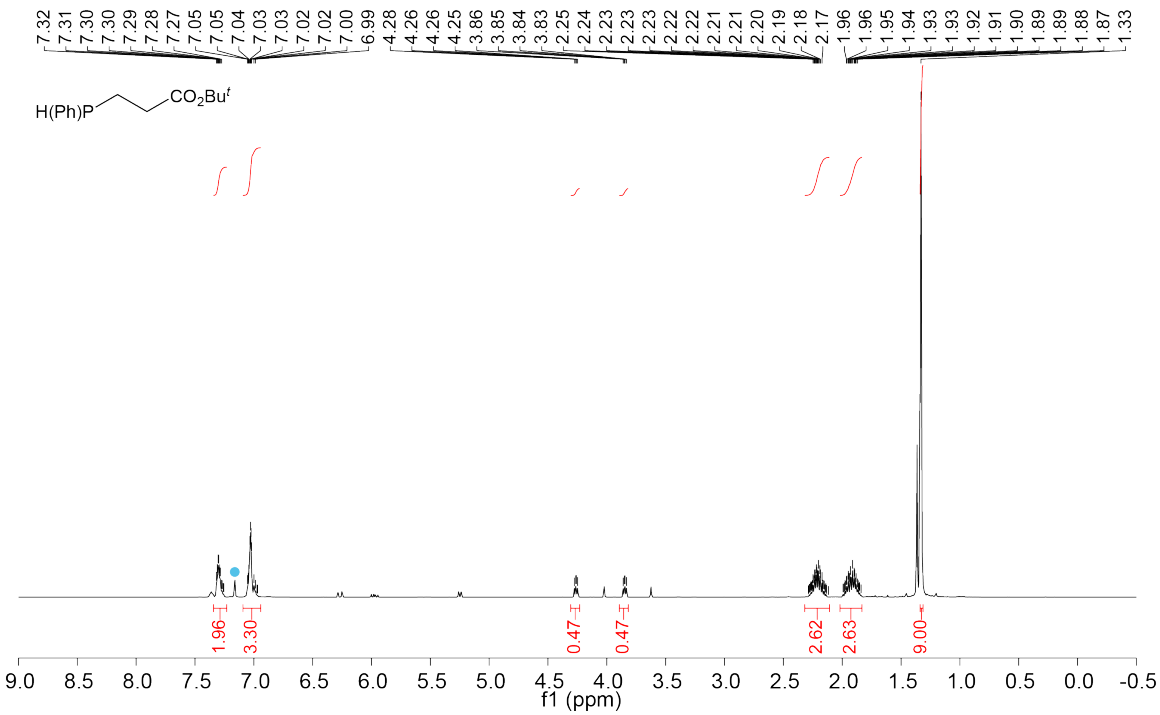

Figure D.25 ^{1}H NMR (500.27 MHz, C_6D_6) spectrum of P(Ph)(H)($CH_2CH_2CO_2Bu^t$). Residual proteo-solvent (•).

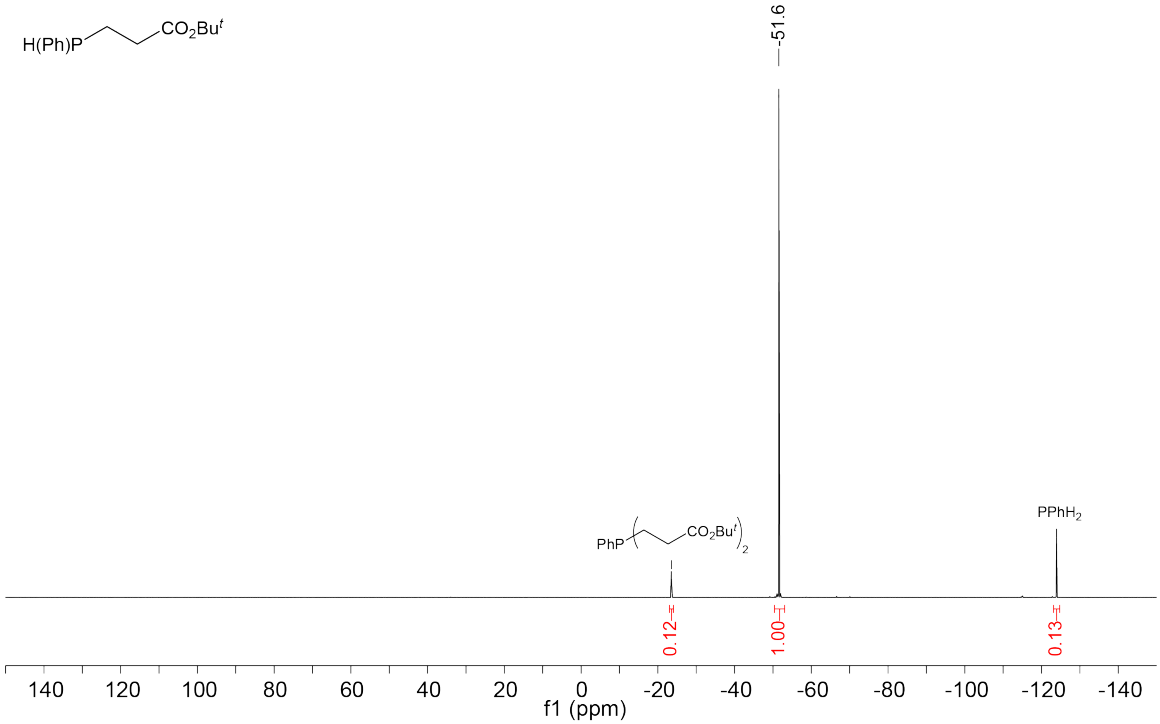

Figure D.26 ^{31}P{^{1}H} NMR (202.51 MHz, C_6D_6) spectrum of P(Ph)(H)($CH_2CH_2CO_2Bu^t$).

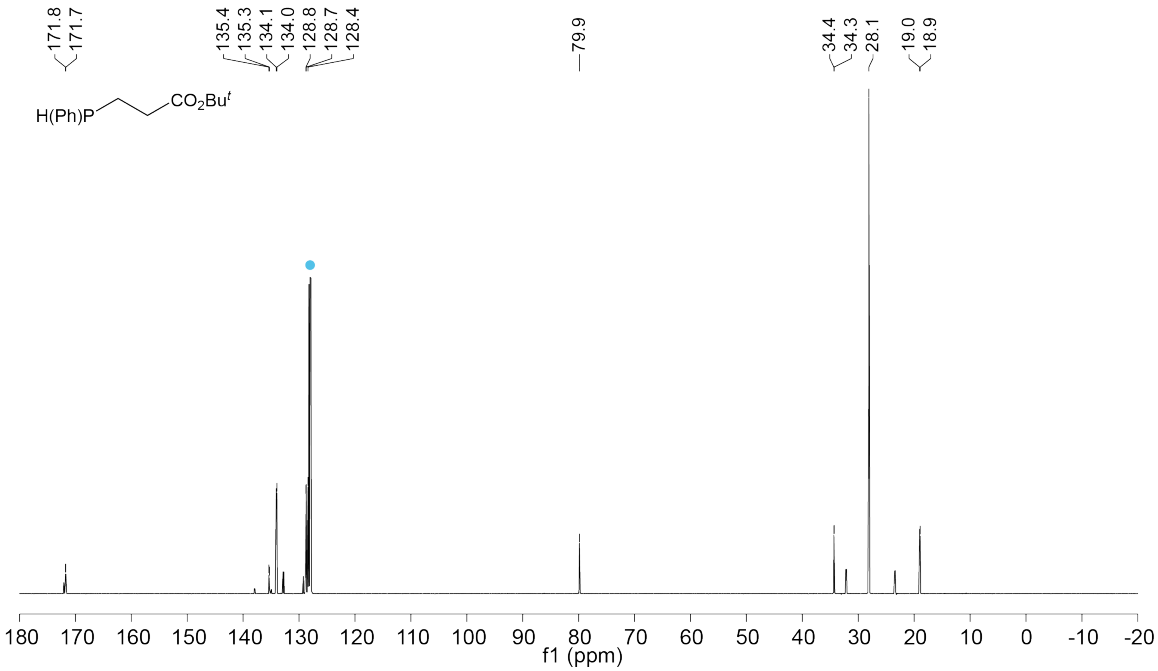

Figure D.27 $^{13}C\{^{1}H\}$ NMR (125.77 MHz, C_6D_6) spectrum of $P(Ph)(H)(CH_2CH_2CO_2Bu^t)$. Deuterated solvent (•).

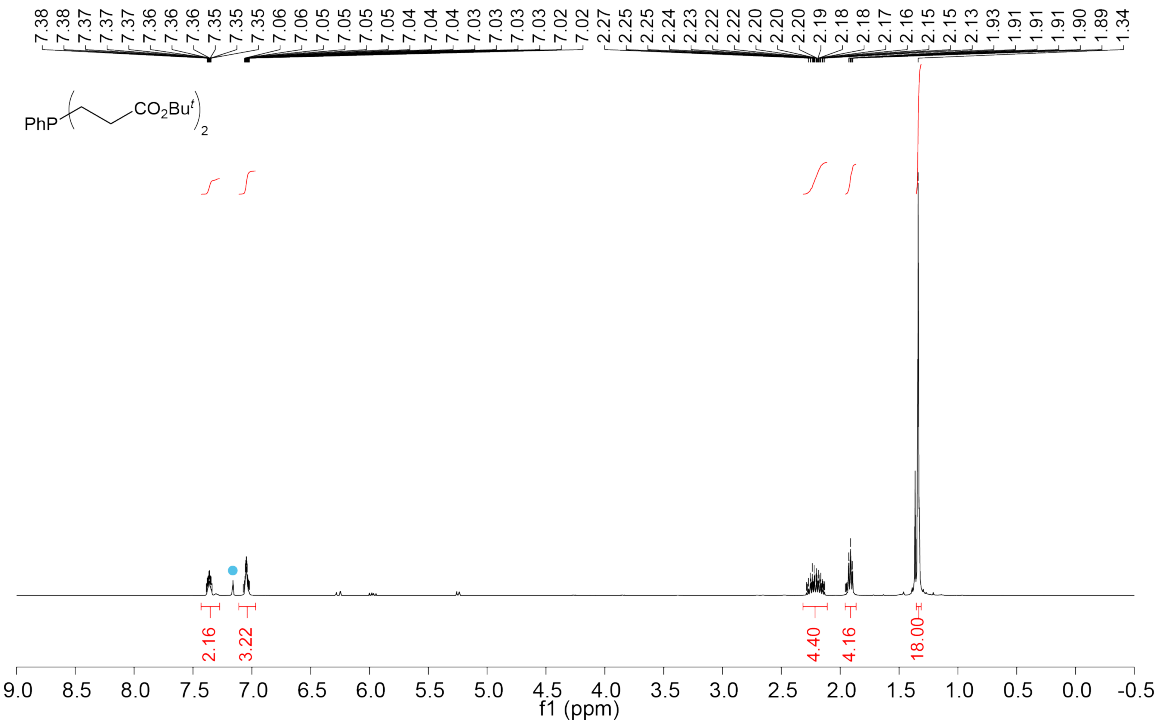

Figure D.28 ^{1}H NMR (500.27 MHz, C_6D_6) spectrum of $Ph_2P(CH_2CH_2CO_2Bu^t)$ (7 days reactions). Residual proteo-solvent (•).

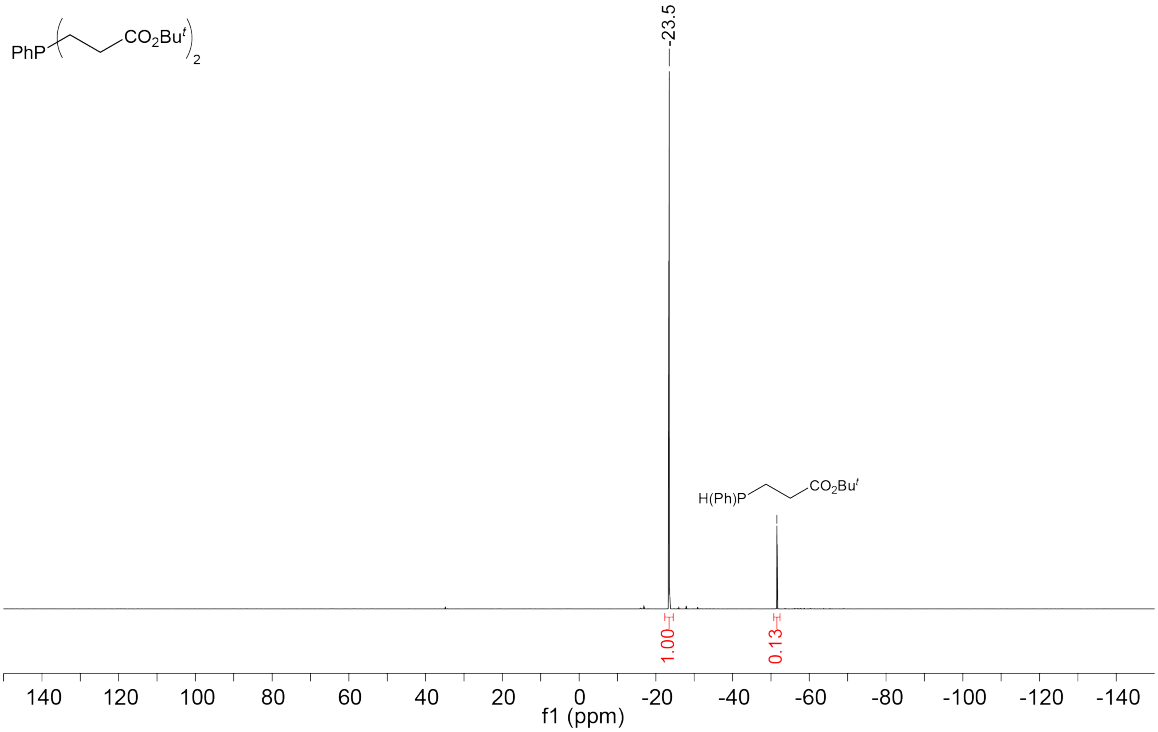

Figure D.29 $^{31}P\{^{1}H\}$ NMR (202.51 MHz, C_6D_6) spectrum of $Ph_2P(CH_2CH_2CO_2Bu^t)$ (7 days reactions).

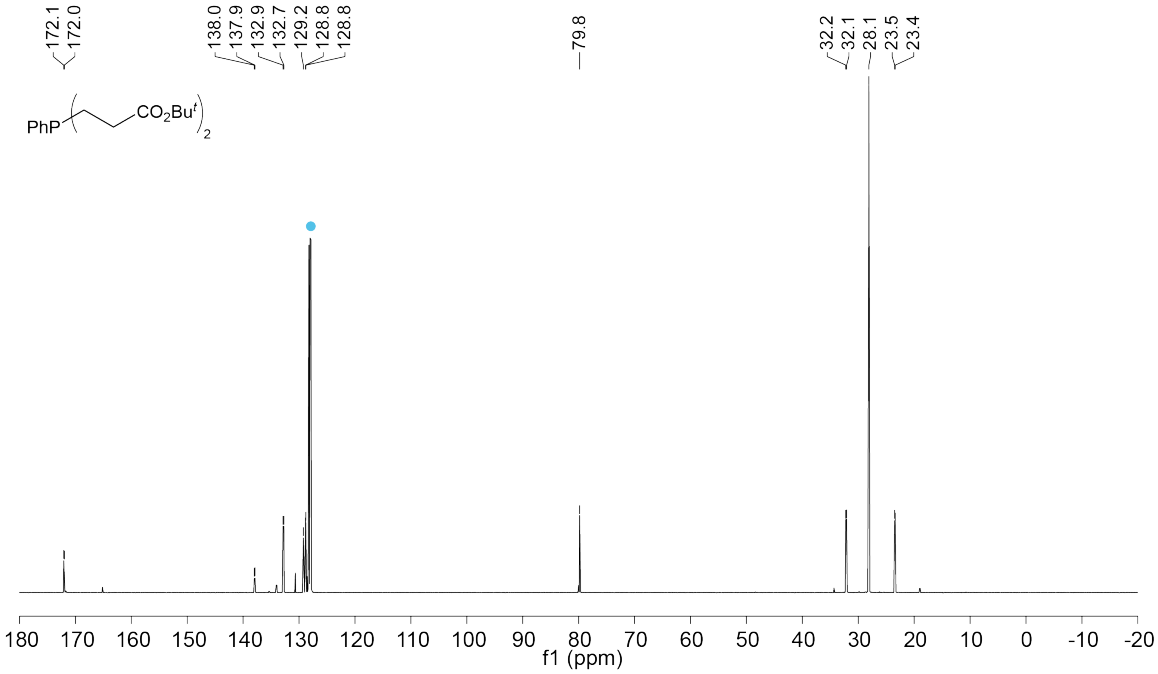

Figure D.30 $^{13}C\{^{1}H\}$ NMR (125.77 MHz, C_6D_6) spectrum of $Ph_2P(CH_2CH_2CO_2Bu^t)$ (7 days reactions). Deuterated solvent (•).

Appendix E – Survey of Co phosphido complexes

One of the most crucial aspects of the reaction mechanism (Chapters 4 and 5) is whether or not a Co phosphido intermediate (Co-PR_2) exists and in what form. As a result, I briefly reviewed the literature to compile a list of known Co phosphido complexes and their spectroscopy data (Table E.1), which may help identify potential Co-PR_2 in our Cp*Co system. Table E.1 includes most examples of isolatable Co-PR_2 complexes. Some heteronuclear bridging phosphido complexes (M-Co) containing Co and observed Co-PR_2 intermediates are not included.

Table E.1 List of isolatable Co phosphido complexes.

Complex	δ ^{31}P	X-ray	Reference
Co = Co^{III} Co = Co^{II} Co = Co^{I}			
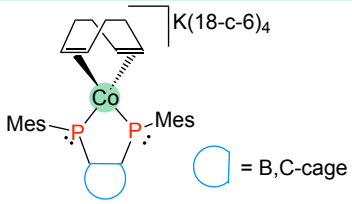	101.3	Yes	Hey-Hawkins & Wolf 2021
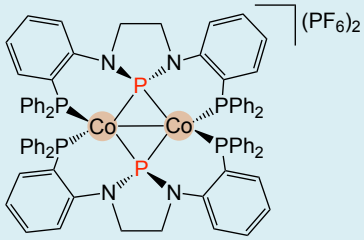	225.9	Yes	Thomas 2020
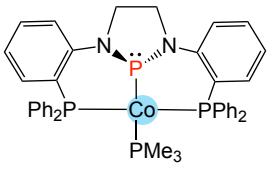	251.2	Yes	Thomas 2018
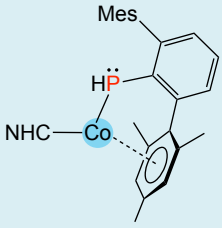	−28.3 ~ −35.0	Yes	Deng 2018

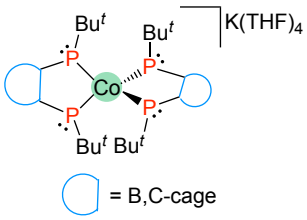	201.8	Yes	Hey-Hawkins & Wolf 2017[8]
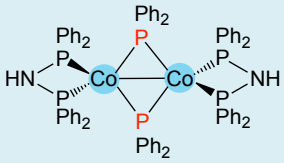	112.2	Yes	Kornev 2012
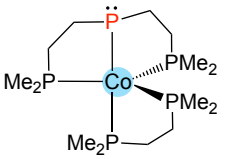	94.6	no	Edwards 1994
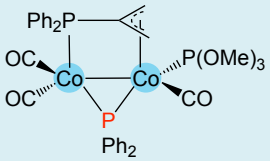	48.7	Yes	Tiripicchio 1993
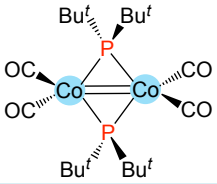	331.4	no	Chandler 1989
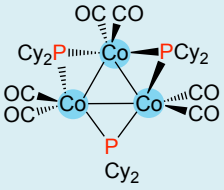	319.2	Yes	Albright, Bard & Jones 1988
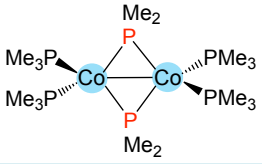	Not reported	Yes	Klein 1988
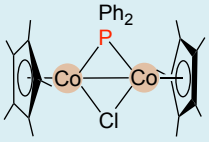	Not reported	no	Koelle 1986
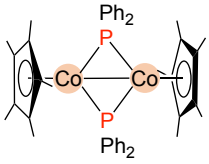	Not reported (not stable)	no	Koelle 1986

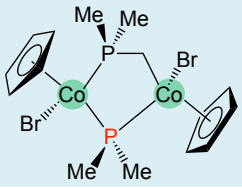	95.9	Yes	Werner 1986
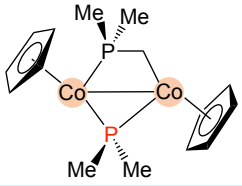	115.69	no	Werner 1985
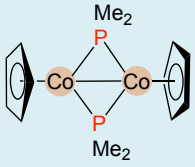	Not reported	Yes	Werner 1985
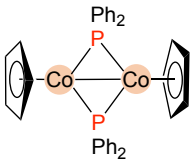	119.6	no	Meek 1985 William 1964
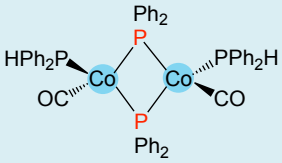	182.7	Yes	Geoffroy 1985 Geoffroy 1983
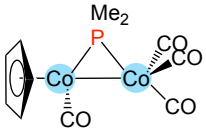	Not reported	Yes	Keller 1978

As shown in Table E.1, most reported examples are from the last century. Only a small amount of terminal phosphido complexes have been identified and isolated in these examples, while the main majority of Co-PR_2 is a bridging phosphido complex. In terms of the oxidation state of Co, Co(I) is the most common, followed by Co(II); only two examples of Co(III) have been reported.

Co bridging phosphido complexes have a wide range of ^{31}P shifts, often more than 100 ppm (Table E.1). Nearly all these Co bridging phosphido complexes have Co-Co bonds, which are confirmed by X-ray crystallography. Due to these Co-Co bonds, paramagnetic Co(II) complexes can be observed in the typical NMR region. Moreover,

these dimeric Co(II) complexes are not sufficiently stable and can dissociate to the monomers in solution. Their Co-Co bonds are easily broken by adding specific small molecules. Although some reactivities on Co phosphido species have been reported in the preceding cases, no one has reported employing these complexes in the hydrophosphination and dehydrocoupling of phosphines.

The insights gained from reviewing literature examples of Co-PR_2 is that: 1) Co(III)-PR_2 species might be too reactive to isolate or observe. 2) With regard to the first part (1), I wonder if Co(III)-PR_2 is a vial intermediate for catalyzing hydrophosphination or whether there are alternative forms of Co-PR_2 (e.g., low valent Co-PR_2) that are the real intermediates. Indeed, I demonstrate in this chapter 4 that the Co(II)-PR_2 is more stable and capable of catalyzing hydrophosphination in our system than high valent Co(III).

References:

(1) Coburger, P.; Leitl, J.; Scott, D. J.; Hierlmeier, G.; Shenderovich, I. G.; Hey-Hawkins, E.; Wolf, R. Synthesis of a Carborane-Substituted Bis(Phosphanido) Cobaltate(i), Ligand Substitution, and Unusual P4fragmentation. *Chem. Sci.* **2021**, *12*, 11225–11235.

(2) Poitras, A. M.; Bezpalko, M. W.; Moore, C. E.; Dickie, D. A.; Foxman, B. M.; Thomas, C. M. A Series of Dimeric Cobalt Complexes Bridged by N-Heterocyclic Phosphido Ligands. *Inorg. Chem.* **2020**, *59*, 4729–4740.

(3) Poitras, A. M.; Knight, S. E.; Bezpalko, M. W.; Foxman, B. M.; Thomas, C. M. Addition of H 2 Across a Cobalt–Phosphorus Bond. *Angew. Chem.* **2018**, *130*, 1513–1516.

(4) Wang, D.; Chen, Q.; Leng, X.; Deng, L. Reactions of Low-Coordinate Cobalt(0)-N-Heterocyclic Carbene Complexes with Primary Aryl Phosphines. *Inorg. Chem.* **2018**, *57* (24), 15600–15609.

(5) Coburger, P.; Demeshko, S.; Rödl, C.; Hey-Hawkins, E.; Wolf, R. Oxidative P-P-Bindungsaddition an Cobalt(−I): Bildung Eines Low-Spin-Cobalt(III)-Phosphanidokomplexes. *Angew. Chem.* **2017**, *129*, 16087–16091.

(6) Kornev, A. N.; Sushev, V. V.; Panova, Y. S.; Belina, N. V.; Lukoyanova, O. V.; Fukin, G. K.; Ketkov, S. Y.; Abakumov, G. A.; Lönnecke, P.; Hey-Hawkins, E. The Intramolecular Rearrangement of Phosphinohydrazides [R′ $_2$P-NR-NR-M] → [RN=PR′$_2$-NR-M]: General Rules and Exceptions. Transformations of Bulky Phosphinohydrazines (R-NH-N(PPh$_2$)$_2$, R = ^{t}Bu, Ph$_2$P). *Inorg. Chem.* **2012**, *51*, 874–881.

(7) Edwards, P. G.; Read, P. W.; Hursthouse, M. B.; Malik, K. M. A. Synthesis and Structure of a Series of Unique Cobalt Phosphides. *J. Chem. Soc. Dalton Trans.* **1994**, No. 7, 971–975.

(8) Caffyn, A. J. M.; Mays, M. J.; Solan, G. A.; Conole, G.; Tiripicchio, A. Synthesis of [Co$_2$(μ-PPh$_2$C$_3$H$_4$)(μ-PPh$_2$)(CO)$_4$]; Its Reactions with P(OMe)$_3$ and with Alkynes. *J. Chem. Soc. Dalton Trans.* **1993**, No. 15, 2345–2352.

(9) Chandler, D. J.; Jones, R. A.; Ratliff, K. S.; Stuart, A. L.; Viswanathan, N.; Geoffroy, G. L. Tetracarbonylbis(μ-Di-Tert-Butylphosphido)Dicobalt(+1) [Co(μ-T-Bu$_2$P)(Co)$_2$]$_2$. *Inorg. Synth.* **1989**, 177–179.

(10) Albright, T. A.; Kang, S. K.; Arif, A. M.; Bard, A. J.; Jones, R. A.; Leland, J. K.; Schwab, S. T. The Balance of Steric and Electronic Factors in Co$_3$ Cluster Geometry: Synthesis, Structure, Computations, and Electrochemistry of [Co(μ-Cy$_2$P)(CO)$_2$]$_3$ (Cy = Cyclohexyl). *Inorg. Chem.* **1988**, *27*, 1246–1253.

(11) Klein, H. F.; Gaß, M.; Zucha, U.; Eisenmann, B. Di(μ-Phosphido)Cobalt- Und -Nickel-Verbindungen Mit Trimethylphosphanliganden. *Z. Naturforsch. - Sect. B J. Chem. Sci.* **1988**, *43*, 927–932.

(12) Koelle, U.; Fuss, B.; Raabe, E. Pentamethylcyclopentadlenyl Transition Metal Complexes. 9.1 Reactions and Solid-State and Solution Behavior of Dinuclear Cobalt(II) Complexes [C$_5$Me$_5$Co(μ-X)]$_2$. *Organometallics* **1986**, *5*, 980–987.

(13) Zolk, R.; Werner, H. Metallkomplexe Mit Verbrückenden Dimethylphosphido-Liganden. III. Oxidative Additionsreaktionen Des Zweikernkomplexes [C$_5$H$_5$Co(μ-PMe$_2$)]$_2$ Mit Elementarem Halogen Und Dihalogenmethanen. Kristall- Und

Molekülstruktur von Trans-{[$C_5H_5(Br)Co]_2(\mu$-$PMe_2)(\mu$-$CH_2PMe_2)$} *J. Organomet. Chem.* **1986**, *303*, 233–250.

(14) Werner, H.; Hofmann, W.; Zolk, R.; Dahl, L. F.; Kocal, J.; Kühn, A. Synthesis and Reactions of a Nucleophilic Bis(μ-Dimethylphosphido)Dicobalt Complex. The Crystal and Molecular Structure of $[C_5H_5Co(\mu$-$PMe_2)]_2$ and $[(C_5H_5Co)_2(\mu$-$H)(\mu$-$PMe_2)_2]BPh_4$. *J. Organomet. Chem.* **1985**, *289*, 173–188.

(15) Chen, L.; Kountz, D. J.; Meek, D. W. New Bimetallic Cobalt(II) Complexes of Chelated, Bridged Phosphido Ligands. *Organometallics* **1985**, *4*, 598–601.

(16) Hayter, R. G.; Williams, L. F. Phosphorus- and Arsenic-Bridged Complexes of Metal Carbonyls-VIII. Cyclopentadienylcobalt and -Manganese Complexes. *J. Inorg. Nucl. Chem.* **1964**, *26*, 1977–1983.

(17) Mercer, W. C.; Whittle, R. R.; Vastag, S.; Markó, L.; Geoffroy, G. L. Further Examples of (Diphenylphosphido)-Bridged Dicobalt Complexes: $Co_2(\mu$-$PPh_2)_2(CO)_4(PPh_2H)_2$ and $Co_2(\mu$-$PPh_2)_2(CO)_2(PPh_2H)_2$. *Inorg. Chem.* **1985**, *24*, 3771–3774.

(18) Harley, A. D.; Guskey, G. J.; Geoffroy, G. L. Interconversion of Phosphido-Bridged Polynuclear Cobalt Carbonyl Complexes. Cleavage of the Phosphido Bridge during Hydroformylation Catalysis. *Organometallics* **1983**, *2*, 53–59.

(19) Harley, A. D.; Whittle, R. R.; Geoffroy, G. L. $Co_2(\mu$-$PPh_2)_2(CO)_2(PEt_2Ph)_2$, a Phosphido-Bridged Compound with a Formal Cobalt-Cobalt Double Bond. *Organometallics* **1983**, *2*, 60–63.

(20) Keller, E.; Vahrenkamp, H. Stereochemie Der Metall-Metall-Bindung: Darstellung Und Struktur von $Co_2(CO)_4C_5H_5P(CH_3)_2$. *Z. Naturforsch. - Sect. B J. Chem. Sci.* **1978**, *33*, 537–541.

Appendix F – ^{1}H and $^{31}P\{^{1}H\}$ NMR spectra from Chapter 5

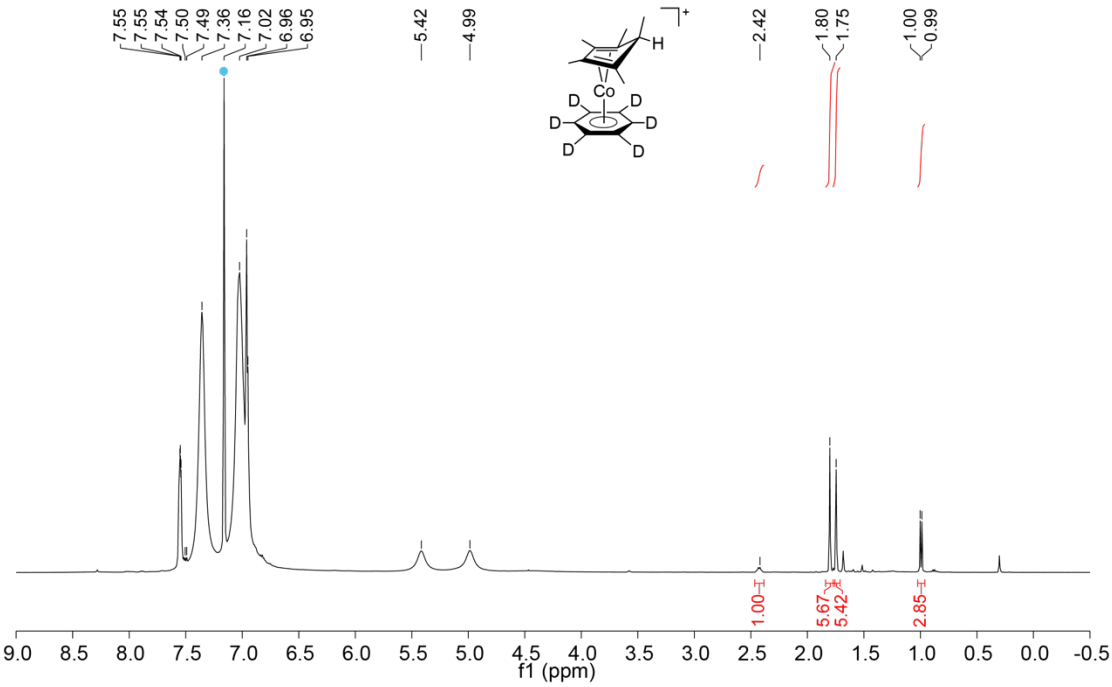

Figure F.1 ^{1}H NMR (500.27 MHz, C_6D_6) spectrum of dehydrocoupling reaction of PPh_2H catalyzed by 10 mol% **Co-1** and 20 mol% DBU after 24 h, showing the formation of the cation **Co-10**. Residual proteo-solvent (•).

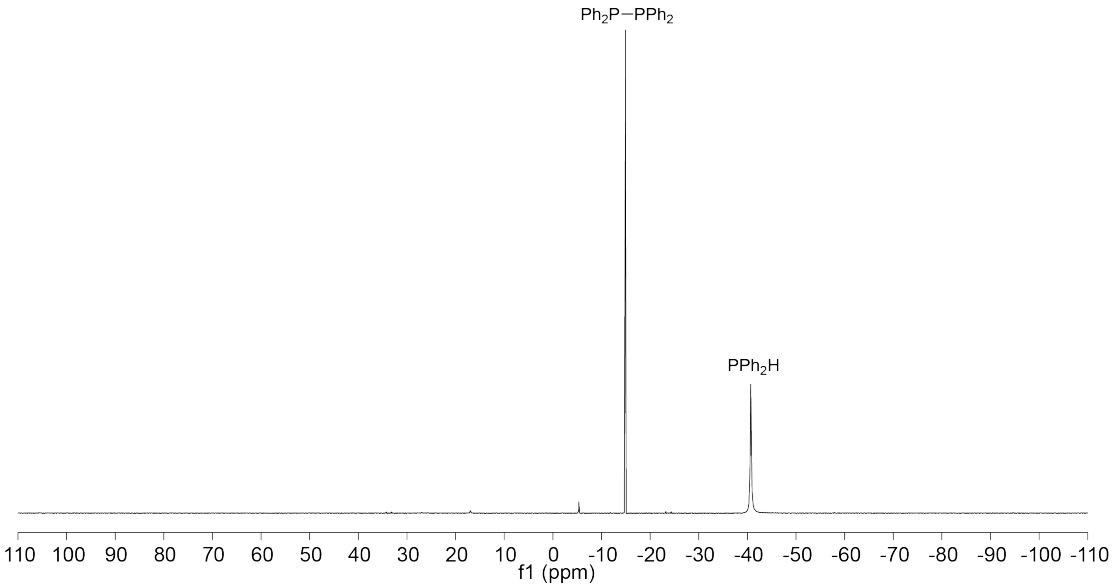

Figure F.2 $^{31}P\{^{1}H\}$ NMR (202.51 MHz, C_6D_6) spectrum of dehydrocoupling reaction of PPh_2H catalyzed by 10 mol% **Co-1** and 20 mol% DBU after 24 h, showing that no Co-P complex is observed by ^{31}P NMR.

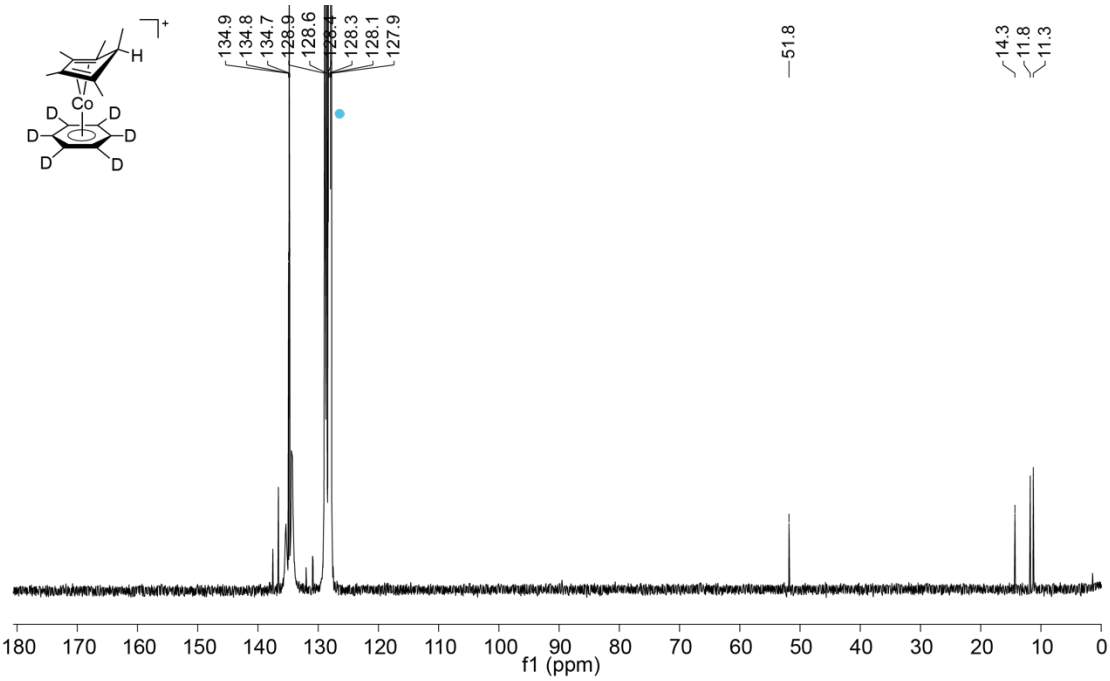

Figure F.3 $^{13}C\{^{1}H\}$ NMR (125.77 MHz, C_6D_6) spectrum of the dehydrocoupling reaction of PPh_2H catalyzed by 10 mol% **Co-1** and 20 mol% DBU after 24 h. Deuterated solvent (•).

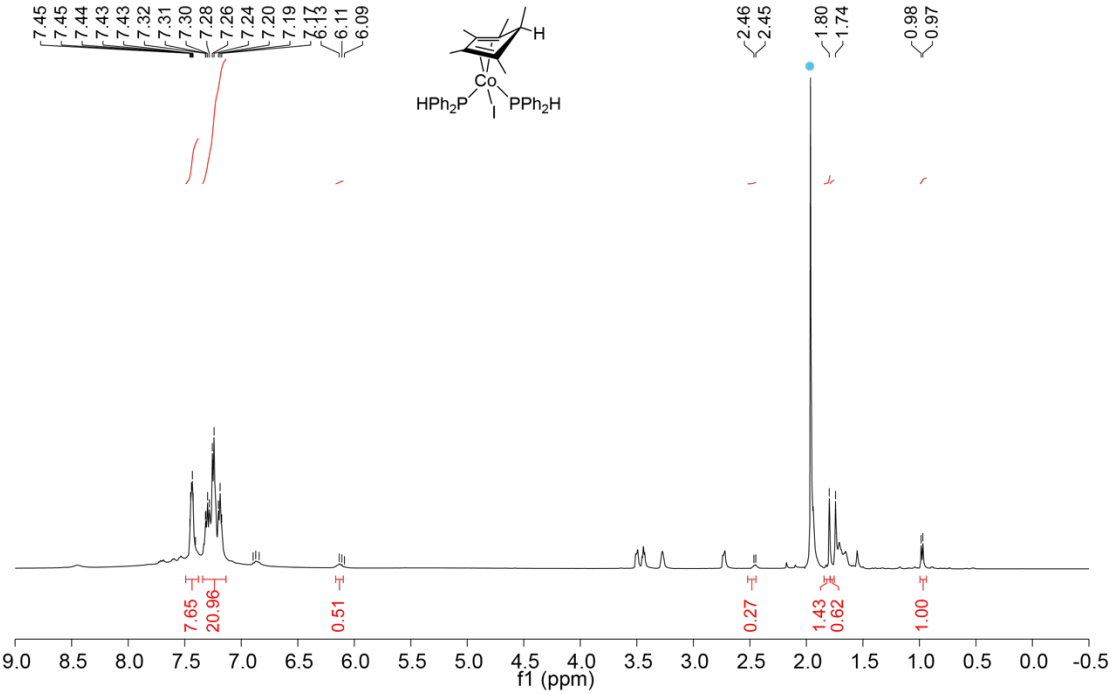

Figure F.4 ^{1}H NMR (500.27 MHz, CD_3CN) spectrum of the dehydrocoupling reaction of PPh_2H catalyzed by 10 mol% **Co-1** and 20 mol% DBU after 24 h.

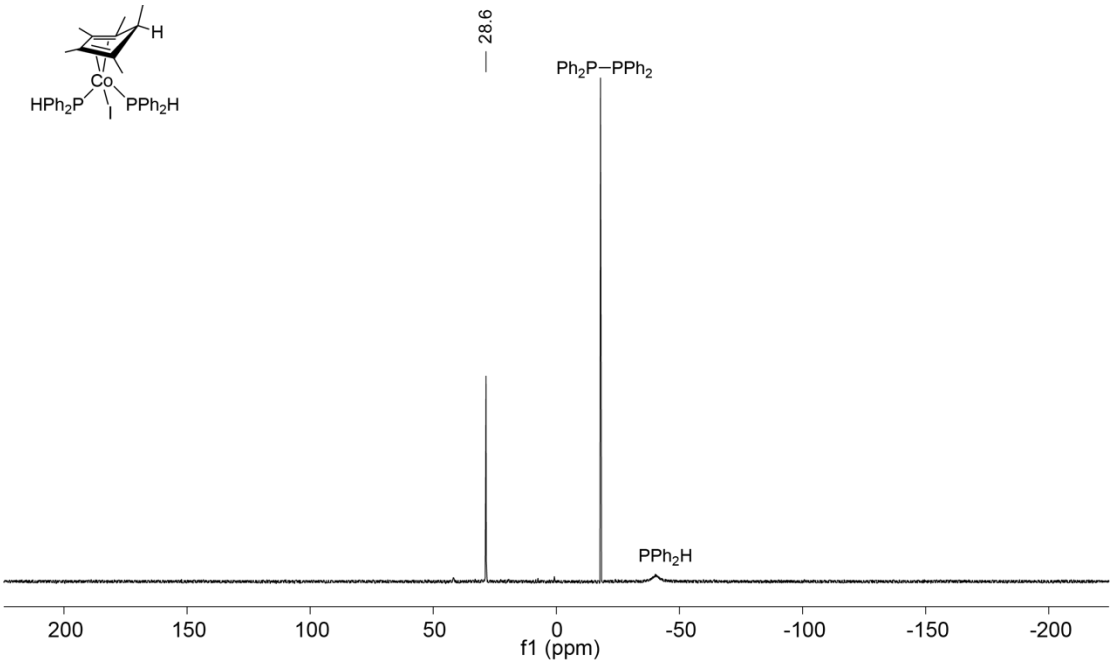

Figure F.5 $^{31}P\{^{1}H\}$ NMR (202.51 MHz, CD_3CN) spectrum of the dehydrocoupling reaction of PPh_2H catalyzed by 10 mol% **Co-1** and 20 mol% DBU after 24 h.

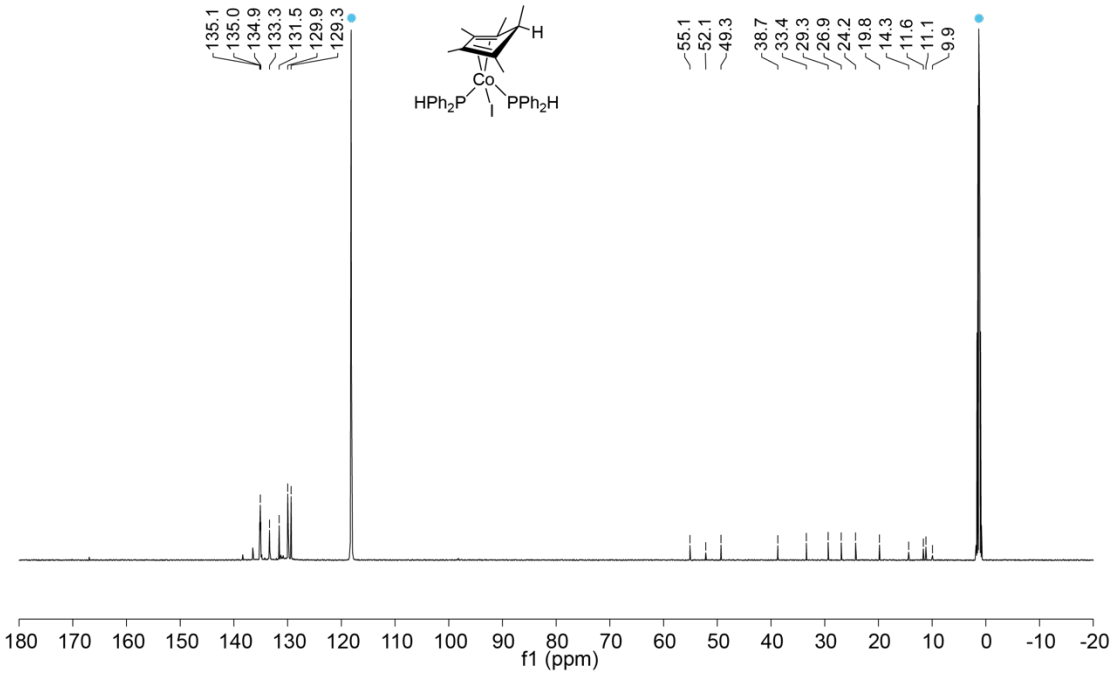

Figure F.6 $^{13}C\{^{1}H\}$ NMR (125.77 MHz, C_6D_6) spectrum of the dehydrocoupling reaction of PPh_2H catalyzed by 10 mol% **Co-1** and 20 mol% DBU after 24 h. Deuterated solvent (•).

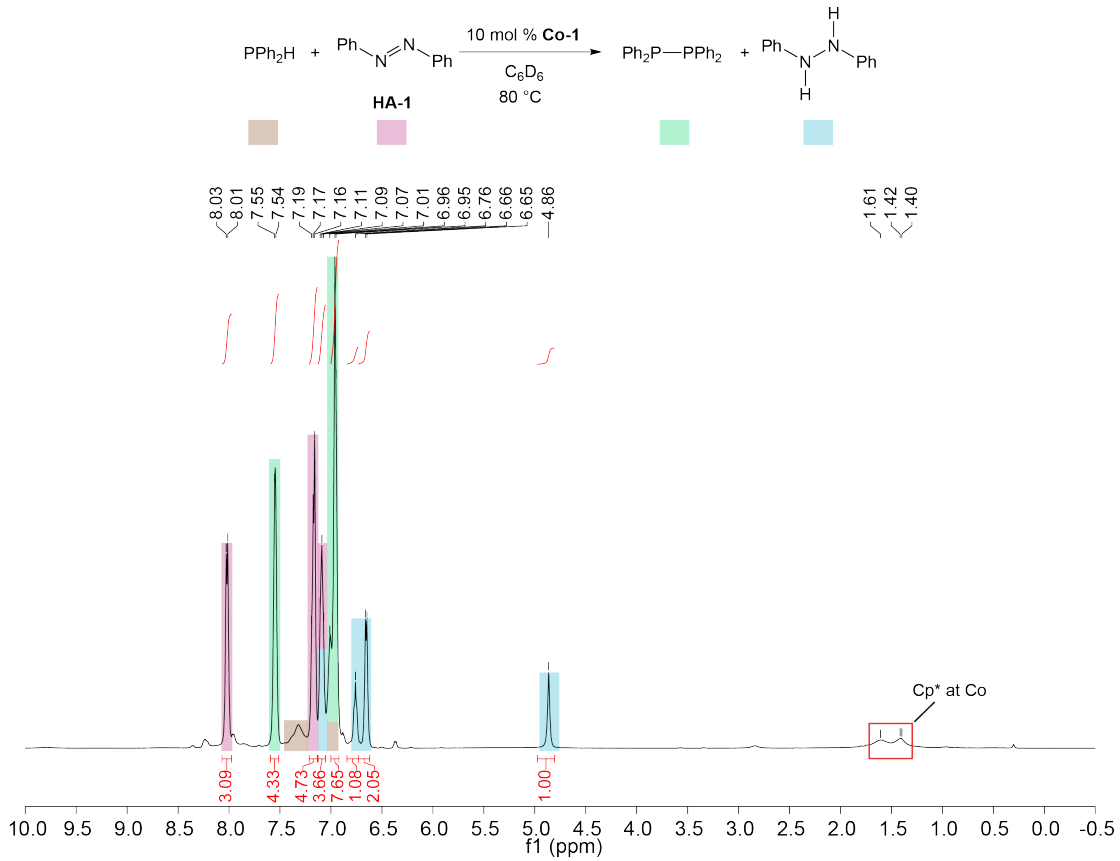

Figure F.7 ^{1}H NMR (300.27 MHz, C_6D_6) spectrum of the dehydrocoupling reaction of PPh_2H with azobenzene (**HA-1**) catalyzed by 10 mol% **Co-1** after 24 h.

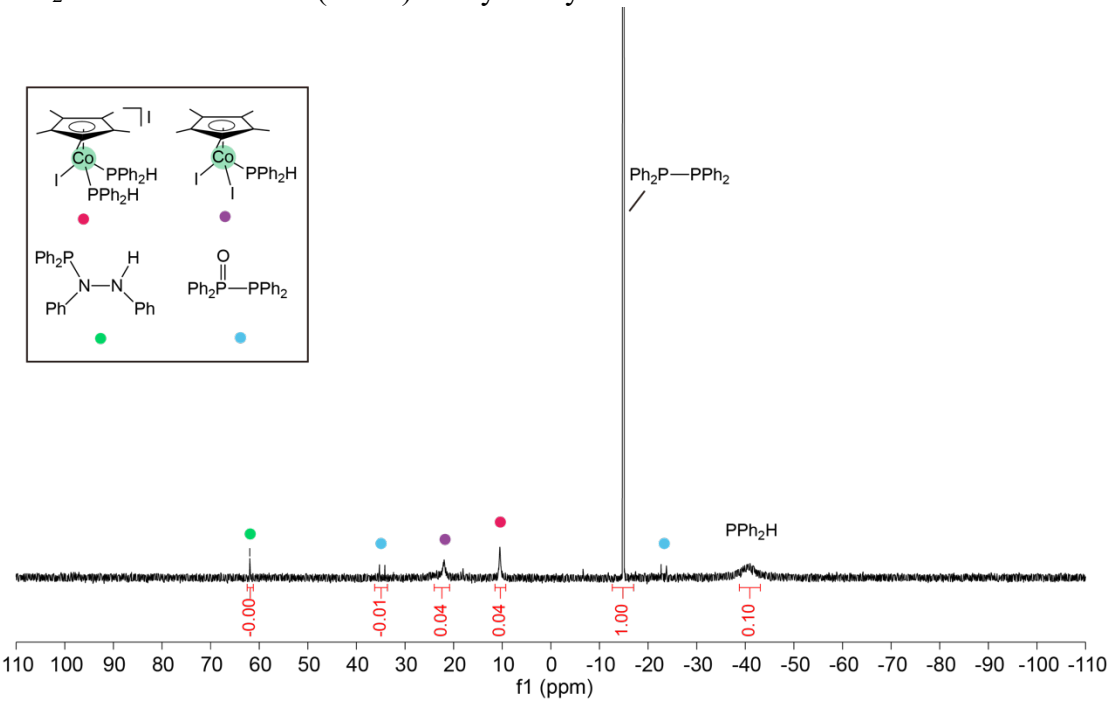

Figure F.8 $^{31}P\{^{1}H\}$ NMR (121.55 MHz, C_6D_6) spectrum of dehydrocoupling reaction of PPh_2H with azobenzene (**HA-1**) catalyzed by 10 mol% **Co-1** after 24 h.

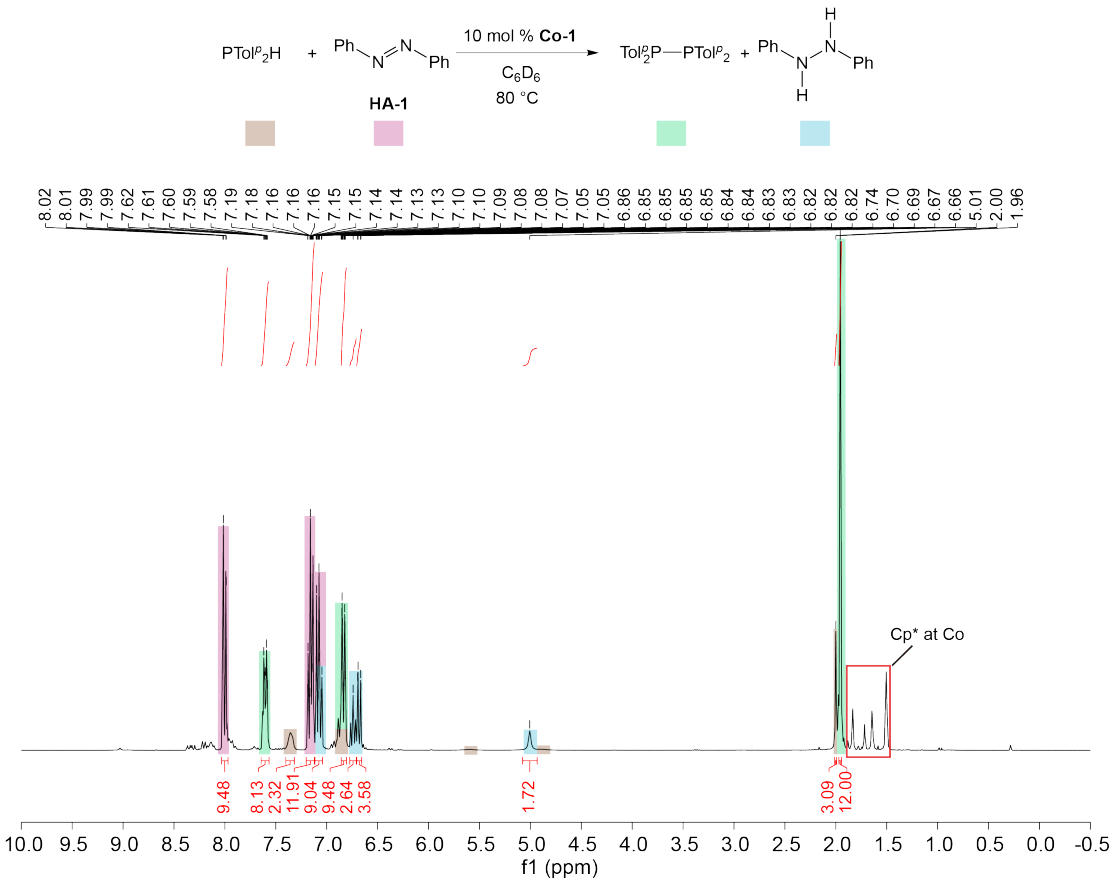

Figure F.9 ^{1}H NMR (300.27 MHz, C_6D_6) spectrum of the dehydrocoupling reaction of PTol$^p_2$H with azobenzene (**HA-1**) catalyzed by 10 mol% **Co-1** after 24 h.

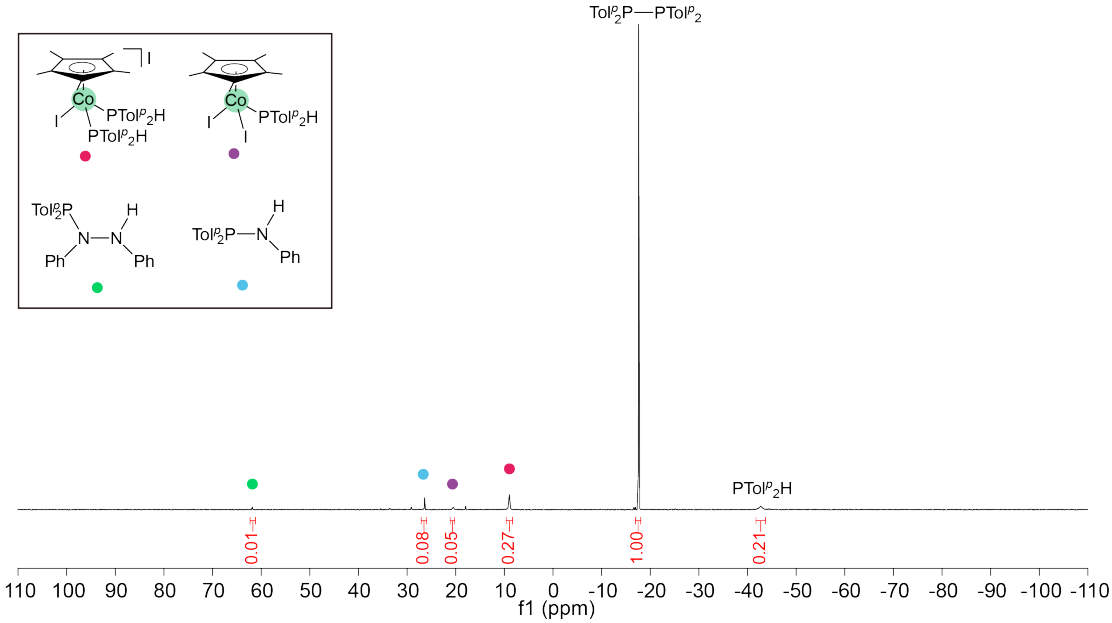

Figure F.10 ^{31}P{^{1}H} NMR (121.55 MHz, C_6D_6) spectrum of the dehydrocoupling reaction of PTol$^p_2$H with azobenzene (**HA-1**) catalyzed by 10 mol% **Co-1** after 24 h.

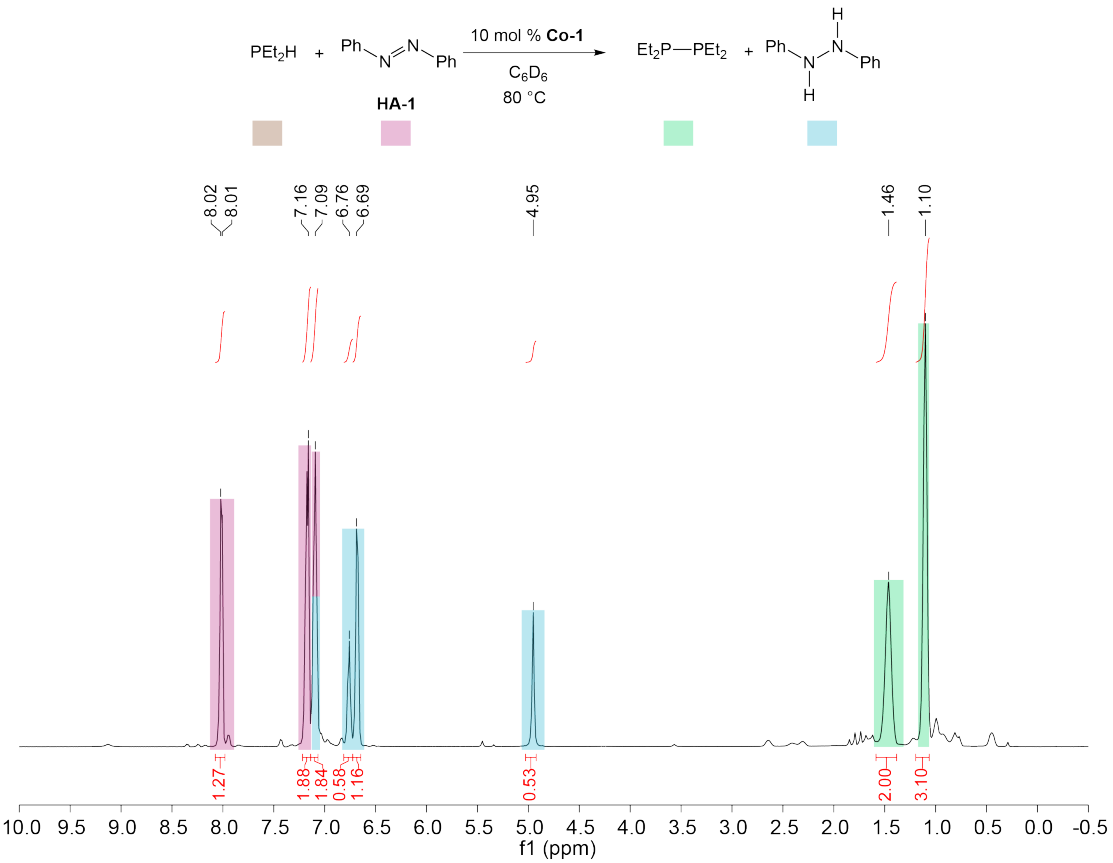

Figure F.11 ^{1}H NMR (300.27 MHz, C_6D_6) spectrum of the dehydrocoupling reaction of PEt_2H with azobenzene (**HA-1**) catalyzed by 10 mol% **Co-1** after 24 h.

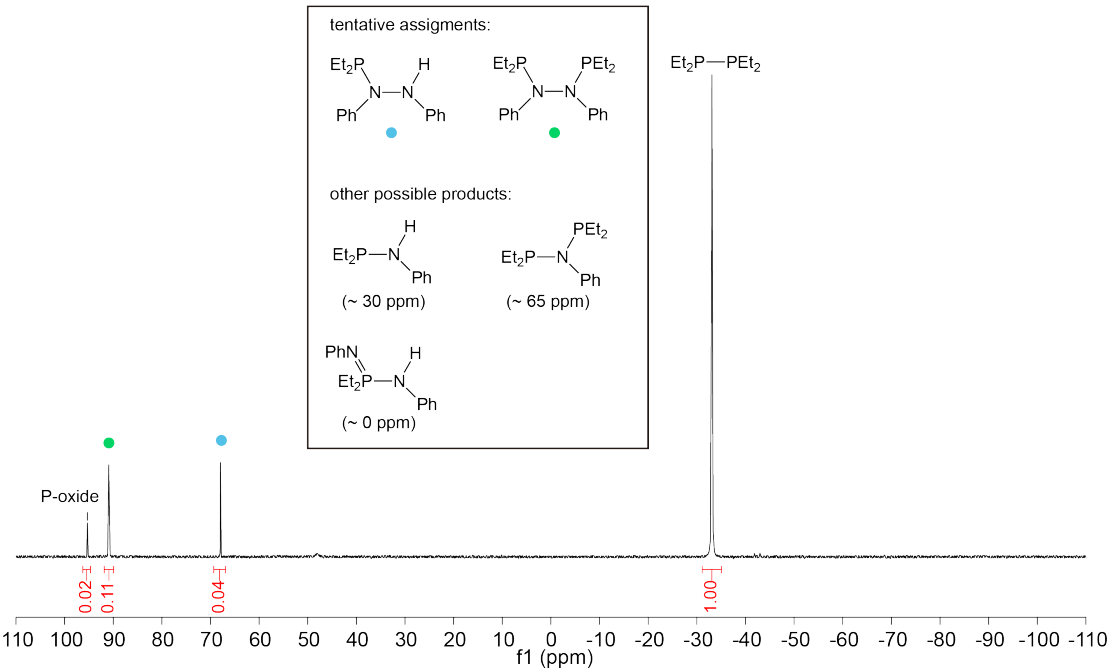

Figure F.12 ^{31}P{^{1}H} NMR (121.55 MHz, C_6D_6) spectrum of the dehydrocoupling reaction of $PTol^{p}_2H$ with azobenzene (**HA-1**) catalyzed by 10 mol% **Co-1** after 24 h.

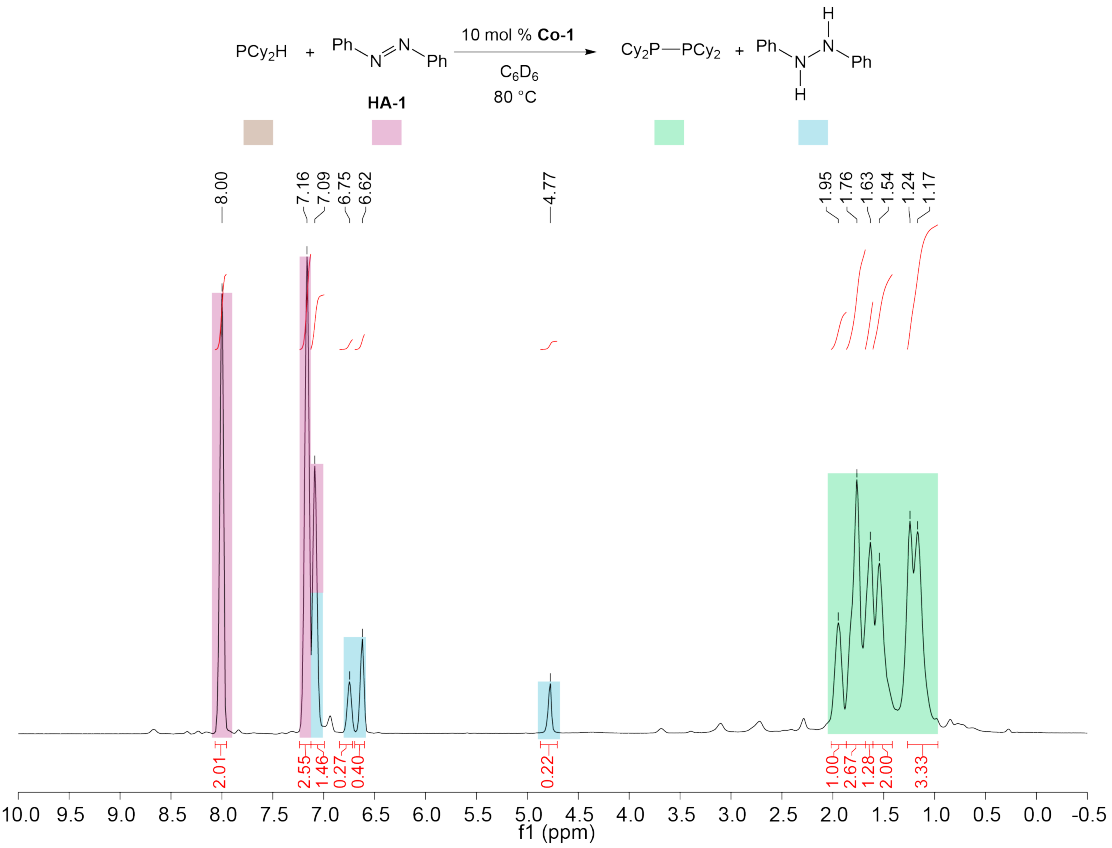

Figure F.13 ^{1}H NMR (300.27 MHz, C_6D_6) spectrum of the dehydrocoupling reaction of PCy_2H with azobenzene (**HA-1**) catalyzed by 10 mol% **Co-1** after 24 h.

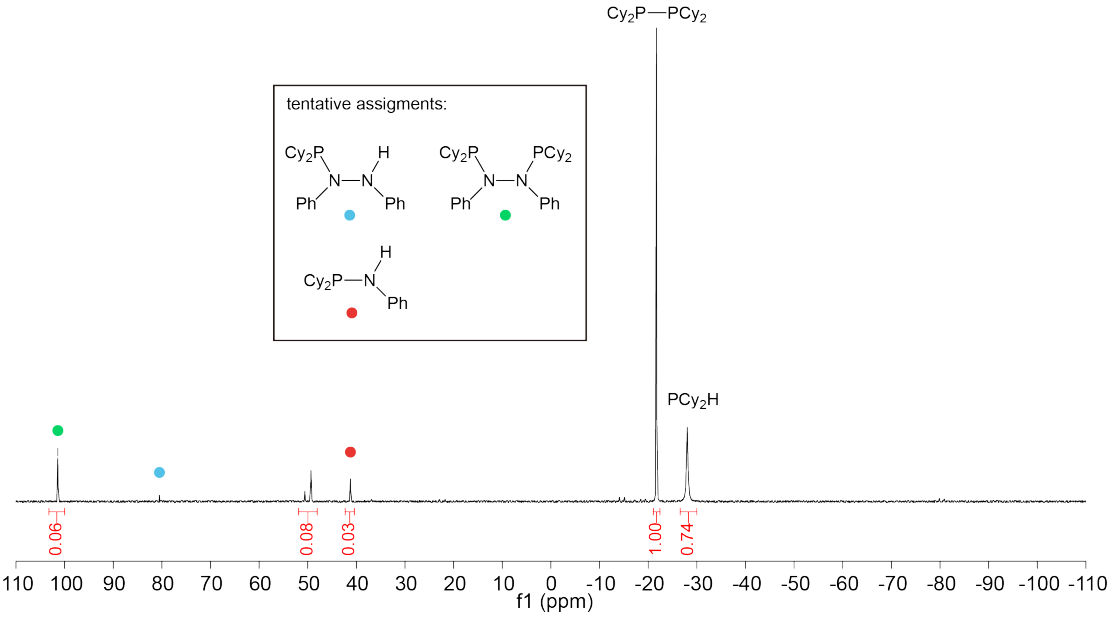

Figure F.14 $^{31}P\{^{1}H\}$ NMR (121.55 MHz, C_6D_6) spectrum of the dehydrocoupling reaction of PCy_2H with azobenzene (**HA-1**) catalyzed by 10 mol% **Co-1** after 24 h.

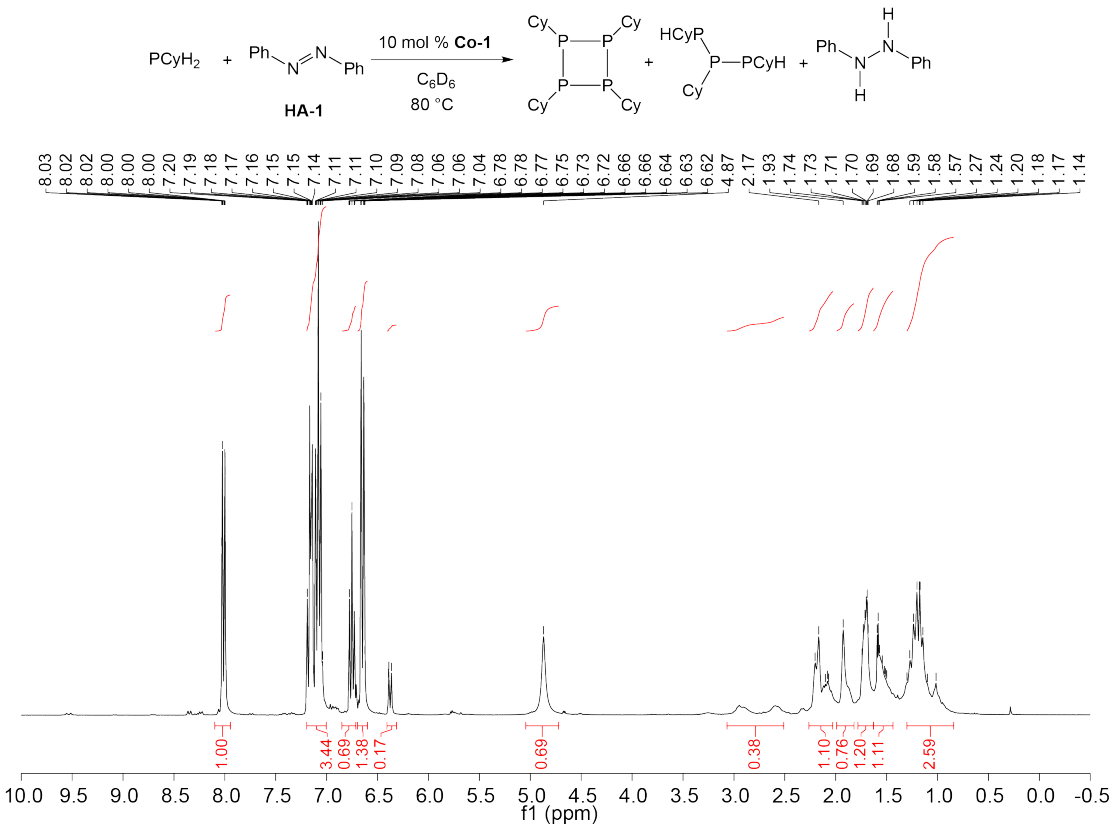

Figure F.15 ^{1}H NMR (300.27 MHz, C_6D_6) spectrum of the dehydrocoupling reaction of $PCyH_2$ with azobenzene (**HA-1**) catalyzed by 10 mol% **Co-1** after 2 h.

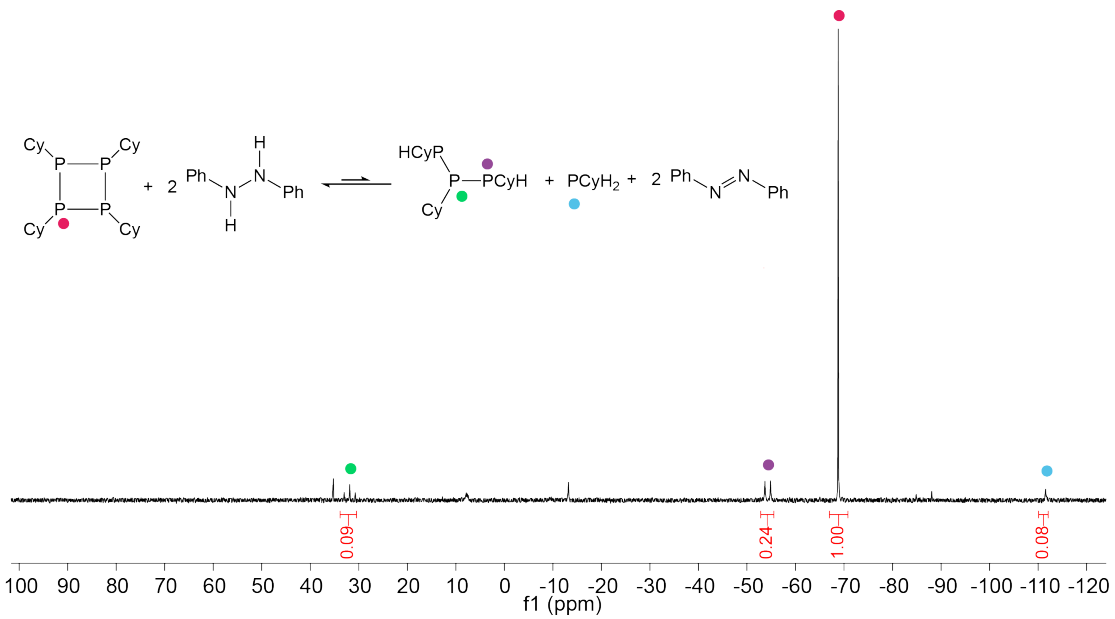

Figure F.16 ^{31}P{^{1}H} NMR (121.55 MHz, C_6D_6) spectrum of the dehydrocoupling reaction of $PCyH_2$ with azobenzene (**HA-1**) catalyzed by 10 mol% **Co-1** after 2 h.

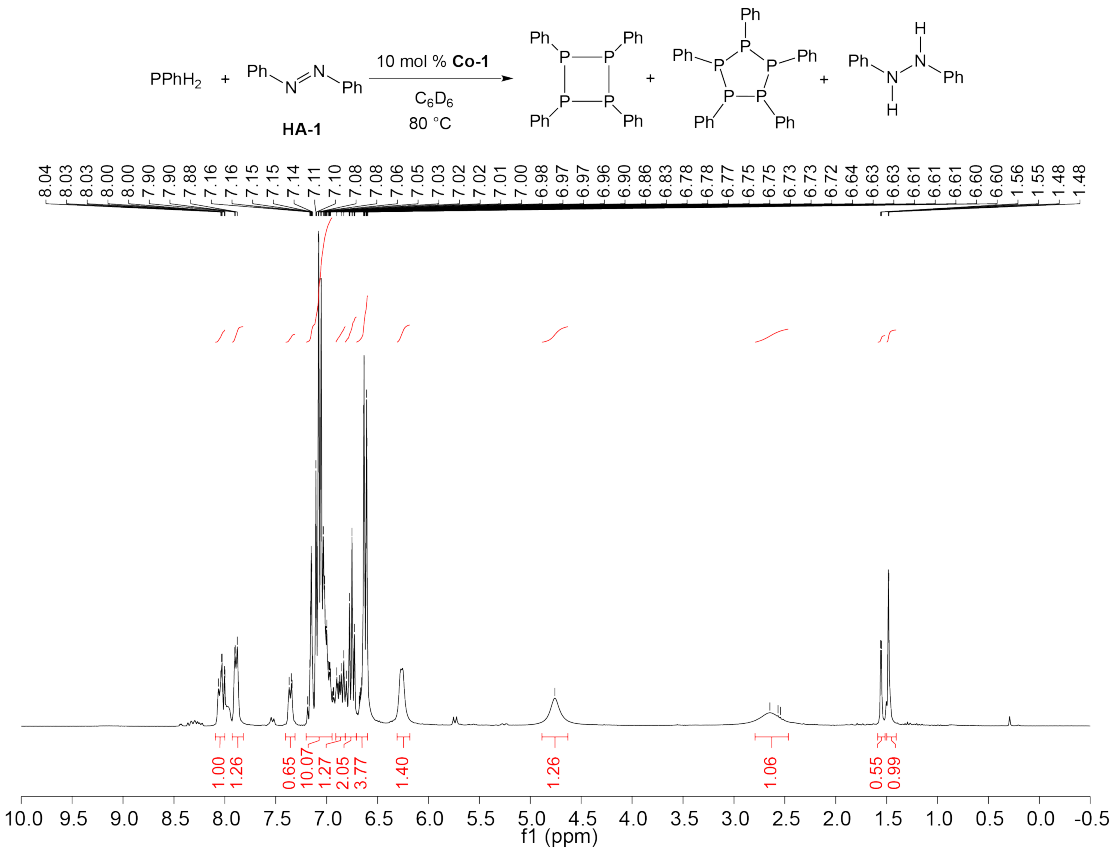

Figure F.17 ^{1}H NMR (300.27 MHz, C_6D_6) spectrum of the dehydrocoupling reaction of $PPhH_2$ with azobenzene (**HA-1**) catalyzed by 10 mol% **Co-1** after 2 h.

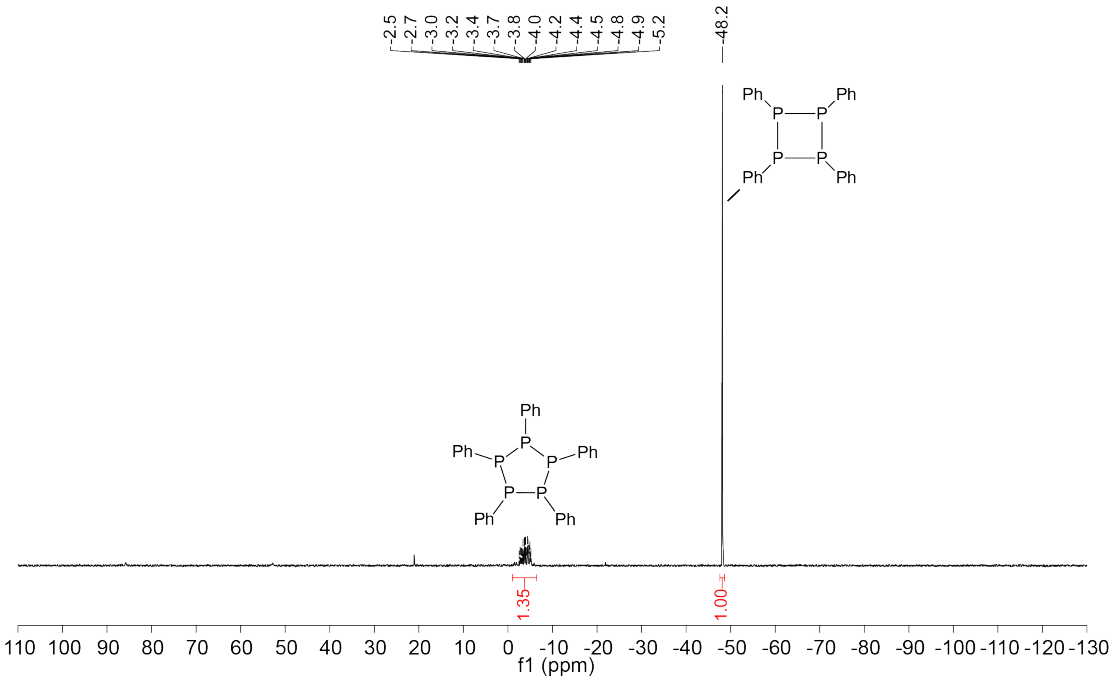

Figure F.18 ^{31}P{^{1}H} NMR (121.55 MHz, C_6D_6) spectrum of the dehydrocoupling reaction of $PPhH_2$ with azobenzene (**HA-1**) catalyzed by 10 mol% **Co-1** after 2 h

Appendix G – X-ray crystallographic structure report for complex Co-1

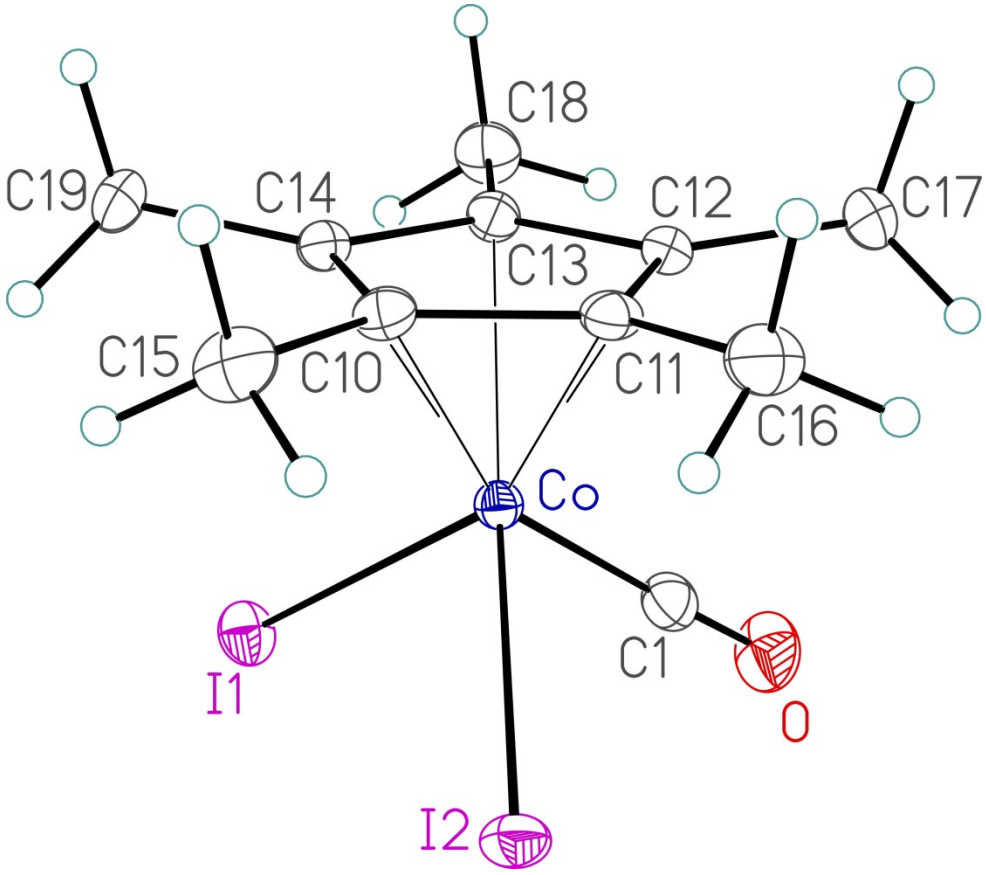

Figure G.1 Perspective view of the Co(η^5-Cp*)I_2(CO) (**Co-1**) molecule showing the atom labelling scheme. Non-hydrogen atoms are represented by Gaussian ellipsoids at the 30% probability level. Hydrogen atoms are shown with arbitrarily small thermal parameters.

The crystal contains half equiv of I_2, thus the compound analyzed is actually Co(η^5-Cp*)I_2(CO)•$^1/_2I_2$. This structure determination, as well as that of complex **Co-2c**, **Co-3c**, **Co-6a** and **Co-6c** in the following Appendix, were carried out by Dr. Robert McDonald at the X-Ray Crystallography Laboratory, Department of Chemistry, University of Alberta, Edmonton, Alberta, Canada T6G 2G2. E-mail: Bob.McDonald@ualberta.ca. Phone: 1-(780)-492-2485.

Table G.1 Crystallographic Experimental Details

A. Crystal Data	
formula	$C_{11}H_{15}CoI_3O$
formula weight	602.86
crystal dimensions (mm)	0.46 × 0.36 × 0.11
crystal system	triclinic
space group	$P\bar{1}$ (No. 2)
unit cell parameters[a]	
a (Å)	7.6158 (4)
b (Å)	8.2142 (4)
c (Å)	13.9988 (7)
α (deg)	79.6322 (7)
β (deg)	85.6243 (6)
γ (deg)	66.5194 (6)
V (Å^3)	790.09 (7)
Z	2
ρ_{calcd} (g cm^{-3})	2.534
μ (mm^{-1})	6.928
B. Data Collection and Refinement Conditions	
diffractometer	Bruker PLATFORM/APEX II CCD[b]
radiation (λ [Å])	graphite-monochromated Mo Kα (0.71073)
temperature (°C)	–80
scan type	ω scans (0.4°) (10 s exposures)
data collection 2θ limit (deg)	56.71
total data collected	6524 (-10 ≤ h ≤ 10, -10 ≤ k ≤ 10, -18 ≤ l ≤ 18)
independent reflections	3916 (R_{int} = 0.0162)
number of observed reflections (*NO*)	3677 [$F_o^2 \geq 2\sigma(F_o^2)$]
structure solution method	intrinsic phasing (*SHELXT-2014*[c])
refinement method	full-matrix least-squares on F^2 (*SHELXL–2014*[d])
absorption correction method	Gaussian integration (face-indexed)
range of transmission factors	0.6391–0.1556
data/restraints/parameters	3916 / 0 / 151
extinction coefficient (x)[e]	0.0066(3)
goodness-of-fit (S)[f] [all data]	1.092
final R indices[g]	
R_1 [$F_o^2 \geq 2\sigma(F_o^2)$]	0.0208
wR_2 [all data]	0.0488
largest difference peak and hole	0.611 and –0.851 e Å^{-3}

(continued)

Table G.1 Crystallographic Experimental Details (continued)

[a]Obtained from least-squares refinement of 5008 reflections with $5.48° < 2\theta < 56.68°$.

[b]Programs for diffractometer operation, data collection, data reduction and absorption correction were those supplied by Bruker.

[c]Sheldrick, G. M. *Acta Crystallogr.* **2015**, *A71*, 3–8.

[d]Sheldrick, G. M. *Acta Crystallogr.* **2015**, *C71*, 3–8.

[e]$F_c^* = kF_c[1 + x\{0.001F_c^2\lambda^3/\sin(2\theta)\}]^{-1/4}$ where k is the overall scale factor.

[f]$S = [\Sigma w(F_o^2 - F_c^2)^2/(n-p)]^{1/2}$ (n = number of data; p = number of parameters varied; $w = [\sigma^2(F_o^2) + (0.0174P)^2 + 0.6800P]^{-1}$ where $P = [\text{Max}(F_o^2, 0) + 2F_c^2]/3$).

[g]$R_1 = \Sigma||F_o| - |F_c||/\Sigma|F_o|$; $wR_2 = [\Sigma w(F_o^2 - F_c^2)^2/\Sigma w(F_o^4)]^{1/2}$.

Table G.2 Atomic Coordinates and Equivalent Isotropic Displacement Parameters

Atom	*x*	*y*	*z*	U_{eq}, Å^2
I1	0.58234(3)	0.41632(3)	0.19631(2)	0.03149(6)*
I2	0.68868(2)	-0.02792(3)	0.36034(2)	0.03086(6)*
Co	0.38827(5)	0.24119(5)	0.28861(2)	0.01933(8)*
O	0.3668(4)	0.4224(4)	0.45240(18)	0.0485(6)*
C1	0.3783(4)	0.3504(4)	0.3905(2)	0.0305(6)*
C10	0.3110(4)	0.0926(4)	0.20324(19)	0.0237(5)*
C11	0.2258(4)	0.0847(4)	0.29886(19)	0.0244(5)*
C12	0.1065(4)	0.2653(4)	0.31138(19)	0.0248(5)*
C13	0.1211(4)	0.3847(4)	0.22505(19)	0.0239(5)*
C14	0.2428(4)	0.2742(4)	0.15772(19)	0.0229(5)*
C15	0.4365(5)	-0.0651(4)	0.1575(2)	0.0362(7)*
C16	0.2416(5)	-0.0821(5)	0.3670(2)	0.0376(7)*
C17	-0.0193(4)	0.3183(5)	0.3975(2)	0.0366(7)*
C18	0.0173(4)	0.5838(4)	0.2047(2)	0.0364(7)*
C19	0.2775(4)	0.3393(5)	0.05406(19)	0.0325(6)*
I3	0.88203(3)	0.11181(3)	0.06191(2)	0.03176(6)*

Anisotropically-refined atoms are marked with an asterisk (*). The form of the anisotropic displacement parameter is: $\exp[-2\pi^2(h^2a^{*2}U_{11} + k^2b^{*2}U_{22} + l^2c^{*2}U_{33} + 2klb^*c^*U_{23} + 2hla^*c^*U_{13} + 2hka^*b^*U_{12})]$.

Table G.3 Selected Interatomic Distances (Å)

Atom1	Atom2	Distance
I1	Co	2.5801(4)
I2	Co	2.5789(4)
Co	C1	1.798(3)
Co	C10	2.114(3)
Co	C11	2.093(3)
Co	C12	2.079(3)
Co	C13	2.076(3)
Co	C14	2.133(3)
O	C1	1.114(4)
C10	C11	1.445(4)
C10	C14	1.411(4)
C10	C15	1.490(4)
C11	C12	1.433(4)
C11	C16	1.489(4)
C12	C13	1.440(4)
C12	C17	1.497(4)
C13	C14	1.441(3)
C13	C18	1.490(4)
C14	C19	1.496(4)
I3	I3’	2.7654(4)[a]

[a]I3 is related to I3’ via the crystallographic inversion center (1, 0, 0).

Table G.4 Selected Interatomic Angles (deg)

Atom1	Atom2	Atom3	Angle	Atom1	Atom2	Atom3	Angle
I1	Co	I2	93.660(13)	Co	C10	C14	71.34(15)
I1	Co	C1	88.17(10)	Co	C10	C15	129.02(19)
I1	Co	C10	114.24(8)	C11	C10	C14	108.3(2)
I1	Co	C11	154.08(7)	C11	C10	C15	125.8(3)
I1	Co	C12	140.28(8)	C14	C10	C15	125.8(3)
I1	Co	C13	101.19(8)	Co	C11	C10	70.71(15)
I1	Co	C14	89.90(7)	Co	C11	C12	69.42(15)
I2	Co	C1	90.02(10)	Co	C11	C16	130.34(19)
I2	Co	C10	94.65(7)	C10	C11	C12	107.5(2)
I2	Co	C11	93.05(8)	C10	C11	C16	126.0(3)
I2	Co	C12	126.06(8)	C12	C11	C16	126.2(3)
I2	Co	C13	160.04(8)	Co	C12	C11	70.41(14)
I2	Co	C14	127.88(7)	Co	C12	C13	69.59(14)
C1	Co	C10	156.67(12)	Co	C12	C17	128.24(19)
C1	Co	C11	116.84(12)	C11	C12	C13	108.3(2)
C1	Co	C12	91.68(12)	C11	C12	C17	125.4(3)
C1	Co	C13	103.59(12)	C13	C12	C17	126.3(3)
C1	Co	C14	142.09(12)	Co	C13	C12	69.86(15)
C10	Co	C11	40.17(10)	Co	C13	C14	72.14(14)
C10	Co	C12	67.18(10)	Co	C13	C18	127.2(2)
C10	Co	C13	67.16(10)	C12	C13	C14	107.2(2)
C10	Co	C14	38.80(11)	C12	C13	C18	126.9(2)
C11	Co	C12	40.17(11)	C14	C13	C18	125.7(3)
C11	Co	C13	67.89(11)	Co	C14	C10	69.86(14)
C11	Co	C14	66.42(10)	Co	C14	C13	67.86(14)
C12	Co	C13	40.55(11)	Co	C14	C19	132.17(19)
C12	Co	C14	66.75(10)	C10	C14	C13	108.7(2)
C13	Co	C14	40.00(9)	C10	C14	C19	125.5(2)
Co	C1	O	177.7(3)	C13	C14	C19	125.6(3)
Co	C10	C11	69.12(14)	Co	C10	C14	71.34(15)

Table G.5 Torsional Angles (deg)

Atom1	Atom2	Atom3	Atom4	Angle	(continued)				
I1	Co	C10	C11	-174.65(13)	I1	Co	C12	C17	-100.7(3)
I1	Co	C10	C14	-55.74(15)	I2	Co	C12	C11	-40.48(17)
I1	Co	C10	C15	65.6(3)	I2	Co	C12	C13	-159.64(12)
I2	Co	C10	C11	89.22(15)	I2	Co	C12	C17	79.7(3)
I2	Co	C10	C14	-151.87(14)	C1	Co	C12	C11	-131.73(17)
I2	Co	C10	C15	-30.5(3)	C1	Co	C12	C13	109.11(18)
C1	Co	C10	C11	-11.7(4)	C1	Co	C12	C17	-11.6(3)
C1	Co	C10	C14	107.2(3)	C10	Co	C12	C11	38.12(15)
C1	Co	C10	C15	-131.4(4)	C10	Co	C12	C13	-81.03(16)
C11	Co	C10	C14	118.9(2)	C10	Co	C12	C17	158.3(3)
C11	Co	C10	C15	-119.7(3)	C11	Co	C12	C13	-119.2(2)
C12	Co	C10	C11	-38.12(16)	C11	Co	C12	C17	120.2(3)
C12	Co	C10	C14	80.79(17)	C13	Co	C12	C11	119.2(2)
C12	Co	C10	C15	-157.8(3)	C13	Co	C12	C17	-120.7(3)
C13	Co	C10	C11	-82.29(16)	C14	Co	C12	C11	80.44(16)
C13	Co	C10	C14	36.62(15)	C14	Co	C12	C13	-38.71(15)
C13	Co	C10	C15	158.0(3)	C14	Co	C12	C17	-159.4(3)
C14	Co	C10	C11	-118.9(2)	I1	Co	C13	C12	-167.15(14)
C14	Co	C10	C15	121.4(3)	I1	Co	C13	C14	76.21(15)
I1	Co	C11	C10	11.2(3)	I1	Co	C13	C18	-45.5(3)
I1	Co	C11	C12	-106.89(19)	I2	Co	C13	C12	55.5(3)
I1	Co	C11	C16	132.5(2)	I2	Co	C13	C14	-61.1(3)
I2	Co	C11	C10	-93.60(14)	I2	Co	C13	C18	177.19(17)
I2	Co	C11	C12	148.29(14)	C1	Co	C13	C12	-76.33(18)
I2	Co	C11	C16	27.7(3)	C1	Co	C13	C14	167.04(17)
C1	Co	C11	C10	174.83(17)	C1	Co	C13	C18	45.3(3)
C1	Co	C11	C12	56.72(19)	C10	Co	C13	C12	81.07(17)
C1	Co	C11	C16	-63.9(3)	C10	Co	C13	C14	-35.56(16)
C10	Co	C11	C12	-118.1(2)	C10	Co	C13	C18	-157.3(3)
C10	Co	C11	C16	121.2(3)	C11	Co	C13	C12	37.45(15)
C12	Co	C11	C10	118.1(2)	C11	Co	C13	C14	-79.19(17)
C12	Co	C11	C16	-120.6(3)	C11	Co	C13	C18	159.1(3)
C13	Co	C11	C10	80.32(16)	C12	Co	C13	C14	-116.6(2)
C13	Co	C11	C12	-37.79(15)	C12	Co	C13	C18	121.7(3)
C13	Co	C11	C16	-158.4(3)	C14	Co	C13	C12	116.6(2)
C14	Co	C11	C10	36.77(15)	C14	Co	C13	C18	-121.7(3)
C14	Co	C11	C12	-81.34(16)	I1	Co	C14	C10	131.10(14)
C14	Co	C11	C16	158.0(3)	I1	Co	C14	C13	-107.69(15)
I1	Co	C12	C11	139.11(13)	I1	Co	C14	C19	11.0(3)
I1	Co	C12	C13	20.0(2)	I2	Co	C14	C10	36.54(18)

Table G.5 Torsional Angles (continued)

Atom1	Atom2	Atom3	Atom4	Angle	(continued)				
I2	Co	C14	C13	157.75(13)	C15	C10	C14	Co	-125.1(3)
I2	Co	C14	C19	-83.6(3)	C15	C10	C14	C13	178.1(3)
C1	Co	C14	C10	-142.0(2)	C15	C10	C14	C19	2.9(4)
C1	Co	C14	C13	-20.8(3)	Co	C11	C12	C13	59.53(18)
C1	Co	C14	C19	97.9(3)	Co	C11	C12	C17	-123.6(3)
C10	Co	C14	C13	121.2(2)	C10	C11	C12	Co	-60.78(17)
C10	Co	C14	C19	-120.1(3)	C10	C11	C12	C13	-1.3(3)
C11	Co	C14	C10	-38.04(15)	C10	C11	C12	C17	175.6(2)
C11	Co	C14	C13	83.18(17)	C16	C11	C12	Co	125.6(3)
C11	Co	C14	C19	-158.2(3)	C16	C11	C12	C13	-174.9(3)
C12	Co	C14	C10	-81.98(17)	C16	C11	C12	C17	2.0(4)
C12	Co	C14	C13	39.23(16)	Co	C12	C13	C14	62.93(17)
C12	Co	C14	C19	157.9(3)	Co	C12	C13	C18	-122.0(3)
C13	Co	C14	C10	-121.2(2)	C11	C12	C13	Co	-60.04(17)
C13	Co	C14	C19	118.6(3)	C11	C12	C13	C14	2.9(3)
Co	C10	C11	C12	59.96(17)	C11	C12	C13	C18	178.0(3)
Co	C10	C11	C16	-126.4(3)	C17	C12	C13	Co	123.1(3)
C14	C10	C11	Co	-60.87(18)	C17	C12	C13	C14	-174.0(3)
C14	C10	C11	C12	-0.9(3)	C17	C12	C13	C18	1.1(5)
C14	C10	C11	C16	172.7(3)	Co	C13	C14	C10	57.97(18)
C15	C10	C11	Co	123.8(3)	Co	C13	C14	C19	-126.9(3)
C15	C10	C11	C12	-176.3(3)	C12	C13	C14	Co	-61.44(17)
C15	C10	C11	C16	-2.6(4)	C12	C13	C14	C10	-3.5(3)
Co	C10	C14	C13	-56.76(18)	C12	C13	C14	C19	171.7(3)
Co	C10	C14	C19	128.1(3)	C18	C13	C14	Co	123.4(3)
C11	C10	C14	Co	59.48(17)	C18	C13	C14	C10	-178.7(3)
C11	C10	C14	C13	2.7(3)	C18	C13	C14	C19	-3.5(4)
C11	C10	C14	C19	-172.4(2)					

Table G.6 Least-Squares Planes

Plane	Coefficients[a]	Defining Atoms with Deviations (Å)[b]			
1	6.977(4) 4.082(10) 6.460(16) 3.850(4)				
		C10	0.0106(16)	C11	0.0012(16)
		C12	-0.0123(16)	C13	0.0186(16)
		C14	-0.0182(16)		
		Co	1.7077(12)	C15	-0.053(5)
		C16	-0.129(5)	C17	-0.118(5)
		C18	-0.024(5)	C19	-0.180(5)

[a]Coefficients are for the form $ax+by+cz = d$ where x, y and z are crystallographic coordinates.

[b]Underlined atoms were not included in the definition of the plane.

Distance: Co–C_{cent} = 1.708 Å (C_{cent} = C10–C11–C12–C13–C14 centroid)

Angles: C_{cent}–Co–I1 = 123.8º, C_{cent}–Co–I2 = 123.9º, C_{cent}–Co–C1 = 126.8º

Table G.7 Anisotropic Displacement Parameters (U_{ij}, Å^2)

Atom	U_{11}	U_{22}	U_{33}	U_{23}	U_{13}	U_{12}
I1	0.03547(11)	0.03056(12)	0.03398(10)	-0.00458(8)	0.00514(7)	-0.01996(8)
I2	0.02312(9)	0.03015(11)	0.03360(10)	-0.00131(8)	-0.00637(7)	-0.00505(7)
I3	0.02897(10)	0.03478(12)	0.03220(10)	-0.00291(8)	0.00124(7)	-0.01452(8)
Co	0.01879(16)	0.01957(18)	0.01952(16)	-0.00422(13)	0.00004(12)	-0.00700(13)
O	0.0603(16)	0.0587(17)	0.0399(13)	-0.0248(13)	0.0088(11)	-0.0318(13)
C1	0.0285(14)	0.0338(17)	0.0316(14)	-0.0055(13)	0.0026(11)	-0.0151(12)
C10	0.0237(12)	0.0220(14)	0.0260(12)	-0.0050(10)	-0.0044(9)	-0.0082(10)
C11	0.0209(12)	0.0265(15)	0.0275(13)	0.0008(11)	-0.0050(9)	-0.0125(10)
C12	0.0180(11)	0.0330(16)	0.0217(12)	-0.0040(11)	-0.0002(9)	-0.0086(10)
C13	0.0203(11)	0.0230(14)	0.0247(12)	-0.0039(10)	-0.0003(9)	-0.0046(10)
C14	0.0209(11)	0.0246(14)	0.0223(12)	-0.0041(10)	-0.0016(9)	-0.0077(10)
C15	0.0398(16)	0.0265(16)	0.0418(17)	-0.0170(14)	-0.0059(13)	-0.0066(13)
C16	0.0372(16)	0.0345(18)	0.0427(17)	0.0092(14)	-0.0069(13)	-0.0212(14)
C17	0.0253(14)	0.053(2)	0.0279(14)	-0.0064(14)	0.0055(11)	-0.0120(13)
C18	0.0313(15)	0.0273(17)	0.0416(17)	-0.0035(13)	-0.0018(12)	-0.0029(12)
C19	0.0356(15)	0.0398(18)	0.0192(12)	-0.0017(12)	-0.0019(10)	-0.0129(13)
I1	0.03547(11)	0.03056(12)	0.03398(10)	-0.00458(8)	0.00514(7)	-0.01996(8)
I2	0.02312(9)	0.03015(11)	0.03360(10)	-0.00131(8)	-0.00637(7)	-0.00505(7)
I3	0.02897(10)	0.03478(12)	0.03220(10)	-0.00291(8)	0.00124(7)	-0.01452(8)
Co	0.01879(16)	0.01957(18)	0.01952(16)	-0.00422(13)	0.00004(12)	-0.00700(13)
O	0.0603(16)	0.0587(17)	0.0399(13)	-0.0248(13)	0.0088(11)	-0.0318(13)
C1	0.0285(14)	0.0338(17)	0.0316(14)	-0.0055(13)	0.0026(11)	-0.0151(12)
C10	0.0237(12)	0.0220(14)	0.0260(12)	-0.0050(10)	-0.0044(9)	-0.0082(10)
C11	0.0209(12)	0.0265(15)	0.0275(13)	0.0008(11)	-0.0050(9)	-0.0125(10)
C12	0.0180(11)	0.0330(16)	0.0217(12)	-0.0040(11)	-0.0002(9)	-0.0086(10)
C13	0.0203(11)	0.0230(14)	0.0247(12)	-0.0039(10)	-0.0003(9)	-0.0046(10)
C14	0.0209(11)	0.0246(14)	0.0223(12)	-0.0041(10)	-0.0016(9)	-0.0077(10)
C15	0.0398(16)	0.0265(16)	0.0418(17)	-0.0170(14)	-0.0059(13)	-0.0066(13)

The form of the anisotropic displacement parameter is:

$\exp[-2\pi^2(h^2a^{*2}U_{11} + k^2b^{*2}U_{22} + l^2c^{*2}U_{33} + 2klb^*c^*U_{23} + 2hla^*c^*U_{13} + 2hka^*b^*U_{12})]$

Table G.8 Derived Atomic Coordinates and Displacement Parameters for Hydrogen Atoms

Atom	*x*	*y*	*z*	U_{eq}, Å^2
H15A	0.3576	-0.1032	0.1219	0.043
H15B	0.5083	-0.1643	0.2081	0.043
H15C	0.5262	-0.0316	0.1126	0.043
H16A	0.2261	-0.0582	0.4339	0.045
H16B	0.3677	-0.1774	0.3595	0.045
H16C	0.1416	-0.1206	0.3525	0.045
H17A	-0.1420	0.3101	0.3892	0.044
H17B	-0.0416	0.4422	0.4032	0.044
H17C	0.0432	0.2373	0.4565	0.044
H18A	0.1008	0.6377	0.1677	0.044
H18B	-0.0192	0.6304	0.2661	0.044
H18C	-0.0979	0.6144	0.1669	0.044
H19A	0.2566	0.4667	0.0460	0.039
H19B	0.1891	0.3246	0.0122	0.039
H19C	0.4097	0.2691	0.0360	0.039

Appendix H – X-ray crystallographic structure report for complex Co-2c

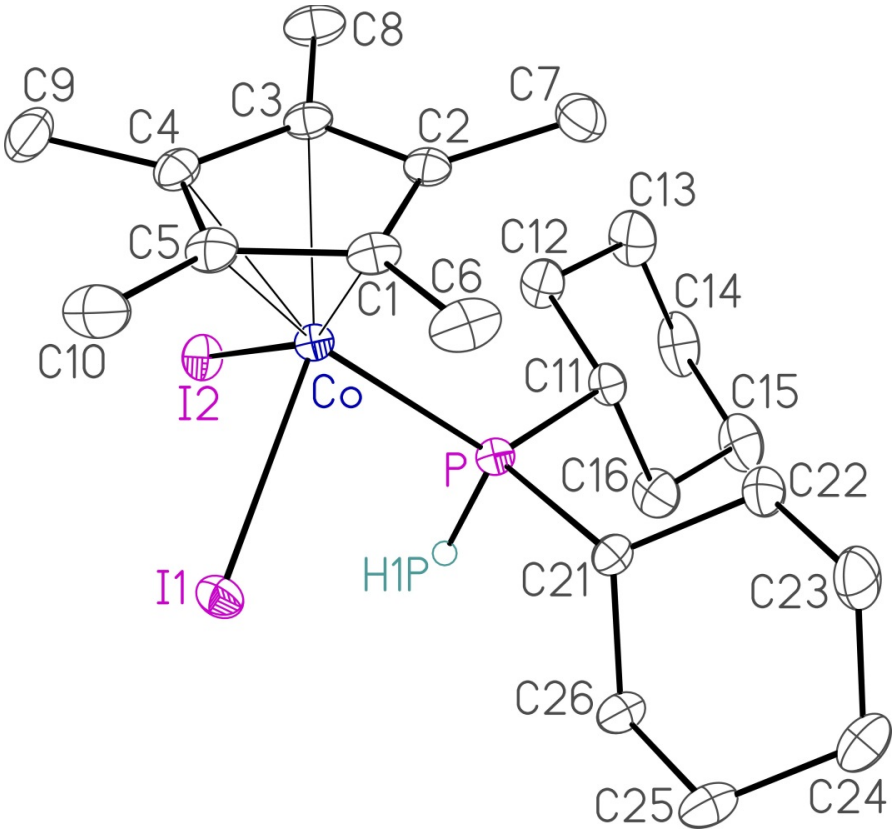

Figure H.1 Perspective view of the Co(η^5-Cp*)I_2(PCy_2H) (**Co-2c**) molecule showing the atom labelling scheme. Non-hydrogen atoms are represented by Gaussian ellipsoids at the 30% probability level. The phosphorus-bound hydrogen atom (H1P) is shown with an arbitrarily small thermal parameter; all other hydrogens are not shown.

Table H.1 Crystallographic Experimental Details

A. Crystal Data	
formula	$C_{22}H_{38}CoI_2P$
formula weight	646.22
crystal dimensions (mm)	0.43 × 0.19 × 0.05
crystal system	monoclinic
space group	$P2_1/c$ (No. 14)
unit cell parameters[a]	
a (Å)	9.0567 (6)
b (Å)	29.6018 (18)
c (Å)	9.2506 (6)
β (deg)	93.1536 (8)
V (Å^3)	2476.3 (3)
Z	4
ρ_{calcd} (g cm^{-3})	1.733
μ (mm^{-1})	3.256
B. Data Collection and Refinement Conditions	
diffractometer	Bruker PLATFORM/APEX II CCD[b]
radiation (λ [Å])	graphite-monochromated Mo Kα (0.71073)
temperature (°C)	–80
scan type	ω scans (0.5°) (10 s exposures)
data collection 2θ limit (deg)	56.77
total data collected	21345 (-12 ≤ h ≤ 12, -39 ≤ k ≤ 39, -12 ≤ l ≤ 12)
independent reflections	6094 (R_{int} = 0.0314)
number of observed reflections (*NO*)	5232 [$F_o^2 \geq 2\sigma(F_o^2)$]
structure solution method	Patterson/structure expansion (*DIRDIF–2008*[c])
refinement method	full-matrix least-squares on F^2 (*SHELXL–2014*[d])
absorption correction method	Gaussian integration (face-indexed)
range of transmission factors	0.8757–0.3509
data/restraints/parameters	6094 / 0 / 244
goodness-of-fit (*S*)[e] [all data]	1.039
final R indices[f]	
R_1 [$F_o^2 \geq 2\sigma(F_o^2)$]	0.0282
wR_2 [all data]	0.0682
largest difference peak and hole	1.122 and –0.496 e Å^{-3}

[a]Obtained from least-squares refinement of 4937 reflections with 4.50° < 2θ < 47.62°.

[b]Programs for diffractometer operation, data collection, data reduction and absorption correction were those supplied by Bruker.

(continued)

Table H.1 Crystallographic Experimental Details (continued)

[c]Beurskens, P. T.; Beurskens, G.; de Gelder, R.; Smits, J. M. M.; Garcia-Granda, S.; Gould, R. O. (2008). The *DIRDIF-2008* program system. Crystallography Laboratory, Radboud University Nijmegen, The Netherlands.

[d]Sheldrick, G. M. *Acta Crystallogr.* **2015**, *C71*, 3–8.

[e]$S = [\Sigma w(F_o^2 - F_c^2)^2/(n - p)]^{1/2}$ (n = number of data; p = number of parameters varied; $w = [\sigma^2(F_o^2) + (0.0322P)^2 + 1.2224P]^{-1}$ where $P = [\mathrm{Max}(F_o^2, 0) + 2F_c^2]/3$).

[f]$R_1 = \Sigma||F_o| - |F_c||/\Sigma|F_o|$; $wR_2 = [\Sigma w(F_o^2 - F_c^2)^2/\Sigma w(F_o^4)]^{1/2}$.

Table H.2 Atomic Coordinates and Equivalent Isotropic Displacement Parameters

Atom	*x*	*y*	*z*	U_{eq}, Å^2
I1	-0.28922(2)	0.07159(2)	0.18694(2)	0.03077(6)*
I2	-0.22146(2)	0.15835(2)	-0.10040(2)	0.02992(6)*
Co	-0.13095(4)	0.14463(2)	0.16723(4)	0.02062(8)*
P	0.04474(8)	0.09823(2)	0.09502(7)	0.02178(14)*
C1	-0.0845(3)	0.15828(9)	0.3850(3)	0.0262(6)*
C2	0.0057(3)	0.18595(9)	0.2986(3)	0.0258(6)*
C3	-0.0894(3)	0.21323(10)	0.2082(3)	0.0270(6)*
C4	-0.2395(3)	0.20354(10)	0.2405(3)	0.0290(6)*
C5	-0.2360(3)	0.17060(10)	0.3507(3)	0.0298(6)*
C6	-0.0355(4)	0.12690(11)	0.5040(3)	0.0406(8)*
C7	0.1714(4)	0.19096(12)	0.3162(4)	0.0389(8)*
C8	-0.0427(4)	0.25055(11)	0.1111(4)	0.0401(8)*
C9	-0.3747(4)	0.22728(12)	0.1778(4)	0.0462(9)*
C10	-0.3650(4)	0.15530(12)	0.4319(4)	0.0475(9)*
C11	0.2098(3)	0.11667(10)	0.0000(3)	0.0261(6)*
C12	0.1851(4)	0.15941(11)	-0.0922(4)	0.0377(8)*
C13	0.3244(4)	0.17219(14)	-0.1676(4)	0.0482(9)*
C14	0.3750(4)	0.13362(15)	-0.2614(4)	0.0497(10)*
C15	0.3977(4)	0.09062(14)	-0.1759(4)	0.0465(9)*
C16	0.2597(4)	0.07809(12)	-0.0971(4)	0.0401(8)*
C21	0.1138(3)	0.05648(9)	0.2346(3)	0.0240(6)*
C22	0.2708(3)	0.06441(11)	0.2991(4)	0.0362(7)*
C23	0.3067(4)	0.03120(13)	0.4229(4)	0.0445(9)*
C24	0.2877(4)	-0.01746(12)	0.3718(4)	0.0453(9)*
C25	0.1328(4)	-0.02543(11)	0.3058(4)	0.0382(8)*
C26	0.0949(4)	0.00750(10)	0.1818(3)	0.0310(7)*
H1P	-0.017(3)	0.0724(10)	-0.004(3)	0.027(8)

Anisotropically-refined atoms are marked with an asterisk (*). The form of the anisotropic displacement parameter is: $\exp[-2\pi^2(h^2a^{*2}U_{11} + k^2b^{*2}U_{22} + l^2c^{*2}U_{33} + 2klb^*c^*U_{23} + 2hla^*c^*U_{13} + 2hka^*b^*U_{12})]$.

Table H.3 Selected Interatomic Distances (Å)

Atom1	Atom2	Distance
I1	Co	2.6062(4)
I2	Co	2.5967(4)
Co	P	2.2319(8)
Co	C1	2.075(3)
Co	C2	2.083(3)
Co	C3	2.096(3)
Co	C4	2.131(3)
Co	C5	2.134(3)
P	H1P	1.30(3)
P	C11	1.857(3)
P	C21	1.870(3)
C1	C2	1.431(4)
C1	C5	1.438(4)
C1	C6	1.489(4)
C2	C3	1.419(4)
C2	C7	1.508(4)
C3	C4	1.437(4)
C3	C8	1.499(4)
C4	C5	1.410(4)
C4	C9	1.500(4)
C5	C10	1.494(4)
C11	C12	1.535(4)
C11	C16	1.536(4)
C12	C13	1.522(5)
C13	C14	1.521(6)
C14	C15	1.507(5)
C15	C16	1.527(4)
C21	C22	1.530(4)
C21	C26	1.537(4)
C22	C23	1.530(4)
C23	C24	1.523(5)
C24	C25	1.517(5)
C25	C26	1.530(4)

Table H.4 Selected Interatomic Angles (deg)

Atom1	Atom2	Atom3	Angle	Atom1	Atom2	Atom3	Angle
I1	Co	I2	92.891(13)	Co	C2	C1	69.57(16)
I1	Co	P	85.08(2)	Co	C2	C3	70.64(16)
I1	Co	C1	100.17(8)	Co	C2	C7	132.6(2)
I1	Co	C2	139.27(8)	C1	C2	C3	108.0(3)
I1	Co	C3	152.28(8)	C1	C2	C7	126.2(3)
I1	Co	C4	113.05(8)	C3	C2	C7	125.1(3)
I1	Co	C5	88.41(8)	Co	C3	C2	69.66(16)
I2	Co	P	90.21(2)	Co	C3	C4	71.44(16)
I2	Co	C1	158.71(8)	Co	C3	C8	131.3(2)
I2	Co	C2	127.64(8)	C2	C3	C4	108.3(2)
I2	Co	C3	93.72(8)	C2	C3	C8	126.2(3)
I2	Co	C4	92.77(8)	C4	C3	C8	125.0(3)
I2	Co	C5	124.81(9)	Co	C4	C3	68.82(16)
P	Co	C1	107.50(9)	Co	C4	C5	70.82(17)
P	Co	C2	97.21(8)	Co	C4	C9	129.9(2)
P	Co	C3	121.76(8)	C3	C4	C5	107.7(3)
P	Co	C4	161.41(9)	C3	C4	C9	126.0(3)
P	Co	C5	144.69(9)	C5	C4	C9	126.1(3)
C1	Co	C2	40.27(11)	Co	C5	C1	67.83(16)
C1	Co	C3	67.12(11)	Co	C5	C4	70.58(16)
C1	Co	C4	66.68(11)	Co	C5	C10	133.3(2)
C1	Co	C5	39.92(12)	C1	C5	C4	108.6(3)
C2	Co	C3	39.71(11)	C1	C5	C10	125.1(3)
C2	Co	C4	66.64(11)	C4	C5	C10	125.9(3)
C2	Co	C5	66.48(12)	P	C11	C12	114.1(2)
C3	Co	C4	39.74(11)	P	C11	C16	109.2(2)
C3	Co	C5	65.84(11)	C12	C11	C16	109.0(3)
C4	Co	C5	38.60(11)	C11	C12	C13	111.1(3)
Co	P	H1P	106.7(13)	C12	C13	C14	111.0(3)
Co	P	C11	124.50(10)	C13	C14	C15	111.8(3)
Co	P	C21	114.64(9)	C14	C15	C16	111.4(3)
C11	P	H1P	99.6(14)	C11	C16	C15	111.9(3)
C11	P	C21	105.88(13)	P	C21	C22	115.9(2)
C21	P	H1P	102.3(13)	P	C21	C26	112.15(19)
Co	C1	C2	70.16(15)	C22	C21	C26	110.7(2)
Co	C1	C5	72.25(16)	C21	C22	C23	110.3(3)
Co	C1	C6	129.2(2)	C22	C23	C24	111.1(3)
C2	C1	C5	107.4(2)	C23	C24	C25	111.0(3)
C2	C1	C6	127.9(3)	C24	C25	C26	111.5(3)
C5	C1	C6	124.3(3)	C21	C26	C25	110.3(2)

Table H.5 Torsional Angles (deg)

Atom1	Atom2	Atom3	Atom4	Angle	continued				
I1	Co	P	C11	163.09(11)	P	Co	C2	C3	132.70(15)
I1	Co	P	C21	-64.02(10)	P	Co	C2	C7	12.3(3)
I2	Co	P	C11	70.21(11)	C1	Co	C2	C3	-118.7(2)
I2	Co	P	C21	-156.90(10)	C1	Co	C2	C7	121.0(4)
C1	Co	P	C11	-97.78(14)	C3	Co	C2	C1	118.7(2)
C1	Co	P	C21	35.10(13)	C3	Co	C2	C7	-120.4(4)
C2	Co	P	C11	-57.82(14)	C4	Co	C2	C1	80.95(18)
C2	Co	P	C21	75.07(13)	C4	Co	C2	C3	-37.72(16)
C3	Co	P	C11	-24.30(15)	C4	Co	C2	C7	-158.1(3)
C3	Co	P	C21	108.58(14)	C5	Co	C2	C1	38.72(17)
C4	Co	P	C11	-29.2(3)	C5	Co	C2	C3	-79.95(18)
C4	Co	P	C21	103.7(3)	C5	Co	C2	C7	159.7(3)
C5	Co	P	C11	-116.67(18)	I1	Co	C3	C2	105.0(2)
C5	Co	P	C21	16.22(18)	I1	Co	C3	C4	-13.6(3)
I1	Co	C1	C2	168.31(15)	I1	Co	C3	C8	-134.2(3)
I1	Co	C1	C5	-75.04(16)	I2	Co	C3	C2	-151.60(15)
I1	Co	C1	C6	45.1(3)	I2	Co	C3	C4	89.86(16)
I2	Co	C1	C2	-64.7(3)	I2	Co	C3	C8	-30.8(3)
I2	Co	C1	C5	51.9(3)	P	Co	C3	C2	-59.04(18)
I2	Co	C1	C6	172.1(2)	P	Co	C3	C4	-177.58(14)
P	Co	C1	C2	80.30(16)	P	Co	C3	C8	61.8(3)
P	Co	C1	C5	-163.05(15)	C1	Co	C3	C2	38.00(17)
P	Co	C1	C6	-42.9(3)	C1	Co	C3	C4	-80.54(18)
C2	Co	C1	C5	116.6(2)	C1	Co	C3	C8	158.8(3)
C2	Co	C1	C6	-123.2(4)	C2	Co	C3	C4	-118.5(2)
C3	Co	C1	C2	-37.47(17)	C2	Co	C3	C8	120.8(4)
C3	Co	C1	C5	79.18(18)	C4	Co	C3	C2	118.5(2)
C3	Co	C1	C6	-160.7(3)	C4	Co	C3	C8	-120.6(4)
C4	Co	C1	C2	-80.84(18)	C5	Co	C3	C2	81.69(18)
C4	Co	C1	C5	35.81(17)	C5	Co	C3	C4	-36.85(17)
C4	Co	C1	C6	156.0(3)	C5	Co	C3	C8	-157.5(3)
C5	Co	C1	C2	-116.6(2)	I1	Co	C4	C3	173.18(14)
C5	Co	C1	C6	120.1(4)	I1	Co	C4	C5	54.46(18)
I1	Co	C2	C1	-17.8(2)	I1	Co	C4	C9	-67.0(3)
I1	Co	C2	C3	-136.47(14)	I2	Co	C4	C3	-92.49(16)
I1	Co	C2	C7	103.2(3)	I2	Co	C4	C5	148.79(17)
I2	Co	C2	C1	155.50(14)	I2	Co	C4	C9	27.3(3)
I2	Co	C2	C3	36.83(19)	P	Co	C4	C3	6.5(4)
I2	Co	C2	C7	-83.5(3)	P	Co	C4	C5	-112.2(3)
P	Co	C2	C1	-108.63(16)	P	Co	C4	C9	126.3(3)

Table H.5 Torsional Angles (continued)

Atom1	Atom2	Atom3	Atom4	Angle	continued				
C1	Co	C4	C3	81.73(18)	C5	C1	C2	C3	-2.6(3)
C1	Co	C4	C5	-36.99(18)	C5	C1	C2	C7	168.4(3)
C1	Co	C4	C9	-158.5(3)	C6	C1	C2	Co	124.8(3)
C2	Co	C4	C3	37.68(16)	C6	C1	C2	C3	-174.7(3)
C2	Co	C4	C5	-81.04(19)	C6	C1	C2	C7	-3.6(5)
C2	Co	C4	C9	157.5(3)	Co	C1	C5	C4	-59.0(2)
C3	Co	C4	C5	-118.7(2)	Co	C1	C5	C10	128.2(3)
C3	Co	C4	C9	119.8(4)	C2	C1	C5	Co	61.74(18)
C5	Co	C4	C3	118.7(2)	C2	C1	C5	C4	2.8(3)
C5	Co	C4	C9	-121.5(4)	C2	C1	C5	C10	-170.0(3)
I1	Co	C5	C1	107.95(16)	C6	C1	C5	Co	-125.8(3)
I1	Co	C5	C4	-131.49(17)	C6	C1	C5	C4	175.2(3)
I1	Co	C5	C10	-10.0(3)	C6	C1	C5	C10	2.4(5)
I2	Co	C5	C1	-159.63(13)	Co	C2	C3	C4	61.3(2)
I2	Co	C5	C4	-39.1(2)	Co	C2	C3	C8	-126.9(3)
I2	Co	C5	C10	82.4(4)	C1	C2	C3	Co	-59.81(19)
P	Co	C5	C1	28.8(2)	C1	C2	C3	C4	1.5(3)
P	Co	C5	C4	149.31(15)	C1	C2	C3	C8	173.3(3)
P	Co	C5	C10	-89.2(4)	C7	C2	C3	Co	129.0(3)
C1	Co	C5	C4	120.6(3)	C7	C2	C3	C4	-169.7(3)
C1	Co	C5	C10	-118.0(4)	C7	C2	C3	C8	2.1(5)
C2	Co	C5	C1	-39.06(17)	Co	C3	C4	C5	60.4(2)
C2	Co	C5	C4	81.50(19)	Co	C3	C4	C9	-124.6(3)
C2	Co	C5	C10	-157.0(4)	C2	C3	C4	Co	-60.18(19)
C3	Co	C5	C1	-82.64(18)	C2	C3	C4	C5	0.2(3)
C3	Co	C5	C4	37.91(18)	C2	C3	C4	C9	175.2(3)
C3	Co	C5	C10	159.4(4)	C8	C3	C4	Co	127.9(3)
C4	Co	C5	C1	-120.6(3)	C8	C3	C4	C5	-171.7(3)
C4	Co	C5	C10	121.5(4)	C8	C3	C4	C9	3.2(5)
Co	P	C11	C12	-29.2(3)	Co	C4	C5	C1	57.3(2)
Co	P	C11	C16	-151.48(18)	Co	C4	C5	C10	-130.0(3)
C21	P	C11	C12	-165.4(2)	C3	C4	C5	Co	-59.15(19)
C21	P	C11	C16	72.3(2)	C3	C4	C5	C1	-1.9(3)
Co	P	C21	C22	-109.3(2)	C3	C4	C5	C10	170.9(3)
Co	P	C21	C26	122.33(19)	C9	C4	C5	Co	125.9(3)
C11	P	C21	C22	31.8(3)	C9	C4	C5	C1	-176.8(3)
C11	P	C21	C26	-96.6(2)	C9	C4	C5	C10	-4.1(5)
Co	C1	C2	C3	60.48(19)	P	C11	C12	C13	-179.5(2)
Co	C1	C2	C7	-128.5(3)	C16	C11	C12	C13	-57.2(4)
C5	C1	C2	Co	-63.10(19)	P	C11	C16	C15	-178.6(2)

Table H.5 Torsional Angles (continued)

Atom1	Atom2	Atom3	Atom4	Angle	continued				
C12	C11	C16	C15	56.1(4)	P	C21	C26	C25	-172.2(2)
C11	C12	C13	C14	57.4(4)	C22	C21	C26	C25	56.7(3)
C12	C13	C14	C15	-55.5(4)	C21	C22	C23	C24	56.9(4)
C13	C14	C15	C16	54.2(4)	C22	C23	C24	C25	-56.3(4)
C14	C15	C16	C11	-55.2(4)	C23	C24	C25	C26	56.1(4)
P	C21	C22	C23	173.7(2)	C24	C25	C26	C21	-56.2(4)
C26	C21	C22	C23	-57.2(3					

Table H.6 Least-Squares Planes

Plane	Coefficients[a]		Defining Atoms with Deviations (Å)[b]			
1	0.052(13)	21.08(3)				
	6.481(9)	5.844(4)				
			C1	-0.0158(17)	C2	0.0121(17)
			C3	-0.0038(18)	C4	-0.0062(18)
			C5	0.0137(18)		
			Co	-1.7174(13)	C6	0.096(5)
			C7	0.240(5)	C8	0.156(5)
			C9	0.081(6)	C10	0.211(6)

[a]Coefficients are for the form $ax+by+cz = d$ where x, y and z are crystallographic coordinates.

[b]Underlined atoms were not included in the definition of the plane.

Distance: $Co–C_{cent}$ = 1.718 Å (C_{cent} = C1–C2–C3–C4–C5 centroid)

Angles: C_{cent}–Co–Il = 122.2º, C_{cent}–Co–I2 = 122.9º, C_{cent}–Ru–P = 132.0º

Table H.7 Anisotropic Displacement Parameters (U_{ij}, Å^2)

Atom	U_{11}	U_{22}	U_{33}	U_{23}	U_{13}	U_{12}
I1	0.02973(11)	0.02991(11)	0.03306(11)	0.00003(8)	0.00509(8)	-0.00728(8)
I2	0.03081(11)	0.03720(12)	0.02154(10)	0.00335(7)	-0.00035(7)	0.00243(8)
Co	0.02393(19)	0.02066(18)	0.01752(17)	0.00030(14)	0.00346(14)	-0.00022(14)
P	0.0244(3)	0.0225(3)	0.0186(3)	-0.0003(3)	0.0029(3)	0.0001(3)
C1	0.0402(17)	0.0245(14)	0.0143(12)	-0.0028(10)	0.0054(11)	0.0000(12)
C2	0.0322(15)	0.0243(14)	0.0211(13)	-0.0062(11)	0.0035(11)	-0.0019(11)
C3	0.0362(16)	0.0221(14)	0.0234(14)	-0.0022(11)	0.0073(12)	-0.0008(12)
C4	0.0338(16)	0.0269(15)	0.0266(14)	-0.0055(12)	0.0027(12)	0.0041(12)
C5	0.0372(17)	0.0289(15)	0.0240(14)	-0.0056(12)	0.0097(12)	-0.0001(13)
C6	0.071(2)	0.0331(17)	0.0182(14)	0.0007(12)	0.0025(14)	0.0047(16)
C7	0.0345(17)	0.0411(19)	0.0409(18)	-0.0101(15)	0.0002(14)	-0.0040(14)
C8	0.062(2)	0.0249(16)	0.0341(18)	0.0048(13)	0.0107(16)	-0.0046(15)
C9	0.043(2)	0.042(2)	0.054(2)	-0.0085(17)	-0.0006(17)	0.0168(16)
C10	0.053(2)	0.039(2)	0.054(2)	-0.0083(16)	0.0327(18)	-0.0091(16)
C11	0.0234(13)	0.0322(15)	0.0230(13)	0.0025(11)	0.0038(11)	-0.0014(11)
C12	0.0343(17)	0.0416(19)	0.0381(18)	0.0132(14)	0.0098(14)	0.0005(14)
C13	0.0386(19)	0.059(2)	0.048(2)	0.0196(18)	0.0138(16)	-0.0047(17)
C14	0.0311(18)	0.091(3)	0.0277(17)	0.0072(18)	0.0108(14)	0.0018(19)
C15	0.0312(17)	0.072(3)	0.0380(19)	-0.0069(18)	0.0137(14)	0.0002(17)
C16	0.0342(18)	0.048(2)	0.0394(19)	-0.0102(15)	0.0162(14)	0.0000(15)
C21	0.0276(14)	0.0242(14)	0.0201(13)	0.0014(11)	0.0012(11)	0.0029(11)
C22	0.0308(17)	0.0370(18)	0.0400(18)	0.0033(14)	-0.0061(14)	0.0006(13)
C23	0.0379(19)	0.055(2)	0.0391(19)	0.0075(16)	-0.0106(15)	0.0023(16)
C24	0.053(2)	0.040(2)	0.0429(19)	0.0116(16)	-0.0002(16)	0.0142(16)
C25	0.056(2)	0.0246(15)	0.0335(17)	0.0037(13)	0.0011(15)	0.0060(14)
C26	0.0410(17)	0.0239(15)	0.0280(15)	0.0001(12)	-0.0007(13)	0.0041(13)

The form of the anisotropic displacement parameter is:

$\exp[-2\pi^2(h^2a^{*2}U_{11} + k^2b^{*2}U_{22} + l^2c^{*2}U_{33} + 2klb^*c^*U_{23} + 2hla^*c^*U_{13} + 2hka^*b^*U_{12})]$

Table H.8 Derived Atomic Coordinates and Displacement Parameters for Hydrogen Atoms

Atom	*x*	*y*	*z*	U_{eq}, Å^2
H6A	0.070689	0.121086	0.499766	0.049
H6B	-0.089896	0.098375	0.493014	0.049
H6C	-0.055083	0.140585	0.597482	0.049
H7A	0.212702	0.192350	0.220540	0.047
H7B	0.213399	0.164995	0.369794	0.047
H7C	0.195936	0.218793	0.369635	0.047
H8A	-0.056638	0.279718	0.158569	0.048
H8B	-0.102773	0.249576	0.019734	0.048
H8C	0.061820	0.246755	0.091515	0.048
H9A	-0.393081	0.254349	0.235085	0.055
H9B	-0.460026	0.206985	0.179774	0.055
H9C	-0.359212	0.236015	0.077566	0.055
H10A	-0.386898	0.177933	0.505043	0.057
H10B	-0.341355	0.126423	0.479615	0.057
H10C	-0.451356	0.151491	0.364465	0.057
H11	0.291351	0.122914	0.074653	0.031
H12A	0.103295	0.154127	-0.165728	0.045
H12B	0.156197	0.184675	-0.029602	0.045
H13A	0.304523	0.199235	-0.228529	0.058
H13B	0.404003	0.179823	-0.094007	0.058
H14A	0.300051	0.128393	-0.341692	0.060
H14B	0.468838	0.142131	-0.304274	0.060
H15A	0.482135	0.094483	-0.104403	0.056
H15B	0.422061	0.065770	-0.242133	0.056
H16A	0.280602	0.050914	-0.036998	0.048
H16B	0.178570	0.070586	-0.169148	0.048
H21	0.047557	0.059703	0.317001	0.029
H22A	0.279879	0.095760	0.335820	0.043
H22B	0.342390	0.060416	0.222975	0.043
H23A	0.409807	0.035931	0.460947	0.053
H23B	0.240420	0.037018	0.502456	0.053
H24A	0.360696	-0.024175	0.298956	0.054
H24B	0.306626	-0.038155	0.454802	0.054
H25A	0.060523	-0.021751	0.381510	0.046
H25B	0.124946	-0.056794	0.269076	0.046
H26A	-0.008411	0.002589	0.144549	0.037
H26B	0.160690	0.001893	0.101650	0.037

Appendix I – X-ray crystallographic structure report for complex Co-3c

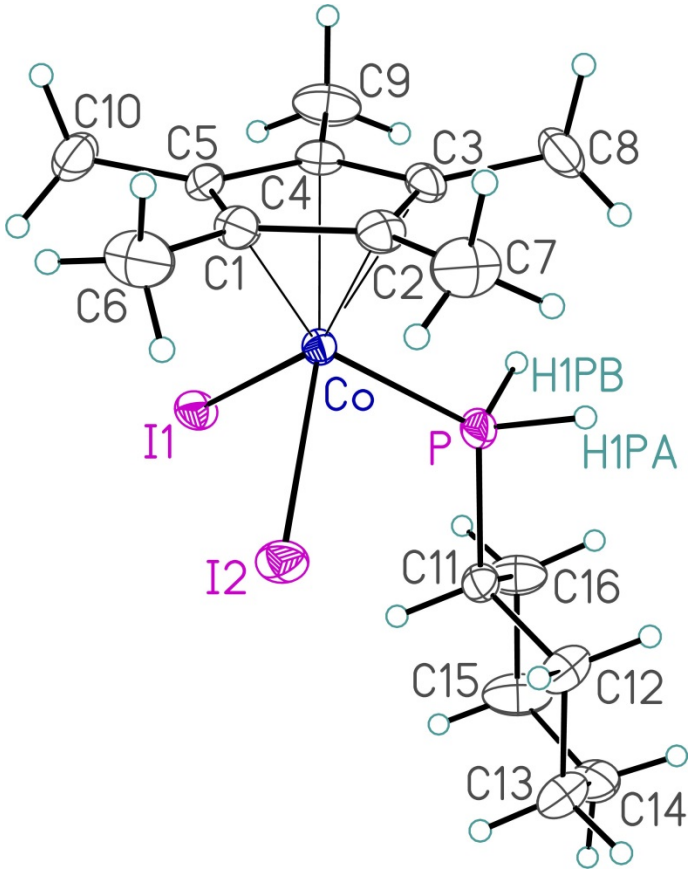

Figure I.1 Perspective view of the Co(η^5-Cp*)I_2($PCyH_2$) (**Co-3c**) molecule showing the atom labelling scheme. Non-hydrogen atoms are represented by Gaussian ellipsoids at the 30% probability level. Hydrogen atoms are shown with arbitrarily small thermal parameters.

Table I.1 Crystallographic Experimental Details

A. Crystal Data	
formula	$C_{16}H_{28}CoI_2P$
formula weight	564.08
crystal dimensions (mm)	0.27 × 0.15 × 0.10
crystal system	orthorhombic
space group	$P2_12_12_1$ (No. 19)
unit cell parameters[a]	
a (Å)	9.6450 (3)
b (Å)	12.3673 (4)
c (Å)	16.6630 (6)
V (Å^3)	1987.61 (11)
Z	4
ρ_{calcd} (g cm^{-3})	1.885
μ (mm^{-1})	4.041
B. Data Collection and Refinement Conditions	
diffractometer	Bruker PLATFORM/APEX II CCD[b]
radiation (λ [Å])	graphite-monochromated Mo Kα (0.71073)
temperature (°C)	–80
scan type	ω scans (0.3°) (15 s exposures)
data collection 2θ limit (deg)	56.70
total data collected	17704 (-12 ≤ *h* ≤ 12, -16 ≤ *k* ≤ 16, -22 ≤ *l* ≤ 22)
independent reflections	4914 (R_{int} = 0.0221)
number of observed reflections (*NO*)	4723 [$F_o^2 \geq 2\sigma(F_o^2)$]
structure solution method	Patterson/structure expansion (*DIRDIF–2008*[c])
refinement method	full-matrix least-squares on F^2 (*SHELXL–2014*[d])
absorption correction method	Gaussian integration (face-indexed)
range of transmission factors	0.7579–0.4326
data/restraints/parameters	4914 / 0 / 194
Flack absolute structure parameter[e]	0.001(8)
goodness-of-fit (*S*)[f] [all data]	1.036
final *R* indices[g]	
R_1 [$F_o^2 \geq 2\sigma(F_o^2)$]	0.0188
wR_2 [all data]	0.0412
largest difference peak and hole	0.372 and –0.391 e Å^{-3}

[a]Obtained from least-squares refinement of 9988 reflections with 4.88° < 2θ < 55.96°.

[b]Programs for diffractometer operation, data collection, data reduction and absorption correction were those supplied by Bruker.

Table I.1 Crystallographic Experimental Details (continued)

[c]Beurskens, P. T.; Beurskens, G.; de Gelder, R.; Smits, J. M. M.; Garcia-Granda, S.; Gould, R. O. (2008). The *DIRDIF-2008* program system. Crystallography Laboratory, Radboud University Nijmegen, The Netherlands.

[d]Sheldrick, G. M. *Acta Crystallogr.* **2015**, *C71*, 3–8.

[e]Flack, H. D. *Acta Crystallogr.* **1983**, *A39*, 876–881; Flack, H. D.; Bernardinelli, G. *Acta Crystallogr.* **1999**, *A55*, 908–915; Flack, H. D.; Bernardinelli, G. *J. Appl. Cryst.* **2000**, *33*, 1143–1148. The Flack parameter will refine to a value near zero if the structure is in the correct configuration and will refine to a value near one for the inverted configuration.

[f]$S = [\Sigma w(F_o^2 - F_c^2)^2/(n-p)]^{1/2}$ (n = number of data; p = number of parameters varied; $w = [\sigma^2(F_o^2) + (0.0177P)^2 + 0.6923P]^{-1}$ where $P = [\mathrm{Max}(F_o^2, 0) + 2F_c^2]/3$).

[g]$R_1 = \Sigma||F_o| - |F_c||/\Sigma|F_o|$; $wR_2 = [\Sigma w(F_o^2 - F_c^2)^2/\Sigma w(F_o^4)]^{1/2}$.

Table I.2 Atomic Coordinates and Equivalent Isotropic Displacement Parameters

Atom	*x*	*y*	*z*	U_{eq}, Å^2
I1	-0.06039(3)	0.16071(2)	0.15877(2)	0.03737(7)*
I2	0.23543(3)	0.24018(2)	0.30341(2)	0.04174(7)*
Co	0.18353(4)	0.09002(4)	0.19897(3)	0.02431(9)*
P	0.08100(10)	-0.00609(8)	0.29124(6)	0.0332(2)*
C1	0.3642(4)	0.1275(3)	0.1313(2)	0.0366(9)*
C2	0.3863(4)	0.0379(3)	0.1854(2)	0.0363(8)*
C3	0.2931(4)	-0.0464(3)	0.1628(2)	0.0336(8)*
C4	0.2095(4)	-0.0080(3)	0.0993(2)	0.0336(8)*
C5	0.2563(4)	0.0997(3)	0.0792(2)	0.0345(8)*
C6	0.4493(6)	0.2284(4)	0.1275(4)	0.0677(16)*
C7	0.5002(5)	0.0313(5)	0.2462(3)	0.0649(15)*
C8	0.2968(5)	-0.1593(3)	0.1956(3)	0.0585(13)*
C9	0.1027(5)	-0.0728(4)	0.0556(3)	0.0593(14)*
C10	0.2042(5)	0.1662(5)	0.0107(3)	0.0609(14)*
C11	-0.0385(4)	0.0500(3)	0.3668(2)	0.0312(8)*
C12	0.0270(4)	0.0521(4)	0.4493(2)	0.0478(11)*
C13	-0.0736(4)	0.1006(4)	0.5114(2)	0.0473(10)*
C14	-0.2068(5)	0.0383(4)	0.5137(3)	0.0508(11)*
C15	-0.2729(5)	0.0322(5)	0.4313(3)	0.0642(15)*
C16	-0.1738(5)	-0.0148(4)	0.3684(3)	0.0523(12)*
H1PA	0.164(5)	-0.068(4)	0.332(3)	0.054(13)
H1PB	0.015(4)	-0.091(4)	0.263(3)	0.045(12)

Anisotropically-refined atoms are marked with an asterisk (*). The form of the anisotropic displacement parameter is: $\exp[-2\pi^2(h^2a^{*2}U_{11} + k^2b^{*2}U_{22} + l^2c^{*2}U_{33} + 2klb^*c^*U_{23} + 2hla^*c^*U_{13} + 2hka^*b^*U_{12})]$.

Table I.3 Selected Interatomic Distances (Å)

Atom1	Atom2	Distance
I1	Co	2.5977(5)
I2	Co	2.5938(5)
Co	P	2.1805(10)
Co	C1	2.127(4)
Co	C2	2.072(4)
Co	C3	2.079(3)
Co	C4	2.071(4)
Co	C5	2.120(3)
P	H1PA	1.30(5)
P	H1PB	1.31(4)
P	C11	1.843(4)
C1	C2	1.445(5)
C1	C5	1.398(6)
C1	C6	1.495(6)
C2	C3	1.427(5)
C2	C7	1.497(6)
C3	C4	1.413(5)
C3	C8	1.501(5)
C4	C5	1.446(5)
C4	C9	1.494(6)
C5	C10	1.493(5)
C11	C12	1.512(5)
C11	C16	1.531(6)
C12	C13	1.541(6)
C13	C14	1.498(6)
C14	C15	1.516(7)
C15	C16	1.533(6)

Table I.4 Selected Interatomic Angles (deg)

Atom1	Atom2	Atom3	Angle	Atom1	Atom2	Atom3	Angle
I1	Co	I2	96.133(16)	Co	C1	C6	130.9(3)
I1	Co	P	87.39(3)	C2	C1	C5	108.0(3)
I1	Co	C1	122.12(12)	C2	C1	C6	125.8(4)
I1	Co	C2	158.67(11)	C5	C1	C6	126.0(4)
I1	Co	C3	131.18(11)	Co	C2	C1	71.9(2)
I1	Co	C4	95.70(10)	Co	C2	C3	70.2(2)
I1	Co	C5	92.16(11)	Co	C2	C7	129.5(3)
I2	Co	P	90.27(3)	C1	C2	C3	107.6(3)
I2	Co	C1	92.38(11)	C1	C2	C7	125.0(4)
I2	Co	C2	96.54(11)	C3	C2	C7	127.0(4)
I2	Co	C3	132.62(12)	Co	C3	C2	69.6(2)
I2	Co	C4	159.01(11)	Co	C3	C4	69.8(2)
I2	Co	C5	121.83(11)	Co	C3	C8	131.4(3)
P	Co	C1	149.82(12)	C2	C3	C4	108.2(3)
P	Co	C2	109.62(12)	C2	C3	C8	124.7(4)
P	Co	C3	89.58(10)	C4	C3	C8	126.8(4)
P	Co	C4	107.54(12)	Co	C4	C3	70.4(2)
P	Co	C5	147.69(11)	Co	C4	C5	71.6(2)
C1	Co	C2	40.22(15)	Co	C4	C9	128.4(3)
C1	Co	C3	66.86(14)	C3	C4	C5	107.8(3)
C1	Co	C4	66.63(15)	C3	C4	C9	125.3(4)
C1	Co	C5	38.45(16)	C5	C4	C9	126.7(4)
C2	Co	C3	40.21(15)	Co	C5	C1	71.1(2)
C2	Co	C4	67.44(15)	Co	C5	C4	68.04(19)
C2	Co	C5	66.56(15)	Co	C5	C10	129.8(3)
C3	Co	C4	39.80(15)	C1	C5	C4	108.3(3)
C3	Co	C5	66.73(14)	C1	C5	C10	126.1(4)
C4	Co	C5	40.34(15)	C4	C5	C10	125.4(4)
Co	P	C11	124.10(13)	P	C11	C12	111.5(3)
Co	P	H1PA	114(2)	P	C11	C16	110.3(3)
Co	P	H1PB	114(2)	C12	C11	C16	110.5(3)
C11	P	H1PA	104(2)	C11	C12	C13	110.7(3)
C11	P	H1PB	103.9(19)	C12	C13	C14	110.9(4)
H1PA	P	H1PB	91(3)	C13	C14	C15	111.3(4)
Co	C1	C2	67.8(2)	C14	C15	C16	112.0(4)
Co	C1	C5	70.5(2)	C11	C16	C15	110.2(4)

Table I.5 Torsional Angles (deg)

Atom1	Atom2	Atom3	Atom4	Angle	continued				
I1	Co	P	C11	-53.57(15)	C4	Co	C2	C3	-37.1(2)
I2	Co	P	C11	42.56(15)	C4	Co	C2	C7	-159.2(5)
C1	Co	P	C11	137.8(3)	C5	Co	C2	C1	36.0(2)
C2	Co	P	C11	139.60(19)	C5	Co	C2	C3	-81.1(2)
C3	Co	P	C11	175.18(19)	C5	Co	C2	C7	156.8(5)
C4	Co	P	C11	-148.73(18)	I1	Co	C3	C2	151.91(18)
C5	Co	P	C11	-143.5(2)	I1	Co	C3	C4	32.5(3)
I1	Co	C1	C2	-163.92(18)	I1	Co	C3	C8	-89.3(5)
I1	Co	C1	C5	-44.0(2)	I2	Co	C3	C2	-31.9(3)
I1	Co	C1	C6	77.2(5)	I2	Co	C3	C4	-151.36(18)
I2	Co	C1	C2	97.3(2)	I2	Co	C3	C8	86.8(4)
I2	Co	C1	C5	-142.8(2)	P	Co	C3	C2	-121.9(2)
I2	Co	C1	C6	-21.6(5)	P	Co	C3	C4	118.7(2)
P	Co	C1	C2	2.7(4)	P	Co	C3	C8	-3.2(4)
P	Co	C1	C5	122.6(2)	C1	Co	C3	C2	38.7(2)
P	Co	C1	C6	-116.3(4)	C1	Co	C3	C4	-80.7(2)
C2	Co	C1	C5	119.9(3)	C1	Co	C3	C8	157.4(5)
C2	Co	C1	C6	-118.9(5)	C2	Co	C3	C4	-119.4(3)
C3	Co	C1	C2	-38.7(2)	C2	Co	C3	C8	118.8(5)
C3	Co	C1	C5	81.2(2)	C4	Co	C3	C2	119.4(3)
C3	Co	C1	C6	-157.6(5)	C4	Co	C3	C8	-121.8(5)
C4	Co	C1	C2	-82.2(2)	C5	Co	C3	C2	80.7(2)
C4	Co	C1	C5	37.7(2)	C5	Co	C3	C4	-38.7(2)
C4	Co	C1	C6	158.9(5)	C5	Co	C3	C8	-160.6(5)
C5	Co	C1	C2	-119.9(3)	I1	Co	C4	C3	-156.0(2)
C5	Co	C1	C6	121.2(6)	I1	Co	C4	C5	86.6(2)
I1	Co	C2	C1	40.2(4)	I1	Co	C4	C9	-36.0(4)
I1	Co	C2	C3	-77.0(4)	I2	Co	C4	C3	79.9(4)
I1	Co	C2	C7	161.0(3)	I2	Co	C4	C5	-37.4(4)
I2	Co	C2	C1	-85.9(2)	I2	Co	C4	C9	-160.1(3)
I2	Co	C2	C3	156.9(2)	P	Co	C4	C3	-67.0(2)
I2	Co	C2	C7	34.9(5)	P	Co	C4	C5	175.68(19)
P	Co	C2	C1	-178.58(19)	P	Co	C4	C9	53.0(4)
P	Co	C2	C3	64.3(2)	C1	Co	C4	C3	81.4(2)
P	Co	C2	C7	-57.8(5)	C1	Co	C4	C5	-36.0(2)
C1	Co	C2	C3	-117.1(3)	C1	Co	C4	C9	-158.6(5)
C1	Co	C2	C7	120.8(5)	C2	Co	C4	C3	37.5(2)
C3	Co	C2	C1	117.1(3)	C2	Co	C4	C5	-79.8(2)
C3	Co	C2	C7	-122.1(5)	C2	Co	C4	C9	157.5(5)
C4	Co	C2	C1	80.0(2)	C3	Co	C4	C5	-117.4(3)

Table I.5 Torsional Angles (continued)

Atom1	Atom2	Atom3	Atom4	Angle	continued				
C3	Co	C4	C9	120.0(5)	C2	C1	C5	C10	-176.5(4)
C5	Co	C4	C3	117.4(3)	C6	C1	C5	Co	-126.9(4)
C5	Co	C4	C9	-122.6(5)	C6	C1	C5	C4	175.1(4)
I1	Co	C5	C1	143.9(2)	C6	C1	C5	C10	-1.0(6)
I1	Co	C5	C4	-96.3(2)	Co	C2	C3	C4	59.3(2)
I1	Co	C5	C10	22.2(5)	Co	C2	C3	C8	-126.9(4)
I2	Co	C5	C1	45.3(2)	C1	C2	C3	Co	-62.6(3)
I2	Co	C5	C4	165.15(18)	C1	C2	C3	C4	-3.2(4)
I2	Co	C5	C10	-76.4(5)	C1	C2	C3	C8	170.5(3)
P	Co	C5	C1	-127.5(2)	C7	C2	C3	Co	125.1(4)
P	Co	C5	C4	-7.7(3)	C7	C2	C3	C4	-175.6(4)
P	Co	C5	C10	110.7(4)	C7	C2	C3	C8	-1.9(6)
C1	Co	C5	C4	119.8(3)	Co	C3	C4	C5	62.3(2)
C1	Co	C5	C10	-121.7(5)	Co	C3	C4	C9	-123.8(4)
C2	Co	C5	C1	-37.6(2)	C2	C3	C4	Co	-59.2(3)
C2	Co	C5	C4	82.2(2)	C2	C3	C4	C5	3.0(4)
C2	Co	C5	C10	-159.3(5)	C2	C3	C4	C9	177.0(4)
C3	Co	C5	C1	-81.6(2)	C8	C3	C4	Co	127.2(4)
C3	Co	C5	C4	38.2(2)	C8	C3	C4	C5	-170.5(4)
C3	Co	C5	C10	156.7(5)	C8	C3	C4	C9	3.5(6)
C4	Co	C5	C1	-119.8(3)	Co	C4	C5	C1	59.8(3)
C4	Co	C5	C10	118.5(5)	Co	C4	C5	C10	-124.0(4)
Co	P	C11	C12	-107.9(3)	C3	C4	C5	Co	-61.5(2)
Co	P	C11	C16	129.0(3)	C3	C4	C5	C1	-1.7(4)
Co	C1	C2	C3	61.5(3)	C3	C4	C5	C10	174.5(4)
Co	C1	C2	C7	-126.0(4)	C9	C4	C5	Co	124.7(4)
C5	C1	C2	Co	-59.2(3)	C9	C4	C5	C1	-175.5(4)
C5	C1	C2	C3	2.2(4)	C9	C4	C5	C10	0.6(6)
C5	C1	C2	C7	174.8(4)	P	C11	C12	C13	179.2(3)
C6	C1	C2	Co	125.3(4)	C16	C11	C12	C13	-57.7(5)
C6	C1	C2	C3	-173.3(4)	P	C11	C16	C15	-179.9(4)
C6	C1	C2	C7	-0.7(6)	C12	C11	C16	C15	56.4(5)
Co	C1	C5	C4	-58.0(2)	C11	C12	C13	C14	57.5(5)
Co	C1	C5	C10	125.9(4)	C12	C13	C14	C15	-55.5(5)
C2	C1	C5	Co	57.6(3)	C13	C14	C15	C16	55.1(6)
C2	C1	C5	C4	-0.4(4)	C14	C15	C16	C11	-55.0(6)

Table I.6 Least-Squares Planes

Plane	Coefficients[a]		Defining Atoms with Deviations (Å)[b]			
1	6.422(14)	-4.64(2)				
		-10.75(2)				
		0.329(7)				
			C1	0.007(2)	C2	-0.016(2)
			C3	0.019(2)	C4	-0.014(2)
			C5	0.004(2)		
			Co	-1.7061(17)	C6	0.127(7)
			C7	0.092(8)	C8	0.213(7)
			C9	0.071(7)	C10	0.097(7)

Distance: Co–C_{cent} = 1.707 Å (C_{cent} = C1–C2–C3–C4–C5 centroid)
Angles: C_{cent}–Co–I1 = 123.5º, C_{cent}–Co–I2 = 124.1º, C_{cent}–Co–P = 125.3º

[a]Coefficients are for the form $ax+by+cz = d$ where x, y and z are crystallographic coordinates.

[b]Underlined atoms were not included in the definition of the plane.

Table I.7 Anisotropic Displacement Parameters (U_{ij}, Å^2)

Atom	U_{11}	U_{22}	U_{33}	U_{23}	U_{13}	U_{12}
I1	0.03506(12)	0.04040(13)	0.03664(12)	-0.00361(11)	-0.00513(11)	0.01309(11)
I2	0.04938(16)	0.03763(13)	0.03820(13)	-0.01071(11)	0.00200(12)	-0.01202(11)
Co	0.0256(2)	0.0225(2)	0.0248(2)	0.00071(19)	-0.00026(18)	0.00005(17)
P	0.0361(5)	0.0282(4)	0.0352(5)	0.0060(4)	0.0088(4)	0.0031(4)
C1	0.037(2)	0.0305(19)	0.042(2)	-0.0009(15)	0.0129(17)	-0.0059(16)
C2	0.0259(18)	0.045(2)	0.037(2)	-0.0034(17)	0.0007(15)	0.0065(15)
C3	0.0326(19)	0.0271(17)	0.0412(19)	0.0015(16)	0.0125(16)	0.0038(14)
C4	0.0277(18)	0.039(2)	0.0343(18)	-0.0100(16)	0.0038(15)	0.0015(16)
C5	0.042(2)	0.0375(19)	0.0244(16)	0.0038(14)	0.0070(16)	0.0105(18)
C6	0.067(3)	0.049(3)	0.087(4)	-0.014(3)	0.036(3)	-0.027(3)
C7	0.044(2)	0.093(4)	0.058(3)	-0.012(3)	-0.017(2)	0.020(3)
C8	0.069(3)	0.031(2)	0.075(3)	0.012(2)	0.031(3)	0.018(2)
C9	0.045(3)	0.070(3)	0.063(3)	-0.034(3)	0.000(2)	-0.004(2)
C10	0.074(3)	0.072(3)	0.037(2)	0.018(2)	0.014(2)	0.031(3)
C11	0.0309(19)	0.0315(18)	0.0313(17)	0.0027(14)	0.0038(14)	0.0012(15)
C12	0.036(2)	0.074(3)	0.033(2)	0.002(2)	0.0007(17)	0.002(2)
C13	0.041(2)	0.070(3)	0.0314(19)	0.0003(19)	0.0013(18)	-0.003(2)
C14	0.052(3)	0.052(3)	0.048(2)	-0.003(2)	0.020(2)	-0.003(2)
C15	0.033(2)	0.091(4)	0.068(3)	-0.033(3)	0.014(2)	-0.008(3)
C16	0.037(2)	0.066(3)	0.054(3)	-0.022(2)	0.008(2)	-0.009(2)

The form of the anisotropic displacement parameter is:

$\exp[-2\pi^2(h^2a^{*2}U_{11} + k^2b^{*2}U_{22} + l^2c^{*2}U_{33} + 2klb^*c^*U_{23} + 2hla^*c^*U_{13} + 2hka^*b^*U_{12})]$

Table I.8 Derived Atomic Coordinates and Displacement Parameters for Hydrogen Atoms

Atom	*x*	*y*	*z*	U_{eq}, Å^2
H6A	0.404420	0.280631	0.091663	0.081
H6B	0.541877	0.211143	0.106950	0.081
H6C	0.457325	0.259613	0.181344	0.081
H7A	0.521265	0.103980	0.266266	0.078
H7B	0.583208	0.000396	0.221236	0.078
H7C	0.470681	-0.014699	0.290921	0.078
H8A	0.364671	-0.202195	0.165594	0.070
H8B	0.204860	-0.192326	0.190361	0.070
H8C	0.323256	-0.157230	0.252401	0.070
H9A	0.146990	-0.112791	0.011789	0.071
H9B	0.031928	-0.024332	0.033645	0.071
H9C	0.059216	-0.123952	0.092870	0.071
H10A	0.195895	0.241793	0.027549	0.073
H10B	0.113211	0.139226	-0.006190	0.073
H10C	0.269382	0.161062	-0.034292	0.073
H11	-0.061052	0.126040	0.351197	0.037
H12A	0.112977	0.095792	0.447598	0.057
H12B	0.052191	-0.022385	0.465462	0.057
H13A	-0.029941	0.099301	0.565123	0.057
H13B	-0.093162	0.176913	0.497378	0.057
H14A	-0.271724	0.073693	0.551459	0.061
H14B	-0.188460	-0.035747	0.533562	0.061
H15A	-0.301753	0.105574	0.414417	0.077
H15B	-0.357066	-0.013524	0.434196	0.077
H16A	-0.153540	-0.091288	0.381411	0.063
H16B	-0.218005	-0.012342	0.314835	0.063

Appendix J – X-ray crystallographic structure report for complex Co-4e

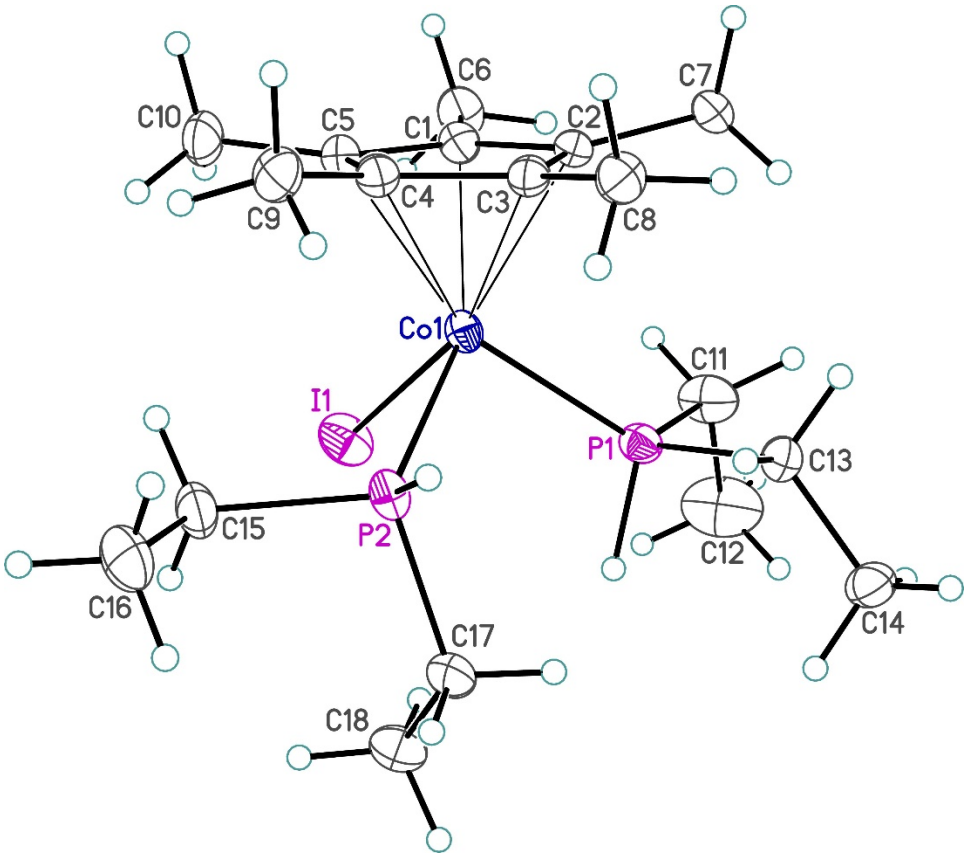

Figure J.1 Perspective view of the $[Cp^*CoI(PEt_2H)_2]^+$ cation showing the atom labelling scheme. Only the major orientation of the two disordered ethyl groups is shown. Non-hydrogen atoms are represented by Gaussian ellipsoids at the 30% probability level. Hydrogen atoms are shown with arbitrarily small thermal parameters.

Table J.1 Crystallographic Experimental Details

A. Crystal Data	
formula	$C_{18}H_{37}CoI_2P_2$
formula weight	628.14
crystal dimensions (mm)	0.32 × 0.10 × 0.04
crystal system	orthorhombic
space group	*Pbca* (No. 61)
unit cell parameters[a]	
a (Å)	16.6349(7
b (Å)	15.9310(6)
c (Å)	18.4362(7)
V (Å^3)	4885.8(3)
Z	8
ρ_{calcd} (g cm^{-3})	1.708
μ (mm^{-1})	3.360
B. Data Collection and Refinement Conditions	
diffractometer	Bruker PLATFORM/APEX II CCD[b]
radiation (λ [Å])	graphite-monochromated Mo Kα (0.71073)
temperature (°C)	–80
scan type	ω scans (0.3°) (20 s exposures)
data collection 2θ limit (deg)	52.78
total data collected	36995 (-20 ≤ *h* ≤ 20, -19 ≤ *k* ≤ 19, -23 ≤ *l* ≤ 23)
independent reflections	4999 (R_{int} = 0.0379)
number of observed reflections (*NO*)	4294 [$F_o^2 \geq 2\sigma(F_o^2)$]
structure solution method	intrinsic phasing (*SHELXT-2014*[c])
refinement method	full-matrix least-squares on F^2 (*SHELXL–2016*[d])
absorption correction method	Gaussian integration (face-indexed)
range of transmission factors	0.9048–0.4429
data/restraints/parameters	4999 / 2[e] / 241
goodness-of-fit (*S*)[e] [all data]	1.257
final *R* indices[f]	
R_1 [$F_o^2 \geq 2\sigma(F_o^2)$]	0.0330
wR_2 [all data]	0.0652
largest difference peak and hole	0.556 and –0.529 e Å^{-3}

[a]Obtained from least-squares refinement of 9910 reflections with 4.42° < 2θ < 51.02°.

[b]Programs for diffractometer operation, data collection, data reduction and absorption correction were those supplied by Bruker.

(continued)

Table J.1 Crystallographic Experimental Details (continued)

[c]Sheldrick, G. M. *Acta Crystallogr.* **2015**, *A71*, 3–8. (*SHELXT-2014*)

[d]Sheldrick, G. M. *Acta Crystallogr.* **2015**, *C71*, 3–8. (*SHELXL-2016*)

[e]The C–C distances within the disordered ethyl groups were restrained to be approximately equivalent by use of the *SHELXL* **SADI** instruction.

[f]$S = [\Sigma w(F_o^2 - F_c^2)^2/(n - p)]^{1/2}$ (n = number of data; p = number of parameters varied; $w = [\sigma^2(F_o^2) + (0.0001P)^2 + 16.0305P]^{-1}$ where $P = [\text{Max}(F_o^2, 0) + 2F_c^2]/3$).

[g]$R_1 = \Sigma||F_o| - |F_c||/\Sigma|F_o|$; $wR_2 = [\Sigma w(F_o^2 - F_c^2)^2/\Sigma w(F_o^4)]^{1/2}$.

Table J.2 Atomic Coordinates and Equivalent Isotropic Displacement Parameters

Atom	*x*	*y*	*z*	U_{eq}, Å^2
I1	0.01517(2)	0.27780(2)	0.25395(2)	0.04838(10)*
I2	0.29510(2)	0.38135(2)	-0.04185(2)	0.04439(9)*
Co1	0.12262(3)	0.20790(4)	0.17376(3)	0.02720(13)*
P1	0.21019(7)	0.29885(7)	0.21451(6)	0.0309(2)*
H1	0.182(2)	0.377(3)	0.214(2)	0.031(11)
P2	0.08791(7)	0.28787(8)	0.08123(6)	0.0325(3)*
H2	0.128(2)	0.270(2)	0.022(2)	0.026(11)
C1	0.1239(3)	0.0942(3)	0.2317(2)	0.0327(10)*
C2	0.2002(2)	0.1068(3)	0.1988(2)	0.0291(9)*
C3	0.1878(2)	0.1149(3)	0.1222(2)	0.0290(9)*
C4	0.1036(3)	0.1005(3)	0.1080(2)	0.0334(10)*
C5	0.0646(2)	0.0889(3)	0.1756(2)	0.0327(10)*
C6	0.1087(3)	0.0782(3)	0.3108(2)	0.0444(12)*
C7	0.2806(2)	0.0990(3)	0.2356(3)	0.0380(11)*
C8	0.2511(3)	0.1201(3)	0.0647(2)	0.0380(10)*
C9	0.0686(3)	0.0875(3)	0.0338(3)	0.0419(11)*
C10	-0.0219(3)	0.0653(3)	0.1866(3)	0.0466(12)*
C11	0.2394(4)	0.2912(3)	0.3099(3)	0.0518(14)*
C12[a]	0.231(3)	0.3721(9)	0.3485(10)	0.085(8)*
C12A[b]	0.276(2)	0.3617(16)	0.3494(12)	0.064(7)*
C13	0.3020(3)	0.3106(3)	0.1613(3)	0.0373(10)*
C14	0.3423(3)	0.3959(3)	0.1668(3)	0.0425(11)*
C15	-0.0172(3)	0.2775(3)	0.0526(3)	0.0433(12)*
C16	-0.0313(3)	0.2858(4)	-0.0286(3)	0.0577(15)*
C17	0.1067(3)	0.4010(3)	0.0806(3)	0.0486(13)*
C18[c]	0.0560(6)	0.4532(6)	0.1213(5)	0.047(3)*
C18A[d]	0.0704(7)	0.4583(7)	0.0273(7)	0.055(4)*

Anisotropically-refined atoms are marked with an asterisk (*). The form of the anisotropic displacement parameter is: $\exp[-2\pi^2(h^2a^{*2}U_{11} + k^2b^{*2}U_{22} + l^2c^{*2}U_{33} + 2klb^*c^*U_{23} + 2hla^*c^*U_{13} + 2hka^*b^*U_{12})]$. Refined occupancies of 0.56(5)[a], 0.44(5)[b], 0.533(10)[c] and 0.467(10)[d].

Table J.3 Selected Interatomic Distances (Å)

Atom1	Atom2	Distance
I1	Co1	2.5731(6)
Co1	P1	2.1876(13)
Co1	P2	2.2060(13)
Co1	C1	2.103(4)
Co1	C2	2.115(4)
Co1	C3	2.068(4)
Co1	C4	2.120(4)
Co1	C5	2.128(4)
P1	C11	1.829(5)
P1	C13	1.825(5)
P1	H1	1.33(4)
P2	C15	1.834(4)
P2	C17	1.830(5)
P2	H2	1.32(4)
C1	C2	1.420(6)
C1	C5	1.432(6)
C1	C6	1.502(6)
C2	C3	1.434(6)
C2	C7	1.505(6)
C3	C4	1.443(6)
C3	C8	1.495(6)
C4	C5	1.417(6)
C4	C9	1.501(6)
C5	C10	1.501(6)
C11	C12	1.479(11)
C11	C12A	1.472(13)
C13	C14	1.520(6)
C15	C16	1.521(7)
C17	C18	1.403(9)
C17	C18A	1.470(9)

Table J.4 Selected Interatomic Angles (deg)

Atom1	Atom2	Atom3	Angle	Atom1	Atom2	Atom3	Angle
I1	Co1	P1	88.77(4)	C15	P2	H2	103.1(16)
I1	Co1	P2	90.72(4)	C17	P2	H2	96.7(17)
I1	Co1	C1	95.06(12)	Co1	C1	C2	70.8(2)
I1	Co1	C2	128.89(12)	Co1	C1	C5	71.1(2)
I1	Co1	C3	159.82(12)	Co1	C1	C6	129.6(3)
I1	Co1	C4	125.04(12)	C2	C1	C5	108.4(4)
I1	Co1	C5	93.53(12)	C2	C1	C6	126.0(4)
P1	Co1	P2	93.29(5)	C5	C1	C6	125.1(4)
P1	Co1	C1	112.91(12)	Co1	C2	C1	69.9(2)
P1	Co1	C2	91.30(12)	Co1	C2	C3	68.2(2)
P1	Co1	C3	106.47(12)	Co1	C2	C7	134.7(3)
P1	Co1	C4	146.09(13)	C1	C2	C3	107.7(4)
P1	Co1	C5	152.48(12)	C1	C2	C7	126.2(4)
P2	Co1	C1	153.23(12)	C3	C2	C7	125.4(4)
P2	Co1	C2	140.22(12)	Co1	C3	C2	71.7(2)
P2	Co1	C3	101.27(12)	Co1	C3	C4	71.8(2)
P2	Co1	C4	89.13(13)	Co1	C3	C8	130.9(3)
P2	Co1	C5	114.08(12)	C2	C3	C4	107.7(4)
C1	Co1	C2	39.36(16)	C2	C3	C8	127.0(4)
C1	Co1	C3	67.09(17)	C4	C3	C8	124.3(4)
C1	Co1	C4	66.22(17)	Co1	C4	C3	67.9(2)
C1	Co1	C5	39.57(16)	Co1	C4	C5	70.8(2)
C2	Co1	C3	40.08(16)	Co1	C4	C9	133.7(3)
C2	Co1	C4	66.53(16)	C3	C4	C5	107.8(4)
C2	Co1	C5	66.11(16)	C3	C4	C9	124.3(4)
C3	Co1	C4	40.27(16)	C5	C4	C9	127.2(4)
C3	Co1	C5	66.82(16)	Co1	C5	C1	69.3(2)
C4	Co1	C5	38.96(17)	Co1	C5	C4	70.2(2)
Co1	P1	C11	117.58(19)	Co1	C5	C10	131.3(3)
Co1	P1	C13	116.10(15)	C1	C5	C4	108.2(4)
C11	P1	C13	107.6(3)	C1	C5	C10	125.3(4)
Co1	P1	H1	112.2(17)	C4	C5	C10	126.2(4)
C11	P1	H1	99.7(17)	P1	C11	C12	112.3(9)
C13	P1	H1	101.3(17)	P1	C11	C12A	122.3(11)
Co1	P2	C15	114.83(16)	P1	C13	C14	115.1(3)
Co1	P2	C17	121.94(18)	P2	C15	C16	115.0(4)
C15	P2	C17	104.5(2)	P2	C17	C18	118.5(5)
Co1	P2	H2	112.9(17)	P2	C17	C18A	123.0(6)

Table J.5 Torsional Angles (deg)

Atom1	Atom2	Atom3	Atom4	Angle	continued				
I1	Co1	P1	C11	68.2(2)	C3	Co1	C1	C5	-80.8(3)
I1	Co1	P1	C13	-162.36(17)	C3	Co1	C1	C6	158.7(4)
P2	Co1	P1	C11	158.8(2)	C4	Co1	C1	C2	81.4(3)
P2	Co1	P1	C13	-71.70(17)	C4	Co1	C1	C5	-36.8(2)
C1	Co1	P1	C11	-26.8(3)	C4	Co1	C1	C6	-157.2(5)
C1	Co1	P1	C13	102.7(2)	C5	Co1	C1	C2	118.2(4)
C2	Co1	P1	C11	-60.7(2)	C5	Co1	C1	C6	-120.4(5)
C2	Co1	P1	C13	68.8(2)	I1	Co1	C2	C1	36.4(3)
C3	Co1	P1	C11	-98.4(2)	I1	Co1	C2	C3	156.11(19)
C3	Co1	P1	C13	31.1(2)	I1	Co1	C2	C7	-85.0(4)
C4	Co1	P1	C11	-107.8(3)	P1	Co1	C2	C1	125.9(2)
C4	Co1	P1	C13	21.6(3)	P1	Co1	C2	C3	-114.4(2)
C5	Co1	P1	C11	-27.1(4)	P1	Co1	C2	C7	4.4(4)
C5	Co1	P1	C13	102.4(3)	P2	Co1	C2	C1	-137.4(2)
I1	Co1	P2	C15	-59.31(19)	P2	Co1	C2	C3	-17.7(3)
I1	Co1	P2	C17	68.5(2)	P2	Co1	C2	C7	101.2(4)
P1	Co1	P2	C15	-148.12(19)	C1	Co1	C2	C3	119.7(4)
P1	Co1	P2	C17	-20.3(2)	C1	Co1	C2	C7	-121.5(5)
C1	Co1	P2	C15	43.5(3)	C3	Co1	C2	C1	-119.7(4)
C1	Co1	P2	C17	171.3(3)	C3	Co1	C2	C7	118.8(5)
C2	Co1	P2	C15	115.9(3)	C4	Co1	C2	C1	-80.6(3)
C2	Co1	P2	C17	-116.3(3)	C4	Co1	C2	C3	39.1(2)
C3	Co1	P2	C15	104.4(2)	C4	Co1	C2	C7	158.0(5)
C3	Co1	P2	C17	-127.8(2)	C5	Co1	C2	C1	-37.9(2)
C4	Co1	P2	C15	65.7(2)	C5	Co1	C2	C3	81.8(3)
C4	Co1	P2	C17	-166.4(2)	C5	Co1	C2	C7	-159.3(5)
C5	Co1	P2	C15	34.9(2)	I1	Co1	C3	C2	-66.0(4)
C5	Co1	P2	C17	162.7(2)	I1	Co1	C3	C4	50.5(5)
I1	Co1	C1	C2	-152.4(2)	I1	Co1	C3	C8	170.5(3)
I1	Co1	C1	C5	89.4(2)	P1	Co1	C3	C2	71.7(2)
I1	Co1	C1	C6	-31.0(4)	P1	Co1	C3	C4	-171.9(2)
P1	Co1	C1	C2	-61.6(3)	P1	Co1	C3	C8	-51.8(4)
P1	Co1	C1	C5	-179.8(2)	P2	Co1	C3	C2	168.6(2)
P1	Co1	C1	C6	59.8(4)	P2	Co1	C3	C4	-75.0(2)
P2	Co1	C1	C2	105.9(3)	P2	Co1	C3	C8	45.1(4)
P2	Co1	C1	C5	-12.3(4)	C1	Co1	C3	C2	-36.7(2)
P2	Co1	C1	C6	-132.8(3)	C1	Co1	C3	C4	79.7(3)
C2	Co1	C1	C5	-118.2(4)	C1	Co1	C3	C8	-160.2(4)
C2	Co1	C1	C6	121.3(5)	C2	Co1	C3	C4	116.5(4)
C3	Co1	C1	C2	37.4(2)	C2	Co1	C3	C8	-123.5(5)

Table J.5 Torsional Angles (continued)

Atom1	Atom2	Atom3	Atom4	Angle	continued				
C4	Co1	C3	C2	-116.5(4)	C3	Co1	C5	C10	-159.1(5)
C4	Co1	C3	C8	120.0(5)	C4	Co1	C5	C1	119.3(4)
C5	Co1	C3	C2	-79.9(3)	C4	Co1	C5	C10	-121.4(5)
C5	Co1	C3	C4	36.6(2)	Co1	P1	C11	C12	-128.1(19)
C5	Co1	C3	C8	156.6(4)	Co1	P1	C11	C12A	-160.2(18)
I1	Co1	C4	C3	-161.0(2)	C13	P1	C11	C12	98.6(19)
I1	Co1	C4	C5	-41.6(3)	C13	P1	C11	C12A	66.5(19)
I1	Co1	C4	C9	82.0(5)	Co1	P1	C13	C14	152.8(3)
P1	Co1	C4	C3	14.1(4)	C11	P1	C13	C14	-73.1(4)
P1	Co1	C4	C5	133.5(2)	Co1	P2	C15	C16	-145.1(4)
P1	Co1	C4	C9	-102.9(4)	C17	P2	C15	C16	78.7(5)
P2	Co1	C4	C3	108.7(2)	Co1	P2	C17	C18	-77.0(6)
P2	Co1	C4	C5	-131.9(2)	Co1	P2	C17	C18A	-167.3(7)
P2	Co1	C4	C9	-8.3(4)	C15	P2	C17	C18	55.2(6)
C1	Co1	C4	C3	-82.1(3)	C15	P2	C17	C18A	-35.1(8)
C1	Co1	C4	C5	37.4(2)	Co1	C1	C2	C3	-57.8(3)
C1	Co1	C4	C9	160.9(5)	Co1	C1	C2	C7	131.3(4)
C2	Co1	C4	C3	-38.9(2)	C5	C1	C2	Co1	61.5(3)
C2	Co1	C4	C5	80.5(3)	C5	C1	C2	C3	3.7(5)
C2	Co1	C4	C9	-155.9(5)	C5	C1	C2	C7	-167.1(4)
C3	Co1	C4	C5	119.4(4)	C6	C1	C2	Co1	-125.6(5)
C3	Co1	C4	C9	-117.0(5)	C6	C1	C2	C3	176.6(4)
C5	Co1	C4	C3	-119.4(4)	C6	C1	C2	C7	5.8(7)
C5	Co1	C4	C9	123.6(5)	Co1	C1	C5	C4	59.7(3)
I1	Co1	C5	C1	-93.7(2)	Co1	C1	C5	C10	-126.6(5)
I1	Co1	C5	C4	147.0(2)	C2	C1	C5	Co1	-61.3(3)
I1	Co1	C5	C10	25.6(4)	C2	C1	C5	C4	-1.6(5)
P1	Co1	C5	C1	0.4(4)	C2	C1	C5	C10	172.1(4)
P1	Co1	C5	C4	-118.9(3)	C6	C1	C5	Co1	125.7(5)
P1	Co1	C5	C10	119.7(4)	C6	C1	C5	C4	-174.6(4)
P2	Co1	C5	C1	173.9(2)	C6	C1	C5	C10	-0.9(7)
P2	Co1	C5	C4	54.6(3)	Co1	C2	C3	C4	-63.2(3)
P2	Co1	C5	C10	-66.8(5)	Co1	C2	C3	C8	127.9(4)
C1	Co1	C5	C4	-119.3(4)	C1	C2	C3	Co1	58.9(3)
C1	Co1	C5	C10	119.3(5)	C1	C2	C3	C4	-4.3(5)
C2	Co1	C5	C1	37.7(2)	C1	C2	C3	C8	-173.2(4)
C2	Co1	C5	C4	-81.7(3)	C7	C2	C3	Co1	-130.2(4)
C2	Co1	C5	C10	157.0(5)	C7	C2	C3	C4	166.6(4)
C3	Co1	C5	C1	81.6(3)	C7	C2	C3	C8	-2.4(7)
C3	Co1	C5	C4	-37.8(2)	Co1	C3	C4	C5	-59.8(3)

Table J.5 Torsional Angles (continued)

Atom1	Atom2	Atom3	Atom4	Angle	continued				
Co1	C3	C4	C9	128.7(4)	Co1	C4	C5	C10	127.3(5)
C2	C3	C4	Co1	63.1(3)	C3	C4	C5	Co1	58.0(3)
C2	C3	C4	C5	3.4(5)	C3	C4	C5	C1	-1.1(5)
C2	C3	C4	C9	-168.1(4)	C3	C4	C5	C10	-174.7(4)
C8	C3	C4	Co1	-127.6(4)	C9	C4	C5	Co1	-130.8(5)
C8	C3	C4	C5	172.7(4)	C9	C4	C5	C1	170.1(4)
C8	C3	C4	C9	1.2(7)	C9	C4	C5	C10	-3.5(7)
Co1	C4	C5	C1	-59.1(3)					

Table J.6 Least-Squares Planes

Plane	Coefficients[a]	Defining Atoms with Deviations (Å)[b]			
1	-2.4881 (352) 15.7022 (59) 1.4456 (406) 1.4902 (86)				
		C1	0.0154 (27)	C2	-0.0236 (27)
		C3	0.0226 (27)	C4	-0.0133 (27)
		C5	-0.0012 (27)		
		Co	1.7205 (19)	C6	-0.0841 (84)
		C7	-0.2928 (76)	C8	-0.1350 (78)
		C9	-0.2385 (80)		
		C10	-0.1400 (83)		

Distance: Co–C_{cent} = 1.721 Å (C_{cent} = C1–C2–C3–C4–C5 centroid)

Angles: C_{cent}–Co–Pl = 126.3º, C_{cent}–Co–P2 = 123.5º, C_{cent}–Ru–I1 = 123.9º

[a]Coefficients are for the form $ax+by+cz = d$ where x, y and z are crystallographic coordinates.

[b]Underlined atoms were not included in the definition of the plane.

Table J.7 Anisotropic Displacement Parameters (U_{ij}, Å^2)

Atom	U_{11}	U_{22}	U_{33}	U_{23}	U_{13}	U_{12}
I1	0.04409(18)	0.0564(2)	0.04462(18)	-0.00092(17)	0.01709(15)	0.01498(16)
I2	0.04004(17)	0.0597(2)	0.03345(16)	-0.00504(15)	-0.00079(13)	0.00092(15)
Co1	0.0233(3)	0.0314(3)	0.0269(3)	-0.0017(2)	0.0008(2)	0.0032(2)
P1	0.0344(6)	0.0282(6)	0.0302(6)	-0.0017(5)	-0.0052(5)	0.0033(5)
P2	0.0251(5)	0.0425(7)	0.0299(6)	0.0025(5)	-0.0013(5)	0.0030(5)
C1	0.030(2)	0.032(2)	0.036(2)	0.0013(19)	0.0001(18)	0.0013(18)
C2	0.026(2)	0.024(2)	0.038(2)	-0.0027(18)	-0.0011(18)	0.0024(17)
C3	0.028(2)	0.026(2)	0.032(2)	-0.0048(18)	0.0011(17)	0.0002(17)
C4	0.032(2)	0.029(2)	0.040(2)	-0.0050(19)	-0.004(2)	0.0020(18)
C5	0.027(2)	0.032(2)	0.040(2)	0.001(2)	-0.0012(19)	-0.0005(18)
C6	0.040(3)	0.055(3)	0.038(3)	0.010(2)	0.003(2)	0.001(2)
C7	0.031(2)	0.033(2)	0.050(3)	0.001(2)	-0.008(2)	0.0052(19)
C8	0.035(2)	0.039(3)	0.040(3)	-0.006(2)	0.009(2)	0.001(2)
C9	0.043(3)	0.043(3)	0.040(3)	-0.011(2)	-0.009(2)	-0.002(2)
C10	0.029(2)	0.053(3)	0.058(3)	0.010(3)	-0.001(2)	-0.008(2)
C11	0.076(4)	0.046(3)	0.033(3)	-0.002(2)	-0.017(3)	0.004(3)
C12	0.15(2)	0.071(9)	0.037(7)	-0.023(6)	-0.025(12)	0.012(11)
C12A	0.080(15)	0.079(13)	0.033(8)	-0.002(8)	-0.016(10)	-0.020(11)
C13	0.030(2)	0.033(2)	0.049(3)	-0.003(2)	-0.005(2)	-0.0018(19)
C14	0.047(3)	0.034(3)	0.047(3)	0.003(2)	-0.011(2)	-0.006(2)
C15	0.030(2)	0.053(3)	0.048(3)	0.007(2)	-0.009(2)	0.000(2)
C16	0.052(3)	0.068(4)	0.053(3)	0.008(3)	-0.023(3)	0.002(3)
C17	0.039(3)	0.041(3)	0.065(3)	0.021(3)	-0.008(3)	0.001(2)
C18	0.052(6)	0.037(5)	0.051(6)	-0.002(4)	0.002(5)	0.013(4)
C18A	0.045(6)	0.041(7)	0.078(9)	0.026(6)	-0.022(6)	-0.004(5)

The form of the anisotropic displacement parameter is:
$\exp[-2\pi^2(h^2a^{*2}U_{11} + k^2b^{*2}U_{22} + l^2c^{*2}U_{33} + 2klb^*c^*U_{23} + 2hla^*c^*U_{13} + 2hka^*b^*U_{12})]$

Table J.8 Derived Atomic Coordinates and Displacement Parameters for Hydrogen Atoms

Atom	*x*	*y*	*z*	U_{eq}, Å^2
H6A	0.097999	0.018307	0.318306	0.053
H6B	0.062182	0.111028	0.326737	0.053
H6C	0.156136	0.094696	0.338948	0.053
H7A	0.302622	0.042841	0.226974	0.046
H7B	0.274145	0.107899	0.287919	0.046
H7C	0.317534	0.141266	0.216011	0.046
H8A	0.253892	0.066665	0.038557	0.046
H8B	0.303225	0.131930	0.087270	0.046
H8C	0.237598	0.165250	0.030705	0.046
H9A	0.080660	0.030403	0.017234	0.050
H9B	0.092004	0.128145	0.000014	0.050
H9C	0.010188	0.095322	0.035802	0.050
H10A	-0.027330	0.004112	0.185061	0.056
H10B	-0.054685	0.090424	0.148142	0.056
H10C	-0.040149	0.086097	0.233868	0.056
H11A[a]	0.205363	0.248610	0.334169	0.062
H11B[a]	0.295929	0.272069	0.313003	0.062
H11C[b]	0.190542	0.275019	0.337228	0.062
H11D[b]	0.277228	0.243399	0.313718	0.062
H12A[a]	0.247461	0.365111	0.399196	0.102
H12B[a]	0.265677	0.414223	0.325279	0.102
H12C[a]	0.175121	0.390767	0.346443	0.102
H12D[b]	0.287168	0.344759	0.399509	0.077
H12E[b]	0.326554	0.377744	0.325621	0.077
H12F[b]	0.239182	0.409615	0.349316	0.077
H13A	0.340798	0.267144	0.176973	0.045
H13B	0.289020	0.299699	0.109685	0.045
H14A	0.390789	0.396469	0.136632	0.051
H14B	0.305109	0.439464	0.149974	0.051
H14C	0.357002	0.406837	0.217411	0.051
H15A	-0.037320	0.221952	0.068509	0.052
H15B	-0.049406	0.320816	0.077815	0.052
H16A	-0.088740	0.279473	-0.038989	0.069
H16B	-0.013146	0.341225	-0.044913	0.069
H16C	-0.001034	0.242157	-0.054238	0.069
H17A[c]	0.162437	0.410210	0.097778	0.058
H17B[c]	0.104516	0.420207	0.029548	0.058
H17C[d]	0.091235	0.422204	0.129093	0.058
H17D[d]	0.165689	0.408294	0.076637	0.058

Table J.8 Derived Parameters for Hydrogen Atoms (continued)

Atom	*x*	*y*	*z*	U_{eq}, Å^2
H18A[c]	0.073202	0.511718	0.115880	0.056
H18B[c]	0.000630	0.447214	0.104033	0.056
H18C[c]	0.058836	0.437168	0.172598	0.056
H18D[d]	0.088556	0.515738	0.036854	0.066
H18E[d]	0.086832	0.441572	-0.021672	0.066
H18F[d]	0.011749	0.455600	0.031228	0.066

Refined occupancies of 0.56(5)[a], 0.44(5)[b], 0.533(10)[c] and 0.467(10)[d].

Appendix K – X-ray crystallographic structure report for complex Co-6a

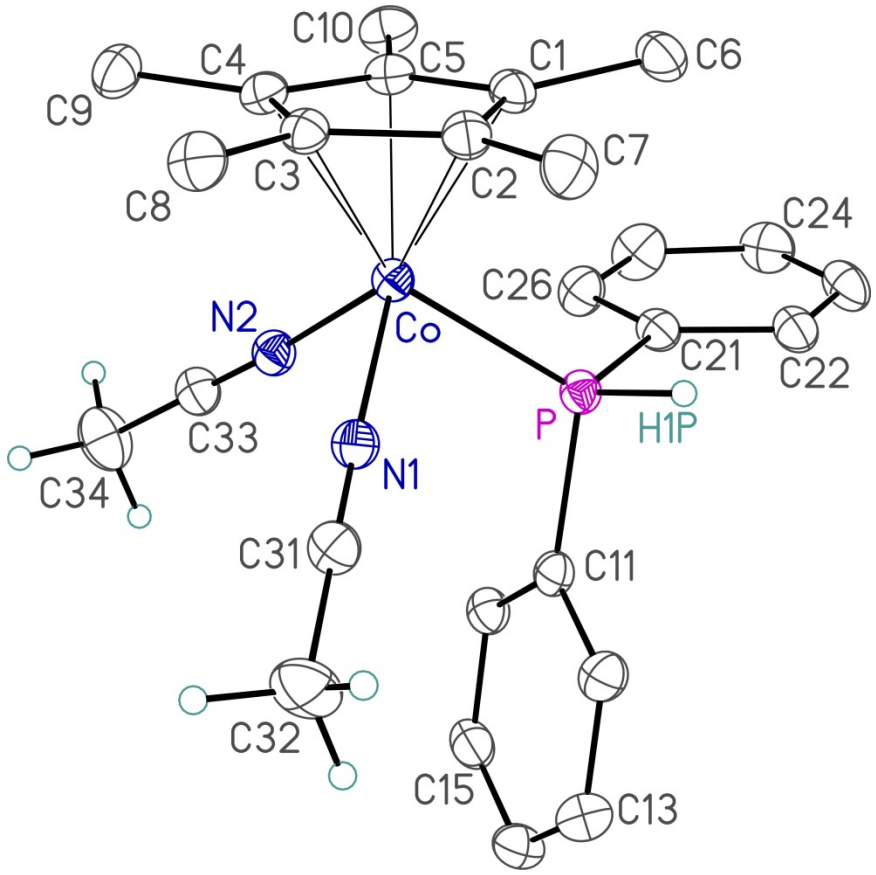

Figure K.1 Perspective view of the $[Co(\eta^5\text{–}Cp^*)(NCCH_3)_2(PPh_2H)]^{2+}$ complex ion showing the atom labelling scheme. Non-hydrogen atoms are represented by Gaussian ellipsoids at the 30% probability level. The hydrogen atom attached to the phosphorus atom and the hydrogens of the acetonitrile ligands are shown with arbitrarily small thermal parameters; all other hydrogens are not shown.

Table K.1 Crystallographic Experimental Details

A. Crystal Data	
formula	$C_{30}H_{38}CoF_{12}N_4PSb_2$
formula weight	1016.04
crystal dimensions (mm)	0.25 × 0.20 × 0.15
crystal system	triclinic
space group	$P\bar{1}$ (No. 2)
unit cell parameters[a]	
a (Å)	9.1591 (4)
b (Å)	11.8767 (5)
c (Å)	18.4531 (8)
α (deg)	97.5581 (5)
β (deg)	99.6645 (5)
γ (deg)	92.1815 (5)
V (Å^3)	1957.93 (15)
Z	2
ρ_{calcd} (g cm^{-3})	1.723
μ (mm^{-1})	1.913
B. Data Collection and Refinement Conditions	
diffractometer	Bruker D8/APEX II CCD[b]
radiation (λ [Å])	graphite-monochromated Mo Kα (0.71073)
temperature (°C)	–100
scan type	ω scans (0.3°) (15 s exposures)
data collection 2θ limit (deg)	56.65
total data collected	18614 (-12 ≤ h ≤ 12, -15 ≤ k ≤ 15, -24 ≤ l ≤ 23)
independent reflections	9531 (R_{int} = 0.0150)
number of observed reflections (*NO*)	8042 [$F_o^2 \geq 2\sigma(F_o^2)$]
structure solution method	Patterson/structure expansion (*DIRDIF–2008*[c])
refinement method	full-matrix least-squares on F^2 (*SHELXL–2014*[d])
absorption correction method	Gaussian integration (face-indexed)
range of transmission factors	0.7971–0.6810
data/restraints/parameters	9531 / 0 / 545
goodness-of-fit (S)[e] [all data]	1.052
final R indices[f]	
R_1 [$F_o^2 \geq 2\sigma(F_o^2)$]	0.0341
wR_2 [all data]	0.0959
largest difference peak and hole	1.233 and –0.946 e Å^{-3}

[a]Obtained from least-squares refinement of 9908 reflections with 4.40° < 2θ < 50.14°.

(continued)

Table K.1 Crystallographic Experimental Details (continued)

[b]Programs for diffractometer operation, data collection, data reduction and absorption correction were those supplied by Bruker.

[c]Beurskens, P. T.; Beurskens, G.; de Gelder, R.; Smits, J. M. M.; Garcia-Granda, S.; Gould, R. O. (2008). The *DIRDIF-2008* program system. Crystallography Laboratory, Radboud University Nijmegen, The Netherlands.

[d]Sheldrick, G. M. *Acta Crystallogr.* **2015**, *C71*, 3–8.

[e]$S = [\Sigma w(F_o^2 - F_c^2)^2/(n - p)]^{1/2}$ (n = number of data; p = number of parameters varied; $w = [\sigma^2(F_o^2) + (0.0520P)^2 + 0.9943P]^{-1}$ where $P = [\text{Max}(F_o^2, 0) + 2F_c^2]/3$).

[f]$R_1 = \Sigma||F_o| - |F_c||/\Sigma|F_o|$; $wR_2 = [\Sigma w(F_o^2 - F_c^2)^2/\Sigma w(F_o^4)]^{1/2}$.

Table K.2 Atomic Coordinates and Equivalent Isotropic Displacement Parameters

(a) atoms of the $[(\eta^5\text{–}C_5Me_5)Co(NCMe)_2(PPh_2H)]^{2+}$ ion

Atom	*x*	*y*	*z*	U_{eq}, Å^2
Co	0.17160(3)	0.21235(3)	0.31960(2)	0.02624(8)*
P	0.12854(7)	0.20505(5)	0.19627(3)	0.02884(13)*
N1	0.3251(2)	0.32966(19)	0.32439(12)	0.0327(4)*
N2	0.3113(2)	0.09455(19)	0.31992(12)	0.0328(4)*
C1	-0.0560(3)	0.2146(2)	0.32053(14)	0.0328(5)*
C2	0.0206(3)	0.3183(2)	0.35839(14)	0.0329(5)*
C3	0.1220(3)	0.2910(2)	0.42160(14)	0.0305(5)*
C4	0.1129(3)	0.1723(2)	0.41991(14)	0.0318(5)*
C5	0.0062(3)	0.1232(2)	0.35579(14)	0.0325(5)*
C6	-0.1890(3)	0.2050(3)	0.25968(16)	0.0442(7)*
C7	-0.0095(4)	0.4352(2)	0.34124(18)	0.0448(7)*
C8	0.2164(3)	0.3747(2)	0.47941(16)	0.0420(6)*
C9	0.1939(3)	0.1073(3)	0.47618(16)	0.0430(6)*
C10	-0.0420(3)	-0.0002(2)	0.33701(17)	0.0441(7)*
C11	0.2947(3)	0.2153(2)	0.15609(13)	0.0315(5)*
C12	0.3424(3)	0.3192(2)	0.13860(16)	0.0404(6)*
C13	0.4688(4)	0.3275(3)	0.10671(19)	0.0512(8)*
C14	0.5471(3)	0.2322(3)	0.09220(18)	0.0491(7)*
C15	0.5015(3)	0.1286(3)	0.11022(16)	0.0422(6)*
C16	0.3750(3)	0.1201(2)	0.14278(14)	0.0348(5)*
C21	0.0120(3)	0.0900(2)	0.13844(14)	0.0328(5)*
C22	-0.0891(3)	0.1133(3)	0.07794(15)	0.0374(6)*
C23	-0.1783(3)	0.0251(3)	0.03326(16)	0.0461(7)*
C24	-0.1660(4)	-0.0849(3)	0.04784(17)	0.0509(8)*
C25	-0.0618(4)	-0.1089(3)	0.10661(18)	0.0529(8)*
C26	0.0268(3)	-0.0213(2)	0.15247(16)	0.0419(6)*
C31	0.4147(3)	0.4000(2)	0.32636(15)	0.0371(6)*
C32	0.5297(4)	0.4891(3)	0.3281(2)	0.0568(9)*
C33	0.3997(3)	0.0298(2)	0.32692(15)	0.0368(6)*
C34	0.5134(4)	-0.0512(3)	0.3365(2)	0.0578(9)*
H1P	0.064(4)	0.288(3)	0.1760(18)	0.046(9)

(b) atoms of the hexfluoroantimonate ions

Atom	*x*	*y*	*z*	U_{eq}, Å^2
Sb1	0.28287(2)	0.74671(2)	0.49124(2)	0.03790(7)*
F11A[a]	0.4683(5)	0.8182(6)	0.5160(4)	0.122(2)*
F12A[a]	0.0976(5)	0.6759(5)	0.4672(3)	0.1042(18)*
F13A[a]	0.2494(7)	0.8223(4)	0.4085(2)	0.0979(16)*
F14A[a]	0.3119(7)	0.6761(6)	0.5741(3)	0.118(2)*

Table K.2 Atomic Coordinates and Displacement Parameters (continued)

Atom	*x*	*y*	*z*	U_{eq}, Å^2
F15A[a]	0.3565(7)	0.6290(4)	0.4353(4)	0.111(3)*
F16A[a]	0.2090(6)	0.8677(3)	0.5452(3)	0.0769(15)*
F11B[b,c]	0.4463(14)	0.6781(19)	0.5241(10)	0.209(6)*
F12B[b,c]	0.1122(14)	0.8076(19)	0.4636(10)	0.209(6)*
F13B[b,c]	0.387(2)	0.8505(7)	0.4572(12)	0.183(7)*
F14B[b,c]	0.178(2)	0.6417(7)	0.5308(12)	0.183(7)*
F15B[b,c]	0.280(2)	0.6428(16)	0.4100(9)	0.197(8)*
F16B[b,c]	0.2888(19)	0.8401(16)	0.5773(8)	0.197(8)*
Sb2A[d]	0.36097(19)	0.71335(14)	0.13588(11)	0.0590(3)*
F21A[d]	0.4594(18)	0.6189(11)	0.0752(7)	0.131(5)*
F22A[d]	0.2822(18)	0.8161(11)	0.1971(8)	0.127(4)*
F23A[d]	0.5239(14)	0.7136(12)	0.2084(6)	0.203(6)*
F24A[d]	0.2084(9)	0.7168(7)	0.0595(4)	0.118(2)*
F25A[d]	0.2792(17)	0.5910(5)	0.1631(8)	0.177(4)*
F26A[d]	0.4425(12)	0.8391(6)	0.1013(8)	0.155(3)*
Sb2B[c,e]	0.3799(4)	0.7187(3)	0.13254(18)	0.0922(9)*
F21B[c,e]	0.435(2)	0.6173(15)	0.0565(10)	0.086(3)*
F22B[c,e]	0.289(2)	0.8086(14)	0.2094(11)	0.086(3)*
F23B[c,e]	0.415(3)	0.6158(16)	0.1979(7)	0.192(7)*
F24B[c,e]	0.326(3)	0.8140(15)	0.0703(7)	0.192(7)*
F25B[c,e]	0.1753(15)	0.6490(19)	0.1046(11)	0.194(6)*
F26B[c,e]	0.5477(19)	0.7910(19)	0.1618(11)	0.194(6)*

(c) solvent acetonitrile atoms

Atom	*x*	*y*	*z*	U_{eq}, Å^2
N1S	0.8744(5)	0.4304(3)	0.1334(2)	0.0868(11)*
C1S	0.8480(5)	0.4905(3)	0.0912(3)	0.0720(11)*
C2S	0.8142(8)	0.5682(4)	0.0374(3)	0.120(2)*
N2S	0.2350(8)	0.2814(6)	0.6525(4)	0.140(2)*
C3S	0.1484(10)	0.2903(5)	0.6911(3)	0.114(3)*
C4S	0.0320(11)	0.3007(5)	0.7361(4)	0.163(4)*

Anisotropically-refined atoms are marked with an asterisk (*). The form of the anisotropic displacement parameter is: $\exp[-2\pi^2(h^2a^{*2}U_{11} + k^2b^{*2}U_{22} + l^2c^{*2}U_{33} + 2klb^*c^*U_{23} + 2hla^*c^*U_{13} + 2hka^*b^*U_{12})]$. [a]Refined with an occupancy factor of 0.65. [b]Refined with an occupancy factor of 0.35. [c]The following pairs of atoms were refined with common anisotropic displacement parameters: {F11B, F12B}, {F13B, F14B}, {F15B, F16B}, {F21B, F22B}, {F23B, F24B}, {F25B, F26B}. [d]Refined with an occupancy factor of 0.6. [e]Refined with an occupancy factor of 0.4.

Table K.3 Selected Interatomic Distances (Å)

(a) atoms of the $[(\eta^5\text{–}C_5Me_5)Co(NCMe)_2(PPh_2H)]^{2+}$ *ion*

Atom1	Atom2	Distance	Atom1	Atom2	Distance
Co	P	2.2330(7)	C3	C8	1.490(4)
Co	N1	1.924(2)	C4	C5	1.443(4)
Co	N2	1.931(2)	C4	C9	1.491(4)
Co	C1	2.089(2)	C5	C10	1.493(4)
Co	C2	2.058(2)	C11	C12	1.389(4)
Co	C3	2.116(2)	C11	C16	1.390(4)
Co	C4	2.119(2)	C12	C13	1.390(4)
Co	C5	2.065(2)	C13	C14	1.384(5)
P	C11	1.808(3)	C14	C15	1.383(5)
P	C21	1.807(3)	C15	C16	1.398(4)
P	H1P	1.23(3)	C21	C22	1.391(4)
N1	C31	1.141(3)	C21	C26	1.388(4)
N2	C33	1.141(3)	C22	C23	1.388(4)
C1	C2	1.429(4)	C23	C24	1.373(5)
C1	C5	1.426(4)	C24	C25	1.387(5)
C1	C6	1.502(4)	C25	C26	1.389(4)
C2	C3	1.444(4)	C31	C32	1.458(4)
C2	C7	1.490(4)	C33	C34	1.450(4)
C3	C4	1.405(3)			

(b) within the hexfluoroantimonate ions

Atom1	Atom2	Distance	Atom1	Atom2	Distance
Sb1	F11A	1.828(4)	Sb2A	F21A	1.847(13)
Sb1	F12A	1.823(3)	Sb2A	F22A	1.807(14)
Sb1	F13A	1.859(4)	Sb2A	F23A	1.829(7)
Sb1	F14A	1.824(4)	Sb2A	F24A	1.816(6)
Sb1	F15A	1.844(4)	Sb2A	F25A	1.777(7)
Sb1	F16A	1.854(4)	Sb2A	F26A	1.876(8)
Sb1	F11B	1.786(9)	Sb2B	F21B	1.876(19)
Sb1	F12B	1.773(9)	Sb2B	F22B	1.98(2)
Sb1	F13B	1.771(8)	Sb2B	F23B	1.828(11)
Sb1	F14B	1.843(8)	Sb2B	F24B	1.742(10)
Sb1	F15B	1.807(11)	Sb2B	F25B	1.977(11)
Sb1	F16B	1.805(10)	Sb2B	F26B	1.700(12)

(c) within the solvent acetonitrile molecules

Atom1	Atom2	Distance	Atom1	Atom2	Distance
N1S	C1S	1.127(5)	N2S	C3S	1.151(10)
C1S	C2S	1.445(6)	C3S	C4S	1.456(11)

Table K.4 Selected Interatomic Angles (deg)

(a) atoms of the $[(\eta^5\text{–}C_5Me_5)Co(NCMe)_2(PPh_2H)]^{2+}$ *ion*

Atom1	Atom2	Atom3	Angle	Atom1	Atom2	Atom3	Angle
P	Co	N1	88.53(7)	C2	C1	C5	108.0(2)
P	Co	N2	94.56(7)	C2	C1	C6	125.7(3)
P	Co	C1	90.16(7)	C5	C1	C6	126.0(3)
P	Co	C2	106.10(8)	Co	C2	C1	71.00(14)
P	Co	C3	146.06(7)	Co	C2	C3	71.95(14)
P	Co	C4	151.89(7)	Co	C2	C7	127.6(2)
P	Co	C5	111.57(8)	C1	C2	C3	107.7(2)
N1	Co	N2	92.30(9)	C1	C2	C7	126.5(2)
N1	Co	C1	133.36(10)	C3	C2	C7	125.5(2)
N1	Co	C2	96.02(10)	Co	C3	C2	67.60(14)
N1	Co	C3	89.84(9)	Co	C3	C4	70.71(14)
N1	Co	C4	118.79(9)	Co	C3	C8	128.49(19)
N1	Co	C5	156.85(10)	C2	C3	C4	108.0(2)
N2	Co	C1	134.24(10)	C2	C3	C8	125.8(2)
N2	Co	C2	157.86(10)	C4	C3	C8	126.2(2)
N2	Co	C3	119.38(10)	Co	C4	C3	70.54(14)
N2	Co	C4	91.03(10)	Co	C4	C5	67.86(14)
N2	Co	C5	97.21(10)	Co	C4	C9	129.40(19)
C1	Co	C2	40.30(10)	C3	C4	C5	108.5(2)
C1	Co	C3	66.96(10)	C3	C4	C9	126.3(2)
C1	Co	C4	66.74(10)	C5	C4	C9	125.1(2)
C1	Co	C5	40.14(10)	Co	C5	C1	70.80(14)
C2	Co	C3	40.45(10)	Co	C5	C4	71.82(14)
C2	Co	C4	66.99(10)	Co	C5	C10	128.71(19)
C2	Co	C5	68.11(10)	C1	C5	C4	107.5(2)
C3	Co	C4	38.75(10)	C1	C5	C10	127.1(2)
C3	Co	C5	67.09(10)	C4	C5	C10	124.9(2)
C4	Co	C5	40.33(10)	P	C11	C12	119.7(2)
Co	P	C11	114.03(8)	P	C11	C16	120.5(2)
Co	P	C21	120.43(9)	C12	C11	C16	119.9(2)
Co	P	H1P	112.4(15)	C11	C12	C13	120.1(3)
C11	P	C21	105.82(12)	C12	C13	C14	120.0(3)
C11	P	H1P	101.4(15)	C13	C14	C15	120.4(3)
C21	P	H1P	100.3(15)	C14	C15	C16	119.8(3)
Co	N1	C31	178.9(2)	C11	C16	C15	119.9(3)
Co	N2	C33	173.3(2)	P	C21	C22	119.5(2)
Co	C1	C2	68.70(14)	P	C21	C26	120.4(2)
Co	C1	C5	69.06(14)	C22	C21	C26	120.0(3)
Co	C1	C6	132.63(19)	C21	C22	C23	119.6(3)
C22	C23	C24	120.5(3)	C21	C26	C25	119.6(3)
C23	C24	C25	120.0(3)	N1	C31	C32	179.3(3)
C24	C25	C26	120.1(3)	N2	C33	C34	179.2(3)

Table K.4 Selected Interatomic Angles (continued)

(b) within the hexfluoroantimonate ions

Atom1	Atom2	Atom3	Angle	Atom1	Atom2	Atom3	Angle
F11A	Sb1	F12A	179.6(2)	F21A	Sb2A	F22A	173.8(6)
F11A	Sb1	F13A	88.8(3)	F21A	Sb2A	F23A	86.9(5)
F11A	Sb1	F14A	91.6(4)	F21A	Sb2A	F24A	90.7(5)
F11A	Sb1	F15A	90.1(3)	F21A	Sb2A	F25A	89.1(5)
F11A	Sb1	F16A	89.6(3)	F21A	Sb2A	F26A	89.1(6)
F12A	Sb1	F13A	91.4(3)	F22A	Sb2A	F23A	89.4(5)
F12A	Sb1	F14A	88.2(3)	F22A	Sb2A	F24A	92.7(5)
F12A	Sb1	F15A	90.3(3)	F22A	Sb2A	F25A	96.0(6)
F12A	Sb1	F16A	90.0(2)	F22A	Sb2A	F26A	86.1(6)
F13A	Sb1	F14A	178.0(2)	F23A	Sb2A	F24A	175.7(6)
F13A	Sb1	F15A	89.4(3)	F23A	Sb2A	F25A	91.2(6)
F13A	Sb1	F16A	88.9(2)	F23A	Sb2A	F26A	91.5(6)
F14A	Sb1	F15A	92.6(3)	F24A	Sb2A	F25A	92.3(5)
F14A	Sb1	F16A	89.1(2)	F24A	Sb2A	F26A	84.9(4)
F15A	Sb1	F16A	178.3(2)	F25A	Sb2A	F26A	176.6(5)
F11B	Sb1	F12B	174.9(7)	F21B	Sb2B	F22B	170.0(7)
F11B	Sb1	F13B	91.9(9)	F21B	Sb2B	F23B	91.3(7)
F11B	Sb1	F14B	87.4(9)	F21B	Sb2B	F24B	90.6(7)
F11B	Sb1	F15B	82.2(9)	F21B	Sb2B	F25B	88.9(7)
F11B	Sb1	F16B	94.3(10)	F21B	Sb2B	F26B	97.2(7)
F12B	Sb1	F13B	93.1(9)	F22B	Sb2B	F23B	86.3(7)
F12B	Sb1	F14B	87.6(8)	F22B	Sb2B	F24B	90.8(7)
F12B	Sb1	F15B	98.8(10)	F22B	Sb2B	F25B	81.2(6)
F12B	Sb1	F16B	84.3(9)	F22B	Sb2B	F26B	92.7(7)
F13B	Sb1	F14B	177.5(10)	F23B	Sb2B	F24B	174.0(11)
F13B	Sb1	F15B	93.3(8)	F23B	Sb2B	F25B	87.4(10)
F13B	Sb1	F16B	90.6(8)	F23B	Sb2B	F26B	94.2(11)
F14B	Sb1	F15B	89.0(8)	F24B	Sb2B	F25B	86.9(10)
F14B	Sb1	F16B	87.1(7)	F24B	Sb2B	F26B	91.2(11)
F15B	Sb1	F16B	174.8(10)	F25B	Sb2B	F26B	173.6(7)

(c) within the solvent acetonitrile molecules

Atom1	Atom2	Atom3	Angle	Atom1	Atom2	Atom3	Angle
N1S	C1S	C2S	179.6(5)	N2S	C3S	C4S	176.6(8)

Table K.5 Torsional Angles (deg)

Atom1	Atom2	Atom3	Atom4	Angle	continued				
N1	Co	P	C11	40.75(12)	N2	Co	C2	C3	28.8(3)
N1	Co	P	C21	168.21(12)	N2	Co	C2	C7	150.2(3)
N2	Co	P	C11	-51.44(12)	C1	Co	C2	C3	116.8(2)
N2	Co	P	C21	76.02(12)	C1	Co	C2	C7	-121.9(3)
C1	Co	P	C11	174.12(12)	C3	Co	C2	C1	-116.8(2)
C1	Co	P	C21	-58.42(12)	C3	Co	C2	C7	121.3(3)
C2	Co	P	C11	136.59(12)	C4	Co	C2	C1	-80.65(16)
C2	Co	P	C21	-95.95(13)	C4	Co	C2	C3	36.12(14)
C3	Co	P	C11	128.29(15)	C4	Co	C2	C7	157.5(3)
C3	Co	P	C21	-104.26(16)	C5	Co	C2	C1	-36.86(15)
C4	Co	P	C11	-152.26(18)	C5	Co	C2	C3	79.90(16)
C4	Co	P	C21	-24.80(19)	C5	Co	C2	C7	-158.8(3)
C5	Co	P	C11	-151.05(12)	P	Co	C3	C2	12.4(2)
C5	Co	P	C21	-23.60(13)	P	Co	C3	C4	132.26(14)
P	Co	C1	C2	-115.18(14)	P	Co	C3	C8	-106.3(2)
P	Co	C1	C5	124.53(14)	N1	Co	C3	C2	99.49(15)
P	Co	C1	C6	4.3(3)	N1	Co	C3	C4	-140.60(15)
N1	Co	C1	C2	-27.0(2)	N1	Co	C3	C8	-19.2(2)
N1	Co	C1	C5	-147.34(15)	N2	Co	C3	C2	-167.96(14)
N1	Co	C1	C6	92.5(3)	N2	Co	C3	C4	-48.05(17)
N2	Co	C1	C2	148.28(15)	N2	Co	C3	C8	73.3(3)
N2	Co	C1	C5	28.0(2)	C1	Co	C3	C2	-38.86(15)
N2	Co	C1	C6	-92.2(3)	C1	Co	C3	C4	81.05(16)
C2	Co	C1	C5	-120.3(2)	C1	Co	C3	C8	-157.6(3)
C2	Co	C1	C6	119.5(3)	C2	Co	C3	C4	119.9(2)
C3	Co	C1	C2	39.01(15)	C2	Co	C3	C8	-118.7(3)
C3	Co	C1	C5	-81.27(16)	C4	Co	C3	C2	-119.9(2)
C3	Co	C1	C6	158.5(3)	C4	Co	C3	C8	121.4(3)
C4	Co	C1	C2	81.32(16)	C5	Co	C3	C2	-82.63(16)
C4	Co	C1	C5	-38.97(15)	C5	Co	C3	C4	37.28(15)
C4	Co	C1	C6	-159.2(3)	C5	Co	C3	C8	158.7(3)
C5	Co	C1	C2	120.3(2)	P	Co	C4	C3	-118.72(17)
C5	Co	C1	C6	-120.2(3)	P	Co	C4	C5	1.7(2)
P	Co	C2	C1	70.37(15)	P	Co	C4	C9	119.8(2)
P	Co	C2	C3	-172.86(13)	N1	Co	C4	C3	46.40(17)
P	Co	C2	C7	-51.5(3)	N1	Co	C4	C5	166.85(14)
N1	Co	C2	C1	160.58(15)	N1	Co	C4	C9	-75.1(3)
N1	Co	C2	C3	-82.65(15)	N2	Co	C4	C3	139.59(15)
N1	Co	C2	C7	38.7(3)	N2	Co	C4	C5	-99.96(15)
N2	Co	C2	C1	-87.9(3)	N2	Co	C4	C9	18.1(2)

Table K.5 Torsional Angles (continued)

Atom1	Atom2	Atom3	Atom4	Angle	continued				
C1	Co	C4	C3	-81.66(16)	C5	C1	C2	C3	-5.0(3)
C1	Co	C4	C5	38.79(15)	C5	C1	C2	C7	-178.8(3)
C1	Co	C4	C9	156.8(3)	C6	C1	C2	Co	-128.0(3)
C2	Co	C4	C3	-37.66(15)	C6	C1	C2	C3	169.0(2)
C2	Co	C4	C5	82.79(16)	C6	C1	C2	C7	-4.8(4)
C2	Co	C4	C9	-159.2(3)	Co	C1	C5	C4	62.83(17)
C3	Co	C4	C5	120.5(2)	Co	C1	C5	C10	-124.5(3)
C3	Co	C4	C9	-121.5(3)	C2	C1	C5	Co	-57.77(17)
C5	Co	C4	C3	-120.5(2)	C2	C1	C5	C4	5.1(3)
C5	Co	C4	C9	118.0(3)	C2	C1	C5	C10	177.7(2)
P	Co	C5	C1	-62.36(15)	C6	C1	C5	Co	128.2(3)
P	Co	C5	C4	-179.13(12)	C6	C1	C5	C4	-169.0(2)
P	Co	C5	C10	60.3(3)	C6	C1	C5	C10	3.7(4)
N1	Co	C5	C1	86.3(3)	Co	C2	C3	C4	-59.35(17)
N1	Co	C5	C4	-30.5(3)	Co	C2	C3	C8	122.2(3)
N1	Co	C5	C10	-151.0(3)	C1	C2	C3	Co	62.40(17)
N2	Co	C5	C1	-160.19(15)	C1	C2	C3	C4	3.0(3)
N2	Co	C5	C4	83.04(15)	C1	C2	C3	C8	-175.4(2)
N2	Co	C5	C10	-37.5(3)	C7	C2	C3	Co	-123.7(3)
C1	Co	C5	C4	-116.8(2)	C7	C2	C3	C4	176.9(2)
C1	Co	C5	C10	122.7(3)	C7	C2	C3	C8	-1.5(4)
C2	Co	C5	C1	37.00(15)	Co	C3	C4	C5	-57.34(17)
C2	Co	C5	C4	-79.77(16)	Co	C3	C4	C9	125.2(3)
C2	Co	C5	C10	159.7(3)	C2	C3	C4	Co	57.42(17)
C3	Co	C5	C1	80.91(16)	C2	C3	C4	C5	0.1(3)
C3	Co	C5	C4	-35.86(14)	C2	C3	C4	C9	-177.4(2)
C3	Co	C5	C10	-156.4(3)	C8	C3	C4	Co	-124.1(3)
C4	Co	C5	C1	116.8(2)	C8	C3	C4	C5	178.5(2)
C4	Co	C5	C10	-120.6(3)	C8	C3	C4	C9	1.0(4)
Co	P	C11	C12	-98.4(2)	Co	C4	C5	C1	-62.17(17)
Co	P	C11	C16	81.4(2)	Co	C4	C5	C10	125.0(3)
C21	P	C11	C12	126.9(2)	C3	C4	C5	Co	58.99(17)
C21	P	C11	C16	-53.3(2)	C3	C4	C5	C1	-3.2(3)
Co	P	C21	C22	138.71(18)	C3	C4	C5	C10	-176.0(2)
Co	P	C21	C26	-43.7(2)	C9	C4	C5	Co	-123.5(3)
C11	P	C21	C22	-90.2(2)	C9	C4	C5	C1	174.4(2)
C11	P	C21	C26	87.4(2)	C9	C4	C5	C10	1.5(4)
Co	C1	C2	C3	-63.01(17)	P	C11	C12	C13	-179.1(2)
Co	C1	C2	C7	123.2(3)	C16	C11	C12	C13	1.1(4)
C5	C1	C2	Co	57.99(17)	P	C11	C16	C15	178.6(2)

Table K.5 Torsional Angles (continued)

Atom1	Atom2	Atom3	Atom4	Angle	continued				
C12	C11	C16	C15	-1.5(4)	P	C21	C26	C25	-178.8(2)
C11	C12	C13	C14	0.1(5)	C22	C21	C26	C25	-1.2(4)
C12	C13	C14	C15	-0.9(5)	C21	C22	C23	C24	-0.9(4)
C13	C14	C15	C16	0.5(5)	C22	C23	C24	C25	-1.4(5)
C14	C15	C16	C11	0.7(4)	C23	C24	C25	C26	2.3(5)
P	C21	C22	C23	179.8(2)	C24	C25	C26	C21	-1.0(5)
C26	C21	C22	C23	2.1(4)					

Table K.6 Least-Squares Planes

Plane	Coefficients[a]			Defining Atoms with Deviations (Å)[b]			
1	-7.539(7)	0.392(15)					
	12.773(17)	4.571(7)					
				C1	0.0298(16)	C2	-0.0237(16)
				C3	0.0087(15)	C4	0.0095(15)
				C5	-0.0242(15)		
				Co	-1.6989(11)	C6	0.252(5)
				C7	0.030(5)	C8	0.069(5)
				C9	0.092(5)	C10	0.051(5)

Distance: Co–C_{cent} = 1.700 Å (C_{cent} = C1–C2–C3–C4–C5 centroid)

Angles: C_{cent}–Co–P = 125.7º, C_{cent}–Ru–N1 = 122.5º, C_{cent}–Ru–N2 = 123.6º

[a]Coefficients are for the form $ax+by+cz = d$ where x, y and z are crystallographic coordinates.

[b]Underlined atoms were <u>not</u> included in the definition of the plane.

Table K.7 Anisotropic Displacement Parameters (U_{ij}, Å^2)

Atom	U_{11}	U_{22}	U_{33}	U_{23}	U_{13}	U_{12}
Co	0.02708(16)	0.02526(16)	0.02521(16)	0.00045(12)	0.00374(12)	0.00091(12)
P	0.0291(3)	0.0306(3)	0.0260(3)	0.0019(2)	0.0036(2)	0.0032(2)
N1	0.0335(11)	0.0341(11)	0.0285(11)	0.0005(9)	0.0038(8)	-0.0005(9)
N2	0.0330(11)	0.0350(11)	0.0291(11)	0.0014(9)	0.0041(8)	0.0019(9)
C1	0.0280(12)	0.0400(14)	0.0299(12)	0.0004(10)	0.0070(10)	0.0041(10)
C2	0.0340(13)	0.0347(13)	0.0300(13)	0.0006(10)	0.0078(10)	0.0065(10)
C3	0.0317(12)	0.0313(12)	0.0285(12)	0.0007(10)	0.0081(10)	0.0029(9)
C4	0.0342(12)	0.0340(13)	0.0284(12)	0.0038(10)	0.0097(10)	0.0006(10)
C5	0.0330(12)	0.0325(13)	0.0329(13)	0.0022(10)	0.0113(10)	-0.0007(10)
C6	0.0302(13)	0.0621(19)	0.0374(15)	-0.0002(13)	0.0029(11)	0.0021(12)
C7	0.0510(17)	0.0378(15)	0.0467(17)	0.0062(12)	0.0089(13)	0.0144(12)
C8	0.0471(16)	0.0396(15)	0.0348(14)	-0.0065(11)	0.0055(12)	-0.0053(12)
C9	0.0492(16)	0.0442(16)	0.0378(15)	0.0135(12)	0.0071(12)	0.0066(13)
C10	0.0492(16)	0.0357(14)	0.0467(16)	0.0002(12)	0.0137(13)	-0.0093(12)
C11	0.0319(12)	0.0369(13)	0.0246(12)	0.0032(10)	0.0022(9)	0.0021(10)
C12	0.0421(15)	0.0381(14)	0.0429(15)	0.0115(12)	0.0080(12)	0.0038(11)
C13	0.0471(17)	0.0583(19)	0.0526(19)	0.0196(16)	0.0130(14)	-0.0026(14)
C14	0.0334(14)	0.070(2)	0.0459(17)	0.0114(15)	0.0114(13)	0.0013(13)
C15	0.0324(13)	0.0556(17)	0.0365(15)	0.0012(13)	0.0030(11)	0.0072(12)
C16	0.0348(13)	0.0370(13)	0.0312(13)	0.0014(10)	0.0037(10)	0.0042(10)
C21	0.0298(12)	0.0388(13)	0.0281(12)	-0.0025(10)	0.0055(10)	0.0021(10)
C22	0.0323(13)	0.0460(15)	0.0319(13)	-0.0015(11)	0.0048(10)	0.0058(11)
C23	0.0332(14)	0.065(2)	0.0339(14)	-0.0100(13)	0.0000(11)	0.0053(13)
C24	0.0486(17)	0.058(2)	0.0377(16)	-0.0135(14)	0.0026(13)	-0.0110(14)
C25	0.068(2)	0.0400(16)	0.0455(18)	-0.0042(13)	0.0042(15)	-0.0081(15)
C26	0.0472(16)	0.0402(15)	0.0356(14)	0.0016(12)	0.0028(12)	-0.0019(12)
C31	0.0387(14)	0.0349(13)	0.0365(14)	0.0023(11)	0.0052(11)	0.0001(11)
C32	0.0479(18)	0.0469(18)	0.072(2)	0.0051(17)	0.0071(16)	-0.0165(15)
C33	0.0360(13)	0.0374(14)	0.0356(14)	0.0013(11)	0.0045(11)	0.0042(11)
C34	0.0506(18)	0.0497(18)	0.069(2)	0.0006(16)	0.0018(16)	0.0182(15)
Sb1	0.03654(11)	0.03412(11)	0.04362(12)	0.00204(8)	0.01139(8)	0.00167(7)
F11A	0.057(2)	0.164(6)	0.129(4)	-0.033(4)	0.027(3)	-0.055(3)
F12A	0.058(2)	0.126(4)	0.114(4)	-0.049(3)	0.037(2)	-0.048(3)
F13A	0.150(4)	0.098(3)	0.061(2)	0.038(2)	0.034(3)	0.044(3)
F14A	0.136(4)	0.144(5)	0.102(4)	0.083(4)	0.039(3)	0.052(4)
F15A	0.139(5)	0.0387(19)	0.184(7)	-0.001(3)	0.119(5)	0.019(3)
F16A	0.121(4)	0.0330(15)	0.092(4)	-0.0001(18)	0.069(3)	0.009(2)
F11B[a]	0.100(6)	0.349(18)	0.226(12)	0.155(13)	0.055(7)	0.127(9)
F12B[a]	0.100(6)	0.349(18)	0.226(12)	0.155(13)	0.055(7)	0.127(9)
F13B[a]	0.288(14)	0.039(3)	0.298(15)	0.033(6)	0.259(13)	0.022(6)

Table K.7 Anisotropic Displacement Parameters (continued)

Atom	U_{11}	U_{22}	U_{33}	U_{23}	U_{13}	U_{12}
F14B[a]	0.288(14)	0.039(3)	0.298(15)	0.033(6)	0.259(13)	0.022(6)
F15B[a]	0.208(13)	0.236(14)	0.123(8)	-0.128(9)	0.109(9)	-0.120(10)
F16B[a]	0.208(13)	0.236(14)	0.123(8)	-0.128(9)	0.109(9)	-0.120(10)
Sb2A	0.0772(4)	0.0321(4)	0.0601(8)	0.0020(4)	-0.0081(4)	0.0115(3)
F21A	0.196(10)	0.102(5)	0.091(8)	-0.014(5)	0.020(7)	0.085(6)
F22A	0.194(8)	0.115(6)	0.061(5)	-0.012(4)	-0.008(4)	0.096(6)
F23A	0.193(9)	0.185(9)	0.172(9)	-0.066(7)	-0.098(7)	0.127(8)
F24A	0.126(5)	0.113(5)	0.089(4)	-0.027(3)	-0.029(4)	0.030(4)
F25A	0.293(13)	0.054(3)	0.221(11)	0.044(5)	0.129(9)	0.034(6)
F26A	0.167(8)	0.061(3)	0.235(11)	0.018(5)	0.033(7)	-0.002(4)
Sb2B	0.167(2)	0.0636(13)	0.0451(9)	0.0068(8)	0.0054(12)	0.0528(12)
F21B[a]	0.123(6)	0.069(4)	0.060(5)	-0.005(3)	0.009(4)	0.008(5)
F22B[a]	0.123(6)	0.069(4)	0.060(5)	-0.005(3)	0.009(4)	0.008(5)
F23B[a]	0.364(19)	0.156(11)	0.085(5)	0.065(6)	0.055(9)	0.155(13)
F24B[a]	0.364(19)	0.156(11)	0.085(5)	0.065(6)	0.055(9)	0.155(13)
F25B[a]	0.128(7)	0.227(13)	0.198(12)	-0.111(10)	0.076(8)	-0.068(8)
F26B[a]	0.128(7)	0.227(13)	0.198(12)	-0.111(10)	0.076(8)	-0.068(8)
N1S	0.094(3)	0.068(2)	0.094(3)	0.025(2)	-0.010(2)	0.012(2)
C1S	0.078(3)	0.0431(19)	0.083(3)	0.0060(19)	-0.019(2)	0.0015(18)
C2S	0.180(6)	0.056(3)	0.101(4)	0.022(3)	-0.043(4)	-0.008(3)
N2S	0.165(6)	0.139(5)	0.102(4)	0.034(4)	-0.022(4)	-0.048(4)
C3S	0.204(8)	0.073(3)	0.054(3)	0.021(3)	-0.010(4)	-0.026(4)
C4S	0.355(13)	0.058(3)	0.084(4)	0.003(3)	0.066(6)	-0.006(5)

The form of the anisotropic displacement parameter is:
$\exp[-2\pi^2(h^2a^{*2}U_{11} + k^2b^{*2}U_{22} + l^2c^{*2}U_{33} + 2klb^*c^*U_{23} + 2hla^*c^*U_{13} + 2hka^*b^*U_{12})]$.

[a]The following pairs of atoms were refined with common anisotropic displacement parameters: {F11B, F12B}, {F13B, F14B}, {F15B, F16B}, {F21B, F22B}, {F23B, F24B}, {F25B, F26B}.

Table K.8 Derived Atomic Coordinates and Displacement Parameters for Hydrogen Atoms

Atom	*x*	*y*	*z*	U_{eq}, Å^2
H6A	-0.1798	0.2647	0.2285	0.053
H6B	-0.2791	0.2137	0.2815	0.053
H6C	-0.1949	0.1302	0.2293	0.053
H7A	0.0835	0.4828	0.3524	0.054
H7B	-0.0796	0.4681	0.3715	0.054
H7C	-0.0520	0.4317	0.2885	0.054
H8A	0.3086	0.3407	0.4980	0.050
H8B	0.1629	0.3957	0.5205	0.050
H8C	0.2396	0.4429	0.4578	0.050
H9A	0.2898	0.1474	0.4980	0.052
H9B	0.2101	0.0312	0.4522	0.052
H9C	0.1350	0.1004	0.5153	0.052
H10A	-0.0920	-0.0159	0.2851	0.053
H10B	-0.1106	-0.0199	0.3695	0.053
H10C	0.0449	-0.0457	0.3441	0.053
H12	0.2885	0.3847	0.1484	0.048
H13	0.5015	0.3987	0.0949	0.061
H14	0.6326	0.2379	0.0697	0.059
H15	0.5560	0.0635	0.1005	0.051
H16	0.3440	0.0493	0.1558	0.042
H22	-0.0970	0.1892	0.0672	0.045
H23	-0.2484	0.0410	-0.0077	0.055
H24	-0.2290	-0.1446	0.0177	0.061
H25	-0.0509	-0.1853	0.1155	0.064
H26	0.0972	-0.0375	0.1932	0.050
H32A	0.5751	0.4744	0.2836	0.068
H32B	0.6058	0.4896	0.3724	0.068
H32C	0.4857	0.5631	0.3295	0.068
H34A	0.5894	-0.0219	0.3795	0.069
H34B	0.5591	-0.0627	0.2919	0.069
H34C	0.4687	-0.1239	0.3444	0.069
H2SA	0.9041	0.6146	0.0359	0.144
H2SB	0.7377	0.6178	0.0517	0.144
H2SC	0.7780	0.5248	-0.0117	0.144
H4SA	-0.0558	0.3295	0.7080	0.196
H4SB	0.0674	0.3536	0.7816	0.196
H4SC	0.0060	0.2259	0.7490	0.196

Appendix L – X-ray crystallographic structure report for complex Co-6c

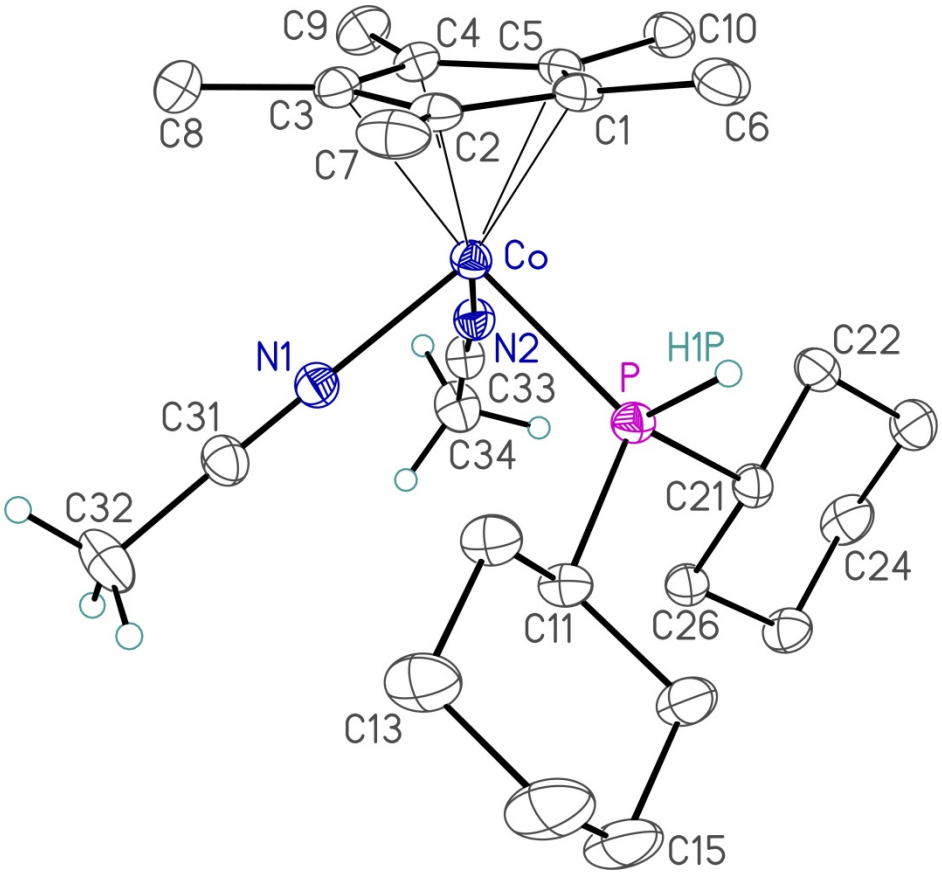

Figure L.1 Perspective view of the $[Co(\eta^5\text{–}Cp^*)(NCCH_3)_2(PCy_2H)]^{2+}$ complex ion showing the atom labelling scheme. Non-hydrogen atoms are represented by Gaussian ellipsoids at the 30% probability level. The hydrogen atom attched to the phosphorus atom and the hydrogens of the acetonitrile ligands are shown with arbitrarily small thermal parameters; all other hydrogens are not shown.

Table L.1 Crystallographic Experimental Details

A. Crystal Data	
formula	$C_{28}H_{47}CoF_{12}N_3PSb_2$
formula weight	987.08
crystal dimensions (mm)	0.35 × 0.34 × 0.23
crystal system	monoclinic
space group	$P2_1/n$ (an alternate setting of $P2_1/c$ [No. 14])
unit cell parameters[a]	
a (Å)	13.8708 (6)
b (Å)	16.4526 (7)
c (Å)	16.7924 (7)
β (deg)	94.7465 (5)
V (Å^3)	3819.1 (3)
Z	4
ρ_{calcd} (g cm^{-3})	1.717
μ (mm^{-1})	1.957
B. Data Collection and Refinement Conditions	
diffractometer	Bruker D8/APEX II CCD[b]
radiation (λ [Å])	graphite-monochromated Mo Kα (0.71073)
temperature (°C)	–100
scan type	ω scans (0.3°) (15 s exposures)
data collection 2θ limit (deg)	56.58
total data collected	34701 (-18 ≤ h ≤ 18, -21 ≤ k ≤ 21, -22 ≤ l ≤ 22)
independent reflections	9361 (R_{int} = 0.0215)
number of observed reflections (*NO*)	8032 [$F_o^2 \geq 2\sigma(F_o^2)$]
structure solution method	Patterson/structure expansion (*DIRDIF–2008*[c])
refinement method	full-matrix least-squares on F^2 (*SHELXL–2014*[d])
absorption correction method	Gaussian integration (face-indexed)
range of transmission factors	0.7732–0.6111
data/restraints/parameters	9361 / 0 / 472
goodness-of-fit (*S*)[e] [all data]	1.054
final R indices[f]	
R_1 [$F_o^2 \geq 2\sigma(F_o^2)$]	0.0260
wR_2 [all data]	0.0661
largest difference peak and hole	0.585 and –0.402 e Å^{-3}

[a]Obtained from least-squares refinement of 9863 reflections with 4.68° < 2θ < 53.40°.

[b]Programs for diffractometer operation, data collection, data reduction and absorption correction were those supplied by Bruker.

(continued)

Table L.1 Crystallographic Experimental Details (continued)

[c]Beurskens, P. T.; Beurskens, G.; de Gelder, R.; Smits, J. M. M.; Garcia-Granda, S.; Gould, R. O. (2008). The *DIRDIF-2008* program system. Crystallography Laboratory, Radboud University Nijmegen, The Netherlands.

[d]Sheldrick, G. M. *Acta Crystallogr.* **2015**, *C71*, 3–8.

[e]$S = [\Sigma w(F_o^2 - F_c^2)^2/(n - p)]^{1/2}$ (n = number of data; p = number of parameters varied; $w = [\sigma^2(F_o^2) + (0.0301P)^2 + 2.1384P]^{-1}$ where $P = [\mathrm{Max}(F_o^2, 0) + 2F_c^2]/3$).

[f]$R_1 = \Sigma||F_o| - |F_c||/\Sigma|F_o|$; $wR_2 = [\Sigma w(F_o^2 - F_c^2)^2/\Sigma w(F_o^4)]^{1/2}$.

Table L.2 Atomic Coordinates and Equivalent Isotropic Displacement Parameters

(a) atoms of the $[(\eta^5\text{–}C_5Me_5)Co(PHCy_2)(NCMe)_2]^{2+}$ ion

Atom	*x*	*y*	*z*	U_{eq}, Å^2
Co	0.01813(2)	0.23707(2)	0.16606(2)	0.02542(6)*
P	0.15579(4)	0.25356(3)	0.24831(3)	0.02802(11)*
N1	0.07954(13)	0.27874(11)	0.07576(10)	0.0312(4)*
N2	-0.03171(13)	0.34379(11)	0.18682(10)	0.0304(4)*
C1	-0.00532(15)	0.12121(12)	0.21399(13)	0.0304(4)*
C2	0.01137(15)	0.11617(12)	0.13130(13)	0.0317(4)*
C3	-0.06542(16)	0.15999(13)	0.08698(13)	0.0327(4)*
C4	-0.12498(15)	0.19440(13)	0.14184(13)	0.0309(4)*
C5	-0.08662(15)	0.17217(12)	0.22135(12)	0.0301(4)*
C6	0.04659(19)	0.07258(14)	0.27999(16)	0.0433(6)*
C7	0.08522(19)	0.06467(14)	0.09606(17)	0.0460(6)*
C8	-0.0807(2)	0.16609(16)	-0.00197(14)	0.0459(6)*
C9	-0.21485(17)	0.24246(16)	0.12223(16)	0.0444(6)*
C10	-0.13445(18)	0.19053(15)	0.29613(14)	0.0412(5)*
C11	0.26782(15)	0.27308(14)	0.19923(14)	0.0343(5)*
C12	0.28750(16)	0.19998(15)	0.14595(14)	0.0389(5)*
C13	0.37910(19)	0.21188(19)	0.10277(18)	0.0547(7)*
C14	0.4657(2)	0.2281(2)	0.1618(2)	0.0706(9)*
C15	0.44702(19)	0.3002(2)	0.2144(2)	0.0643(8)*
C16	0.35546(17)	0.28802(17)	0.25909(15)	0.0455(6)*
C21	0.15610(16)	0.32463(13)	0.33287(12)	0.0310(4)*
C22	0.07055(17)	0.30993(15)	0.38301(13)	0.0384(5)*
C23	0.0775(2)	0.36608(18)	0.45640(14)	0.0492(6)*
C24	0.08463(19)	0.45473(17)	0.43254(16)	0.0481(6)*
C25	0.16936(18)	0.46830(15)	0.38266(14)	0.0404(5)*
C26	0.16337(17)	0.41417(13)	0.30855(13)	0.0340(5)*
C31	0.11492(18)	0.30442(14)	0.02306(13)	0.0370(5)*
C32	0.1634(2)	0.33623(17)	-0.04414(16)	0.0556(7)*
C33	-0.05810(16)	0.40850(14)	0.19194(12)	0.0322(4)*
C34	-0.08810(19)	0.49256(13)	0.20054(15)	0.0425(5)*
H1P	0.1795(17)	0.1889(14)	0.2881(14)	0.038(6)

(b) atoms of the hexfluoroantimonate ions

Atom	*x*	*y*	*z*	U_{eq}, Å^2
Sb1	0.17088(2)	0.56070(2)	0.08072(2)	0.03768(5)*
F11	0.27857(15)	0.49371(14)	0.08279(13)	0.0881(6)*
F12	0.06271(15)	0.62744(13)	0.07980(14)	0.0864(6)*
F13	0.24885(15)	0.65207(11)	0.07098(10)	0.0738(6)*
F14	0.09277(15)	0.47027(11)	0.09022(12)	0.0770(6)*

Table L2. Atomic Coordinates and Displacement Parameters (continued)

Atom	*x*	*y*	*z*	U_{eq}, Å^2
F15	0.18779(16)	0.57059(10)	0.19181(9)	0.0669(5)*
F16	0.15742(15)	0.55117(12)	-0.03020(9)	0.0723(5)*
Sb2	0.20508(2)	0.07112(2)	0.85884(2)	0.03665(5)*
F21	0.33829(13)	0.07738(14)	0.86028(14)	0.0850(7)*
F22	0.07016(13)	0.06718(12)	0.85556(15)	0.0838(6)*
F23A[a]	0.1897(8)	0.1618(10)	0.7922(8)	0.102(4)*
F24A[a]	0.2188(12)	-0.0191(10)	0.9225(8)	0.108(5)*
F25A[a]	0.1939(9)	0.0063(9)	0.7716(6)	0.085(4)*
F26A[a]	0.2148(13)	0.1404(9)	0.9476(9)	0.096(4)*
F23B[a]	0.2052(10)	0.1466(10)	0.7784(7)	0.110(5)*
F24B[a]	0.2026(12)	-0.0070(10)	0.9382(7)	0.074(3)*
F25B[a]	0.2061(9)	-0.0128(9)	0.7813(7)	0.094(4)*
F26B[a]	0.2009(13)	0.1516(9)	0.9331(10)	0.093(4)*

(c) solvent acetonitrile atoms

Atom	*x*	*y*	*z*	U_{eq}, Å^2
N1S	-0.0279(4)	0.1190(2)	0.4852(2)	0.1090(14)*
C1S	0.0340(3)	0.0976(2)	0.5295(2)	0.0740(10)*
C2S	0.1113(3)	0.0711(2)	0.5860(2)	0.0788(11)*

Anisotropically-refined atoms are marked with an asterisk (*). The form of the anisotropic displacement parameter is: $\exp[-2\pi^2(h^2a^{*2}U_{11} + k^2b^{*2}U_{22} + l^2c^{*2}U_{33} + 2klb^*c^*U_{23} + 2hla^*c^*U_{13} + 2hka^*b^*U_{12})]$. [a]Refined with an occupancy factor of 0.5.

Table L.3 Selected Interatomic Distances (Å)

(a) within the $[(\eta^5\text{–}C_5Me_5)Co(PHCy_2)(NCMe)_2]^{2+}$ ion

Atom1	Atom2	Distance	Atom1	Atom2	Distance
Co	P	2.2784(6)	C3	C8	1.495(3)
Co	N1	1.9257(18)	C4	C5	1.443(3)
Co	N2	1.9293(18)	C4	C9	1.490(3)
Co	C1	2.105(2)	C5	C10	1.499(3)
Co	C2	2.073(2)	C11	C12	1.537(3)
Co	C3	2.112(2)	C11	C16	1.532(3)
Co	C4	2.113(2)	C12	C13	1.527(3)
Co	C5	2.082(2)	C13	C14	1.516(4)
P	C11	1.846(2)	C14	C15	1.515(4)
P	C21	1.839(2)	C15	C16	1.540(4)
P	H1P	1.28(2)	C21	C22	1.530(3)
N1	C31	1.129(3)	C21	C26	1.534(3)
N2	C33	1.131(3)	C22	C23	1.537(3)
C1	C2	1.429(3)	C23	C24	1.518(4)
C1	C5	1.419(3)	C24	C25	1.515(3)
C1	C6	1.502(3)	C25	C26	1.527(3)
C2	C3	1.441(3)	C31	C32	1.458(3)
C2	C7	1.489(3)	C33	C34	1.455(3)
C3	C4	1.406(3)			

(b) within the hexfluoroantimonate ions

Atom1	Atom2	Distance	Atom1	Atom2	Distance
Sb1	F11	1.8543(19)	Sb2	F23A	1.866(12)
Sb1	F12	1.8584(19)	Sb2	F24A	1.830(16)
Sb1	F13	1.8671(16)	Sb2	F25A	1.808(10)
Sb1	F14	1.8550(16)	Sb2	F26A	1.872(12)
Sb1	F15	1.8678(15)	Sb2	F23B	1.834(9)
Sb1	F16	1.8633(16)	Sb2	F24B	1.855(13)
Sb2	F21	1.8488(18)	Sb2	F25B	1.899(13)
Sb2	F22	1.8689(18)	Sb2	F26B	1.823(12)

(c) within the solvent acetonitrile molecules

Atom1	Atom2	Distance	Atom1	Atom2	Distance
N1S	C1S	1.143(5)	C1S	C2S	1.440(6)

Table L.4 Selected Interatomic Angles (deg)

(a) within the [(η^5–C_5Me_5)Co($PHCy_2$)($NCMe)_2$]$^{2+}$ ion

Atom1	Atom2	Atom3	Angle	Atom1	Atom2	Atom3	Angle
P	Co	N1	91.82(6)	C2	C1	C5	108.23(18)
P	Co	N2	94.41(5)	C2	C1	C6	125.5(2)
P	Co	C1	91.40(6)	C5	C1	C6	125.9(2)
P	Co	C2	107.52(6)	Co	C2	C1	71.21(11)
P	Co	C3	147.30(6)	Co	C2	C3	71.31(12)
P	Co	C4	152.02(6)	Co	C2	C7	129.88(15)
P	Co	C5	111.80(6)	C1	C2	C3	107.49(18)
N1	Co	N2	90.39(7)	C1	C2	C7	126.2(2)
N1	Co	C1	135.72(8)	C3	C2	C7	125.6(2)
N1	Co	C2	97.62(8)	Co	C3	C2	68.41(11)
N1	Co	C3	88.52(8)	Co	C3	C4	70.60(12)
N1	Co	C4	115.88(8)	Co	C3	C8	127.81(16)
N1	Co	C5	154.69(8)	C2	C3	C4	108.19(19)
N2	Co	C1	133.32(8)	C2	C3	C8	125.9(2)
N2	Co	C2	156.30(8)	C4	C3	C8	125.8(2)
N2	Co	C3	118.29(8)	Co	C4	C3	70.51(12)
N2	Co	C4	89.55(8)	Co	C4	C5	68.75(11)
N2	Co	C5	96.46(8)	Co	C4	C9	128.44(16)
C1	Co	C2	39.99(8)	C3	C4	C5	108.21(19)
C1	Co	C3	66.58(8)	C3	C4	C9	126.5(2)
C1	Co	C4	66.44(8)	C5	C4	C9	125.2(2)
C1	Co	C5	39.61(8)	Co	C5	C1	71.05(11)
C2	Co	C3	40.28(8)	Co	C5	C4	71.03(11)
C2	Co	C4	66.87(8)	Co	C5	C10	130.08(15)
C2	Co	C5	67.45(8)	C1	C5	C4	107.70(18)
C3	Co	C4	38.88(8)	C1	C5	C10	127.0(2)
C3	Co	C5	66.77(8)	C4	C5	C10	124.7(2)
C4	Co	C5	40.23(8)	P	C11	C12	108.69(15)
Co	P	C11	116.37(7)	P	C11	C16	112.74(16)
Co	P	C21	119.48(7)	C12	C11	C16	109.76(19)
Co	P	H1P	112.4(11)	C11	C12	C13	111.8(2)
C11	P	C21	106.61(10)	C12	C13	C14	111.0(2)
C11	P	H1P	100.8(11)	C13	C14	C15	110.8(3)
C21	P	H1P	98.1(10)	C14	C15	C16	111.7(2)
Co	N1	C31	178.84(19)	C11	C16	C15	110.1(2)
Co	N2	C33	173.28(18)	P	C21	C22	111.84(15)
Co	C1	C2	68.80(11)	P	C21	C26	113.63(14)
Co	C1	C5	69.34(11)	C22	C21	C26	111.68(18)
Co	C1	C6	133.23(15)	C21	C22	C23	110.25(19)
C22	C23	C24	111.5(2)	C21	C26	C25	110.08(18)
C23	C24	C25	111.0(2)	N1	C31	C32	178.2(3)
C24	C25	C26	111.9(2)	N2	C33	C34	177.5(3)

Table L.4 Selected Interatomic Angles (continued)

(b) within the hexfluoroantimonate ions

Atom1	Atom2	Atom3	Angle	Atom1	Atom2	Atom3	Angle
F11	Sb1	F12	179.36(10)	F21	Sb2	F25B	89.2(4)
F11	Sb1	F13	90.49(11)	F21	Sb2	F26B	92.2(6)
F11	Sb1	F14	89.83(10)	F22	Sb2	F23A	86.9(4)
F11	Sb1	F15	89.92(9)	F22	Sb2	F24A	92.6(5)
F11	Sb1	F16	89.00(10)	F22	Sb2	F25A	86.4(4)
F12	Sb1	F13	89.81(10)	F22	Sb2	F26A	92.9(6)
F12	Sb1	F14	89.87(10)	F22	Sb2	F23B	93.6(4)
F12	Sb1	F15	89.51(10)	F22	Sb2	F24B	85.4(5)
F12	Sb1	F16	91.57(10)	F22	Sb2	F25B	91.1(4)
F13	Sb1	F14	179.66(10)	F22	Sb2	F26B	87.6(6)
F13	Sb1	F15	89.52(7)	F23A	Sb2	F24A	178.8(7)
F13	Sb1	F16	89.48(8)	F23A	Sb2	F25A	89.3(7)
F14	Sb1	F15	90.57(8)	F23A	Sb2	F26A	89.3(8)
F14	Sb1	F16	90.43(8)	F24A	Sb2	F25A	89.6(6)
F15	Sb1	F16	178.53(9)	F24A	Sb2	F26A	91.8(7)
F21	Sb2	F22	178.47(10)	F25A	Sb2	F26A	178.5(7)
F21	Sb2	F23A	91.6(4)	F23B	Sb2	F24B	178.4(7)
F21	Sb2	F24A	89.0(5)	F23B	Sb2	F25B	89.3(7)
F21	Sb2	F25A	93.6(4)	F23B	Sb2	F26B	90.8(8)
F21	Sb2	F26A	87.1(6)	F24B	Sb2	F25B	89.4(6)
F21	Sb2	F23B	84.9(4)	F24B	Sb2	F26B	90.5(7)
F21	Sb2	F24B	96.1(5)	F25B	Sb2	F26B	178.6(7)

(c) within the solvent acetonitrile molecules

Atom1	Atom2	Atom3	Angle
N1S	C1S	C2S	179.3(5)

Table L.5 Torsional Angles (deg)

Atom1	Atom2	Atom3	Atom4	Angle	continued				
N1	Co	P	C11	-13.44(10)	N2	Co	C2	C3	30.2(3)
N1	Co	P	C21	116.85(9)	N2	Co	C2	C7	151.5(2)
N2	Co	P	C11	-103.97(10)	C1	Co	C2	C3	116.76(17)
N2	Co	P	C21	26.32(9)	C1	Co	C2	C7	-122.0(3)
C1	Co	P	C11	122.39(10)	C3	Co	C2	C1	-116.76(17)
C1	Co	P	C21	-107.32(10)	C3	Co	C2	C7	121.3(3)
C2	Co	P	C11	85.14(10)	C4	Co	C2	C1	-80.39(13)
C2	Co	P	C21	-144.57(10)	C4	Co	C2	C3	36.37(12)
C3	Co	P	C11	76.66(14)	C4	Co	C2	C7	157.6(3)
C3	Co	P	C21	-153.05(13)	C5	Co	C2	C1	-36.57(12)
C4	Co	P	C11	158.65(15)	C5	Co	C2	C3	80.18(13)
C4	Co	P	C21	-71.06(15)	C5	Co	C2	C7	-158.5(3)
C5	Co	P	C11	157.27(10)	P	Co	C3	C2	12.57(18)
C5	Co	P	C21	-72.44(10)	P	Co	C3	C4	132.26(12)
P	Co	C1	C2	-116.08(12)	P	Co	C3	C8	-106.9(2)
P	Co	C1	C5	123.60(11)	N1	Co	C3	C2	103.63(13)
P	Co	C1	C6	3.2(2)	N1	Co	C3	C4	-136.68(13)
N1	Co	C1	C2	-22.04(17)	N1	Co	C3	C8	-15.8(2)
N1	Co	C1	C5	-142.36(13)	N2	Co	C3	C2	-166.73(11)
N1	Co	C1	C6	97.3(2)	N2	Co	C3	C4	-47.04(15)
N2	Co	C1	C2	146.52(12)	N2	Co	C3	C8	73.8(2)
N2	Co	C1	C5	26.20(17)	C1	Co	C3	C2	-38.71(12)
N2	Co	C1	C6	-94.2(2)	C1	Co	C3	C4	80.98(13)
C2	Co	C1	C5	-120.32(17)	C1	Co	C3	C8	-158.2(2)
C2	Co	C1	C6	119.3(3)	C2	Co	C3	C4	119.69(18)
C3	Co	C1	C2	38.98(12)	C2	Co	C3	C8	-119.5(3)
C3	Co	C1	C5	-81.34(13)	C4	Co	C3	C2	-119.69(18)
C3	Co	C1	C6	158.3(3)	C4	Co	C3	C8	120.8(3)
C4	Co	C1	C2	81.54(13)	C5	Co	C3	C2	-82.01(13)
C4	Co	C1	C5	-38.78(12)	C5	Co	C3	C4	37.68(13)
C4	Co	C1	C6	-159.2(3)	C5	Co	C3	C8	158.5(2)
C5	Co	C1	C2	120.32(17)	P	Co	C4	C3	-121.54(14)
C5	Co	C1	C6	-120.4(3)	P	Co	C4	C5	-2.0(2)
P	Co	C2	C1	70.32(12)	P	Co	C4	C9	116.8(2)
P	Co	C2	C3	-172.92(10)	N1	Co	C4	C3	49.67(15)
P	Co	C2	C7	-51.7(2)	N1	Co	C4	C5	169.22(12)
N1	Co	C2	C1	164.67(12)	N1	Co	C4	C9	-72.0(2)
N1	Co	C2	C3	-78.57(13)	N2	Co	C4	C3	139.88(13)
N1	Co	C2	C7	42.7(2)	N2	Co	C4	C5	-100.56(12)
N2	Co	C2	C1	-86.6(2)	N2	Co	C4	C9	18.2(2)

Table L.5 Torsional Angles (continued)

Atom1	Atom2	Atom3	Atom4	Angle	continued				
C1	Co	C4	C3	-81.37(14)	C5	C1	C2	C3	-4.2(2)
C1	Co	C4	C5	38.19(12)	C5	C1	C2	C7	-175.6(2)
C1	Co	C4	C9	157.0(2)	C6	C1	C2	Co	-128.7(2)
C2	Co	C4	C3	-37.64(13)	C6	C1	C2	C3	168.8(2)
C2	Co	C4	C5	81.92(13)	C6	C1	C2	C7	-2.5(3)
C2	Co	C4	C9	-159.3(2)	Co	C1	C5	C4	61.94(14)
C3	Co	C4	C5	119.56(18)	Co	C1	C5	C10	-126.4(2)
C3	Co	C4	C9	-121.7(3)	C2	C1	C5	Co	-57.92(14)
C5	Co	C4	C3	-119.56(18)	C2	C1	C5	C4	4.0(2)
C5	Co	C4	C9	118.8(3)	C2	C1	C5	C10	175.7(2)
P	Co	C5	C1	-63.75(12)	C6	C1	C5	Co	129.1(2)
P	Co	C5	C4	179.00(10)	C6	C1	C5	C4	-169.0(2)
P	Co	C5	C10	59.2(2)	C6	C1	C5	C10	2.7(3)
N1	Co	C5	C1	94.1(2)	Co	C2	C3	C4	-59.60(15)
N1	Co	C5	C4	-23.2(2)	Co	C2	C3	C8	121.8(2)
N1	Co	C5	C10	-143.0(2)	C1	C2	C3	Co	62.42(14)
N2	Co	C5	C1	-161.14(12)	C1	C2	C3	C4	2.8(2)
N2	Co	C5	C4	81.61(13)	C1	C2	C3	C8	-175.8(2)
N2	Co	C5	C10	-38.2(2)	C7	C2	C3	Co	-126.2(2)
C1	Co	C5	C4	-117.25(17)	C7	C2	C3	C4	174.2(2)
C1	Co	C5	C10	122.9(3)	C7	C2	C3	C8	-4.4(3)
C2	Co	C5	C1	36.91(12)	Co	C3	C4	C5	-58.59(14)
C2	Co	C5	C4	-80.34(13)	Co	C3	C4	C9	124.0(2)
C2	Co	C5	C10	159.8(2)	C2	C3	C4	Co	58.24(14)
C3	Co	C5	C1	80.80(13)	C2	C3	C4	C5	-0.3(2)
C3	Co	C5	C4	-36.45(12)	C2	C3	C4	C9	-177.8(2)
C3	Co	C5	C10	-156.3(2)	C8	C3	C4	Co	-123.2(2)
C4	Co	C5	C1	117.25(17)	C8	C3	C4	C5	178.2(2)
C4	Co	C5	C10	-119.8(3)	C8	C3	C4	C9	0.8(4)
Co	P	C11	C12	-61.26(17)	Co	C4	C5	C1	-61.96(14)
Co	P	C11	C16	176.83(14)	Co	C4	C5	C10	126.2(2)
C21	P	C11	C12	162.61(16)	C3	C4	C5	Co	59.69(15)
C21	P	C11	C16	40.7(2)	C3	C4	C5	C1	-2.3(2)
Co	P	C21	C22	50.17(17)	C3	C4	C5	C10	-174.2(2)
Co	P	C21	C26	-77.40(17)	C9	C4	C5	Co	-122.8(2)
C11	P	C21	C22	-175.32(16)	C9	C4	C5	C1	175.2(2)
C11	P	C21	C26	57.11(18)	C9	C4	C5	C10	3.3(3)
Co	C1	C2	C3	-62.48(14)	P	C11	C12	C13	179.66(19)
Co	C1	C2	C7	126.2(2)	C16	C11	C12	C13	-56.6(3)
C5	C1	C2	Co	58.25(14)	P	C11	C16	C15	177.6(2)

Table L.5 Torsional Angles (continued)

Atom1	Atom2	Atom3	Atom4	Angle	continued				
C12	C11	C16	C15	56.3(3)	P	C21	C26	C25	-176.56(15)
C11	C12	C13	C14	56.3(3)	C22	C21	C26	C25	55.8(2)
C12	C13	C14	C15	-55.6(4)	C21	C22	C23	C24	55.5(3)
C13	C14	C15	C16	56.7(4)	C22	C23	C24	C25	-56.0(3)
C14	C15	C16	C11	-57.3(4)	C23	C24	C25	C26	56.5(3)
P	C21	C22	C23	175.79(17)	C24	C25	C26	C21	-56.0(3)
C26	C21	C22	C23	-55.6(3)					

Table L.6 Least-Squares Planes

Plane	Coefficients[a]			Defining Atoms with Deviations (Å)[b]			
1	7.933(12)	13.458(10)					
	0.238(17)	1.664(4)					
				C1	-0.0243(12)	C2	0.0206(13)
				C3	-0.0093(13)	C4	-0.0055(13)
				C5	0.0185(13)		
				Co	1.7096(9)	C6	-0.251(4)
				C7	-0.095(4)	C8	-0.069(4)
				C9	-0.076(4)	C10	-0.096(4)

Distance: $Co–C_{cent}$ = 1.710 Å (C_{cent} = C1–C2–C3–C4–C5 centroid)

Angles: C_{cent}–Co–P = 126.6º, C_{cent}–Co–N1 = 122.0º, C_{cent}–Co–N2 = 122.2º

[a]Coefficients are for the form $ax+by+cz = d$ where x, y and z are crystallographic coordinates.

[b]Underlined atoms were not included in the definition of the plane.

Table L.7 Anisotropic Displacement Parameters (U_{ij}, Å^2)

Atom	U_{11}	U_{22}	U_{33}	U_{23}	U_{13}	U_{12}
Co	0.02681(14)	0.02368(13)	0.02613(13)	-0.00075(10)	0.00430(10)	-0.00118(10)
P	0.0286(3)	0.0256(2)	0.0298(3)	0.0001(2)	0.0025(2)	-0.0023(2)
N1	0.0354(10)	0.0288(9)	0.0296(9)	-0.0012(7)	0.0035(7)	-0.0012(7)
N2	0.0310(9)	0.0305(9)	0.0296(9)	-0.0004(7)	0.0027(7)	0.0002(7)
C1	0.0296(10)	0.0234(10)	0.0384(11)	0.0015(8)	0.0032(8)	-0.0049(8)
C2	0.0299(11)	0.0248(10)	0.0411(11)	-0.0050(8)	0.0075(9)	-0.0065(8)
C3	0.0338(11)	0.0304(11)	0.0340(11)	-0.0043(8)	0.0033(8)	-0.0068(9)
C4	0.0256(10)	0.0316(11)	0.0351(11)	-0.0027(8)	-0.0001(8)	-0.0033(8)
C5	0.0291(10)	0.0285(10)	0.0335(10)	-0.0012(8)	0.0067(8)	-0.0060(8)
C6	0.0440(14)	0.0323(12)	0.0530(15)	0.0118(10)	0.0004(11)	-0.0066(10)
C7	0.0406(13)	0.0326(12)	0.0674(17)	-0.0129(11)	0.0204(12)	-0.0052(10)
C8	0.0537(15)	0.0498(14)	0.0337(12)	-0.0076(10)	0.0012(10)	-0.0111(12)
C9	0.0319(12)	0.0478(14)	0.0523(14)	-0.0042(11)	-0.0039(10)	0.0023(10)
C10	0.0407(13)	0.0446(13)	0.0399(12)	-0.0035(10)	0.0134(10)	-0.0067(10)
C11	0.0287(11)	0.0331(11)	0.0415(12)	-0.0036(9)	0.0061(9)	-0.0035(9)
C12	0.0336(12)	0.0366(12)	0.0473(13)	-0.0071(10)	0.0084(10)	-0.0005(9)
C13	0.0394(14)	0.0596(17)	0.0678(18)	-0.0173(14)	0.0201(13)	-0.0025(12)
C14	0.0317(14)	0.090(2)	0.092(2)	-0.0241(19)	0.0171(15)	-0.0030(15)
C15	0.0315(14)	0.085(2)	0.077(2)	-0.0224(17)	0.0086(13)	-0.0164(14)
C16	0.0341(12)	0.0525(15)	0.0495(14)	-0.0091(12)	0.0016(10)	-0.0082(11)
C21	0.0360(11)	0.0308(11)	0.0262(10)	0.0000(8)	0.0022(8)	-0.0026(8)
C22	0.0410(13)	0.0407(13)	0.0343(11)	0.0020(9)	0.0081(9)	-0.0074(10)
C23	0.0457(14)	0.0711(18)	0.0323(12)	-0.0044(12)	0.0119(10)	-0.0075(13)
C24	0.0440(14)	0.0555(15)	0.0452(14)	-0.0204(12)	0.0067(11)	-0.0002(12)
C25	0.0418(13)	0.0373(12)	0.0421(12)	-0.0091(10)	0.0038(10)	-0.0040(10)
C26	0.0378(12)	0.0308(11)	0.0332(11)	-0.0005(9)	0.0022(9)	-0.0047(9)
C31	0.0466(13)	0.0313(11)	0.0338(11)	0.0001(9)	0.0075(10)	-0.0008(10)
C32	0.074(2)	0.0498(15)	0.0464(15)	0.0118(12)	0.0260(14)	-0.0011(14)
C33	0.0349(11)	0.0338(11)	0.0280(10)	0.0011(8)	0.0026(8)	0.0026(9)
C34	0.0560(15)	0.0293(11)	0.0430(13)	0.0000(10)	0.0086(11)	0.0090(10)
Sb1	0.04369(10)	0.03699(9)	0.03219(8)	0.00060(6)	0.00214(6)	-0.00823(6)
F11	0.0719(13)	0.0999(16)	0.0915(15)	-0.0096(12)	0.0005(11)	0.0327(12)
F12	0.0727(13)	0.0786(14)	0.1053(16)	-0.0089(12)	-0.0078(11)	0.0256(11)
F13	0.0981(14)	0.0724(12)	0.0504(9)	0.0041(8)	0.0029(9)	-0.0497(11)
F14	0.0966(15)	0.0584(11)	0.0803(13)	-0.0164(9)	0.0325(11)	-0.0417(10)
F15	0.1115(16)	0.0549(10)	0.0344(8)	0.0014(7)	0.0078(9)	-0.0165(9)
F16	0.0897(14)	0.0900(14)	0.0356(8)	-0.0058(8)	-0.0038(8)	-0.0277(11)
Sb2	0.03727(9)	0.03936(9)	0.03374(8)	0.00192(6)	0.00545(6)	-0.00657(6)
F21	0.0347(9)	0.1101(17)	0.1090(17)	-0.0354(13)	-0.0013(10)	-0.0071(9)
F22	0.0435(10)	0.0769(13)	0.1334(19)	0.0117(12)	0.0218(11)	-0.0117(9)

Table L.7 Anisotropic Displacement Parameters (continued)

Atom	U_{11}	U_{22}	U_{33}	U_{23}	U_{13}	U_{12}
F23A	0.051(3)	0.087(5)	0.163(10)	0.071(6)	-0.026(4)	-0.022(3)
F24A	0.147(11)	0.056(4)	0.106(8)	0.029(5)	-0.064(7)	-0.033(7)
F25A	0.063(3)	0.140(10)	0.050(3)	-0.048(4)	-0.006(3)	-0.017(4)
F26A	0.126(8)	0.105(9)	0.063(3)	-0.046(5)	0.037(4)	-0.063(7)
F23B	0.126(9)	0.132(10)	0.068(3)	0.068(5)	-0.010(4)	-0.063(7)
F24B	0.112(5)	0.063(5)	0.047(3)	0.027(3)	0.006(3)	-0.002(4)
F25B	0.099(7)	0.086(5)	0.106(7)	-0.054(4)	0.060(5)	-0.055(5)
F26B	0.114(6)	0.046(3)	0.126(10)	-0.033(5)	0.060(7)	-0.009(3)
N1S	0.176(4)	0.087(3)	0.061(2)	0.0039(18)	-0.007(2)	0.015(3)
C1S	0.114(3)	0.064(2)	0.0458(17)	-0.0020(15)	0.0184(19)	-0.007(2)
C2S	0.074(2)	0.098(3)	0.066(2)	-0.0068(19)	0.0169(18)	-0.013(2)

The form of the anisotropic displacement parameter is:
exp[-2π2(h2a*2U11 + k2b*2U22 + l2c*2U33 + 2klb*c*U23 + 2hla*c*U13 + 2hka*b*U12)]

Table L.8 Derived Atomic Coordinates and Displacement Parameters for Hydrogen Atoms

Atom	*x*	*y*	*z*	U_{eq}, Å^2
H6A	0.0447	0.1018	0.3307	0.052
H6B	0.1140	0.0645	0.2684	0.052
H6C	0.0149	0.0196	0.2840	0.052
H7A	0.0570	0.0116	0.0814	0.055
H7B	0.1409	0.0572	0.1353	0.055
H7C	0.1064	0.0913	0.0483	0.055
H8A	-0.0193	0.1563	-0.0253	0.055
H8B	-0.1045	0.2205	-0.0169	0.055
H8C	-0.1282	0.1254	-0.0220	0.055
H9A	-0.2089	0.2732	0.0729	0.053
H9B	-0.2244	0.2803	0.1660	0.053
H9C	-0.2704	0.2056	0.1149	0.053
H10A	-0.1908	0.1551	0.2991	0.049
H10B	-0.1553	0.2474	0.2954	0.049
H10C	-0.0885	0.1811	0.3427	0.049
H11	0.2577	0.3223	0.1646	0.041
H12A	0.2943	0.1503	0.1793	0.047
H12B	0.2317	0.1921	0.1060	0.047
H13A	0.3912	0.1626	0.0713	0.066
H13B	0.3700	0.2582	0.0653	0.066
H14A	0.4792	0.1794	0.1954	0.085
H14B	0.5232	0.2390	0.1323	0.085
H15A	0.4395	0.3498	0.1811	0.077
H15B	0.5034	0.3082	0.2538	0.077
H16A	0.3646	0.2410	0.2958	0.055
H16B	0.3441	0.3369	0.2914	0.055
H21	0.2158	0.3124	0.3684	0.037
H22A	0.0705	0.2525	0.4006	0.046
H22B	0.0092	0.3205	0.3502	0.046
H23A	0.0197	0.3583	0.4864	0.059
H23B	0.1352	0.3512	0.4921	0.059
H24A	0.0240	0.4713	0.4016	0.058
H24B	0.0927	0.4889	0.4812	0.058
H25A	0.2304	0.4568	0.4156	0.048
H25B	0.1706	0.5260	0.3660	0.048
H26A	0.2216	0.4223	0.2792	0.041
H26B	0.1059	0.4293	0.2727	0.041
H32A	0.2332	0.3271	-0.0348	0.067
H32B	0.1507	0.3946	-0.0496	0.067
H32C	0.1388	0.3084	-0.0933	0.067

Table L.8 Derived Parameters for Hydrogen Atoms (continued)

Atom	*x*	*y*	*z*	U_{eq}, Å^2
H34A	-0.0512	0.5275	0.1669	0.051
H34B	-0.0760	0.5092	0.2565	0.051
H34C	-0.1573	0.4976	0.1841	0.051
H2SA	0.1736	0.0860	0.5665	0.095
H2SB	0.1081	0.0120	0.5922	0.095
H2SC	0.1049	0.0973	0.6377	0.095